Reaction mechanism of the enzymatic chlorination of amino compounds catalyzed by the myeloperoxidase-hydrogen peroxide-chloride ion system. A kinetic and computational approach.

Autor: Daniel Rodríguez Ramos

Tesis doctoral UDC / 2019

Director: Juan Arturo Santaballa López

Directora: María Victoria García Dopico

Tutor: Juan Arturo Santaballa López

Programa de doctorado en Química Ambiental y Fundamental

UNIVERSIDADE DA CORUÑA

If it's not true, it's well invented.

Giordano Bruno,
in De gli Eroici Furore

ACKNOWLEDGEMENTS

I am indebted to:

Protein Biochemistry research group (University of Natural Resources and Life Sciences, Vienna)
The former Laboratorio de Química Computacional (Universitat Jaume I, Castelló)
Centro de Supercomputación de Galicia (Santiago de Compostela)
Synchrotron Radiation Source (Daresbury Laboratory, Daresbury, Cheshire)

for all the assistance provided, and to:

Xunta de Galicia
Universidad de A Coruña
Fundación Segundo Gil Dávila
Dirección General de Enseñanza Superior e Investigación Científica
Diputación Provincial de A Coruña

for financial support.

A todos los que me habéis ayudado, apoyado, animado y acompañado
a lo largo de este camino que parecía interminable,
gracias.

Reaction mechanism of the enzymatic chlorination of amino compounds catalyzed by the myeloperoxidase-hydrogen peroxide-chloride ion system.
A kinetic and computational approach.

Myeloperoxidase is a key enzyme of the immune system, quite abundant in neutrophils. It is actively involved in the protection against exogenous microorganisms and represents a significant factor in the development of numerous diseases.

Unlike other peroxidases, unable to oxidize chloride anion, the main reaction catalyzed by this enzyme is the chlorination of nitrogen compounds. There are numerous studies on myeloperoxidase, particularly from a clinical or biochemical point of view, but the precise reaction mechanism of the chlorination process catalyzed by the enzyme was still unknown.

A detailed knowledge of the structure and reactivity of myeloperoxidase, the substrates, and obtained chlorinated products, as well as the interaction between them, is essential for a comprehensive understanding of its enzymatic activity and the development of treatments and drugs.

The main aim of this dissertation is to unravel the mechanism of the myeloperoxidase-mediated chlorination, and to explain the source of its high oxidation potential, and other unique features, relative to other peroxidases. Furthermore, subsequent decomposition of some chlorinated nitrogen compounds and the particular behaviour of the amino acid cysteine and the antioxidant glutathione when reacting with these chloramines are analyzed.

Mecanismo de cloración encimática de compostos nitroxenados catalizada polo sistema mieloperoxidasa-peróxido de hidróxeno-anión cloruro.
Aproximación cinética e computacional.

A mieloperoxidasa é un encima clave do sistema inmunolóxico, moi abundante en neutrófilos, que participa activamente na protección contra microorganismos esóxenos e representa un factor relevante no desenvolvemento de numerosas enfermidades.

Ó contrario doutras peroxidasas, incapaces de oxidar o anión cloruro, a principal reacción catalizada por este encima é a cloración de compostos nitroxenados. Existen numerosos estudos centrados na mieloperoxidasa, en particular dende un punto de vista clínico ou bioquímico, mais descoñecíase o mecanismo de reacción preciso polo que este encima cataliza o proceso de cloración.

O coñecemento detallado da estrutura e reactividade da mieloperoxidasa, os seus substratos e os produtos clorados obtidos así como a interacción entre eles, resulta imprescindible tanto para a comprensión global da súa actividade encimática como para o desenvolvemento de tratamentos e fármacos.

Nesta tese doutoral preténdese determinar o mecanismo encimático de cloración catalizado pola mieloperoxidasa, así como examinar a orixe do seu elevado potencial de oxidación respecto doutras peroxidasas e outras características distintivas. Ademais analízase a posterior descomposición dalgúns compostos nitroxenados clorados e o particular comportamento do aminoácido cisteína e do antioxidante glutatión na súa reacción con estas cloraminas.

Mecanismo de cloración enzimática de compuestos nitrogenados catalizada por el sistema mieloperoxidasa-peróxido de hidrógeno-anión cloruro.
Aproximación cinética y computacional.

La mieloperoxidasa es un enzima clave del sistema inmunológico, muy abundante en neutrófilos, que participa activamente en la protección contra microorganismos exógenos y representa un factor relevante en el desarrollo de numerosas enfermedades.

Al contrario de otras peroxidasas, incapaces de oxidar el anión cloruro, la principal reacción catalizada por este enzima es la cloración de compuestos nitrogenados. Existen numerosos estudios centrados en la mieloperoxidasa, en particular desde un punto de vista clínico o bioquímico, pero se desconocía el mecanismo de reacción preciso por el que este enzima cataliza el proceso de cloración.

El conocimiento detallado de la estructura y reactividad de la mieloperoxidasa, sus sustratos y los productos clorados obtenidos así como la interacción entre ellos, resulta imprescindible tanto para la comprensión global de su actividad enzimática como para el desarrollo de tratamientos y fármacos.

En esta tesis doctoral se pretende determinar el mecanismo enzimático de cloración catalizado por la mieloperoxidasa, así como examinar el origen de su elevado potencial de oxidación respecto a otras peroxidasas y otras características distintivas. Además se analiza la posterior descomposición de algunos compuestos nitrogenados clorados y el particular comportamiento del aminoácido cisteína y del antioxidante glutatión en su reacción con estas cloraminas.

INDEX

INTRODUCTION AND OBJECTIVES

Anna, you mustn't speak of oxidized muriatic acid anymore, from now on you must say chlorine.

Jöns Jacob Berzelius, in 1820, to his cook,
who had complained of the smell of the flask she was cleaning

Halogenation is a fundamental process in chemical and biological reactivity. The elemental form of stable halogens, *i.e.* fluorine, chlorine, bromine, and iodine, is a diatomic molecule. However, due to their high reactivity, only halogenated compounds or ions are found in the environment, where their occurrence is ubiquitous. Chlorine is the most frequent halogen, present in seawater at a high concentration, but also in several minerals and multiple organic compounds.

Thousands of natural halogenated organic compounds are known, while many others of anthropogenic origin are constantly developed. They are extensively used in the production of multiple manufactured goods (plastic polymers, solvents, textiles, dyes, agrochemicals, pharmaceuticals, fire retardants, nutrition supplements, etc), as well as in other industrial processes and applications. Among them, chlorination is the widest disinfection method, and it is the most used technique of water treatment worldwide, despite the well-known formation of harmful by-products.[1-3]

Furthermore, chlorine presents several biological functions of essential importance in living organisms. Chloride is the major anion found in the extracellular fluid and in blood plasma. Thus, it is essential in the balance of body fluids, in brain function, and is an important constituent of gastric acid. Chlorination plays a critical role in innate immune system, participating in leukocyte protection against infection and hence damaging the host tissues in inflammatory diseases.[4, 5]

Peroxidases are a large family of enzymes that catalyze the oxidation of a substrate while reducing a peroxide (typically hydrogen peroxide, H_2O_2). Myeloperoxidase (MPO, EC number 1.11.1.7), an enzyme that belongs to the peroxidase-cyclooxygenase superfamily,[6] is the most abundant protein in neutrophils, as it represents 5 % of their dry weight.[7] MPO plays a very important role in immune system in mammals, catalyzing the formation of several reactive oxygen species (ROS) during respiratory burst.[8] MPO compound I presents a very high oxidation potential;[9] as a result, the major enzyme reaction is the generation of the strong oxidizing and chlorinating agent hypochlorous acid (HClO) from H_2O_2 and chloride anion (Cl^-).[10] HClO is an extremely effective biocide and the most reactive two-electron oxidant produced in significant amounts in human body.[11]

Taurine is an aminosulfonic acid ubiquitous in mammalian tissues, and the most abundant free amino acid in the heart, retina, skeletal muscle, brain, and leukocytes.[12] Concentration of cytosolic taurine up to 50 mM has been reported for human leukocytes.[13] Thus, it is considered the main chlorination target of MPO-derived HClO, producing the more stable but less toxic taurine chloramine (*N*-Cl Tau). This chemical is capable of chlorinating and oxidizing other molecules and, therefore, retains relevant bacterial activity.[14, 15] Furthermore, *N*-Cl Tau has revealed as a powerful modulator of immunity,[13] and it also participates in inflammatory diseases associated with oxidative stress.[16] Many other chemicals, preferentially containing amino or thiol functional groups, may undergo chlorination during the oxidative burst of neutrophils.[17]

Organosulfur compounds react with HClO much faster than any other cellular constituent. Among them, cysteine, methionine, and glutathione (γ-L-glutamyl-L-cysteinyl-glycine) are of great biological importance. Thus, the two α-amino acids are the most reactive targets of HClO-mediated oxidation of proteins,[18] which may lead to irreversible degradation; whereas the tripeptide participates in regulation of cellular redox potential,[19] and also acts as antioxidant.[20]

Amines are converted to chloramines upon reaction with HClO, but at much slower rates than sulfur-containing species. They retain the chlorinating ability, being able to oxidize other molecules, in particular preceding organosulfur compounds.[21, 22] Thus, long-lived chloramines are reactive chlorine species that have potent antimicrobial activities, participate in HClO-mediated cellular damage, and contribute to the propagation of inflammatory diseases.[23, 24] However, many of them are unstable and may decompose readily.

The research proposal for the PhD study was focused on some particular aspects of the reactions considered in the short revision above. Detailed knowledge on the specific reactivity of some important biological processes was incomplete or needed further clarification. Consequently, the following studies were intended for the present doctoral thesis.

The starting point of this research was a 1994 paper entitled *Chlorination of taurine by myeloperoxidase. Kinetic evidence for an enzyme-bound intermediate*,[25] where the proposed reaction mechanism included an enzymatic intermediate acting as chlorinating agent. However, we found some inconsistencies between kinetic results and their mathematical

interpretation. ***Therefore, the main objective of this dissertation was to unravel the mechanism of the MPO-mediated chlorination reaction***.

Enzymes are selective and very efficient catalysts that work by binding substrates and stabilising transition states. Similarly, some intramolecular reactions display rates several orders of magnitude faster than corresponding intermolecular processes.[26] In both cases, the high acceleration arises, at least in part, from an noticeable entropy reduction,[27] and is related to the close proximity and correct orientation of the reacting groups.[28] Thus, intramolecular catalysis has been considered an adequate model of enzyme catalysis for a long time. Therefore, it also seems a suitable first approach to mechanistic studies of catalyzed reactions.

Chlorinated substrates undergo other reactions, which may be of great importance and their study is necessary to understand their participation in biological processes. Formation and decomposition of many chloramines have been thoroughly studied;[29, 30] this research group has already provided relevant contributions on this field.[31] Chlorination of these compounds is generally fast and they decompose at a much slower rate. However, some species like secondary *N*-halo ethanolamines are more unstable. Their ready decomposition in basic media involves an intramolecular elimination and an intramolecular fragmentation, leading to free chloride anion[32] and, therefore, functioning as efficient HClO scavengers. ***A comprehensive study of the fast decomposition of* N-*Cl ethanolamines was considered important enough to be chosen as another goal of this research***.

Other chloramines are more stable and do not scavenge HClO but, upon formation, they may undergo different subsequent reactions, as further chlorination of other substrates. Besides presenting faster kinetics with HClO, thiol chlorination is more thermodynamically favoured than on nitrogen atom. Thus, thiols can be easily halogenated by reaction with chloramines.

The α-amino acid cysteine contains a side chain with a thiol group, which is a major site of chlorination within proteins.[33] Previous studies have explored the reaction mechanism of cysteine chlorination by HClO and *N*-Cl Tau.[15, 18] Three different macroscopic pK_a values have been determined for this species and, while pK_{a1} = 2.00 is clearly assigned to carboxylic acid, the assignment of pK_{a2} (8.35, –SH) and pK_{a3} (10.39, $–NH_2^+$) was made on the basis of acidity theories, without any solid experimental confirmation.[34, 35] Besides, a value of 8.22 has been measured for thiol pK_a by isothermal titration calorimetry, also supporting that this group is more acidic.[36] However, obtained kinetic results suggested that the amino group deprotonates at pH around eight, being more acidic than the thiol group.[15, 18]

The correct assignment of cysteine pK_a values is a relevant issue to understand its reactivity. ***Thus, this compound has also been studied with the aim of establishing unequivocally its protonation state under biological conditions***.

This dissertation is organized as follows: the first part collects studies on the base-catalyzed decomposition of secondary *N*-halo ethanolamines and subsequent reactions, the second part is focused on cysteine ionization, and the last part compiles the research concerning heme peroxidases, primarily human MPO. Besides, the work has been divided into 14 chapters, each of them with the structure of a scientific paper. Then, an addendum summarizes other studies also carried out, research in progress, and some planned further work. Finally, general conclusions of the whole research close this PhD thesis.

Since these chapters were written with some independence there is no continuity in the manuscript, but still I hope that this extensive report provides a good and comprehensive insight on the research and subjects addressed in the current doctoral level research.

1. J. Hu, W. Chu, M. Sui, B. Xu, N. Gao, and S. Ding, *Comparison of drinking water treatment processes combinations for the minimization of subsequent disinfection by-products formation during chlorination and chloramination.* Chem. Eng. J., 2018 **335** 352-361.
2. C. Postigo and S. D. Richardson, *Transformation of pharmaceuticals during oxidation/disinfection processes in drinking water treatment.* J. Hazard. Mater., 2014 **279** 461-475.
3. S. D. Richardson and T. A. Ternes, *Water analysis: Emerging contaminants and current issues.* Anal. Chem., 2018 **90** (1) 398-428.
4. C. S. Foote, T. E. Goyne, and R. I. Lehrer, *Assessment of chlorination by human neutrophils.* Nature, 1983 **301** (5902) 715-716.
5. S. J. Klebanoff, *Myeloperoxidase-halide-hydrogen peroxide antibacterial system.* J. Bacteriol., 1968 **95** (6) 2131-2138.
6. M. Zamocky, C. Jakopitsch, P. G. Furtmüller, C. Dunand, and C. Obinger, *The peroxidase-cyclooxygenase superfamily: reconstructed evolution of critical enzymes of the innate immune system.* Proteins, 2008 **72** (2) 589-605.
7. M. J. Davies, *Myeloperoxidase-derived oxidation: mechanisms of biological damage and its prevention.* J. Clin. Biochem. Nutr., 2011 **48** (1) 8-19.
8. H. Parker and C. C. Winterbourn, *Reactive oxidants and myeloperoxidase and their involvement in neutrophil extracellular traps.* Front. Immunol., 2013 **3** 424.
9. J. Arnhold, P. G. Furtmüller, and C. Obinger, *Redox properties of myeloperoxidase.* Redox Rep., 2003 **8** (4) 179-186.
10. C. C. Winterbourn and A. J. Kettle, *Biomarkers of myeloperoxidase-derived hypochlorous acid.* Free Radic. Biol. Med., 2000 **29** (5) 403-409.
11. A. J. Kettle, A. M. Albrett, A. L. Chapman, N. Dickerhof, L. V. Forbes, I. Khalilova, and R. Turner, *Measuring chlorine bleach in biology and medicine.* Biochim. Biophys. Acta, 2014 **1840** (2) 781-793.
12. G. B. Schuller-Levis and E. Park, *Taurine: new implications for an old amino acid.* FEMS Microbiol. Lett., 2003 **226** (2) 195-202.
13. G. B. Schuller-Levis and E. Park, *Taurine and its chloramine: modulators of immunity.* Neurochem. Res., 2004 **29** (1) 117-126.
14. M. Nagl, M. W. Hess, K. Pfaller, P. Hengster, and W. Gottardi, *Bactericidal activity of micromolar N-chlorotaurine: evidence for its antimicrobial function in the human defense system.* Antimicrob. Agents Chemother., 2000 **44** (9) 2507-2513.
15. M. I. Fernández, M. V. García, X. L. Armesto, M. Canle L., and J. A. Santaballa, *Unravelling the mechanism of intracellular oxidation of thiols by (N-Cl)-Taurine.* J. Phys. Org. Chem., 2013 **26** (12) 1098-1104.
16. J. Marcinkiewicz and E. Kontny, *Taurine and inflammatory diseases.* Amino Acids, 2014 **46** (1) 7-20.
17. M. J. Gray, W. Y. Wholey, and U. Jakob, *Bacterial responses to reactive chlorine species.* Annu. Rev. Microbiol., 2013 **67** (1) 141-160.
18. X. L. Armesto, M. Canle L., M. I. Fernández, M. V. García, and J. A. Santaballa, *First steps in the oxidation of sulfur-containing amino acids by hypohalogenation: very fast generation of intermediate sulfenyl halides and halosulfonium cations.* Tetrahedron, 2000 **56** (8) 1103-1109.
19. E. V. Kalinina, N. N. Chernov, and M. D. Novichkova, *Role of glutathione, glutathione transferase, and glutaredoxin in regulation of redox-dependent processes.* Biochemistry (Moscow), 2014 **79** (13) 1562-1583.

20. E. E. Battin and J. L. Brumaghim, *Antioxidant activity of sulfur and selenium: a review of reactive oxygen species scavenging, glutathione peroxidase, and metal-binding antioxidant mechanisms.* Cell Biochem. Biophys., 2009 **55** (1) 1-23.

21. D. I. Pattison, C. L. Hawkins, and M. J. Davies, *Hypochlorous acid-mediated protein oxidation: how important are chloramine transfer reactions and protein tertiary structure?* Biochemistry, 2007 **46** (34) 9853-9864.

22. D. I. Pattison, M. J. Davies, and C. L. Hawkins, *Reactions and reactivity of myeloperoxidase-derived oxidants: differential biological effects of hypochlorous and hypothiocyanous acids.* Free Radic. Res., 2012 **46** (8) 975-995.

23. E. Malle, P. G. Furtmüller, W. Sattler, and C. Obinger, *Myeloperoxidase: a target for new drug development?* Br. J. Pharmacol., 2007 **152** (6) 838-854.

24. W. Gottardi, D. Debabov, and M. Nagl, *N-Chloramines, a promising class of well-tolerated topical anti-infectives.* Antimicrob. Agents Chemother., 2013 **57** (3) 1107-1114.

25. L. A. Marquez and H. B. Dunford, *Chlorination of taurine by myeloperoxidase. Kinetic evidence for an enzyme-bound intermediate.* J. Biol. Chem., 1994 **269** (11) 7950-7956.

26. A. J. Kirby, *Effective molarities for intramolecular reactions.* Adv. Phys. Org. Chem., 1980 **17** 183-278.

27. M. I. Page and W. P. Jencks, *Entropic contributions to rate accelerations in enzymic and intramolecular reactions and the chelate effect.* Proc. Natl. Acad. Sci. U.S.A., 1971 **68** (8) 1678-1683.

28. F. M. Menger, *On the source of intramolecular and enzymatic reactivity.* Acc. Chem. Res., 1985 **18** (5) 128-134.

29. P. Kovacic, M. K. Lowery, and K. W. Field, *Chemistry of N-bromamines and N-chloramines.* Chem. Rev., 1970 **70** (6) 639-665.

30. E. L. Thomas, M. B. Grisham, and M. M. Jefferson, *[40] Preparation and characterization of chloramines.* Methods Enzymol., 1986 **132** (Immunochemical techniques part J) 569-585.

31. X. L. Armesto, M. Canle L., M. V. García, and J. A. Santaballa, *Aqueous chemistry of N-halo-compounds.* Chem. Soc. Rev., 1998 **27** (6) 453-460.

32. X. L. Armesto, M. Canle L., P. Carretero, M. V. García, and J. A. Santaballa, *Evidence for an intramolecular elimination mechanism in the aqueous decomposition of (N-Cl)-alcoholamines.* Tetrahedron, 1997 **53** (7) 2565-2572.

33. M. J. Davies, *The oxidative environment and protein damage.* Biochim. Biophys. Acta, 2005 **1703** (2) 93-109.

34. A. E. Martell and R. M. Smith, *Critical stability constants. Amino acids*. Vol. 1. 1989, New York: Plenum Press.

35. M. Friedman, *The chemistry and biochemistry of the sulfhydryl groups in amino acids, peptides and proteins*. 1973, Elmsford, NY: Pergamon Press.

36. S. G. Tajc, B. S. Tolbert, R. Basavappa, and B. L. Miller, *Direct determination of thiol pK_a by isothermal titration microcalorimetry.* J. Am. Chem. Soc., 2004 **126** (34) 10508-10509.

PART I

Amines

If you perceive that there are four possible ways in which a procedure can go wrong and circumvent these, then a fifth way will develop.

Murphy's Twelfth Law

CHAPTER 1

Understanding the mechanism of base-assisted decomposition of *N*-halo,*N*-alkylalcoholamines

Nature will tell you a direct lie if she can.

Charles Darwin

1.1 Introduction

Halogenation is of considerable relevance in the cell metabolism of mammalians.[1] Thus, enzymatic chlorination of amino derivatives, such as taurine, has proved to be essential in leucocyte protection against infection in mammalians,[2-4] and has also been related to cell lysis[4] and other disorders related to inflammation.[5] On the other hand, chlorination is still the most used method of water treatment,[6] with well documented benefits and drawbacks.[7] Relationships between water chlorination and cancer have been reported.[8]

Alcoholamines are widely used in industry,[9] and as a result occur in residual and wastewaters. Recent studies[10, 11] explained the base-promoted decomposition of some secondary *N*-X alcoholamines (X = Cl, Br) in terms of a cooperative four-pathway mechanism as depicted in Scheme 1.1, *i.e.*: Hofmann and Zaitsev intermolecular eliminations,[12] a Grob fragmentation,[13] and an intramolecular elimination.[10] The main process was found to be intramolecular elimination for the HO^--promoted decomposition of *N*-Cl,*N*-ethylethanolamine, and Grob fragmentation in the case of the HO^--promoted decomposition of *N*-Cl,*N*-tertbutylethanolamine.[10]

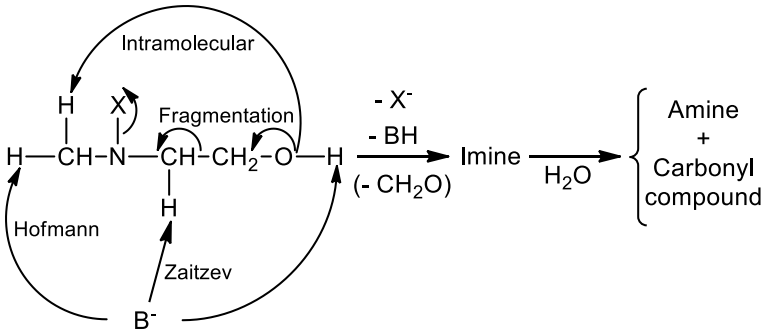

Scheme 1.1. Potential decomposition pathways for *N*-X,*N*-alkylalcoholamines.

Here, we report a joint kinetic and theoretical study of the base-promoted decomposition of *N*-X,*N*-methylethanolamine. The mechanism of the process differs from the one previously proposed[10] in the intramolecular elimination process being concerted and general-base catalyzed and, more particularly, in that the proposed fragmentation step corresponds to an unprecedented concerted base-assisted fragmentation.

1.2 Experimental

1.2.1 Chemicals and solutions

N-Methylethylamine (Fluka, 95%) and *N*-methylethanolamine (Merck, >98%) were halogenated *in situ* using fresh HClO and HBrO solutions, as described elsewhere,[10, 14] to obtain 2 mM aqueous solutions of *N*-X amines in all cases. Solutions of NaOH (Merck, *p.a.*), and buffers of 2,2,2-trifluoroethanol / 2,2,2-trifluoroethoxide (Aldrich, 99%+, pK_a=12.43),[15] and 1,1,1,3,3,3-hexafluoro-2-propanol / 1,1,1,3,3,3-hexafluoro-2-propoxide (Aldrich, 99%+, pK_a=9.30),[15] were used to control pH. Ionic strength was set to 1.0 M using NaCl or KCl (Merck, *p.a.*), the latter in the kinetic runs involving buffers. All other chemicals were of the highest purity available and used without further purification. Organic matter-free, twice-distilled water was used to make up all solutions.

1.2.2 Kinetic measurements

Reactions were studied in all cases under pseudo-first order conditions, following the decrease of the UV bands of the *N*-X amines (λ_{max} (*N*-Cl) = 265 nm, λ_{max} (*N*-Br) = 303 nm). A double-beam Varian® Cary 1E spectrophotometer and a Hi-Tech Scientific® SF-61 stopped-flow spectrophotometer were used.

Samples were placed in Suprasil quartz cells and thermostated at 298.15 ± 0.1 K, unless otherwise indicated. pH

measurements were carried out using a properly calibrated combined glass electrode.

1.2.3 Product analysis

Product analyses of formaldehyde and amines, reported in Table 1.1, were carried out by HPLC with UV detection. All analyses were performed at least in duplicate and the results averaged.

Quantitative determination of amines was made by derivatization to the corresponding phenylthioureas with phenyl isothiocyanate (Fluka, *puriss.* ≥ 99%) at 313 K and pH *ca.* 7 (50 mM phosphate buffer) during 30 min, then brought to completion at room temperature. The absorbance of the derivatized products was measured at 248 nm. The mobile phase used was CH_3CN/H_2O (50:50 v:v), flowing at 1 $mL \cdot min^{-1}$, 20 µL of sample being injected in all cases. The linearity of response of the detector to all analyzed products was checked. A reversed-phase 250 mm length, 4.6 mm internal diameter Sugelabor® column, packed with C-18 Inertsil ODS2, 5 µm, was used in an Agilent® 1100 series chromatograph. Using this method, the retention times found were: 3.27 min for ethanolamine, 3.76 min for *N*-methylethanolamine, 4.15 min for methylamine, 5.18 min for ethylamine and 5.86 min for *N*-methylethylamine.

Table 1.1. Amount of final reaction products found per mol of reacted *N*-X,*N*-methylethanolamine in the presence of HO^-.

Product	*N*-Cl compound	*N*-Br compound
CH_3NH_2	0.67 ± 0.01	0.55 ± 0.02
$NH_2CH_2CH_2OH$	0.33 ± 0.01	0.45 ± 0.02
CH_2O	1.41 ± 0.05	1.80 ± 0.09

Analysis of formaldehyde was also performed by derivatization with dinitrophenylhydrazine (Merck, *p.a.*).[16] A reversed-phase 250 mm length, 4.6 mm internal diameter Sugelabor® column, packed with C-18 Partisil ODS3, 5 µm, and protected with a 7.5 mm length, 4.6 mm internal diameter Sugelabor® precolumn, filled with the same stationary phase, were used in a Waters® 600s/717plus/996 chromatograph. The presence of reaction products other than aldehydes was proved to interfere under the study conditions, leading to deviations from the real formaldehyde concentrations.

1.2.4 Computational details

All calculations have been performed using the Gaussian 98 suite of programs.[17] Density functional theory calculations were carried out by using the B3LYP/6-31++G** level.[18-20]

The model comprises a molecule of *N*-Cl,*N*-methylethanolamine, a HO^- in the vicinity of the hydroxylic hydrogen, and to roughly simulate the first solvation shell two water molecules were also included, one located close to the HO^- and the other close to the amino group. Geometry, energy, and frequencies of stationary points for the fragmentation pathway, *i.e.* isolated reactants (R), reactant interaction complex (RIC), transition structure (TS), product interaction complex (PIC), and isolated products (P), have been characterized. In all cases real frequencies were obtained, except for the transition structure where only one imaginary frequency was found. Wyberg bond indexes[21] have also been computed over the optimized structures by using the natural bond orbital (NBO) analysis as implemented in Gaussian 98.[17, 22, 23] To include the bulk effect of solvation, single point calculations were carried out over the *in vacuo* optimized structures, using the polarizable continuum model (PCM).[24]

1.3 Results and discussion

In alkaline media and at constant hydroxide ion concentration, the reaction follows a pseudo-first order rate dependence on the *N*-X,*N*-methylethanolamine concentration:

$$r = k_{obs} \cdot [N\text{-X},N\text{-methylethanolamine}] \quad (1)$$

The observed rate constant, k_{obs}, is linearly dependent on [HO^-], as shown in Figure 1.1.

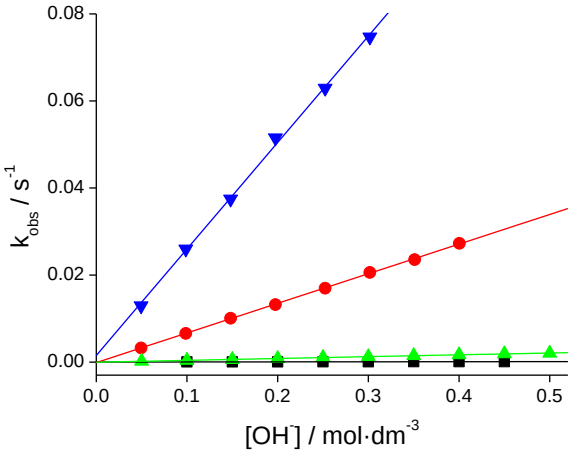

Figure 1.1. Dependence of k_{obs} *vs.* [HO^-]. (●) *N*-Cl,*N*-methylethanolamine, (■) *N*-Cl,*N*-methylethylamine, (▼) *N*-Br,*N*-methylethanolamine, (▲) *N*-Br,*N*-methylethylamine. [*N*-X amine] = $2.00 \cdot 10^{-3}$ mol·dm^{-3}, I = 1.0 mol·dm^{-3}, T = 298.15 K.

Linear dependences on base concentration are also observed when other bases are present *i.e.*:

$$k_{obs} = \Sigma\, k_B \cdot [B] \qquad (2) \qquad (2)$$

where k_B is the second order rate constant corresponding to each base present in the reaction media. The values of k_B are collected in Table 1.2.

Table 1.2. Second order rate constants observed for the base-promoted decomposition of different *N*-X amines and *N*-X alcoholamines. I = 1.0 mol·dm^{-3}, T = 298.15 K unless stated.

Compound	$k_{HO} \times 10^4$ / $mol^{-1} \cdot dm^3 \cdot s^{-1}$	$k_{TFE} \times 10^4$ / $mol^{-1} \cdot dm^3 \cdot s^{-1}$ [a]	$k_{HFPr} \times 10^4$ / $mol^{-1} \cdot dm^3 \cdot s^{-1}$ [a]
N-Cl,*N*-methylethanolamine	402 ± 4[b]		
N-Cl,*N*-methylethanolamine	681 ± 5	152 ± 9	0.50 ± 0.03
N-Cl,*N*-methylethanolamine	1205 ± 18[c]		
N-Cl,*N*-methylethanolamine	1904 ± 19[d]		
N-Br,*N*-methylethanolamine	2447 ± 47		
N-Cl,*N*-methylethylamine	1.88 ± 0.07		
N-Br,*N*-methylethylamine	42.2 ± 0.4		
N-Cl,*N*-ethylethanolamine	8200[e]		
N-Cl,*N*-diethylamine	2.03[e]		

[a] TFE = 2,2,2-trifluoroethoxide ion; HFPr = 1,1,1,3,3,3-hexafluoro-2-propoxide ion, [b] 293.15 K, [c] 303.15 K, [d] 308.15 K, [e] Ref. 10

N-X alcoholamines decompose much faster than the corresponding parent *N*-X amines in all cases. In accordance with this, k_{HO} for reaction of *N*-X,*N*-methylethanolamine with HO^- is two orders of magnitude higher than for the corresponding reaction of *N*-X,*N*-methylethylamine under similar conditions. In both cases the decomposition rate of the *N*-Br alcoholamine is *ca.* one order of magnitude faster than for the analogous *N*-Cl derivative. Taking this into account, and considering the fact that the change of inductive effect due to the replacement of $–CH_3$ by $–CH_2OH$ at one of the reaction centres of the molecule (σ^* ($–CH_2OH$) = 0.56, σ^* ($–CH_3$) = 0.00)[25] would not explain a rate enhancement of two orders of magnitude, it follows that the decomposition through Zaitsev elimination must be minimal. A parallelism can be established with the base-promoted decomposition of aliphatic secondary *N*-X amines,[26] so that the contribution of Hofmann

elimination should be also negligible. Thus, the intramolecular elimination and fragmentation pathways depicted in Scheme 1.1 remain to be considered.

The reaction mechanism shown in Scheme 1.2 has been proposed for the base-promoted decomposition of *N*-Cl,N-ethylethanolamine, involving a fast ionization of the –OH group that leads to the corresponding alkoxide, which may decompose through two different pathways.[10]

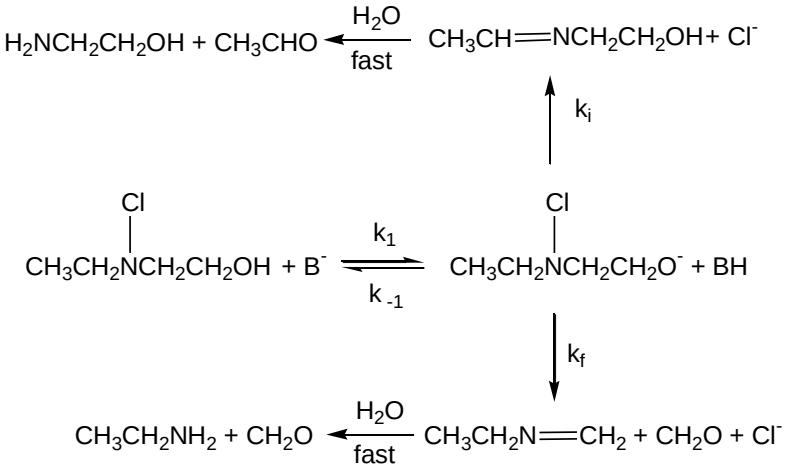

Scheme 1.2. Mechanism proposed for the base-promoted decomposition of *N*-Cl,*N*-ethylethanolamine.[10]

Product analyses allow determination of the relative weight, and hence rate constants, of each of the two pathways. The reaction products expected for the base-promoted decomposition of *N*-X,*N*-methylethanolamine through each of the pathways depicted in Scheme 1.1 are summarised in Table 1.3.

Table 1.3. Reaction products expected for the base-promoted decomposition of one mole of *N*-X,*N*-methylethanolamine when the reaction takes place through the pathways shown in Scheme 1.1.

Hofmann elimination	Zaitsev elimination	Intramolecular elimination	Fragmentation
CH_2O	$HOCH_2CHO$	CH_2O	2 CH_2O
$NH_2CH_2CH_2OH$	CH_3NH_2	$NH_2CH_2CH_2OH$	CH_3NH_2
X^-	X^-	X^-	X^-

Since methylamine and ethanolamine were obtained in similar concentrations (Table 1.1), both intramolecular elimination and fragmentation pathways must take place concurrently and contribute to the rate.

The yields of formaldehyde obtained (Table 1.1) can only be understood in terms of the fragmentation pathway being relevant in the overall decomposition mechanism: one mole of the starting *N*-X,*N*-methylethanolamine leads to two moles of formaldehyde. Consequently, the two main paths in the decomposition of *N*-X,*N*-methylethanolamine are intramolecular elimination and fragmentation. The corresponding contribution of each one, estimated from product analysis is collected in Table 1.4.

Assuming the fast acid-base preequilibrium (K_1) shown in Scheme 1.2 is displaced towards reactants, due to the high basicity of the alkoxide,[10] the corresponding rate equation is:

$$r = k \cdot K_1 \cdot ([B^-]/[BH]) \cdot [N\text{-X,N-methylethanolamine}] \quad (3)$$

where $k = k_f + k_i$. Taking into account the acidity constants of the base ($K_{a(BH)}$) and of the hydroxyl group of the alcoholamine ($K_{a(-OH)}$), and considering that $K_1 = K_{a(BH)}/K_{a(-OH)}$, equation 3 becomes:

$$r = (k \cdot K_{a(-OH)}/K_w) \cdot [HO^-] \cdot [N\text{-X},N\text{-methylethanolamine}] \quad (4)$$

where K_w is the self-ionization constant of water.

Table 1.4. Estimated contributions of intramolecular elimination and base-assisted fragmentation to the base-promoted decomposition of *N*-X,*N*-alkylethanolamines.

System	%Fragmentation	%Intramol. Elim.
N-Cl,*N*-methylethanolamine + HO^-	67	33
N-Br,*N*-methylethanolamine + HO^-	55	45
N-Cl,*N*-methylethanolamine + $CF_3CH_2O^-$	67	33
N-Cl,*N*-methylethanolamine + $(CF_3)_2CHO^-$	33	67
N-Cl,*N*-ethylethanolamine + HO^-	14[a]	86[a]

[a] Ref. 10

Thus, $k_{obs} = (k_f + k_i) \cdot K_{a(-OH)}/K_w) \cdot [HO^-]$, *i.e.*, the rate equation derived from the mechanism in Scheme 1.2 implies specific base catalysis, whereas general base catalysis is found here (Eq. 2). Both pathways show second order rate constants that are dependent on base strength, as shown in Figure 1.2.

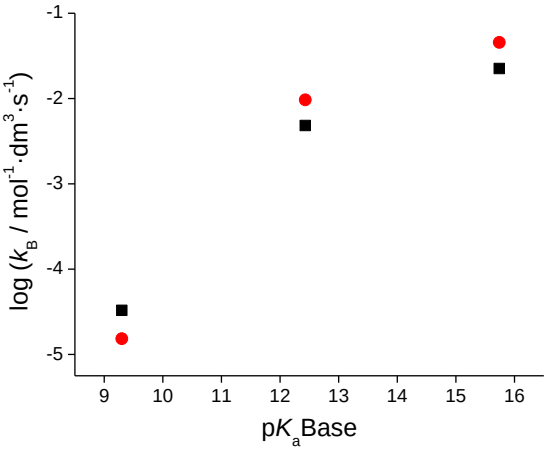

Figure 1.2. Dependence of the second order rate constant (k_B) on base strength for *N*-Cl,*N*-methylethanolamine. (●) Fragmentation, (■) Intramolecular elimination.

Although product analyses are in agreement with the overall reaction scheme (Scheme 1.2), the fast ionization preequilibrium at the –OH group is not appropriately accounted for by the current results, making necessary revisiting the mechanism of decomposition of *N*-Cl,*N*-ethylethanolamine.

On the basis of the dependence of the second order rate constants with the pK_a of the base (Figure 1.2), a proton transfer from the –OH to the base could be suggested as the rate limiting step. However, the differences obtained in the rate of decomposition of *N*-Br,*N*-methylethanolamine and *N*-Cl,*N*-methylethanolamine rule out this possibility (Table 1.2). The dependence of the observed rate constants on the concentration of any base present in the medium together with the correlation between the second order rate constant and the pK_a of the base point to base-assisted processes. In order to

avoid an acid-base preequilibrium, the concerted process shown in Scheme 1.3 can be proposed as reaction mechanism. Since the hydrolysis of imines is fast, in the rest of this paper we refer to the initial stages, prior to imine hydrolysis. Thus, the corresponding rate law would be:

$$r = k\cdot[B^-]\cdot[N\text{-X},N\text{-methylethanolamine}] \quad (5)$$

where $k = k_f + k_i$ and $k_{obs} = k\cdot[B^-]$. Thus, the proton transfer from the –OH group would be dependent on base strength. The fact that Br^- is a better nucleofuge than Cl^- agrees with a concerted mechanism, explaining the higher rate of decomposition observed for *N*-Br,*N*-methylethanolamine.

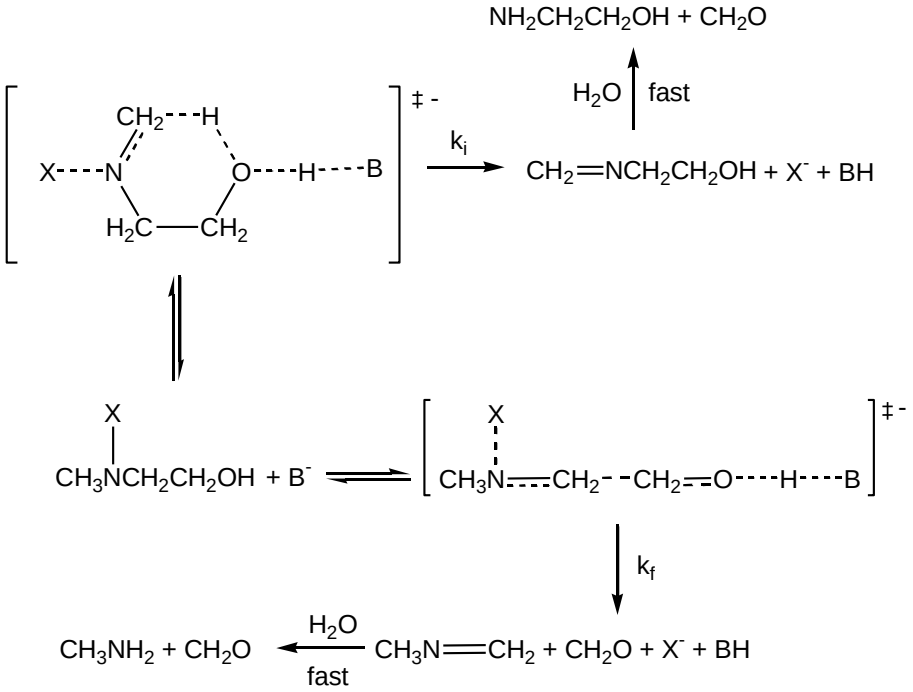

Scheme 1.3. Mechanism proposed for the base-assisted decomposition of *N*-X,*N*-alkylethanolamines.

Transition states can be put forward for both pathways in which six bonds would be simultaneously involved, the most characteristic being a C=O bond formation and C–C bond breaking for the base-assisted fragmentation, and an H–O bond formation and C–H bond breaking for the intramolecular elimination. Although a simple estimation based on bond energies[27] suggests the intramolecular process (*ca.* –359 kJ) to be twice as exothermic as the base-assisted fragmentation (*ca.* –143 kJ), the product yields (Table 1.4) point to a similar $\Delta G^{\ddagger}$ for both processes. Additional information is supplied by the activation parameters, obtained from the study of the effect of temperature on the rate constants for the reaction between *N*-Cl,*N*-methylethanolamine and HO^- (Table 1.5), and using the product distribution to resolve the two pathways.

Due to the limited temperature range used for the determination of the activation parameters, and the fact that the experimental rate constants have been dissected into the rate constants of the two parallel reactions on the basis of product distribution, the significance of the activation parameters should be taken with caution. The values obtained show that in fact $\Delta G^{\ddagger}$ is very similar for both processes, and agree with the proposed mechanism. Taking into account the bonds involved in the transition state, $\Delta H^{\ddagger}$ is expected to be rather similar for both processes, which is found. The $\Delta S^{\ddagger}$ values point to a more ordered transition state for the intramolecular elimination. This is reasonable, as achieving the cyclic disposition at the TS is more entropy demanding than reaching an open transition state. A value of $\Delta S^{\ddagger} \approx 0$ would be expected for the base-assisted fragmentation, its sign depending on the extent to which the bonds involved at the transition state are formed or broken, as well as on solvation changes.

Table 1.5. Experimental activation parameters obtained for the HO^--assisted decomposition of *N*-Cl,*N*-methylethanolamine.

	Base-assisted fragmentation	**Intramolecular elimination**
$\Delta H^{\ddagger}$ / kJ·mol^{-1}	77 ± 2	74 ± 2
$\Delta S^{\ddagger}$ / J·K^{-1}·mol^{-1}	-11 ± 6	-29 ± 8
$\Delta G^{\ddagger}$ (298.0 K)/ kJ·mol^{-1}	81 ± 2	82 ± 3

A further step in the characterization of the transition states is the use of reaction maps.[28, 29] Strictly speaking such bidimensional representations would only be appropriate to describe processes in which two major molecular events are involved, while in this case six bonds are breaking and forming cooperatively. Still, for a concerted process a plot of its progress in terms of proton transfer to the base and N–X bond breaking, should be a reasonable approximate approach. The estimation of the concertedness of the process and of the structure of the transition state can be done in terms of Brønsted's β_H, and of the Brønsted-like parameter β_{lg}, *i.e.*, the slopes of the plot of log (k_B / $M^{-1}\cdot s^{-1}$) *vs.* pK_a (BH) and log (k_X / $M^{-1}\cdot s^{-1}$) *vs.* pK_a (XH), respectively. The linearity of such plots is understood as evidence for the reaction with different bases and / or leaving groups having rather similar transition states. The synchronicity of the concerted process can be estimated as $|\beta_H - |\beta_{lg}||$, a value of 0 being obtained for a synchronous process and 1 for an uncoupled stepwise reaction.

Due to the nature of the reaction under study, only two points are available to make a crude estimation of the degree of N–X bond breaking (β_{lg}). On the other hand, the Brønsted plot is not linear for either pathway, as evident from Figure 1.2, which implies a variable degree of proton transfer to the base depending on its strength. The weaker the base the steeper the slope, *i.e.*, the degree of proton transfer is higher as the pK_a of the base decreases. Keeping this in mind and assuming that a linearization of the log (k_B / $M^{-1}\cdot s^{-1}$) *vs.* pK_a (BH) plot is an oversimplification, both TS's can be located on a reaction map (Figure 1.3).[28, 29] It must be noted here that the free energy surfaces are different for the two processes, *i.e.*: the species on the upper right corner are not the same for each pathway. However, as the proton transfer and the N–X bond breaking are the processes under consideration, plotting them together allows comparison of the location of transition states. The error bars shown represent the change in the slopes in the Brønsted plot (Figure 1.2) as the strength of the base decreases: from 0.20 to 0.98 for the base-assisted fragmentation and from 0.19 to 0.67 for the intramolecular elimination.

Accordingly, as the points lie outside the axes, both pathways can be described as concerted, the degree of synchronicity depending on the base strength. Both processes are almost synchronous with stronger bases, the hydrogen abstraction from the –OH group being slightly ahead of the N–X bond breaking. As the base weakens, the imbalance[30] increases and the degree of proton transfer changes, being well ahead of the N–X bond breaking. In this case fragmentation is highly asynchronous. When $(CF_3)_2CHO^-$ is involved, the proton is almost fully transferred, whereas the N–X bond is only 25% broken. Such facts are in agreement with the change on the yield of reaction products on going from HO^- to $(CF_3)_2CHO^-$ (Table 1.4).

From the $\Delta G^{\ddagger}$ values for the decomposition of *N*-Br,*N*-methylethanolamine, it could be interpreted that the change from N–Cl to the weaker N–Br bond accelerates both the base-assisted fragmentation process by lowering $\Delta G^{\ddagger}$ *ca.* 3 kJ·mol^{-1} and the intramolecular elimination pathway by decreasing $\Delta G^{\ddagger}$ *ca.* 4 kJ·mol^{-1}. The fact that the intramolecular elementary process is favoured supports the proposed mechanism; this pathway should be more sensitive to changes in the nucleofuge.

Table 1.4 reflects a dramatic change in the relative contribution of the two pathways for the HO^--assisted decomposition of *N*-Cl,*N*-ethylethanolamine, the intramolecular elimination being the most favourable pathway in that case. Such a difference can be easily explained in terms of the increased acidity of the hydrogen being transferred and the enhanced stability of the N–C double bond being formed due to the presence of the methyl group on the C transferring the hydrogen, which lowers the intramolecular elimination energy barrier. Considering again the effect of this change on $\Delta G^{\ddagger}$, the fragmentation pathway shows a $\Delta G^{\ddagger}$ that is lower by *ca.* 2 kJ·mol^{-1} than that of *N*-Cl,*N*-methylethanolamine, rather similar

to the effect observed when changing –Cl to –Br on the N. The effect observed on the intramolecular elimination is a reduction of *ca.* 8-9 kJ·mol^{-1} in $\Delta G^{\ddagger}$, in agreement with the previous statements.

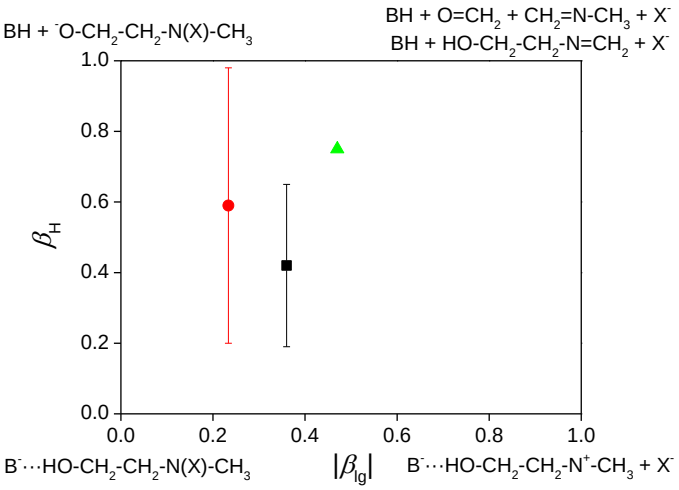

Figure 1.3. Reaction map for the processes under consideration. (■) Intramolecular elimination, experimental; (●) base-assisted fragmentation, experimental; (▲) base-assisted fragmentation, computational.

Electronic structure calculations of the *in vacuo* HO^--assisted fragmentation of *N*-Cl,*N*-methylethanolamine led to the same mechanism proposed on an experimental basis, *i.e.*, a two-step mechanism (Scheme 1.3) in which the first step corresponds to the fragmentation and the second to the hydrolysis of the *N*-methylmethanimine intermediate, yielding a second molecule of formaldehyde and methylamine. The results obtained cannot be explained in terms of the three-step mechanism, involving a Grob fragmentation as rate limiting step, proposed previously for the reaction between *N*-Cl,*N*-ethylethanolamine and HO^-.[10] Attempts to find a stepwise mechanism via proton transfer followed by N–Cl cleavage were unsuccessful.

The –OH proton withdrawal is accompanied by a major internal reorganization taking place at the TS. It has been found that not only H–O and N–Cl bonds, but six bonds form and break concertedly. The theoretical TS for the rate limiting step is depicted in Figure 1.4.

A plot of the theoretically-determined progress of O–H and Cl–N bond breakages at the TS is shown on the reaction map of Figure 1.3. The difference can be attributed to the approximations underlying the experimental reaction maps, etc. For instance, to experimentally estimate β_H several bases are used, and thus the value reported for the degree of proton transfer is an average rather than a specific value for each base, the same being true for the nucleofuges. Conversely, the computationally obtained value is estimated for the reactants involved in the calculation, *N*-Cl,*N*-methylethanolamine and HO^-. Another common experimental assumption is the conservation of bond order at the transition state. Computational results suggest this is not the case for this process. Figure 1.4 shows the Wiberg bond indexes at the TS, and it follows that the sum of bond orders involved in the proton transfer is not one, and the pattern will not change on moving from the transition structure to the transition state.

Wiberg bond indexes have been used to analyze the synchronicity of the base-assisted fragmentation, which can be estimated by means of the Sy parameter proposed by Moyano *et al*.[31] Sy = 1 meaning fully synchronous bond reorganization, while Sy = 0 implies a stepwise mechanism. Here, we find Sy = 0.77, *i.e.*: the HO^--assisted fragmentation of *N*-Cl,*N*-methylethanolamine is a slightly asynchronous process. This value can be compared to the experimental one, 0.95,

estimated as $(1 - |\beta_H - |\beta_{lg}||)$. Having in mind the approximations underlying this value (*vide supra*) the agreement is acceptable.

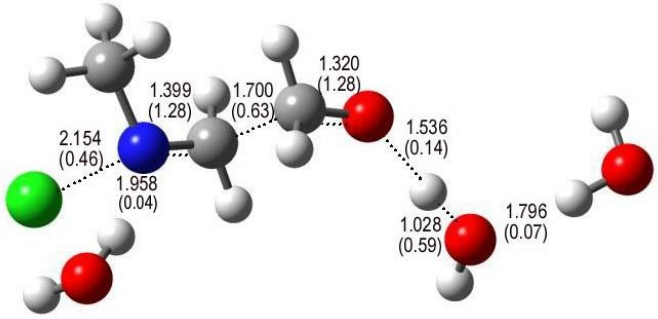

Figure 1.4. Theoretically obtained TS for the HO^--assisted fragmentation of *N*-Cl,*N*-methylethanolamine *in vacuo* obtained at the B3LYP/6-31++G** computational level. Dotted lines indicate bond-breaking / bond-forming processes. Distances between relevant atoms are shown and the corresponding Wiberg bond orders given between parenthesis.

Thermodynamic parameters for the fragmentation process were theoretically calculated considering RIC, transition structure, and PIC as the relevant stationary points along the reaction coordinate (Table 1.6).

Table 1.6. B3LYP/6-31++G** thermodynamic parameters obtained for the HO^--assisted fragmentation of *N*-Cl,*N*-methylethanolamine.

	RIC to TS		**RIC to PIC**
$\Delta H^{\ddagger}$ / kJ·mol^{-1}	28	$\Delta H°$ / kJ·mol^{-1}	–139
$\Delta S^{\ddagger}$ / J·K^{-1}·mol^{-1}	1	$\Delta S°$ / J·K^{-1}·mol^{-1}	67
$\Delta G^{\ddagger}$ (298.0 K)/ kJ·mol^{-1}	27	$\Delta G°$ / kJ·mol^{-1}	–159

As usual, theoretical and experimental activation values are different.[32] The experimental $\Delta S^{\ddagger} = -11 \pm 6$ J·K^{-1}·mol^{-1}, a small negative value, does not clearly show the bimolecularity of the rate limiting step. Likewise, the theoretical value of $\Delta S^{\ddagger} = 1$ J·K^{-1}·mol^{-1}, is close to zero but still the computational results clearly describe this process as bimolecular. Furthermore, these data are very similar to the value obtained for the intermolecular elimination of *N*-Cl,*N*-methylethylamine, $\Delta S^{\ddagger} = -4 \pm 26$ J·K^{-1}·mol^{-1}, which is also accepted as a bimolecular process.[11, 26] The reaction proceeds from two reactant molecules, *N*-Cl,*N*-methylethanolamine and HO^-, to products, four molecules: *N*-methylmethanimine, formaldehyde, Cl^-, and a discrete H_2O molecule. Thus, a noticeable increment of entropy is expected as the reaction progresses. The increase of ΔS from RIC to PIC has been theoretically calculated as 67 J·K^{-1}·mol^{-1}, therefore, the activation entropy for this process corresponds to a change from a two-molecule RIC into a TS that is a cluster of four partially bonded molecules. This explains the low absolute value obtained for $\Delta S^{\ddagger}$. It is a remarkable fact that the calculated value for the enthalpy change from RIC to PIC (–139 kJ·mol^{-1}) is in good agreement with the value of the reaction enthalpy change estimated from average bond enthalpies (–143 kJ·mol^{-1}).[27]

Single point calculations on the previously optimized structures using the polarizable continuum model (PCM)[24] were carried out to include bulk solvation. The free energy of solvation values for RIC, TS, and PIC are –215, –227, and –177 kJ·mol^{-1}, respectively. The variation comes from the change in solvation on going from the HO^- to Cl^- as the reaction proceeds. The net effect of solvation using PCM is to reduce both the activation barrier and the exergonicity of the reaction. Calculations with more sophisticated models to better match the experimental values are in progress.

More important than the coincidence of the thermodynamic computational and experimental values seems the fact that both experiment and calculation support a concerted asynchronous process, where the proton transfer from the –OH group to the HO^- is ahead of the N–Cl bond cleavage.

1.4 Conclusions

The presence of the –OH group in *N*-X,*N*-methylethanolamine increases the rate of decomposition relative to the parent *N*-X,*N*-methylethylamine to an extent that cannot be explained just in terms of inductive effect. The rate enhancement observed, as well as the analysis of the products generated, led us to the conclusion that only two pathways, an intramolecular elimination and a base-assisted bimolecular fragmentation, are involved.

Both routes take place via two consecutive steps. The first one in both cases is a bimolecular step involving the attack of the base to the hydroxylic hydrogen of the *N*-X,*N*-methylethanolamine. In the elementary intramolecular elimination process such attack triggers the proton transfer from the methyl group to the hydroxylic oxygen and the departure of the halide. In the elementary base-assisted fragmentation, the proton transfer from the hydroxyl group forces the breakage of the molecule, formaldehyde acts as electrofuge group, the halide anion plays the nucleofuge role, and *N*-methylmethanimine is formed. Kinetic evidences suggest both the elementary base-assisted fragmentation and the intramolecular elimination take place through concerted asynchronous steps. The attack of the base on the hydroxylic hydrogen is ahead of the rest of the molecular events, the weaker the base the more asynchronous the process becomes. Subsequent fast hydrolysis of the intermediate imine formed through each route explains the percentages of products found. B3LYP/6-31++G** density functional calculations on the elementary base-assisted fragmentation step support the mechanism proposed.

This study has been published as: J. Andrés, X. L. Armesto, M. Canle L., M. V. García, D. R. Ramos, and J. A. Santaballa, Org. Biomol. Chem., 2003 **1** (23) 4323-4328.

1.5 References

1. E. L. Thomas, M. B. Grisham, and M. M. Jefferson, *[41] Cytotoxicity of chloramines.* Methods Enzymol., 1986 **132** (Immunochemical Techniques Part J) 585-593.
2. S. J. Klebanoff, *Myeloperoxidase-halide-hydrogen peroxide antibacterial system.* J. Bacteriol., 1968 **95** (6) 2131-2138.
3. E. L. Thomas, M. B. Grisham, and M. M. Jefferson, *Myeloperoxidase-dependent effect of amines on functions of isolated neutrophils.* J. Clin. Invest., 1983 **72** (2) 441-454.
4. I. U. Schraufstatter, K. Browne, A. Harris, P. A. Hyslop, J. H. Jackson, O. Quehenberger, and C. G. Cochrane, *Mechanisms of hypochlorite injury of target cells.* J. Clin. Invest., 1990 **85** (2) 554-562.
5. S. J. Klebanoff, *Oxygen metabolites from phagocytes*, in *Inflammation: basic principles and clinical correlates*, J.I. Gallin and R. Snyderman, Editors. 1999, Lippincott Williams & Wilkins: Philadelphia. 721.
6. S. Miller, *Disinfection products in water treatment.* Environ. Sci. Technol., 1993 **27** (12) 2292-2294.
7. D. Henschler, *Toxicity of chlorinated organic compounds: effects of the introduction of chlorine in organic molecules.* Angew. Chem. Int. Ed. Engl., 1994 **33** (19) 1920-1935.
8. R. Franzén and L. Kronberg, *Determination of chlorinated 5-methyl-5-hydroxyfuranones in drinking water, in chlorinated humic water, and in pulp bleaching liquor.* Environ. Sci. Technol., 1994 **28** (12) 2222-2227.

9. *The Merck index: an encyclopedia of chemicals, drugs, and biologicals*. 12th ed, ed. S. Budavari. 1996, New Jersey: Whitehouse Station.
10. X. L. Armesto, M. Canle L., P. Carretero, M. V. García, and J. A. Santaballa, *Evidence for an intramolecular elimination mechanism in the aqueous decomposition of (N-Cl)-alcoholamines.* Tetrahedron, 1997 **53** (7) 2565-2572.
11. X. L. Armesto, M. Canle L., M. V. García, and J. A. Santaballa, *Aqueous Chemistry of N-halo-compounds.* Chem. Soc. Rev., 1998 **27** (6) 453-460.
12. W. Hückel and M. Hanack, *Eliminations in cyclic cis-trans-isomers.* Angew. Chem. Int. Ed. Engl., 1967 **6** (6) 534-544.
13. C. A. Grob and P. W. Schiess, *Heterolytic fragmentation. A class of organic reactions.* Angew. Chem., Int. Ed. Engl., 1967 **6** (1) 1-15.
14. X. L. Armesto, M. Canle L., M. Losada, and J. A. Santaballa, *An operational approach to N-Cl-α-amino acids decomposition.* Int. J. Chem. Kinet., 1993 **25** (5) 331-339.
15. M. I. Page, P. S. Webster, and L. Ghosez, *The hydrolysis of azetidinyl amidinium salts. Part 2. Substituent effects, buffer catalysis, and the reaction mechanism.* J. Chem. Soc., Perkin Trans. 2, 1990 (5) 813-823.
16. EPA, *Method 8315A, Determination of carbonyl compounds by high performance liquid chromatography (HPLC)*. 1996.
17. M. J. Frisch, G. W. Trucks, H. B. Schlegel, G. E. Scuseria, M. A. Robb, J. R. Cheeseman, V. G. Zakrzewski, J. A. Montgomery, R. E. Stratmann, J. C. Burant, S. Dapprich, J. M. Millam, A. D. Daniels, K. N. Kudin, M. C. Strain, O. Farkas, J. Tomasi, V. Barone, M. Cossi, R. Cammi, B. Mennucci, C. Pomelli, C. Adamo, S. Clifford, J. Ochterski, G. A. Petersson, P. Y. Ayala, Q. Cui, K. Morokuma, D. K. Malick, A. D. Rabuck, K. Raghavachari, J. B. Foresman, J. Cioslowski, J. V. Ortiz, B. B. Stefanov, G. Liu, A. Liashenko, P. Piskorz, I. Komaromi, R. Gomperts, R. L. Martin, D. J. Fox, T. Keith, M. A. Al-Laham, C. Y. Peng, A. Nanayakkara, C. Gonzalez, M. Challacombe, P. M. W. Gill, B. G. Johnson, W. Chen, M. W. Wong, J. L. Andres, M. Head-Gordon, E. S. Replogle, and J. A. Pople, *Gaussian 98*. 1998, Gaussian, Inc.: Pittsburgh PA.
18. A. D. Becke, *Density-functional thermochemistry. III. The role of exact exchange.* J. Chem. Phys., 1993 **98** (7) 5648-5652.
19. T. Clark, J. Chandrasekhar, G. W. Spitznagel, and P. v. R. Schleyer, *Efficient diffuse function-augmented basis sets for anion calculations. III. The 3-21+G basis set for first-row elements, Li–F.* J. Comput. Chem., 1983 **4** (3) 294-301.
20. C. Lee, W. Yang, and R. G. Parr, *Development of the Colle-Salvetti correlation-energy formula into a functional of the electron density.* Phys. Rev. B, 1988 **37** (2) 785-789.
21. K. B. Wiberg, *Application of the pople-santry-segal CNDO method to the cyclopropylcarbinyl and cyclobutyl cation and to bicyclobutane.* Tetrahedron, 1968 **24** (3) 1083-1096.
22. A. E. Reed, R. B. Weinstock, and F. J. Weinhold, *Natural population analysis.* J. Chem. Phys., 1985 **83** (2) 735-746.
23. A. E. Reed, L. A. Curtiss, and F. Weinhold, *Intermolecular interactions from a natural bond orbital, donor-acceptor viewpoint.* Chem. Rev., 1988 **88** (6) 899-926.
24. S. Miertuš, E. Scrocco, and J. Tomasi, *Electrostatic interaction of a solute with a continuum. A direct utilization of ab initio molecular potentials for the prevision of solvent effects.* Chem. Phys., 1981 **55** (1) 117-129.
25. C. Hansch and A. Leo, *Substituent constants for correlation analysis in chemistry and biology*. 1979, New York: Wiley Interscience.
26. L. Abia, *Estudio cinético de cloración de aminas alifáticas secundarias*. 1993, Universidade da Coruña: A Coruña, Spain.

27. *CRC Handbook of chemistry and physics*. 83rd ed. 2002, Boca Raton, FL: CRC Press, Inc.

28. W. P. Jencks, *A primer for the Bema Hapothle. An empirical approach to the characterization of changing transition-state structures.* Chem. Rev., 1985 **85** (6) 511-527.

29. R. A. More O'Ferrall, *Relationships between E2 and E1cB mechanisms of β-elimination.* J. Chem. Soc. (B), 1970 (0) 274-277.

30. C. F. Bernasconi, *The principle of non-perfect synchronization.* Adv. Phys. Org. Chem., 1992 **27** 119-238.

31. A. Moyano, M. A. Pericàs, and A. Valentí, *A theoretical study on the mechanism of the thermal and the acid-catalyzed decarboxylation of 2-oxetanones (b-lactones).* J. Org. Chem., 1989 **54** (3) 573-582.

32. F. Jensen, *Introduction to computational chemistry*. 1999, Chichester: John Wiley & Sons.

CHAPTER 2

Density functional study of the Hofmann elimination of *N*-Cl,*N*-methylethanolamine in gas phase and in aqueous solution

The only existing things are atoms and empty space,
all else is mere opinion.

Democritus (460 to 370 BC)

2.1 Introduction

Chemical reactivity involving *N*-X compounds (X=halogen) has been widely studied at a macroscopic level over the past 40 years due to their importance in both environmental and biological chemistry.[1-8] Recent experimental studies opened the door to the detailed analysis of the corresponding molecular mechanism. Kinetic results show that these compounds easily decompose in basic media, but the reaction mechanism is still a matter of controversy;[7, 9, 10] to our knowledge, there have been no computational attempts to model in detail this reaction.

Experimental and computational studies devoted to the determination of reaction mechanisms are an issue of major concern in chemistry. Theoretical characterization of potential energy surfaces (PES) has significantly improved our understanding of intrinsic reactivity, helping to unravel the molecular mechanism of chemical reactions. In this work, we present model electronic structure calculations in order to shed light on the reaction between *N*-Cl,*N*-methylethanolamine and hydroxide ion to yield 2-methyleneamino-ethanol (see Scheme 2.1). To explore the effect of water as a solvent, we have included in the model up to two discrete water molecules and/or a continuum method.

2.2 Computational procedures and model systems

Density functional theory calculations were carried out with the GAUSSIAN98 package of programs.[11] The minima and TSs were fully optimized by B3LYP[12, 13] using the 6-31++G** basis set. B3LYP was selected to qualitatively reveal the solvent effects on the elimination reaction rather than obtaining quantitative data. Although the title reaction is different, quantitative conclusions should be avoided as energy barrier underestimation by this functional in gas-phase identity S_N2 reactions at neutral nitrogen involving N–X bonds has been reported.[14]

The nature of the molecular mechanism has been elucidated by characterizing on the PES the geometry and energy of the stationary points: reactants, transition structure (TS), products and putative intermediates. The nature of each stationary point was established by calculating analytically and diagonalizing the matrix of the energy second derivatives to determine the number of imaginary frequencies, zero for local minima and one for TS. Harmonic frequencies were calculated in order to confirm the nature of the stationary points, and to obtain zero point energies (ZPE) and thermal corrections to enthalpies and free energies at 298.15 K in the usual rigid rotor harmonic oscillator approximation.[15] The unique imaginary frequency associated with the transition vector (TV) of the different TSs has been analyzed.[16] The components of the TV allow us to decide which variables control the transformation. The intrinsic reaction coordinate, from the TSs down to the two lower energy structures, has been traced using the second order Gonzalez-Schlegel integration method in order to verify that each saddle point links the two putative minima.[17-19] Evolution of relevant bonds along the reaction pathways has been estimated on the basis of changes in net atomic charges calculated using the natural population analysis of Weinhold *et al*.[11, 20-22]

Modelling chemical reactions involving ionic species in aqueous solution can be carried out by means of implicit solvation models, supermolecule approach, and/or continuum-based models. These methods have contributed to the elucidation of the role of solvent in the energy and geometry of relevant stationary points. High-level *ab initio* electronic structure calculations including even a modest number of solvent molecules are prohibitive computationally. Microsolvated models including one and two discrete water molecules have been computed, and finally the continuum model was taken into account. Model I corresponds to the reaction between *N*-Cl,*N*-methylethanolamine and HO^- in vacuum (Figure 2.1). Previous conformational analysis rendered the most stable conformer of *N*-Cl,*N*-methylethanolamine. One discrete water molecule interacting with the incoming HO^- is considered in model II (Figure 2.1). Model III comprises model II and another discrete water molecule that acts as H^+ donor/acceptor to/from the nitrogen/oxygen atom of *N*-Cl,*N*-methylethanolamine, respectively (Figure 2.1). In order to model solvated reactants and products in a more realistic way, the hydrogen bonds involving water molecules both at the bound reactant-like complex (called hereafter reactant interaction complex (RIC)), and at the product interaction complex (PIC), that opens the channel to reach the products, were preserved in separate reactants (R) and products (P). Thus, they were grouped as follows, according to the model: HO^- together with one water

molecule, and *N*-Cl,*N*-methylethanolamine bonded to another water molecule are the reactants, while Cl^- bonded to one or two molecules of water, and the imine with another water molecule are the products. Finally, to assess the long-distance stabilization of solvent, a continuum solvation approach was included on previous three models. Single point calculations based on the polarized continuum model (PCM) developed by Tomasi and Persico were carried out to reveal the effect of bulk water (ε = 78.39 [11]) on each of the stationary points.[23]

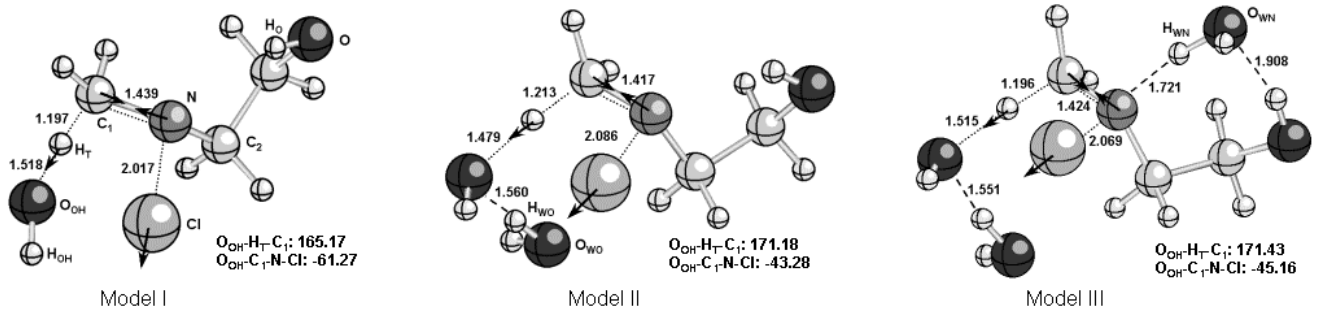

Figure 2.1. Optimized transition structures for the three model systems by using DFT at B3LYP/6-31++G** level. Distances in Å and bond angles in degrees. Vibrational mode components in mass-weighted coordinates are also included.

2.3 Results and discussion

2.3.1 Microsolvated models

Figure 2.2 shows the free energy profiles for the three model systems. Three stationary points have been characterized on the PES: the RIC, the TS, and the corresponding PIC; for comparison purposes the reactants were taken as reference. Calculated thermodynamic parameters are reported in Table 2.1.

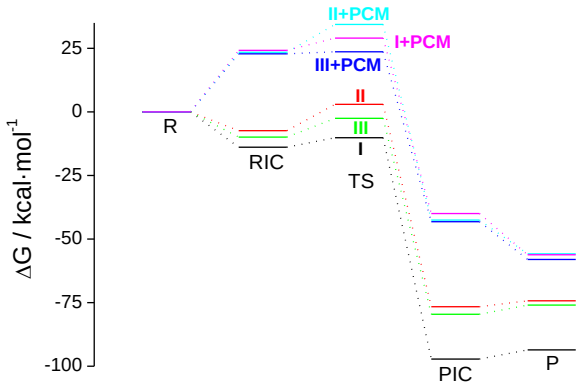

Figure 2.2. Gibbs free energy profiles for the Hofmann elimination obtained with all six microsolvated and microsolvated plus continuum models by using DFT at B3LYP/6-31++G** level. Reactants (R) were taken as reference.

The reaction pathway derived from the minimum energy path, shown in Figure 2.2, can be divided in three sharply separable parts: (a) activationless approach of the incoming HO^- and *N*-Cl,*N*-methylethanolamine to form the RIC; (b) bond-breaking/forming processes corresponding to the Hofmann elimination (Scheme 2.1). In this step, the N–Cl bond is broken, the C–N single bond is transformed into a C=N double bond, and H_t is transferred from the terminal carbon of *N*-Cl,*N*-methylethanolamine to the incoming HO^-. The corresponding geometries of TSs, connecting RIC and PIC, for each model system are shown in Figure 2.1; (c) formation of products from PIC by diffusional separation of the just generated water

molecule, imine and Cl^-.

Table 2.1. Thermodynamic parameters, ΔH, TΔS and ΔG, in kcal·mol^{-1} for the Hofmann elimination obtained by using DFT at B3LYP/6-31++G** level. Reactants (R) were taken as reference. Values obtained with PCM continuum model in italics. ΔG_{int} values refer to intrinsic activation barrier ($\Delta G_{int} = \Delta G_{TS} - \Delta G_{RIC}$).

RIC	**ΔH**	**TΔS**	**ΔG**			
Model I	–21.76	–7.87	–13.89	*24.20*		
Model II	–16.12	–8.75	–7.37	*23.44*		
Model III	–19.03	–9.12	–9.91	*22.84*		
TS	**ΔH**	**TΔS**	**ΔG**		**ΔG_{int}**	
Model I	–18.69	–8.54	–10.14	*29.02*	3.75	*4.82*
Model II	–7.15	–10.13	2.98	*34.39*	10.35	*10.95*
Model III	–12.91	–10.40	–2.52	*23.62*	7.39	*0.78*
PIC	**ΔH**	**TΔS**	**ΔG**			
Model I	–99.36	–2.16	–97.20	*–39.95*		
Model II	–79.93	–3.31	–76.62	*–42.54*		
Model III	–83.96	–4.40	–79.57	*–43.16*		

The formation of RIC from reactants always corresponds to an activationless process, while the step from RIC to TS involves an energy barrier (ΔG_{int}), and PIC and products are energetically stable systems. RICs are destabilized by addition of water molecules, more in model II than in III, due to the weakening of hydrogen bonds with respect to reactants and/or model I. The geometries of stationary points for model III present two hydrogen bonds in a 7-membered cyclic arrangement, one water molecule acting both as H^+ donor/acceptor to/from the nitrogen/oxygen atom of *N*-Cl,*N*-methylethanolamine, respectively. This cyclic structure contributes to stabilize the TS, the results supporting a water-assisted reaction. Stabilization by a cyclic structure involving water molecules was reported in a theoretical study of the formation of *N*-Cl compounds.[24] Activation parameters point out that the effect of the water molecules arises from the enthalpic contribution. Thus, $\Delta H^{\ddagger}$ decreases from –7.15 kcal·mol^{-1} (model II) to –12.91 kcal·mol^{-1} (model III), and the decrease in $\Delta G^{\ddagger}$ has the same value due to the similar entropic contribution (Table 2.1). Therefore, this effect in model III is due to a synergetic role of the cyclic structure, where the N–Cl bond breaking and the H_t transfer to the HO^- are facilitated by the presence of the discrete water molecule properly oriented. A third effect of solvation by discrete water molecules is the strong destabilization of the final stage, PICs and products.

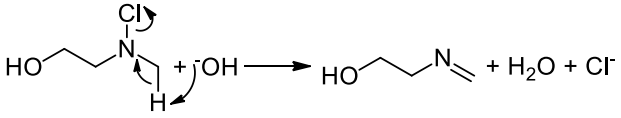

Scheme 2.1. Hofmann elimination in the reaction between HO^- and *N*-Cl,*N*-methylethanolamine.

The components of the TV for the different TSs are mainly associated with the H_t transfer from the carbon atom, C_1, of *N*-Cl,*N*-methylethanolamine to the oxygen atom, O_{OH}, of the incoming HO^-, the formation of a double bond, C_1=N, and the N–Cl bond breaking, with Cl^- as nucleofuge. In models II and III, the discrete water molecules also participate in the TV. These results point out that this elimination reaction corresponds with an asynchronous concerted bimolecular elimination mechanism ($A_{XH}D_HD_N$).[25] The two possible limiting stepwise mechanisms either $D_N^{\ddagger}+A_{XH}D_H$ (N–Cl cleavage and proton transfer to the HO^- taking place in separate steps), or $(A_{XH}D_H)^{\ddagger}+D_N$ (proton transfer to HO^- followed by departure of Cl^-) were not found during the calculations.

Table 2.2 shows the evolution of relevant bonds along the reaction pathway, with similar values for the three models, the

TS being reactant-like.[26] Negative charge transfer takes place along the reaction from the incoming HO^- to the leaving Cl^- (Table 2.3). The net atomic charge of the H_t atom being transferred to the HO^- increases along the process due to the enhancement of the polarity of the bonds being formed/broken. The net atomic charge of H_t at the TS is around 0.30 a.u. in the three models; therefore, the reaction has a proton transfer character. Besides, at the TS the net negative charge transferred from the hydroxide moiety is around 0.35 a.u. for the three models, and the net negative charge of the chlorine fragment is in the range 0.25 - 0.30 a.u. Therefore, there is a synergetic charge flow generating an anion at the Cl-end. In addition, in model III, the cyclic structure produces a better nucleofuge, Cl^-, via hydrogen bonding of one discrete water molecule with *N*-Cl,*N*-methylethanolamine; in fact the net atomic charge on the nitrogen atom for both TSs of models I and II is around –0.25 a.u., while this value decreases to –0.43 a.u. in model III. Thus, there is a polarization of the nitrogen centre that promotes the Cl^- departure.

Table 2.2. Percentage of negative charge transferred from the HO^-, dipole moment, and degree of evolution for selected bonds at RIC and TS.

	Model I		**Model II**		**Model III**	
	RIC	**TS**	**RIC**	**TS**	**RIC**	**TS**
% $q_{transferred}$	31.0	58.3	–0.5	43.2	4.1	41.4
μ	6.44	6.31	5.82	4.26	6.88	4.08
% Evolution						
O_{OH}–H_T	5.0	31.3	6.5	34.3	7.9	31.4
H_T–C_1	5.5	27.6	9.6	31.5	10.8	28.6
C_1–N	–0.7	11.0	1.2	16.8	1.2	14.5
N–Cl	1.0	22.5	2.8	28.4	4.3	26.8

Table 2.3. Mulliken atomic charges for the Hofmann elimination obtained by using DFT at B3LYP/6-31++G** level.

	Mulliken charges												
	C_1	**N**	**Cl**	**C_2**	**O**	**H_T**	**H_O**	**O_{OH}**	**H_{OH}**	**O_{WO}**	**H_{WO}**	**O_{WN}**	**H_{WN}**
Model I													
R	–0.33	–0.27	–0.03	–0.19	–0.46	0.16	0.37	–1.20	0.20	-	-	-	-
RIC	–0.37	–0.29	–0.07	–0.27	–0.51	0.23	0.37	–1.09	0.28	-	-	-	-
TS	–0.42	–0.26	–0.26	–0.20	–0.49	0.30	0.38	–0.90	0.25	-	-	-	-
PIC	–0.18	–0.18	–0.85	–0.28	–0.49	0.32	0.37	–0.71	0.29	-	-	-	-
P	–0.15	–0.12	–0.90	–0.34	–0.46	0.31	0.36	–0.72	0.31	-	-	-	-
Model II													
R	–0.33	–0.27	–0.03	–0.19	–0.46	0.16	0.37	–1.05	0.25	–0.93	0.48	-	-
RIC	–0.39	–0.23	–0.07	–0.22	–0.48	0.21	0.36	–1.11	0.30	–0.85	0.47	-	-
TS	–0.40	–0.23	–0.30	–0.21	–0.48	0.30	0.38	–0.96	0.32	–0.83	0.47	-	-
PIC	–0.15	–0.18	–0.83	–0.32	–0.48	0.32	0.37	–0.76	0.34	–0.74	0.38	-	-
P	–0.15	–0.12	–0.84	–0.34	–0.46	0.31	0.36	–0.76	0.34	–0.75	0.38	-	-
Model III													
R	–0.33	–0.44	0.05	–0.21	–0.50	0.15	0.42	–1.05	0.25	–0.93	0.48	–0.77	0.46
RIC	–0.33	–0.45	–0.05	–0.09	–0.52	0.22	0.40	–1.09	0.30	–0.87	0.48	–0.78	0.47
TS	–0.38	–0.43	–0.27	–0.04	–0.52	0.29	0.40	–0.96	0.31	–0.83	0.47	–0.80	0.49
PIC	–0.22	–0.22	–0.80	–0.20	–0.52	0.32	0.41	–0.76	0.34	–0.75	0.39	–0.79	0.44
P	–0.12	–0.18	–0.84	–0.30	–0.51	0.31	0.42	–0.76	0.34	–0.75	0.38	–0.78	0.43

2.3.2 Microsolvated plus continuum model

The calculated Gibbs free energy including continuum model for the three microsolvated models is reported in Table 2.1 and shown in Figure 2.2. The formation of RICs is an activated process, presenting a barrier around 23 kcal·mol^{-1} in the three models, while the corresponding TSs are located above the reference R. In the initial step partial desolvation of the reagents, mainly HO^-, gives rise to a free energy barrier in contrast to microsolvated models. This result is consistent with those obtained for other reactions involving HO^- attack calculated by different computational methods, *i.e.* PCM-B3LYP,[27] Monte Carlo,[28] or QM/MM molecular dynamics.[29] The value for the free energy barrier between RIC and TS (ΔG_{int}) is similar to the values obtained with simple microsolvation in models I and II, but this is not the case for model III, where the value is reduced from 7.39 kcal·mol^{-1} to 0.78 kcal·mol^{-1}. This result can be explained by considering the differences in charge stabilization between both stationary points, TS and RIC; thus, polar media stabilize the former more efficiently than the latter. Consequently, the rate increases when incorporating the continuum model to simulate the aqueous solvent.

Some authors endorsed the suitability of a hybrid approach using a combination of explicit solvent molecules and continuum model for the calculation of the solvation thermodynamic properties of ions, in particular HO^-.[30-33] It is important to remark that this kind of computational model must be used with some caution. We do not claim that the inclusion of two discrete water molecules plus a continuum represented by a dielectric constant are enough for modelling the aqueous solvent, but apparently the inclusion of the continuum model and two water molecules could produce a reasonable picture of the elimination process both in terms of structure and energy. Certainly, a more detailed dynamical treatment should be performed in order to confirm the role of the structural and dynamical properties of ions in water. In a recent study, Chen *et al*[34] carried out Car-Parrinello molecular dynamics simulations to identify the structural and dynamic behavior of HO^- in water, and its relationship with the formation of hydroxide ion-water complexes. Nevertheless, in the present study quantum chemical calculations revealed the role of water in the title reaction, and the characteristics of the elimination obtained with water clusters and PCM should hold in the reaction in bulk solvent. Discrete water molecules directly participate in the TS, making its geometry less strained and more favourable for the reaction to proceed, thereby facilitating the formation and cleavage of bonds that lead to products, while the continuum model stabilizes the localized charges at the TS reducing its energy, and speeding up the chemical reaction.

2.4 Conclusions

We report a comprehensive study of the Hofmann elimination in the reaction between *N*-Cl,*N*-methylethanolamine and HO^- to yield 2-methyleneamino-ethanol, water, and Cl^- both in the gas phase and in aqueous solution. Our results can be summarized as follows: (i) the process corresponds to an asynchronous concerted $A_{XH}D_HD_N$ mechanism. (ii) Specific solvent effects were also taken into account, including in the computations up to two explicit water molecules. Our results indicate that two discrete water molecules lower the reaction barrier, enhancing the N-Cl bond-breaking, which leads to the formation of Cl^-. To be efficient in such process, one of the water molecules acts both as H^+ donor/acceptor to/from the nitrogen/oxygen atom of *N*-Cl,*N*-methylethanolamine, respectively. This water molecule, not involved in a proton relay mechanism, causes a polarization effect, essentially on the N atom, favouring the nucleofuge departure. This observation suggests cooperative hydrogen structural motif involving a water molecule, which may be important in the chemical reaction. This cooperative effect enhances the charge redistribution at the TS. The reaction can be viewed as a prototype for water-assisted elimination rearrangement. (iii) Bulk solvent effects, described by PCM continuum model, change significantly the energy profile: the formation of RICs is an activated process, and the corresponding TSs are located above the reactants. In the case of the hybrid discrete-continuum model described by two water molecules plus PCM, the step leading to the TS becomes nearly barrierless. This work contributes to a qualitative understanding of solvent effects on chemical reactivity.

This study has been published as: D. R. Ramos, R. Castillo, M. Canle L., M. V. García, J. Andrés, and J. A. Santaballa, Chem.

Phys. Lett., 2006 **429** (4-6) 425-429.

2.5 References

1. S. J. Klebanoff, *Myeloperoxidase-halide-hydrogen peroxide antibacterial system.* J. Bacteriol., 1968 **95** (6) 2131-2138.
2. E. L. Thomas, M. B. Grisham, and M. M. Jefferson, *Myeloperoxidase-dependent effect of amines on functions of isolated neutrophils.* J. Clin. Invest., 1983 **72** (2) 441-454.
3. I. U. Schraufstatter, K. Browne, A. Harris, P. A. Hyslop, J. H. Jackson, O. Quehenberger, and C. G. Cochrane, *Mechanisms of hypochlorite injury of target cells.* J. Clin. Invest., 1990 **85** (2) 554-562.
4. S. Miller, *Disinfection products in water treatment.* Environ. Sci. Technol., 1993 **27** (12) 2292-2294.
5. D. Henschler, *Toxicity of chlorinated organic compounds: effects of the introduction of chlorine in organic molecules.* Angew. Chem. Int. Ed. Engl., 1994 **33** (19) 1920-1935.
6. R. Franzén and L. Kronberg, *Determination of chlorinated 5-methyl-5-hydroxyfuranones in drinking water, in chlorinated humic water, and in pulp bleaching liquor.* Environ. Sci. Technol., 1994 **28** (12) 2222-2227.
7. X. L. Armesto, M. Canle L., M. V. García, and J. A. Santaballa, *Aqueous Chemistry of N-halo-compounds.* Chem. Soc. Rev., 1998 **27** (6) 453-460.
8. S. J. Klebanoff, *Oxygen metabolites from phagocytes*, in *Inflammation: basic principles and clinical correlates*, J.I. Gallin and R. Snyderman, Editors. 1999, Lippincott Williams & Wilkins: Philadelphia. 721.
9. X. L. Armesto, M. Canle. L., P. Carretero, M. V. García, and J. A. Santaballa, *Evidence for an intramolecular elimination mechanism in the aqueous decomposition of (N-Cl)-alcoholamines.* Tetrahedron, 1997 **53** (7) 2565-2572.
10. J. Andrés, X. L. Armesto, M. Canle L., M. V. García, D. R. Ramos, and J. A. Santaballa, *Understanding the mechanism of base-assisted decomposition of (N-halo),N-alkylalcoholamines.* Org. Biomol. Chem., 2003 **1** (23) 4323-4328.
11. M. J. Frisch, G. W. Trucks, H. B. Schlegel, G. E. Scuseria, M. A. Robb, J. R. Cheeseman, V. G. Zakrzewski, J. A. Montgomery, R. E. Stratmann, J. C. Burant, S. Dapprich, J. M. Millam, A. D. Daniels, K. N. Kudin, M. C. Strain, O. Farkas, J. Tomasi, V. Barone, M. Cossi, R. Cammi, B. Mennucci, C. Pomelli, C. Adamo, S. Clifford, J. Ochterski, G. A. Petersson, P. Y. Ayala, Q. Cui, K. Morokuma, D. K. Malick, A. D. Rabuck, K. Raghavachari, J. B. Foresman, J. Cioslowski, J. V. Ortiz, B. B. Stefanov, G. Liu, A. Liashenko, P. Piskorz, I. Komaromi, R. Gomperts, R. L. Martin, D. J. Fox, T. Keith, M. A. Al-Laham, C. Y. Peng, A. Nanayakkara, C. Gonzalez, M. Challacombe, P. M. W. Gill, B. G. Johnson, W. Chen, M. W. Wong, J. L. Andres, M. Head-Gordon, E. S. Replogle, and J. A. Pople, *Gaussian 98*. 1998, Gaussian, Inc.: Pittsburgh PA.
12. A. D. Becke, *Density-functional exchange-energy approximation with correct asymptotic behavior.* Phys. Rev. A, 1988 **38** (6) 3098-3100.
13. A. D. Becke, *Density-functional thermochemistry. III. The role of exact exchange.* J. Chem. Phys., 1993 **98** (7) 5648-5652.
14. Y. Ren, J. L. Wolk, and S. Hoz, *The performance of density function theory in describing gas-phase S_N2 reactions at saturated nitrogen.* Int. J. Mass. Spectrom., 2002 **221** (1) 59-65.
15. D. A. McQuarrie, *Statistical Mechanics*. 2000, Sausalito, CA: University Science Books.
16. J. W. McIver, *Structure of transition states. Are they symmetric?* Acc. Chem. Res., 1974 **7** (3) 72-77.
17. K. Fukui, *Formulation of the reaction coordinate.* J. Phys. Chem., 1970 **74** (23) 4161-4163.
18. C. Gonzalez and H. B. Schlegel, *Reaction path following in mass-weighted internal coordinates.* J. Phys. Chem., 1990

94 (14) 5523-5527.

19. C. Gonzalez and H. B. Schlegel, *Improved algorithms for reaction path following: Higher-order implicit algorithms.* J. Chem. Phys., 1991 **95** (8) 5853-5860.
20. J. E. Carpenter and F. Weinhold, *Analysis of the geometry of the hydroxymethyl radical by the "different hybrids for different spins" natural bond orbital procedure.* J. Mol Struct.-Theochem, 1988 **169** 41-62.
21. E. D. Glendening, A. E. Reed, J. E. Carpenter, and F. Weinhold, *NBO Version 3.1*.
22. A. E. Reed, L. A. Curtiss, and F. Weinhold, *Intermolecular interactions from a natural bond orbital, donor-acceptor viewpoint.* Chem. Rev., 1988 **88** (6) 899-926.
23. J. Tomasi and M. Persico, *Molecular interactions in solution: An overview of methods based on continuous distributions of the solvent.* Chem. Rev., 1994 **94** (7) 2027-2094.
24. J. Andrés, M. Canle L., M. V. García, L. F. Rodríguez Vázquez, and J. A. Santaballa, *A B3LYP/6-31G** study on the chlorination of ammonia by hypochlorous acid.* Chem. Phys. Lett., 2001 **342** (3-4) 405-410.
25. R. D. Guthrie and W. P. Jencks, *IUPAC recommendations for the representation of reaction mechanisms.* Acc. Chem. Res., 1989 **22** (10) 343-349.
26. H. Maskill, *The physical basis of organic chemistry*. 1986, Oxford: Oxford University Press.
27. J. Kóňa, W. M. F. Fabian, and P. Zahradník, *Ab initio and DFT studies on the mechanism of ring-opening reactions of 4H-1-benzopyran-4-one with hydroxide ion.* J. Chem. Soc., Perkin Trans. 2, 2001 (3) 422-426.
28. J. D. Madura and W. L. Jorgensen, *Ab initio and Monte Carlo calculations for a nucleophilic addition reaction in the gas phase and in aqueous solution.* J. Am. Chem. Soc., 1986 **108** (10) 2517-2527.
29. T. Hori, H. Takahashi, and T. Nitta, *Hybrid QM/MM molecular dynamics simulations for an ionic S_N2 reaction in the supercritical water: $OH^- + CH_3Cl \rightarrow CH_3OH + Cl^-$.* J. Comput. Chem., 2003 **24** (2) 209-221.
30. I. Tuñón, D. Rinaldi, M. F. Ruiz-López, and J. L. Rivail, *Hydroxide ion in liquid water: structure, energetics, and proton transfer using a mixed discrete-continuum ab initio model.* J. Phys. Chem., 1995 **99** (11) 3798-3805.
31. A. R. Grimm, G. B. Bacskay, and A. D. J. Haymet, *Quantum chemical studies of the solvation of the hydroxide ion.* Mol. Phys., 1995 **86** (3) 369-384.
32. C. Cappelli, B. Mennucci, C. O. da Silva, and J. Tomasi, *Refinements on solvation continuum models: Hydrogen-bond effects on the OH stretch in liquid water and methanol.* J. Chem. Phys., 2000 **112** (12) 5382-5392.
33. C. G. Zhan and D. A. Dixon, *First-principles determination of the absolute hydration free energy of the hydroxide ion.* J. Phys. Chem. A, 2002 **106** (42) 9737-9744.
34. B. Chen, I. Ivanov, J. M. Park, M. Parrinello, and M. L. Klein, *Solvation structure and mobility mechanism of OH^-: a Car–Parrinello molecular dynamics investigation of alkaline solutions.* J. Phys. Chem. B, 2002 **106** (46) 12006-12016.

CHAPTER 3

A theoretical study on the mechanism of the base-promoted decomposition of *N*-Cl,*N*-methylethanolamine

Life can only be understood backwards,
but it must be lived forwards.

Søren Aabye Kierkegaard

3.1 Introduction

Experimental and computational research devoted to the determination of reaction mechanisms is an issue of major concern in chemistry.[1] Theoretical characterization of geometry and energy of stationary points on potential energy surfaces (PESs) has significantly improved our understanding of intrinsic reactivity, helping to unravel the molecular mechanism of chemical reactions. However, molecular modelling of chemical processes in solution is a very demanding task; in this sense one of the currently accepted solvation models is to combine explicit water molecules, to mimic specific solute-solvent interactions at the first solvation shell, and a dielectric continuum to model bulk solvent properties.

Chemical reactivity involving *N*-halo compounds has been widely studied at a macroscopic level over the past 40 years due to their relevance to both environmental and biological chemistry.[2] In this sense, chlorination is still the most used method of water treatment,[3] despite its presumed relationship with cancer.[4] This fact together with the inability of aqueous chlorine to inactivate certain microorganisms have promoted the search of safer alternative water treatment methods, jointly known as advanced oxidation processes.[5] On the other hand, chlorination is essential in leukocyte protection against infection in mammals,[6-8] and it has also been related to cell lysis[7] and other disorders related to inflammation.[9] When leukocites are activated, the enzyme myeloperoxidase reacts with chloride ion and hydrogen peroxide to generate either HClO or an oxidizing enzyme complex, which chlorinate a wide variety of nitrogenated compounds.[10-12]

Formation and decomposition of numerous halogenated nitrogen species has been examined experimentally.[2] Chlorination of amines and amino acids by HClO shows a complex dependence on acidity, its maximum rate appearing near neutral pH. After its formation, *N*-Cl compounds decompose; the higher the basicity of the medium, the faster their decomposition rate. Base-promoted decomposition of *N*-Cl derivatives of aliphatic secondary amines in aqueous solution is not particularly fast; for example the corresponding second-order rate constant for the HO^--promoted decomposition of $CH_3N(Cl)CH_2CH_3$ is *ca.* 2×10^{-4} $mol \cdot dm^{-3}.s^{-1}$ at 298 K. The currently accepted mechanism for the base-promoted decomposition of *N*-Cl amines involves two consecutive steps. The first one is the rate-determining step of the reaction and corresponds with an elimination reaction, Hofmann or Zaitsev (see Scheme 3.1). The second step is the fast hydrolysis of the so-formed imine. Noticeable rate enhancement is observed when parent *N*-Cl ethanolamines are considered;[13, 14] for example the observed second order rate constant for the HO^--promoted decomposition of $CH_3N(Cl)CH_2CH_2OH$ is 360-fold higher than that of *N*-Cl,*N*-methylethylamine.[14] Such a rate increase could be ascribed to the inductive effect due to the –OH group, which should make more acidic the hydrogen being transferred, but product analysis did not support such a hypothesis. Unexpected production of formaldehyde was observed in the case of *N*-Cl,*N*-methylethanolamine, which was contrary to such an inductive effect; furthermore, non-stoichiometric amounts were found.

These facts are in agreement with two additional competitive pathways for the rate-determining base-promoted decomposition of secondary *N*-Cl ethanolamines: bimolecular fragmentation and intramolecular elimination, which are responsible for the reaction rate enhancement (Scheme 3.1). Experimental data point to all four pathways being asynchronous concerted processes.[14]

Aminoalcohols are widely used as feedstock in the production of chemical intermediates, pharmaceuticals, polishes, detergents, and emulsifiers. They have also relevant applications as corrosion inhibitors or for scrubbing certain acidic gases.[15] In particular, *N*-methylethanolamine is involved in the biosynthesis of choline, a precursor of acetylcholine in mammals, a neurotransmitter of the peripheral and the central nervous system.[16] It has also been proposed to play a role in the prebiotic synthesis of vitamin B6-type systems.[17] These compounds have beneficial therapeutic effect on cardiac diseases, as cardiac fibrosis,[18] and might play a role in the regulation of synaptic vesicle filling.[19] *N*-Methylethanolamine is the simplest choice of the family, and thus was selected as model compound for the electronic structure calculation of the mechanism of decomposition of secondary *N*-halo ethanolamines in alkaline medium. Hofmann elimination has been recently analyzed computationally by B3LYP using the 6-31++G(d,p) basis set,[20] and the description of the detailed mechanism is consistent with the experimental data.[14]

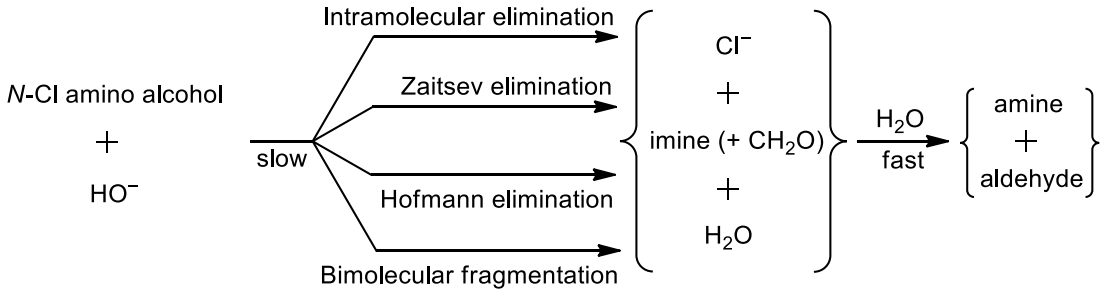

Scheme 3.1 General mechanism for the base-promoted decomposition of aliphatic secondary *N*-Cl ethanolamines in aqueous solution.

In this work, we present electronic structure calculations to shed light on the four parallel reaction pathways associated to the base-promoted decomposition of secondary *N*-halo ethanolamines: Hofmann, Zaitsev and intramolecular eliminations, and bimolecular fragmentation (see Scheme 3.1). The model that revealed to be more appropriate[20] is used here at a higher computational level to examine the reaction between *N*-Cl,*N*-methylethanolamine and hydroxide ion. To model solvent effects, we have included two explicit water molecules simulating specific solute-solvent interactions, and further utilized the continuum method to take into account the effect of bulk solvent. The results are compared with previously obtained experimental data.[14]

3.2 Computational methods

All calculations have been carried out with the Gaussian98 suite of programs.[21] Minima and transition structures were fully optimized at MP2=full/6-31++G(d,p) computational level; the perturbation theory of Møller-Plesset truncated at second order was used to consider the correlation energy.[22] The nature of the molecular mechanisms has been elucidated by characterizing stationary points on the PES: reactants (R), bound reactant-like complexes (called hereafter reactant interaction complex (RIC)), transition structures (TS), and product interaction complexes (PIC), which open the channel to reach the products (P). It should be mentioned that, for the four considered decomposition reactions, any attempt to localize a stepwise mechanism involving HO^--promoted H^+ removal and N–Cl bond breaking was unsuccessful.

Harmonic frequencies were calculated in order to confirm the nature of the stationary points, one imaginary frequency for TSs and zero for local minima. Zero point energies and thermal corrections to enthalpies and free energies at 298.15 K have been taken into account. The unique imaginary frequency associated with the transition vector (TV) of the different TSs has been analyzed.[23] The intrinsic reaction coordinate has been traced from the TSs down to the two lower energy structures (RIC and PIC), in order to verify that each saddle point links the two putative minima.[24-26]

Among the different procedures to describe solute-solvent interactions at the quantum level, the use of discrete water molecules and continuum models have been selected. High-level *ab initio* electronic structure calculations including even a modest number of solvent molecules are prohibitive computationally. On the other hand, continuum models are very popular due to their combination of simplicity and efficiency, however they are unlikely to be adequate for the description of the reaction under study in water, as a cavity is built around the bare solute and therefore short-range solvent-solute interactions are not explicitly considered. The model employed in this work consists of *N*-Cl,*N*-methylethanolamine and HO^-, which promotes the reaction, with one discrete water molecule interacting with the incoming HO^- and another molecule acting as H^+ donor to the nitrogen atom of the amine. This cluster showed a good behaviour when studying the Hofmann elimination;[20] it can describe adequately the solute-solvent interaction in the first solvation layer by stabilization of localized charges, but long-distance solvent stabilization is ignored. Some authors endorsed the suitability of a hybrid approach using a combination of explicit solvent molecules and continuum model for the calculation of the solvation thermodynamic properties of ions, in particular HO^-.[27-30] Thus, a hybrid cluster-continuum model was

considered. Single-point calculations were performed over the optimized microsolvated structures, using the polarized continuum model (PCM)[31] to estimate the Gibbs free energy of solvation, allowing a better description of the process in bulk water.[32]

It is important to remark that this kind of computational model must be used with caution. We do not claim that the inclusion of two discrete water molecules plus a continuum represented by a dielectric constant are enough for rigorously modelling the aqueous solvent, but apparently the inclusion of the continuum model and two water molecules produces a reasonable picture of the processes under study both in terms of structure and energy.

Evolution of relevant bonds along each reaction pathway was calculated using the natural population analysis of Weinhold *et al*.[21, 33-35] In order to analyze the synchronicity of the four pathways, the S_Y parameter proposed by Moyano *et al* has been used.[36, 37]

3.3 Results

3.3.1 Energy and reactivity

Figure 3.1 shows the free energy profiles for the four decomposition processes under study. Figure 3.1A collects microsolvated data, *i.e.*, including two discrete water molecules, and Figure 3.1B shows the results obtained with the hybrid microsolvated-continuum model. Three stationary points have been characterized on the PES: the RIC, the TS, and the corresponding PIC; for comparison purposes the reactants were taken as reference. Although the four pathways correspond to different chemical processes, and thus the reaction centres and products are not the same (Scheme 3.2), the free energy profiles obtained are similar. Reaction pathways produced by the microsolvated model present an inverted energy profile in all cases (Figure 3.1A), while the deep effect of solvation is evident in Figure 3.1B.

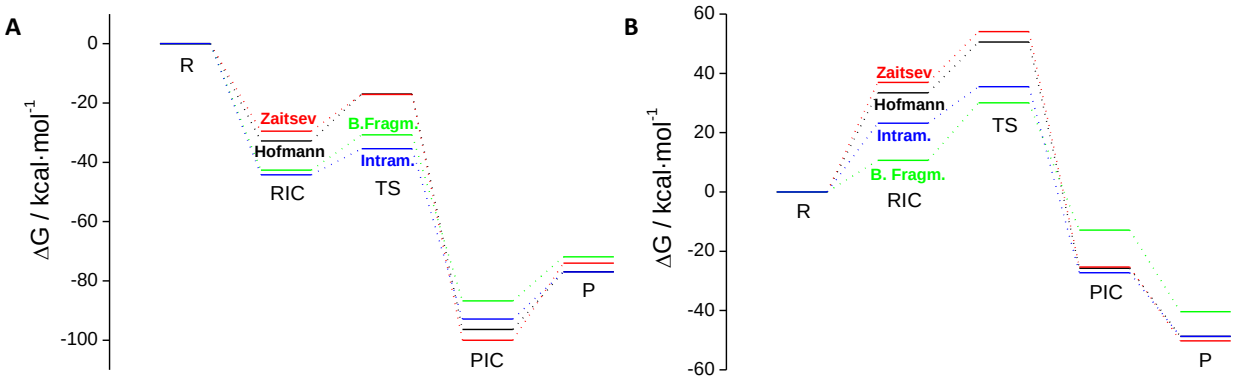

Figure 3.1. Gibbs free energy profiles for the four pathways found for the HO^--promoted decomposition of *N*-Cl,*N*-methylethanolamine at the MP2=full/6-31++G(d,p) computational level. Reactants (R) were taken as reference. Data obtained with (A) microsolvated and (B) microsolvated plus continuum models.

Despite the fact that RIC and/or PIC do not represent true minima on the PES when the continuum model is used to describe reactions in solution, we have retained them in the computational study with the hybrid cluster-continuum model. A physical meaning has been traditionally assigned to RIC and PIC in solution. Many bimolecular steps in solution can be described similarly to the mechanism of proton transfer first proposed by Eigen;[38] such bimolecular processes involve the passage through three well defined stages: 1) diffusion together of reactants to give an encounter complex (here named RIC); 2) electron and/or molecular rearrangement, *i.e.*, the chemical change associated to the bond-breaking/bond-forming

processes involved in TSs; and, if appropriate, 3) dissociation of the products encounter complex (here named PIC) into separate products.[38] This conceptual scheme can be also translated quantitatively into kinetics by using Marcus theory:[38]

$$\Delta G^{\circ\ddagger} = w^r + \Delta G^{\circ\ddagger}_0 \left(1 + \frac{\Delta G^\circ_e}{4\Delta G^\circ_0}\right)$$

where the work term w^r represents the standard molar free-energy involved in bringing reactants together in the right configuration for the chemical event to take place, *i.e.* ΔG°(R→RIC). The meaning of other terms is described elsewhere.[38]

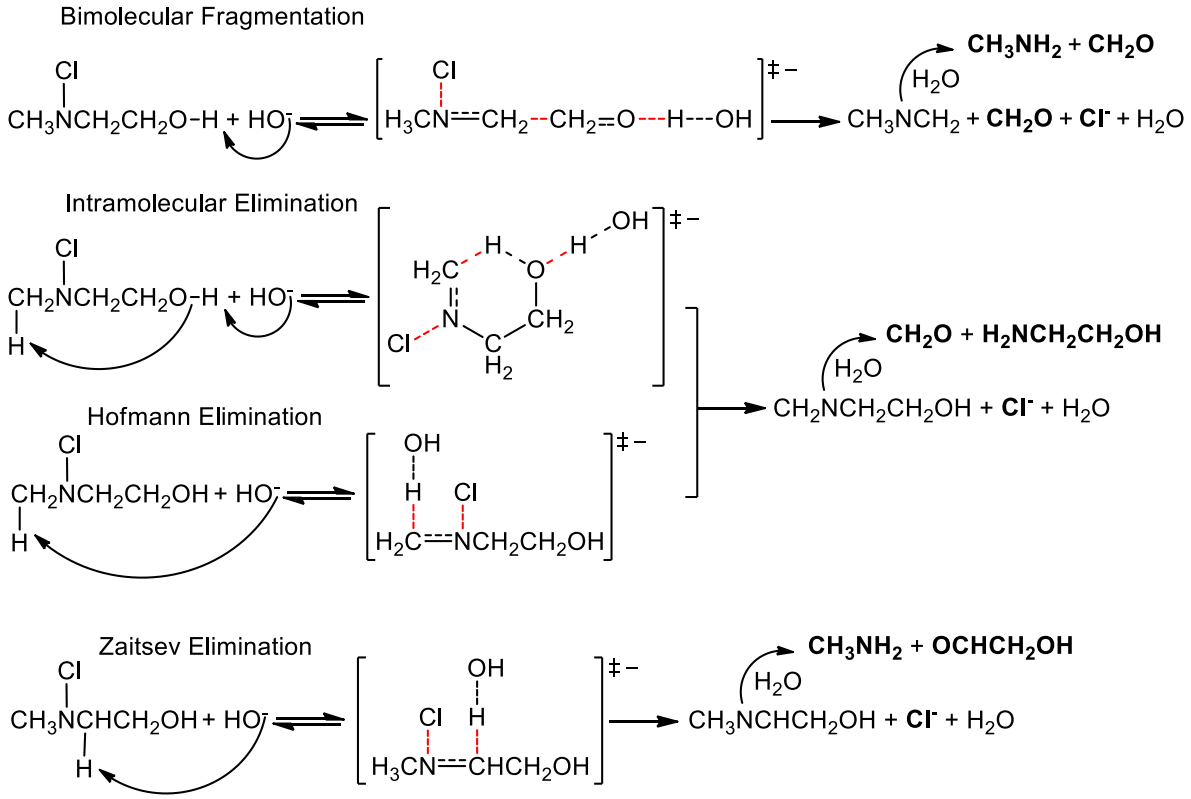

Scheme 3.2. The four parallel pathways involved in the rate-determining step of the HO^--promoted decomposition of *N*-Cl,*N*-methylethanolamine. Bonds being broken (in red) and formed (in black) are shown as dashed lines. End products through each pathway are shown in bold. Notice that the products of Hofmann and intramolecular eliminations are the same, and thus these two pathways are indistinguishable by product analysis.

Calculated thermodynamic parameters are reported in Table 3.1. In both models, reactions can be described as three sharply separable parts: (a) the formation of RIC from reactants corresponds to an activationless process in the microsolvated model, while the approach of the incoming HO^- and *N*-Cl,*N*-methylethanolamine to form the RIC requires a minimum of 20 kcal·mol^{-1} in the hybrid microsolvated-continuum model. In the microsolvated model, energy reduction comes from the stabilization of ions (HO^-) by hydrogen bonding with the amine and/or water molecules, whereas in the hybrid discrete-continuum model, bulk solvation stabilizes more the charge present in reactants than the more diffused charge in RIC; (b) bond-breaking/bond-forming processes corresponding to the formation of the TSs of the four parallel pathways under study. The N–Cl bond is always broken, a C–N single bond is transformed into a C=N double bond (imine), and the corresponding H atom is transferred from *N*-Cl,*N*-methylethanolamine to the incoming HO^-. Further reorganization is also carried out according to each molecular process (Scheme 3.2); (c) formation of energetically more stable PIC and

products (P). The position of P with respect to PIC also depends on the presence of the continuum model.

Table 3.1. Thermodynamic parameters, ΔH, TΔS and ΔG (in kcal·mol^{-1}) for the four parallel pathways of HO^--promoted decomposition of *N*-Cl,*N*-methylethanolamine obtained at MP2=full/6-31++G(d,p) level (T = 298.15 K). Reactants (R) were taken as reference (total energy of R in kcal·mol^{-1}: H = –587266.68, T×S = 63.88, G = –587330.57, $G_{solvation}$ = –117.16). ΔG_{int} values refer to intrinsic activation barrier ($\Delta G_{int} = \Delta G_{TS} - \Delta G_{RIC}$). Values of Gibbs free energy obtained with PCM continuum model in italics. w^r parameter from Marcus equation corresponds to ∆G(R→RIC) (Ref. 38). Values between parentheses calculated at the DFT/B3LYP/6-31++G(d,p) level (Refs. 14 & 20). $\Delta G^{\ddagger}_{exp}$ refers to the experimental activation barriers (Ref. 14). Values rounded to show two significant figures.

RIC	**ΔH°**	**TΔS°**	**ΔG°**	**w^r**			
Hofmann elim.	–59	–26	–33	*34*			
Zaitsev elim.	–56	–26	–29	*37*			
Bimol. fragm.	–68	–25	–43	*11*			
Intram. elim.	–69	–25	–44	*23*			
TS	**ΔH°**	**TΔS°**	**ΔG°**		**ΔG_{int}**		**$\Delta G^{\ddagger}_{exp}$**
Hofmann elim.	–45	–28	–17	*51*	16 *17*	(7.5 *0.78)*	*24*
Zaitsev elim.	–43	–26	–17	*54*	12 *17*		*23*
Bimol. fragm.	–53	–22	–31	*30*	12 *19*	(6.5 *3.6)*	*19*
Intram. elim.	–60	–24	–35	*35*	8.8 *12*		*20*
PIC	**ΔH°**	**TΔS°**	**ΔG°**				
Hofmann elim.	–120	–23	–96	*–26*			
Zaitsev elim.	–124	–24	–100	*–25*			
Bimol. fragm.	–105	–18	–87	*–13*			
Intram. elim.	–113	–20	–93	*–27*			
P	**ΔH°**	**TΔS°**	**ΔG°**				
Hofmann elim.	–67	9.6	–77	*–49*			
Zaitsev elim.	–63	11	–74	*–50*			
Bimol. fragm.	–50	22	–72	*–40*			
Intram. elim.	–67	9.6	–77	*–49*			

In the microsolvated model (Figure 3.1A) the Gibbs free energy of activation corresponds to the intrinsic free energy barrier going from RIC to TS, labelled $\Delta G°_{int}$. According to this model, the intramolecular elimination pathway exhibits the lowest free energy of activation (Table 3.1). The obtained order of reactivity is: intramolecular elimination > bimolecular fragmentation > Zaitsev elimination > Hofmann elimination.

Although the structural parameters were not modified, addition of PCM bulk solvent, *i.e.*, hybrid cluster-continuum model, led to an effective change in all free energy reaction profiles, as reported in Table 3.1 and shown in Figure 3.1B. The formation of structures with RIC geometries is an activated process, while the corresponding TSs are now located above the reference R. In the initial, step partial desolvation of the reagents, mainly HO^-, gives rise to a free energy barrier in contrast to the microsolvated model. This result is consistent with those obtained for other reactions involving HO^- attack calculated by different computational methods, such as PCM-B3LYP,[39] Monte Carlo,[40] or QM/MM molecular dynamics.[41] In all cases, $\Delta G°_{int}$ increases when PCM solvation is incorporated (Table 3.1). The lowest free energy intrinsic barrier of the four processes is again obtained for the intramolecular elimination. Similar activation Gibbs energy values were calculated for the Hofmann and Zaitsev eliminations, while bimolecular fragmentation presents the largest value of the barrier height.

A detailed analysis of solvation in going from RIC to TS, in the hybrid cluster-continuum model, shows the main and energetically favourable contribution comes from the electrostatic term (Table 3.2), while the average contribution of the non-electrostatic term is positive and amounts to about 0.5 kcal·mol^{-1}. The RIC of bimolecular fragmentation shows the most negative solvation energy, whereas similar values are found for the rest of RICs. The same pattern applies for TSs, but stabilization due to solvation is lower, and consequently destabilization is obtained in going from RIC to TS, this effect being stronger in the case of bimolecular fragmentation. Although there is no unique way to separate electrostatic and non-electrostatic contributions to the free energy of solvation,[42] results will not differ using other partition schemes.

Table 3.2 Contribution of the electrostatic and non-electrostatic terms to the solvation energy in the four parallel base-promoted decomposition pathways. All values in kcal·mol^{-1}. Values rounded to show two significant figures.

	Hofmann elim.	**Zaitsev elim.**	**Bimol. fragm.**	**Intram. elim.**
RIC				
Electrostatic term	–60	–60	–74	–59
Non-electrostatic term	7.2	7.8	7.9	7.5
TS				
Electrostatic term	–58	–55	–66	–55
Non-electrostatic term	6.7	7.5	7.3	7.2
RIC→TS				
$\Delta G_{electrostatic}$	1.8	5.1	8.2	3.9
$\Delta G_{non\text{-}electrostatic}$	–0.52	–0.37	–0.66	–0.34
$\Delta G_{solvation}$	1.3	4.8	7.5	3.5

Values for absolute activation Gibbs free energies, $\Delta G°(R \rightarrow TS)$, with the cluster-continuum hybrid model (Table 3.1) have been calculated by using the thermochemical cycle shown in Scheme 3.3. The corresponding values have been corrected in order to use consistent standard states.[43]

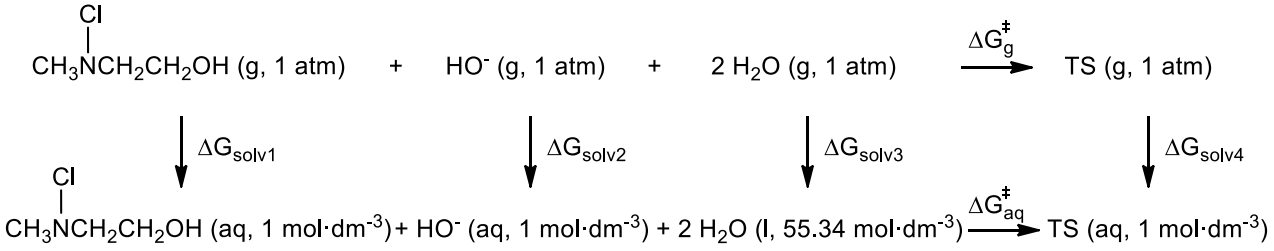

$$\Delta G^{‡}_{aq} = \Delta G^{‡}_{g} - \Delta G_{solv1} - \Delta G_{solv2} - 2\cdot\Delta G_{solv3} + \Delta G_{solv4}$$

Scheme 3.3. Thermochemical cycle used to estimate the activation Gibbs free energy in aqueous solution.

3.3.2 Geometry

Geometries of TSs, connecting RIC and PIC, for each model system are shown in Figure 3.2, and representative structural parameters of calculated stationary points are collected in the supplementary information.

TSs for Hofmann, Zaitsev, and intramolecular elimination processes exhibit cyclic arrangements (Figure 3.2), but only in the latter some bonds of the ring are broken/formed (see Scheme 3.2). These cyclic assemblies contribute to stabilize the TSs, distributing more uniformly atomic charges; in fact their dipole moments are lower than that of bimolecular fragmentation

(see supplementary information). In the intramolecular elimination a six-membered ring is formed by the bent backbone of *N*-methylethanolamine; both edges are linked by the hydrogen atom that is being transferred from methyl carbon atom (C_1) to the alcoholic oxygen (Figure 3.2). Non reaction-active 7-membered cycles are obtained in the TSs of the intermolecular eliminations, Hofmann and Zaitsev; such cyclic arrangements involve the ethanolamine fragment of the *N*-Cl compound and one of the discrete water molecules used to model specific solute-solvent interactions (Figure 3.2).

Those 7-membered cyclic assemblies present two hydrogen bonds: the water molecule acts both as H^+ donor/acceptor to/from the nitrogen/oxygen atom of *N*-Cl,*N*-methylethanolamine, respectively. A linear arrangement is obtained in the TS of the bimolecular fragmentation (Figure 3.2).

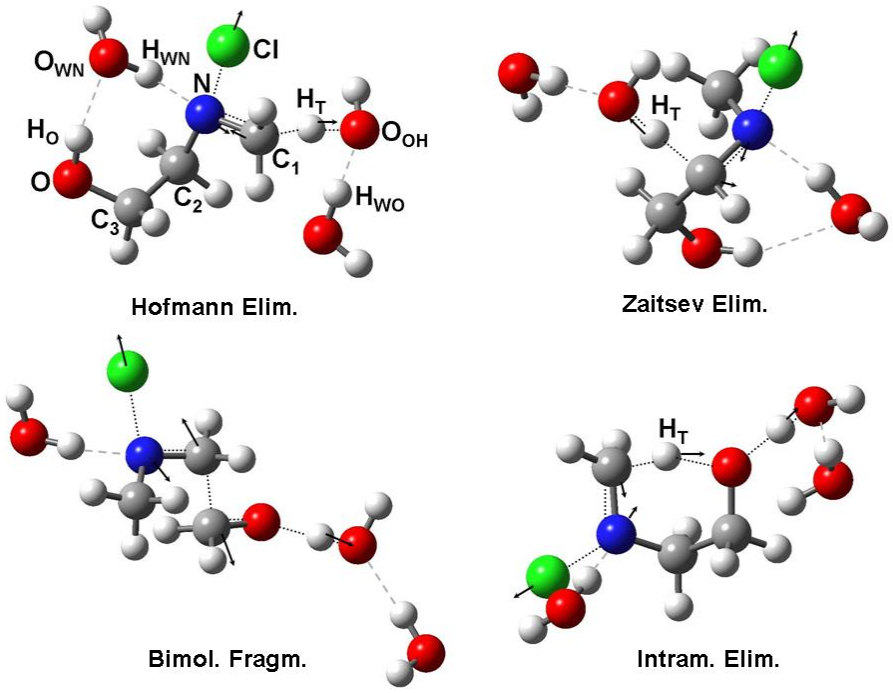

Figure 3.2. Optimized transition structures for the four decomposition pathways obtained at the MP2=full/6-31++G(d,p) level. Breaking/forming bonds are displayed as dotted lines, while hydrogen bonds are represented by dashed lines. Vibrational mode components in mass-weighted coordinates are also included. Atom numbering used through the paper is indicated: H_T is the proton transferred from a carbon atom, either C_1 or C_2, in the elimination reactions; H_O labels the proton initially bound to the alcohol group; two explicit hydrogen bonded water molecules are taken into account, one acting as H^+ donor to the O atom of incoming HO^- and the other to the N atom, these are labelled as WO and WN, respectively.

3.3.3 Transition vectors and bonds evolution

The transition vectors for the different TSs are represented in Figure 3.2. The components of TV for the different pathways are clearly associated with the bond-forming/bond-breaking processes. Thus, in the four pathways TVs are coupled with a proton transfer (H_T or H_O) to the oxygen atom (O_{OH}) of the incoming HO^-, formation of a C=N double bond (imine), and Cl^- acting as nucleofuge. In all cases the discrete water molecules also participate in the TV.

Evolution of relevant bonds along the reaction coordinate (supplementary information) confirms the behaviour revealed by TVs analysis. Four different bonds are concertedly formed/broken in the intermolecular Hofmann and Zaitsev eliminations, while six bonds are converted in the other two processes (Scheme 3.2). Again, the shared features of the four pathways are imine formation, N–Cl cleavage, and proton transfer to the incoming HO^-, the latter being ahead of the other

molecular processes. This indicates that HO^- approach and subsequent proton abstraction triggers the decomposition mechanism.

3.3.4 Atomic charges

Electron flow takes place along the reaction from the incoming HO^- to the leaving Cl^- (relevant Mulliken atomic charge values are collected as supplementary information). The net atomic charge of the H atoms being transferred at the TSs increases from R to TS due to the enhancement of the polarity of the bonds being formed/broken. This value ranges from 0.30 to 0.56 a.u. In addition, at the TSs the net negative charge displaced from the hydroxide moiety varies in the range 44 - 71 % of the total charge transferred along the whole process, and the chlorine fragment holds a net negative charge between 0.23 - 0.48 a.u. depending on the pathway under consideration.

3.4 Discussion

It has been observed experimentally that the decomposition reaction of *N*-Cl,*N*-methylethanolamine in basic medium fulfils a second-order rate law, being first order relative to both chloramine and base,[14] *i.e.*, in the present case:

$$r = k_{obs} \cdot [N\text{-Cl},N\text{-methylethanolamine}] \cdot [HO^-]$$

As stated above, the net reaction is more complex, the final products being Cl^-, an aldehyde, and an amine with at least one carbon less. Kinetic experiments are consistent with the Cl^- leaving as a nucleofuge, the imine formation and the proton cleavage taking place in the rate-limiting step,[2, 13, 14] which could be classified as an asynchronous concerted process.[14] Subsequent hydrolysis of the imine is much faster than its formation, *i.e.*, such hydrolysis has no influence on the observed rate of *N*-Cl,*N*-methylethanolamine decomposition.[2]

Previous density functional theory (DFT) calculations on the Hofmann rearrangement[20] allowed us to establish a suitable model to simulate the reaction in water, and therefore, it was employed again, this time at the *ab initio* MP2=full/6-31++G(d,p) computational level. Transition vectors (Figure 3.2) obtained for the four pathways taking place in the HO^--promoted decomposition of *N*-Cl,*N*-methylethanolamine, agree with each process being a bimolecular concerted step, which fits to overall second-order kinetics as well.

Description of those molecular processes is consistent with the proposed detailed reaction pathways coming from experimental studies.[2, 14] Six bonds are involved along the breaking/forming processes of the intramolecular elimination and bimolecular fragmentation, while only four bonds are directly involved in the Hofmann and Zaitsev eliminations (Scheme 3.2 and supplementary information).[14]

At the TSs all H atoms being transferred to HO^- increase their positive charge between 0.14 and 0.37 a.u.; therefore, the reaction has a proton transfer character. The other H atom "in flight" in the intramolecular elimination (H_T) is also 0.16 a.u. more positive at TS; the process can also be considered as a proton transfer. All proton transfer processes take place along geometrical linear arrangements (bond angles > 170°), except that of the 6-membered ring in the intramolecular elimination (155°). At the TSs the bond between H^+ and HO^- is more than 55% formed (supplementary information), but in the Zaitsev elimination, where this value is lower (34%). Bond evolution values indicate that proton transfer to HO^- triggers the rest of the molecular events (Scheme 3.2).

In the four pathways the corresponding imine is formed, and Cl^- acts as nucleofuge; additionally, formaldehyde works as electrofuge in the bimolecular fragmentation. Depending on the elementary step the N–Cl bond is broken between 7.1% and 37.5% at the TS. The increase of the Cl atom negative charge along the reaction coordinate is coupled with the decrease of the charge on the oxygen of the HO^- moiety; therefore, there is a synergetic charge flow generating an anion at the Cl-end (charges and bond evolution data are collected as supplementary information).

The net charge on N atom does not vary, relative to reactants, in either the Hofmann or Zaitsev eliminations, whereas it is less negative in the other two pathways; this is consistent with the degree of N–Cl bond breaking at the different TSs. The

interaction of the discrete water molecule in the neighbourhood of the amino group is reflected in the more negative charge on the N atom both at RIC and PIC. Consequently, there is a polarization effect on this water molecule, which stays fairly constant for each pathway when moving from RIC to PIC. Similar behaviour is obtained for the discrete water molecule near HO^-; in this case the negative charge of the oxygen decreases on going from RIC to TS due to the partial conversion of hydroxide ion into a water molecule. Finally, charge on the C atom involved in the formation of C–N double bond, C_1 or C_2, acquires its most negative value at TS.

The synchronicity values, S_y, as calculated from the bonds being formed or broken along the four reaction pathways, are collected as supplementary information. $S_y = 1$ implies fully synchronous bond reorganization, while $S_y = 0$ characterizes a stepwise mechanism. Thus, the S_y values support our previous analysis, *i.e.*, all pathways are concerted but not fully synchronous, the order of synchronicity being: Zaitsev elimination < Hofmann elimination < intramolecular elimination < bimolecular fragmentation. The value obtained here for the bimolecular fragmentation is similar to that found with the DFT(B3LYP)/6-31++G(d,p) model.[14]

Synchronicity can also be calculated from empirical kinetics as $(1 - |\beta_H - |\beta_{lg}||)$,[14] where Brønsted β_H gives an estimation of the O–H_O bond breaking at the TS, and the Brønsted-like parameter β_{lg} measures the degree of N–Cl bond breaking at the TS.[38] Brønsted β_H values for intramolecular elimination and bimolecular fragmentation pathways are 0.45 and 0.60 respectively.[14] These values are consistent with what was obtained here, the evolution of O–H_O bond breaking at the TSs being calculated as 83.3% (β_H = 0.833) for the elimination, and 82.8% (β_H = 0.828) for the fragmentation. Experimental values have large uncertainties due to the curvature of the Brønsted plot, an observation already found for analogous base-promoted processes.[44] On the other hand, values of β_{lg}, estimated from experimental reaction rates obtained for the process under study for the chlorinated and brominated species, are –0.2 and –0.35 for bimolecular fragmentation and intramolecular elimination, respectively, their uncertainty being unknown as only two values were used to calculate β_{lg}.[14] Thus, empirical values for synchronicity are 0.60 for the fragmentation and 0.90 for the elimination. Keeping in mind the approximations underlying those values, the agreement with the theoretical ones is acceptable (see supplementary information). These results imply that the four pathways correspond with asynchronous concerted bimolecular processes.

Free energy activation barriers, and therefore kinetic constants, differ significantly from experimental data (Table 3.1). According to the microsolvated model the intramolecular elimination is the preferred pathway; its activation free energy being the lowest of the four competitive processes, as experimentally predicted by the extremely slow rate measured for *N*-Cl,*N*-*tert*butylethanolamine decomposition reaction.[13] On the other hand, the experimental study with *N*-Cl,*N*-methylethanolamine and HO^- pointed to the bimolecular fragmentation as the main decomposition pathway (67%), while the intramolecular pathway accounted for the remaining 33% of the reaction.[14] This partition into pathways was based on product analysis.

Addition of PCM to the microsolvated model increases activation barriers for all pathways in the present study, whereas the opposite was found for Hofmann elimination and bimolecular fragmentation at the less-demanding DFT-based B3LYP/6-31++G(d,p) level (see Table 3.1).[14, 20] Values for $\Delta H°$, $T\Delta S°$, and $\Delta G°$ are more negative when MP2 instead of DFT is used. On the other hand, energy barriers increase with the former when single point PCM calculations are included. This indicates that both computational methods, using the same basis set, differ on the free energy assignment of continuum-solvated models of RICs and TSs, thus yielding opposed solvation effects on the $\Delta G°_{int}$ values. Activation free energy increases, since charge polarization, and therefore, solvent stabilization, on the RIC is higher than in the TS (see Mulliken charges and dipolar moment at the supplementary information). Thus, polar solvents like water stabilize the former more efficiently than the latter. When PCM solvation is considered, the reactivity pattern is different from that in the case of the microsolvated model; then the intramolecular elimination is still the fastest pathway, while the bimolecular fragmentation becomes the slowest one.

One could wonder which barrier really corresponds to the activation free energy, $\Delta G°$(RIC→TS) (*i.e.*, $\Delta G°_{int}$), or $\Delta G°$(R→TS). In the absence of bulk solvation, there is no doubt that $\Delta G°_{int}$ is the energy barrier, whereas $\Delta G°$(R→TS) could be adequate

for processes in solution when non-inverted free energy reaction profiles are found (Figure 3.1B). This is caused by the partial desolvation of approaching reactants that is not sufficiently compensated by the additional interaction energies; in that case, RIC and PIC are not stationary structures. As stated before, geometries of PCM-solvated structures were not optimized, we just performed single-point calculations including the continuum model. Attempts to obtain unconstrained optimized structures of some of the stationary points including PCM were unsuccessful, even with Gaussian03.

All activation free energy values mentioned above have been obtained as ΔG°_{int}. However, the picture changes when the energy barrier is calculated from R to TS as depicted in Figure 3.1B. In this case the kinetically favoured process is the bimolecular fragmentation, as experimentally found,[14] followed by the sequence: intramolecular, Hofmann, and Zaitsev eliminations.

Both microsolvated and microsolvated plus PCM models predict a high acceleration of the decomposition reaction, *i.e.*, lower activation free energies, when the alcohol group is directly involved in the reaction, which is consistent with the dramatic (360-fold) rate acceleration experimentally observed when alcoholamines instead of parent amines are studied.[14] Fully optimized electronic structure calculations at the relatively sophisticated level MP2=full/6-31++G(d,p) and with a hybrid-continuum model to describe solvation effects often, like here, misjudge the absolute thermodynamic values even for simple reactions. However, the relative acceleration caused by the alcohol group is properly predicted.

The title decomposition reaction has only been described up to the point where the chloride anion departs and the imine is formed, while much less attention was paid to the subsequent hydrolysis of imines, even though the partition on different pathways is based on product analysis from such hydrolysis.[14] Imine hydrolysis has been considered to take place as suggested by Jencks and coworkers,[45, 46] and repeatedly verified afterwards. This process involves an uncatalyzed pathway, and is also subject to general base catalysis.[47] Thus, under the experimental conditions, the process would be accelerated. This second process seems to be faster, so that the previously described processes represent the rate-limiting step in all cases. Although decomposition reaction rates, and therefore observed kinetic rate constants, are not affected by the subsequent faster imine hydrolysis, this second step should be carefully taken into account since partition into pathways is performed on the basis of products analysis.[14] As shown in Scheme 3.2, imines produced through different pathways are not identical: the –OH group of the parent ethanolamine remains in imines coming from the three elimination processes, whereas it is absent in the imine formed in the bimolecular fragmentation pathway. Furthermore, when multiple functionality is present elsewhere in the molecule, imines may suffer from other side reactions,[48] like tautomerization. Thus, unexpected products are feasible, which could lead to misinterpret the relative contribution of the four pathways involved in the rate-determining step of the base promoted decomposition of aliphatic secondary *N*-Cl ethanolamines.

3.5 Conclusions

In this work, the rate-limiting step of the HO^--induced decomposition of *N*-Cl,*N*-methylethanolamine in water has been investigated using the MP2=full/6-31++G(d,p) method. To give an appropriate picture of this process, a microsolvated model (in which two explicit water molecules simulate the specific solvent effects) and a hybrid cluster-continuum model (by applying PCM on the previous results, to account for the bulk effect of solvent) have been explored. Our calculations showed that the reaction takes place via four different competitive pathways (bimolecular fragmentation, and Hofmann, Zaitsev, and intramolecular eliminations). The results indicated that all pathways can be considered as bimolecular asynchronous concerted processes, where proton transfer to HO^- is more advanced than all other molecular events, whereas imine formation is delayed. TSs of Hofmann, Zaitsev, and intramolecular eliminations have cyclic structures, only the latter being reactive. Hofmann and Zaitsev mechanisms involve a water molecule that acts both as H^+ donor/acceptor to/from the nitrogen/oxygen atom of *N*-Cl,*N*-methylethanolamine, respectively.

Computational studies agree with experimental findings in the global description of the processes, even accounting for the dramatic acceleration of the decomposition process due to the addition of an alcoholic group on C_β to the amino group of

N-Cl,*N*-methylethylamine.

According to the microsolvated model, intramolecular elimination is the most favourable decomposition pathway. On the other hand, our results indicate that the continuum increases all reaction barriers, lowering the computed rate constants, and when considering the free energy of activation from reactants, $\Delta G(R \rightarrow TS)$, bimolecular fragmentation is the preferred decomposition pathway, as found empirically in the reaction between HO^- and *N*-Cl,*N*-methylethanolamine.[14] To the best of our knowledge, this work is the first comprehensive computational study on the molecular mechanism for the reaction between *N*-chloro aliphatic secondary ethanolamines and bases.

This study has been published as: D. R. Ramos, R. Castillo, M. Canle L., M. V. García, J. Andrés, and J. A. Santaballa, Org. Biomol. Chem., 2009 **7** (9) 1807-1814.

3.6 References

1. H. Maskill, *The investigation of organic reactions and their mechanisms*. 2006, Oxford: Blackwell Publishing.
2. X. L. Armesto, M. Canle L., M. V. García, and J. A. Santaballa, *Aqueous chemistry of N-halo-compounds.* Chem. Soc. Rev., 1998 **27** (6) 453-460.
3. S. Miller, *Disinfection products in water treatment.* Environ. Sci. Technol., 1993 **27** (12) 2292-2294.
4. M. T. Do, N. J. Birkett, K. C. Johnson, D. Krewski, P. Villeneuve, and Canadian Cancer Registries Epidemiology Research Group, *Chlorination disinfection by-products and pancreatic cancer risk.* Environ. Health Perspect., 2005 **113** (4) 418-424.
5. T. Oppenländer, *Photochemical purification of water and air: advanced oxidation processes (AOPs): principles, reaction mechanisms, reactor concepts*. 2003, Weinheim: Wiley-VCH.
6. S. J. Klebanoff, *Myeloperoxidase-halide-hydrogen peroxide antibacterial system.* J. Bacteriol., 1968 **95** (6) 2131-2138.
7. I. U. Schraufstätter, K. Browne, A. Harris, P. A. Hyslop, J. H. Jackson, O. Quehenberger, and C. G. Cochrane, *Mechanisms of hypochlorite injury of target cells.* J. Clin. Invest., 1990 **85** (2) 554-562.
8. E. L. Thomas, M. B. Grisham, and M. M. Jefferson, *Myeloperoxidase-dependent effect of amines on functions of isolated neutrophils.* J. Clin. Invest., 1983 **72** (2) 441-454.
9. S. J. Klebanoff, *Oxygen metabolites from phagocytes*, in *Inflammation: basic principles and clinical correlates*, J. I. Gallin and R. Snyderman, Editors. 1999, Lippincott Williams & Wilkins: Philadelphia. 721.
10. C. S. Foote, T. E. Goyne, and R. I. Lehrer, *Assessment of chlorination by human neutrophils.* Nature, 1983 **301** (5902) 715-716.
11. D. R. Ramos, M. V. García, M. Canle L., J. A. Santaballa, P. G. Furtmüller, and C. Obinger, *Myeloperoxidase-catalyzed taurine chlorination: Initial versus equilibrium rate.* Arch. Biochem. Biophys., 2007 **466** (2) 221-233.
12. D. R. Ramos, M. V. García, M. Canle L., J. A. Santaballa, P. G. Furtmüller, and C. Obinger, *Myeloperoxidase-catalyzed chlorination: The quest for the active species.* J. Inorg. Biochem., 2008 **102** (5-6) 1300-1311.
13. X. L. Armesto, M. Canle. L., P. Carretero, M. V. García, and J. A. Santaballa, *Evidence for an intramolecular elimination mechanism in the aqueous decomposition of (N-Cl)-alcoholamines.* Tetrahedron, 1997 **53** (7) 2565-2572.
14. J. Andrés, X. L. Armesto, M. Canle L., M. V. García, D. R. Ramos, and J. A. Santaballa, *Understanding the mechanism of base-assisted decomposition of (N-halo),N-alkylalcoholamines.* Org. Biomol. Chem., 2003 **1** (23) 4323-4328.
15. J. Xiao, C. W. Li, and M. H. Li, *Kinetics of absorption of carbon dioxide into aqueous solutions of 2-amino-2-methyl-*

1-propanol + monoethanolamine. Chem. Eng. Sci., 2000 **55** (1) 161-175.

16. D. L. Nelson and M. M. Cox, *Lehninger Principles of Biochemistry*. 2008, New York: W. H. Freeman.
17. S. M. Austin and T. G. Waddell, *Prebiotic synthesis of vitamin B6-type compounds.* Orig. Life Evol. Biosph., 1999 **29** (3) 287-296.
18. K. Yamamoto, Y. Takahashi, T. Mano, Y. Sakata, N. Nishikawa, J. Yoshida, Y. Oishi, M. Hori, T. Miwa, S. Inoue, and T. Masuyama, *N-Methylethanolamine attenuates cardiac fibrosis and improves diastolic function: inhibition of phospholipase D as a possible mechanism.* Eur. Heart J., 2004 **25** (14) 1221-1229.
19. C. Liao and R. A. Nicholson, *Ethanolamine and related amino alcohols increase basal and evoked release of [3H]-D-aspartic acid from synaptosomes by enhancing the filling of synaptic vesicles.* Eur. J. Pharmacol., 2007 **566** (1-3) 103-112.
20. D. R. Ramos, R. Castillo, M. Canle L., M. V. García, J. Andrés, and J. A. Santaballa, *Density functional study of the Hoffmann elimination of (N-Cl),N-methylethanolamine in gas phase and in aqueous solution.* Chem. Phys. Lett., 2006 **429** (4-6) 425-429.
21. M. J. Frisch, G. W. Trucks, H. B. Schlegel, G. E. Scuseria, M. A. Robb, J. R. Cheeseman, V. G. Zakrzewski, J. A. Montgomery, R. E. Stratmann, J. C. Burant, S. Dapprich, J. M. Millam, A. D. Daniels, K. N. Kudin, M. C. Strain, O. Farkas, J. Tomasi, V. Barone, M. Cossi, R. Cammi, B. Mennucci, C. Pomelli, C. Adamo, S. Clifford, J. Ochterski, G. A. Petersson, P. Y. Ayala, Q. Cui, K. Morokuma, D. K. Malick, A. D. Rabuck, K. Raghavachari, J. B. Foresman, J. Cioslowski, J. V. Ortiz, B. B. Stefanov, G. Liu, A. Liashenko, P. Piskorz, I. Komaromi, R. Gomperts, R. L. Martin, D. J. Fox, T. Keith, M. A. Al-Laham, C. Y. Peng, A. Nanayakkara, C. Gonzalez, M. Challacombe, P. M. W. Gill, B. G. Johnson, W. Chen, M. W. Wong, J. L. Andres, M. Head-Gordon, E. S. Replogle, and J. A. Pople, *Gaussian 98*. 1998, Gaussian, Inc.: Pittsburgh PA.
22. C. Møller and M. S. Plesset, *Note on an approximation treatment for many-electron systems.* Phys. Rev., 1934 **46** (7) 618-622.
23. J. W. McIver, *Structure of transition states. Are they symmetric?* Acc. Chem. Res., 1974 **7** (3) 72-77.
24. K. Fukui, *Formulation of the reaction coordinate.* J. Phys. Chem., 1970 **74** (23) 4161-4163.
25. C. Gonzalez and H. B. Schlegel, *Reaction path following in mass-weighted internal coordinates.* J. Phys. Chem., 1990 **94** (14) 5523-5527.
26. C. Gonzalez and H. B. Schlegel, *Improved algorithms for reaction path following: Higher-order implicit algorithms.* J. Chem. Phys., 1991 **95** (8) 5853-5860.
27. C. Cappelli, B. Mennucci, C. O. da Silva, and J. Tomasi, *Refinements on solvation continuum models: Hydrogen-bond effects on the OH stretch in liquid water and methanol.* J. Chem. Phys., 2000 **112** (12) 5382-5392.
28. A. R. Grimm, G. B. Bacskay, and A. D. J. Haymet, *Quantum chemical studies of the solvation of the hydroxide ion.* Mol. Phys., 1995 **86** (3) 369-384.
29. I. Tuñón, D. Rinaldi, M. F. Ruiz-López, and J. L. Rivail, *Hydroxide ion in liquid water: structure, energetics, and proton transfer using a mixed discrete-continuum ab initio model.* J. Phys. Chem., 1995 **99** (11) 3798-3805.
30. C. G. Zhan and D. A. Dixon, *First-principles determination of the absolute hydration free energy of the hydroxide ion.* J. Phys. Chem. A, 2002 **106** (42) 9737-9744.
31. J. Tomasi and M. Persico, *Molecular interactions in solution: An overview of methods based on continuous distributions of the solvent.* Chem. Rev., 1994 **94** (7) 2027-2094.
32. J. R. Pliego Jr. and J. M. Riveros, *The cluster-continuum model for the calculation of the solvation free energy of ionic species.* J. Phys. Chem. A, 2001 **105** (30) 7241-7247.

33. J. E. Carpenter and F. Weinhold, *Analysis of the geometry of the hydroxymethyl radical by the "different hybrids for different spins" natural bond orbital procedure.* J. Mol Struct.-Theochem, 1988 **169** 41-62.
34. E. D. Glendening, A. E. Reed, J. E. Carpenter, and F. Weinhold, *NBO Version 3.1*.
35. A. E. Reed, L. A. Curtiss, and F. Weinhold, *Intermolecular interactions from a natural bond orbital, donor-acceptor viewpoint.* Chem. Rev., 1988 **88** (6) 899-926.
36. K. B. Wiberg, *Application of the pople-santry-segal CNDO method to the cyclopropylcarbinyl and cyclobutyl cation and to bicyclobutane.* Tetrahedron, 1968 **24** (3) 1083-1096.
37. A. Moyano, M. A. Pericàs, and A. Valentí, *A theoretical study on the mechanism of the thermal and the acid-catalyzed decarboxylation of 2-oxetanones (β-lactones).* J. Org. Chem., 1989 **54** (3) 573-582.
38. H. Maskill, *The physical basis of organic chemistry*. 1986, Oxford: Oxford University Press.
39. J. Kóňa, W. M. F. Fabian, and P. Zahradník, *Ab initio and DFT studies on the mechanism of ring-opening reactions of 4H-1-benzopyran-4-one with hydroxide ion.* J. Chem. Soc., Perkin Trans. 2, 2001 (3) 422-426.
40. J. D. Madura and W. L. Jorgensen, *Ab initio and Monte Carlo calculations for a nucleophilic addition reaction in the gas phase and in aqueous solution.* J. Am. Chem. Soc., 1986 **108** (10) 2517-2527.
41. T. Hori, H. Takahashi, and T. Nitta, *Hybrid QM/MM molecular dynamics simulations for an ionic S_N2 reaction in the supercritical water: $OH^- + CH_3Cl \rightarrow CH_3OH + Cl^-$*. J. Comput. Chem., 2003 **24** (2) 209-221.
42. A. V. Marenich, C. J. Cramer, and D. G. Truhlar, *Perspective on foundations of solvation modeling: the electrostatic contribution to the free energy of solvation.* J. Chem. Theory Comput., 2008 **4** (6) 877-887.
43. C. J. Cramer, *Essentials of computational chemistry. Theories and models*. 2004, Chichester: John Wiley & Sons.
44. X. L. Armesto, M. Canle L., M. V. García, M. Losada, P. Rodríguez, and J. A. Santaballa, *Alkoxide-promoted decomposition of N-halo-α-amino acids in aqueous medium.* Tetrahedron, 1994 **50** (7) 2265-2276.
45. W. P. Jencks, *Studies on the mechanism of oxime and semicarbazone formation.* J. Am. Chem. Soc., 1959 **81** (2) 475-481.
46. B. M. Anderson and W. P. Jencks, *The effect of structure on reactivity in semicarbazone formation.* J. Am. Chem. Soc., 1960 **82** (7) 1773-1777.
47. E. H. Cordes and W. P. Jencks, *The mechanism of hydrolysis of Schiff bases derived from aliphatic amines.* J. Am. Chem. Soc., 1963 **85** (18) 2843-2848.
48. Z. Huang, D. Wan, and J. Huang, *Hydrolysis of Schiff bases promoted by UV light.* Chem. Lett., 2001 **30** (7) 708-709.

CHAPTER 4

Neutral hydrolysis of aliphatic imines: A quantum chemical study

The cure for boredom is curiosity.
There is no cure for curiosity.

Attributed to Dorothy Parker or Ellen Parr

4.1 Introduction

Imines display a distinctive carbon-nitrogen double bond, when the nitrogen atom is linked to an alkyl or aryl group they may be named Schiff bases. This arrangement occurs, as intermediate, in a large number of enzymatic processes.[1-3] They also take part in many organic reactions,[4-9] and are common ligands in coordination chemistry.[10] Besides, imines have been widely used as reversible protective group of the amino function in organic synthesis.[11]

Imines are unstable in aqueous solution and thus, some aspects of their reactivity and properties are still rather unknown. They undergo a fast hydrolysis process in water, which attracted the attention of some researchers in the 1950's decade. This reaction has been extensively investigated by Jencks and others empirically:[12] the uncatalyzed reaction involves a water molecule and proceeds via a stepwise mechanism, the mechanism of formation of the heminaminal intermediate was also described. Latterly not many other studies have been focused on these processes. Furthermore, no theoretical computations have been dedicated to the analysis of the molecular mechanism of imine neutral hydrolysis, and it is important to examine whether a computational approach can properly describe the reaction and the role of water.

Theoretical characterization of potential energy surfaces (PES) has significantly furthered our understanding of intrinsic reactivity, and helps us to unravel the molecular mechanism of chemical reactions. In this work, we present electronic structure calculations in order to shed light on the hydrolysis of imines at neutral pH. A detailed mechanistic study of the process undergone by imines in water will permit a much better understanding of other reactions where imines participate. However, to our knowledge there have not been computational attempts to model this process in detail.

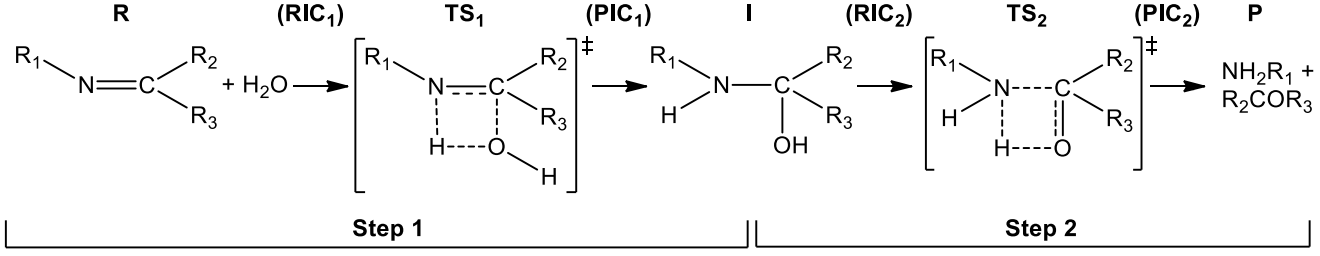

Scheme 4.1. Schematic description of the observed hydrolysis process used as starting point for the computational analysis of the reaction.

In this study we have included discrete water molecules either alone or together with a continuum method, in order to explore the effects of water. Discrete water molecules must be added to properly account for the role of water in the hydrolysis process: a water molecule has the central function of promoting and participating in the reaction of imine decomposition. This molecule acts as H^+ donor to the nitrogen atom and HO^- donor to the carbon atom of the N=C group, *i.e.* hydrolysis of imines implies the nucleophilic addition to a double bond. The reaction proceeds via a stepwise mechanism, as empirically proposed.[12] The attack of the water molecule onto the N=C double bond takes place in the first step, subsequently the so-formed hemiaminal collapses: the C–N single bond is broken and the C–O bond becomes double, leading to the corresponding amine and carbonyl compounds as products (see Scheme 4.1).

Other water molecules were added to describe the solute-solvent interaction in the first solvation layer, while the PCM model was used to assess the effect of bulk water. Quantum chemical calculations revealed the role of water in the title reaction, and the characteristics of the process obtained with water clusters and PCM should hold in the reaction in bulk solvent.

The geometry and energy of all relevant stationary points for several simple imines (R_1, R_2, and R_3 = H, CH_3, or CH_2CH_3, see Scheme 4.1) were calculated. The present study opens the door to the detailed analysis of the molecular mechanism of the hydrolysis of imines.

4.2 Computational procedure

The nature of the molecular mechanism has been elucidated by characterizing on the PES the geometry and energy of the stationary points (Scheme 4.1): reactants (R), bound reactant-like complex (called hereafter reactant interaction complex (RIC_1)), transition structure for the addition of water to the N=C double bond (TS_1), intermediate that corresponds to the hemiaminal (I), transition structure for the C–N bond breaking and formation of carbonyl group (TS_2), and product interaction complex (PIC_2) that opens the channel to reach the products (P). Two other interaction complexes, similar to the intermediate I, are also obtained (PIC_1 and RIC_2, Scheme 4.1). The unique imaginary frequency associated with the transition vector of the different TSs has been analyzed.[13] The intrinsic reaction coordinate (IRC), from the TSs down to the corresponding two lower energy structures (RIC & PIC), has been traced using the second order Gonzalez-Schlegel integration method in order to verify that each saddle point links the two putative minima.[14-16] Thus, in all cases the intermediate stands for the hemiaminal together with corresponding water molecules, whereas there are only conformational differences in water location between PIC_1 and RIC_2. In order to calculate adequate activation barriers, each TS has been used together with the corresponding RIC obtained from the IRC.

Among the different procedures to describe solute-solvent interactions at the quantum level, a combination of discrete water molecules and continuum models has been used. High-level *ab initio* electronic structure calculations including even a modest number of solvent molecules are prohibitive computationally. On the other hand, continuum models are very popular due to their combination of simplicity and efficiency, however they are unlikely to be adequate for the description of the reaction under study in water, as a cavity is built around the bare solute and therefore short-range solvent-solute interactions are not explicitly considered. Thus, apart from the water molecule that actively participates in the reaction, other discrete water molecules were considered; they were situated hydrogen-bonded to charged atoms and their possible catalytic role was studied. Specific interactions of the solute with the solvent molecules can either reduce the activation free energy of the reaction by stabilization of localized charges, or even promote an alternative pathway through which hydrolysis could occur more readily.

The use of all possible combinations of H, CH_3, and CH_2CH_3 as R_1, R_2, and R_3 substituents leads to several stereoisomer pairs. Preliminary studies concluded that *E* isomers were more thermodynamically stable than corresponding *Z* ones. Furthermore, the *E* reactant was always obtained from corresponding most stable TS_1, following IRC and geometry optimization. Thus, only data for the *E* species are here presented.

The four models described below, and shown in Figure 4.1, were used for the smallest compounds (R_1, R_2, and R_3 = H or CH_3). Model I is the simplest model, it involves the imine and one water molecule, which is added onto the N=C_I double bond. In model II a second water was included as H^+ donor to the oxygen atom producing the carbonyl group (O_C), *i.e.*, this is the oxygen of the first water molecule (step 1) and of the alcoholic group of hemiaminal (step 2), see Figure 4.1. Model III also considers two discrete water molecules but in this case the second one acts as H^+ donor to the nitrogen atom (Figure 4.1). In order to take into account the possibility of addition of HO^- and H^+ onto N=C_I bond from different solvent water molecules, in model IV two water molecules actively participate in the reaction (Figure 4.1): H^+ donated to nitrogen (H_1) comes from the first water molecule, while the second molecule donates its HO^- to the carbon atom and its H^+ to the first water (step 1); subsequently, the so-formed water molecule donates a second H^+ to N atom of the hemiaminal (H_2) while accepting another H^+ from the alcohol group (step 2). The expected transition structures for the two elementary steps of these four models are depicted in Figure 4.1. Model IV showed a much better performance, yielding lower activation barriers and, therefore, was selected for calculations with imines containing ethyl substituents (R_1, R_2, and/or R_3 = CH_2CH_3).

Furthermore, a hybrid microsolvated-continuum model was considered. Polarized continuum model (PCM)[17] was applied over the geometries calculated with previous models without further optimization to obtain free energy of solvation (ΔG_{solv}). The corresponding values have been corrected in order to use consistent standard states.[18] This arrangement should yield a more realistic energy profile in aqueous medium as it includes both the short-range interaction with the molecules in the first solvation shell and the solvation effect of bulk solvent, stabilizing net atomic charges. Extra spheres

were added when necessary, as centred on some hydrogen atoms in flight at the TSs.

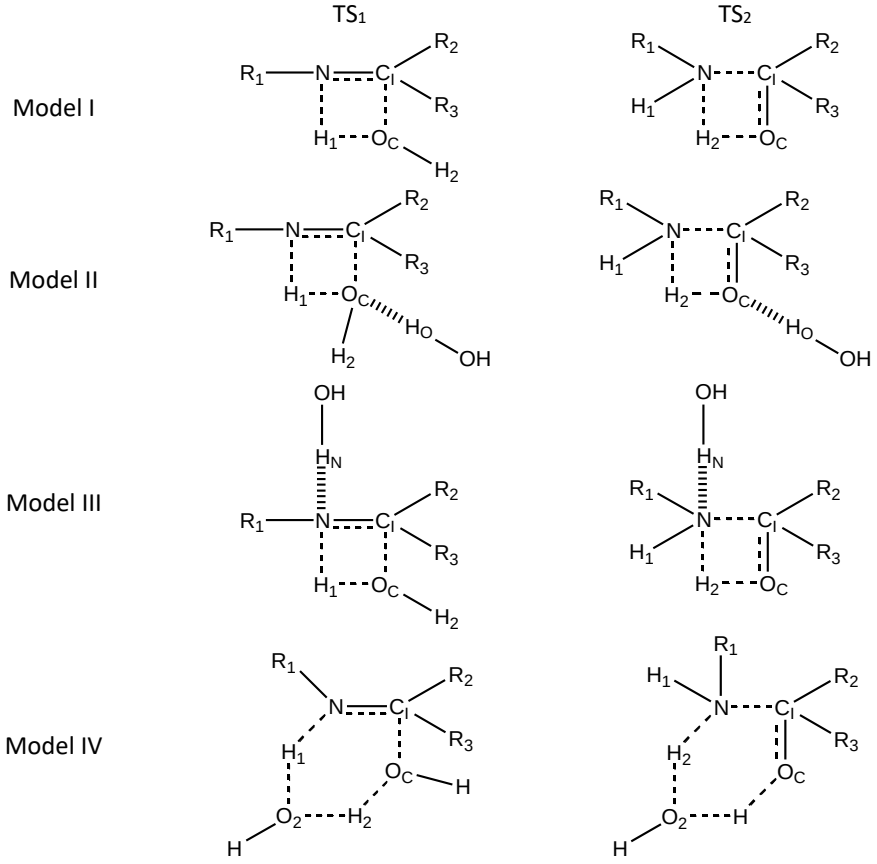

Figure 4.1. Schematic description of the transition structures calculated for both steps and with models I to IV. N and C_I are the two atoms forming the imine bond (N=C_I) in the reactant. H_1 and H_2 are the hydrogen atoms transferred from water to N at first and second steps, respectively. O_C is the oxygen atom first transferred to C_I and then forming the carbonyl group. H_O and H_N are the hydrogen atoms hydrogen-bonded to O_C and N at models II and III, respectively. O_2 is the oxygen atom of the second water molecule that participates in the proton-relay mechanism at model IV.

The minima and TSs for models I to IV were fully optimized by using density functional theory (DFT) at the B3LYP level[19-21] together with the double-ζ 6-31++G** basis set incorporating polarization and diffuse functions. All calculations were carried out with the Gaussian03 program,[22]default values of this package have been used for all applicable parameters.

Evolution of relevant bonds along the reaction pathway of CH_2=NH hydrolysis for each computational model was calculated using the natural population analysis of Weinhold *et al*.[23-25] Reactions were considered here in the direction described above, *i.e.*, imine hydrolysis, but, taking into account the reversibility of these processes, some relevant results obtained for the back reaction are also provided, *i.e.*, alkylimino-de-oxo-bisubstitution or imine formation from carbonyl compound and amine, which is a typical condensation reaction.

4.3 Results

The reaction always takes place in the two-step mechanism shown in Scheme 4.1. The attack of water to the imine to form the corresponding hemiaminal intermediate takes place in the first step, then this carbinolamine intermediate collapses to

release the parent amine (or ammonia) and ketone (or aldehyde) (step 2). Any attempt to obtain a concerted mechanism, *i.e.*, just one step, or a stepwise mechanism via more than two separate steps has been unsuccessful. Figure 4.2 shows optimized TSs corresponding to the hydrolysis of CH_2=NH according to the four proposed models. Relevant distances and Mulliken charges for the hydrolysis of this compound are collected in Tables 4.1 and 4.2, respectively. Similar values were observed with other compounds (Tables S4.1 and S4.2 of the supplementary material). Values of free energy of activation obtained for these six compounds are collected in Table 4.3; they correspond to the intrinsic free energy barriers going from RICs to TSs, labelled ΔG°_{int}. Other detailed thermodynamic data are available at the supplementary information (Tables S4.3 and S4.4).

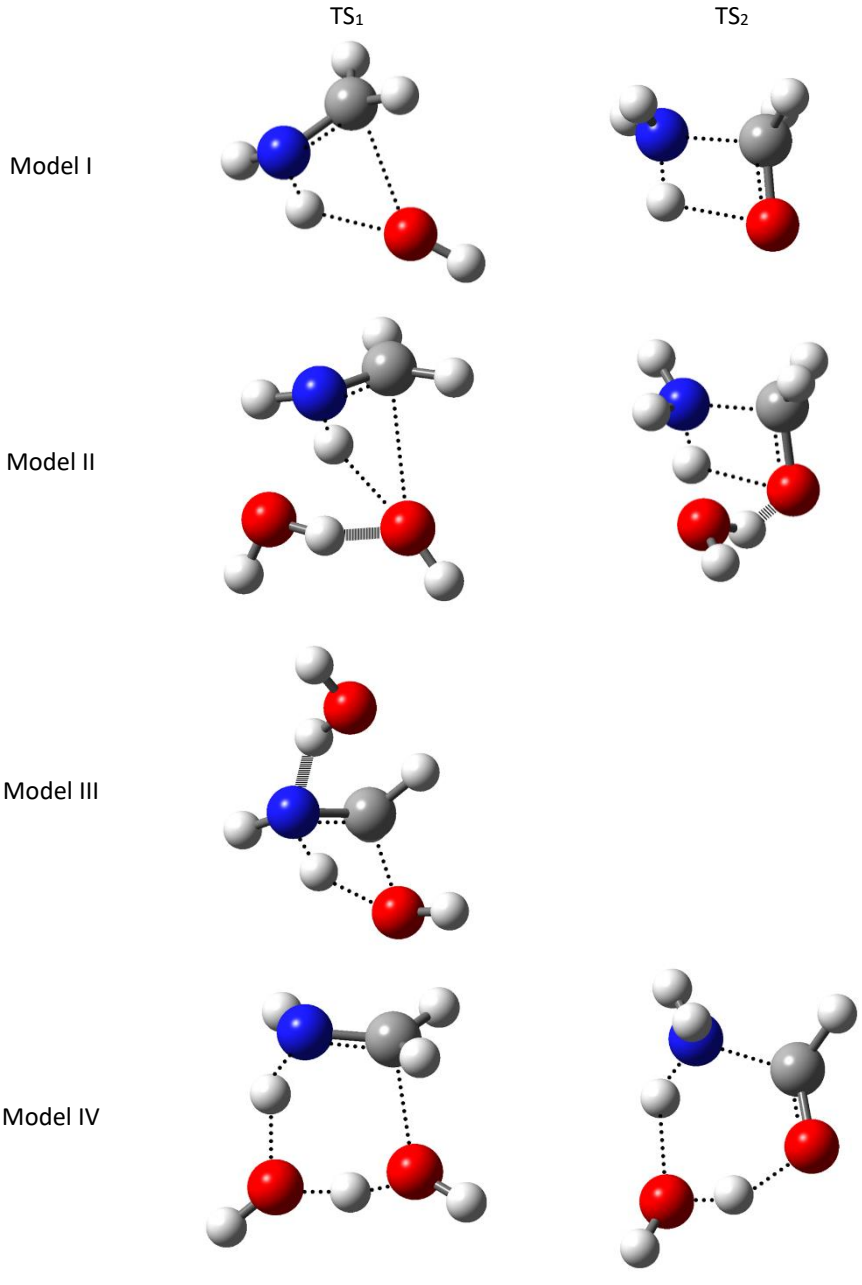

Figure 4.2. Geometries obtained for the TSs of the hydrolysis of CH_2=NH with models I - IV and at the B3LYP/6-31++G** computational level.

Table 4.1. Relevant distances in Å and corresponding bond orders (shown in parentheses) at the different stationary points obtained for the hydrolysis of CH_2=NH with models I to IV at the B3LYP/6-31++G** computational level.

Model	Stationary Point	N–C_I	N–H_1	N–H_2	C_I–O_C	O_C–H_1	O_C–H_2	O_C–H_O	N–H_N	O_2–H_1	O_2–H_2
	R	1.272	-	-	-	0.965	0.965	-	-	0.965	-
		(2.03)				(0.76)	(0.76)			(0.76)	
	I	1.428	1.016	3.198	1.444	2.610	0.968	-	-	-	-
		(1.07)	(0.83)	(0.02)	(0.89)	(0.00)	(0.75)				
	P	-	1.016	1.016	1.209	-	-	-	-	-	-
			(0.86)	(0.86)	(1.92)						
I	RIC_1	1.273	1.944	3.393	3.573	0.979	0.964	-	-	-	-
		(2.00)	(0.05)	(0.00)	(0.00)	(0.70)	(0.77)				
	TS_1	1.307	1.069	3.285	2.274	1.656	0.969	-	-	-	-
		(1.58)	(0.63)	(0.01)	(0.32)	(0.12)	(0.77)				
	PIC_1	1.428	1.016	3.198	1.444	2.610	0.968	-	-	-	-
		(1.07)	(0.83)	(0.02)	(0.89)	(0.00)	(0.75)				
	RIC_2	1.452	1.016	2.405	1.417	2.746	0.969	-	-	-	-
		(1.02)	(0.83)	(0.01)	(0.94)	(0.00)	(0.73)				
	TS_2	1.585	1.021	1.186	1.346	2.897	1.420	-	-	-	-
		(0.82)	(0.80)	(0.48)	(1.13)	(0.01)	(0.26)				
	PIC_2	2.850	1.017	1.017	1.213	4.099	3.151	-	-	-	-
		(0.04)	(0.85)	(0.85)	(1.87)	(0.00)	(0.00)				
II	RIC_1	1.270	1.896	3.368	4.012	0.985	0.964	1.871	-	-	-
		(2.00)	(0.06)	(0.00)	(0.00)	(0.67)	(0.75)	(0.05)			
	TS_1	1.290	1.038	3.379	2.449	1.893	0.967	1.621	-	-	-
		(1.68)	(0.69)	(0.00)	(0.19)	(0.05)	(0.77)	(0.13)			
	PIC_1	1.418	1.015	3.210	1.467	2.653	0.968	1.894	-	-	-
		(1.10)	(0.83)	(0.02)	(0.85)	(0.00)	(0.74)	(0.04)			
	RIC_2	1.444	1.017	2.405	1.434	2.736	0.970	1.919	-	-	-
		(1.04)	(0.81)	(0.01)	(0.91)	(0.00)	(0.72)	(0.04)			
	TS_2	1.538	1.022	1.212	1.376	2.688	1.392	1.791	-	-	-
		(0.88)	(0.78)	(0.46)	(1.06)	(0.00)	(0.28)	(0.08)			
	PIC_2	2.666	1.022	1.017	1.220	3.053	3.570	1.909	-	-	-
		(0.08)	(0.81)	(0.85)	(1.80)	(0.00)	(0.00)	(0.04)			
III	RIC_1	1.276	3.308	4.484	3.293	0.982	0.964	-	1.845	-	-
		(1.98)	(0.00)	(0.00)	(0.01)	(0.69)	(0.76)		(0.08)		
	TS_1	1.366	1.370	2.942	1.771	1.209	0.974	-	1.881	-	-
		(1.31)	(0.35)	(0.01)	(0.56)	(0.37)	(0.73)		(0.06)		
	PIC_1	1.440	1.018	3.193	1.435	2.572	0.967	-	1.942	-	-
		(1.04)	(0.82)	(0.02)	(0.90)	(0.00)	(0.74)		(0.06)		
IV	RIC_1	1.276	1.845	3.308	3.293	-	0.982	-	-	0.989	1.827
		(1.98)	(0.08)	(0.00)	(0.01)		(0.69)			(0.66)	(0.06)
	TS_1	1.309	1.142	2.462	2.083	-	1.140	-	-	1.413	1.307
		(1.58)	(0.53)	(0.00)	(0.30)		(0.43)			(0.24)	(0.30)
	PIC_1	1.418	1.017	2.838	1.467	-	1.894	-	-	2.400	0.977
		(1.10)	(0.81)	(0.00)	(0.85)		(0.04)			(0.01)	(0.70)
	RIC_2	1.476	1.018	1.918	1.403	-	2.673	-	-	3.408	0.986
		(0.98)	(0.83)	(0.07)	(0.97)		(0.00)			(0.00)	(0.68)
	TS_2	1.598	1.020	1.119	1.333	-	2.364	-	-	3.052	1.471
		(0.79)	(0.80)	(0.56)	(1.16)		(0.00)			(0.00)	(0.21)
	PIC_2	2.666	1.017	1.022	1.220	-	3.053	-	-	3.607	2.139
		(0.08)	(0.85)	(0.81)	(1.80)		(0.00)			(0.00)	(0.02)

4.3.1 Model I

Results computed with the simplest system (model I) show that N–C_I distance increases along the whole reaction, as the

double bond weakens to single bond in the first step and breaks in the second. Accordingly, negative charge on N atom slightly increases with the conversion of the reactant imine into a primary/secondary amine upon addition of H_1 and N–H_1 bond formation, and then into ammonia/primary amine upon addition of H_2 and N–H_2 bond formation. On the other hand, C_I–O_C distance decreases along the reaction: in the first step these two atoms bind yielding a single bond and H_1 is transferred to N (O_C–H_1 distance increases while N–H_1 decreases due to the proton transfer), then a carbonyl group is formed in the second step, as H_2 is transferred to N (O_C–H_2 distance increases and N–H_2 decreases). The negative charge on the oxygen atom added to the double bond (O_C) decreases along the reaction, mostly upon water addition across the N–C_I double bond and, to a lesser extent, as the alcohol group converts to carbonyl oxygen, but it should be noted that the net charge is higher at the TSs than at the corresponding RICs and PICs. The charge on C_I atom is also affected, it may be negative at the reactant and hemiaminal but greatly increases along the second process to yield a positively charged carbonyl C_I atom.

Table 4.2. Mulliken charges on relevant atoms at the different stationary points obtained for the hydrolysis of CH_2=NH with models I to IV at the B3LYP/6-31++G** computational level.

Model	Stationary Point	N	C_I	O_C	H_1	H_2	H_O	H_N
	R	–0.32	–0.20	–0.69	0.34	0.34	0.34	0.34
	I	–0.58	–0.15	–0.50	0.30	0.33	0.34	0.34
	P	–0.85	0.11	–0.32	0.28	0.28	0.34	0.34
I	RIC_1	–0.43	–0.14	–0.75	0.42	0.33	-	-
	TS_1	–0.36	–0.09	–0.95	0.38	0.34	-	-
	PIC_1	–0.58	–0.15	–0.50	0.30	0.33	-	-
	RIC_2	–0.57	–0.17	–0.48	0.30	0.35	-	-
	TS_2	–0.60	0.00	–0.65	0.32	0.39	-	-
	PIC_2	–0.91	0.17	–0.35	0.29	0.32	-	-
II	RIC_1	–0.41	–0.17	–0.77	0.42	0.36	0.41	-
	TS_1	–0.35	–0.08	–1.07	0.39	0.37	0.44	-
	PIC_1	–0.57	–0.16	–0.57	0.30	0.35	0.42	-
	RIC_2	–0.56	–0.19	–0.54	0.33	0.37	0.41	-
	TS_2	–0.62	–0.04	–0.67	0.37	0.38	0.40	-
	PIC_2	–0.96	0.18	–0.38	0.37	0.30	0.40	-
III	RIC_1	–0.47	–0.14	–0.78	0.42	0.35	-	0.45
	TS_1	–0.78	–0.10	–0.57	0.40	0.36	-	0.46
	PIC_1	–0.75	–0.12	–0.47	0.33	0.36	-	0.43
IV	RIC_1	–0.47	–0.14	–0.78	0.45	0.42	-	-
	TS_1	–0.41	–0.16	–0.77	0.44	0.51	-	-
	PIC_1	–0.57	–0.16	–0.57	0.33	0.42	-	-
	RIC_2	–0.70	–0.13	–0.49	0.31	0.44	-	-
	TS_2	–0.66	–0.07	–0.58	0.35	0.47	-	-
	PIC_2	–0.96	0.18	–0.38	0.30	0.37	-	-

Transferred hydrogen atoms exhibit positive charge at the TSs (*i.e.*, H_1 at TS_1 and H_2 at TS_2), showing that the process has a proton transfer character. It should be taken into account that the transference of H_1 is more advanced than other molecular events at TS_1, as shown by N–H_1 distance and bond order, similar to PIC_1. Besides, this atom is hydrogen-bonded to N at RIC_1, causing polarization between both atoms. Consequently, H_1 charge is even more positive at RIC_1 than at TS_1 (when it is already moderately bonded to N), while charge on H_2 is actually higher at TS_2.

The analysis of the thermodynamic parameters (Tables 4.3 & S4.3) reveals that the reaction is enthalpy controlled. The enthalpic term in going from RIC to TS is relevant, while the entropy only accounts for less than 10% of the free energy in the step leading to the hemiaminal, and is almost negligible in the final step. However, diffusion together of reactants to

give RIC_1 is an activated process, as the negative enthalpy that results from the interaction between imine and water is fully compensated by a greater entropic term due to the loss of degrees of freedom at this arrangement.

When bulk solvation (PCM) is applied to model I, a Gibbs free energy stabilization is observed, greater on TSs than on corresponding RICs and PICs, leading to reduced activation barriers (20 to 30 kJ·mol^{-1} lower, Tables 4.3 and S4.3). The proton transfer character of both elementary processes, as well as the higher net charge on some atoms at the transition structures may explain the decrease in the free energy barrier. In any case, free activation energy is always higher for TS_1 (at least 50 kJ·mol^{-1}), indicating that this is the rate-limiting step.

Table 4.3. Intrinsic activation barriers ($\Delta G^\circ_{int} = \Delta G^\circ_{TS} - \Delta G^\circ_{RIC}$) in kJ·mol^{-1} for both steps of the hydrolysis of imines with R_1, R_2, and R_3 = H or CH_3, obtained with models I to IV at the B3LYP/6-31++G** computational level.

Step 1										
Compound			**ΔG°_{int} (*in vacuo*)**				**ΔG°_{int} (PCM)**			
R_1	**R_2**	**R_3**	**Model I**	**Model II**	**Model III**	**Model IV**	**Model I**	**Model II**	**Model III**	**Model IV**
H	H	H	196.01	163.94	198.90	114.46	175.47	135.11	182.75	89.40
H	H	CH_3	202.50	-	204.54	123.93	185.77	-	193.53	107.86
H	CH_3	CH_3	195.48	-	199.84	118.76	176.77	-	190.51	99.60
CH_3	H	H	200.83	163.33	216.22	119.56	170.88	130.19	200.78	94.42
CH_3	H	CH_3	206.15	168.61	217.01	125.64	177.12	133.59	195.37	105.68
CH_3	CH_3	CH_3	192.99	150.32	204.32	117.48	168.22	116.01	185.04	98.40
Step 2										
Compound			**ΔG°_{int} (*in vacuo*)**				**ΔG°_{int} (PCM)**			
R_1	**R_2**	**R_3**	**Model I**	**Model II**	**Model III**	**Model IV**	**Model I**	**Model II**	**Model III**	**Model IV**
H	H	H	157.53	142.14	-	86.29	123.27	126.87	-	43.70
H	H	CH_3	152.25	139.41	-	81.98	120.91	123.05	-	41.31
H	CH_3	CH_3	148.94	134.97	-	80.66	121.24	120.33	-	43.13
CH_3	H	H	147.93	130.39	-	76.92	118.18	120.85	-	41.94
CH_3	H	CH_3	141.92	127.60	-	71.74	116.90	118.06	-	39.82
CH_3	CH_3	CH_3	137.98	123.01	-	70.74	113.75	115.65	-	40.74

4.3.2 Model II

The atoms with the most negative Mulliken charge along the reaction are O_C and N. The interaction of solvent water at these points must be more relevant and has been explicitly taken into account. Therefore, a discrete water molecule was incorporated into models II and III, hydrogen-bonded to O_C and N, respectively. These water molecules are not involved in the proton transfer, but cause a polarization effect favouring the nucleofuge departure. This observation suggests cooperative hydrogen structural motif involving the water molecule, which may be important in the chemical reaction. This effect enhances charge distribution at the TSs.

The effect of the extra water molecule in model II is evident on O_C. Thus, according to C_I–O_C distance and bond order, the approach of O_C to C_I in the first step turned more delayed with respect to other events. This may arise from the stabilization of the transient HO^- anion at TS_1 through hydrogen bonding: net negative charge on O_C increases with respect to model I (0.05 - 0.12 a.u.), while H_O presents higher proton character than at reactant H_2O (0.10 - 0.13 a.u.). TS_1 could not be obtained with model II for the compounds with R_1 = H and R_3 = CH_3. Likely N–C_I bond polarization prevents the addition of a more stable water molecule. Geometry and charge distribution reveal almost unaffected at the second step.

The water molecule hydrogen-bonded to O_C exerts a catalytic effect, mostly at the first step, where the intrinsic activation barrier lowers (32 - 42 kJ·mol^{-1}), mainly due to enthalpy reduction, but also at the second step (13 - 18 kJ·mol^{-1}), where the

entropy term partially counteracts the activation free energy decrease. The high positive charge on O_C might explain that the transition structure is particularly stabilized by a water molecule hydrogen-bonded to this atom, particularly at the first elementary reaction, where the charge is larger. Addition of PCM results in further stabilization of TS_1 (free activation energy decreases 40 to 52 kJ·mol^{-1} with respect to model I), whereas in TS_2 the combination of model II and PCM shows no improvement, or even higher free energy barriers, with respect to solvated model I.

4.3.3 Model III

Some differences in geometry and charge distribution are also observed in model III. Lengthening and weakening of N–C_I bond occurs upon hydrogen bonding on N atom, and the charge on this position becomes more stable, so the net negative charge increases, mostly at TS_1 and PIC_1. It is observed at RIC_1 that hydrogen bonding from the two available water molecules does not take place simultaneously, *i.e.*, when N–H_N < 2 Å, then N–H_1 rises over 3 Å, and vice versa. As a result, contrary to other stationary points, charge on N is barely stabilized at RIC_1. Furthermore, as N and H_N form an effective hydrogen bond, the transfer of H_1 to N becomes delayed: N–H_1 bond order computed for CH_2=NH decreases from 0.63 to 0.35 at TS_1. On the other hand, addition of HO^- to the double bond is more advanced, as revealed by the increase of C_I–O_C bond order at TS_1 (0.32 to 0.56) and corroborated by lower negative charge (O_C + H_2), closer to hemiaminal values (PIC_1 or I). N–H_1 and C_I–O_C bond distances obtained for other compounds also support this change in reaction synchronicity.

TS_2 could not be obtained in any case. This fact may arise from steric hindrance around N atom or the hydrogen bonding inducing an inadequate electronic configuration on this atom for reaction to proceed.

N atom also presents a relevant negative net charge, higher at the imine and RIC_1 than at TS_1 in previous models. The addition of a water molecule interacting with this atom in model III inverts this charge scheme, particularly increasing the negative charge on N in TS_1. Besides preventing the rearrangement of hemiaminal to yield products, the water molecule hydrogen-bonded to N does not exert any catalytic effect: the activation barrier of TS_1 is slightly higher than with model I *in vacuo* (2 - 15 kJ·mol^{-1}) and with PCM solvation (7 - 30 kJ·mol^{-1}).

4.3.4 Model IV

In model IV two water molecules participate in the hydrolysis but, contrary to previous models II and III where one water molecule just simulates the specific hydrogen bonding by aqueous solvent, both molecules actively take part in the molecular reorganization. Besides, six bonds are breaking and forming cooperatively in both steps, while only four bonds were directly involved in the other models (see Figure 4.1). Despite the proton and the hydroxide added to N=C_I double bond come from two different water molecules (TS_1), and although a proton translocation process takes place through a water molecule instead a direct proton transfer from the hydroxyl group to N (TS_2), many structural values are quite similar to model I.

At RIC_1 the atoms N and H_1 are closer and hence situated more adequately for the reaction to proceed. This is also the case of C_I and O_C atoms when R_2 = R_3 = H, although steric hindrance avoids such approach at other compounds with substituents on C_I. This is possible because H_1 and O_C belong to two different water molecules, which allows a less stressed conformation. In fact, the atoms directly involved in the process are arranged in a six-membered cyclic assembly that is also present at TS_1. This particular organization remains in the second step, resulting again in a shorter N–H_2 distance at RIC_2. Concertedly to other molecular events, H_2 is transferred from one water molecule to the other (involving O_C–H_2 bond breaking and O_2–H_2 bond formation) in TS_1, and from the resulting water molecule to N (O_2–H_2 bond breaking and N–H_2 bond formation) in TS_2. At the TSs the charge of exchanged hydrogens ranges from 0.41 to 0.52 a.u., such values show that they transfer as protons.

Obtained results with model IV indicate that the hydrolysis process takes place via six-membered cyclic transition structures with three molecules (two in TS_2) closely involved. As a result, the activation entropic term is more unfavourable (2 - 11 kJ·mol^{-1}) with respect to model I, indicating the loss of degrees of freedom corresponding to such ordered structure. However, these cyclic assemblies contribute to stabilize the TSs, as revealed by the important decrease in activation enthalpy (around 85 kJ·mol^{-1} for TS_1 and 75 kJ·mol^{-1} for TS_2). Therefore, obtained $\Delta G°_{int}$ values range from 114 to 126

kJ·mol^{-1} for step 1 and 71 to 86 kJ·mol^{-1} for step 2, the performance of model IV being much better than the others. Free energy barrier is even lower when considering PCM solvation, so $\Delta G°_{int}$ is 89 to 108 kJ·mol^{-1} for the first elementary reaction, and 40 to 44 kJ·mol^{-1} for the second one. PIC_1 and RIC_2 present geometries more different than in previous models, but their conversion only implies slight rotational or translational changes in the remaining water molecule, so that there is not any activation barrier and the energy of both stationary points is quite similar.

The effect of the second molecule in model IV cannot be described with just a charge stabilization scheme. In this case, the hydrolysis is a cooperative process where, in the first step, proton addition to nitrogen, proton transfer from one water molecule to the other, hydroxide addition to carbon, and weakening of the $N=C_I$ double bond take place in a concerted mechanism. Similarly, in the second step, proton addition to nitrogen, proton transfer from hydroxyl group to the water molecule, formation of carbonyl $C_I=O_C$ double bond, and $N–C_I$ bond breaking occur concertedly. This particular arrangement notably lowers the activation free energy of the transition structure, thus the reaction is facilitated through water-assisted proton transfer along the hydrogen-bonded water molecules.

The possibility of addition onto the $N=C_I$ double bond of H^+ and HO^- ions from different water molecules is considered in this model. This allows shorter $N–H_1$ and $C–O_C$ distances at the reactants, while the imine may adopt a more relaxed structure at TS_1. Thus, the proximity of the reacting species permit that both addition processes take place more simultaneously, whereas the reaction when only one water molecule was involved, although still concerted, was quite asynchronous. Besides, in step two, an intramolecular proton transfer takes place in models I to III. Since TS_2 organizes in a four-membered ring, the distance between O_C and N is adequate but it does not permit the favourable N···H···O linear arrangement for a proton transfer process. Participation of other water molecules in the reaction may solve this problem, as in model IV, where inclusion of one extra discrete water allows a more relaxed six-membered cyclic geometry. The consideration of a higher number of water molecules would also prevent formation of strained structures leading to either macrocyclic or acyclic TSs. In fact, when the reaction takes place in aqueous solution, several water molecules must be involved in the addition and proton transfer processes. Thus, although a rough simulation of solvent participation in the reaction, model IV seems more adequate to reproduce the experimental process than previous models.

4.4 Discussion

Gibbs free energy profiles of the hydrolysis reaction of $CH_2=NH$ *in vacuo* are depicted in Figure 4.3A for the four considered models. Formation of RIC_1 from reactants corresponds to an almost activationless process (Table S4.3). This small free energy increase (about 10 kJ·mol^{-1} with model I, *ca.* 20 kJ·mol^{-1} with other models) can be ascribed to an important negative entropic term (as the independent reactants diffuse together to form RIC_1 structure) that fully counteracts the enthalpy decrease, arising from the exothermic formation of hydrogen bonding. The free energy of activation corresponds to the intrinsic free energy barrier going from RICs to TSs, labelled $\Delta G°_{int}$. According to this scheme, the first step is always rate limiting, and model IV exhibits the lowest free energy of activation for both elementary reactions (Table 4.3).

Reaction products are more stable than reactants when R_1 = H *in vacuo*, and therefore the reaction is both exothermic and exergonic. However, this is not always the case when $R_1 = CH_3$, as the enthalpic contribution of NH_3 is higher than that of CH_3NH_2 with respect to corresponding starting imines. On the other hand, substituted carbonyl products are enthalpically favoured, resulting in more thermodynamically spontaneous reactions as the substitution at the carbon increases.

Although the geometries obtained *in vacuo* were not further optimized, addition of PCM bulk solvent led to important differences in the free energy reaction profiles, as shown in Figure 4.3B. Formation of complexes with RIC_1 geometries is an activated process, yielding values up to 46 kJ·mol^{-1} above reference R (Table S4.3). In the initial step, partial desolvation of the separate reactants leads to an important free energy rise in contrast to *in vacuo* calculations and, as a general rule, the approach of the imine and one water molecule to yield the encounter complex in model I requires a smaller amount of free energy than when reagents involve two water molecules (models II – IV).

Despite the fact that RICs and PICs do not represent free energy minima in solution, we have retained them in the

computational study since a physical meaning can be assigned. Many bimolecular reactions in solution may be described as in the mechanism of proton transfer proposed by Eigen, involving three distinct steps: 1) approach of reactants by diffusion to give an encounter complex (RIC), 2) molecular rearrangements involved in TS, and 3) dissociation of the product encounter complex (PIC) into separate products.[26] An analysis of this conceptual scheme establishes a connection to Marcus equation:[27]

$$\Delta G^{\circ\ddagger} = w^{r} + \Delta G^{\circ\ddagger}_{0}\left(1 + \frac{\Delta G^{\circ}_{e}}{4\Delta G^{\circ}_{0}}\right)$$

Which relates the Gibbs free activation energy ($\Delta G^{\circ\ddagger}$) with the intrinsic barrier $\Delta G^{\circ}_{0}{}^{\ddagger}$ (here called ΔG°_{int}). The work term w^{r} represents the energy required for initial structural reorganization, *i.e.*, ΔG°(R→RIC$_1$). In all cases, ΔG°_{int} decreases with the continuum model (Table 4.3), and the lowest free energy intrinsic barrier is again obtained for model IV.

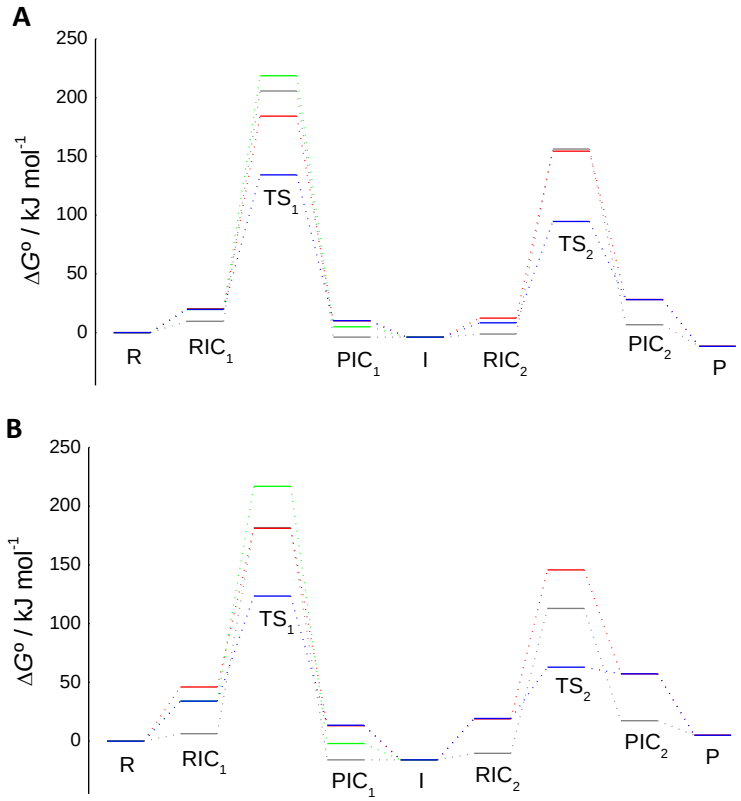

Figure 4.3. Gibbs free energy profiles for the reaction of hydrolysis of CH_2=NH in vacuo (A) and with PCM solvation (B) at the B3LYP/6-31++G** computational level and for the four considered models: model I (—), model II (—), model III (—), and model IV (—).

The situation is slightly different for the second step, the formation of the amino and carbonyl compounds from the carbinolamine intermediate (Scheme 4.1). In this case, the elementary reaction cannot start from separate hemiaminal and water molecule (models II - IV, in model I the intermediate consists of just one molecule). Both molecules derive from the preliminary addition of water onto N=C$_I$ double bond, and their conformation and relative position after the first step is very adequate for the subsequent process, as shown by the almost identical geometries obtained for complexes PIC$_1$ and RIC$_2$ (Table S4.1). In fact, the most evident difference is the conformation of the hydrogen atom transferred to N in the second step (H_2). This atom adjusts its starting orientation in PIC$_1$ to a position directed towards the acceptor N in RIC$_2$, this results in a free energy difference of only 1 to 11 kJ·mol^{-1} between both stationary points (Table S4.3). Thus, we consider that this intermediate complex does not disaggregate after first elementary reaction, but reacts straightforward to yield

products and, therefore, the intrinsic barrier is calculated from RIC_2 to TS_2.

Again, calculations with PCM reveal that the second process is faster than the rate-limiting first step for all considered models (Figure 4.3B). Best results were also obtained with model IV, with the lowest activation barriers (Table 4.3). PCM-solvated reaction products present free energy values slightly more unstable than in the previous *in vacuo* models (1 to 17 kJ·mol $^{-1}$), although analogous substituents effect is observed.

Table 4.4. Intrinsic activation barriers ($\Delta G^\circ_{int} = \Delta G^\circ_{TS} - \Delta G^\circ_{RIC}$) in kJ·mol^{-1} for both steps of the reverse reaction (imine formation from carbonyl compound and amine) with R_1, R_2, and R_3 = H or CH_3, obtained with models I to IV at the B3LYP/6-31++G** computational level.

Step 1										
Compound			**ΔG°_{int} (*in vacuo*)**				**ΔG°_{int} (PCM)**			
R_1	**R_2**	**R_3**	**Model I**	**Model II**	**Model III**	**Model IV**	**Model I**	**Model II**	**Model III**	**Model IV**
H	H	H	149.60	126.36	-	66.53	95.58	88.46	-	5.69
H	H	CH_3	168.40	151.08	-	90.71	116.52	110.29	-	30.84
H	CH_3	CH_3	183.31	170.46	-	111.48	132.97	132.21	-	55.67
CH_3	H	H	126.84	106.77	-	47.84	80.31	81.62	-	–0.65
CH_3	H	CH_3	148.39	132.46	-	74.11	104.46	104.35	-	22.48
CH_3	CH_3	CH_3	171.59	158.16	-	102.32	125.03	130.55	-	54.00
Step 2										
Compound			**ΔG°_{int} (*in vacuo*)**				**ΔG°_{int} (PCM)**			
R_1	**R_2**	**R_3**	**Model I**	**Model II**	**Model III**	**Model IV**	**Model I**	**Model II**	**Model III**	**Model IV**
H	H	H	209.50	174.25	213.68	124.10	197.75	168.02	218.91	110.00
H	H	CH_3	200.20	-	201.91	116.85	189.49	-	203.37	104.22
H	CH_3	CH_3	180.22	-	182.94	101.05	168.00	-	185.95	87.50
CH_3	H	H	192.43	154.42	207.96	109.20	179.29	135.21	220.72	100.62
CH_3	H	CH_3	185.93	145.08	194.85	101.03	171.24	120.73	193.13	90.62
CH_3	CH_3	CH_3	166.49	119.22	175.64	85.39	151.59	99.39	172.59	74.01

Despite the reaction is not always exergonic, the process is kinetically controlled, *i.e.*, activation barriers for the forward reaction (imine hydrolysis) differ from those for the backward reaction (alkylimino-de-oxo-bisubstitution). According to the principle of microscopic reversibility[28] the backward reaction is also stepwise, its second step being rate limiting (Table 4.4). Upon intermediate formation, the course to hydrolysis products is kinetically more favourable than the backward progress to yield imine. Furthermore, at dilute aqueous solution imine formation from carbonyl compound and amine is slowed by the low concentration of reactants, whereas water molecules (55.5 M) are ubiquitous and ready to react with any imine molecule present. Thus, the high instability of imines in water can be explained.

According to model IV, the imine and two molecules of water interact to form an encounter complex (RIC_1) where reactants are conveniently close and aligned to facilitate both elementary reactions of the imine hydrolysis. Although hydrogen bonding is much weaker than covalent bonding, they share some features, as directionality, and therefore, hydrogen bonds are also capable of some molecule orientation.[29] The use of a larger number of water molecules could lead to cyclic TSs with C_l and N linked through a chain of hydrogen-bonded water molecules, enforcing a relay of proton transfers coupled to water addition onto $N{=}C_l$ double bond. However, these forces compete with solvation in aqueous solution, and the interaction of water with hydrogen-bond donors and acceptors is usually strong and may be quite significant. Thus, the use of this kind of computational model, with a TS stabilized through water-assisted H^+ transfer along the chain may be an artifact caused by the lack of explicit consideration of hydrogen bonding within bulk solvent. Although this approach has

been used in other computational studies, we consider that such an ordered arrangement would not be entropically favourable and that it actually does not take place in water solvation. Furthermore, by using the pattern depicted in model IV we do not assume that the hydrolysis process takes place by the solely action of two water molecules participating in a six-membered cyclic assembly but that, contrary to previous models, the reaction involves at least two different solvent water molecules, and model IV stands for the simplest molecular system considering this aspect. Thus, in the step leading to hemiaminal the HO^- and H^+ ions added onto $N=C_I$ bond derive from different water molecules, and in the following step two different protons are intermolecularly transferred among water and hydroxyl and amine groups, while an intramolecular proton transfer occurred in models I to III. The structure here employed is just the smallest available model to simulate that aqueous solvent, and not a single discrete water molecule, donates and accepts the corresponding protons and hydroxyl anions. Besides, a polarizable continuum represented by a dielectric constant is used to reproduce bulk solvation. We accept that this rough computational scheme is not enough for rigorously modelling the actual effect of water solvent on this hydrolysis reaction; however, it can be presumed that it may yield a reasonable picture of the processes under study in terms of structure and energy, and thus, this is the model selected for further calculations and following discussion.

Table 4.5. Intrinsic activation barriers ($\Delta G^\circ_{int} = \Delta G^\circ_{TS} - \Delta G^\circ_{RIC}$) in kJ mol^{-1} for both steps of the hydrolysis of imines with R_1, R_2, and R_3 = H, CH_3, or CH_2CH_3, obtained with model IV at the PCM/B3LYP/6-31++G** computational level.

Substituents			ΔG°_{int} (PCM)	
R_1	**R_2**	**R_3**	**Step 1**	**Step 2**
H	H	H	89.40	43.70
H	H	CH_3	107.86	41.31
H	H	CH_2CH_3	85.34	40.70
H	CH_3	CH_3	99.60	43.13
H	CH_3	CH_2CH_3	99.50	47.33
H	CH_2CH_3	CH_2CH_3	100.41	41.92
CH_3	H	H	94.42	41.94
CH_3	H	CH_3	105.68	39.82
CH_3	H	CH_2CH_3	85.09	39.35
CH_3	CH_3	CH_3	98.40	40.74
CH_3	CH_3	CH_2CH_3	95.54	40.75
CH_3	CH_2CH_3	CH_2CH_3	98.33	42.39
CH_2CH_3	H	H	93.32	40.35
CH_2CH_3	H	CH_3	104.12	38.63
CH_2CH_3	H	CH_2CH_3	85.81	38.48
CH_2CH_3	CH_3	CH_3	96.69	39.46
CH_2CH_3	CH_3	CH_2CH_3	96.04	37.97
CH_2CH_3	CH_2CH_3	CH_2CH_3	95.10	36.33

Model IV was used to calculate the stationary points of the compounds containing ethyl substituents. Values of intrinsic barriers in solution for all the studied imines are collected in Table 4.5 (other parameters: bond distances, charges, and more thermodynamical data are shown in supplementary information, Tables S4.4, S4.5, S4.6, S4.7, and S4.8). Once more, formation of hemiaminal is the rate-limiting step in all cases. The intrinsic free energy calculated for this step is, on average, 55 $kJ \cdot mol^{-1}$ higher than for the subsequent fragmentation step. This outcome is consistent with the experimentally obtained results from Cordes and Jencks, stating that the attack on the protonated Schiff base is rate-determining in the pH independent hydrolysis of imines.[12] Furthermore, the formation of the hemiaminal and its collapse to corresponding imine (or ammonia) and ketone (or aldehyde) take place concertedly in highly asynchronous concerted processes, where proton transfer from water is nearly complete at the transition structures (Table 4.1). This result agrees with the fact that,

according to previously mentioned authors, the imine must be protonated before water or hydroxide anion can bond the carbon atom, and it also follows from the obtained results that in more acidic media the second step becomes rate determining.[12]

The differences in the activation barriers arise from the effect of substituents attached to both ends of the N=C_I group, and this effect can be analyzed in terms of linear free energy relationships (LFER). The effect of substituents on both steps of the hydrolysis has been examined by means of the Hammett equation. This equation relates reaction rates with substituent constants, according to the following equation:

$$\log\frac{k}{k_0} = \rho\sigma$$

Where k_0 is the reference reaction rate of the unsubstituted reactant, and k that of a substituted reactant, while ρ and σ represent the reaction and substituent constants, respectively. Kinetic constants were obtained with Eyring equation, and the electronic substituent constants considering inductive and/or resonance effects as defined by polar σ^* scale, or only inductive effect (σ_i scale), were employed.[30] It has been observed that bulky substituents as t-butyl do not show any important steric influence on the reaction rate.[12] Thus, electronic effects have been primarily considered.

The contribution of substituents on each side was considered separately, as the electron-releasing effect of the alkyl substituents on N and C_I atoms may be different and associated to their particular charge evolution along the reaction. Thus, a multiple linear regression analysis was used:

$$\log\frac{k}{k_0} = \rho_N\sigma_{(N)} + \rho_{C_I}\sigma_{(C_I)}$$

Where the subscripts (N) and (C_I) indicate parameters for substituents on N and C_I atoms, respectively. The contribution of the electronic effect on each side (ρ_N and ρ_{C_I} reaction constants) was optimized in order to achieve the best possible linear fit. Adequate linear plots were obtained for the second step (Figure 4.4), whereas data points of step 1 yielded random distributions. Thus, we subsequently tested the validity of Taft equation[31] within the process here studied, particularly in the first step:

$$\log\frac{k}{k_0} = \delta E_S$$

Where E_S indicates the steric substituent constant.

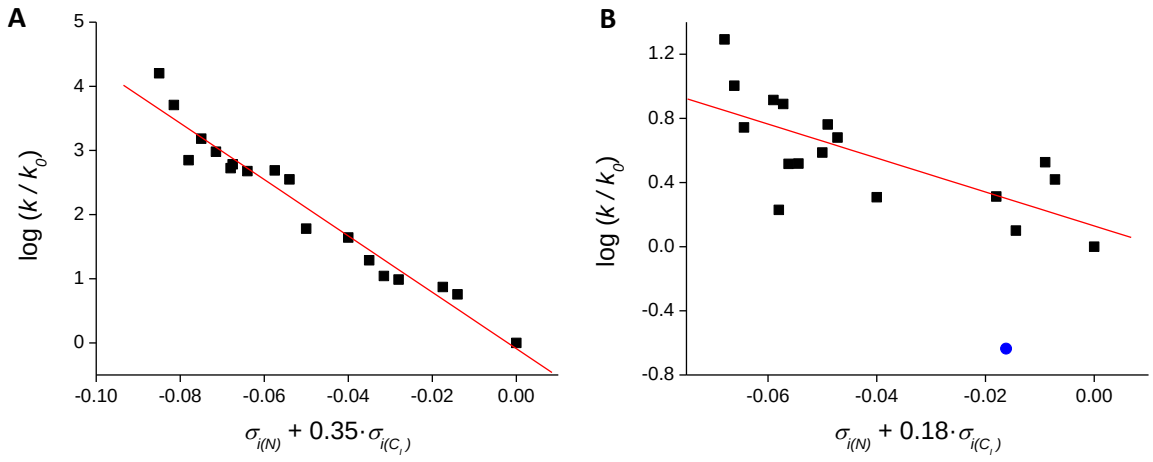

Figure 4.4. Hammett plots employing inductive σ_I scale for the second step of the hydrolysis reaction calculated *in vacuo* (A) and with PCM solvation (B) at the B3LYP/6-31++G** computational level and with model IV.

The scatter plot of the rate constants obtained for step 2 with model IV *in vacuo* vs. σ_i (Figure 4.4A) presents a very good linear correlation. Similar fits can be obtained with σ^* or E_S, although the coefficient of determination (r^2) is slightly lower and the standard deviation is higher, showing that apparently the inductive effect of substituents better controls the intrinsic activation barrier. A similar outcome is obtained with the values computed with PCM (Figure 4.4B): σ_i shows again the best possible fit. In this case an outlier was discarded and the scatter plot displays more dispersion. This deviation may arise from the use of the geometries calculated *in vacuo* for the determination of solvation energies. Scatter plots for the first step are displayed in Figure S4.1. Random point clouds were always obtained, independently of the substituent parameter used for the representation. Obtained reaction factors are collected in Table 4.6.

Table 4.6. Reaction constants obtained from the linear correlation of computed kinetic constants *vs.* inductive σ_i substituent parameter. Only 17 data pairs were used for the linear fit of the second step with PCM solvation (see Figure 4.4).

	Step 1		**Step 2**	
	In vacuo	**PCM**	***In vacuo***	**PCM**
$\rho_{(N)}$	-3.3 ± 3.2	-5.6 ± 5.7	-43.9 ± 2.5	-10.6 ± 2.7
$\rho_{(C_I)}$	-4.7 ± 4.5	7.0 ± 7.2	-15.4 ± 0.9	-1.9 ± 0.5

The values of the three considered substituent constants present very similar ratios (σ_i = 0.00 / –0.04 / –0.05, σ^* = 0.00 / –0.49 / –0.59, and E_S = 0.00 / –1.24 / –1.31 for H / CH_3 / CH_2CH_3, respectively) and, therefore, the corresponding effects cannot be easily discriminated. Thus, all of them yield adequate fits for the kinetic rates of step 2 (σ_i slightly better), while linear arranged scatter plots cannot be obtained for the first step in any case. Still, best linear correlations of step 1 data with respect to σ_i scale are collected in Table 4.6 as well.

Reaction constants for step 1 present errors similar to (or even higher than) the values, so that these constants could be close to zero or of opposite sign. Thus, substituent effects for this elementary reaction cannot be analyzed. On the other hand, there is an evident inductive effect of the substituents on the rate of the second step. The high negative reaction constant obtained for substitution on N, particularly *in vacuo*, indicates that electron-releasing groups, like the alkyl groups here employed, increase the reaction rate. However, contrary to expected, the addition of methyl or ethyl substituents on this atom causes the reduction of its negative charge (Tables S4.2 & S4.6), so that the observed behaviour seems not to be easily explained by means of a charge stabilization process. However, the observed rate acceleration by electron donating groups is consistent with the almost complete proton transfer from one water molecule to the nitrogen at the transition states of model IV, *i.e.*, regarding the proton transfer, the TSs can be considered as virtually iminium (TS_1) or aminium (TS_2) cations. This could explain the electronic effect of alkyl substituents. A negative value was also obtained for ρ_{CI}, notably lower than ρ_N, indicating an analogous effect of the substituents on C_I but to a lower extent, consistent with a higher distance from the positively charged N.

The cumulative effect of substituents on both steps of the hydrolysis reaction has been examined by means of a multiparametric Taft-like equation,[31] including both electronic (σ_i or σ^*) and steric (E_S) effects, but the complete analysis is not included here. It suggests that substituents on C_I atom exert a much more relevant effect than that on N in both steps. Again, negative reaction factors are obtained for the electronic parameters, but it is observed in this case that reaction rate decreases as the size of the substituents on C_i increases, mainly in the first step. This effect may arise from the fact that a proton is transferred to N in this step, but a bulkier hydroxyl anion is added onto C_i.

4.5 Conclusions

The molecular mechanism of the hydrolysis of imines has been theoretically characterized by using DFT at the B3LYP/6-

31++G** computing level (Gaussian03): the geometry and energy of all relevant stationary points for several simple imines were calculated. The role of water as solvent was analyzed by using discrete and hybrid discrete-polarized continuum models to describe both the solute-solvent interaction in the first solvation shell and the effect of bulk water.

Model I was the simplest model, it only comprises a single water molecule, and adequately predicts that the hydrolysis of imines takes place in two subsequent steps, formation of hemiaminal being rate-limiting step. Model II, comprising a second water molecule hydrogen-bonded to O_C, showed an important advantage with respect to previous model both *in vacuo* and with PCM solvation. However, this model does not work for some of the compounds under study. Besides, the catalytic effect of the extra water molecule is not so evident in the second step, mostly when bulk aqueous solvent (PCM) is considered. The reaction does not take place beyond hemiaminal formation with model III, characterized by a water molecule linked to N through hydrogen bonding, while the activation free energy obtained for this step is higher than in model I. The best results were obtained with model IV, both *in vacuo* and in solution, as the process is notably accelerated when two water molecules are directly involved in the hydrolysis reaction. Here, both water molecules participate in a cooperative process where bonds are formed and broken among all species, mimicking the possibility of HO^- and H^+ ions from different water molecules. This arrangement resulted in a much more favourable formation of TSs.

The addition of explicit water molecules shows a strong effect on reaction free energy profile and PCM solvation improves the description of imine hydrolysis in water, further reducing activation barriers. Therefore, solvent plays a fundamental role in this kind of chemical process, and the specific solvation patterns found in this mechanism could also appear in other analogous hydrolysis reactions.

The reaction proceeds via a stepwise mechanism, as experimentally observed. The attack of a water molecule on the N=C double bond (asynchronous concerted addition of H^+ and HO^-) takes place in the first step, which is rate limiting in the pH independent hydrolysis of imines. Subsequently, the so-formed hemiaminal collapses, leading to the parent amine (or ammonia) and carbonyl (or aldehyde) compounds. This step becomes rate limiting in more acidic media. In both steps proton-transfer from water to the nitrogen atom is well ahead of the rest of bond-forming / bond-breaking processes.

4.6 References

1. G. A. Hamilton and F. H. Westheimer, *On the mechanism of the enzymatic decarboxylation of acetoacetate.* J. Am. Chem. Soc., 1959 **81** (23) 6332-6333.
2. B. L. Horecker, S. Pontremoli, C. Ricci, and T. Cheng, *On the nature of the transaldolase-dihydroxyacetone complex.* Proc. Natl. Acad. Sci. U. S. A., 1961 **47** (12) 1949-1955.
3. A. C. Eliot and J. F. Kirsch, *Pyridoxal phosphate enzymes: mechanistic, structural, and evolutionary considerations.* Annu. Rev. Biochem., 2004 **73** (1) 383-415.
4. J. Stieglitz and P. N. Leech, *The molecular rearrangement of triarylmethylhydroxylamines and the "Beckmann" rearrangement of ketoximes.* J. Am. Chem. Soc., 1914 **36** (2) 272-301.
5. K. F. Schmidt, *Über den Imin-Rest.* Ber. Dtsch. Chem. Ges., 1924 **57** (4) 704-706.
6. F. Asinger, *Über die gemeinsame Einwirkung von Schwefel und Ammoniak auf Ketone.* Angew. Chem., 1956 **68** (12) 413-413.
7. S. D. Larsen and P. A. Grieco, *Aza Diels-Alder reactions in aqueous solution: cyclocondensation of dienes with simple iminium salts generated under Mannich conditions.* J. Am. Chem. Soc., 1985 **107** (6) 1768-1769.
8. X. L. Armesto, M. Canle L., M. V. García, and J. A. Santaballa, *Aqueous chemistry of N-halo-compounds.* Chem. Soc. Rev., 1998 **27** (6) 453-460.
9. S. Kobayashi and H. Ishitani, *Catalytic enantioselective addition to imines.* Chem. Rev., 1999 **99** (5) 1069-1094.
10. R. Hernández-Molina and A. Mederos, *1.19 - Acyclic and macrocyclic Schiff base ligands*, in *Comprehensive*

Coordination Chemistry II, J. A. McCleverty and T. J. Meyer, Editors. 2003, Elsevier Science. 411-446.

11. P. Bey and J. P. Vevert, *Synthesis of α-alkyl and α-functionalized methyl-α-amino acids.* Tetrahedron Lett., 1977 **18** (17) 1455-1458.
12. E. H. Cordes and W. P. Jencks, *The mechanism of hydrolysis of Schiff bases derived from aliphatic amines.* J. Am. Chem. Soc., 1963 **85** (18) 2843-2848.
13. J. W. McIver, *Structure of transition states. Are they symmetric?* Acc. Chem. Res., 1974 **7** (3) 72-77.
14. K. Fukui, *Formulation of the reaction coordinate.* J. Phys. Chem., 1970 **74** (23) 4161-4163.
15. C. Gonzalez and H. B. Schlegel, *Reaction path following in mass-weighted internal coordinates.* J. Phys. Chem., 1990 **94** (14) 5523-5527.
16. C. Gonzalez and H. B. Schlegel, *Improved algorithms for reaction path following: Higher-order implicit algorithms.* J. Chem. Phys., 1991 **95** (8) 5853-5860.
17. J. Tomasi and M. Persico, *Molecular interactions in solution: An overview of methods based on continuous distributions of the solvent.* Chem. Rev., 1994 **94** (7) 2027-2094.
18. C. J. Cramer, *Essentials of computational chemistry. Theories and models*. 2004, Chichester: John Wiley & Sons.
19. A. D. Becke, *Density-functional thermochemistry. III. The role of exact exchange.* J. Chem. Phys., 1993 **98** (7) 5648-5652.
20. C. Lee, W. Yang, and R. G. Parr, *Development of the Colle-Salvetti correlation-energy formula into a functional of the electron density.* Phys. Rev. B, 1988 **37** (2) 785-789.
21. B. Miehlich, A. Savin, H. Stoll, and H. Preuss, *Results obtained with the correlation energy density functionals of Becke and Lee, Yang and Parr.* Chem. Phys. Lett., 1989 **157** (3) 200-206.
22. M. J. Frisch, G. W. Trucks, H. B. Schlegel, G. E. Scuseria, M. A. Robb, J. R. Cheeseman, J. A. Montgomery Jr., T. Vreven, K. N. Kudin, J. C. Burant, J. M. Millam, S. S. Iyengar, J. Tomasi, V. Barone, B. Mennucci, M. Cossi, G. Scalmani, N. Rega, G. A. Petersson, H. Nakatsuji, M. Hada, M. Ehara, K. Toyota, R. Fukuda, J. Hasegawa, M. Ishida, T. Nakajima, Y. Honda, O. Kitao, H. Nakai, M. Klene, X. Li, J. E. Knox, H. P. Hratchian, J. B. Cross, C. Adamo, J. Jaramillo, R. Gomperts, R. E. Stratmann, O. Yazyev, A. J. Austin, R. Cammi, C. Pomelli, J. W. Ochterski, P. Y. Ayala, K. Morokuma, G. A. Voth, P. Salvador, J. J. Dannenberg, V. G. Zakrzewski, S. Dapprich, A. D. Daniels, M. C. Strain, O. Farkas, D. K. Malick, A. D. Rabuck, K. Raghavachari, J. B. Foresman, J. V. Ortiz, Q. Cui, A. G. Baboul, S. Clifford, J. Cioslowski, B. B. Stefanov, G. Liu, A. Liashenko, P. Piskorz, I. Komaromi, R. L. Martin, D. J. Fox, T. Keith, M. A. Al-Laham, C. Y. Peng, A. Nanayakkara, M. Challacombe, P. M. W. Gill, B. Johnson, W. Chen, M. W. Wong, C. Gonzalez, and J. A. Pople, *Gaussian 03*. 2004, Gaussian, Inc.: Wallingford CT.
23. J. E. Carpenter and F. Weinhold, *Analysis of the geometry of the hydroxymethyl radical by the "different hybrids for different spins" natural bond orbital procedure.* J. Mol Struct.-Theochem, 1988 **169** 41-62.
24. E. D. Glendening, A. E. Reed, J. E. Carpenter, and F. Weinhold, *NBO Version 3.1*.
25. A. E. Reed, L. A. Curtiss, and F. Weinhold, *Intermolecular interactions from a natural bond orbital, donor-acceptor viewpoint.* Chem. Rev., 1988 **88** (6) 899-926.
26. H. Maskill, *The physical basis of organic chemistry*. 1986, Oxford: Oxford University Press.
27. J. P. Richard, T. L. Amyes, and K. B. Williams, *Intrinsic barriers to the formation and reaction of carbocations.* Pure & Appl. Chem., 1998 **70** (10) 2007-2014.
28. A. D. McNaught and A. Wilkinson, *Compendium of chemical terminology*. 2 ed. IUPAC Chemical Data. 1997, Oxford: Blackwell Science.
29. P. A. Kollman, *Theory of hydrogen bond directionality.* J. Am. Chem. Soc., 1972 **94** (6) 1837-1842.

30. C. Hansch and A. Leo, *Substituent constants for correlation analysis in chemistry and biology*. 1979, New York: John Wiley & Sons, Inc.

31. R. W. Taft Jr., *Polar and steric substituent constants for aliphatic and o-benzoate groups from rates of esterification and hydrolysis of esters.* J. Am. Chem. Soc., 1952 **74** (12) 3120-3128.

CHAPTER 5

Density functional study of the decomposition of ethanolimines: Hydrolysis and fragmentation reactions

Curioser and curioser.

Lewis Carroll,
in Alice's Adventures in Wonderland

5.1 Introduction

An important discrepancy was observed between empirical and computational results for the decomposition of *N*-Cl ethanolamines (Chapters 1 to 3).[1-3] Experimental data suggest that a base-assisted bimolecular fragmentation process is the fastest reaction and, therefore, most of the decomposition takes place through this pathway, while electronic density calculations point to an intramolecular elimination as the most relevant process. It should be taken into account that kinetic measurements were performed on the first steps of the decomposition reaction but the weight of the different pathways was distributed according to final products ratios. In order to solve this disagreement, we decided to also analyze the subsequent steps of the process, *i.e.*, the hydrolysis of imine intermediates.

The bimolecular fragmentation yields simple imines, with no other functional groups present elsewhere in the molecule. Hydrolysis of these compounds has been already explained by empirical studies,[4] and we have also corroborated the reaction mechanism by computational methods as discussed in the previous chapter. However, the intramolecular elimination leads to *N*-(2-hydroxyethyl) imines (hereinafter referred to as ethanolimines) as intermediates. The hydrolysis of these compounds containing an alcohol function may be altered, or they could even undergo side reactions leading to unexpected products. Thus, we have studied computationally this process to explain the observed discrepancies. Relevant information about these compounds can be hardly found in the literature. This is surely due to the fact that they decompose readily, even in the absence of water, as described below. To our knowledge, this is the first study on the reactivity of this kind of species by means of electronic structure calculations.

5.2 Computational procedure

The most important outcomes of the hydrolysis process already studied for simple imines have been used as starting point to compute the reaction of ethanolimines. Thus, the methodology that was successfully applied is then here repeated. First, the hydrolysis of the simplest ethanolimine (CH_2=NCH_2CH_2OH) was performed using the same models I to IV employed in Chapter 4, and also a model V, considering a water molecule hydrogen-bonded to the oxygen atom of the alcohol group (O_{OH}). Then, model IV (*i.e.*, the molecular model comprising the imine plus two water molecules actively participating in the reaction) has been employed to estimate the activation barriers for the hydrolysis process of related compounds, as this system yielded again lower activation values.

Besides, another reaction has been analysed: alcohol donates its proton to imine carbon (C_I) via a six-membered cyclic transition structure (TS_{Frag}) and a full reorganization of the molecular bonds takes place leading to formaldehyde ($O=CH_2$) and another imine. This process is denominated intramolecular fragmentation throughout the text (in a few cases, namely with model V, the fragmentation is a bimolecular reaction). Both studied reactions are collected in Scheme 5.1.

Different molecular models have been also employed with this reaction. Model I only considers the ethanolimine without any discrete water molecules. Models II and III incorporate a discrete water molecule hydrogen-bonded to O_{OH} and to imine nitrogen (N), respectively. Model IV combines the two previous models, applying microsolvation on both O_{OH} and N atoms with two water molecules. Finally, model V considers a bimolecular process, where the hydroxyl functional group donates the proton to water while another proton is transferred from the solvent to C_I. As in model IV of the hydrolysis, the simplest arrangement consists of a single water molecule that concertedly accepts and donates a proton via an eight-membered cyclic TS.

In all cases, the polarized continuum model (PCM)[5] was applied over the geometries calculated *in vacuo* to obtain the free energy of solvation (ΔG_{solv}). The corresponding values have been corrected in order to use consistent standard states.[6]

All stationary points were fully optimized by using density functional theory (DFT) at the B3LYP level[7-9] together with the double-ζ 6-31++G** basis set incorporating polarization and diffuse functions. All calculations were carried out with the Gaussian03 program,[10] default values of this package have been used for all applicable parameters.

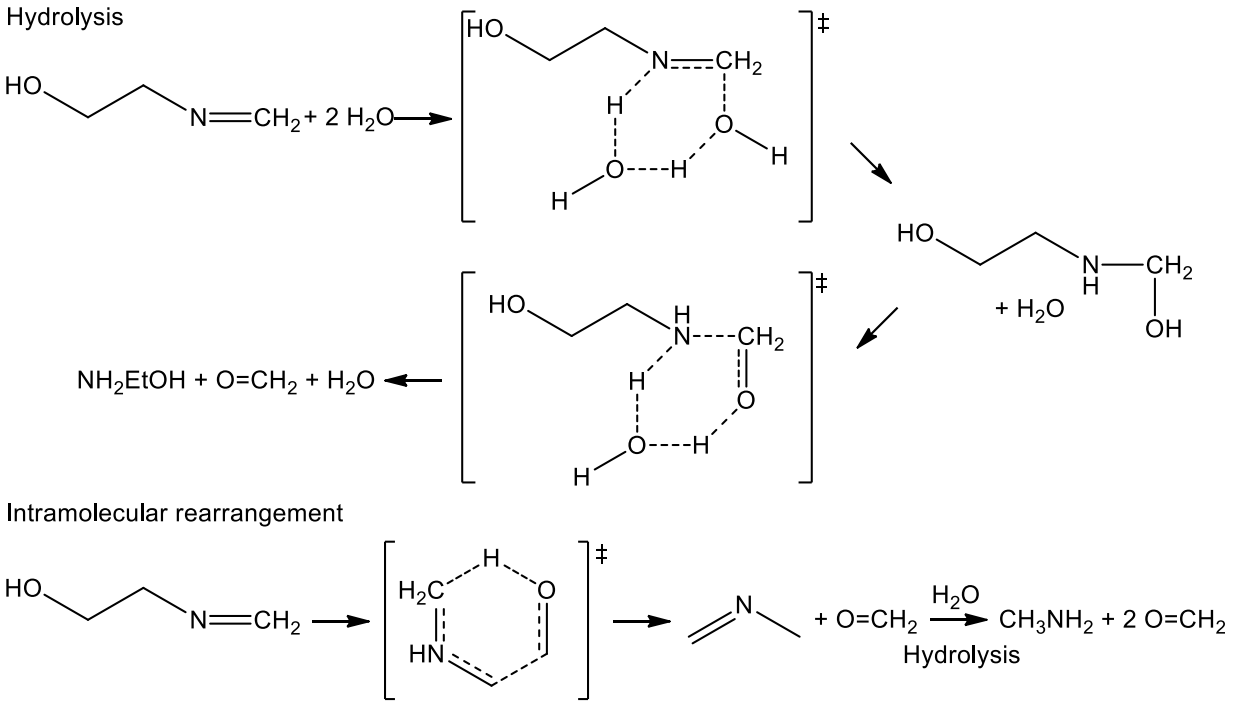

Scheme 5.1. Schematic description of the reactions undergone by CH_2=NCH_2CH_2OH. The hydrolysis process is shown with participation of a second water molecule (model IV), while the intramolecular fragmentation does not consider any discrete water molecule (model I).

5.3 Results and discussion

The first process analyzed is the typical hydrolysis of imines. Free energy activation barriers obtained for CH_2=NCH_2CH_2OH are collected in Table 5.1. Model II shows some catalytic effect with respect to model I. Model III yields higher activation barriers for step 1 while TS_2 could not be obtained, as already observed with imines lacking the alcohol function. Model IV is again preferred as it yields lower values for both steps of the reaction. Finally, the water molecule interacting with the alcohol group (model V) does not produce any decrease in the energy of activation and the values obtained are similar to model I. Step 1 is rate limiting with all five models. Besides, addition of PCM to consider bulk solvation enhances greatly the reaction rate as the activation barriers are lower (10 to 45 kJ mol^{-1}) than *in vacuo*. More detailed thermodynamic information is collected in Supplementary Information (Table S5.1).

Table 5.1. Intrinsic activation barriers ($\Delta G°_{int} = \Delta G°_{TS} - \Delta G°_{RIC}$) in kJ mol^{-1} for the hydrolysis and fragmentation processes of the simplest ethanolimine (CH_2=NCH_2CH_2OH), obtained with models I to V at the B3LYP/6-31++G** computational level.

	Hydrolysis				Fragmentation	
	Step 1		Step 2			
Model	***In vacuo***	**PCM**	***In vacuo***	**PCM**	***In vacuo***	**PCM**
I	200.87	159.44	152.16	121.70	177.04	185.58
II	166.85	128.78	135.07	124.65	179.97	183.86
III	225.63	211.41	-	-	177.60	180.16
IV	101.60	78.34	76.64	41.49	201.17	203.81
V	205.80	160.91	153.29	123.00	241.39	230.05

The transition structures obtained for both hydrolysis steps (TS_1 and TS_2) with model IV are depicted in Figure 5.1. This is the simplest molecular model that considers the addition onto N=C_I double bond of HO^- and H^+ ions from different water molecules and it is selected for the use along the study. Most stable conformational isomers have been calculated for both structures. In TS_1 the hydroxyl function interacts with the oxygen atom attaching to C_I. This hydrogen bond presents a distance of only 1.567 Å, stabilizing the negatively charged HO^- group and, as a result, both proton transfers are quite advanced (bonds forming in this step yield distances of 1.066 and 1.085 Å at the TS) with respect to C_I–O bond formation (2.616 Å). This process is more asynchronous than the observed for the parent imine CH_2=NCH_2CH_3 (see Table S4.5). On the other hand, this alcohol does not interact with any other atom in the thermodynamically preferred conformer obtained for TS_2, and the bond evolution (solely evaluated by bond distances) is then fully equivalent in both compounds (CH_2=NCH_2CH_2OH and CH_2=NCH_2CH_3).

The addition of the alcohol group causes a decrease in the activation barrier of step 1 (Table S5.1). However, $\Delta G°_{int}$ of step 2 does not show any significant difference between CH_2=NCH_2CH_2OH and CH_2=NCH_2CH_3. Therefore, the only presence of the hydroxyl apparently does not produce any relevant inductive effect as it should affect both elementary reactions, but has an influence on the first step just by interaction with one of the water molecules via strong hydrogen bonding.

The fragmentation process has been analyzed with five different computational models as well (Figure 5.1). Free energy activation barriers calculated for this process are in general higher than for hydrolysis (Table 5.1). In models I to IV the proton of the alcoholic group is intramolecularly transferred to imine carbon atom (C_I) forming a six-membered cycle, and six bonds are formed and broken concertedly. Thus, the molecule collapses and two fragments are obtained as products, formaldehyde and another simple imine, which may undergo hydrolysis in water.

The addition of a water molecule hydrogen-bonded to charged atoms (models II and III) leads to a slight change in the barrier, it increases *in vacuo* but a small decrease of a few (2 - 5) kJ·mol^{-1} is observed with PCM. As this water molecule does not take part in the reaction, the geometry obtained for both TSs is not very affected. Hydrogen-bond distances range from 1.92 to 1.96 Å, the interaction is not as strong as that observed in TS_1 of hydrolysis. Proton transfer is more advanced upon water interaction with O_{OH} (model II), but delayed when water interacts with N (model III). Model IV incorporates both discrete water molecules. They form three hydrogen bonds, two of them directed to the N and O_{OH} atoms of the ethanolimine and a third one between them. The hydrogen bond to N atom is in this case much weaker and, as a consequence, the effect in the geometry of the addition of two water molecules is quite similar to that of model II: the interaction with O_{OH} leads to some advance of the proton transfer. However, their effect on the stability of the stationary points was unexpected, as the free energy of activation increases ca. 20 kJ·mol^{-1} both *in vacuo* and with PCM solvation.

Model V includes a water molecule that participates actively in the chemical process, donating a proton to C_I while accepting the proton from the alcohol. This arrangement represents the simplest possibility of an intermolecular fragmentation with direct participation of the aqueous solvent in the reaction, as the model IV used for hydrolysis. In this particular case, eight bonds are formed and broken concertedly in an eight-membered cyclic transition structure. Both proton transfers occur simultaneously and the advance of the reaction at the TS is analogous to model I, *i.e.,* the relevant bond distances are quite similar. However, this system seems more unstable and yields a higher activation barrier than the previous models considering intramolecular processes.

The use of discrete water molecules in the microsolvated models of the fragmentation process does not show an important improvement in the description of the reaction or in the free energy profile. Furthermore, the use of PCM solvation increases the activation barriers, and solvent interaction seems to hinder the reaction. Thus, the intramolecular fragmentation obtained with model I is taken as standard method for the calculation with other compounds.

Some analogies can be drawn between this reaction and an enol imine ⇆ enaminone tautomerization.[11] A similar bond rearrangement occurs upon the proton transfer from the hydroxyl group to the imine moiety. However, in this case the proton is not added on N but on C_I atom, and the double bond formed is not a C=C bond but another imine. Furthermore, the lack of a double bond in position α to the alcohol is responsible for the molecule breakdown, and thus the fragmentation

process is not readily reversible as in the case of a tautomerism.

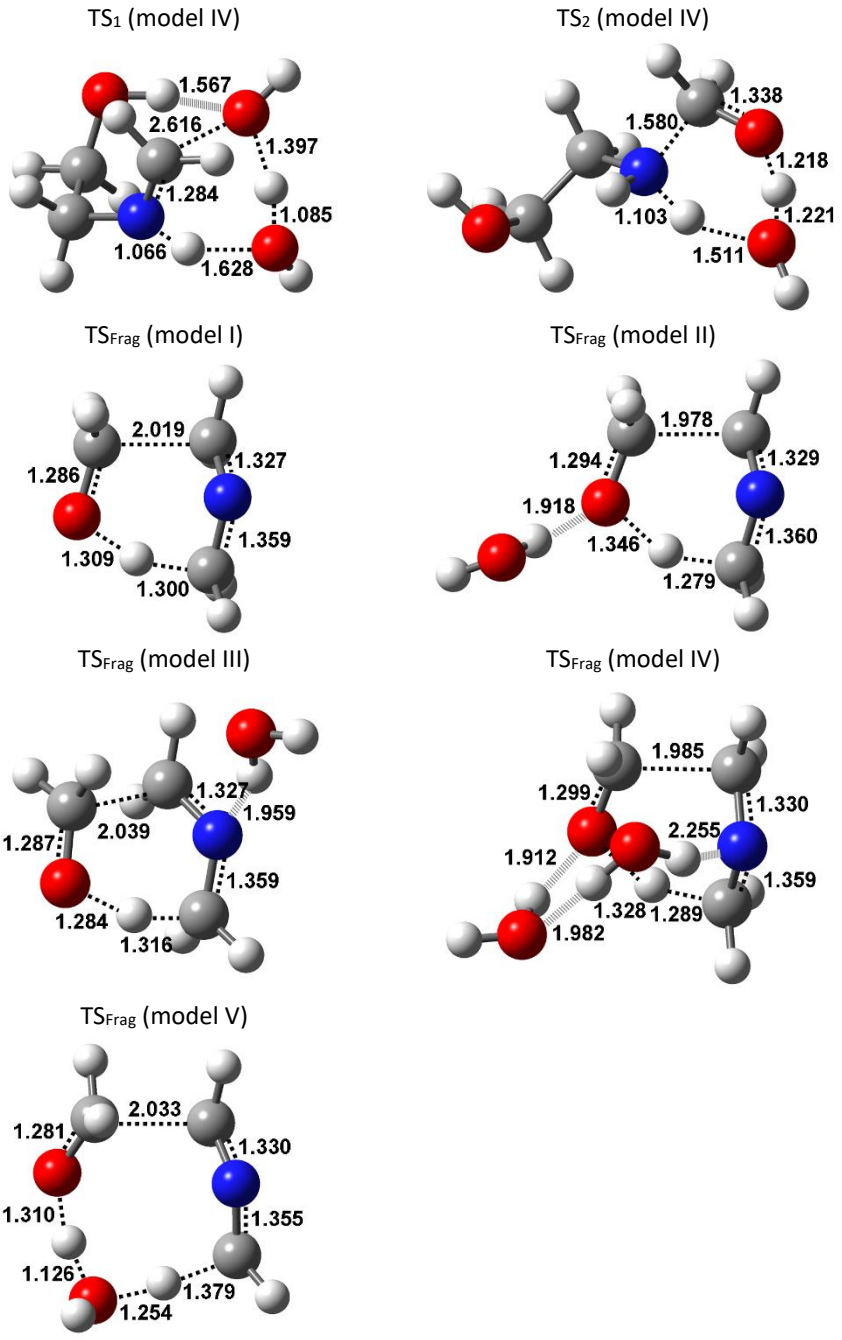

Figure 5.1. Geometries obtained for the TSs for both steps of the hydrolysis process of CH_2=NCH_2CH_2OH with model IV and for the fragmentation reaction with models I to V at the B3LYP/6-31++G** computational level. Bonds being formed and broken are represented with dotted lines and hydrogen bonds are represented with ⁞⁞⁞⁞⁞. Distances in Å.

Several theories on intramolecular reactivity propose different reasons for their higher reaction rates obtained with respect to the intermolecular counterparts: proximity or adequate distance between reactants, correct orientation, or a more favourable entropic contribution.[12-14] Six-membered cyclic transition structures, as the TS obtained for the

intramolecular fragmentation, are typically very stable and indicative of fast reaction rates. The process here considered is surely much faster than the equivalent intermolecular reaction (it was already observed with model V), yielding a high effective molarity, but it is still slower than the hydrolysis. This pathway also presents six-membered TSs and, as an intermolecular reaction, the entropy from RICs to TSs is not so favourable, but it is fully compensated by the enthalpic term (Table S5.1).

Table 5.2. Intrinsic activation barriers ($\Delta G°_{int} = \Delta G°_{TS} - \Delta G°_{RIC}$) in kJ·mol^{-1} for the hydrolysis and intramolecular fragmentation processes of ethanolimines with R_1 and R_2 = H, CH_3, or CH_2CH_3, obtained with models IV and I, respectively, at the PCM/B3LYP/6-31++G** computational level.

Substituents		Hydrolysis		Intramolecular fragmentation
R_1	R_2	Step 1	Step 2	
H	H	78.34	41.49	185.58
H	CH_3	86.39	40.28	204.17
H	CH_2CH_3	87.00	39.82	203.79
CH_3	CH_3	76.27	40.34	215.25
CH_3	CH_2CH_3	74.04	39.37	214.09
CH_2CH_3	CH_2CH_3	76.20	41.74	209.82

The addition of substituents on C_I shows little influence on the activation barriers of the hydrolysis (4 - 9 kJ·mol^{-1} for TS_1, and 0 - 2 kJ·mol^{-1} for TS_2, Table 5.2). A more important change is observed for the fragmentation: the activation value increases by 20 - 30 kJ·mol^{-1}, and the effect reveals more significant with methyl substituents than with ethyl groups. Therefore, hydrolysis is the preferred pathway for the decomposition process of all the studied ethanolimines in water, and the difference in reaction rates between both processes increases upon substitution on C_I.

Figure 5.2 displays the reaction profiles *in vacuo* and with PCM for the two processes under study and following the reaction to final products, *i.e.*, for the intramolecular fragmentation the subsequent hydrolysis of the produced imine (CH_2=NCH_3) is also shown. All intermediates (either hemiaminals or formaldehyde + imine) have been represented, despite independent hemiaminals are not observed since, in both imine hydrolysis processes, the complexes PIC_1 and RIC_2 are pretty similar in thermodynamics and geometry.

In the case of the fragmentation reaction PCM solvation has no relevant influence on the activation free energy, while it shows an important catalytic effect on both steps of the hydrolysis. Besides, it is evident that the reduction in the first step is mostly due to RIC_1 as it presents higher relative energy with PCM than *in vacuo*, and not because of further stabilization of TS_1. However, the free energy value of RIC_{Frag} is very similar to that of separate reactants, both *in vacuo* and with PCM. The difference between these two stationary points has been explained in the previous chapter with reference to the work term in Marcus equation. It represents the energy rise for the adequate arrangement of the reactants, necessary for the hydrolysis reaction to proceed, but it is negligible for the fragmentation, as R and RIC_{Frag} present similar energies. Therefore, if we use $\Delta G°^{\ddagger}$ values, *i.e.* $\Delta G°_{TS} - \Delta G°_{R}$, as activation energies, the barriers obtained for both processes are more similar, although the hydrolysis would still be faster.

Hydrolysis pathway needs water molecules to proceed and the interaction with bulk solvent as modelled with PCM shows an important catalytic effect. The reaction in aqueous solution presents a low activation barrier and is kinetically preferred to fragmentation. On the other hand, the latter process cannot be distinctly accelerated by microsolvation with discrete water molecules, and the use of the PCM model yields reactants and RICs more stabilized upon solvation than TSs, that is, the activation energy increases. However, water is unnecessary for the intramolecular fragmentation reaction and the process may proceed also *in vacuo* or with any other solvent. For this reason *N*-ethanolimines must be quite unstable even in the absence of water.

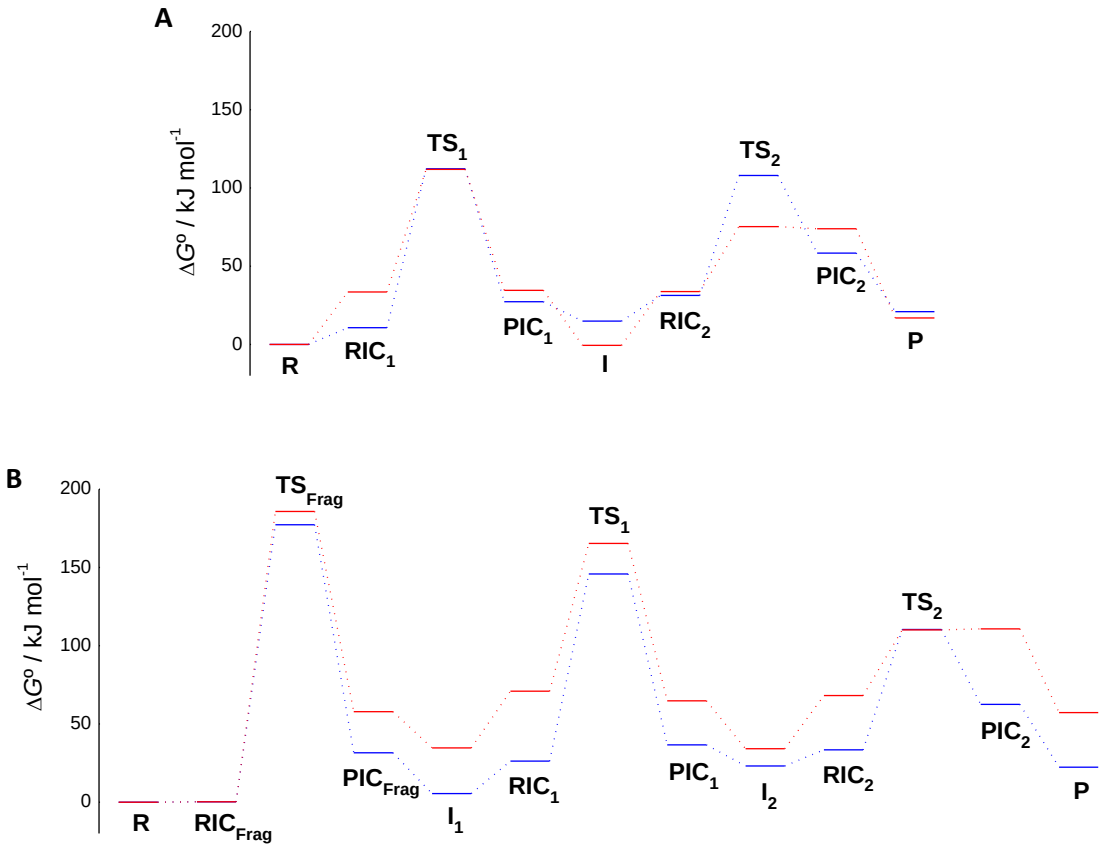

Figure 5.2. Gibbs free energy profiles for the decomposition of CH_2=NCH_2CH_2OH *in vacuo* (—) and with PCM solvation (—) at the B3LYP/6-31++G** computational level. (A) Hydrolysis process with model IV, (B) intramolecular fragmentation with model I plus subsequent hydrolysis of CH_2=NCH_3 (model IV).

5.4 Conclusions

A detailed mechanistic study of the decomposition process carried out by *N*-(2-hydroxyethyl) imines or ethanolimines has been performed to provide a better understanding of the reactions in which they take part as intermediates. Furthermore, it is also helpful in explaining the observed discrepancies between empirical and computational approaches to the decomposition of secondary *N*-halo ethanolamines.

The decomposition may take place via two concurrent pathways: hydrolysis and intramolecular fragmentation reactions. Ethanolimines in aqueous solvation undergo preferentially the hydrolysis process yielding ethanolamine and a carbonyl compound, and the intramolecular fragmentation is slower. However, while water is required as a reactant in the hydrolysis reaction, fragmentation can proceed even in the absence of water, leading to formaldehyde and another imine, which could subsequently hydrolyze if water is present.

Therefore, these compounds reveal quite unstable since they readily decompose with or without water present. This is a plausible reason for the lack of information about the properties and reactivity of ethanolimines in the literature.

5.5 References

1. J. Andrés, X. L. Armesto, M. Canle L., M. V. García, D. R. Ramos, and J. A. Santaballa, *Understanding the mechanism of base-assisted decomposition of (N-halo),N-alkylalcoholamines.* Org. Biomol. Chem., 2003 **1** (23) 4323-4328.

2. D. R. Ramos, R. Castillo, M. Canle L., M. V. García, J. Andrés, and J. A. Santaballa, *Density functional study of the Hoffmann elimination of (N-Cl),N-methylethanolamine in gas phase and in aqueous solution.* Chem. Phys. Lett., 2006 **429** (4-6) 425-429.

3. D. R. Ramos, R. Castillo, M. Canle L., M. V. García, J. Andrés, and J. A. Santaballa, *A theoretical study on the mechanism of the base-promoted decomposition of N-chloro,N-methylethanolamine.* Org. Biomol. Chem., 2009 **7** (9) 1807-1814.

4. E. H. Cordes and W. P. Jencks, *The mechanism of hydrolysis of Schiff bases derived from aliphatic amines.* J. Am. Chem. Soc., 1963 **85** (18) 2843-2848.

5. J. Tomasi and M. Persico, *Molecular interactions in solution: An overview of methods based on continuous distributions of the solvent.* Chem. Rev., 1994 **94** (7) 2027-2094.

6. C. J. Cramer, *Essentials of computational chemistry. Theories and models*. 2004, Chichester: John Wiley & Sons.

7. B. Miehlich, A. Savin, H. Stoll, and H. Preuss, *Results obtained with the correlation energy density functionals of Becke and Lee, Yang and Parr.* Chem. Phys. Lett., 1989 **157** (3) 200-206.

8. C. Lee, W. Yang, and R. G. Parr, *Development of the Colle-Salvetti correlation-energy formula into a functional of the electron density.* Phys. Rev. B, 1988 **37** (2) 785-789.

9. A. D. Becke, *Density-functional thermochemistry. III. The role of exact exchange.* J. Chem. Phys., 1993 **98** (7) 5648-5652.

10. M. J. Frisch, G. W. Trucks, H. B. Schlegel, G. E. Scuseria, M. A. Robb, J. R. Cheeseman, J. A. Montgomery Jr., T. Vreven, K. N. Kudin, J. C. Burant, J. M. Millam, S. S. Iyengar, J. Tomasi, V. Barone, B. Mennucci, M. Cossi, G. Scalmani, N. Rega, G. A. Petersson, H. Nakatsuji, M. Hada, M. Ehara, K. Toyota, R. Fukuda, J. Hasegawa, M. Ishida, T. Nakajima, Y. Honda, O. Kitao, H. Nakai, M. Klene, X. Li, J. E. Knox, H. P. Hratchian, J. B. Cross, C. Adamo, J. Jaramillo, R. Gomperts, R. E. Stratmann, O. Yazyev, A. J. Austin, R. Cammi, C. Pomelli, J. W. Ochterski, P. Y. Ayala, K. Morokuma, G. A. Voth, P. Salvador, J. J. Dannenberg, V. G. Zakrzewski, S. Dapprich, A. D. Daniels, M. C. Strain, O. Farkas, D. K. Malick, A. D. Rabuck, K. Raghavachari, J. B. Foresman, J. V. Ortiz, Q. Cui, A. G. Baboul, S. Clifford, J. Cioslowski, B. B. Stefanov, G. Liu, A. Liashenko, P. Piskorz, I. Komaromi, R. L. Martin, D. J. Fox, T. Keith, M. A. Al-Laham, C. Y. Peng, A. Nanayakkara, M. Challacombe, P. M. W. Gill, B. Johnson, W. Chen, M. W. Wong, C. Gonzalez, and J. A. Pople, *Gaussian 03*. 2004, Gaussian, Inc.: Wallingford CT.

11. W. M. F. Fabian, L. Antonov, D. Nedeltcheva, F. S. Kamounah, and P. J. Taylor, *Tautomerism in hydroxynaphthaldehyde anils and azo analogues: a combined experimental and computational study.* J. Phys. Chem. A, 2004 **108** (37) 7603-7612.

12. M. I. Page and W. P. Jencks, *Entropic contributions to rate accelerations in enzymic and intramolecular reactions and the chelate effect.* Proc. Natl. Acad. Sci. U. S. A., 1971 **68** (8) 1678-1683.

13. F. M. Menger, *On the source of intramolecular and enzymatic reactivity.* Acc. Chem. Res., 1985 **18** (5) 128-134.

14. L. Mandolini, *Entropy control in intramolecular reactions.* Bull. Soc. Chim. Fr., 1988 **2** 173-176.

CHAPTER 6

A joint experimental-computational approach to concurrent reaction mechanisms: Decomposition of secondary *N*-halo ethanolamines

It is also a good rule not to put too much confidence in experimental results until they have been confirmed by theory.

Sir Arthur Eddington

6.1 Introduction

Numerous valuable tools can be employed in the experimental elucidation of reaction mechanisms, such as determination of rate equation, product analysis, kinetic isotope effects, intermediates identification, etc. However, these methods present a somewhat limited application when the mechanism presents great complexity, in particular multi-step reactions initiated by the rate-limiting step or when some steps are partially rate determining, mechanisms with elusive intermediates, and concurrent pathways yielding identical products. On the other hand, electronic density calculations allow the accurate characterization of the molecular mechanism of chemical reactions. A computational analysis can discriminate every elementary step, it allows the analysis of any particular pathway independently of any other parallel reactions, and the characterization of all proposed intermediates is feasible. Unfortunately, computational methods do not always reproduce thermodynamic values satisfactorily, except for small systems using highly sophisticated methods, which may involve huge computational resources, and so-obtained results must be validated by comparison with corresponding empirical data. Therefore, the combined use of experimental measurements and computational data is much more effective than a separate approach for the comprehensive elucidation of complex reaction mechanisms.

Halogenation is fundamental in many chemical and biological processes. Chlorination is widely employed in water disinfection,[1] whereas peroxidases catalyze halogenation in vivo, in particular, myeloperoxidase-mediated chlorination of the aminosulfonic acid taurine plays a central role in the immune response against infection in mammals[2-4] and in several inflammatory diseases.[5] Additionally, aminoalcohols are widely used in the production of different chemicals, also have relevant industrial applications, and take part in several metabolic pathways.[6-10] Thus, formation, reactivity, and decomposition of diverse *N*-halo compounds have been thoroughly studied,[11] and the *N*-halo derivatives of aminoalcohols have received some attention as well.[12, 13]

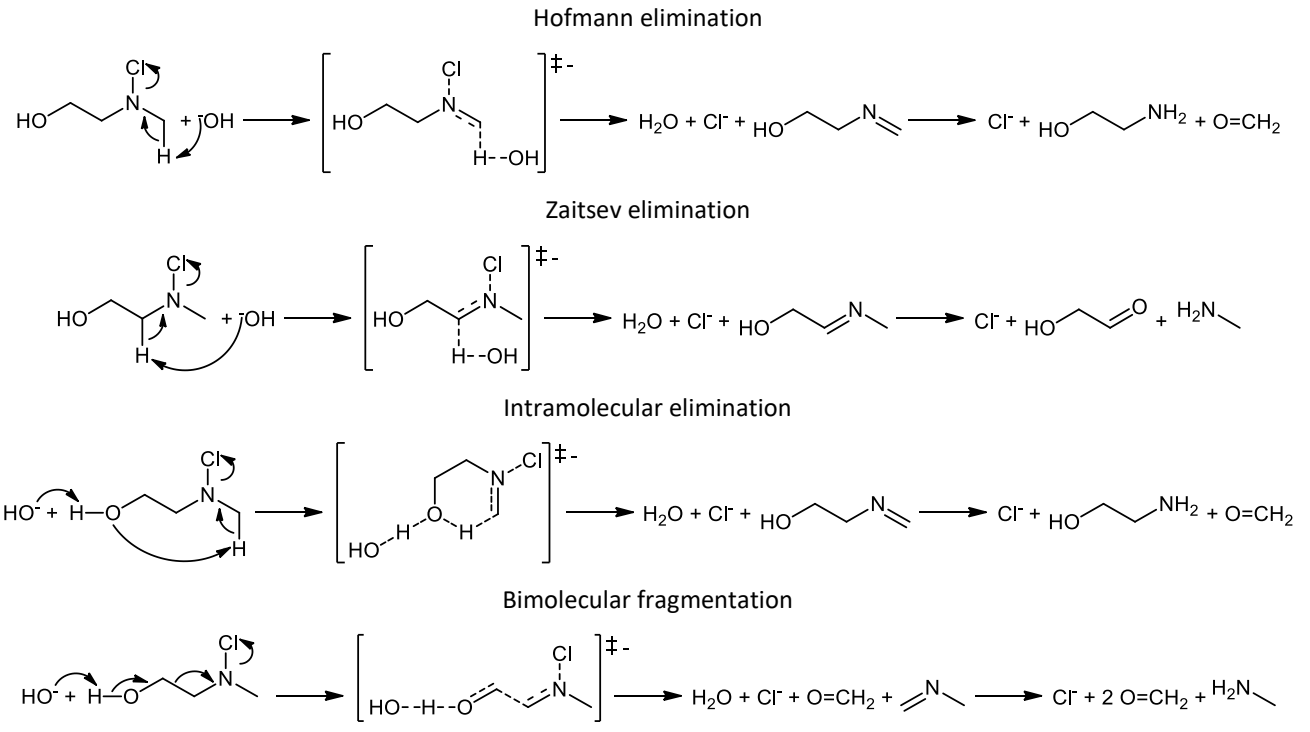

Scheme 6.1. Reaction mechanism proposed for the HO^--promoted decomposition of *N*-Cl,*N*-methylethanolamine according to experimental findings.

Base-promoted decomposition of secondary *N*-halo amines involves two consecutive steps. The first step is rate determining and corresponds to an elimination reaction, Hofmann or Zaitsev, (see Scheme 6.1) whereas the second step is the fast hydrolysis of the so-formed imine. Kinetic studies on the decomposition of secondary *N*-halo ethanolamines have shown that the striking rate enhancement observed with respect to corresponding parent *N*-halo ethylamines arises from the presence of the hydroxyl functional group, but to an extent that cannot be explained just in terms of inductive effect. Thus, the proposed mechanism involves two additional competitive pathways, an intramolecular elimination and a bimolecular fragmentation, comprising a total of four cooperative reactions (Scheme 6.1).[12, 13]

Analysis of final products of *N*-Cl,*N*-methylethanolamine decomposition showed a higher amount of methylamine, supporting bimolecular fragmentation as primary decomposition pathway.[12] However, a previous study revealed that *N*-Cl,*N*-*tert*-butylethanolamine, where this process is feasible but intramolecular elimination is impossible, decomposes at a far lower rate, indicating a much greater contribution of the latter.[13] These discrepancies led us to perform a computational analysis on this reaction. Contrary to our experimental research, this study suggests that intramolecular elimination is the main process, with a considerably lower activation barrier. Kinetic measurements do not yield any information about the steps later than rate-limiting step. Consequently, subsequent imine hydrolysis and other competitive pathways were also computationally studied.

The aim of this work is the determination of the complete reaction mechanism of the base-assisted decomposition of secondary *N*-halo ethanolamines. This chemical process revealed far more challenging than initially expected, as it involves many concurrent pathways, which yield misleading final products ratios. Therefore, experimental results and electronic structure calculations on the reaction between *N*-Cl,*N*-methylethanolamine and hydroxide ion, and successive processes, were contrasted to obtain a more detailed and accurate knowledge of the proper reaction path.

6.2 Experimental and computational methods

Most important procedures employed in the study are described below. *N*-Methylethylamine and *N*-methylethanolamine were halogenated with HClO(aq). Kinetics of the base-assisted decomposition of the *N*-chloro compounds was monitored using UV-Vis spectrophotometry upon reaction with NaOH. Brominated amines were obtained with HBrO(aq), and decomposition initiated by other bases was also followed. Same procedure has been performed for other amine couples. Quantitative determination of produced amines was made by derivatization and HPLC analysis.

The four pathways proposed for the HO^--mediated decomposition of *N*-Cl, *N*-methylethanolamine were calculated at the MP2=full/6-31++G** computational level with the Gaussian98 suite of programs.[14] Besides, calculations of subsequent processes were carried out with Gaussian03 at the B3LYP/6-31++G** computational level.[15] Hybrid cluster-continuum models, incorporating PCM (polarized continuum model) solvation[16] over microsolvated optimized structures, were employed to depict the process in water, considering both the solute-solvent interactions and the effect of bulk water. More detailed information on the employed methodology can be found in previous chapters.

6.3 Results and discussion

Decomposition in basic media of four different secondary *N*-halo ethanolamines has been studied both experimentally and computationally: *N*-X,*N*-methylethanolamine, *N*-X,*N*-ethylethanolamine, *N*-X,*N*-isopropylethanolamine, and *N*-X,*N*-benzylethanolamine (X=halogen). Parent *N*-halo ethylamines were also investigated for comparison. The reaction between *N*-Cl,*N*-methylethanolamine and HO^- is analyzed thoroughly below, results obtained for other compound were consistent. According to kinetic measurements a 360-fold rate increase is observed for the HO^--initiated decomposition of *N*-Cl,*N*-methylethanolamine with respect to the same reaction of *N*-Cl,*N*-methylethylamine, due to the participation of two additional pathways. This rise is even higher for other couples (Table 6.1).

Table 6.1. Second-order kinetic rate constants measured for the HO^--mediated decomposition of several secondary *N*-Cl,*N*-ethanolamines and corresponding parent secondary *N*-Cl,*N*-ethylamines at T = 298.15 K, and ratio between them. [a] Ref. [13]

Amine	k_{HO^-} ($M^{-1}\cdot s^{-1}$)	Ethanolamine	k_{HO^-} ($M^{-1}\cdot s^{-1}$)	Ratio
N-methylethylamine	1.88×10^{-4}	*N*-methylethanolamine	6.81×10^{-2}	362
diethylamine	2.03×10^{-4} [a]	*N*-ethylethanolamine	0.82[a]	4039
N-isopropylethylamine	3.27×10^{-2}	*N*-isopropylethanolamine	2.06	63
N-benzylethylamine	3.22×10^{-3}	*N*-benzylethanolamine	6.94	2155
		N-*tert*-butylethanolamine	8.28×10^{-5} [a]	-

Addition of substituents on the methyl end showed an important influence on the reaction rate. Quantitative structure-activity relationship models are helpful to understand the effect exerted by substituents in the reaction and to predict the reactivity of similar compounds. Application of Hammett equation[17] with different electronic parameters to analyze inductive and resonance effects did not yield any dependence. Addition of the steric effect of the substituents according to Taft approach[18] did not permit the establishment of any correlation either. Therefore, mechanistic information cannot be inferred from these models.

The relative contribution of each pathway on the overall decomposition rate has been worked out from the ratio of produced amines, and corresponding rate constants were determined. Thus, according to experimental data, bimolecular fragmentation (67 %) is preferred over intramolecular elimination (Chapter 1).

Product analysis of other amines yielded pretty different results. Substituents do not only affect reaction rate constant, but they influence the weight of the different pathways. Thus, substitution of a H atom in *N*-methylethanolamine by a phenyl group in *N*-benzylethanolamine meant a major change in pathways ratio of the decomposition reaction. For *N*-Cl,*N*-methylethanolamine bimolecular fragmentation is preferred, while main decomposition reaction for *N*-Cl,*N*-benzylethanolamine is intramolecular elimination (68 %). These substituents are linked to a C atom involved in Hofmann and intramolecular eliminations. They may also affect the neighbouring N atom, either facilitating or hindering the release of the leaving group (Cl^-), but this would have a similar effect in all four pathways.

Determination of the rate equation plus product analysis are core tools for the establishment of reaction mechanisms. However, while these obtained empirical results are facts, the proposed mechanism derived from them is only a postulate, which could be an artifact that just fits experimental data. This statement is particularly valid in the case of very complex reactions as in the present example. Kinetic studies are consistent with the base-assisted decomposition of *N*-halo ethanolamines showing extra pathways. Besides, second-order rate constants revealed that these processes are bimolecular. Thus, a base-mediated intramolecular elimination and a bimolecular fragmentation are proposed (Chapter 1).

It is possible to study reaction mechanisms using other experimental procedures that yield additional information. Different bases, HO^-, 2,2,2-trifluoroethoxide, and 1,1,1,3,3,3-hexafluoro-2-propoxide anions, and two leaving groups, Cl^- and Br^-, have been employed. These measurements revealed some details about the process, namely, the two main pathways are asynchronous concerted processes, but they did not enable us to establish unequivocally the reaction pathway either.

Product analysis seemed to be more helpful, as it allowed some discrimination among the four possible concurrent pathways. Still, ethanolamine is common to Hofmann and intramolecular eliminations, methylamine to Zaitsev and fragmentation processes, and formaldehyde is produced through all reactions but Zaitsev elimination. Since decomposition of the alcoholamine is much faster than that of the parent amine, contribution of Hofmann and Zaitsev eliminations were neglected, and thus the participation of intramolecular elimination and bimolecular fragmentation in the whole reaction were distributed according to [ethanolamine] / [methylamine] ratio.

Kinetic isotope effects (KIEs) could also be employed to obtain a more comprehensive mechanism and to determine the major decomposition reaction pathway. Primary or secondary KIEs can be studied by hydrogen - deuterium exchange.

However, substitution of the hydrogen on the hydroxyl group does not permit a differentiation between intramolecular elimination and bimolecular fragmentation. Replacement of other hydrogens is much more difficult and they do not allow a full differentiation among the four processes either. Only primary KIEs are usually relevant in the case of heavy atoms, but they cannot be applied on N and Cl, as these atoms take part similarly in all reactions. Besides, alcoholic oxygen participates in two pathways and only carbon in α position to hydroxyl group is just involved in bimolecular fragmentation but not in any other reaction. These experiments are complex and, as explained below, they would not be conclusive as they only take into account the first step of the decomposition, and do not consider subsequent reactions other than hydrolysis. Isotope-labelled products could be also analyzed, but same issues as with KIEs would arise.

Computational description of reaction mechanisms and characterization of transient intermediates revealed invaluable for a correct understanding of the base-assisted decomposition of secondary *N*-halo ethanolamines. Electronic density calculations can analyze concurrent pathways independently, also considering hypothetical structures, like transition structures or postulated undetected intermediates, and very detailed reaction mechanisms can be obtained. However, computational methods suffer from low thermodynamic accuracy, except for high-level methods, which are computationally expensive. Furthermore, while kinetic measurements only provide information on the elementary steps prior to rate-limiting step, computational studies report on the whole reaction.

Decomposition processes have been described computationally. Kinetic results are consistent with determined transitions structures, showing that the four pathways are concerted, with base attack and halide leaving taking place in the same initial step. Free energy intrinsic activation barriers ($\Delta G^\circ_{int} = \Delta G^\circ_{TS} - \Delta G^\circ_{RIC}$) obtained computationally are underestimated if compared with experimental values, but the bimolecular fragmentation (Table 6.2). The acceleration with respect to parent *N*-Cl,*N*-methylethylamine was correctly predicted with the best microsolvated model (420-fold), while the hybrid approach yielded a more dramatic increase (1640). However, these data suggest that intramolecular elimination is the preferred pathway, accounting for more than 99% of the overall reaction. This fully differs from experimental values, as product analysis indicated that bimolecular fragmentation is the main decomposition pathway (67%), but it is consistent with the fact that *N*-Cl,*N*-*tert*-butylethanolamine decomposes at an extremely slow rate.[13]

Table 6.2. Gibbs free energy activation barriers in $kJ \cdot mol^{-1}$ determined experimentally and computationally for the HO^--assisted decomposition of *N*-Cl,*N*-methylethanolamine and subsequent reactions. Experimental data were worked out from kinetic constants. Computational values correspond to calculated intrinsic activation barriers with the corresponding cluster-continuum model.

Compound	Process	Experimental	Computational
N-Cl,*N*-methylethanolamine	Hofmann elimination	100.22	71.59
	Zaitsev elimination	94.52	71.63
	Intramolecular elimination	82.43	51.55
	Bimolecular fragmentation	80.68	81.04
N-ethanolmethanimine	Hydrolysis step 1	-	78.34
	Hydrolysis step 2	-	41.49
	Intramolecular fragmentation	-	185.58
N-methylmethanimine	Hydrolysis step 1	-	94.42
	Hydrolysis step 2	-	41.94

Decomposition reaction rates are controlled by the combination of these four concurrent processes, as the initial step is rate limiting. However, following steps should be considered as well, since the contribution of the different pathways was estimated from final products concentration ratio. Therefore, subsequent decomposition of imines and ethanolimines has been also computationally studied. Hydrolysis of imines has been thoroughly analyzed some decades ago.[19] However, also alcoholimines are produced in the degradation processes under study. Thus, while hydroxyl group converts to carbonyl

group in the bimolecular fragmentation pathway, it remains as part of the formed imine in the intramolecular elimination reaction as *N*-(2-hydroxyethyl)methanimine or simply, *N*-ethanolmethanimine. Stability of ethanolimines has never been empirically investigated, and the alcohol group may present more than just a substituent effect, as already observed in the base-assisted decomposition of *N*-halo ethanolamines. Electronic structure calculations have been also performed on the hydrolysis of simple imines (Chapter 4) and ethanolamines, and on the rearrangement of the latter via an intramolecular fragmentation (Chapter 5).

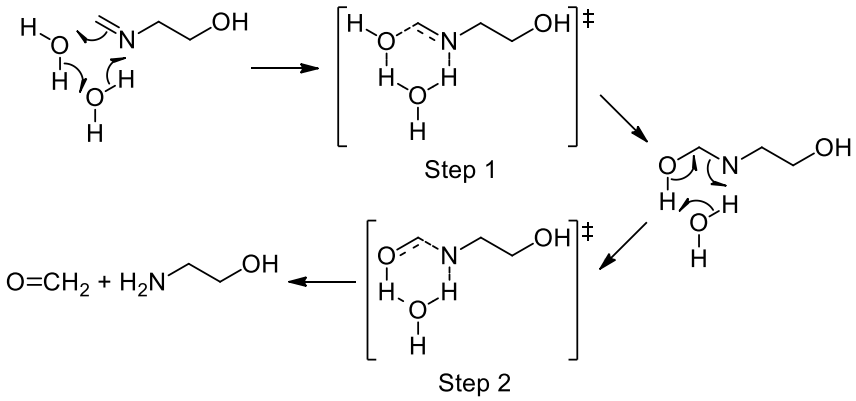

Scheme 6.2. Two-step mechanism of hydrolysis of *N*-ethanolmethanimine according to the model employed in the computational study.

A stepwise mechanism was obtained for pH-independent hydrolysis of imines, as suggested by previous experimental studies by Cordes and Jencks.[19] The reaction is initiated by the attack of water to the imine leading to a hemiaminal. It collapses yielding an amine and a carbonyl compound in a second step. In all cases the first step was rate limiting, as also stated by those authors (Chapter 4).

Ethanolimines present quite different reactivity from that of simple imines due to the extra alcohol function. Apart from hydrolysis, a side reaction occurs, leading to other products. Both processes have been studied computationally (Chapter 5). Hydrolysis of ethanolimines revealed similar to that of parent imines. Thus, analysis of both imines and ethanolimines was performed with the same computational model, including two discrete water molecules that actively participate in the reaction. Then, the process takes place via more relaxed six-membered cyclic transition structures in the two steps (Scheme 6.2). It yielded best outcomes in both cases and the results were altered by the presence of the hydroxyl group, mainly with a decrease in the activation barrier of step 1.

An intramolecular fragmentation followed by hydrolysis of the produced imine has been also studied. In this case, several models present very similar good performance, so the simplest model, only comprising the reacting molecule without any discrete waters, was selected. In this process a proton is transferred from alcohol to imine carbon, coupled with a full reorganization of the molecular bonds, via a six-membered cyclic transition structure, leading to formaldehyde and *N*-methylmethanimine, which then undergoes hydrolysis (Scheme 6.3).

Thermodynamics of both competitive pathways, imine hydrolysis and intramolecular fragmentation, must be compared in order to estimate their relative weight in the decomposition reaction of ethanolimines. A diagram of Gibbs free energy calculated for *N*-ethanolmethanimine decomposition *vs*. reaction coordinate is displayed in Figure 6.1. Gibbs free energy of the transition structure of hydrolysis step 1 is lower than that of intramolecular fragmentation. Thus, activation energy, also the intrinsic value, is more favourable for hydrolysis, which corresponds to a much faster reaction rate. Therefore, intramolecular fragmentation would only account for a negligible percentage of the overall reaction and, apparently, it could not justify the divergence between experimental and computational studies on the base-assisted degradation of *N*-

halo ethanolamines.

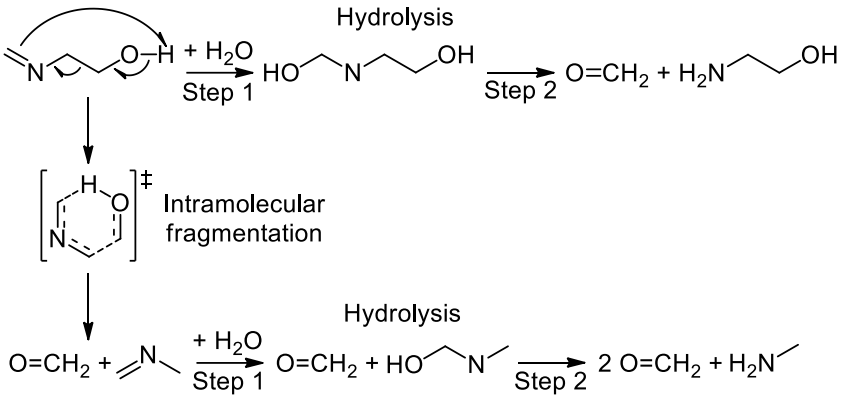

Scheme 6.3. Decomposition pathways of *N*-ethanolmethanimine: direct imine hydrolysis and intramolecular fragmentation plus imine hydrolysis. The fragmentation is described in more detail according to the model employed in the computational study.

We can take into account the reversibility of imine hydrolysis. The backward reaction presents an activation barrier similar to the forward process, but the large excess of water favours the latter. Besides, the second step is much faster, so the reaction back to starting imine may not have a relevant effect on the reaction kinetics. On the other hand, the RIC of the intramolecular fragmentation of *N*-ethanolmethanimine is quite similar to the PIC obtained for intramolecular elimination of *N*-Cl,*N*-methylethanolamine. Thus, these two successive processes may take place immediately, without any relevant rearrangement in between. This would favour this pathway but, according to our computational results, hydrolysis would still be much preferred.

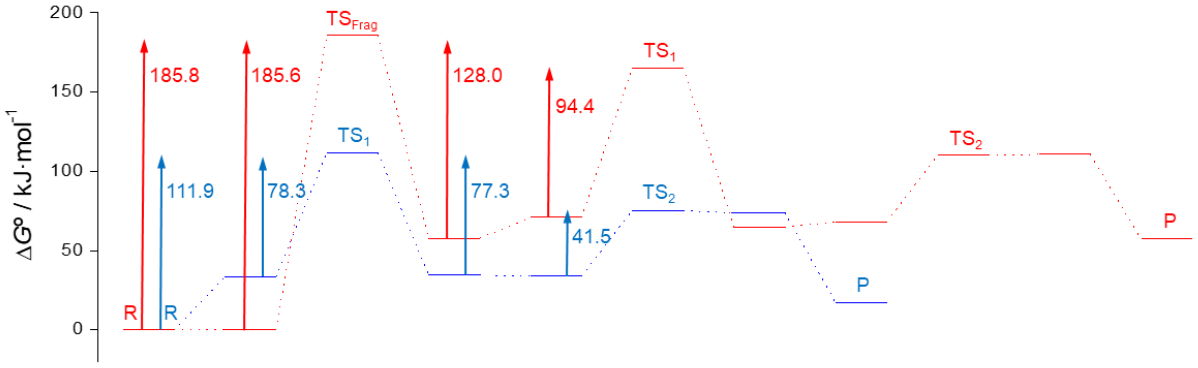

Figure 6.1. Energy profile diagram for the decomposition pathways for *N*-ethanolmethanimine: (—) direct imine hydrolysis, (—) intramolecular fragmentation plus imine hydrolysis. For the sake of clarity, reaction intermediates are not shown. Calculated (intrinsic) activation barriers for some direct and reverse steps are displayed. Gibbs free energy data calculated at PCM//B3LYP/631++G** level.

Considering reversibility of every step, the reaction would be under thermodynamic control instead of being kinetically controlled. However, as observed in Figure 6.1, the products obtained through hydrolysis are more stable, and again this pathway would be more favoured. Thus, experimental results could only be obtained if hydrolysis process was reversible and intramolecular fragmentation irreversible, but this does not seem to be the case.

The outcome is not consistent with products ratio. Therefore, according to the slow decomposition rate observed for *N*-Cl,*N*-*tert*-butylethanolamine, the base-assisted decomposition of secondary *N*-halo ethanolamines must take place preferentially via an intramolecular elimination followed by concurrent imine hydrolysis and intramolecular fragmentation together with a final hydrolysis of the produced imine. Relative contribution of these two pathways controls the distribution of products. Transition structures calculated for this whole reaction are collected in Figure 6.2.

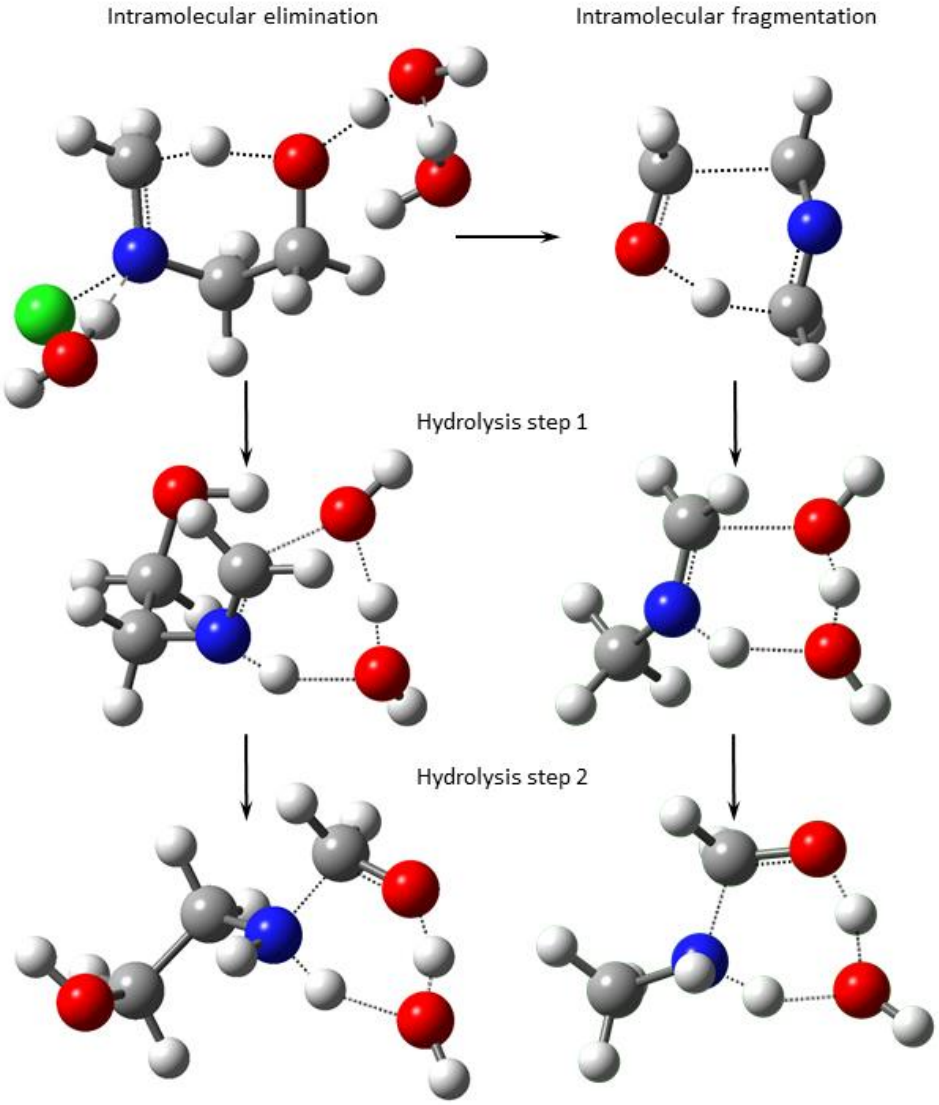

Figure 6.2. Calculated transition structures at the corresponding microsolvated models, obtained along the proposed bifurcated pathway for the HO^--assisted decomposition of *N*-Cl,*N*-methylethanolamine.

According to this scheme, the degradation of *N*-Cl,*N*-methylethanolamine solely takes place via the intramolecular elimination, while parent *N*-Cl,*N*-methylethylamine reacts mostly through Zaitsev elimination. Thus, effective molarity for this reaction, estimated from the ratio between intramolecular and Hofmann eliminations, is around 4000 (without molar units, as both processes are bimolecular), while the ratio for other *N*-halo ethanolamines would be still higher.

6.4 Conclusions

The reaction between HO^- and *N*-Cl,*N*-methylethanolamine has been comparatively characterized by experimental and computational means. Despite obtained data are not conclusive, the results clearly point to a decomposition reaction mostly controlled by a base-assisted intramolecular elimination, followed by hydrolysis in a two-step mechanism coupled with a more prevalent concurrent reorganization of the produced ethanolimine, which can be best described as an intramolecular fragmentation. The imine produced in this process also suffers hydrolysis to yield the final products, which exactly correspond to the products expected from the bimolecular fragmentation plus imine hydrolysis pathway. This outcome can be also generalized to base-mediated decomposition of other secondary *N*-halo ethanolamines, but with a different ratio of the competitive processes.

6.5 References

1. S. Miller, *Disinfection products in water treatment.* Environ. Sci. Technol., 1993 **27** (12) 2292-2294.
2. S. J. Klebanoff, *Myeloperoxidase-halide-hydrogen peroxide antibacterial system.* S. J. Klebanoff, J. Bacteriol., 1968, 95, 2131 1968 **95** (6) 2131-2138.
3. I. U. Schraufstätter, K. Browne, A. Harris, P. A. Hyslop, J. H. Jackson, O. Quehenberger, and C. G. Cochrane, *Mechanisms of hypochlorite injury of target cells.* J. Clin. Invest., 1990 **85** (2) 554-562.
4. E. L. Thomas, M. B. Grisham, and M. M. Jefferson, *Myeloperoxidase-dependent effect of amines on functions of isolated neutrophils.* J. Clin. Invest., 1983 **72** (2) 441-454.
5. S. J. Klebanoff, *Oxygen metabolites from phagocytes*, in *Inflammation: basic principles and clinical correlates*, J. I. Gallin and R. Snyderman, Editors. 1999, Lippincott Williams & Wilkins: Philadelphia. 721-768.
6. J. Xiao, C. W. Li, and M. H. Li, *Kinetics of absorption of carbon dioxide into aqueous solutions of 2-amino-2-methyl-1-propanol+monoethanolamine.* Chem. Eng. Sci., 2000 **55** (1) 161-175.
7. D. L. Nelson, A. L. Lehninger, and M. M. Cox, *Lehninger principles of biochemistry*. 2008, New York: W. H. Freeman.
8. S. M. Austin and T. G. Waddell, *Prebiotic synthesis of vitamin B6-type compounds.* Orig. Life Evol. Biosph., 1999 **29** (3) 287-296.
9. K. Yamamoto, Y. Takahashi, T. Mano, Y. Sakata, N. Nishikawa, J. Yoshida, Y. Oishi, M. Hori, T. Miwa, S. Inoue, and T. Masuyama, *N-methylethanolamine attenuates cardiac fibrosis and improves diastolic function: inhibition of phospholipase D as a possible mechanism.* Eur. Heart J., 2004 **25** (14) 1221-1229.
10. C. Liao and R. A. Nicholson, *Ethanolamine and related amino alcohols increase basal and evoked release of [^{3}H]-D-aspartic acid from synaptosomes by enhancing the filling of synaptic vesicles.* Eur. J. Pharmacol., 2007 **566** (1-3) 103-112.
11. X. L. Armesto, M. Canle L., M. V. García, and J. A. Santaballa, *Aqueous chemistry of N-halo-compounds.* Chem. Soc. Rev., 1998 **27** (6) 453-460.
12. J. Andrés, X. L. Armesto, M. Canle L., M. V. García, D. R. Ramos, and J. A. Santaballa, *Understanding the mechanism of base-assisted decomposition of (N-halo),N-alkylalcoholamines.* Org. Biomol. Chem., 2003 **1** (23) 4323-4328.
13. X. L. Armesto, M. Canle L., P. Carretero, M. V. García, and J. A. Santaballa, *Evidence for an intramolecular elimination mechanism in the aqueous decomposition of (N-Cl)-alcoholamines.* Tetrahedron, 1997 **53** (7) 2565-2572.
14. M. J. Frisch, G. W. Trucks, H. B. Schlegel, G. E. Scuseria, M. A. Robb, J. R. Cheeseman, V. G. Zakrzewski, J. A. Montgomery, R. E. Stratmann, J. C. Burant, S. Dapprich, J. M. Millam, A. D. Daniels, K. N. Kudin, M. C. Strain, O. Farkas, J. Tomasi, V. Barone, M. Cossi, R. Cammi, B. Mennucci, C. Pomelli, C. Adamo, S. Clifford, J. Ochterski, G. A. Petersson, P. Y. Ayala, Q. Cui, K. Morokuma, D. K. Malick, A. D. Rabuck, K. Raghavachari, J. B. Foresman, J.

Cioslowski, J. V. Ortiz, B. B. Stefanov, G. Liu, A. Liashenko, P. Piskorz, I. Komaromi, R. Gomperts, R. L. Martin, D. J. Fox, T. Keith, M-. A. Al-Laham, C. Y. Peng, A. Nanayakkara, C. Gonzalez, M. Challacombe, P. M. W. Gill, B. G. Johnson, W. Chen, M. W. Wong, J. L. Andres, M. Head-Gordon, E. S. Replogle, and J. A. Pople, *Gaussian98*. 1998, Gaussian, Inc.: Pittsburgh PA.

15. M. J. Frisch, G. W. Trucks, H. B. Schlegel, G. E. Scuseria, M. A. Robb, J. R. Cheeseman, J. J. A. Montgomery, T. Vreven, K. N. Kudin, J. C. Burant, J. M. Millam, S. S. Iyengar, J. Tomasi, V. Barone, B. Mennucci, M. Cossi, G. Scalmani, N. Rega, G. A. Petersson, H. Nakatsuji, M. Hada, M. Ehara, K. Toyota, R. Fukuda, J. Hasegawa, M. Ishida, T. Nakajima, Y. Honda, O. Kitao, H. Nakai, M. Klene, X. Li, J. E. Knox, H. P. Hratchian, J. B. Cross, C. Adamo, J. Jaramillo, R. Gomperts, R. E. Stratmann, O. Yazyev, A. J. Austin, R. Cammi, C. Pomelli, J. W. Ochterski, P. Y. Ayala, K. Morokuma, G. A. Voth, P. Salvador, J. J. Dannenberg, V. G. Zakrzewski, S. Dapprich, A. D. Daniels, M. C. Strain, O. Farkas, D. K. Malick, A. D. Rabuck, K. Raghavachari, J. B. Foresman, J. V. Ortiz, Q. Cui, A. G. Baboul, S. Clifford, J. Cioslowski, B. B. Stefanov, G. Liu, A. Liashenko, P. Piskorz, I. Komaromi, R. L. Martin, D. J. Fox, T. Keith, M. A. Al-Laham, C. Y. Peng, A. Nanayakkara, M. Challacombe, P. M. W. Gill, B. Johnson, W. Chen, M. W. Wong, C. Gonzalez, and J. A. Pople, *Gaussian 03*. 2004, Gaussian, Inc.: Wallingford CT.

16. J. Tomasi and M. Persico, *Molecular interactions in solution: an overview of methods based on continuous distributions of the solvent.* Chem. Rev., 1994 **94** (7) 2027-2094.

17. L. P. Hammett, *Some relations between reaction rates and equilibrium constants*. Chem. Rev., 1935 **17** (1) 125-136.

18. R. W. Taft Jr., *Polar and steric substituent constants for aliphatic and o-benzoate groups from rates of esterification and hydrolysis of esters.* J. Am. Chem. Soc., 1952 **74** (12) 3120-3128.

19. E. H. Cordes and W. P. Jencks, *The mechanism of hydrolysis of Schiff bases derived from aliphatic amines.* J. Am. Chem. Soc., 1963 **85** (18) 2843-2848.

PART II

Thiols

Let us place at the end of every chapter (…) the two letters used by Roman judges when they did not understand a pleading: N. L., Non Liquet, it is not clear.

Voltaire,
in Philosophical Dictionary

CHAPTER 7

A DFT study on the microscopic ionization of cysteine in water

I have not failed,

I have only discovered 10,000 ways that didn't work.

Thomas A. Edison

7.1 Introduction

The central role played by proton transfer reactions in many scientific areas makes the evaluation of reliable pK_a values a topic of significant importance.[1, 2] Experimental pK_a measurements yield information about macroscopic equilibria. Thus, correlation with corresponding molecular processes is limited to rough estimations based on existing data of similar systems or theories dealing with acidity classification of different functional groups. Discrepancies arise when empirical pK_a values are assigned to molecules with more than one ionizable group, or when the acid-base function of interest is embedded in a complex system such as a protein, a membrane, or a micelle, and also when its pK_a is very close to that of the surrounding medium. Computational chemistry emerges as a valuable tool for evaluating the right sequence of deprotonation. This explains the many attempts to develop reliable methods for the calculation of accurate absolute or relative pK_a values.[3-5] Computational accurate determination of pK_a for more exotic solutes, such as free radicals, zwitterions, and excited states remains elusive.

The essential amino acid cysteine (Cys) holds three ionization sites: carboxyl, thiol, and amino groups. The complete dissociation scheme of Cys at a molecular level includes eight molecular species involving twelve microscopic ionization constants. While the lower macroscopic pK_a (2.00) could be assigned to the carboxyl centre, the subsequent macroscopic values are 8.35 and 10.39, *i.e.*, the other two groups deprotonate within a narrow pH range. The assigned molecular equilibria of deprotonation of HS-CH_2-CH(NH_3^+)-CO_2^- are 8.55 for the thiol and 8.88 for the amino group.[6] Thus, –SH is more acidic and the loss of the proton attached to the sulfur atom could be mainly ascribed to the 8.35 macroscopic value. However, a difference of only 0.33 units in the molecular equilibria seems not solid enough for the unambiguous assignment of the macroscopic values. On the other hand, a value of 8.22 ± 0.16 has been recently obtained for pK_a of the thiol of Cys by isothermal titration calorimetry,[7] supporting the previously proposed deprotonation order.

Solely considering these two controversial ionizable groups, two macroscopic constants should be considered. Cys could be present in the form of four species: ionic (Cys 2), diionic (Cys 4), and zwitterionic (Cys 1 and Cys 3). They are related by four molecular ionization equilibria, three of them independent (Scheme 7.1). This system proves ideal for examining the reliability of different computational methodologies to calculate molecular pK_a values.

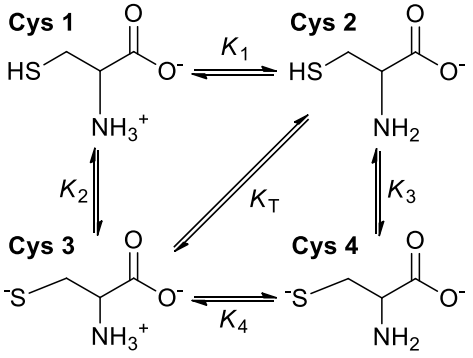

Scheme 7.1. Molecular equilibria involved in the second and third ionization processes of Cys.

Calculations were performed using the Gaussian98 suite of programs.[8] *Ab initio* calculations have been performed by using DFT at B3LYP/6-31++G** level.[9-11] Default values of Gaussian98 have been used for all applicable parameters. The four structures have been fully optimized. Equilibrium constants were obtained by calculating Gibbs free energy for independent reactants and products of every process.

Among the different procedures to describe solute-solvent interactions at the quantum level, the use of discrete water molecules and continuum models have been selected.

Solvent was simulated by adding discrete water molecules (n, m = 0 - 6), see Scheme 7.2, adjacent to every single compound for an adequate description of the solute-solvent interaction in the first solvation layer (microsolvated model). Additionally, values were extrapolated to n = m = ∞.

$$AH{\cdot}nH_2O + H_2O{\cdot}mH_2O \overset{K_{AH}}{\rightleftharpoons} A^-{\cdot}nH_2O + H_3O^+{\cdot}mH_2O$$

Scheme 7.2. Allocation of discrete water molecules in the microsolvated model.

The Onsager[12, 13] and the polarized continuum (PCM)[14] models were used to assess the effect of bulk water. In situations where there are strong and specific solute-solvent interactions, as ions solvated in water, the use of a discrete-continuum approach can lead to a substantial improvement of the solvation model.[15, 16] Finally, hybrid microsolvated-continuum methods were tested, in which both continuum models were applied over the supermolecule arrangements.

7.2 Microsolvated model

Firstly, calculations have been performed *in vacuo* (n = m = 0). Previous conformational analysis rendered the most stable conformers of the four species considered, where stabilization was found by intramolecular hydrogen bonding between –SH or $–NH_2$/$–NH_3^+$ and $–CO_2^–$, and between $–S^–$ and $–NH_2$/$–NH_3^+$ groups (Figure 7.1, Table 7.1). When optimizing the geometry of Cys 1, one proton transferred from $–NH_3^+$ to $–CO_2^–$, and further conformational analysis led in all cases to the same proton transfer. Then, three discrete water molecules have been added (n = 3) forming an arrangement controlled by hydrogen bonds, *i.e.*, each water molecule was placed next to one of the three ionizable groups, and the so-obtained structures were fully optimized without any movement restriction. For n = 6 three additional molecules of water were included over the previous structures, and optimized following the same procedure. Similarly, discrete water molecules (m = 1 - 6) were added to H_2O and H_3O^+, and the supermolecule model optimized (Table 7.2). The experimental value $G°_f(H^+_{(aq)})$ = –270.26 kcal·mol^{-1} has been proposed to correct calculated pK_a values.[17, 18] The use of such number contributes to lower the pK_a data, but they are still far from the experimental results.

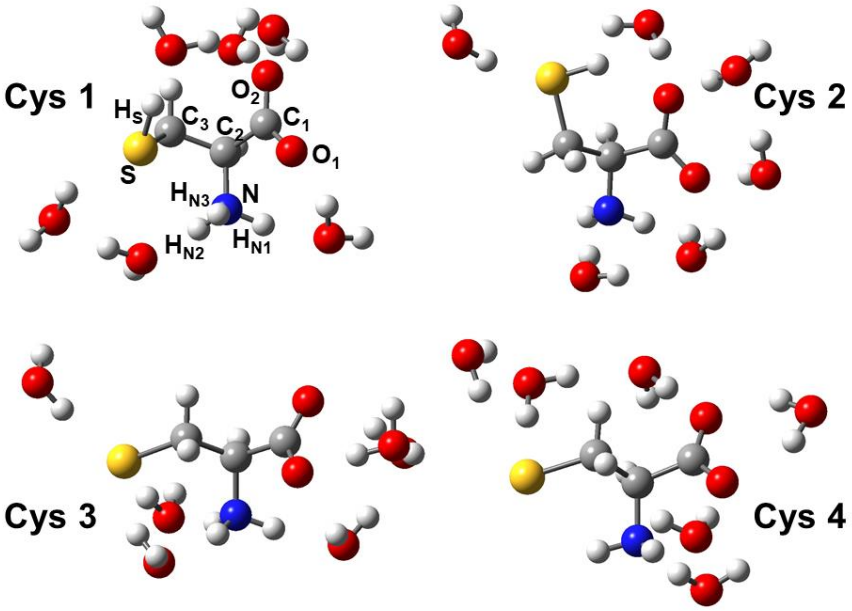

Figure 7.1. Geometries attained at B3LYP/6-31++G** level and n = 6 for the four Cys species considered.

Table 7.1. Selected geometrical parameters for structures calculated at B3LYP/6-31++G** level. Values obtained with the Onsager solvation method in italics.

Compound	n	C_1–O_1		C_1–O_2		N–H_{N1}		N–H_{N2}		N–H_{N3}		S–H_S	
Cys 1	0	1.339	*1.337*	1.212	*1.214*	0.988[a]	*0.993*[a]	1.015	*1.015*	1.020	*1.020*	1.349	*1.349*
	3	1.266	*1.252*	1.246	*1.273*	1.077	*1.028*	1.027	*1.063*	1.033	*1.029*	1.372	*1.351*
	6	1.254	*1.250*	1.262	*1.277*	1.040	*1.044*	1.027	*1.070*	1.041	*1.025*	1.374	*1.350*
Cys 2	0	1.255	*1.261*	1.269	*1.267*	1.024	*1.020*	1.016	*1.016*	-	-	1.387	*1.364*
	3	1.259	*1.266*	1.269	*1.268*	1.019	*1.017*	1.016	*1.017*	-	-	1.354	*1.350*
	6	1.256	*1.265*	1.272	*1.268*	1.019	*1.019*	1.016	*1.018*	-	-	1.351	*1.348*
Cys 3	0	1.275	*1.271*	1.245	*1.249*	1.052	*1.047*	1.017	*1.017*	1.086	*1.078*	-	-
	3	1.275	*1.263*	1.247	*1.266*	1.046	*1.032*	1.031	*1.040*	1.038	*1.043*	-	-
	6	1.273	*1.275*	1.253	*1.254*	1.040	*1.039*	1.036	*1.038*	1.037	*1.037*	-	-
Cys 4	0	1.270	*1.267*	1.266	*1.267*	1.022	*1.022*	1.024	*1.022*	-	-	-	-
	3	1.279	*1.274*	1.263	*1.268*	1.019	*1.019*	1.023	*1.023*	-	-	-	-
	6	1.269	*1.265*	1.272	*1.274*	1.020	*1.020*	1.025	*1.024*	-	-	-	-

Compound	n	C_1–C_2–N		C_1–C_2–C_3–S		N–C_2–C_3–S	
Cys 1	0	109.14	*108.79*	–70.59	*–68.74*	55.08	*56.35*
	3	104.09	*109.10*	–79.94	*–61.75*	38.86	*61.72*
	6	109.54	*111.82*	–70.79	*–60.88*	52.03	*64.82*
Cys 2	0	110.43	*109.43*	67.68	*71.26*	–169.40	*–166.33*
	3	110.39	*110.72*	70.88	*74.76*	–167.90	*–163.23*
	6	110.05	*109.25*	74.38	*79.69*	–164.26	*–157.93*
Cys 3	0	106.09	*106.86*	–154.52	*–153.66*	–37.76	*–36.59*
	3	105.90	*107.95*	–176.16	*–181.36*	–54.52	*–58.29*
	6	109.10	*109.57*	–172.07	*–170.89*	–49.89	*–48.59*
Cys 4	0	110.03	*110.11*	–177.59	*–179.99*	–54.51	*–56.90*
	3	110.24	*110.47*	–176.66	*–181.97*	–52.54	*–57.44*
	6	111.31	*110.88*	175.36	*175.13*	–59.18	*–60.15*

[a] Distance O_1–H_{N1}

Table 7.2. pK_a values calculated at B3LYP/6-31++G** level, and experimental values for reference.[6]

Dielectric continuum	n,m	pK_1	pK_2	pK_3	pK_4	pK_T
None	0	122.54	128.04	187.75	182.25	5.50
	3	67.98	72.11	131.90	127.77	4.12
	6	53.27	56.70	107.49	104.06	3.43
	∞	50.46	53.56	50.56	37.90	3.09
Onsager	0	122.66	128.37	189.98	184.27	5.71
	3	87.89	90.93	138.07	135.02	3.05
	6	71.04	78.09	111.33	104.28	7.05
PCM	0	10.86	7.47	12.31	15.70	–3.39
	3	17.31	11.24	10.10	16.17	–6.06
	6	8.90	5.53	7.27	10.64	–3.38
Experimental		**pK_1**	**pK_2**	**pK_3**	**pK_4**	**pK_T**
		8.88	8.55	9.87	10.20	–0.33

All four pK_a values decrease dramatically when going from n = 0 to 6 due to the interaction of Cys with the surrounding solvent molecules. As expected, water acts as H donor with $–S^-$ and $–CO_2^-$ groups, as H acceptor with $–NH_3^+$, and as both H donor and acceptor with –SH and $–NH_2$ resulting in net charge and, consequently, free energy stabilization of the ions and

zwitterions. The carboxylate group is more affected than any other group as shown by the greater increase of its net negative charge as n increases (Table 7.3). This water stabilization prevents H^+ transfer in Cys 1 when n > 0. Despite being more relaxed, the other three Cys species show geometries that are similar to gas phase structures, presumably due to the remaining intramolecular hydrogen bonding. The net charge and its distribution on Cys 4 could explain the higher stabilization of this species, and therefore the greater drop (*ca*. 9 units) of pK_3 and pK_4 with respect to pK_2 and pK_1 when changing from n = 0 to 6. However, computational values obtained with n = 6 still overestimate pK_a values (see Table 7.2). In all cases, according to the supermolecule approach, Cys first ionizes at the amino group (Scheme 7.1, equilibrium K_1).

Table 7.3. Mulliken charges on the ionizable groups and dipole moment of all structures calculated at B3LYP/6-31++G** level.

Dielectric continuum	n	Cys 1 (net charge = 0)[a,b]				Cys 2 (net charge = –1)			
		$-CO_2^-$	**–SH**	**$-NH_3^+$**	**μ**	**$-CO_2^-$**	**–SH**	**$-NH_2$**	**μ**
None	0	–0.06[a]	0.12	0.12[b]	4.72	–0.89	–0.17	0.09	3.86
	3	–0.89	0.02	0.62	10.46	–0.90	–0.04	0.04	5.21
	6	–0.94	0.04	0.59	6.03	–0.97	–0.06	0.06	9.15
Onsager	0	–0.09[a]	0.12	0.14[b]	5.58	–0.98	–0.12	0.08	6.74
	3	–0.86	0.13	0.79	26.16	–1.06	–0.04	0.04	11.38
	6	–0.82	0.12	0.76	31.51	–1.22	0.04	0.02	14.65
PCM	0	–0.13[a]	0.08	0.14[b]	6.25	–1.01	–0.14	0.08	7.06
	3	–0.98	–0.02	0.71	12.80	–1.02	–0.03	0.07	9.48
	6	–1.04	0.04	0.69	7.70	–1.04	–0.04	0.08	8.59
Dielectric continuum	**N**	**Cys 3 (net charge = –1)**				**Cys 4 (net charge = -2)**			
		$-CO_2^-$	**$-S^-$**	**$-NH_3^+$**	**μ**	**$-CO_2^-$**	**$-S^-$**	**$-NH_2$**	**μ**
None	0	–0.69	–0.68	0.53	8.99	–0.84	–1.02	0.00	17.56
	3	–1.25	–0.54	0.45	4.55	–1.18	–0.80	0.06	15.54
	6	–1.42	–0.57	0.40	8.37	–1.29	–0.73	0.16	16.39
Onsager	0	–0.71	–0.69	0.58	6.04	–0.83	–1.06	0.01	2.78
	3	–1.38	–0.59	0.48	13.89	–1.16	–0.82	0.08	3.73
	6	–1.58	–0.57	0.38	3.96	–1.21	–0.74	0.17	5.07
PCM	0	–0.82	–0.81	0.69	6.60	–0.94	–0.98	0.06	1.87
	3	–1.32	–0.67	0.53	6.33	–1.27	–0.89	0.04	3.53
	6	–1.43	–0.67	0.46	2.74	–1.45	–0.80	0.21	3.15

[a] The optimized structure *in vacuo* (n = 0) for Cys 1 is not the zwitterion. These values correspond to $-CO_2H$ group.
[b] To $-NH_2$ group.

This model has a severe limitation though, *i.e.*, it only takes into account the energy stabilization due to the first solvation shell. Although these water molecules must have the highest contribution to charge delocalization and to the effective solvation of the solute, the effect of bulk water must be considered in order to get a proper characterization of the equilibria in solution. The pK_a values obtained with discrete water molecules show an exponential behaviour and, therefore, can be extrapolated to ∞. Figure 7.2A shows the extrapolation to m = ∞ for pK_1 and n = 0. This was repeated for n = 3 and n = 6, and subsequently the values for pK_1 and m = ∞ were extrapolated (Figure 7.2B) to obtain the result for n = m = ∞. Thus, the stabilization effect of both the first solvation layer and the bulk solvent together was calculated. The procedure has been reproduced for the other 3 ionization equilibria (Table 7.2).

As bulk solvation is roughly taken into account, this approach yields pK_a values that are lower than for the simple microsolvated method. However, since the optimized structure of Cys 1 in the gas phase is not the zwitterion, extrapolated values of pK_1 and pK_2 must be affected. For this reason this model must be considered with caution.

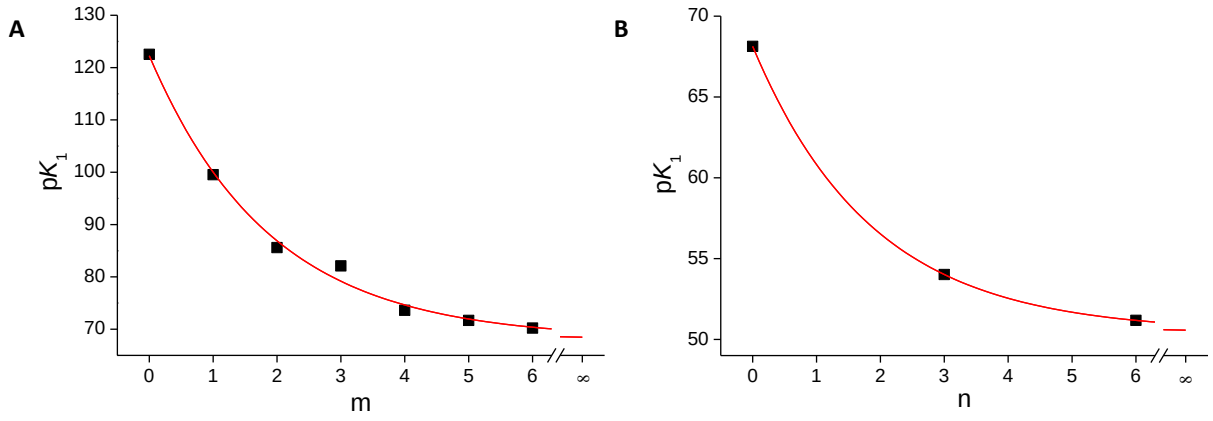

Figure 7.2. Extrapolation to ∞ of pK_1 values obtained at B3LYP/6-31++G** level: (A) n = 0, m = 0 - 6; (B) m = ∞, n = 0 - 6.

7.3 Continuum models

According to the literature, very accurate pK_a values (absolute error < 0.6 units) have been calculated applying the thermodynamic cycle showed in Scheme 7.3, together with PCM solvation model at DFT computing level.[5] All four Cys species were fully optimized using the Onsager solvation method. Radii used to generate the Onsager cavities were calculated with the Volume keyword of Gaussian98. Attained geometries fully resemble those obtained *in vacuo*, solvation being unable to prevent the H^+ transference in Cys 1 (see above), which shows the inadequacy of this model for charge stabilization. Single point PCM solvation calculations were performed on the *in vacuo* structures without further geometry optimization, and the thermodynamic cycle shown in Scheme 7.3 was applied (Table 7.2). The percentage of electronic charge placed outside the cavity is low, always inferior to 1.5 %. In both cases the use of the experimental free energy value for $H^+_{(aq)}$ did not give better results.

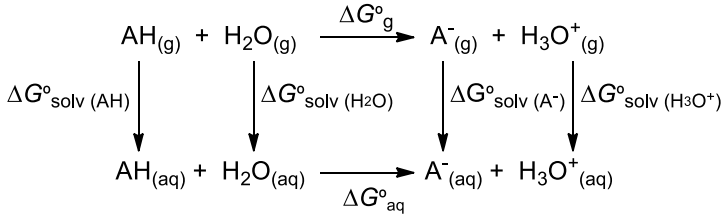

Scheme 7.3. Thermodynamic cycle used to determine pK_a values in solution with the PCM model.

Onsager pK_a values do not substantially differ from gas phase values. This probably derives from the large cavities required to accommodate quite diffuse electronic charge. Therefore, this model does not yield any improvement with respect to calculations *in vacuo*.

Conversely, all species are greatly stabilized by PCM solvation, and the pK_a values obtained are much lower than those of the supermolecule model. pK_3 and pK_4 decrease 45 - 65 units more than pK_1 and pK_2 when moving from gas phase to PCM solvation. This different stabilization arises from both the net charge and the charge distribution of the involved species (Table 7.3). Similarly, calculated solvation free energy of Cys 2 is much lower (12.13 kcal·mol^{-1}) than that of Cys 3 and, as a result, pK_2 and pK_3 decrease about 9 units more than pK_1 and pK_4 respectively. Consequently, according to this model, pK_2 is lower than pK_1, *i.e.*, ionization of Cys firstly occurs on the thiol group as suggested by experimental studies.[6]

7.4 Microsolvated plus continuum model

Continuum models were applied on the supermolecule system. A computational model including discrete water molecules plus the continuum represented by a dielectric constant is not enough to model the whole solvent system, but should yield a reasonable picture of the solvation effect on the studied equilibria. Thus, structures for n = 3 and 6, and m = 1 - 6 were fully optimized with the Onsager method, whereas corresponding microsolvated geometries were used for calculating PCM solvation energy followed by application of Scheme 7.3.

As described in the previous section, structural parameters calculated either with Onsager plus supermolecule method or using only the supermolecule approach are fully equivalent (Table 7.1). However energy values differ in this case; the hybrid model shows defective solvation ability, resulting in large pK_a values, even higher than the results obtained only with discrete solvent molecules. Despite this difference it must be noted that the same deprotonation sequence was always obtained (via Cys 2).

The microsolvated-PCM approach rendered pK_a values that do not follow any pattern related to the number of water molecules. Results are greatly improved with respect to simple microsolvated model, due to the better stabilization of charges that yields lower pK_as, but this is not the case with respect to plain PCM method, for which some results resemble better the experimental data, while others do not. Also, percentage of escaped charge is lower than in the previous section. Although this model uses the zwitterion for Cys 1 to obtain absolute values of pK_1 and pK_2, these still differ from the experimental ones. pK_2 keeps always below pK_1 ($G°_f$ (Cys $3_{(aq)}$) is 4.61 - 8.27 kcal·mol^{-1} lower than $G°_f$ (Cys $2_{(aq)}$)), while pK_3 reduces its magnitude as much as for turning into the lowest in some cases, which can be interpreted as an incorrect solvation capability of the method.

Accurate calculated pK_a values have been reported for several acids,[5] in fact the supermolecule-PCM model estimates correctly the ionization constants associated with the amino group, but fails with the pK_a values of the thiol group. Results involving the ionization constants of the –SH group suggest both the PCM formalism and supermolecule-PCM approach should be improved to properly handle the solvation of species containing this group.

We do not claim that this procedure can substitute QM/MM calculations incorporating a sphere of solvent molecules interacting with the solute. However it takes into account the main QM interactions of the first solvation layer, while the effect of the other further solvent molecules is also considered.

7.5 Conclusions

The present work deals with the pK_a calculation of two anions, one of them a dianion, and two zwitterions, one of them incorporating three different charged groups.

The results of systematic calculations carried out by using discrete, continuum, and mixed discrete-continuum solvation models were analyzed. The disparity in the calculated reaction free energies when going from gas phase to the best solvation model is larger than 1000 kcal·mol^{-1}. More important than the absolute values are the relative energies that allow discriminating the correct deprotonation sequence. Therefore, two scenarios must be distinguished:

a) gas phase, microsolvated and Onsager values. Computed acidity constants always differ significantly from experimental data. The observed variance does not qualitatively affect the ionization pattern, all results suggesting that deprotonation of Cys 1 takes place on the amino group. Calculations incorporating discrete water molecules improve the description of the studied equilibria with respect to calculations performed *in vacuo*, while the Onsager and the hybrid Onsager-supermolecule methods fail in solvating properly the different species considered. An innovative approach to solvation was presented: a rough estimation of the stabilization promoted by a high number of discrete solvent molecules was made by extrapolation of small numbers of water molecules to ∞.

This study has been published as: M. Canle L., D. R. Ramos, and J. A. Santaballa, Chem. Phys. Lett., 2006 **417** (1-3) 28-33.

7.6 References

1. C. Hansch, P. G. Sammes, and J. B. Taylor, eds. *Quantitative drug design*. Comprehensive medicinal chemistry. Vol. 4. 1990, Pergamon Press: Oxford, UK.
2. G. Shüürmann, *Ecotoxicology*, G. Shüürmann and B. Markert, Editors. 1998, Wiley: New York. 665.
3. D. M. Chipman, *Computation of pK_a from dielectric continuum theory.* J. Phys. Chem. A, 2002 **106** (32) 7413-7422.
4. J. R. Pliego Jr. and J. M. Riveros, *Theoretical calculation of pK_a using the cluster-continuum model.* J. Phys. Chem. A, 2002 **106** (32) 7434-7439.
5. G. A. A. Saracino, R. Improta, and V. Barone, *Absolute pK_a determination for carboxylic acids using density functional theory and the polarizable continuum model.* Chem. Phys. Lett., 2003 **373** (3-4) 411-415.
6. R. Stewart, *The proton: Applications to organic chemistry*. 1985, Orlando: Academic Press, Inc.
7. S. G. Tajc, B. S. Tolbert, R. Basavappa, and B. L. Miller, *Direct determination of thiol pK_a by isothermal titration microcalorimetry.* J. Am. Chem. Soc., 2004 **126** (34) 10508-10509.
8. M. J. Frisch, G. W. Trucks, H. B. Schlegel, G. E. Scuseria, M. A. Robb, J. R. Cheeseman, V. G. Zakrzewski, J. A. Montgomery, R. E. Stratmann, J. C. Burant, S. Dapprich, J. M. Millam, A. D. Daniels, K. N. Kudin, M. C. Strain, O. Farkas, J. Tomasi, V. Barone, M. Cossi, R. Cammi, B. Mennucci, C. Pomelli, C. Adamo, S. Clifford, J. Ochterski, G. A. Petersson, P. Y. Ayala, Q. Cui, K. Morokuma, D. K. Malick, A. D. Rabuck, K. Raghavachari, J. B. Foresman, J. Cioslowski, J. V. Ortiz, B. B. Stefanov, G. Liu, A. Liashenko, P. Piskorz, I. Komaromi, R. Gomperts, R. L. Martin, D. J. Fox, T. Keith, M. A. Al-Laham, C. Y. Peng, A. Nanayakkara, C. Gonzalez, M. Challacombe, P. M. W. Gill, B. G. Johnson, W. Chen, M. W. Wong, J. L. Andres, M. Head-Gordon, E. S. Replogle, and J. A. Pople, *Gaussian 98*. 1998, Gaussian, Inc.: Pittsburgh PA.
9. A. D. Becke, *Density-functional thermochemistry. III. The role of exact exchange.* J. Chem. Phys., 1993 **98** (7) 5648-5652.
10. T. Clark, J. Chandrasekhar, G. W. Spitznagel, and P. v. R. Schleyer, *Efficient diffuse function-augmented basis sets for anion calculations. III. The 3-21+G basis set for first-row elements, Li–F.* J. Comput. Chem., 1983 **4** (3) 294-301.
11. C. Lee, W. Yang, and R. G. Parr, *Development of the Colle-Salvetti correlation-energy formula into a functional of the electron density.* Phys. Rev. B, 1988 **37** (2) 785-789.
12. J. G. Kirkwood, *Theory of solutions of molecules containing widely separated charges with special application to zwitterions.* J. Chem. Phys., 1934 **2** (7) 351-361.
13. L. Onsager, *Electric moments of molecules in liquids.* J. Am. Chem. Soc., 1936 **58** (8) 1486-1493.
14. S. Miertuš, E. Scrocco, and J. Tomasi, *Electrostatic interaction of a solute with a continuum. A direct utilization of ab initio molecular potentials for the prevision of solvent effects.* Chem. Phys., 1981 **55** (1) 117-129.
15. J. R. Pliego Jr. and J. M. Riveros, *The cluster-continuum model for the calculation of the solvation free energy of ionic species.* J. Phys. Chem. A, 2001 **105** (30) 7241-7247.
16. F. Aquilante, M. Cossi, O. Crescenzi, G. Scalmani, and V. Barone, *Computation of the acetone ultraviolet spectrum in gas phase and in aqueous solution by a mixed discrete/continuum model.* Mol. Phys., 2003 **101** (13) 1945-1953.
17. M. D. Tissandier, K. A. Cowen, W. Y. Feng, E. Gundlach, M. H. Cohen, A. D. Earhart, J. V. Coe, and T. R. Tuttle Jr., *The proton's absolute aqueous enthalpy and Gibbs free energy of solvation from cluster-ion solvation data.* J. Phys. Chem. A, 1998 **102** (40) 7787-7794.
18. I. A. Topol, G. J. Tawa, S. K. Burt, and A. A. Rashin, *On the structure and thermodynamics of solvated monoatomic ions using a hybrid solvation model.* J. Chem. Phys., 1999 **111** (24) 10998-11014.

PART III

Myeloperoxidase

If the Lord Almighty had consulted me before embarking on creation, I should have recommended something simpler.

Alphonso X of Castile, the Wise (1221-1284)
Also quoted by Adam Riess in his Nobel Prize lecture (2011)

CHAPTER 8

Myeloperoxidase-catalyzed taurine chlorination: Initial *versus* equilibrium rate

It always seems impossible until it's done.

Nelson Mandela

8.1 Introduction

Myeloperoxidase (MPO)[1] is a heme-containing dominant granule enzyme present in circulating polymorphonuclear neutrophils, which represent the cornerstone of cell-mediated antimicrobial activity in the human innate immune system. Neutrophils endocytose pathogens and deposit their granule contents intracellularly into target phagosomes.[1] The principal reaction catalyzed by MPO under physiological conditions is thought to be the oxidation of Cl^- by H_2O_2 to yield the highly-reactive oxidizing and chlorinating agent HClO.[1]. In this respect MPO is unique among the members of the animal peroxidase superfamily[2] because the high reduction potential of its redox intermediate compound I (MPO-I) allows the two-electron oxidation of Cl^-.[3] HClO can participate in subsequent nonenzymatic reactions such as oxidation and chlorination of target cell components, and can also react with substances in the immediate environment that modulate its biological effects. For example HClO chlorinates ammonia and amines to yield chloramines, which also have oxidizing and chlorinating activity.[4] The most important role of HClO and chloramines in leukocyte function is probably to attack essential microbial cell components.

Taurine (Tau, 2-aminoethane-sulfonic acid) is one of the most abundant free amino acids in mammalian tissues, and accounts for a large part of the amines that are available for reaction with chlorinating reagents. Intracellular concentrations between 22 and 26 mM were reported for human leukocytes.[5, 6] Although Tau is found in the cytoplasm of neutrophils and not released into phagosomes, it has been proposed that it could play a role in scavenging of HClO released from the phagosomes.[4] Thereby, the long-lived oxidant monochlorotaurine (*N*-Cl Tau) is formed, which is a hydrophilic anionic membrane-impermeable oxidant with relatively low toxicity.[7] Monochlorotaurine was reported to be uptaken by red blood cells and, finally, reduced by intracellular components, such as glutathione or hemoglobin, to Tau,[4] which accumulates inside these cells.[8] These results suggest that red blood cells contribute to elimination of *N*-Cl Tau *in vivo*, preventing its accumulation in the extracellular phase and protecting other blood cells, plasma components, and tissues from oxidative attack.[8]

At pH 7.0 the formation of *N*-Cl Tau from Tau and HClO (Reaction 3 in Table 8.1) takes place with a measured rate constant of $4.8 \times 10^5\ M^{-1}{\cdot}s^{-1}$,[9] whereas at pH 4.7 the rate constant is $3.5 \times 10^3\ M^{-1}{\cdot}s^{-1}$.[10] Further chlorination to Tau-dichloramine, which is more toxic than *N*-Cl Tau and has significant cytolytic activity,[8] is relatively slow. Generally, dichlorination is much slower than monochlorination. This is best demonstrated by the fact that formation of *N*-Cl methylamine ($2 \times 10^8\ M^{-1}{\cdot}s^{-1}$) is about 5 orders of magnitude faster than the consecutive reaction between HClO and *N*-Cl methylamine,[11] or by the published rate of ammonia chlorination by HClO ($6.1 \times 10^6\ M^{-1}{\cdot}s^{-1}$), which is about 4 orders of magnitude faster than further chlorination of monochloroamine.[12] Since Tau is not an electron donor for either compound I (MPO-I) or compound II (MPO-II), it is an ideal molecule to investigate the mechanism of its chlorination by MPO.[10, 13]

The chlorination of Tau by MPO has been studied by Marquez and Dunford.[10, 13] However, in order to avoid consideration of the complex scenario of reactions outside the chlorination cycle of MPO (Table 8.1), the authors conducted most of their measurements at low pH (4.7) and focused only on initial rate data of Tau chlorination to eliminate the effect of formation of Tau-dichloramine.[10, 13] From their kinetic data they could conclude that the chlorination reaction mediated by MPO *in vivo* may involve an enzyme intermediate species rather than free HClO. Nevertheless, the authors did not include MPO-typical reactions, which play an important role in catalysis *in vitro* and *in vivo*, and thus significantly affect chlorination reactions, especially at high pH. These reactions need to be considered when investigating chlorination of Tau over the whole period of the reaction. This is possible since, as mentioned above, formation of Tau-dichloramine is negligible. Additionally, the influence of pH should be studied in order to determine whether protons intervene in the reaction mechanism.

The reactions involved in the so-called chlorination cycle of MPO are the formation of MPO-I, which has been described to be slightly reversible (Reaction 1 in Table 8.1)[14, 15] and its direct reaction back to the ferric enzyme (Reaction 2 in Table 8.1). Moreover, both Fe(III)-MPO and MPO-I could participate in protonation reactions (Reactions 4 and 5 in Table 8.1). In addition to a redox reaction with H_2O_2, protonated native MPO can also bind Cl^- forming a high-spin complex (MPO-H-Cl,

Reaction 6 in Table 8.1); this binding constant has been accurately measured as a function of pH.[16-18] Very important is the role of H_2O_2 as one-electron donor reducing MPO-I to MPO-II and forming $HO_2^{\cdot}$ (hydroperoxyl) radical (Reaction 7 in Table 8.1). Compound II is outside the halogenation cycle. The rate constant for the reduction of MPO-I to MPO-II by H_2O_2 was reported to be 8.2×10^4 $M^{-1}{\cdot}s^{-1}$ at pH 7.0,[14, 15] so this reaction is competitive with MPO-I reduction by Cl^- at neutral pH regions.[19] The only alternative of a compound I to compound II transition in the system MPO/H_2O_2/Cl^-/Tau (*i.e.*, in the absence of an exogenous one-electron donor) is intramolecular electron transfer that quenches the porphyryl radical of compound I and oxidizes an amino acid of the protein matrix. This is known to occur with MPO but is extremely slow and thus of no significance in the presence of H_2O_2. [14, 15]

Table 8.1. Mechanisms of MPO-catalyzed Tau chlorination proposed to fit experimental kinetic data

Mechanism	Reaction	No.
I	$\mathrm{MPO} + \mathrm{H_2O_2} \overset{K_1}{\underset{\leftarrow}{\rightarrow}} \mathrm{MPO\text{–}I} + \mathrm{H_2O}$	1
	$\mathrm{MPO\text{-}I} + \mathrm{Cl^-} + \mathrm{H^+} \overset{k_2}{\rightarrow} \mathrm{MPO} + \mathrm{HClO}$	2
	$\mathrm{HClO} + \mathrm{Tau} \overset{k_3}{\rightarrow} N\text{-Cl Tau} + \mathrm{H_2O}$	3
	$\mathrm{MPO} + \mathrm{H^+} \overset{K_4}{\underset{\leftarrow}{\rightarrow}} \mathrm{MPO\text{–}H}$	4
	$\mathrm{MPO\text{–}I} + \mathrm{H^+} \overset{K_5}{\underset{\leftarrow}{\rightarrow}} \mathrm{MPO\text{–}I\text{–}H}$	5
	$\mathrm{MPO\text{–}H} + \mathrm{Cl^-} \overset{K_6}{\underset{\leftarrow}{\rightarrow}} \mathrm{MPO\text{–}H\text{–}Cl}$	6
	$\mathrm{MPO\text{–}I} + \mathrm{H_2O_2} \overset{K_7}{\underset{\leftarrow}{\rightarrow}} \mathrm{MPO\text{–}II} + \mathrm{HO_2^{\cdot}} + \mathrm{H^+}$	7
	$\mathrm{MPO\text{–}II} + \mathrm{HO_2^{\cdot}} + \mathrm{H^+} \overset{k_8}{\rightarrow} \mathrm{MPO} + \mathrm{H_2O} + \mathrm{O_2}$	8
II	$\mathrm{MPO} + \mathrm{H_2O_2} \overset{K_1}{\underset{\leftarrow}{\rightarrow}} \mathrm{MPO\text{–}I} + \mathrm{H_2O}$	1
	$\mathrm{MPO\text{–}I} + \mathrm{Cl^-} \overset{k_{2b}}{\rightarrow} \mathrm{MPO\text{–}I\text{–}Cl}$	2b
	$\mathrm{MPO\text{-}I\text{-}Cl} + \mathrm{Tau} + \mathrm{H^+} \overset{k_{3b}}{\longrightarrow} N\text{-Cl Tau} + \mathrm{MPO} + \mathrm{H_2O}$	3b
	$\mathrm{MPO} + \mathrm{H^+} \overset{K_4}{\underset{\leftarrow}{\rightarrow}} \mathrm{MPO\text{–}H}$	4
	$\mathrm{MPO\text{–}I} + \mathrm{H^+} \overset{K_5}{\underset{\leftarrow}{\rightarrow}} \mathrm{MPO\text{–}I\text{–}H}$	5
	$\mathrm{MPO\text{–}H} + \mathrm{Cl^-} \overset{K_6}{\underset{\leftarrow}{\rightarrow}} \mathrm{MPO\text{–}H\text{–}Cl}$	6
	$\mathrm{MPO\text{–}I} + \mathrm{H_2O_2} \overset{K_7}{\underset{\leftarrow}{\rightarrow}} \mathrm{MPO\text{–}II} + \mathrm{HO_2^{\cdot}} + \mathrm{H^+}$	7
	$\mathrm{MPO\text{–}II} + \mathrm{HO_2^{\cdot}} + \mathrm{H^+} \overset{k_8}{\rightarrow} \mathrm{MPO} + \mathrm{H_2O} + \mathrm{O_2}$	8

The one-electron oxidation of H_2O_2 produces superoxide,[14, 15] which has been reported to mediate MPO-II reduction to the ferric enzyme (Reaction 8 in Table 8.1).[20] As a consequence of these dynamic equilibria the kinetics of *N*-Cl Tau formation exhibits a very complex behaviour. A typical kinetic trace measured at [H_2O_2] ≥ 0.5 mM and pH ≥ 5 is shown in Figure 8.1A. The detailed kinetic analysis should incorporate all feasible concurrent reactions, allowing a more accurate

description of *in vivo* halogenating activity.

Here, we revisit and extend previous studies including equilibrium conditions to incorporate concurrent side reactions. Two mechanisms (Table 8.1) for MPO-catalyzed chlorination using Tau as a trap were tested in the pH range 4.0 - 7.0 that includes actual conditions during phagocytosis and MPO activity *in vivo*. The kinetic data suggest that there is no proton intervening in the direct reaction between MPO-I and Cl^-. Chlorination might be mediated mainly by the MPO-I-Cl complex at the active site or by ClO^- that undergoes protonation to HClO outside the enzyme.

8.2 Experimental procedures

8.2.1 Materials

Stock solutions of 70 mM Tau (Fluka Microselect, ≥ 99.5%), 2.5 M NaCl (Sigma Ultra, min. 99.5%) and 18 mM H_2O_2 (Sigma-Aldrich) were prepared daily and kept in the dark at 4 °C. The H_2O_2 concentration was determined spectrophotometrically using ε_{240} = 39.4 $M^{-1}\cdot cm^{-1}$.[21] Citric acid (Sigma, anhydrous) / Na_2HPO_4 (Sigma, ACS reagent) buffer, 0.5 M, was used to control pH in the range 4.0 - 6.0. Phosphate buffer was used for measurements at pH 7.0.

Highly purified MPO of a purity index (A_{430} / A_{280}) of at least 0.85 was obtained from Planta Natural Products (http://www.planta.at). Its actual concentration was determined spectrophotometrically by using ε_{430} = 91,000 $M^{-1}\cdot cm^{-1}\cdot heme^{-1}$.[22] Cu/Zn superoxide dismutase was purchased from Sigma.

8.2.2 Methods

Based on the published *in vivo* concentrations,[1, 23] the typical chlorination assays contained 100 mM Cl^-, 10 mM Tau and 100 nM MPO. Temperature and pH were set at 25.0 °C and 4.0 - 7.0, respectively. Hydrogen peroxide was varied from 0.2 - 2.0 mM. Samples were prepared immediately before use by mixing solution 1, containing Tau and MPO, with solution 2, containing NaCl and H_2O_2 in 200 mM phosphate/citrate buffer (pH 4.0 - 6.0) or phosphate buffer (pH 7.0), by using the conventional mixing stopped-flow technique (Applied Photophysics® SX-18MV stopped-flow spectrophotometer equipped with a diode array detector). Single-mixing unit syringes were filled up with both sample solutions and, after thermostating at 25.0 ± 0.1 °C, a total of 100 μL were shot for each run. Reactions were studied both at the whole wavelength range as well as at 252 nm, which corresponds to the absorbance maximum of *N*-Cl Tau. The molar extinction coefficient of the mono-chlorinated and dichlorinated product at 252 nm is 429 and 190 $M^{-1}\cdot cm^{-1}$, respectively, but, based on the huge differences in the reaction rate with HClO, formation of the dichlorinated product was negligible, especially in case of high excess of Tau.[11, 12] Exploratory experiments showed no impact of [Tau] on the obtained kinetic data under the working conditions. Kinetic traces at 252 nm were followed until full consumption of H_2O_2, and led to re-formation of native MPO. In order to determine the stoichiometry of H_2O_2 consumption and *N*-Cl Tau formation, the molar extinction coefficient of the absorbing species at the working wavelength had to be taken into account. As the concentration of *N*-Cl Tau at any time t, $[N\text{-Cl Tau}]_t$, can be estimated, then $[H_2O_2]_t$ equals $[H_2O_2]_0 - [N\text{-Cl Tau}]_t$.

In the initial phase of the reaction (Figure 8.1B), the kinetics of absorbance increase at 252 nm showed a curvature that could be fitted to a double exponential equation (Equation 1). This behaviour may arise from the fact that the rate is strongly dependent on both H_2O_2 and the actual MPO-II concentrations. By using Equation 1 any portion of the initial time traces can be fitted properly. Thus, the derivative of the resulting function just after reagents mixing allows the calculation of the initial rate (Figure 8.1C). Approximately 10 replicated runs were fitted and the initial rates obtained from these fits were averaged.

$$y = y_0 + A_1\cdot(1-e^{-x/t_1}) + A_2\cdot(1-e^{-x/t_2}) \quad (1)$$

This procedure seems more precise than classical methods where the initial rate is obtained from the slope of the more or less short portion at the beginning of the kinetic trace; it implies uncertainties in the initial rate values, especially relevant for noisy traces. The approach used here reduces the scatter of kinetic data, and estimates the initial rate after mixing, *i.e.*, just at “zero time”.

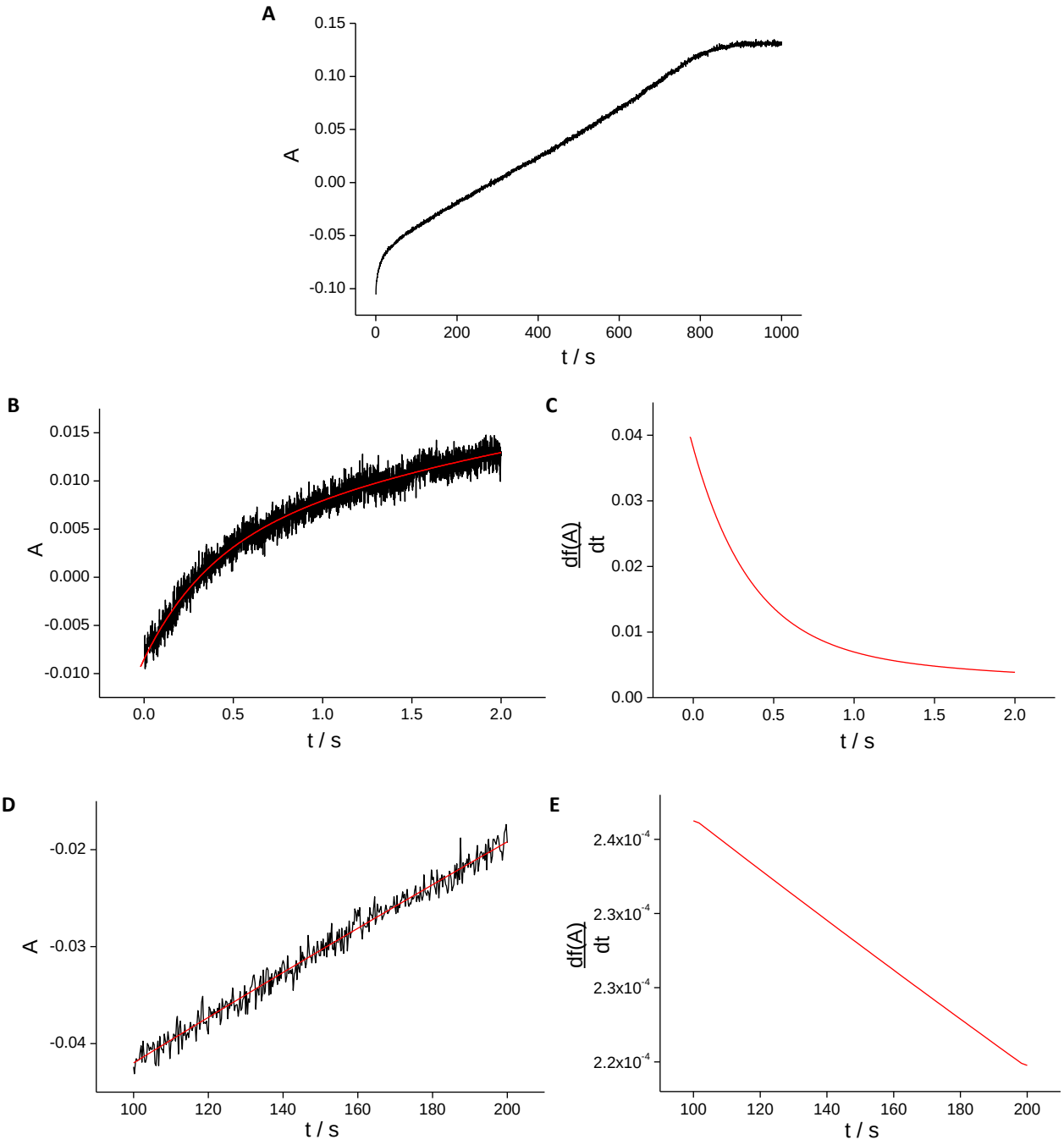

Figure 8.1. (A) Kinetic trace obtained in the stopped-flow spectrophotometer under the following conditions: λ = 252 nm, T = 25.0 °C, [MPO_0] = 100 nM, [Tau] = 10 mM, [Cl^-] = 100 mM, [H_2O_2] = 0.8 mM, pH (100 mM buffer) = 5.5. (B) Initial rate fit and (C) plot of the differentiated function. (D and E) Idem as (B and C) but under "equilibrium" conditions. Each figure is used for illustrative purposes; they do not necessarily belong to the same kinetic run.

Finally, a portion of the residual time trace, after dynamic equilibrium has been achieved, was fitted using the same mathematical expression (Equation 1) yielding the equilibrium rate at a particular time (Figures 8.1D and 8.1E). The total increase in absorbance (ΔA) observed at this point allowed calculation of the amount of *N*-Cl Tau formed and, therefore,

the remaining concentration of H_2O_2, since there is no noticeable loss of H_2O_2 through peroxidative processes. This is consistent with the fact that the presence of Cu/Zn superoxide dismutase had no impact on the equilibrium chlorination rate of Tau (data obtained by Paul G. Furtmüller, results not shown).

8.3 Results

MPO-catalyzed chlorination of Tau follows a rather complex mechanism. So far only the initial stages of this reaction at pH 4.7 have received mechanistic consideration.[10, 13] Here, we followed the formation of *N*-Cl Tau over the whole period of H_2O_2 consumption between pH 4.0 and pH 7.0, varying $[H_2O_2]$. Experimental data were fitted to the two mechanisms summarized in Table 8.1. The basis of these mechanisms has been taken from the literature.[10, 13-20] The novelty in the current study is that we have considered all the known acid/base, binding, and redox equilibria taking place. This enabled the estimation of intrinsic kinetic constants and consequently clarification of the molecular steps involved in the reaction mechanism.

Mechanism I takes into account eight reactions that influence the kinetics of *N*-Cl Tau formation. These include oxidation of Fe(III)-MPO by H_2O_2 to MPO-I (Reaction 1) and the known MPO-typical one-electron reduction of MPO-I to MPO-II by H_2O_2, with subsequent release of $HO_2^{\cdot}$ (Reaction 7).[14, 15] Reduction of MPO-I by Cl^- yields Fe(III)-MPO (Reaction 2) and HClO, which is capable of oxidizing or chlorinating several substrates. These include Tau, which reacts to form *N*-Cl Tau (Reaction 3). Mechanism I also includes protonation equilibria of both Fe(III)-MPO (Reaction 4) and MPO-I (Reaction 5) at the active site, as well as the formation of a high-spin complex by Cl^- binding to protonated Fe(III)-MPO (Reaction 6). Superoxide-mediated reduction of MPO-II to Fe(III)-MPO has been reported,[20] thus Reaction 8 is also included in the reaction mechanism.

In Mechanism II, according to the proposal by Marquez and Dunford,[10, 13] Reactions 2 and 3 are exchanged with Reactions 2b and 3b, *i.e.*, Cl^- binds to MPO-I producing a new enzymatic complex, MPO-I-Cl, (Reaction 2b), which acts as the actual halogenating agent that chlorinates Tau according to Reaction 3b. Despite the noticeable disparity on initial rate values[10, 13] with respect to our data, there are not further reasons to reject this pathway, so both mechanisms are considered as departing point.

8.3.1 Initial rate (v_0) chlorination measurements

In the beginning we investigated the dependence of the initial Tau chlorination rate (v_0) on both the $[H_2O_2]$ and pH. Initial rate of Tau chlorination increased upon raising pH from 4.0 to 7.0. At neutral pH the reaction was too fast even for the stopped-flow technique. Data obtained for five pH values are depicted in Figure 8.2A. They arrange in straight lines. These linear regressions were obtained by using error values as weight, although the corresponding error bars are not shown for the sake of clarity. Figure 8.2A unequivocally demonstrates that saturation of the active site is never reached under the assay conditions (*i.e:* $[H_2O_2] \geq 2000$ [MPO]). In this initial stage of *N*-Cl Tau formation MPO-II does not participate in the enzyme turnover. This is valid based on the published kinetic data of MPO-I reduction. It is well known that at pH 7 MPO-I reduction by Cl^- to Fe(III)-MPO and by H_2O_2 to MPO-II occur at similar rates and that, in contrast to the H_2O_2-mediated reaction, halide oxidation becomes significantly faster with decreasing pH.[14, 15, 19] Moreover, in the different assays $[Cl^-]$ was at least 50-fold that of H_2O_2. As shown in the inset of Figure 8.2A the Soret band appears at 430 nm, which is typical for MPO in its Fe(III) and MPO-I forms. Thus, in Mechanisms I and II only Reactions 1 - 6 have to be considered and Equations 12A (Mechanism I) and 19A (Mechanism II) from the Appendix (Section 8.6) can be applied (Table 8.2).

Uncertainties in initial reaction rates are around 10% at low pH and/or low $[H_2O_2]$, except for the four deviated values at pH 6, where uncertainty goes to 40%. At high pH and $[H_2O_2]$ values kinetics are much faster, which implies less precise measurements. The deviation of the four points at pH 6 is only apparent; the straight line is that of the error-weighted least squares fit, which properly crosses all error bars (not represented). Furthermore, these four deviated data pairs do not clearly point to a curved trace but to a lower slope, since a non-weighted least squares straight line could also be properly

drawn through those data.

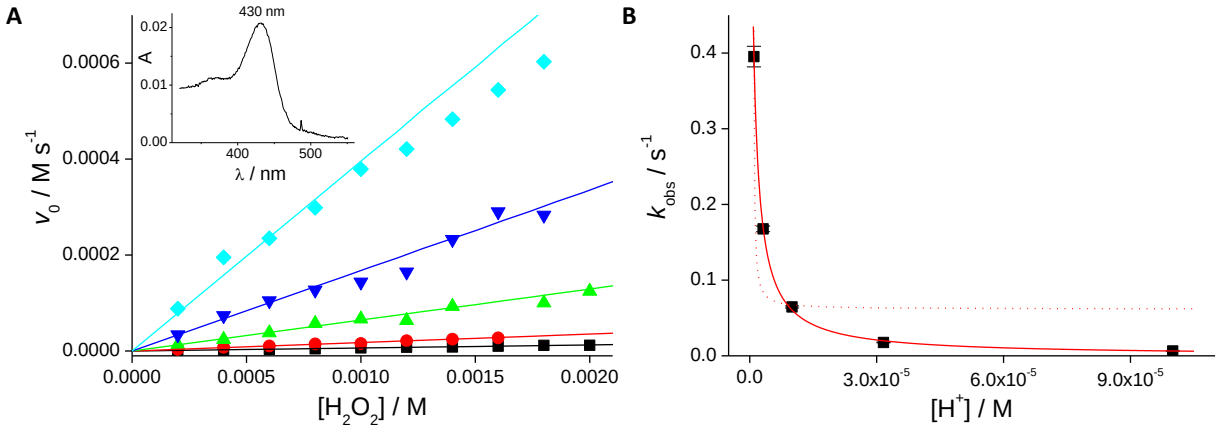

Figure 8.2. (A) Initial rate *vs*. [H_2O_2]. λ = 252 nm, T = 25.0 °C, [MPO_0] = 100 nM, [Tau] = 10 mM, [Cl^-] = 100 mM, [H_2O_2] = 0.2 - 2.0 mM, pH (100 mM buffer) = 4.0 (■), 4.5 (●), 5.0 (▲), 5.5 (▼), and 6.0 (♦). Inset: UV-Vis spectrum obtained at this phase of the reaction showing the Soret band. (B) Observed kinetic constant (k_{obs}) *vs*. [H^+]. Reaction conditions are the same as in (A). Solid line corresponds to Equation 2 fit, dotted line is the best fit with Equation 3.

Table 8.2. Initial rate and equilibrium regime rate equations obtained for Mechanisms I and II.

Mechanism	Initial rate equation	Acidity dependence
I	$v_0 = \frac{k_2 \cdot K_1 [MPO_0] \cdot [H_2O_2] \cdot [Cl^-] \cdot [H^+]}{1 + K_4 [H^+] \cdot (1 + K_6 [Cl^-])}$	$k_{obs} = \frac{v_0}{[H_2O_2]} = \frac{[H^+]}{a + b \cdot [H^+]}$
II	$v_0 = \frac{k_{2b} \cdot K_1 [MPO_0] \cdot [H_2O_2] \cdot [Cl^-]}{1 + K_4 [H^+] \cdot (1 + K_6 [Cl^-])}$	$k_{obs} = \frac{v_0}{[H_2O_2]} = \frac{a}{b + [H^+]}$

Mechanism	Equilibrium regime rate equation
I	$v_{eq} = \frac{k_2 \cdot [MPO_0] \cdot [Cl^-] \cdot [H^+]}{\frac{1 + K_4 [H^+] \cdot (1 + K_6 [Cl^-])}{K_1 \cdot [H_2O_2]} + 1 + K_5 [H^+] + \frac{K_7' \cdot [H_2O_2]}{[H^+]}}$
II	$v_{eq} = \frac{k_{2b} \cdot [MPO_0] \cdot [Cl^-]}{\frac{1 + K_4 [H^+] \cdot (1 + K_6 [Cl^-])}{K_1 \cdot [H_2O_2]} + 1 + K_5 [H^+] + \frac{K_7' \cdot [H_2O_2]}{[H^+]}}$

The dependence of the initial rate of Tau chlorination on pH can be better illustrated by representing the slopes obtained in Figure 8.2A (k_{obs}) *vs*. pH (Figure 8.2B). This pseudoconstant is independent of [H_2O_2], and its meaning becomes apparent by considering Equations 12A and 19A (Table 8.2). Thus, the plotted data have been fitted with two different functions (Equations 2 and 3):

$$k_{obs} = \frac{a}{b + [H^+]} \quad (2)$$

$$k_{obs} = \frac{[H^+]}{a + b \cdot [H^+]} \quad (3)$$

As shown in Figure 8.2B, Equation 2, derived from the initial rate expression of Mechanism II (Equation 19A), fits properly the experimental data, which is an indication of the adequacy of this pathway, while Equation 3 cannot fit the experimental values, suggesting that Mechanism I does not satisfactorily describe the system. Mechanism II includes the formation of a MPO-I-Cl complex, which, finally, chlorinates Tau in a proton dependent reaction (Reaction 3b).

8.3.2 "Equilibrium" rate (v_{eq}) chlorination measurements

Although contradictory at first sight, we decided to use the term "equilibrium" instead of "steady-state" rate in order to describe the study carried out beyond initial rate. Steady-state is the stage in which the concentration of an intermediate remains constant for a period of time. This concept is used in enzyme kinetics when the concentration of the enzyme-substrate complex (E-S) remains invariable and, therefore, the reaction rate being constant, with the corresponding kinetic trace depicting a straight line. On the other hand, the transient state, or pre-steady state, can be defined as the initial phase in which both [E-S] and the reaction rate increase accordingly, until they stabilize and keep constant (steady-state). However, this is not the case in the present study where kinetic traces exhibit a more complex profile. Due to accumulation of MPO-II the initial chlorination rate decelerates rapidly and is followed by a phase, where chlorination proceeds very slowly. Finally, it smoothly increases again due to H_2O_2 consumption and decay of [MPO-II], before it stops due to complete peroxide depletion. The described profile does not suit typical steady-state kinetics. While at the typical pre-steady state the rate should increase to reach a steady-state situation that corresponds to the maximum concentration of active E-S complex, our initial phase exhibits a decrease in reaction rate according to the formation of MPO-II. The monitored subsequent pseudo-straight phase is not due to the constant maximum concentration of active E-S complex, but to the equilibrium of formation, and, therefore, nearly constant concentration of inactive MPO-II. Thus, in order to avoid confusion and highlight the different concept, this stage of the reaction is described as "at equilibrium".

Rates of Tau chlorination measured at equilibrium (v_{eq}) show a fully different profile when plotted against [H_2O_2] (Figure 8.3A). After an initial rise the curves bend down with increasing [H_2O_2], this effect being more significant at higher pH values. Tau chlorination rates for pH ≥ 5.5 and [H_2O_2] ≥ 0.25 mM were very slow, indicating that a significant fraction of MPO is outside the chlorination cycle, the latter including only Fe(III)-MPO and MPO-I. This was the reason why we finally focused on the pH range 4 - 6. Looking at the dominating enzyme redox intermediate in this stage of H_2O_2 consumption revealed that the enzyme gathered as MPO-II, which has its Soret maximum at 456 nm (inset to Figure 8.3A) and a prominent band at 625 nm (not shown). Thus, at equilibrium, *i.e.*, after passing through many chlorination cycles in the initial phase, Reactions 7 and 8 became relevant and need to be considered in Mechanisms I and II. The null effect of the addition of Cu/Zn superoxide dismutase on the equilibrium chlorination rate of Tau, suggests that superoxide is not released from the heme cavity into the bulk medium. Thus, it is reasonable to assume that it does not leave immediately the active site but rapidly reacts in its vicinity where it rebinds to MPO-II (MPO-II-HO_2) before it goes back to MPO-I or donates its electron re-forming Fe(III)-MPO.

Accordingly, MPO-II-HO_2 would be considered as intermediate species. Rebinding to the active site has been also reported to occur for O_2 and NO at the distal heme cavity of myoglobin.[24] Equations 17A (Mechanism I) and 20A (Mechanism II) from the Section 8.6 were applied, with Equation 4 being valid for the two mechanisms (Table 8.2). These sets of data were fitted iteratively (Figures 8.3A - 8.3D), so that *a*- and *b*-values fit to a straight-line with respect to [H^+] (Equation 5) (Figures 8.3B and 8.3C), whereas *c*-values *versus* [H^+] fit to Equation 6 (Figure 8.3D). The effect of [H^+] on *a*, *b*, and *c* parameters has been worked out from the expressions of the rate at equilibrium for valid Mechanism II (Equation 20A) (Table 8.2).

$$v_{\mathrm{eq}} = \frac{1}{\frac{a}{[\mathrm{H_2O_2}]} + b + c \cdot [\mathrm{H_2O_2}]} \tag{4}$$

$$a\ (\text{and}\ b) = a' + b' \cdot [\mathrm{H^+}] \tag{5}$$

$$c = \frac{a''}{[\mathrm{H^+}]} \tag{6}$$

Curvature of the kinetic traces was due to deceleration of the chlorination activity because of accumulation of MPO-II (Figure 8.4A). After reaching the dynamic equilibrium, the chlorination process proceeded very slowly since the concentration of active compounds (MPO and MPO-I) was reduced to a small percentage of the total enzyme. Along the central portion of the kinetic trace the enzyme still cycled consuming H_2O_2 and chlorinating Tau, while [MPO-II] decreased according to H_2O_2 consumption (Figure 8.4B). Formation of compound III[14] was not observed at the concentration of H_2O_2 that was used. Upon depletion of H_2O_2, the absorbance at 430 nm increased indicating accumulation of Fe(III)-MPO (Figure 8.4C).

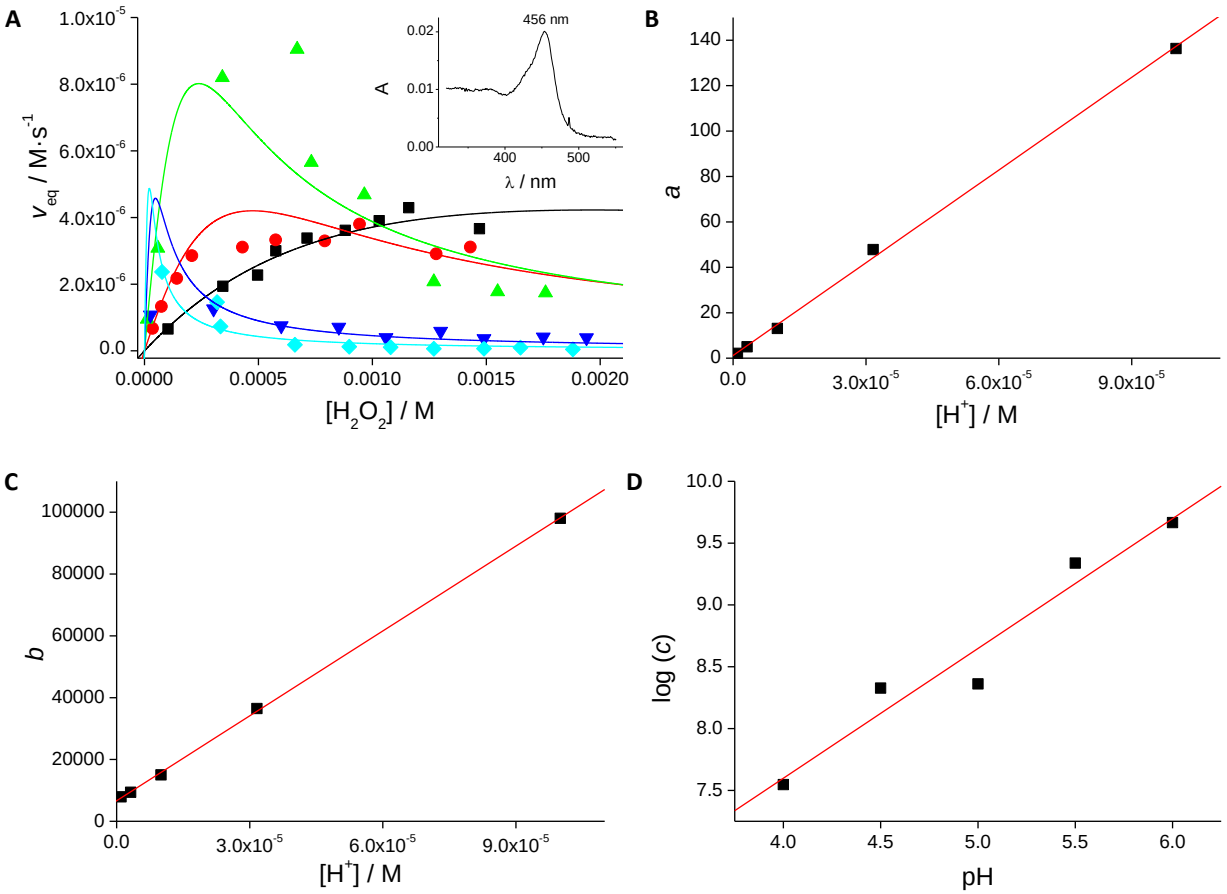

Figure 8.3. (A) Rate at equilibrium *vs*. [H_2O_2]. λ = 252 nm, T = 25.0 °C, [MPO_0] = 100 nM, [Tau] = 10 mM, [Cl^-] = 100 mM, [H_2O_2] = 0.2 - 2.0 mM, pH (100 mM buffer) = 4.0 (■), 4.5 (●), 5.0 (▲), 5.5 (▼), and 6.0 (♦). Inset: UV-Vis spectrum obtained at this phase of the reaction showing the Soret band. (B) *a vs*. [H^+]. (C) *b vs*. [H^+]. (D) log (*c*) *vs*. pH (slope = 1.05 ± 0.14).

These findings show that the decrease in the chlorination rate under equilibrium conditions with respect to initial rates can be ascribed to MPO-II accumulation. From the experimental data (Figures 8.3C and 8.3D) K_7' (= k_7 / (k_{-7} + k_8)) could be calculated to be 0.77 ± 0.13 M. Data from Figures 8.2B and 8.3C yielded a value for K_1 ((8.3 ± 3.7) × 10^3 M^{-1}) very similar to the value calculated in a different manner from Figures 8.2B, 8.3B and 8.3C ((9.3 ± 4.2) × 10^3 M^{-1}), which might reflect the high reduction potential of the redox couple MPO-I/MPO.[3] Besides, the fit shown in Figure 8.3C allowed the calculation of k_{2b} to be (1.58 ± 0.15) × 10^4 $M^{-1}·s^{-1}$, which is very similar to MPO-I reduction rate at physiological [Cl^-].[19, 25]

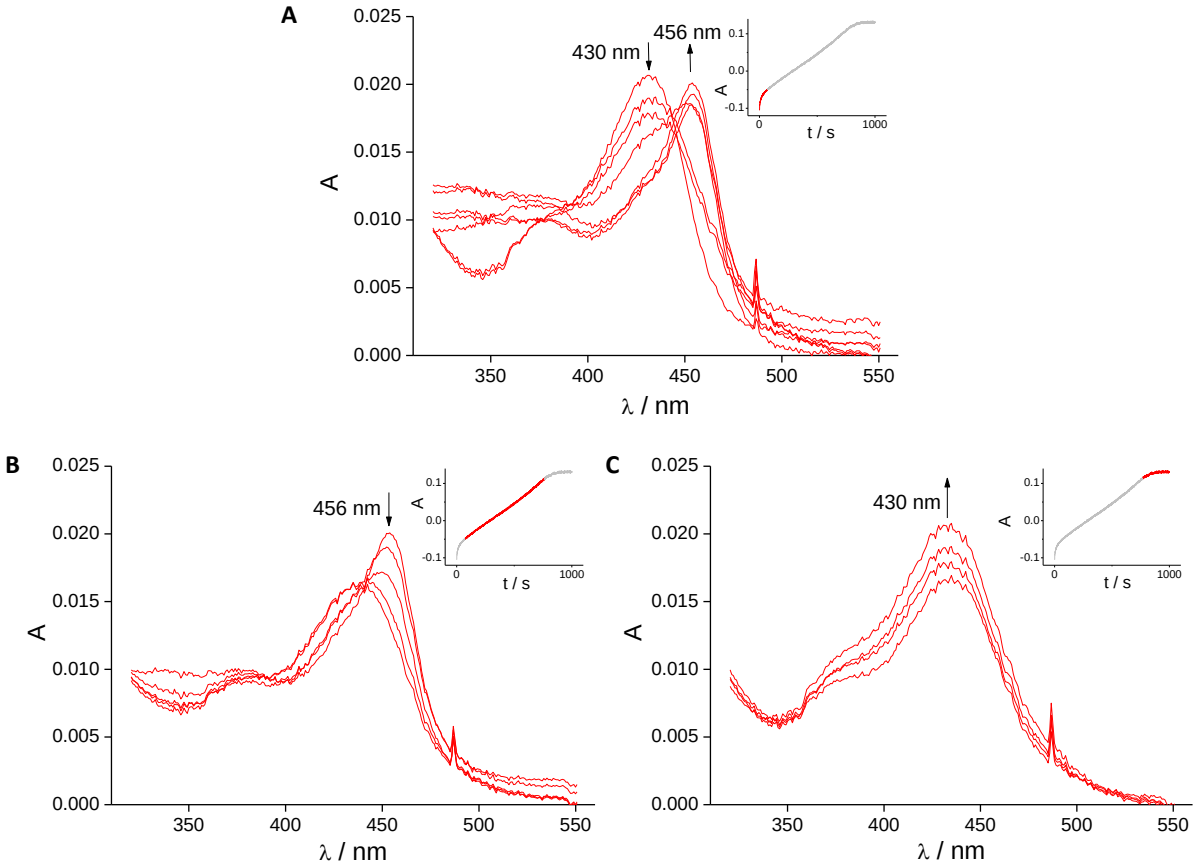

Figure 8.4. Representative UV-Vis spectra obtained from MPO in the initial phase (A), at equilibrium (B), and during H_2O_2 depletion (C), under the following conditions: T = 25.0 °C, [MPO_0] = 100 nM, [Tau] = 10 mM, [Cl^-] = 100 mM, [H_2O_2] = 0.8 mM, pH (100 mM buffer) = 5.5. Insets: Kinetic trace showing Tau chlorination at λ = 252 nm. The corresponding phases from which the representative spectra were taken are highlighted in red.

Additionally, the equilibrium constant of Reaction 5, K_5, was calculated to be $(1.46 \pm 0.16) \times 10^5$ M^{-1}, which corresponds to a pK_a of MPO-I-H of 5.16. It has been demonstrated that the protonated form of MPO-I efficiently oxidizes halides.[19] At acidic pH values halides bind near a protonated site, which has to be very close to the ferryl oxygen since there is a halide-dependent change in the EPR spectrum at acidic pH.[26] The crystal structures of the MPO-bromide and MPO-cyanide-bromide complexes suggest[27] that the distal histidine upon protonation could interact with the ferryl oxygen and the bound halide. Published pK_a values are in the range 4.5 - 5.2,[16, 17, 19, 26] thus underlining the adequacy of Mechanism II.

Applying the published value (170 µM) for the dissociation constant of the MPO-H-Cl complex[14] together with the fitting constants of Figure 8.2B, K_4 was calculated to be $(3.4 \pm 1.1) \times 10^3$ M^{-1}; this corresponds to pK_a(MPO-H) = 3.53, which is close to the published value of 3.95.[18]

8.4 Discussion

The chlorination of Tau by MPO has been investigated by Marquez and Dunford at very specific conditions,[10, 13] namely at pH 4.7 and by linearly fitting the initial portion of the time traces at 252 nm. We have extended these studies including equilibrium conditions and the pH range 4.0 - 7.0. Our data provide some discrepancies with previous studies, [10, 13] and new mechanistic insights regarding formation and nature of the chlorinating agent.

8.4.1 Absence of active site saturation

We could not find that the initial rate of chlorination of Tau exhibits saturation behavior,[10, 13] probably due to two main reasons. The first one is related with the rapid kinetics system. In former work[10, 13] data collection from kinetic runs was triggered 4 ms after mixing; nowadays stopped-flow equipment allows effective mixing below 1 ms, and such difference is important when dealing with the estimation of initial rates for fast kinetics. When considering the rate of formation of MPO-II measured by the same authors (k = (8.2 ± 0.2) x 10^4 $M^{-1}{\cdot}s^{-1}$),[15] it can be noticed that, under conditions used in the study, within 4 ms already some formation of MPO-II occurred, as depicted in Figure 8.1B of the same paper.[15] In case of the discussed paper[10] the time used for the fit seems to be significantly higher (up to 100 ms) to avoid interference of noise in the linear fit.

The present work (Figure 8.5) clearly demonstrates that the decrease of chlorination starts very fast after reactants mixing, and adequate initial rate values should not be measured after 4 ms. At low concentration of H_2O_2 the effect of MPO-II is almost negligible (Figure 8.5A) and the slope obtained after 5 s is still approximately 50% of that at 1 ms. At higher [H_2O_2] MPO-II formation becomes important. Furthermore, this fast (pseudo)inhibition becomes more evident at higher pH values. Figure 8.5B depicts that the mixing time lasts only about 1 ms, and the reaction of chlorination and, more important, the build-up of MPO-II already takes place just after this short time. Within 100 ms the chlorination rate was reduced to 26% of the initial rate. Consequently, we used a different methodology: the kinetic trace at very early stages of the reaction was fitted to an adequate equation and then the initial rate was calculated from its derivative, as explained under Experimental procedures.

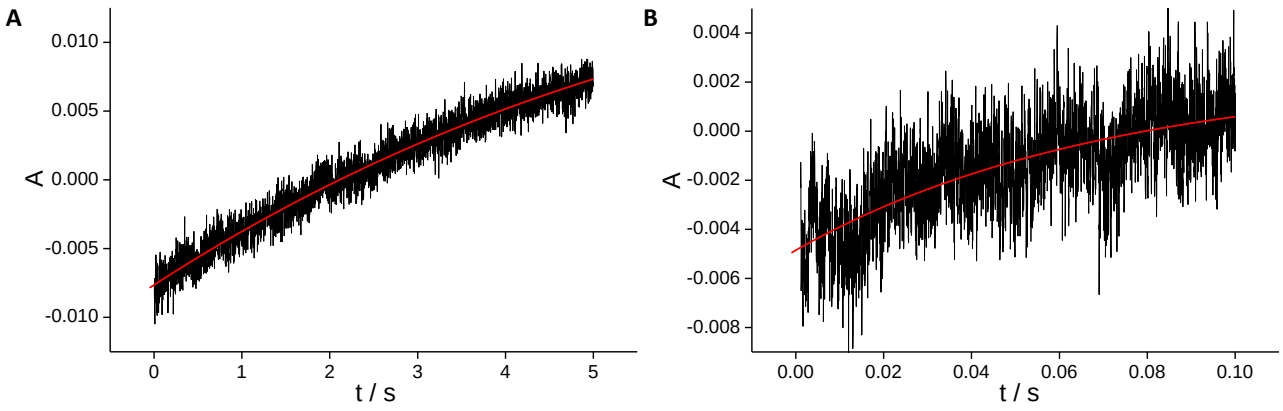

Figure 8.5. Initial kinetic traces obtained in the stopped-flow spectrophotometer under the following conditions: λ = 252 nm, T = 25.0 °C, [MPO_0] = 100 nM, [Tau] = 10 mM, [Cl^-] = 100 mM, (A) [H_2O_2] = 0.2 mM, pH (100 mM buffer) = 5.0, (B) [H_2O_2] = 1.0 mM, pH (100 mM buffer) = 6.0.

Therefore, most likely the previously observed saturation of the active site, which becomes more evident at higher pH values, is an artifact coming from the delay in data collection with respect to the physically available zero time. The reported initial rate values, especially for faster kinetics, certainly are a composite between initial rates and equilibrium regime rates. Thus, apparent saturation is found as the reaction rate decreases upon approaching the equilibrium regime.

On the other hand, the previously proposed mechanism does not take into account acid-base and binding equilibria relevant for derivation of the rate equations. Here, the complementary kinetic information obtained by initial rate and equilibrium rate studies of the same kinetic trace, enables us to draw conclusions up to now not present in the literature.

8.4.2 Chloride oxidation does not depend on proton concentration

The first important outcome of the present work is related to the acidity dependence of the formation of the chlorinating

agent; it has been found that under the working conditions there is no proton intervening in the molecular step between MPO-I and Cl^-. This result rules out molecular steps like Reaction 2, or a modified version of Reaction 2b, *i.e.*:

$$\text{MPO-I} + \text{Cl}^- + \text{H}^+ \overset{k_{2b'}}{\rightarrow} \text{MPO-I-Cl-H}$$

with Tau being chlorinated by this protonated complex (MPO-I-Cl-H) in a subsequent process. Reaction 2b' could be proposed on the basis of the noticeable acceleration of the rate of Cl^- oxidation by MPO at acidic pH values.[16, 18, 19, 28] However, in this case the corresponding initial and equilibrium rate equations would be analogous to those obtained for Mechanism I (Table 8.2), which do not support the observed kinetic behaviour. Equivalent rate equations are also deduced by considering the reversibility of these steps:

$$\text{MPO-I} + \text{Cl}^- + \text{H}^+ \underset{k_{-2}}{\overset{k_2}{\rightleftarrows}} \text{MPO} + \text{HOCl}$$

$$\text{MPO-I} + \text{Cl}^- + \text{H}^+ \underset{k_{-2b'}}{\overset{k_{2b'}}{\rightleftarrows}} \text{MPO-I-Cl-H}$$

In fact, it has been demonstrated that HClO can oxidize Fe(III)-MPO to MPO-I (Reaction –2) similar to the H_2O_2-mediated reaction.[29] Any other mechanistic alternatives involving a proton in the molecular reaction of MPO-I and Cl^- render rate equations similar to Mechanism I, which is not supported by kinetic data. The above indicated acceleration at low pH should be explained by other processes, like the pH-dependent equilibrium of MPO-II formation (Reaction 7). In fact, it has been observed that deceleration of chlorination from this species increases with both [H_2O_2] and pH.

8.4.3 The quest for the chlorinating species

Taking into account that Mechanism II properly describes experimental kinetic rates, opens the door to kinetically indistinguishable mechanisms[30] compatible with the proposals of the literature, the chlorinating agent being either HClO or MPO-I-Cl. As the reaction rate, both initial and equilibrium, is independent of [Tau], the molecular steps where Tau participates must be faster than the formation of the chlorinating agent. Therefore, Mechanism II could be extended beyond the rate-limiting step by the steps depicted in Scheme 8.1 with no effect on the deduced rate equations. Once the intermediate complex MPO-I-Cl is formed (Reaction 2b), it could chlorinate substrates able to diffuse into the heme cavity (Reaction 3b); the equivalent compound I-Cl intermediate has been observed in chloroperoxidase (CPO).[31] Furthermore, it could be involved in an acid-base equilibrium to yield MPO-I-Cl-H (Reaction 10), which has also been found for CPO;[31] this species could merely react with Tau (Reaction 12) and/or likely dissociate to yield Fe(III)-MPO and HClO (Reaction 13), which diffuses away to oxidize a variety of substrates (Reaction 3).

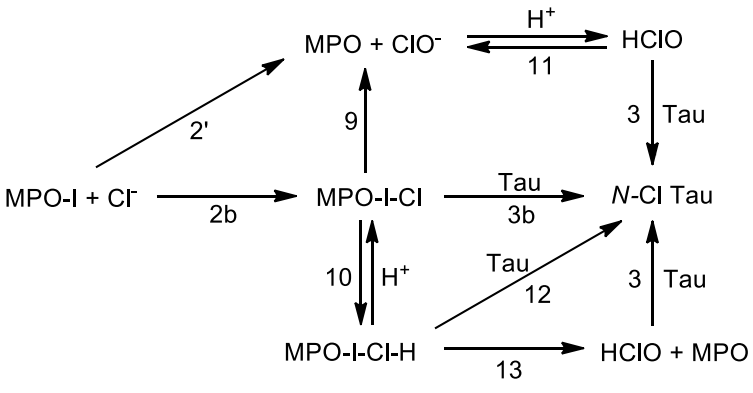

Scheme 8.1. Mechanistic pathways for the formation of MPO-mediated chlorinating agents.

Another feasible pathway is the breaking of MPO-I-Cl to give Fe(III)-MPO and ClO^- (Reaction 9). This species, which is much less oxidizing than HClO, is able to diffuse from the active site. Away from the enzyme, it is readily protonated to HClO (Reaction 11), which is the active chlorinating agent (Reaction 3). It could be argued that under the working conditions for reliable kinetic measurements (pH 4 - 6) ClO^- should have a very short lifetime (pK_a(HClO) = 7.54)[32] in favour of HClO. However, this pK_a value applies for bulk water but not for the inner protein core, where it is produced.[33] Furthermore, the inner environment of the enzyme seems to stabilize negative charged species, Cl^- for instance, and the same must hold for ClO^-. If free HClO was formed inside the enzyme, it could rapidly react with every oxidizable group in the neighbourhood of the heme inhibiting the activity of MPO. High diffusion rate and reactivity of ClO^- and HClO, respectively, impede their direct observation.

Additionally, it could also be possible to propose an independent step to form Fe(III)-MPO and ClO^- (Reaction 2' in Scheme 8.1), instead of a pathway via MPO-I-Cl; even in this case the deduced rate equations would be analogous to those shown in Table 8.2. The same applies if the previous step or the formation of MPO-I-Cl are considered as reversible:

$$\text{MPO-I} + \text{Cl}^- \underset{k_{-2'}}{\overset{k_{2'}}{\rightleftarrows}} \text{MPO} + \text{ClO}^-$$

$$\text{MPO-I} + \text{Cl}^- \underset{k_{-2b}}{\overset{k_{2b}}{\rightleftarrows}} \text{MPO-I-Cl}$$

Summing up all the possibilities exposed above: the deduced rate equation for any reaction mechanism comprising Mechanism II (Table 8.1) and involving some or all steps after MPO-I-Cl formation (Reaction 2b) is the mathematical expression shown in Table 8.2. On the other hand, if both Reactions 2b and 2' are taken into account, the mathematical expression of the rate equations holds but not the meaning of the parameters, *i.e.*, predicted dependence on reactants and acidity is equal, but k_{2b} should be replaced by ($k_{2b} + k_{2'}$). Finally, the solely consideration of Reaction 2' as feasible pathway also leads to the same rate equation, with the kinetic constant $k_{2'}$ taking the place of k_{2b}. Furthermore, according to this reaction scheme (Scheme 8.1), small substrates, like Tau, could be chlorinated both inside the enzyme by the complex MPO-I-Cl, and outside by released ClO^-/HClO, whereas the chlorination of bulkier substrates would only take place outside the heme cavity by reaction with a free released chlorinating agent (ClO^-/HClO).

8.4.4 Role and turnover of compound II

The second important outcome obtained from initial rate and equilibrium rate studies of the same kinetic trace, relates to the effect of formation of MPO-II (or MPO-II-HO_2) on the chlorination cycle. Reactions 7 and 8 (Table 8.1) are responsible for the deceleration of the chlorination reaction rate. This can easily be deduced from the different rate values at initial and equilibrium regimes (Figures 8.2A and 8.3A), and from their appearance in the corresponding mechanism rate equation (Table 8.2 and Equation 20A) associated to the term K_7'. This constant ($K_7' = k_7 / (k_{-7} + k_8)$) involves the rate constant of MPO-II formation, k_7, and of the reverse reaction, k_{-7}, (*i.e.*, re-formation of MPO-I and H_2O_2), and the rate constant for superoxide-mediated MPO-II reduction to Fe(III)-MPO, k_8. It is important to note that following Reaction 8 would mean a net loss of hydrogen peroxide outside the chlorination cycle.

Depending on the relative values of k_{-7} and k_8 two limits can be considered. First limit implies $k_{-7} << k_8$, thus taking into account the values of K_7' (0.77 M) and k_7 (3.3×10^4 $M^{-1}{\cdot}s^{-1}$),[15] the maximum value for k_8 can be calculated as 4.29×10^4 $M^{-1}{\cdot}s^{-1}$, significantly lower than 10^6 $M^{-1}{\cdot}s^{-1}$ proposed in the literature.[34] The latter value would imply a measurable loss of hydrogen peroxide outside the chlorination cycle, which is contrary to our findings. Therefore, the previously reported value should be used with some caution.

The other limit, $k_{-7} >> k_8$ and $K_7' \approx K_7$, means that the equilibrium in Reaction 7 (Table 8.1) is thermodynamically slightly unfavourable, which is in agreement with the required excess of H_2O_2 to drive out the formation of MPO-II.[15] Thus, assuming that the re-formation of MPO-I is faster than the formation of Fe(III)-MPO, *i.e.*, $k_{-7} >> k_8$, and considering that

MPO-II accumulation is the only responsible for the slow rate under equilibrium conditions, we can calculate the fraction of chlorinating-active enzyme (here defined as the concentration of all enzymatic species but MPO-II) and, therefore, [MPO-II] at particular pH and [H_2O_2] conditions:

$$\frac{[MPO_0]-[MPO-II]}{[MPO_0]}=\frac{v_{eq}}{v_{0,calc}} \tag{7}$$

where $v_{0,calc}$ is the estimated value of the initial rate, calculated from fittings shown in Figure 8.2A at the corresponding pH and [H_2O_2].

The one-electron oxidation of Reaction 7 produces $HO_2^{\cdot}$ radicals[14, 15] which have been described to act as electron donors of MPO-II.[35] According to this equilibrium we obtain:

$$K_7=\frac{[MPO-II]\cdot[HO_2^{\cdot}]\cdot[H^+]}{[MPO-I]\cdot[H_2O_2]} \tag{8}$$

Kinetic runs in presence of Cu/Zn superoxide dismutase did not reveal any effect on reaction rate, suggesting that superoxide is not released but rapidly reacts in heme vicinity upon rebinding to MPO-II (MPO-II-HO_2), thus Equation 8 rearranges to:

$$K_7=\frac{[MPO-II-HO_2]\cdot[H^+]}{[MPO-I]\cdot[H_2O_2]};\quad [MPO-II-HO_2]=\frac{K_7\cdot[MPO-I]\cdot[H_2O_2]}{[H^+]} \tag{9}$$

Since the initial amount of enzyme is regained as Fe(III)-MPO following H_2O_2 consumption (Figure 8.4), the formation of this complex must be reversible and it does not lead to MPO permanent inhibition.

Analyzing in detail all reactions involved in valid Mechanism II, we can extract the following dependences. For every pH value, [MPO-I] must be proportional to the fraction of chlorinating-active enzyme ([MPO_0]-[MPO-II-HO_2]) and, according to Reaction 1, the extent of this proportionality depends on the actual [H_2O_2]. Thus, we obtain:

$$[MPO-I]=\alpha\cdot[H_2O_2]\cdot([MPO_0]-[MPO-II-HO_2]) \tag{10}$$

where α is the proportionality constant. Equation 9 changes to:

$$\frac{[MPO-II-HO_2]\cdot[H^+]}{[MPO_0]-[MPO-II-HO_2]}=\alpha\cdot K_7\cdot[H_2O_2]^2 \tag{11}$$

The left term of Equation 11 *versus* $[H_2O_2]^2$ is plotted in Figure 8.6A. Straight lines were obtained for each pH, with the slope representing $\alpha\cdot K_7$, which indicates the correctness of this approach. The effect of protonation equilibria of Fe(III)-MPO and MPO-I (Reactions 4 and 5) on α can also be studied. Thus, for every pH value, [MPO-I] is proportional to the fraction of unprotonated active enzyme (all MPO species minus MPO-II and excluding all other protonated complexes, *i.e.*, [MPO_0] – [MPO-II-HO_2] – [MPO-H] – [MPO-I-H] – [MPO-H-Cl]. The potential protonated MPO-I-Cl-H complex is not considered, as its concentration should be negligible). Besides, [MPO-I] is inversely proportional to [H^+] according to Reaction 5:

$$[MPO-I]=\frac{\beta\cdot[H_2O_2]\cdot([MPO_0]-[MPO-II-HO_2]-[MPO-H]-[MPO-I-H]-[MPO-H-Cl])}{[H^+]} \tag{12}$$

Applying a similar approach to all protonated species, *i.e.*, [MPO-H], [MPO-I-H], and [MPO-H-Cl] must also be proportional to ([MPO_0] – [MPO-II-HO_2]) and, according to Reactions 4 and 5, to [H^+], Equation 12 can be written:

$$[MPO-I]=\frac{\beta\cdot[H_2O_2]\cdot([MPO_0]-[MPO-II-HO_2])\cdot(1-\gamma\cdot[H^+])}{[H^+]} \tag{13}$$

with β and γ representing the proportionality constants of [MPO-I] and concentration of protonated species, respectively. Comparing this expression with Equation 10, the following relationship is obtained:

$$\alpha = \beta \cdot \frac{(1 - \gamma \cdot [H^+])}{[H^+]} \tag{14}$$

The slopes from Figure 8.6A ($\alpha \cdot K_7$) are plotted against $[H^+]$ in Figure 8.6B, and the data fitted to Equation 15:

$$\alpha \cdot K_7 = \frac{a - b \cdot [H^+]}{[H^+]} \tag{15}$$

Considering the different described approximations, Equation 15 reasonably fits the data. This supports the proposed mechanism and the assumptions made to derivate expressions for the rate at equilibrium.

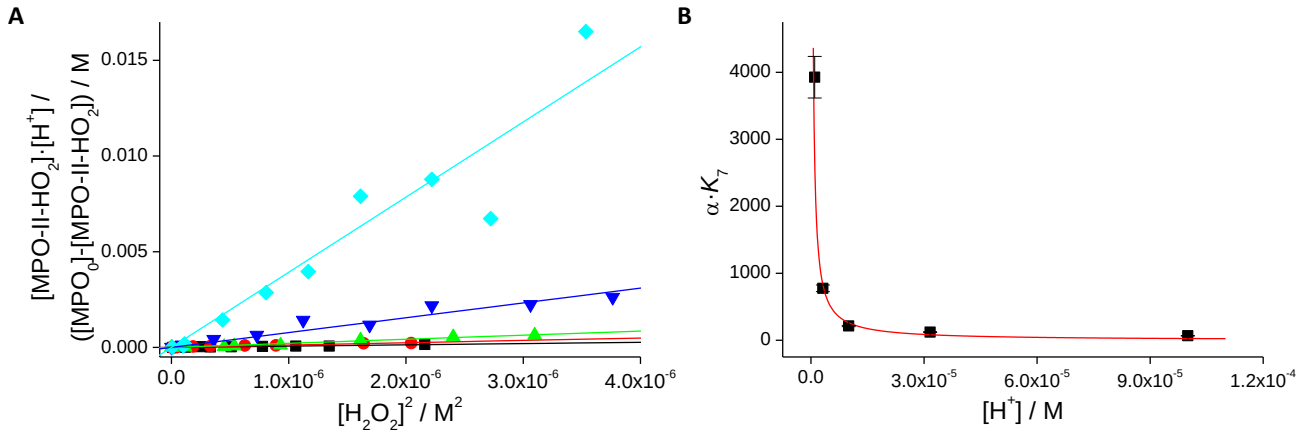

Figure 8.6. (A) ($[MPO\text{-}II\text{-}HO_2] \cdot [H^+] / [MPO_0] - [MPO\text{-}II\text{-}HO_2]$) plotted *vs*. $[H_2O_2]^2$. Values of $[MPO\text{-}II\text{-}HO_2]$ were calculated from the data in Figures 8.2 and 8.3. Conditions are the same as in these figures. (B) Slopes from (A) plotted against $[H^+]$.

Thus, the current data show that formation of MPO-II is the only process that affects the chlorination rate at equilibrium, decelerating it significantly compared to the initial rate. Here, for the first time, quantitative kinetic data are provided that explain this phenomenon. Under working conditions for reliable kinetic measurements (pH 4 - 6), the hydroperoxide radical produced by MPO-I-mediated H_2O_2 oxidation (Reaction 7 in Table 8.1) does not leave the heme cavity, as pointed out by the null effect on Tau chlorination rate when superoxide dismutase is added. Since there was no noticeable loss of H_2O_2 through peroxidative processes like MPO-II reduction by $HO_2^{\cdot}$ to Fe(III)-MPO (Reaction 8 in Table 8.1), it is reasonable to assume that the equilibrium described by Equation 9 mostly determines the ratio [MPO-I]/[MPO-II], and thus the actual Tau chlorination rate at equilibrium.

8.5 Summary

In conclusion, we have demonstrated that kinetic studies on complex enzymatic mechanisms can be performed at different stages of the process, using the same kinetic traces. In the particular case of human myeloperoxidase, the rate dependence on pH and $[H_2O_2]$ shows a different behaviour for initial rates and for rates at equilibrium regime. Despite these data differ from previously published results ,[10, 13] a chlorination pathway via the complex MPO-I-Cl is also supported by the present findings. It is important to notice that the present data also support the possibility of a free chlorinating agent that is released unprotonated (ClO^-) from the active centre and undergoes protonation to HClO outside the heme cavity (Reactions 2' and/or 9 and 11 in Scheme 8.1). In this case, HClO is the actual chlorinating agent. On the other hand, actual results reject mechanisms similar to Mechanism I, which involves formation of the strong oxidizing agent HClO inside the heme cavity by reaction of Cl^- and MPO-I with net consumption of one acid equivalent (Reaction 2 in Table 8.1). The effect of pH on kinetic rates show that the produced halogenating species, at least, prior to and at the rate-limiting step, must be unprotonated, either MPO-I-Cl or ClO^-, which are kinetically indistinguishable. Therefore, determination of factual chlorinating agent

should be carried out by chemical or biological means other than bare kinetic studies.

Evidence for the reversibility of the reaction of MPO-I and H_2O_2 to yield MPO-II has been also provided both mathematically and by the null consumption of H_2O_2 via pathways other than Tau chlorination. The slow chlorination rate under equilibrium conditions could be quantitatively ascribed to the chemical equilibrium between MPO-I and MPO-II. Still, these data do not permit us to completely reject the possibility of MPO turnover via Reaction 8, but they evidence that this pathway must only represent a minor contribution on the overall process. Furthermore, the absence of effect of addition of Cu/Zn superoxide dismutase on the reaction rate indicates that $HO_2^{\cdot}$ radicals are not released from the active site into the bulk medium, which supports the proposal of an enzymatic complex MPO-II-HO_2.

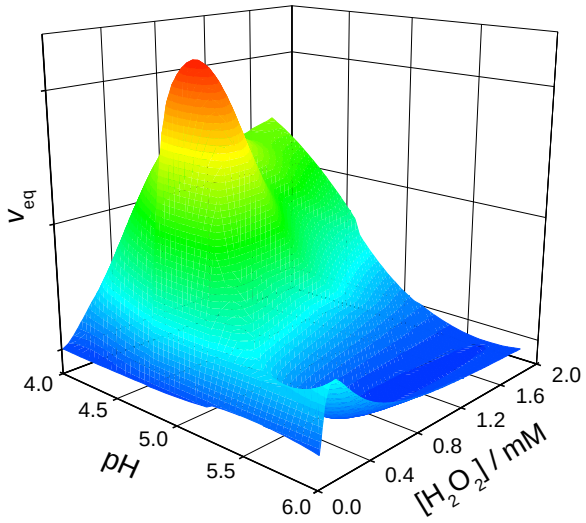

Figure 8.7. Three-dimensional scheme showing the dependence of Tau chlorination rate by MPO on pH and [H_2O_2] at equilibrium (*in vivo* conditions). Conditions are the same as in Figure 8.3A.

Figure 8.7 provides a visual comprehension of the behaviour at equilibrium. Both at high and low [H_2O_2], as well as in the ends of the employed pH range, chlorination keeps at a low rate, whereas the maximum rate is obtained at [H_2O_2] and pH values around 0.4 mM and pH 5, respectively. These results are in agreement with the work of Panasenko and coworkers who found chlorination activity of MPO to be optimal at acidic pH values, while its peroxidative effect takes place around neutral pH.[36, 37] Simulation of the MPO activity in the neutrophil phagosome at pH 7.4 supports the relevance of both processes near neutral pH.[34]

8.6 Appendix. Derivation of the rate equations for Mechanisms I and II

8.6.1 Mechanism I

8.6.1.1 Initial rate

Reaction rate expression from Reaction 3:

$$v_0 = \frac{\mathrm{d}[N\text{-Cl Tau}]}{\mathrm{d}t} = k_3 \cdot [\mathrm{HClO}] \cdot [\mathrm{Tau}] \qquad (1A)$$

Mass balance equation:

$$[\mathrm{MPO}_0] = [\mathrm{MPO}] + [\mathrm{MPO\text{-}I}] + [\mathrm{MPO\text{-}H}] + [\mathrm{MPO\text{-}I\text{-}H}] + [\mathrm{MPO\text{-}H\text{-}Cl}] \qquad (2A)$$

Equilibrium equation for protonation of MPO:

$$K_4 = \frac{[\text{MPO - H}]}{[\text{MPO}]\cdot[\text{H}^+]};\quad [\text{MPO - H}] = K_4\cdot[\text{MPO}]\cdot[\text{H}^+] \tag{3A}$$

Equilibrium equation for proton binding onto MPO-I:

$$K_5 = \frac{[\text{MPO - I - H}]}{[\text{MPO - I}]\cdot[\text{H}^+]};\quad [\text{MPO - I - H}] = K_5\cdot[\text{MPO - I}]\cdot[\text{H}^+] \tag{4A}$$

Equilibrium equation for binding of chloride:

$$K_6 = \frac{[\text{MPO - H - Cl}]}{[\text{MPO - H}]\cdot[\text{Cl}^-]};\quad [\text{MPO - H - Cl}] = K_6\cdot[\text{MPO - H}]\cdot[\text{Cl}^-] \tag{5A}$$

Substituting from Equations 3A - 5A into 2A:

$$[\text{MPO}_0] = [\text{MPO}]\cdot(1+K_4\cdot[\text{H}^+]\cdot(1+K_6\cdot[\text{Cl}^-])) + [\text{MPO - I}]\cdot(1+K_5\cdot[\text{H}^+]) \tag{6A}$$

Equilibrium equation for MPO-I formation:

$$K_1 = \frac{[\text{MPO - I}]}{[\text{MPO}]\cdot[\text{H}_2\text{O}_2]};\quad [\text{MPO}] = \frac{[\text{MPO - I}]}{K_1\cdot[\text{H}_2\text{O}_2]} \tag{7A}$$

Substituting from Equation 7A into 6A:

$$[\text{MPO}_0] = \left(\frac{1+K_4\cdot[\text{H}^+]\cdot(1+K_6\cdot[\text{Cl}^-])}{K_1\cdot[\text{H}_2\text{O}_2]} + 1 + K_5\cdot[\text{H}^+]\right)\cdot[\text{MPO - I}] \tag{8A}$$

Steady-state approximation for HClO:

$$\frac{\text{d}[\text{HClO}]}{\text{d}t} = 0;\quad k_2\cdot[\text{MPO-Cl}]\cdot[\text{Cl}^-]\cdot[\text{Cl}^+] = k_3\cdot[\text{HClO}]\cdot[\text{Tau}] \tag{9A}$$

From Equations 8A and 9A, Equation 1A is converted to:

$$v_0 = k_2\cdot[\text{MPO - I}]\cdot[\text{Cl}^-]\cdot[\text{H}^+] = \frac{k_2\cdot[\text{MPO}_0]\cdot[\text{Cl}^-]\cdot[\text{H}^+]}{\frac{1+K_4\cdot[\text{H}^+]\cdot(1+K_6\cdot[\text{Cl}^-])}{K_1\cdot[\text{H}_2\text{O}_2]} + 1 + K_5\cdot[\text{H}^+]} \tag{10A}$$

Considering:

$$\frac{1+K_4\cdot[\text{H}^+]\cdot(1+K_6\cdot[\text{Cl}^-])}{K_1\cdot[\text{H}_2\text{O}_2]} >> 1+K_5\cdot[\text{H}^+] \tag{11A}$$

which is consistent with the experimental initial rate dependence on the H_2O_2 concentration (Figure 8.2A).

Initial rate expression becomes:

$$v_0 = \frac{K_1\cdot k_2\cdot[\text{MPO}_0]\cdot[\text{H}_2\text{O}_2]\cdot[\text{Cl}^-]\cdot[\text{H}^+]}{1+K_4\cdot[\text{H}^+]\cdot(1+K_6\cdot[\text{Cl}^-])} \tag{12A}$$

8.6.1.2 Rate at equilibrium

Under equilibrium and according to the hypothesis about $HO_2^{\cdot}$ described in the paper, conservation equation changes to:

$$[\text{MPO}_0] = [\text{MPO}] + [\text{MPO - I}] + [\text{MPO - H}] + [\text{MPO - I - H}] + [\text{MPO - H - Cl}] + [\text{MPO - II - HO}_2] \tag{13A}$$

Variation of [MPO-II-HO_2] at equilibrium occurs very slowly, thus steady-state approximation can be applied:

$$\frac{\text{d}[\text{MPO - II - HO}_2]}{\text{d}t} = 0;\quad k_7\cdot[\text{MPO - I}]\cdot[\text{H}_2\text{O}_2] = (k_{-7}+k_8)\cdot[\text{MPO - II - HO}_2]\cdot[\text{H}^+] \tag{14A}$$

Equation 14A converts to:

$$[\text{MPO - II - HO}_2] = \frac{k_7\cdot[\text{MPO - I}]\cdot[\text{H}_2\text{O}_2]}{(k_{-7}+k_8)\cdot[\text{H}^+]} = \frac{K_7^{'}\cdot[\text{MPO - I}]\cdot[\text{H}_2\text{O}_2]}{[\text{H}^+]} \tag{15A}$$

Substituting from Equations 3A - 5A and 15A into Equation 13A:

$$[\mathrm{MPO}_0] = [\mathrm{MPO}]\cdot(1+K_4\cdot[\mathrm{H}^+]\cdot(1+K_6\cdot[\mathrm{Cl}^-])) + [\mathrm{MPO-I}]\cdot\left(1+K_5\cdot[\mathrm{H}^+]+\frac{K_7^{'}\cdot[\mathrm{H_2O_2}]}{[\mathrm{H}^+]}\right) \quad (16A)$$

From Equations 7A, 9A and 16A, rate expression 1A is converted to:

$$v_{eq} = k_2\cdot[\mathrm{MPO-I}]\cdot[\mathrm{Cl}^-]\cdot[\mathrm{H}^+] = \frac{k_2\cdot[\mathrm{MPO}_0]\cdot[\mathrm{Cl}^-]\cdot[\mathrm{H}^+]}{\frac{1+K_4\cdot[\mathrm{H}^+]\cdot(1+K_6\cdot[\mathrm{Cl}^-])}{K_1\cdot[\mathrm{H_2O_2}]}+1+K_5\cdot[\mathrm{H}^+]+\frac{K_7^{'}\cdot[\mathrm{H_2O_2}]}{[\mathrm{H}^+]}} \quad (17A)$$

8.6.2 Mechanism II

8.6.2.1 Initial rate

Mass balance equation:

$$[\mathrm{MPO}_0] = [\mathrm{MPO}]+[\mathrm{MPO-I}]+[\mathrm{MPO-H}]+[\mathrm{MPO-I-H}]+[\mathrm{MPO-H-Cl}]+[\mathrm{MPO-I-Cl}] \quad (18A)$$

Applying steady-state approximation for MPO-I-Cl, considering that [MPO-I-Cl] must be negligible (similarly as HClO, this compound should be a strong oxidant that reacts very rapidly with Tau) and rearranging, the initial rate equation becomes:

$$v_0 = \frac{K_1\cdot k_{2b}\cdot[\mathrm{MPO}_0]\cdot[\mathrm{H_2O_2}]\cdot[\mathrm{Cl}^-]}{1+K_4\cdot[\mathrm{H}^+]\cdot(1+K_6\cdot[\mathrm{Cl}^-])} \quad (19A)$$

8.6.2.2 Rate at equilibrium

The preceding rate expression is converted to:

$$v_{eq} = \frac{k_{2b}\cdot[\mathrm{MPO}_0]\cdot[\mathrm{Cl}^-]}{\frac{1+K_4\cdot[\mathrm{H}^+]\cdot(1+K_6\cdot[\mathrm{Cl}^-])}{K_1\cdot[\mathrm{H_2O_2}]}+1+K_5\cdot[\mathrm{H}^+]+\frac{K_7^{'}\cdot[\mathrm{H_2O_2}]}{[\mathrm{H}^+]}} \quad (20A)$$

This study has been published as: D. R. Ramos, M. V. García, M. Canle L., J. A. Santaballa, P. G. Furtmüller, and C. Obinger, Arch. Biochem. Biophys., 2007 **466** (2) 221-233.

8.7 References

1. S. J. Klebanoff, *Myeloperoxidase: friend and foe.* J. Leukoc. Biol., 2005 **77** (5) 598-625.
2. A. Taurog, *Molecular evolution of thyroid peroxidase.* Biochimie, 1999 **81** (5) 557-562.
3. J. Arnhold, P. G. Furtmüller, and C. Obinger, *Redox properties of myeloperoxidase.* Redox Report, 2003 **8** (4) 179-186.
4. E. L. Thomas and D. B. Learn, *Myeloperoxidase-catalyzed oxidation of chloride and other halides: the role of chloramines*, in *Peroxidases in chemistry and biology*, J. Everse, K. E. Everse, and M. B. Grisham, Editors. 1991, CRC Press: Boston. 83-104.
5. M. B. Grisham, M. M. Jefferson, D. F. Melton, and E. L. Thomas, *Chlorination of endogenous amines by isolated neutrophils. Ammonia-dependent bactericidal, cytotoxic, and cytolytic activities of the chloramines.* J. Biol. Chem., 1984 **259** (16) 10404-10413.
6. K. Fukuda, Y. Hirai, H. Yoshida, T. Nakajima, and T. Usui, *Free amino acid content of lymphocytes and granulocytes compared.* Clin. Chem., 1982 **28** (8) 1758-1761.
7. E. L. Thomas, *Myeloperoxidase-hydrogen peroxide-chloride antimicrobial system: effect of exogenous amines on antibacterial action against Escherichia coli.* Infect. Immun., 1979 **25** (1) 110-116.
8. E. L. Thomas, M. B. Grisham, D. F. Melton, and M. M. Jefferson, *Evidence for a role of taurine in the in vitro oxidative*

toxicity of neutrophils toward erythrocytes. J. Biol. Chem., 1985 **260** (6) 3321-3329.

9. L. K. Folkes, L. P. Candeias, and P. Wardman, *Kinetics and mechanisms of hypochlorous acid reactions.* Arch. Biochem. Biophys., 1995 **323** (1) 120-126.
10. L. A. Marquez and H. B. Dunford, *Chlorination of taurine by myeloperoxidase. Kinetic evidence for an enzyme-bound intermediate.* J. Biol. Chem., 1994 **269** (11) 7950-7956.
11. D. W. Margerum, E. T. Gray, and R. P. Huffman, *Chlorination and formation of N-chloro compounds in water treatment*, in *Organometals and organometalloids: occurrence and fate in the environment*, F. E. Brinckman and J. M. Bellama, Editors. 1978, American Chemical Society: Washington, DC. 278-291.
12. J. C. Morris, *Kinetics of reactions between aqueous chlorine and nitrogen compounds*, in *Principles and applications of water chemistry*, S. D. Faust and J. V. Hunter, Editors. 1967, John Wiley & Sons, Inc.: New York. 23-53.
13. H. B. Dunford and L. A. Marquez-Curtis, *Myeloperoxidase: kinetic evidence for formation of enzyme-bound chlorinating intermediate.* Methods Enzymol., 2002 **354** (Part F) 338-350.
14. B. G. J. M. Bolscher and R. Wever, *A kinetic study of the reaction between human myeloperoxidase, hydroperoxides and cyanide. Inhibition by chloride and thiocyanate.* Biochim. Biophys. Acta, 1984 **788** (1) 1-10.
15. L. A. Marquez, J. T. Huang, and H. B. Dunford, *Spectral and kinetic studies on the formation of myeloperoxidase compounds I and II: roles of hydrogen peroxide and superoxide.* Biochemistry, 1994 **33** (6) 1447-1454.
16. A. R. J. Bakkenist, J. E. G. De Boer, H. Plat, and R. Wever, *The halide complexes of myeloperoxidase and the mechanism of the halogenation reactions.* Biochim. Biophys. Acta, 1980 **613** (2) 337-348.
17. P. C. Andrews and N. I. Krinsky, *A kinetic analysis of the interaction of human myeloperoxidase with hydrogen peroxide, chloride ions, and protons.* J. Biol. Chem., 1982 **257** (22) 13240-13245.
18. M. Ikeda-Saito, *Spectroscopic, ligand binding, and enzymatic properties of the spleen green hemeprotein. A comparison with myeloperoxidase.* J. Biol. Chem., 1985 **260** (21) 11688-11696.
19. P. G. Furtmüller, U. Burner, and C. Obinger, *Reaction of myeloperoxidase compound I with chloride, bromide, iodide, and thiocyanate.* Biochemistry, 1998 **37** (51) 17923-17930.
20. A. J. Kettle and C. C. Winterbourn, *A kinetic analysis of the catalase activity of myeloperoxidase.* Biochemistry, 2001 **40** (34) 10204-10212.
21. D. P. Nelson and L. A. Kiesow, *Enthalpy of decomposition of hydrogen peroxide by catalase at 25 °C (with molar extinction coefficients of H_2O_2 solutions in the UV).* Anal. Biochem., 1972 **49** (2) 474-478.
22. T. Odajima and I. Yamazaki, *Myeloperoxidase of the leukocyte of normal blood. I. Reaction of myeloperoxidase with hydrogen peroxide.* Biochim. Biophys. Acta, 1970 **206** (1) 71-77.
23. D. N. Baron and S. A. Ahmed, *Intracellular concentrations of water and of the principal electrolytes determined by analysis of isolated human leucocytes.* Clin. Sci., 1969 **37** (1) 205-219.
24. M. Ikeda-Saito, Y. Dou, T. Yonetani, J. S. Olson, T. Li, R. Regan, and Q. H. Gibson, *Ligand diffusion in the distal heme pocket of myoglobin. A primary determinant of geminate rebinding.* J. Biol. Chem., 1993 **268** (10) 6855-6857.
25. P. G. Furtmüller, C. Obinger, Y. Hsuanyu, and H. B. Dunford, *Mechanism of reaction of myeloperoxidase with hydrogen peroxide and chloride ion.* Eur. J. Biochem., 2000 **267** (19) 5858-5864.
26. H. C. Lee, K. S. Booth, W. S. Caughey, and M. Ikeda-Saito, *Interaction of halides with the cyanide complex of myeloperoxidase: a model for substrate binding to compound I.* Biochim. Biophys. Acta, 1991 **1076** (2) 317-320.
27. M. Blair-Johnson, T. Fiedler, and R. Fenna, *Human myeloperoxidase: structure of a cyanide complex and its interaction with bromide and thiocyanate substrates at 1.9 Å resolution.* Biochemistry, 2001 **40** (46) 13990-13997.
28. M. Ikeda-Saito, H. C. Lee, K. Adachi, H. S. Eck, R. C. Prince, K. S. Booth, W. S. Caughey, and S. Kimura, *Demonstration*

that spleen green hemeprotein is identical to granulocyte myeloperoxidase. J. Biol. Chem., 1989 **264** (8) 4559-4563.

29. P. G. Furtmüller, U. Burner, W. Jantschko, G. Regelsberger, and C. Obinger, *The reactivity of myeloperoxidase compound I formed with hypochlorous acid.* Redox Report, 2000 **5** (4) 173-178.
30. J. A. Santaballa, H. Maskill, and M. Canle L., *The relationship between mechanism and rate law*, in *Investigation of organic reactions and their mechanisms*, H. Maskill, Editor. 2006, Blackwell Publishing: Singapore. 79-103.
31. H. A. Wagenknecht and W. D. Woggon, *Identification of intermediates in the catalytic cycle of chloroperoxidase.* Chem. Biol., 1997 **4** (5) 367-372.
32. J. C. Morris, *The acid ionization constant of HOCl from 5 to 35°.* J. Phys. Chem., 1966 **70** (12) 3798-3805.
33. T. J. Fiedler, C. A. Davey, and R. E. Fenna, *X-ray crystal structure and characterization of halide-binding sites of human myeloperoxidase at 1.8 Å resolution.* J. Biol. Chem., 2000 **275** (16) 11964-11971.
34. C. C. Winterbourn, M. B. Hampton, J. H. Livesey, and A. J. Kettle, *Modeling the reactions of superoxide and myeloperoxidase in the neutrophil phagosome. Implications for microbial killing.* J. Biol. Chem., 2006 **281** (52) 39860-39869.
35. A. J. Kettle and C. C. Winterbourn, *Superoxide modulates the activity of myeloperoxidase and optimizes the production of hypochlorous acid.* Biochem. J., 1988 **252** (2) 529-536.
36. I. I. Vlasova, J. Arnhold, A. N. Osipov, and O. M. Panasenko, *pH-dependent regulation of myeloperoxidase activity.* Biochem.-Moscow, 2006 **71** (6) 667-677.
37. H. Spalteholtz, O. M. Panasenko, and J. Arnhold, *Formation of reactive halide species by myeloperoxidase and eosinophyl peroxidase.* Arch. Biochem. Biophys., 2006 **445** (2) 225-234.

CHAPTER 9

Myeloperoxidase-catalyzed chlorination: The quest for the active species

Experiments are the only means of knowledge at our disposal. The rest is poetry, imagination.

Max Planck

9.1 Introduction

The primary function of neutrophils is the phagocytosis and destruction of microorganisms.[1] In 1967 Klebanoff for the first time reported that the system myeloperoxidase (MPO) with hydrogen peroxide and iodide, bromide, chloride, or thiocyanate ions can form a powerful antimicrobial system in neutrophils.[2] Of particular interest was the observation that chloride, at physiological concentrations, could meet the halide requirement of the MPO-dependent antimicrobial system.[2] Today, the principal reaction catalyzed by MPO is thought to be the oxidation of Cl^- by H_2O_2 to yield the highly-reactive oxidizing and chlorinating agent HClO.[1] Under physiological conditions besides chloride, thiocyanate and bromide function as electron donors of MPO.[3, 4]

The so-called chlorination cycle of MPO includes H_2O_2-mediated oxidation of ferric MPO to compound I (MPO-I) followed by MPO-I reduction directly to ferric MPO thereby releasing HClO.[5] The latter, with a pK_a of 7.54 in water,[6] exists as a mixture of the undissociated acid and the hypochlorite ion at physiological pH levels. As the pH is lowered HClO predominates, and it can react with excess chloride to form molecular chlorine (Cl_2). Indeed, in one of the first reports about the halogenation activity of MPO, either HClO or Cl_2 were assumed as chlorinating compounds.[7] Both are very reactive towards chlorination and oxidation, and can be converted into each other changing the acidity of the medium, HClO being the dominant species under mild acidic and neutral conditions.[8] These MPO products attack the microorganisms at a variety of chemical targets, *e.g.* sulfhydryl groups, iron-sulfur centres, sulfur-ether groups, unsaturated fatty acids.[9] In addition, HClO reacts with nitrogen-containing compounds to form nitrogen-chlorine derivatives such as monochloramines and dichloramine[10] that retain oxidizing activity. Taurine (Tau, 2-aminoethane-sulfonic acid) is present at high concentration in neutrophil cytoplasm,[11] and reacts with HClO to form taurine chloramine (*N*-Cl Tau), which is less toxic than HClO. This reaction has thus been implicated as a mechanism by which neutrophils are protected from HClO released into the cytoplasm.

Some data in the literature have been accumulated against the assumption about the formation of free HClO by MPO. Chlorination of Tau by MPO has been studied by Marquez and Dunford at pH 4.7.[12, 13] Their proposal implies that the *in vivo* chlorination mediated by MPO may involve an enzyme intermediate species rather than free HClO. According to these authors, Cl^- binds to MPO-I producing a new enzymatic complex, MPO-I-Cl, which acts as halogenating agent.[12, 13] Similarly, the chlorination of monochlorodimedone by chloroperoxidase was demonstrated to occur by an enzyme-bound HClO.[14]

Recently, we have extended the study of Marquez and Dunford[12] by following initial and equilibrium rate of formation of *N*-Cl Tau by MPO at pH 4.0 - 7.0 in order to investigate the viability of several possible chlorination mechanisms.[15] In our model we considered also known side-reactions of system MPO/H_2O_2/Cl^-/Tau (Table 9.1). In detail the model included formation of MPO-I, which has been described to be slightly reversible (Reaction 1),[16, 17] and its direct reaction back to the ferric enzyme (Reaction 2a). It has been demonstrated that ClO^-/HClO can oxidize also Fe(III)-MPO to MPO-I similar to the H_2O_2 mediated reaction,[18] thus the reversibility of Reaction 2a (Reaction –2a) was taken into account. According to the proposal by Marquez and Dunford,[12, 13] Cl^- forms with MPO-I a new enzymatic complex, MPO-I-Cl, (Reaction 2b), which could be also reversible (Reaction –2b). Moreover, both Fe(III)-MPO and MPO-I participate in protonation reactions (Reactions 4 and 5). Additionally, protonated native MPO can bind Cl^- forming a high-spin complex (MPO-H-Cl, Reaction 6); the corresponding binding constant has been accurately measured as a function of pH.[19, 20] Very important is the role of H_2O_2 as one-electron donor reducing MPO-I to MPO-II, which forms a complex with hydroperoxyl radical ($HO_2^{\cdot}$), MPO-II-HO_2 (Reaction 7). Formation of this species has been proposed for explaining the experimentally obtained Tau-chlorination kinetic data, and is supported by the fact that free released $HO_2^{\cdot}$ has not been observed under the working conditions.[15] MPO-II (or MPO-II-HO_2) is outside the halogenation cycle. The rate constant for the reduction of MPO-I to MPO-II by H_2O_2 was reported to be $8.2 \times 10^4\ M^{-1}{\cdot}s^{-1}$ at pH 7.0,[16, 17] so this reaction is competitive with MPO-I reduction by Cl^- at neutral pH values.[21] Moreover, formation of Fe(III)-MPO from MPO-II-HO_2 (Reaction 8) has been also considered in the mechanism, which is supported by the (pseudo-)catalase activity of MPO[22] that could include the cycle Fe(III)-MPO/MPO-

I/MPO-II with overall consumption of two molecules of H_2O_2, as well as by the reactivity of superoxide with MPO.[23]

Table 9.1. Proposed mechanism of MPO-catalyzed chlorination of amino compounds.

Reaction	No.
$\mathrm{MPO} + \mathrm{H_2O_2} \underset{\leftarrow}{\overset{K_1}{\rightarrow}} \mathrm{MPO\text{-}I} + \mathrm{H_2O}$	1
$\mathrm{MPO\text{-}I} + \mathrm{Cl^-} \underset{k_{-2a}}{\overset{k_{2a}}{\rightleftarrows}} \mathrm{MPO} + \mathrm{ClO^-}$	2a, –2a
$\mathrm{MPO\text{-}I} + \mathrm{Cl^-} \underset{k_{-2b}}{\overset{k_{2b}}{\rightleftarrows}} \mathrm{MPO\text{-}I\text{-}Cl}$	2b, –2b
$\mathrm{ClO^-} + \text{Pro-Gly-Gly} + \mathrm{H^+} \xrightarrow{k_{3a}} N\text{-Cl Pro-Gly-Gly} + \mathrm{H_2O}$	3a
$\mathrm{MPO\text{-}I\text{-}Cl} + \text{Pro-Gly-Gly} + \mathrm{H^+} \xrightarrow{k_{3b}} N\text{-Cl Pro-Gly-Gly} + \mathrm{MPO} + \mathrm{H_2O}$	3b
$\mathrm{MPO} + \mathrm{H^+} \underset{\leftarrow}{\overset{K_4}{\rightarrow}} \mathrm{MPO\text{-}H}$	4
$\mathrm{MPO\text{-}I} + \mathrm{H^+} \underset{\leftarrow}{\overset{K_5}{\rightarrow}} \mathrm{MPO\text{-}I\text{-}H}$	5
$\mathrm{MPO\text{-}H} + \mathrm{Cl^-} \underset{\leftarrow}{\overset{K_6}{\rightarrow}} \mathrm{MPO\text{-}H\text{-}Cl}$	6
$\mathrm{MPO\text{-}I} + \mathrm{H_2O_2} \underset{\leftarrow}{\overset{K_7}{\rightarrow}} \mathrm{MPO\text{-}II\text{-}HO_2} + \mathrm{H^+}$	7
$\mathrm{MPO\text{-}II\text{-}HO_2} + \mathrm{H^+} \xrightarrow{k_8} \mathrm{MPO} + \mathrm{H_2O} + \mathrm{O_2}$	8

The obtained kinetic data on Tau chlorination (Chapter 8) demonstrated the importance of Reaction 7 in deceleration of *N*-Cl Tau formation at equilibrium phase, and ruled out a proton participating in the direct reaction between MPO-I and Cl^-. Those findings support the formation of a chlorinating MPO-I-Cl complex and/or of ClO^- stabilized in the inner protein core of MPO.[24] The latter could be formed from MPO-I-Cl or independently of it. Thus, enzymatic chlorination of Tau occurs by either free unprotonated hypochlorite ion (ClO^-), which undergoes fast protonation to the more reactive form HClO (Reaction 3a), or by the MPO-I-Cl complex (Reaction 3b). Our kinetic results did not allow discrimination among these pathways that differ on the nature of the actual chlorinating agent(s), ClO^-/HClO and/or MPO-I-Cl; for both pathways the mechanism rate equations are identical, but the meaning of the calculated rate constants.[25]

If MPO-I-Cl is the chlorinating agent, then substrates must have access to the distal heme cavity. Thus, following the kinetic analysis of MPO-catalyzed chlorination of Tau (Chapter 8) the study has been extended to another substrate, the tripeptide L-prolylglycylglycine (Pro-Gly-Gly). While Tau is a relatively small substrate (M_r = 125.15, 14 atoms), Pro-Gly-Gly is bulkier (M_r = 229.2, 31 atoms), therefore, a decrease in the reaction rate due to the steric hindrance of the tripeptide should be expected if chlorination involves the MPO-I-Cl complex. The halogenated product of Pro-Gly-Gly is relatively stable, and its slow decomposition will not interfere the kinetic measurements. This is in contrast to *N*-halo dipeptides with Gly as the *N*-terminal residue or with a tertiary amide, *i.e.*, substituted peptidic nitrogen, that cause acceleration of their decomposition.[26] Moreover, Pro-Gly-Gly does not contain any other functional group susceptible of chlorination but the terminal amine, and exhibits a high reaction rate in the process of HClO-mediated chlorination, superior to the reaction with Tau.

Here, we investigate MPO-mediated chlorination of the tripeptide Pro-Gly-Gly. Plausibility of the mechanism previously

validated for the MPO-catalyzed chlorination of Tau was again tested in a pH range (pH 4.0 - 6.0) that comprises the actual conditions during phagocytosis and MPO activity *in vivo*.

9.2 Experimental procedures

9.2.1 Materials

Stock solutions of 70 mM Pro-Gly-Gly (Sigma), 70 mM Tau (Fluka Microselect, ≥ 99.5%), 2.5 M NaCl (Sigma Ultra, min. 99.5%), and 18 mM H_2O_2 (Sigma-Aldrich) were prepared daily and kept in the dark at 4 °C. Concentration of HClO, freshly prepared as described elsewhere,[27] and H_2O_2 was determined spectrophotometrically using ε_{292} = 350 $M^{-1}\cdot cm^{-1}$[6] and ε_{240} = 39.4 $M^{-1}\cdot cm^{-1}$,[28] respectively. Citric acid (Sigma, anhydrous)/Na_2HPO_4 (Sigma, ACS reagent) buffer 0.5 M was used to control pH in the range 4.0 - 6.0. The study was not extended to pH values over 6.0, as results with Tau proved the kinetics were too fast to be followed (Chapter 8). Highly purified MPO of a purity index (A_{430} / A_{280}) of at least 0.85 was obtained from Planta Natural Products (http://www.planta.at). Its actual concentration was determined spectrophotometrically by using ε_{430} = 91,000 $M^{-1}\cdot cm^{-1}\cdot heme^{-1}$.[29]

9.2.2 Methods

HClO-mediated chlorination reactions in absence of enzyme were studied following the increase of the UV bands of the *N*-Cl amines (λ_{max} (Pro-Gly-Gly) = 259 nm, λ_{max} (Tau) = 252 nm) at 25.0 ± 0.1 °C. A double-beam Varian® Cary 1E spectrophotometer and a Hi-Tech Scientific® SF-61 stopped-flow spectrophotometer were used for recording spectra and time-resolved traces, respectively.

Based on both the published *in vivo* concentrations[1, 30] and/or previous Tau-chlorination studies,[12, 15] the typical enzyme-catalyzed chlorination assays contained 100 mM Cl^-, 10 mM Pro-Gly-Gly, and 100 nM MPO. Temperature and pH were set at 25.0 °C and 4.0 - 6.0, respectively. H_2O_2 was varied from 0.2 to 2.0 mM. The impact of [Pro-Gly-Gly] on the rate of the MPO-catalyzed reaction was tested in the range 5 - 15 mM.

Samples were prepared immediately before use by mixing solution 1, containing Pro-Gly-Gly and MPO, with solution 2, containing NaCl and H_2O_2 in 200 mM phosphate/citrate buffer (pH 4.0 - 6.0), by using the conventional mixing stopped-flow technique (Applied Photophysics® SX-18MV stopped-flow spectrophotometer equipped with a diode array detector). Single-mixing unit syringes were filled up with both sample solutions and, after thermostating at 25.0 ± 0.1 °C, a total of 100 μL were shot for each run. Reactions were studied both at the whole wavelength range as well as at 270.6 nm, which corresponds to the isosbestic point of the decomposition process of *N*-Cl Pro-Gly-Gly. Kinetic traces at this wavelength (Figure 9.1A) were followed until full consumption of H_2O_2, and led to re-formation of native MPO.

As accounted in the previous chapter, in the initial phase of the reaction (Figure 9.1B), absorbance increases at 270.6 nm, such part of the kinetic trace shows a curvature that could be fitted to a double exponential equation (Equation 1).

$$y = y_0 + A_1\cdot(1-e^{-x/t_1}) + A_2\cdot(1-e^{-x/t_2}) \quad (1)$$

This behaviour may arise from the fact that the rate is strongly dependent on both H_2O_2 and the actual MPO-II-HO_2 concentrations. By using Equation 1 any portion of the initial time traces can be fitted properly. Thus, the derivative of the resulting function just after reagents mixing allows the calculation of the initial rate (inset Figure 9.1B). Approximately 10 replicated runs were fitted, and the so obtained initial-rate values averaged. This procedure seems more precise than classical methods where the initial rate is obtained from the slope of the more or less short portion of the beginning of the trace; it implies uncertainties in the initial rate values, especially relevant for noisy traces. The approach used here reduces the scatter of kinetic data, and estimates the initial rate after mixing, *i.e.*, just at "zero time" (see Chapter 8).

Finally, a portion of the kinetic trace, after equilibrium has been achieved, was fitted (Figure 9.1C) using the same mathematical expression (Equation 1), its derivative yielding the equilibrium rate at a particular time (inset Figure 9.1C). The term equilibrium rate is used in the same sense that in the previous chapter. The change in absorbance (Δ*A*) observed

at this point allowed calculation of the amount of *N*-Cl Pro-Gly-Gly formed and, therefore, the remaining concentration of H_2O_2, since there is no noticeable loss of H_2O_2 through peroxidative processes.

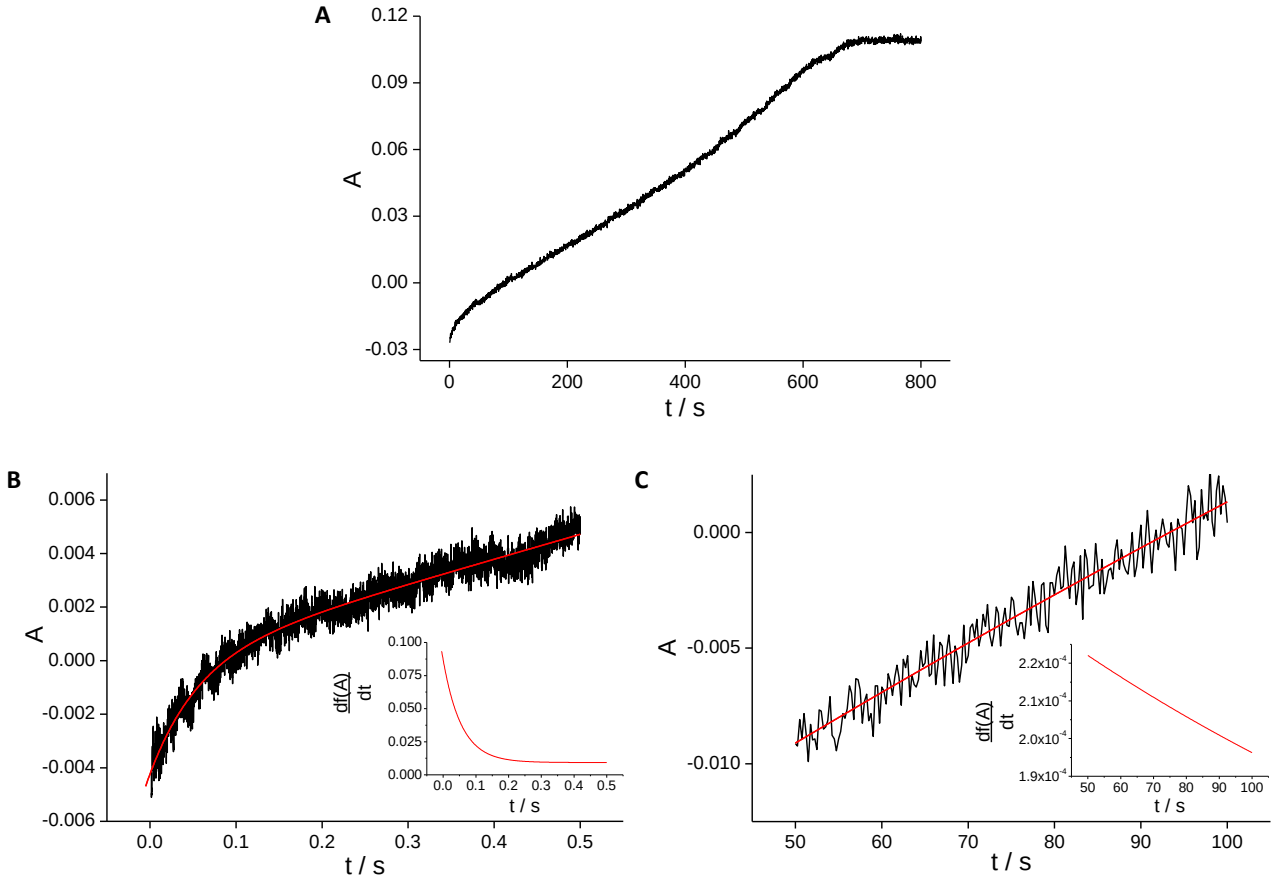

Figure 9.1. MPO-mediated chlorination of Pro-Gly-Gly. (A) Kinetic trace obtained in the stopped-flow spectrophotometer under the following conditions: λ = 270.6 nm, T = 25.0 °C, [MPO_0] = 100 nM, [Pro-Gly-Gly] = 10 mM, [Cl^-] = 100 mM, [H_2O_2] = 0.6 mM, pH (100 mM buffer) = 6.0. (B) Initial rate and fit. (C) Equilibrium rate and fit.

9.2.3 Computational details

Electronic structure calculations were carried out with the Gaussian03 suite of programs[31] in a Hewlett Packard® Integrity Superdome 128 cluster. Previous conformational analysis by using density functional theory at B3LYP computational level with the 3-21G basis set rendered the most stable conformers of both Tau and Pro-Gly-Gly. These structures were then fully optimized at the *ab initio* MP2 level using the 6-31++G** basis set. This computational level yields accurate geometries, very suitable for comparison purposes.

Isoelectric points of many amino acids lie about pH = 6 - 7, thus both substrates were considered to be zwitterions with 0 overall charge, *i.e.*, the carboxylate group negatively charged and the amino group protonated.

9.3 Results

The kinetics of *N*-Cl Pro-Gly-Gly formation, similar to Tau chlorination, exhibits a very complex behaviour (Figure 9.1A). Here, we followed the MPO-mediated formation of *N*-Cl Pro-Gly-Gly over the whole period of H_2O_2 consumption between pH 4.0 and pH 6.0, varying [H_2O_2] and [Pro-Gly-Gly]. Results are compared with the also obtained data studying the non-enzymatic chlorination of Tau and Pro-Gly-Gly by HClO, and with the previous data on the MPO-mediated formation of *N*-

Cl Tau (Chapter 8).

9.3.1 HClO-mediated chlorination in the absence of the enzyme

UV-Vis spectra were obtained for both the HClO-mediated chlorination reaction of Pro-Gly-Gly (Figure 9.2A) and the subsequent decomposition reaction (Figure 9.2B). Under used working conditions, chlorination process finishes in just approximately 4 s, while the much slower decomposition reaction needs hours to completion. *N*-Cl Pro-Gly-Gly shows an UV band with maximum at λ = 259 nm. The decomposition of the chlorinated compound must be described as an elimination reaction[26] yielding chloride ion and a Schiff base, which in turn rapidly hydrolyzes in solvent water to the parent amine and carbonyl compounds.[32] This process presents a prominent band at λ = 238 nm, which could be affected by the solvent cutoff, corresponding to the decomposition product, and an isosbestic point at λ = 270.6 nm. At this latter wavelength the absorbance of *N*-Cl Pro-Gly-Gly, although lower than at λ = 259 nm (approx. –12%), is significant and suitable to study spectrophotometrically the title reaction following the increase of the UV band without any interference from subsequent decomposition processes.

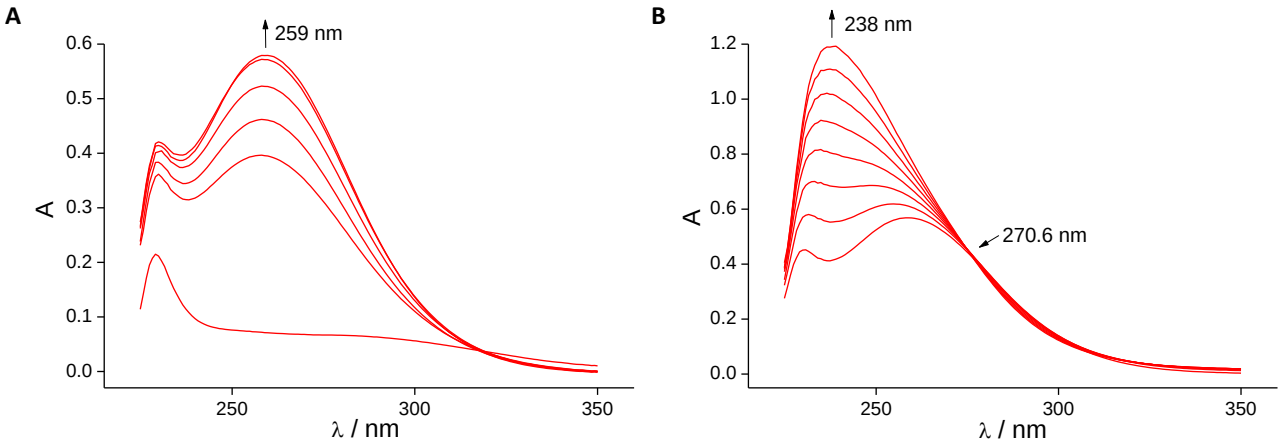

Figure 9.2. Time-resolved UV-Vis spectra for: (A) the reaction between Pro-Gly-Gly and HClO under the following conditions: T = 25.0 °C, [Pro-Gly-Gly] = 2.0 mM, [HClO] = 2.0 mM, pH (100 mM buffer) = 5.0, I = 500 mM ([NaCl] = 400mM). An identical solution, apart from the loss of HClO, was used as blank. First spectrum measured immediately after addition of HClO, subsequent spectra every 1 s. Maximum in absorbance of *N*-Cl Pro-Gly-Gly is indicated at λ = 259 nm. (B) The decomposition reaction of *N*-Cl Pro-Gly-Gly under same reaction conditions. First spectrum measured after full formation of the *N*-Cl compound, subsequent spectra every 600s. Maximum absorbance observed for this process at λ = 238 nm; isosbestic point indicated at λ = 270.6 nm.

Kinetics of HClO-mediated chlorination of Tau and Pro-Gly-Gly in the absence of MPO were measured for pH 4.0 - 6.0. The observed rate equation being first order on both the concentration of HClO and amino compound, and the influence of acidity described by Equation 2. The corresponding data are depicted in Figure 9.3.

$$k_{\mathrm{obs}} = \frac{a}{b + [\mathrm{H^+}]} \tag{2}$$

Under the working conditions, both chlorination rate and observed rate constants were always higher for Pro-Gly-Gly. The mechanism of this reaction has been previously proposed.[32]

9.3.2 MPO-mediated chlorination. Initial rate study

The dependence of the initial rate of MPO-catalyzed chlorination of Pro-Gly-Gly (v_0) on [H_2O_2], [Pro-Gly-Gly] and pH was investigated. Within the used concentration range (5 - 15 mM), initial rate of MPO-mediated Pro-Gly-Gly chlorination is statistically independent of [Pro-Gly-Gly] as shown in Figure 9.4. Initial rate of Pro-Gly-Gly chlorination increased upon raising pH from 4.0 to 6.0. Data pairs of initial rate *vs*. [H_2O_2] obtained for the five pH values arrange in straight lines (Figure

9.5A). Weighted linear regressions were carried out by using error values as weight, the corresponding error bars are not shown for the sake of clarity. Figure 9.5A unequivocally demonstrates that saturation of the active site is never reached under the assay conditions (*i.e.*: $[H_2O_2] \geq 2000$ [MPO]). At this initial stage of *N*-Cl Pro-Gly-Gly formation, MPO-II, or better MPO-II-HO_2, does not participate in the enzyme turnover. This is valid based on the published kinetic data of MPO-I reduction.[16-18] It is well known that at pH 7 MPO-I reduction by Cl^- to Fe(III)-MPO and by H_2O_2 to MPO-II-HO_2 occur at similar rates and that, in contrast to H_2O_2 mediated reaction, halide oxidation becomes significantly faster with decreasing pH. Moreover, in the different assays [Cl^-] was at least 50 fold that of H_2O_2. As shown in the inset to Figure 9.5A the Soret band appears at 430 nm, which is typical for MPO in its Fe(III) and MPO-I forms. Thus, in the mechanism only Reactions 1 - 6 have to be considered, the result being the mechanism rate equation shown in Table 9.2 (corresponding to Equation 18A of the Appendix in Section 9.6).

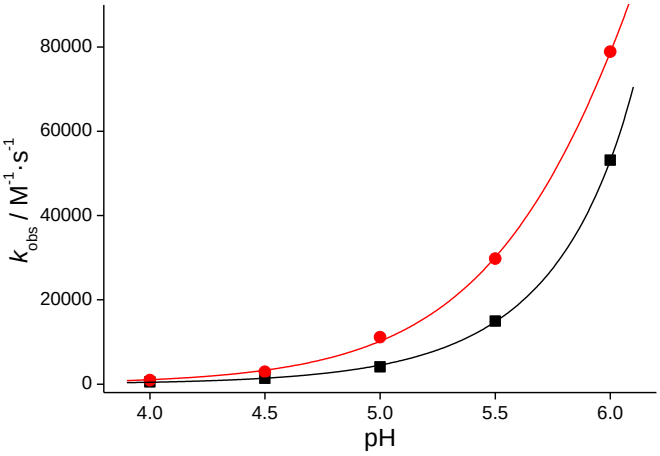

Figure 9.3. Second-order kinetic constant for the HClO-chlorination of Tau (■) and Pro-Gly-Gly (●) *vs*. pH at 25.0 °C and I = 500 mM ([NaCl] = 400 mM). Solid lines correspond to the fitting using Equation 2.

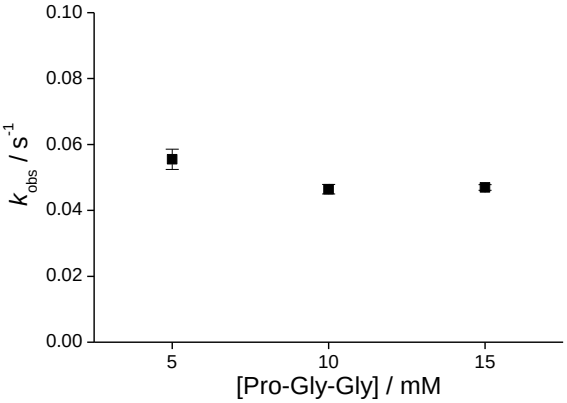

Figure 9.4. Observed kinetic constant (k_{obs}) for the MPO-mediated chlorination of Pro-Gly-Gly *vs*. [Pro-Gly-Gly] measured with initial rates. λ = 270.6 nm, T = 25.0 °C, [MPO_0] = 100 nM, [Pro-Gly-Gly] = 5 - 15 mM, [Cl^-] = 100 mM, [H_2O_2] = 0.2 - 2.0 mM, pH (100 mM buffer) = 5.0.

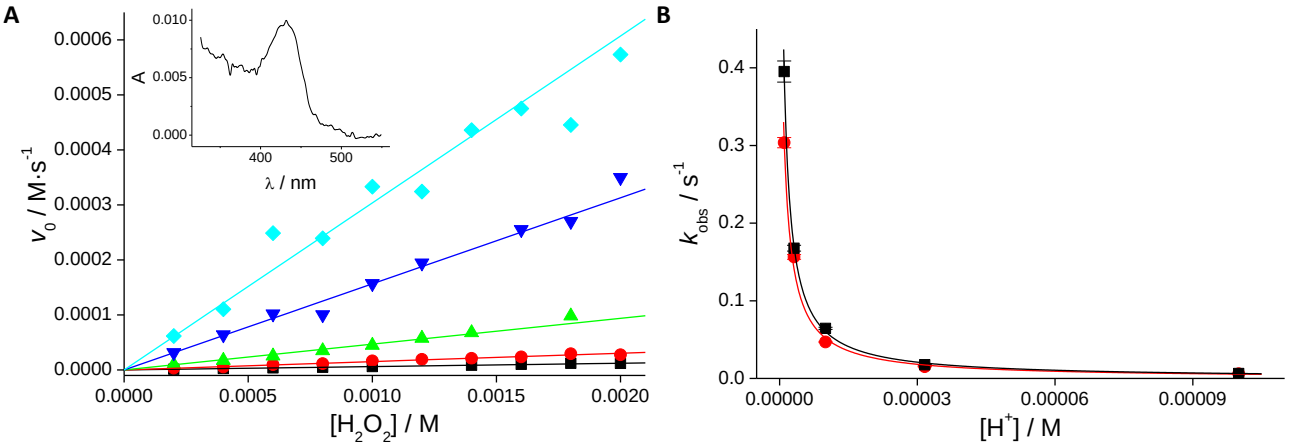

Figure 9.5. MPO-mediated chlorination (A) Initial rate *vs*. [H_2O_2]. λ = 270.6 nm, T = 25.0 °C, [MPO_0] = 100 nM, [Pro-Gly-Gly] = 10 mM, [Cl^-] = 100 mM, [H_2O_2] = 0.2 - 2.0 mM, pH (100 mM buffer) = 4.0 (■), 4.5 (●), 5.0 (▲), 5.5 (▼), and 6.0 (♦). Inset: UV-Vis spectrum obtained at this phase of the reaction showing the Soret band. (B) Observed kinetic constant (k_{obs}) for the MPO-mediated chlorination of Tau (■) and Pro-Gly-Gly (●) *vs*. [H^+]. Reaction conditions are the same as in (A), solid lines calculated using Equation 2.

Table 9.2. Mechanism rate equations and their dependence on pH.

Phase	Rate equation	Acidity dependence
Initial	$v_0 = \frac{k_2 \cdot K_1 [MPO_0] \cdot [H_2O_2] \cdot [Cl^-]}{1 + K_4 [H^+] \cdot (1 + K_6 [Cl^-])}$	$k_{obs} = \frac{v_0}{[H_2O_2]} = \frac{a}{b + [H^+]}$
Equilibrium	$v_{eq} = \frac{k_2 \cdot [MPO_0] \cdot [Cl^-]}{\frac{1 + K_4 [H^+] \cdot (1 + K_6 [Cl^-])}{K_1 \cdot [H_2O_2]} + 1 + K_5 [H^+] + \frac{K_7' \cdot [H_2O_2]}{[H^+]}}$	$v_{eq} = \frac{1}{\frac{a}{[H_2O_2]} + b + c \cdot [H_2O_2]}$ $a \text{ (and } b) = a' + b' \cdot [H^+]$ $c = \frac{a''}{[H^+]}$

$k_2 = k_{2a} + k_{2b}$

Table 9.3. Observed first-order kinetic constants (k_{obs}) obtained from initial rates in the MPO-mediated chlorination of Pro-Gly-Gly and Tau. λ = 270.6 nm (Pro-Gly-Gly) / λ = 252 nm (Tau), T = 25.0 °C, [MPO_0] = 100 nM, [substrate] = 10 mM, [Cl^-] = 100 mM, [H_2O_2] = 0.2 - 2.0 mM, pH (100 mM buffer) = 4.0 - 6.0.

pH	$k_{obs\ (Pro\text{-}Gly\text{-}Gly)} \times 10^2$ (s^{-1})	$k_{obs\ (Tau)} \times 10^2$ (s^{-1})
4.0	0.608 ± 0.006	0.632 ± 0.012
4.5	1.52 ± 0.04	1.76 ± 0.05
5.0	4.69 ± 0.08	6.45 ± 0.14
5.5	15.7 ± 0.4	16.8 ± 0.4
6.0	30.4 ± 0.7	39.5 ± 1.4
	Average difference: 19%	

The dependence of the initial rate of Pro-Gly-Gly chlorination on pH can be better illustrated by plotting the slopes calculated from Figure 9.5A (k_{obs}) *vs*. pH (Figure 9.5B). Data obtained for Tau chlorination under same conditions are also shown. This pseudoconstant is independent of [H_2O_2], and its meaning becomes apparent by considering the initial rate

equation derived from the mechanism (Equation 18A and Table 9.2). Thus, Equation 2 properly fits to the experimental data (Figure 9.5B). On the other hand, the evaluation of the initial rate values for both Pro-Gly-Gly and Tau reveals that the process is always faster, 20% as average, for Tau (Table 9.3).

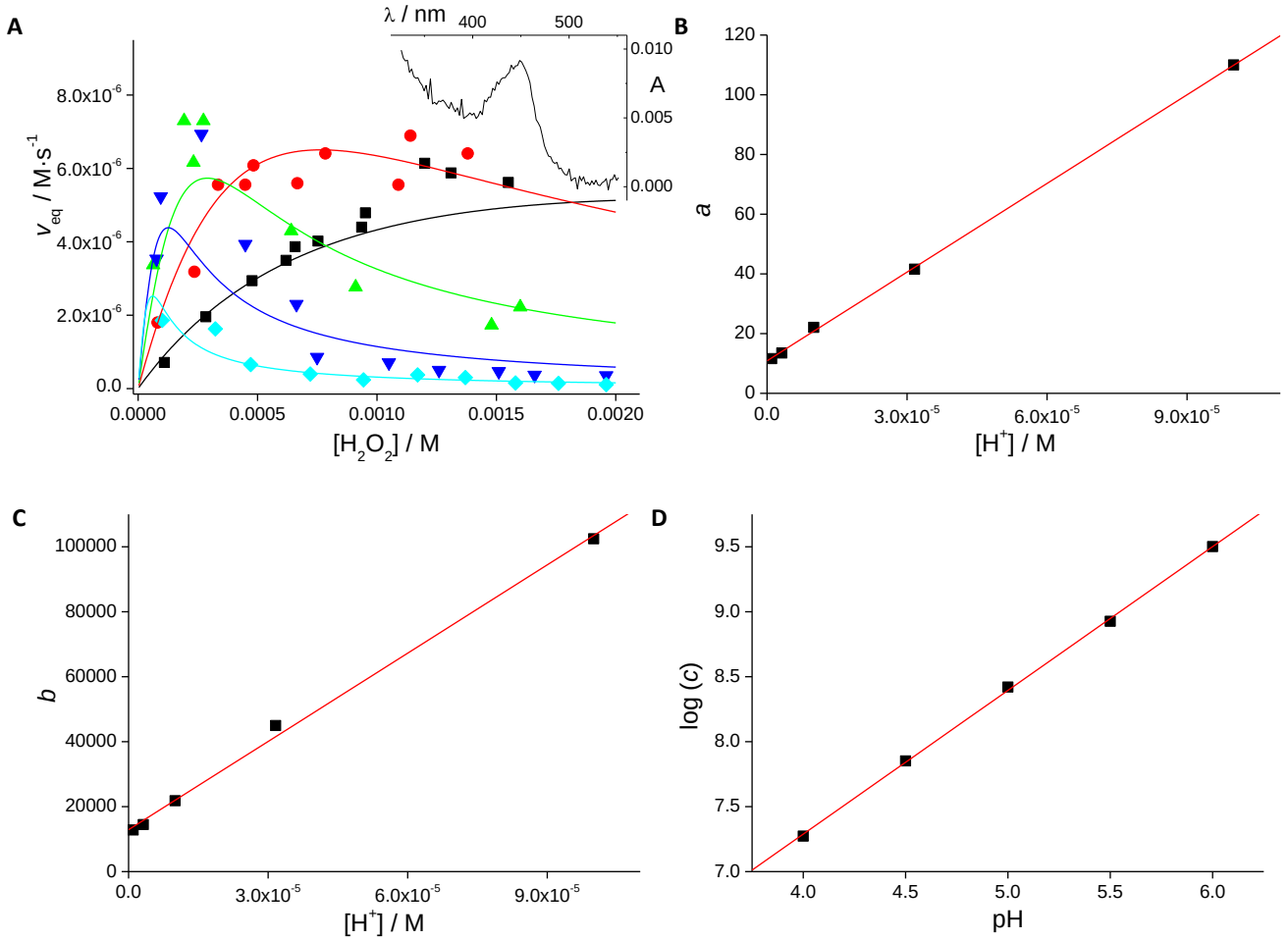

Figure 9.6. MPO-mediated chlorination of Pro-Gly-Gly. (A) Rate at equilibrium *vs*. [H_2O_2]. λ = 270.6 nm, T = 25.0 °C, [MPO_0] = 100 nM, [Pro-Gly-Gly] = 10 mM, [Cl^-] = 100 mM, [H_2O_2] = 0.2 - 2.0 mM, pH (100 mM buffer) = 4.0 (■), 4.5 (●), 5.0 (▲), 5.5 (▼), and 6.0 (♦). Inset: UV-Vis spectrum obtained at this phase of the reaction showing the Soret band. (B) Parameter *a vs*. [H^+]. (C) Parameter *b vs*. [H^+]. (D) log (*c*) *vs*. pH (slope = 1.11 ± 0.02).

9.3.3 MPO-mediated chlorination. Equilibrium rate study

Rates of Pro-Gly-Gly chlorination measured at equilibrium (v_{eq}) show a fully different profile when plotted against [H_2O_2] (Figure 9.6A). After an initial rise the curves bend down with increasing [H_2O_2], this effect being more significant at higher pH. Chlorination rates for pH ≥ 5.5 and [H_2O_2] ≥ 0.75 mM were very slow, indicating that a considerable fraction of MPO is outside the chlorination cycle, the latter including only Fe(III)-MPO and MPO-I. Looking at the dominating enzyme redox intermediate at this stage of H_2O_2 consumption, it clearly showed that the enzyme gathered as MPO-II-HO_2, which has its Soret maximum at 456 nm (inset to Figure 9.6A) and a prominent band at 625 nm (not shown). Thus, at equilibrium, *i.e.*, after passing through many chlorination cycles in the initial phase, Reactions 7 and 8 (Table 9.1) became relevant, and need to be considered in the mechanism, the result being the rate equation 23A (also shown in Table 9.2), which takes the form of Equation 3 in terms of [H_2O_2]. These sets of data were fitted iteratively (Figures 9.6A-D), so that *a*- and *b*-values fit to a

straight-line with respect to [H$^+$] (Equation 4) (Figures 9.6B and 9.6C), whereas *c*-values *vs*. [H$^+$] fit to Equation 5 (Figure 9.6D). The effect of [H$^+$] on *a*, *b*, and *c* parameters has been worked out from the expression of the mechanism equation rate at equilibrium (Table 9.2).

$$v_{\mathrm{eq}} = \frac{1}{\frac{a}{[\mathrm{H_2O_2}]} + b + c \cdot [\mathrm{H_2O_2}]} \tag{3}$$

$$a\ (\text{and}\ b) = a' + b' \cdot [\mathrm{H^+}] \tag{4}$$

$$c = \frac{a''}{[\mathrm{H^+}]} \tag{5}$$

Curvature of the kinetic traces is due to the partial inactivation of the chlorination activity by accumulation of MPO-II-HO_2 at equilibrium. Once the dynamic equilibrium is achieved, the chlorination process proceeded very slowly since the concentration of active compounds (MPO and MPO-I) was reduced to a small percentage of the total enzyme. Along the central portion of the kinetic trace the enzyme still cycled consuming H_2O_2 and chlorinating Pro-Gly-Gly, while [MPO-II-HO_2] decreased according to H_2O_2 consumption. Building up of Fe(III)-MPO was again observed upon depletion of H_2O_2. These findings show that the decrease in the chlorination rate under equilibrium conditions with respect to initial rates can be ascribed to MPO-II-HO_2 accumulation, as in previous chapter.

From the experimental data (Figures 9.6C and 9.6D) K_7' (= k_7 / (k_{-7} + k_8)) could be calculated to be 0.20 $\pm$ 0.08 M. Also, data from Figures 9.5B and 9.6C yielded a value for K_1 ((1.3 $\pm$ 0.3) $\times$ 10^4 M^{-1}) similar to the value calculated in a different manner from Figures 9.5B, 9.6B and 9.6C ((2.1 $\pm$ 0.4) $\times$ 10^4 M^{-1}), which might reflect the high reduction potential of the redox couple MPO-I/MPO.[33] Besides, the fit shown in Figure 9.6C allowed the calculation of (k_{2a} + k_{2b}) to be (7.8 $\pm$ 0.8) $\times$ 10^3 M^{-1}·s^{-1}, which is very similar to MPO-I reduction rate at physiological [Cl$^-$].[18, 21] Additionally, the equilibrium constant of Reaction 5, K_5, was determined to be (7.1 $\pm$ 0.9) $\times$ 10^4 M^{-1}, which corresponds to a pK_a of MPO-I-H of 4.85. It has been demonstrated that the protonated form of MPO-I efficiently oxidizes halides.[21] At acidic pH values halides bind near a protonated site, which has to be very close to the ferryl oxygen since there is a halide-dependent change in the EPR spectrum at acidic pH.[34] The crystal structures of the MPO-bromide and MPO-cyanide-bromide complexes[35] suggest that the distal histidine upon protonation could interact with the ferryl oxygen and the bound halide. Published pK_a values are in the range 4.5 - 5.2,[19-21, 34] thus supporting the adequacy of the proposed mechanism.

Applying the published value (170 µM) for the dissociation constant of the MPO-H-Cl complex[16] together with the fitting constants of Figure 9.5B, K_4 was calculated to be (2.7 $\pm$ 0.2) $\times$ 10^3 M^{-1}; this corresponds to pK_a(MPO-H) = 3.44, which is close to the published value of 3.95.[20] All these values and other published data are summarized in Table 9.4.

Table 9.4. Kinetic and equilibrium constants in the MPO-mediated chlorination of Pro-Gly-Gly and Tau.

Parameter	Pro-Gly-Gly [a]	Tau [b]	Published values
K_1	(1.3 $\pm$ 0.3) $\times$ 10^4 M^{-1}	(8 $\pm$ 4) $\times$ 10^3 M^{-1}	3.1 $\times$ 10^5 M^{-1} [c]
	(2.1 $\pm$ 0.4) $\times$ 10^4 M^{-1}	(9 $\pm$ 4) $\times$ 10^3 M^{-1}	-
k_2	(7.8 $\pm$ 0.8) $\times$ 10^3 M^{-1}·s^{-1}	(1.6 $\pm$ 0.2) $\times$ 10^4 M^{-1}·s^{-1}	-
K_7'	0.20 $\pm$ 0.08 M	0.8 $\pm$ 0.1 M	-
pK_a (MPO-H)	3.44	3.53	3.95 [d]
pK_a (MPO-I-H)	4.85	5.16	4.5 - 5.2 [e]

[a] This work, [b] Chapter 8, [c] Ref. [17], [d] Ref. [20], [e] Refs. [5, 19, 21, 34]

9.3.4 Access to the active site

The active site of MPO is sterically hindered, since substrates must cross a narrow channel to reach the distal heme

cavity.[24, 35] Figure 9.7A depicts the entrance of the substrate channel at the protein surface; heme group can be recognized in the background. To reach the active centre all substrates must enter this opening that is about 15 Å at its maximum and 11 Å at its minimum length. The channel is funnel-shaped, and becomes narrower at the proximity of the active site. The four residues shown in Figure 9.7B form a bow over the heme group; this assembly represents the final access to the heme pocket, which is situated just behind. Relevant distances, either approximately longitudinal (9.27 Å) or perpendicular to the heme group (6.75 Å and 7.79 Å), are indicated. All distances were measured between nuclei of heavy atoms, that is, van der Waals radii and hydrogen atoms have not been considered. Therefore, effective distances are shorter. Computationally calculated structures of Pro-Gly-Gly and Tau are represented in Figures 9.7C and 9.7D, respectively. Dissimilar dimensions of the substrates are illustrated by some significant distances between nuclei and the molecular volume; the latter defined as the volume inside a contour of 0.001 electrons/bohr^3 density. These values show that the size of the tripeptide is twice that of Tau, and comparable to the available gap in the substrate channel, proving that access to the active site must be more difficult for Pro-Gly-Gly. Furthermore, corresponding chlorinated compounds are even bulkier.

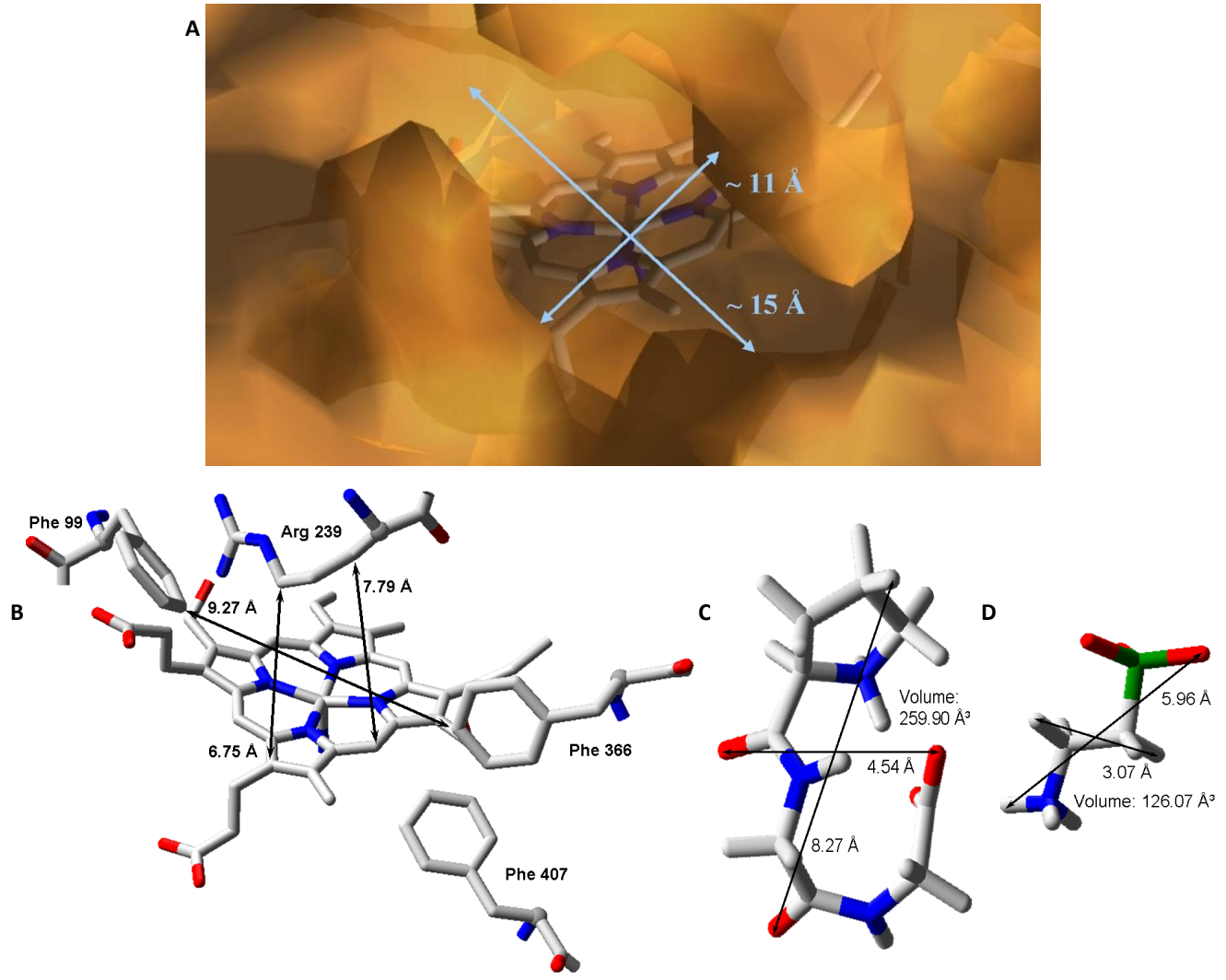

Figure 9.7. MPO-mediated chlorination of Pro-Gly-Gly. (A) Surface of MPO showing the entry of the substrate channel leading to the active site. Heme group is visible in the background. (B) End of the substrate channel of MPO in the proximity of the distal cavity, leading to the active site. Structures of (C) Pro-Gly-Gly and (D) Tau obtained at the MP2/6-31++G** computational level. Volume and relevant distances are indicated in the images.

9.4 Discussion

Kinetic behaviour and rate constants obtained for Pro-Gly-Gly chlorination are consistent with previously published data for Tau (Table 9.4). Three points should be highlighted: (i) within the working conditions, initial and equilibrium rates are independent of the substrate concentration, equilibrium rates being lower than initial ones due to the formation of compound II; (ii) no significant loss of H_2O_2 through peroxidative processes has been found under the working conditions, which is consistent with this activity taking place at higher values of pH;[36-38] and (iii) a maximum of chlorination rate is observed for Pro-Gly-Gly, and also Tau, when $[H_2O_2] \approx 0.3$ - 0.7 mM and pH ≈ 4.5 - 5.0. Some differences between Pro-Gly-Gly and Tau were obtained for kinetic parameters (Table 9.4); it must be taken into account that the estimated values for the kinetic parameters of these two substrates have been measured indirectly, by considering the kinetic traces of the whole chlorination process instead of studying isolated steps.

9.4.1 Role of compound II in chlorination cycle

Reactions 7 and 8 (Table 9.1) slow the chlorination reaction rate at equilibrium, and appear in the corresponding mechanism rate equation (Table 9.2 and Equation 23A) associated to the term involving K_7'. This kinetic constant ($K_7' = k_7 / (k_{-7} + k_8)$), apart from the rate constant of formation of MPO-II-HO_2, k_7, contains both the kinetic constant of the step back to MPO-I + H_2O_2, k_{-7}, and the rate constant forming Fe(III)-MPO, k_8, with net loss of hydrogen peroxide outside the chlorination cycle. Depending on the relative values of k_{-7} and k_8 two limits can be considered. One limit implies $k_{-7} << k_8$, then taking into account the values of K_7' (0.20 M) and k_7 (3.3×10^4 $M^{-1}\cdot s^{-1}$),[12] the maximum value for k_8 would be 1.65×10^5 $M^{-1}\cdot s^{-1}$, lower than 5.5×10^6 $M^{-1}\cdot s^{-1}$ proposed in the literature.[23] High values of k_8 would imply measurable loss of hydrogen peroxide during our kinetic runs, which is contrary to our findings.

The other limit, $k_{-7} >> k_8$ and $K_7' \approx K_7$, means that the equilibrium in Reaction 7 (Table 9.1) is thermodynamically slightly unfavourable, which is in agreement with the required excess of H_2O_2 to drive out the formation of MPO-II.[17] Assuming that the re-formation of MPO-I is faster than the formation of Fe(III)-MPO, *i.e.*, $k_{-7} >> k_8$, and considering that MPO-II accumulation is the only responsible for the slow rate under equilibrium conditions, then it is possible to calculate the fraction of chlorinating-active enzyme and, therefore, [MPO-II-HO_2] at particular pH and $[H_2O_2]$ values:

$$\frac{[\mathrm{MPO_0}] - [\mathrm{MPO\text{-}II\text{-}HO_2}]}{[\mathrm{MPO_0}]} = \frac{v_{eq}}{v_{0,calc}} \tag{6}$$

where $v_{0,calc}$ is the estimated value of the initial rate at the corresponding pH and $[H_2O_2]$. Compound I reduction by H_2O_2 (Reaction 7) produces compound II [16, 17] that, under working conditions, is present in the form of the complex MPO-II-HO_2. According to this equilibrium we obtain:

$$K_7 = \frac{[\mathrm{MPO\text{-}II\text{-}HO_2}]\cdot[\mathrm{H^+}]}{[\mathrm{MPO\text{-}I}]\cdot[\mathrm{H_2O_2}]}; \quad [\mathrm{MPO\text{-}II\text{-}HO_2}] = \frac{K_7\cdot[\mathrm{MPO\text{-}I}]\cdot[\mathrm{H_2O_2}]}{[\mathrm{H^+}]} \tag{7}$$

Considering the species that actively take part on the chlorination process, as well as their dependence on $[H_2O_2]$, Equation 8 is obtained.

$$\frac{[\mathrm{MPO\text{-}II\text{-}HO_2}]\cdot[\mathrm{H^+}]}{[\mathrm{MPO_0}] - [\mathrm{MPO\text{-}II\text{-}HO_2}]} = \alpha\cdot K_7\cdot[\mathrm{H_2O_2}]^2 \tag{8}$$

Figure 9.8A plots the left term of Equation 8 *vs*. $[H_2O_2]^2$. Straight lines were obtained for each pH, with the slope representing $\alpha\cdot K_7$. Applying the protonation equilibria, the effect of pH on the proportionality variable α can be worked out (Equation 9).

$$\alpha = \beta\cdot\frac{(1 - \gamma\cdot[\mathrm{H^+}])}{[\mathrm{H^+}]} \tag{9}$$

The slopes from Figure 9.8A are plotted against $[H^+]$ in the Figure 9.8B, and the data fitted to Equation 10:

$$\alpha \cdot K_7 = \frac{a - b \cdot [H^+]}{[H^+]} \quad (10)$$

Considering the different used approximations, Equation 10 reasonably fits the data, supporting the proposed mechanism; for a more detailed description see chapter 8.

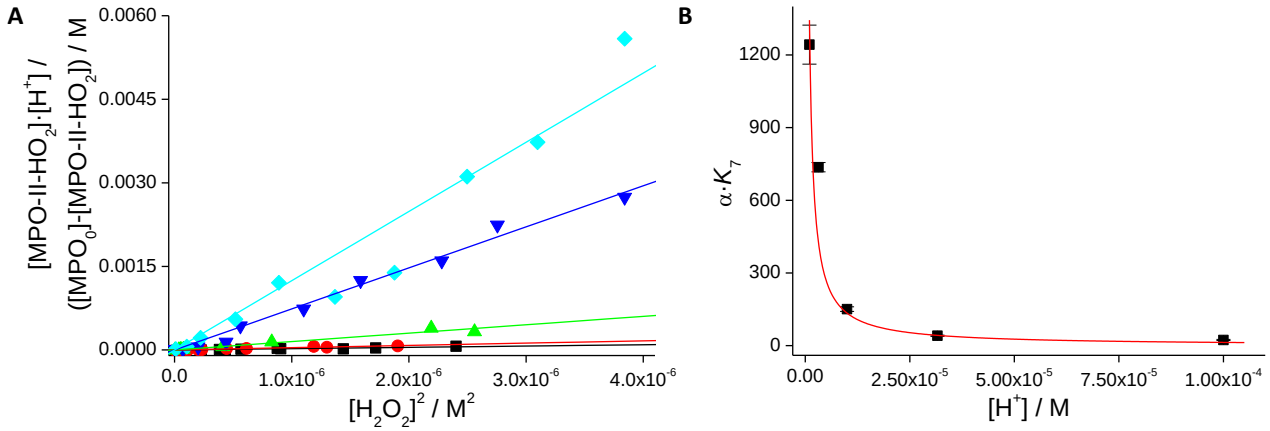

Figure 9.8. MPO-mediated chlorination of Pro-Gly-Gly. (A) ($[MPO\text{-}II\text{-}HO_2] \cdot [H^+] / [MPO_0] - [MPO\text{-}II\text{-}HO_2]$) plotted *vs*. $[H_2O_2]^2$. Values of $[MPO\text{-}II\text{-}HO_2]$ were calculated from the data in Figures 9.5 and 9.6. Conditions are the same as in these figures. (B) Slopes from (A) plotted against $[H^+]$.

9.4.2 Equilibrium chlorination profile for Pro-Gly-Gly

Although initial-rate measurements give information about how the process starts, equilibrium results shed light on most of the progress of *in vivo* chlorination. Both at high and low $[H_2O_2]$, as well as in the ends of the working pH range, chlorination keeps at a low rate, whereas the maximum rate is obtained at $[H_2O_2]$ and pH values around 0.3 - 0.7 mM and 4.5 - 5.0, respectively.

9.4.3 The quest for the active species

The disparity in reaction rates (Figure 9.5B), and the divergence in k_2 values between Pro-Gly-Gly and Tau points out that the MPO-mediated chlorination mechanism is not exactly the same for both substrates, which is not the case for the uncatalyzed process. In fact, the chlorination rate is reversed, Pro-Gly-Gly > Tau in the HClO-mediated reaction (Figure 9.3) *vs*. Pro-Gly-Gly < Tau when the reaction is MPO-mediated (Figure 9.5B).

The independence, within the working conditions, of the chlorination rate on Pro-Gly-Gly or Tau concentration (Figure 9.4) implies that the rate-determining step precedes the chlorinating steps (3a and 3b, Table 9.1), *i.e.*, the reaction rate being controlled by the formation of the putative chlorinating agents, ClO^- and/or MPO-I-Cl (2a and 2b). In other words, the chlorinating steps are faster than the formation of the chlorinating agents and the back reactions to reform MPO-I (-2a and -2b). This fact has been taken into account in the finally deduced mechanism rate equations (Table 9.2) that do not contain k_3. However, this mechanism does not support the observed difference in (k_{2a} + k_{2b}) between Pro-Gly-Gly and Tau. It is reasonable to assume that the rate-determining steps (2a and 2b) do not depend on the chemical features or concentration of Pro-Gly-Gly or Tau as long as the working conditions are identical. Nevertheless, the difference could be ascribed to low or null formation of *N*-Cl Pro-Gly-Gly through Reaction 3b (Table 9.1). As expected, and confirmed by electronic structure calculations, Pro-Gly-Gly is bulkier than Tau, that easily has access to the heme pocket reacting with MPO-I-Cl forming *N*-Cl Tau. There is no diffusion of Pro-Gly-Gly, *i.e.*, there is no formation of *N*-Cl Pro-Gly-Gly through this pathway. This implies $k_{3b,Pro\text{-}Gly\text{-}Gly} = 0$ and k_{2b} should be removed from the mechanism rate equations in the case of Pro-Gly-Gly (Table 9.2).

It could be argued that the discrepancy between k_2 (= k_{2a} + k_{2b}) for Pro-Gly-Gly and Tau (Table 9.4) is an artifact coming from fitting equations to kinetic data, thus whatever is the mechanism, it should be the same for both compounds. The higher reactivity of Tau in the MPO-mediated reaction is obvious from the measured initial rates (Table 9.3). At all pH values the observed kinetic constant, and also the rate (not shown), is always higher for this substrate, 20% in average; random behaviour would be expected if the rates were the same.

9.4.4 Hypochlorite-mediated chlorination

It seems that Pro-Gly-Gly is chlorinated only through the ClO^- pathway, whereas some *N*-Cl Tau is also formed by the MPO-I-Cl pathway; thus, the main chlorinating activity of MPO takes place outside the enzyme, and only smaller substrates could also be chlorinated into the heme pocket. After its formation, ClO^- diffuses away the enzyme cavity, is rapidly protonated according to the equilibrium

$$ClO^- + H^+ \leftrightarrows HClO; \quad pK_a = 7.54 \text{ [6]}$$

and chlorination takes place by HClO. The limited chlorinating power of ClO^- with respect to HClO could prevent or retard self-inactivation of MPO by chlorination of potential targets in the distal heme cavity and/or the substrate channel.

Although the mechanism rate equations (Table 9.2) remain unchanged, strictly speaking Reaction 3a (Table 9.1) is not an elementary step but a composite of three steps (Scheme 9.1A). Equilibria are rapidly achieved, the second equilibrium corresponds to usual pK_a of HClO in aqueous medium, while the last process is the HClO-mediated chlorination in absence of MPO also reported in this work (*vide supra*).

A

$$ClO^-_{in} \leftrightarrows ClO^-_{out}; \quad K_{diffusion}$$

$$ClO^-_{out} + H^+_{out} \leftrightarrows HClO_{out}; \quad K_{a,HOCl}$$

$$HClO_{out} + \text{Pro-Gly-Gly}_{out} \rightarrow N\text{-Cl Pro-Gly-Gly}_{out} + H_2O_{out}; \quad k_{\text{Pro-Gly-Gly}}$$

B

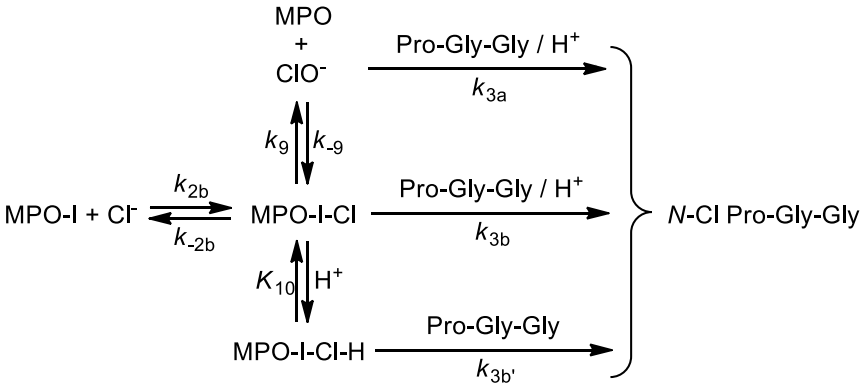

Scheme 9.1. MPO-mediated chlorination of Pro-Gly-Gly. (A) Description of the elementary steps comprised in Reaction 3a as defined in Table 9.1. (B) Alternative mechanistic pathways of MPO-mediated chlorination involving the enzymatic complex MPO-I-Cl.

9.4.5 MPO-I-Cl-mediated chlorination

After formation of MPO-I-Cl (Reaction 2b, Table 9.1), alternative pathways could be proposed (Scheme 9.1B). These possibilities support that either the enzymatic complex (Reaction 3b) (or the corresponding protonated species (Reactions 10 and 3b')) is the chlorinating agent, or ClO^- is released with MPO-I-Cl acting only as a transient reaction intermediate (Reactions 9 and 3a).

The following discussion applies for initial rates, but analogous equations are obtained also for equilibrium rates. Assuming

exclusive chlorination through ClO^- with no application of steady-state approximation to MPO-I-Cl (k_{3b} = $k_{3b'}$ = 0) and, therefore, Reaction 9 is the rate-limiting step, yields a slightly different equation:

$$v_0 = \frac{k_{2b} \cdot k_9 \cdot K_1 \cdot [MPO_0] \cdot [H_2O_2] \cdot [Cl^-]}{k_{-2b} \cdot (1 + K_4 \cdot [H^+] \cdot (1 + K_6 \cdot [Cl^-]))} \quad (11)$$

which also matches the observed behaviour, similarly to that obtained from the mechanism in Table 9.1 (Equation 18A and Table 9.2). But it cannot explain the differences in rate between Pro-Gly-Gly and Tau.

Less detailed information could be extracted from current kinetic data regarding the step involving chlorination inside the distal cavity by MPO-I-Cl (Reaction 3b, Table 9.1). The formation of *N*-Cl Tau could take place by this pathway either in one or in several molecular steps, all of them faster than the formation of MPO-I-Cl. Likely a proton could also be involved, as included in Reaction 3b (Table 9.1); current kinetic data do not allow to confirm it, in fact, same rate equations are obtained without a proton.

Assuming that no ClO^- is formed, *i.e.*, K_9 = 0, MPO-I-Cl is solely responsible for chlorination and the corresponding mechanism rate equation has the form shown in Table 9.2, but without k_{2a}:

$$v_0 = \frac{k_{2b} \cdot K_1 \cdot [MPO_0] \cdot [H_2O_2] \cdot [Cl^-]}{1 + K_4 \cdot [H^+] \cdot (1 + K_6 \cdot [Cl^-])} \quad (12)$$

In this case equal reaction rates are predicted for Pro-Gly-Gly and Tau, which is not supported by the experimental data. Moreover, this approach requires that the tripeptide is able to diffuse into the heme cavity. Considering that the only chlorinating agent is the protonated enzymatic complex MPO-I-Cl-H (Reactions 10 and 3b'), or if both complexes MPO-I-Cl and MPO-I-Cl-H represent the chlorinating species and the two pathways take place simultaneously, the mechanism rate expression is again Equation 12. Therefore, it does not support the observed different rates, and infers that Pro-Gly-Gly must reach the active site. Furthermore, addition of chlorination through ClO^- (Reactions 9 and 3a) to the mechanism does not modify the mechanism rate equation, providing steady-state approximation to ClO^-, MPO-I-Cl and MPO-I-Cl-H holds, which is consistent with Reaction 2a and/or 2b (Table 9.1) being the rate-limiting step.

9.5 Summary

We have demonstrated that kinetic studies on complex enzymatic mechanisms can be carried out at different stages of the process, using the same kinetic traces. In the particular case of human MPO, the rate dependence on pH and $[H_2O_2]$ shows a different behaviour for initial rates and for rates at equilibrium, being slower under equilibrium conditions, which is ascribed to the chemical equilibrium between MPO-I and MPO-II-HO_2. Chlorination of amino compounds, like Pro-Gly-Gly and Tau, achieves its maximum rate at equilibrium when $[H_2O_2]$ ≈ 0.3 - 0.7 mM and pH ≈ 4.5 - 5.0.

In all described cases the mechanism rate equation is formally equivalent to that extracted from kinetic data. A general feature is the absence of rate constants corresponding to the steps where the substrate is being chlorinated (3a, 3b and 3b'); therefore, the reaction rate should be the same irrespective of the substrate. The difference in rate between MPO-mediated chlorination of Pro-Gly-Gly (k_2 = 7.83 × 10^3 $M^{-1}{\cdot}s^{-1}$) and Tau (k_2 = 1.58 × 10^4 $M^{-1}{\cdot}s^{-1}$), despite not substantially different ($k_{2(Tau)} \approx 2\ k_{2(Pro\text{-}Gly\text{-}Gly)}$), is adequately explained in terms of the mechanism proposed in Table 9.1. Bulky substrates are chlorinated only outside the heme pocket by HClO via ClO^- pathway ($k_2 = k_{2a}$), or by other chlorinated species, like *N*-Cl Tau, acting as final chlorinating agents; chlorination of the latter compound and other small substrates can also take place inside the distal cavity by reaction with MPO-I-Cl/MPO-I-Cl-H ($k_2 = k_{2a} + k_{2b}$).

Free generated HClO by MPO/H_2O_2/Cl^- system would be rapidly trapped by thiols or amines available at the close environment of the enzyme (*i.e.*, inside the phagosome). Moreover, MPO itself is known to be (self)inactivated by its own reaction products. The high cytosolic [Tau] reported for human leukocytes could indicate that this compound could help to avoid HClO formation by MPO released to the cytosol. However, although being less toxic than HClO, taurine chloramine is long-lived, thereby providing a mechanism for the prolongation and penetration of the oxidant activity into complex

biological fluids. Evidence has emerged that these MPO-derived oxidants contribute to tissue damage and the initiation and propagation of acute and chronic vascular inflammatory diseases.[39]

9.6 Appendix. Derivation of the rate equations for the mechanism of MPO-catalyzed chlorination of amino compounds

9.6.1 Initial rate

Reaction rate expression from Reactions 3a & 3b:

$$v_0 = \frac{\mathrm{d}[N\text{-Cl Pro-Gly-Gly}]}{\mathrm{d}t} = (k_{3a} \cdot [\mathrm{ClO^-}] + k_{3b} \cdot [\text{MPO-I-Cl}]) \cdot [\text{Pro-Gly-Gly}] \cdot [\mathrm{H^+}] \quad (1A)$$

Mass balance equation:

$$[\mathrm{MPO_0}] = [\mathrm{MPO}] + [\mathrm{MPO-I}] + [\mathrm{MPO-H}] + [\mathrm{MPO-I-H}] + [\mathrm{MPO-H-Cl}] \quad (2A)$$

where it has been assumed that [MPO-I-Cl] must be negligible.

Equilibrium equation for proton binding onto MPO:

$$K_4 = \frac{[\mathrm{MPO-H}]}{[\mathrm{MPO}] \cdot [\mathrm{H^+}]}; \quad [\mathrm{MPO-H}] = K_4 \cdot [\mathrm{MPO}] \cdot [\mathrm{H^+}] \quad (3A)$$

Equilibrium equation for protonation of MPO-I:

$$K_5 = \frac{[\mathrm{MPO-I-H}]}{[\mathrm{MPO-I}] \cdot [\mathrm{H^+}]}; \quad [\mathrm{MPO-I-H}] = K_5 \cdot [\mathrm{MPO-I}] \cdot [\mathrm{H^+}] \quad (4A)$$

Equilibrium equation for binding of chloride:

$$K_6 = \frac{[\mathrm{MPO-H-Cl}]}{[\mathrm{MPO-H}] \cdot [\mathrm{Cl^-}]}; \quad [\mathrm{MPO-H-Cl}] = K_6 \cdot [\mathrm{MPO-H}] \cdot [\mathrm{Cl^-}] \quad (5A)$$

Substituting from Equations 3A, 4A, and 5A into 2A:

$$[\mathrm{MPO_0}] = [\mathrm{MPO}] \cdot (1 + K_4 \cdot [\mathrm{H^+}] \cdot (1 + K_6 \cdot [\mathrm{Cl^-}])) + [\mathrm{MPO-I}] \cdot (1 + K_5 \cdot [\mathrm{H^+}]) \quad (6A)$$

Equilibrium equation for MPO-I formation:

$$K_1 = \frac{[\mathrm{MPO-I}]}{[\mathrm{MPO}] \cdot [\mathrm{H_2O_2}]}; \quad [\mathrm{MPO}] = \frac{[\mathrm{MPO-I}]}{K_1 \cdot [\mathrm{H_2O_2}]} \quad (7A)$$

Substituting from Equation 7A into 6A:

$$[\mathrm{MPO_0}] = \left(\frac{1 + K_4 \cdot [\mathrm{H^+}] \cdot (1 + K_6 \cdot [\mathrm{Cl^-}])}{K_1 \cdot [\mathrm{H_2O_2}]} + 1 + K_5 \cdot [\mathrm{H^+}] \right) \cdot [\mathrm{MPO-I}] \quad (8A)$$

Steady-state approximation for $\mathrm{ClO^-}$:

$$\frac{\mathrm{d}[\mathrm{ClO^-}]}{\mathrm{d}t} = 0; \quad k_{2a} \cdot [\mathrm{MPO-I}] \cdot [\mathrm{Cl^-}] = (k_{-2a} \cdot [\mathrm{MPO}] + k_{3a} \cdot [\text{Pro-Gly-Gly}] \cdot [\mathrm{H^+}]) \cdot [\mathrm{ClO^-}] \quad (9A)$$

Steady-state approximation for MPO-I-Cl:

$$\frac{\mathrm{d}[\mathrm{MPO-I-Cl}]}{\mathrm{d}t} = 0; \quad k_{2b} \cdot [\mathrm{MPO-I}] \cdot [\mathrm{Cl^-}] = (k_{-2b} + k_{3b} \cdot [\text{Pro-Gly-Gly}] \cdot [\mathrm{H^+}]) \cdot [\mathrm{MPO-I-Cl}] \quad (10A)$$

Taking into account that, under conditions used in the study, chlorinating agents cannot be observed:

$$[\mathrm{ClO^-}] \approx 0; \quad k_{2a} \cdot [\mathrm{MPO-I}] \cdot [\mathrm{Cl^-}] >> k_{-2a} \cdot [\mathrm{MPO}] \cdot [\mathrm{ClO^-}] \quad (11A)$$

and

$$[\mathrm{MPO-I-Cl}] \approx 0; \quad k_{2b} \cdot [\mathrm{MPO-I}] \cdot [\mathrm{Cl^-}] >> k_{-2b} \cdot [\mathrm{MPO-I-Cl}] \quad (12A)$$

Equations 9A and 10A simplify to:

$$k_{3a}\cdot[\text{Pro-Gly-Gly}]\cdot[H^+]\cdot[ClO^-] = k_{2a}\cdot[\text{MPO-I}]\cdot[Cl^-] - k_{-2a}\cdot[\text{MPO}]\cdot[ClO^-] \approx k_{2a}\cdot[\text{MPO-I}]\cdot[Cl^-] \quad (13A)$$

$$k_{3b}\cdot[\text{Pro-Gly-Gly}]\cdot[H^+]\cdot[\text{MPO-I-Cl}] = k_{2b}\cdot[\text{MPO-I}]\cdot[Cl^-] - k_{-2b}\cdot[\text{MPO-I-Cl}] \approx k_{2b}\cdot[\text{MPO-I}]\cdot[Cl^-] \quad (14A)$$

This approach is consistent with the observed independence on [Pro-Gly-Gly], which, as indicated in the Discussion, points out that the steps where the substrate is chlorinated (3a and 3b) are faster than the back reactions to reform compound I (-2a and -2b) and the formation of chlorinated compounds (2a and 2b).

From Equations 13A and 14A, Equation 1A is converted to:

$$v_0 = (k_{3a}\cdot[ClO^-] + k_{3b}\cdot[\text{MPO-I-Cl}])\cdot[\text{Pro-Gly-Gly}]\cdot[H^+] = (k_{2a}+k_{2b})\cdot[\text{MPO-I}]\cdot[Cl^-] \quad (15A)$$

which expressed in terms of reactants, applying Equation 8A, becomes:

$$v_0 = \frac{(k_{2a}+k_{2b})\cdot[\text{MPO}_0]\cdot[Cl^-]}{\frac{1+K_4\cdot[H^+]\cdot(1+K_6\cdot[Cl^-])}{K_1\cdot[H_2O_2]}+1+K_5\cdot[H^+]} \quad (16A)$$

Considering:

$$\frac{1+K_4\cdot[H^+]\cdot(1+K_6\cdot[Cl^-])}{K_1\cdot[H_2O_2]} >> 1+K_5\cdot[H^+] \quad (17A)$$

Initial rate expression becomes:

$$v_0 = \frac{k_2\cdot K_1\cdot[\text{MPO}_0]\cdot[H_2O_2]\cdot[Cl^-]}{1+K_4\cdot[H^+]\cdot(1+K_6\cdot[Cl^-])} \quad (18A)$$

where $k_2 = (k_{2a} + k_{2b})$. This rate equation is consistent with the experimental initial rate dependence on $[H_2O_2]$ (Figure 9.5A).

9.6.2 Rate at equilibrium

Under equilibrium and according to the hypothesis about $HO_2^{\cdot}$ described in the paper, conservation equation changes to:

$$[\text{MPO}_0] = [\text{MPO}] + [\text{MPO-I}] + [\text{MPO-H}] + [\text{MPO-I-H}] + [\text{MPO-H-Cl}] + [\text{MPO-II-HO}_2] \quad (19A)$$

Variation of [MPO-II-HO_2] at equilibrium occurs very slowly, thus steady-state approximation can be applied:

$$\frac{d[\text{MPO-II-HO}_2]}{dt} = 0; \quad k_7\cdot[\text{MPO-I}]\cdot[H_2O_2] = (k_{-7}+k_8)\cdot[\text{MPO-II-HO}_2]\cdot[H^+] \quad (20A)$$

$$[\text{MPO-II-HO}_2] = \frac{k_7\cdot[\text{MPO-I}]\cdot[H_2O_2]}{(k_{-7}+k_8)\cdot[H^+]} = \frac{K_7^{'}\cdot[\text{MPO-I}]\cdot[H_2O_2]}{[H^+]} \quad (21A)$$

where $K_7^{'} = \frac{k_7}{k_{-7}+k_8}$.

Substituting from Equations 3A, 4A, 5A, and 21A into Equation 19A:

$$[\text{MPO}_0] = [\text{MPO}]\cdot(1+K_4\cdot[H^+]\cdot(1+K_6\cdot[Cl^-])) + [\text{MPO-I}]\cdot\left(1+K_5\cdot[H^+]+\frac{K_7^{'}\cdot[H_2O_2]}{[H^+]}\right) \quad (22A)$$

From Equations 7A, 13A, 14A, 22A, and the dependence of the reaction rate on the reactants concentration, the rate equation 1A is converted to:

$$v_{eq} = \frac{k_2\cdot[\text{MPO}_0]\cdot[Cl^-]}{\frac{1+K_4\cdot[H^+]\cdot(1+K_6\cdot[Cl^-])}{K_1\cdot[H_2O_2]}+1+K_5\cdot[H^+]+\frac{K_7^{'}\cdot[H_2O_2]}{[H^+]}} \quad (23A)$$

where $k_2 = (k_{2a} + k_{2b})$.

This study has been published as: D. R. Ramos, M. V. García, M. Canle L., J. A. Santaballa, P. G. Furtmüller, and C. Obinger, J. Inorg. Biochem., 2008 **102** (5-6) 1300-1311.

9.7 References

1. S. J. Klebanoff, *Myeloperoxidase: friend and foe.* J. Leukoc. Biol., 2005 **77** (5) 598-625.
2. S. J. Klebanoff, *A peroxidase-mediated antimicrobial system in leukocytes.* J. Clin. Invest., 1967 **46** (6) 1078-1078.
3. C. J. van Dalen, M. W. Whitehouse, C. C. Winterbourn, and A. J. Kettle, *Thiocyanate and chloride as competing substrates for myeloperoxidase.* Biochem. J., 1997 **327** (Pt. 2) 487-492.
4. R. Senthilmohan and A. J. Kettle, *Bromination and chlorination reactions of myeloperoxidase at physiological concentrations of bromide and chloride.* Arch. Biochem. Biophys., 2006 **445** (2) 235-244.
5. P. C. Andrews and N. I. Krinsky, *A kinetic analysis of the interaction of human myeloperoxidase with hydrogen peroxide, chloride ions, and protons.* J. Biol. Chem., 1982 **257** (22) 13240-13245.
6. J. C. Morris, *The acid ionization constant of HOCl from 5 to 35°.* J. Phys. Chem., 1966 **70** (12) 3798-3805.
7. J. E. Harrison and J. Schultz, *Studies on the chlorinating activity of myeloperoxidase.* J. Biol. Chem., 1976 **251** (5) 1371-1374.
8. T. X. Wang and D. W. Margerum, *Kinetics of reversible chlorine hydrolysis: temperature dependence and general-acid/base-assisted mechanisms.* Inorg. Chem., 1994 **33** (6) 1050-1055.
9. C. C. Winterbourn, *Biological reactivity and biomarkers of the neutrophil oxidant, hypochlorous acid.* Toxicology, 2002 **181-182** 223-227.
10. S. L. Hazen, A. d'Avignon, M. M. Anderson, F. F. Hsu, J. W., and Heinecke, *Human neutrophils employ the myeloperoxidase-hydrogen peroxide-chloride system to oxidize alpha-amino acids to a family of reactive aldehydes. Mechanistic studies identifying labile intermediates along the reaction pathway.* J. Biol. Chem., 1998 **273** (9) 4997-5005.
11. D. B. Learn, V. A. Fried, and E. L. Thomas, *Taurine and hypotaurine content of human leukocytes.* J. Leukoc. Biol., 1990 **48** (2) 174-182.
12. L. A. Marquez and H. B. Dunford, *Chlorination of taurine by myeloperoxidase. Kinetic evidence for an enzyme-bound intermediate.* J. Biol. Chem., 1994 **269** (11) 7950-7956.
13. H. B. Dunford and L. A. Marquez-Curtis, *Myeloperoxidase: kinetic evidence for formation of enzyme-bound chlorinating intermediate.* Methods Enzymol., 2002 **354** (Part F) 338-350.
14. H. B. Dunford, A. M. Lambeir, M. A. Kashem, and M. Pickard, *On the mechanism of chlorination by chloroperoxidase.* Arch. Biochem. Biophys., 1987 **252** (1) 292-302.
15. D. R. Ramos, M. V. García, M. Canle L., J. A. Santaballa, P. G. Furtmüller, and C. Obinger, *Myeloperoxidase-catalyzed taurine chlorination: Initial versus equilibrium rate.* Arch. Biochem. Biophys., 2007 **466** (2) 221-233.
16. B. G. J. M. Bolscher and R. Wever, *A kinetic study of the reaction between human myeloperoxidase, hydroperoxides and cyanide. Inhibition by chloride and thiocyanate.* Biochim. Biophys. Acta, 1984 **788** (1) 1-10.
17. L. A. Marquez, J. T. Huang, and H. B. Dunford, *Spectral and kinetic studies on the formation of myeloperoxidase compounds I and II: roles of hydrogen peroxide and superoxide.* Biochemistry, 1994 **33** (6) 1447-1454.
18. P. G. Furtmüller, U. Burner, W. Jantschko, G. Regelsberger, and C. Obinger, *The reactivity of myeloperoxidase compound I formed with hypochlorous acid.* Redox Report, 2000 **5** (4) 173-178.
19. A. R. J. Bakkenist, J. E. G. De Boer, H. Plat, and R. Wever, *The halide complexes of myeloperoxidase and the mechanism of the halogenation reactions.* Biochim. Biophys. Acta, 1980 **613** (2) 337-348.

20. M. Ikeda-Saito, *Spectroscopic, ligand binding, and enzymatic properties of the spleen green hemeprotein. A comparison with myeloperoxidase.* J. Biol. Chem., 1985 **260** (21) 11688-11696.

21. P. G. Furtmüller, U. Burner, and C. Obinger, *Reaction of myeloperoxidase compound I with chloride, bromide, iodide, and thiocyanate.* Biochemistry, 1998 **37** (51) 17923-17930.

22. A. J. Kettle and C. C. Winterbourn, *A kinetic analysis of the catalase activity of myeloperoxidase.* Biochemistry, 2001 **40** (34) 10204-10212.

23. A. J. Kettle, R. F. Anderson, M. B. Hampton, and C. C. Winterbourn, *Reactions of superoxide with myeloperoxidase.* Biochemistry, 2007 **46** (16) 4888-4897.

24. T. J. Fiedler, C. A. Davey, and R. E. Fenna, *X-ray crystal structure and characterization of halide-binding sites of human myeloperoxidase at 1.8 Å resolution.* J. Biol. Chem., 2000 **275** (16) 11964-11971.

25. J. A. Santaballa, H. Maskill, and M. Canle L., *The relationship between mechanism and rate law*, in *Investigation of organic reactions and their mechanisms*, H. Maskill, Editor. 2006, Blackwell Publishing: Singapore. 79-103.

26. X. L. Armesto, M. Canle L., M. I. Fernández, M. V. García, R. S., and J. A. Santaballa, *Intracellular oxidation of dipeptides. Base-promoted elimination from N-halodipeptides to 2-[N-alkyl-N-(2-N-alkylimino-2-alkyl-ethanoyl)amino]-2,2-dialkylethanoic acids.* J. Org. Chem., 2001 **66** (17) 5692-5700.

27. X. L. Armesto, M. Canle L., M. Losada, and J. A. Santaballa, *An operational approach to N-Cl-a-amino acids decomposition.* Int. J. Chem. Kinet., 1993 **25** (5) 331-339.

28. D. P. Nelson and L. A. Kiesow, *Enthalpy of decomposition of hydrogen peroxide by catalase at 25 °C (with molar extinction coefficients of H_2O_2 solutions in the UV).* Anal. Biochem., 1972 **49** (2) 474-478.

29. T. Odajima and I. Yamazaki, *Myeloperoxidase of the leukocyte of normal blood. I. Reaction of myeloperoxidase with hydrogen peroxide.* Biochim. Biophys. Acta, 1970 **206** (1) 71-77.

30. D. N. Baron and S. A. Ahmed, *Intracellular concentrations of water and of the principal electrolytes determined by analysis of isolated human leucocytes.* Clin. Sci., 1969 **37** (1) 205-219.

31. M. J. Frisch, G. W. Trucks, H. B. Schlegel, G. E. Scuseria, M. A. Robb, J. R. Cheeseman, J. J. A. Montgomery, T. Vreven, K. N. Kudin, J. C. Burant, J. M. Millam, S. S. Iyengar, J. Tomasi, V. Barone, B. Mennucci, M. Cossi, G. Scalmani, N. Rega, G. A. Petersson, H. Nakatsuji, M. Hada, M. Ehara, K. Toyota, R. Fukuda, J. Hasegawa, M. Ishida, T. Nakajima, Y. Honda, O. Kitao, H. Nakai, M. Klene, X. Li, J. E. Knox, H. P. Hratchian, J. B. Cross, V. Bakken, C. Adamo, J. Jaramillo, R. Gomperts, R. E. Stratmann, O. Yazyev, A. J. Austin, R. Cammi, C. Pomelli, J. W. Ochterski, P. Y. Ayala, K. Morokuma, G. A. Voth, P. Salvador, J. J. Dannenberg, V. G. Zakrzewski, S. Dapprich, A. D. Daniels, M. C. Strain, O. Farkas, D. K. Malick, A. D. Rabuck, K. Raghavachari, J. B. Foresman, J. V. Ortiz, Q. Cui, A. G. Baboul, S. Clifford, J. Cioslowski, B. B. Stefanov, G. Liu, A. Liashenko, P. Piskorz, I. Komaromi, R. L. Martin, D. J. Fox, T. Keith, M. A. Al-Laham, C. Y. Peng, A. Nanayakkara, M. Challacombe, P. M. W. Gill, B. Johnson, W. Chen, M. W. Wong, C. Gonzalez, and J. A. Pople, *Gaussian03*. 2004, Gaussian, Inc.: Wallingford CT.

32. X. L. Armesto, M. Canle L., M. V. García, and J. A. Santaballa, *Aqueous chemistry of N-halo-compounds.* Chem. Soc. Rev., 1998 **27** (6) 453-460.

33. J. Arnhold, P. G. Furtmüller, and C. Obinger, *Redox properties of myeloperoxidase.* Redox Report, 2003 **8** (4) 179-186.

34. H. C. Lee, K. S. Booth, W. S. Caughey, and M. Ikeda-Saito, *Interaction of halides with the cyanide complex of myeloperoxidase: a model for substrate binding to compound I.* Biochim. Biophys. Acta, 1991 **1076** (2) 317-320.

35. M. Blair-Johnson, T. Fiedler, and R. Fenna, *Human myeloperoxidase: structure of a cyanide complex and its interaction with bromide and thiocyanate substrates at 1.9 Å resolution.* Biochemistry, 2001 **40** (46) 13990-13997.

36. H. Spalteholtz, O. M. Panasenko, and J. Arnhold, *Formation of reactive halide species by myeloperoxidase and*

eosinophyl peroxidase. Arch. Biochem. Biophys., 2006 **445** (2) 225-234.

37. I. I. Vlasova, J. Arnhold, A. N. Osipov, and O. M. Panasenko, *pH-dependent regulation of myeloperoxidase activity.* Biochem. Moscow, 2006 **71** (6) 667-677.

38. C. C. Winterbourn, M. B. Hampton, J. H. Livesey, and A. J. Kettle, *Modeling the reactions of superoxide and myeloperoxidase in the neutrophil phagosome. Implications for microbial killing.* J. Biol. Chem., 2006 **281** (52) 39860-39869.

39. E. Malle, P. G. Furtmüller, W. Sattler, and C. Obinger, *Myeloperoxidase: a target for new drug development?* Br. J. Pharmacol., 2007 **152** (6) 838-854.

CHAPTER 10

Interaction of hydrated electrons with human myeloperoxidase: A pulse radiolysis study

Disappointment is the nurse of wisdom.

Sir Boyle Roche

10.1 Introduction

Myeloperoxidase (MPO), a heme-containing dominant granule enzyme present in circulating polymorphonuclear neutrophils, plays a fundamental role in the production of oxidizing species and thus drives cell-mediated antimicrobial activity in the human innate immune system.[1]

General peroxidase activity of MPO is summarized in Scheme 10.1. Native ferric state of MPO (Fe(III)-MPO) reacts with hydrogen peroxide (H_2O_2) to form a ferryl π-cation radical complex called compound I (MPO-I). A one-electron reduction of this redox intermediate leads to compound II (MPO-II), which may undergo another one-electron reduction to yield starting native Fe(III)-PO. Furthermore, ferric compound may also undergo a one-electron reduction to produce the ferrous species Fe(II)-MPO.

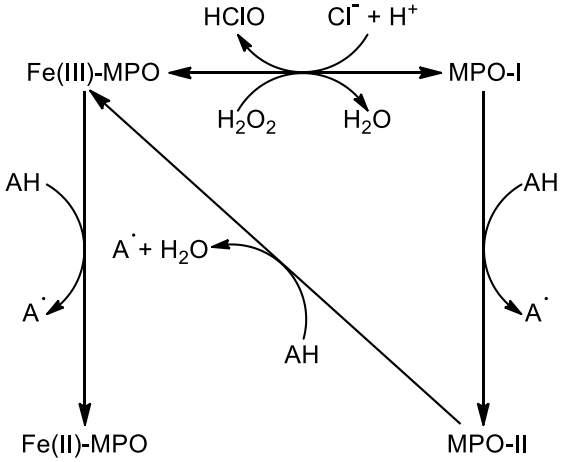

Scheme 10.1. Normal peroxidase cycle applied to MPO and also showing formation of ferrous intermediate and hypochlorous acid (HClO).

The main reaction mediated by MPO under physiological conditions is the oxidation of Cl^- by compound I to yield the highly-reactive chlorinating agent HClO[2] and/or the chlorinating complex MPO-I-Cl.[3] The high reduction potential of MPO-I allows the two-electron oxidation of Cl^-,[4] this confers MPO a unique role within the peroxidase-cyclooxygenase superfamily.[5] The major function of the initial chlorinating agents as well as derived chloramines, which also have oxidizing and chlorinating activity, is probably to attack essential microbial cell elements.

Most cellular components, including proteins, are susceptible of being damaged by harmful chemicals such as reactive oxygen species (ROS).[6] In fact, MPO promotes the generation of several ROS; furthermore, concurrent with MPO release from neutrophils, a burst of NADPH oxidase activity converting oxygen to superoxide anion ($O_2^{\cdot -}$) takes place.[7] Thus, MPO is particularly exposed to these highly reactive species that may modify the protein arrangement, then affecting its normal function. Its structure should be rather resistant to oxidative environments, but possibly this is not the case under highly reductive conditions. As a consequence, this study examines the behaviour of the enzyme when exposed to hydrated electrons, and the vulnerability of MPO to this extremely reactive agent that is also the strongest reductant in water ($E°$ = –2.9 V *vs*. NHE)[8] is assessed by the effect on its chlorination activity.

A few studies have been carried out showing the effect of ionizing radiation or high energy UV radiation on peroxidases. Some researchers studied the photochemical modification of the chromophore of MPO,[9] while other studies focused on the reactions of superoxide anion with several peroxidases,[10-12] including the reactions with the redox intermediates of MPO shown in the previous scheme, extensively investigated by Kettle, Winterbourn, and coworkers,[7, 13, 14] and the reactions promoted by hydroxyl radicals have also been reported.[12, 15, 16]

However, the processes involving hydrated electrons have not been investigated so thoroughly[17, 18] and their interaction

with MPO has not been examined so far. Thus, in this paper we discuss the effect of solvated electrons on MPO in aqueous solution at pH = 5.0, at which *in vivo* MPO chlorination activity is at its maximum,[19-21] and at which phagocytosis takes place,[22] or at pH = 7.0, typical of peroxidation reactions.[19, 20]

Pulse radiolysis is a valuable technique for studying short-lived free radicals and excited states using a beam of highly accelerated electrons, as it permits the selective generation of a radical of interest using appropriate solution conditions. Therefore, it reveals quite useful to assess the vulnerability of MPO to highly reactive species: in this study the enzyme was reacted with solvated electrons, testing the viability of one-electron reduction processes of Fe(III)-MPO, MPO-I, and MPO-II and evaluating the effect on the chlorination activity.

10.2 Material and methods

Highly purified MPO of a purity index (A_{430} / A_{280}) of at least 0.84 was obtained from Planta Natural Products (http://www.planta.at), a stock solution of *ca*. 0.60 μM and pH = 7 (5mM phosphate buffer) was used. Its concentration was determined spectrophotometrically using ε_{430} = 91,000 $M^{-1}\cdot cm^{-1}\cdot heme^{-1}$ for the Soret band of native ferric state.[23]

Stock solutions of glycine (Gly, Fischer Chemicals, Analytical Reagent Grade), potassium chloride (KCl, Sigma-Aldrich, ACS Reagent), and hydrogen peroxide (H_2O_2, Aldrich, 27.5 wt%) were prepared daily and kept in the dark at 4°C. The concentration of H_2O_2 was determined using ε_{240} = 39.4 $M^{-1}\cdot cm^{-1}$.[24] Citric acid ($HOC(COOH)(CH_2COOH)_2$, Sigma, anhydrous) / phosphate (Na_2HPO_4, BDH, AnalaR grade) buffer 0.5 M, was used at pH 5.0, while phosphate buffer (NaH_2PO_4, BDH, AnalaR grade) 0.1 M, was employed at pH 7.0, and *tert*-butanol (*t*-BuOH, Sigma, HPLC grade) was selected as hydroxyl radical scavenger. Irradiated samples were N_2-saturated and the doses per pulse were calibrated from the absorption of the thiocyanate radical (KSCN, BDH, AnalaR grade). All solutions were prepared with deionized water.

Irradiation experiments were performed with 2 μs electron pulses produced by a 12 MeV linear accelerator (Linac) and analyzed with the electron beam pulse radiolysis detection equipment at the SRS Daresbury Laboratory (Cheshire, UK). Prior to measurements a dosimetry of the cell with the KSCN solution was performed, following the production of $(SCN)_2^{\cdot -}$ (G = 2.8, ε_{500} = 7100 $M^{-1}\cdot cm^{-1}$) as described elsewhere.

Ionizing irradiation of the aqueous solution promotes the generation of protons (H^+), hydroxyl radicals ($HO^{\cdot}$), and solvated electrons (e^-_{aq}) according to the following reaction:

$$H_2O \text{ /\!\!\!

Time-resolved spectra of the reaction with hydrated electrons were obtained in the UV-Visible range (350 - 550 nm) after a number of pulses, when response becomes fairly stable. The measurement of transients with low absorption coefficients produces a poor signal-to-noise ratio, then more concentrated samples, containing 500 nM of MPO and 500 μM of H_2O_2 (all other parameters were kept constant), were used. Decay traces were fitted using equations of first-order kinetics to obtain the reaction rate for every single wavelength.

10.2.3 Reduction of Fe(III)-MPO

Finally, this reaction was studied by preparing the corresponding aqueous solutions of MPO at pH 7, with *t*-BuOH but without H_2O_2. The fade-out of ferric species was followed at 430 nm.

10.2.4 Decline of chlorination activity

Damage from irradiation was quantified by monitoring the loss of chlorination activity. This can be easily performed by studying the rate of chlorination of an adequate substrate. Here the simplest α-amino acid, glycine (Gly), was the target of the MPO/H_2O_2/Cl^- enzymatic system.

In vivo MPO chlorination activity takes place at pH near 5, thus this value was employed in the study (100 mM citric/phosphate buffer). Chloride concentration in plasma is as high as 100-140 mM,[26] hence 100 mM of Cl^- was used in all cases. Final concentration of MPO was taken as 20 nM, while [Gly] = 100 mM and [H_2O_2] = 1.0 mM were chosen as this combination yielded appropriate kinetic traces for simple proper fitting.

Radiolysis pulses were applied on N_2-saturated aqueous solutions of MPO *ca*. 40 nM and containing 1 vol% *t*-BuOH prepared in a 1.0 cm-pathlength quartz cuvette. The residual chlorination activity of MPO was determined by measuring its ability to chlorinate Gly. Thus, activity experiments were performed immediately after applying the appropriate total irradiation dose: the cuvette was placed into a diode-array UV-Vis spectrophotometer and the rest of reactants were added to the required concentration. Addition of H_2O_2 triggered the chlorination reaction and spectra were measured between 200 and 500 nm. The formation of *N*-Cl Gly was followed at λ = 260 nm.

Also, *t*-BuOH was previously checked not to interfere with the very reactive active site of MPO, and the chlorination process showed same kinetic rate in the absence or presence of this scavenger.

10.3 Results and discussion

The dose applied to the samples with each 2 μs radiolysis pulse corresponds to ~20 Gy, while the total dose applied in the study of the irradiation effect on enzymatic activity is displayed in the associated figure.

A one-electron reduction of compounds I and II, and ferric MPO yields compound II, native ferric enzyme, and ferrous species, respectively, according to the following reactions:

$$\text{MPO-I} + e^-_{aq} + H^+ \rightarrow \text{MPO-II} \quad (4)$$

$$\text{MPO-II} + e^-_{aq} + H^+ \rightarrow \text{Fe(III)-MPO} + H_2O \quad (5)$$

$$\text{Fe(III)-MPO} + e^-_{aq} + H^+ \rightarrow \text{Fe(II)-MPO} \quad (6)$$

Native MPO and MPO-I show Soret bands with a maximum at 430 nm, although extinction coefficients are rather different, while 456 nm and 476 nm Soret peaks are distinctive of MPO-II and Fe(II)-MPO, respectively. Therefore, samples of MPO-I and MPO-II were irradiated and consequent processes were followed by UV-Vis absorption spectroscopy in the region of those two wavelengths (430 and 450 nm), while pulse radiolysis of Fe(III)-MPO was followed at λ = 430 nm.

Formation of MPO-II according to reaction 4 involves an important absorption increase at λ = 456 nm, whereas a decrease must be observed at λ = 430 nm, as in reduction of Fe(III)-MPO (reaction 6). On the other hand, production of Fe(III)-MPO following reaction 5 features the opposite behaviour. However, absorption traces obtained upon reaction of e^-_{aq} with all oxidation intermediates show hardly any signal (Figure 10.1).

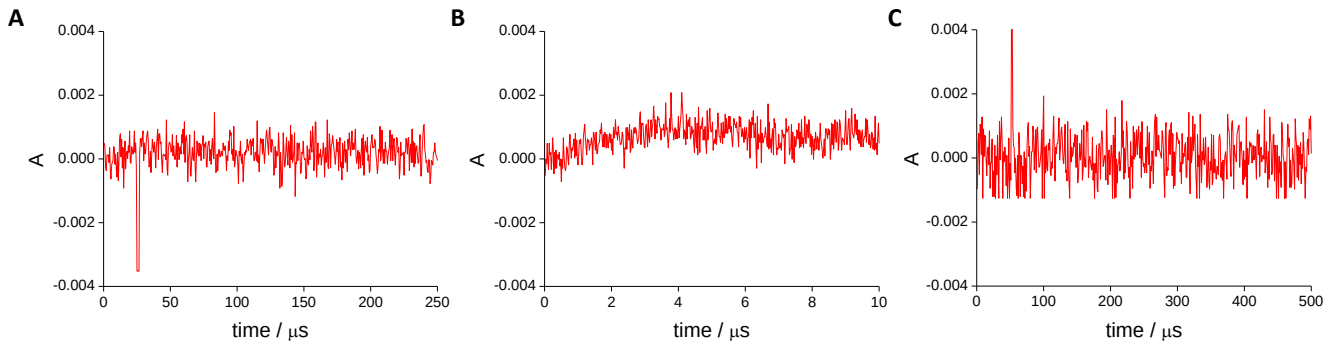

Figure 10.1. Absorption traces measured upon irradiation of (A) MPO-I at λ = 430 nm, (B) MPO-II at λ = 450 nm, and (C) Fe(III)-MPO at λ = 430 nm.

These results are not consistent with reactions 4 to 6. Despite the enzyme concentration is very low, heme group is an important chromophore so that all these enzymatic compounds present high extinction coefficients, *i.e.*, if any of those one-electron reduction processes takes place, a significant response would be expected. Surprisingly, the signal increased with repeated pulses; samples that had been previously irradiated with a great dose showed a much higher response to additional pulses, some traces are shown in Figure 10.2.

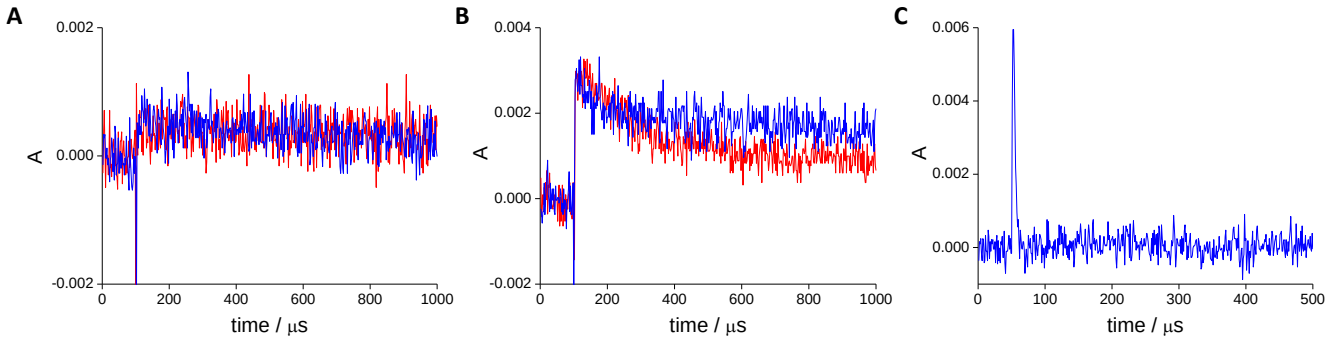

Figure 10.2. Kinetic traces obtained for the relaxation process upon reaction of e^-_{aq} with (A) MPO-I, (B) MPO-II, and (C) Fe(III)-MPO. Data acquired at λ = 430 nm (—) or 450 nm (—).

These traces still cannot account for reactions 4 to 6. The absorbance jump measured for irradiation of MPO-I (Figure 10.2A) is very low, and the obtained product seems to be reasonably stable. However, data collected for MPO-II (Figure 10.2B) correspond to typical relaxation kinetics, stable compounds are not formed and the absorbance change, although higher, is still too low to explain the reduction to Fe(III)-MPO and it is similar at both wavelengths.

Considering that the process observed is different for both compounds and that reactions 4 and 5 do not take place, a plausible explanation could be a reaction of e^-_{aq} with H_2O_2, present in a much higher concentration in the MPO-II sample. This process has been already studied:[27]

$$e^-_{aq} + H_2O_2 \rightarrow HO^- + HO^{\cdot} \qquad (7)$$

It exhibits a rate constant (k = 1.1 × 10^{10} $M^{-1}{\cdot}s^{-1}$) close to the diffusion limit, thus it may have some relevance, although the products are rapidly removed by the buffer and the scavenger (reaction 2). The possibility of hydroxyl radicals produced by reactions 1 and 7 interacting with H_2O_2 could be also considered:

$$HO^{\cdot} + H_2O_2 \rightarrow H_2O + HO_2^{\cdot} \qquad (8)$$

This process ($k = 2.7 \times 10^7$ $M^{-1}{\cdot}s^{-1}$) may compete with the reaction with the scavenger ($k = 6 \times 10^8$ $M^{-1}{\cdot}s^{-1}$),[27] but the rate constant of the reaction of hydroxyl radical with *tert*-butyl alcohol is one magnitude higher than that with hydrogen peroxide. Besides, concentration of the alcohol is much higher, so this compound effectively removes all $HO^{\cdot}$ and reaction 8 does not take place in a significant manner.

Moreover, if the process observed in Figure 10.2B corresponds to any reaction involving H_2O_2, it should be detectable from the first pulse, but this was not the case (Figure 10.1B). Furthermore, an important signal was also obtained with highly irradiated samples of Fe(III)-MPO (Figure 10.2C): the absorbance increase is even higher than with MPO-II and the subsequent decay shows much faster kinetics. This sample does not contain H_2O_2, so the reactions observed must involve the enzyme.

After the initial jump, kinetic traces draw typical relaxation processes. In order to get further information about the reactions undergone upon irradiation, UV-Vis spectra of a MPO-II sample were obtained after a number of pulses when response of further shots was rather stabilized (Figure 10.3). The spectrum is broad, extended over the entire measured range, with no characteristic peak, and showing undefined maxima at λ = 350 and 460 nm. This means either a highly diffused spin or that the reactions take place on different functional groups.

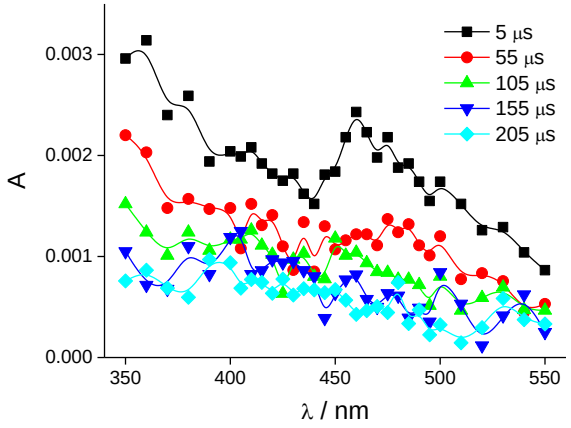

Figure 10.3. Time-resolved spectra following unspecific reduction of MPO by e^-_{aq}.

The kinetic analysis of the decay traces yielded rate constants that are wavelength dependent (Figure 10.4). This supports that hydrated electrons do not react with a single type of functional group but to several different functionalities. Therefore, if multiple reactions take place with hydrated electrons in a very complex molecule as MPO, and the protein structure gets progressively damaged by repetitive irradiation, the process is unlikely to be reproducible, but random effects should be then obtained. This could explain the diverse results obtained for the three different samples. The limited amount of available enzyme prevented the reiterative replication of measurements.

The fact that the initial pulses did not show any response is not yet explained. It can be inferred from previous findings that the enzyme possesses the capacity to remove hydrated electrons through very unspecific reactions, these excitations do not absorb in the studied region, they present extremely low absorption coefficients, or the electrons are very delocalized in the protein moiety. But the so-formed radicals may react within the peptide and after some pulses the protein structure cannot accept more electrons and starts getting damaged. Then, other functional groups are affected and the signal rises. We analyzed the effect of high irradiation doses on the enzymatic activity with the purpose of getting some insight into this damage.

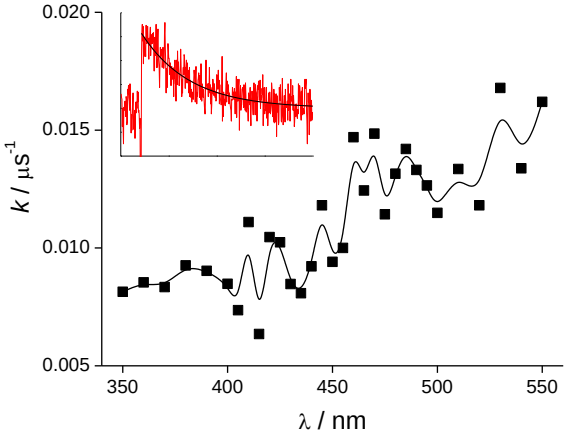

Figure 10.4. Obtained rate constant *vs*. wavelength for the decay process shown in Figure 10.3. Inset shows a typical first-order exponential fit.

Samples of MPO were irradiated with different doses, and the residual chlorination activity of the enzyme was determined by measuring its ability to oxidize the α-amino acid glycine. MPO reacts with H_2O_2, Cl^-, and Gly according to the following summarized reactions:

$$MPO + H_2O_2 + Cl^- + H^+ \rightarrow MPO + HClO + H_2O \quad (9)$$

$$HClO + Gly \rightarrow N\text{-Cl Gly} + H_2O \quad (10)$$

Mechanism 1 (reactions 9 & 10) involves the formation of free HClO, while in mechanism 2 (reactions 11 & 12) an enzymatic intermediate with chlorinating ability reacts directly with the amino acid:[21]

$$Fe(III)\text{-}MPO + H_2O_2 + Cl^- \rightarrow MPO\text{-}I\text{-}Cl + H_2O \quad (11)$$

$$MPO\text{-}I\text{-}Cl + Gly + H^+ \rightarrow Fe(III)\text{-}MPO + N\text{-Cl Gly} + H_2O \quad (12)$$

The overall reaction is the same in both pathways and it does not affect the outcomes inferred from the data obtained in this study.

Initial rate of chlorination (actually, earliest rate after steady state is achieved following the unobserved initial burst. See Chapter 8 for a more detailed discussion) is represented *versus* the total absorbed dose in Figure 10.5. Rate of chlorination decreases with increasing doses but some activity remains after very intense irradiation, which indicates that excitation does not take place at the active site but at the surrounding peptide chains. Previous results already revealed that electrons did not reduce heme Fe centre, but these data also suggest that hydrated electrons do not modify the protein structure at the active site, as in this case a dramatic effect on the enzymatic activity would be obtained.

Substrate binding site of MPO is hidden inside the enzyme, situated in the middle of the molecule,[28, 29] with a narrow channel connecting it to the outer medium and sterically hindered for bulky substrates.[3] Typically, hydrated electrons are situated in a cavity-like structure *ca*. 2.5 Å in radius and surrounded by a cluster of water molecules that may obstruct the access through this funnel-shaped passage. Furthermore, hydrated electrons are the strongest reducing agent in water and are extremely reactive, so we can assume that if entering this substrate channel, they may react with any available oxidizable group situated in the walls, at a short distance away, before reaching the distal cavity and the active site therein. Therefore, hydrated electrons do not enter and react with or in the close proximity of the active site as it remains completely functional. All these results indicate that excitation processes take place with different functional groups on the surface, also in places close to the substrate channel entry. These areas develop damaged, either affecting the protein tertiary structure, hence affecting the oxidation potential of the enzyme, or hindering the access of substrates to the heme pocket,

and then accounting for the slower chlorination rate. Thus, the protein is packed around the heme for shielding from potentially harmful molecules and has a protective role as observed in myoglobin.

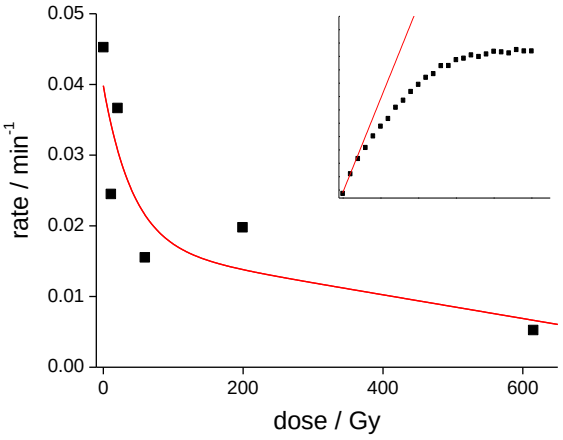

Figure 10.5. Initial chlorination rate of Gly *vs.* irradiation dose. Inset shows a typical fit of the initial rate.

10.4 Conclusions

Pulse radiolysis experiments were performed to study the reactions of hydrated electrons with MPO. One-electron reduction of different oxidation intermediates did not produce any significant signal, indicating that the reaction does not take place at the highly chromophoric heme group, which is hindered in the core of MPO superstructure, but on other parts of the molecule.

The spectrum observed after irradiation was very broad indicating either that the spin is highly diffused or that multiple functional groups undergo reaction. Relaxation kinetics show wavelength-dependent rates, supporting that different processes are being followed and that, therefore, hydrated electrons must react with several functional groups placed at the more accessible surface of the enzyme.

In order to clarify whether the hemes herein, and consequently the active sites, keep unchanged, the effect of irradiation on the chlorinating activity of MPO was analyzed. At low doses, the enzyme itself acts as a scavenger, accepting electrons while showing a modest decrease in its activity. Besides, after a very high irradiation dose the enzyme was still able to chlorinate, indicating that no damage occurs in the active site, hindered at the end of the substrate channel, and that the protein plays a protective role.

10.5 References

1. C. C. Winterbourn, M. C. M. Vissers, and A. J. Kettle, *Myeloperoxidase.* Curr. Opin. Hematol., 2000 **7** (1) 53-58.
2. J. E. Harrison and J. Schultz, *Studies on the chlorinating activity of myeloperoxidase.* J. Biol. Chem., 1976 **251** (5) 1371-1374.
3. D. R. Ramos, M. V. García, M. Canle L., J. A. Santaballa, P. G. Furtmüller, and C. Obinger, *Myeloperoxidase-catalyzed chlorination: the quest for the active species.* J. Inorg. Biochem., 2008 **102** (5-6) 1300-1311.
4. J. Arnhold, P. G. Furtmüller, and C. Obinger, *Redox properties of myeloperoxidase.* Redox Rep., 2003 **8** (4) 179-186.
5. A. Taurog, *Molecular evolution of thyroid peroxidase.* Biochimie, 1999 **81** (5) 557-562.
6. B. S. Berlett and E. R. Stadtman, *Protein oxidation in aging, disease, and oxidative stress.* J. Biol. Chem., 1997 **272** (33) 20313-20316.

7. C. C. Winterbourn and A. J. Kettle, *Reactions of superoxide with myeloperoxidase and its products.* Jpn. J. Infect. Dis., 2004 **57** (5) S31-S33.
8. H. A. Schwarz, *Free radicals generated by radiolysis of aqueous solutions.* J. Chem. Educ., 1981 **58** (2) 101-105.
9. H. Hori and M. Ikeda-Saito, *Photochemically modified myeloperoxidase, with optical spectral properties analogous to those of lactoperoxidase, retains its original catalytic activity.* Biochemistry, 1990 **29** (30) 7106-7112.
10. N. Shimizu, K. Kobayashi, and K. Hayashi, *Kinetics of the reaction of superoxide anion with ferric horseradish peroxidase.* Biochim. Biophys. Acta, 1989 **995** (2) 133-137.
11. L. Gebicka and J. L. Gebicki, *Reactions of radiolytically-generated superoxide anion with higher oxidation states of lactoperoxidase.* Int. J. Radiat. Biol., 1993 **63** (5) 565-568.
12. L. Gebicka and J. L. Gebicki, *Scavenging of oxygen radicals by heme peroxidases.* Acta Biochim. Pol., 1996 **43** (4) 673-678.
13. A. J. Kettle, R. F. Anderson, M. B. Hampton, and C. C. Winterbourn, *Reactions of superoxide with myeloperoxidase.* Biochemistry, 2007 **46** (16) 4888-4897.
14. A. J. Kettle, A. Maroz, G. Woodroffe, C. C. Winterbourn, and R. F. Anderson, *Spectral and kinetic evidence for reaction of superoxide with compound I of myeloperoxidase.* Free Radic. Biol. Med., 2011 **51** (12) 2190-2194.
15. L. Gebicka and J. L. Gebicki, *Modification of horseradish peroxidase induced by hydroxyl radicals. The influence of oxygen.* Biochimie, 1996 **78** (1) 62-65.
16. C. C. Winterbourn, *Myeloperoxidase as an effective inhibitor of hydroxyl radical production. Implications for the oxidative reactions of neutrophils.* J. Clin. Invest., 1986 **78** (2) 545-550.
17. L. Gebicka and J. L. Gebicki, *Reactions of hydrated electrons with horseradish peroxidase: a pulse radiolysis study.* Int. J. Radiat. Biol., 1991 **59** (3) 617-623.
18. L. Gebicka and J. L. Gebicki, *Redox transformations in peroxidases studied by pulse radiolysis technique.* Radiat. Phys. Chem., 1992 **39** (1) 113-116.
19. I. I. Vlasova, J. Arnhold, A. N. Osipov, and O. M. Panasenko, *pH-dependent regulation of myeloperoxidase activity.* Biochemistry (Moscow), 2006 **71** (6) 667-677.
20. H. Spalteholz, O. M. Panasenko, and J. Arnhold, *Formation of reactive halide species by myeloperoxidase and eosinophil peroxidase.* Arch. Biochem. Biophys., 2006 **445** (2) 225-234.
21. D. R. Ramos, M. V. García, M. Canle L., J. A. Santaballa, P. G. Furtmüller, and C. Obinger, *Myeloperoxidase-catalyzed taurine chlorination: initial versus equilibrium rate.* Arch. Biochem. Biophys., 2007 **466** (2) 221-233.
22. M. S. Jensen and D. F. Bainton, *Temporal changes in pH within the phagocytic vacuole of the polymorphonuclear neutrophilic leukocyte.* J. Cell. Biol., 1973 **56** (2) 379-388.
23. T. Odajima and I. Yamazaki, *Myeloperoxidase of the leukocyte of normal blood. I. Reaction of myeloperoxidase with hydrogen peroxide.* Biochim. Biophys. Acta, 1970 **206** (1) 71-77.
24. R. F. Beers and I. W. Sizer, *A spectrophotometric method for measuring the breakdown of hydrogen peroxide by catalase.* J. Biol. Chem., 1952 **195** (1) 133-140.
25. P. G. Furtmüller, C. Obinger, Y. Hsuanyu, and H. B. Dunford, *Mechanism of reaction of myeloperoxidase with hydrogen peroxide and chloride ion.* Eur. J. Biochem., 2000 **267** (19) 5858-5864.
26. C. J. van Dalen, M. W. Whitehouse, C. C. Winterbourn, and A. J. Kettle, *Thiocyanate and chloride as competing substrates for myeloperoxidase.* Biochem. J., 1997 **327** (2) 487-492.
27. G. V. Buxton, C. L. Greenstock, W. P. Helman, and A. B. Ross, *Critical review of rate constants for reactions of hydrated electrons, hydrogen atoms and hydroxyl radicals (·OH/·O⁻) in aqueous solution.* J. Phys. Chem. Ref. Data,

1988 **17** (2) 513-886.

28. T. J. Fiedler, C. A. Davey, and R. E. Fenna, *X-ray crystal structure and characterization of halide-binding sites of human myeloperoxidase at 1.8 A resolution.* J. Biol. Chem., 2000 **275** (16) 11964-11971.

29. M. Blair-Johnson, T. Fiedler, and R. Fenna, *Human myeloperoxidase: structure of a cyanide complex and its interaction with bromide and thiocyanate substrates at 1.9 A resolution.* Biochemistry, 2001 **40** (46) 13990-13997.

CHAPTER 11

Understanding the origin of the shared reactivity and properties of peroxidases: a DFT study

Everything should be made as simple as possible,
but not simpler.

Albert Einstein

11.1 Introduction

Heme-containing proteins and enzymes are ubiquitous and catalyze many different reactions including electron transfer, oxygen binding, oxidations, oxygenations, etc.[1, 2] Heme peroxidases use heme *b* or posttranslationally modified heme to catalyze the hydrogen peroxide-mediated one- and two-electron oxidation of a myriad of molecules including aromatic molecules, cations, anions, or even proteins. Four heme peroxidase superfamilies arose independently during evolution, which differ in overall fold, active site architecture (*e.g.* histidine or cysteine as proximal ligand), and enzymatic activities.[3]

Peroxidases operate in a complex multistep mechanism including several redox intermediates (Scheme 11.1), which were studied by various experimental[4, 5] and computational[6-8] means. In general, native ferric peroxidase (Fe(III)-PO) uses H_2O_2, or other oxidants, to generate a ferryl (Fe(IV)=O) π-cation radical complex called compound I (PO-I) having incorporated one oxygen atom derived from heterolytic cleavage of hydrogen peroxide.[9] This species can be one-electron reduced to compound II (PO-II), which also contains a ferryl group, while reversible reduction of the ferric protein yields the ferrous species (Fe(II)-PO).

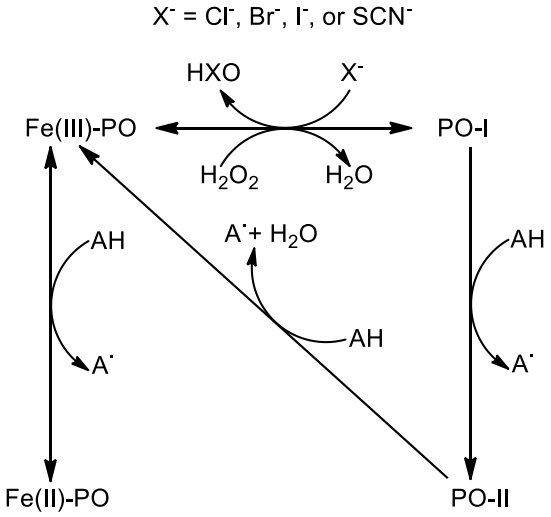

Scheme 11.1. Interconversion between peroxidase species: Fe(III)-PO, ferric state; Fe(II)-PO, ferrous state; PO-I, compound I; PO-II, compound II.

Most experimental studies on the electronic structure and reactivity of peroxidases were carried out under neutral or basic conditions, whereas less attention was paid to acidic pH values despite the fact that the pH optimum of many peroxidase activities is below pH 7. For example, chloride oxidation by human myeloperoxidase (MPO) is significantly more efficient at pH 5 compared to pH 7.[4, 10-12] Under acidic pH conditions the occurrence of H_2O and H^+ rather than HO^- at the distal heme cavity has to be taken into account. Crystal structures of many peroxidases show the presence of a discrete water in an axial position to the heme iron in the distal cavity.[9] Thus, both H_2O and H^+ were considered in the computational model employed in this work in order to probe their impact on the metal centre or ferryl group.

Protons are directly involved in peroxidase reactivity (Scheme 11.1). Protonation of the ferryl centre has been a central issue to justify the different Fe–O bond distances measured with X-ray diffraction structural analysis for compounds I and II.[13] On the other hand, oxo-ferryl stretching frequencies obtained with resonance Raman spectroscopy (RR) suggest that both compounds exhibit a similar short Fe–O distance,[14, 15] indicative of unprotonated ferryl oxygen.[16] Extended X-ray absorption fine structure (EXAFS) experiments also support unprotonated compound II.[17] However, iron photoreduction may occur upon X-ray radiation or even due to laser excitation, leading to some uncertainty about the metal oxidation state in those measurements. Thus, some inconsistencies have been found, as a long Fe–O distance

measured by X-ray diffraction in compound I of cytochrome *c* peroxidase (CCP),[18] or short[17] and long[19] Fe–O distances obtained with EXAFS for horseradish peroxidase (HRP) compound II. Protonation of the ferryl oxygen has been observed for chloroperoxidase (CPO, a heme enzyme with proximal thiolate) compound II by RR[20] and EXAFS[21], whereas myoglobin compound II seems to be unprotonated even at pH 3.9 according to RR and EXAFS measurements.[22] Thus, experimental data are often inconsistent, and compound II of different heme proteins behave differently. On the other hand, neutron diffraction is a reliable technique for characterization and visualization of protons. Moreover, photoreduction does not occur. From CCP the neutron structure of the ferric and compound I states[23] and from ascorbate peroxidase (APX) of compound II[24] are available, and show the presence of a Fe(IV)–OH group in compound II.

A full mechanistic understanding of peroxidases needs, in addition to study the impact of the protein, the knowledge of the underlying chemistry of all relevant redox intermediates, which cannot be provided by experimental means only. Theoretical characterization of geometry and energy of different heme compounds has been successfully performed with different computational methods, confirming many of the empirical observations. For unravelling mechanistic details in (bio)chemistry[25] electronic structure calculations can be very helpful to complement insufficient experimental data. Peroxidases share many properties and have similar molecular structures at the active site. However, the only common part of all these enzymes, at least for three superfamilies, is the Fe-centred porphine ring coordinated to a proximal imidazole. The proximal histidine may display different positions, which have an effect on imidazole rotation, and it is surrounded by pretty dissimilar environments that affect its charge distribution. Heme lateral substituents are also modified in the peroxidase-cyclooxygenase superfamily, and some residues are highly conserved in the distal heme pocket, but their positions with respect to heme also vary. Therefore, it seems that the prevalent behaviour of these enzymes actually arises from just a quite small part of their active site, while the specific performance of a particular peroxidase results from the remaining part of the active site and its environment. This arrangement is also common to other similar enzymes, as for example globins. However, the model revealed not adequate for the study of these proteins.

The aim of this work is the correct description of some common general features of peroxidases by means of electronic structure calculations using a suitable common molecular model together with a computational level that yields reliable data at relatively low computational cost. To this end geometric, electronic, and thermodynamic parameters of a reduced model of the active site of native ferric peroxidase, ferrous peroxidase, peroxidase compounds I and II, and their aquo and protonated complexes have been calculated. Obtained computational data (UV-Vis spectra, pK_a, or reduction potentials) are compared with experimental ones to examine the suitability of both the molecular model and the method of calculation, and to validate protonation states and interactions with distal water molecules. Furthermore, this work offers a simple methodology to obtain additional information on different heme peroxidases that cannot be gathered by experimental techniques, and it also emerges as an adequate starting point for further computational research on these enzymes in general, or for the analysis of more specific properties of single peroxidases by *ad hoc* modification of the molecular model employed to account for the particular structure and specific reactivity.

11.2 Computational details

11.2.1 Models

Computational studies on heme proteins have used several molecular models of the active site, ranging from very few atoms surrounding the heme metal centre to others concerning the whole protein.[26] Some research was performed using full porphyrin and axial imidazole, which was the choice in this study.[16] Peripheral substituents can affect heme configuration; accordingly, a usual approach in electronic structure calculations dealing with heme porphyrins is to use X-ray structures to consider such effects rather than including the covalently bonded residues in heavy geometry optimizations.[27] Questions arose as to whether crystal arrangements are the same as in solution; in fact, some differences between solution (NMR) and crystal geometries of cytochrome *c* have been observed.[28] Furthermore, most X-ray results give the structure of the native enzyme, whereas crystallographic structures are not available for all the species here

considered.

Besides the described general peroxidase behaviour, peroxidases of the four superfamilies[3] exhibit diverse enzymatic activities at different optimum conditions. The origin of these differences is related to variations in the multistep reaction mechanisms, triggered by the protein environment. The use of a specific experimental structure would lead to a particular property, and not to the desired general peroxidase behaviour, which is the aim of this study. On the other hand, the use of geometry optimization on isolated porphyrins may lead to electronic ground states different from those seen in proteins.[29]

Compromising previous evidences, in this work the active site was modelled by using Fe-centred porphine, *i.e.* the porphyrin ring without any side chains, and an imidazole ring coordinated to the metal in an axial position, mimicking the proximal histidine (Figure 11.1). The latter is found in three out of four heme peroxidases superfamilies.[3] This arrangement was selected on account of studies showing that the axial imidazole substantially enhances the binding energy of ligands in contrast to vinyl and propionate side chains,[29-31] which are also modified in the peroxidase-cyclooxygenase superfamily.[3] The distal sixth coordination site is vacant in ferric and ferrous states of peroxidases, while an oxygen atom plays the role of sixth ligand in the case of the ferryl species compounds I and II. According to crystallographic studies, water molecules (or related species) are closer to the heme iron or ferryl oxygen atoms than any other amino acid residue. In addition, protonation reactions might occur. The present computational study considers all possible scenarios (even the untenable ferric and ferrous species with protonated iron) in order to perform an exhaustive analysis.

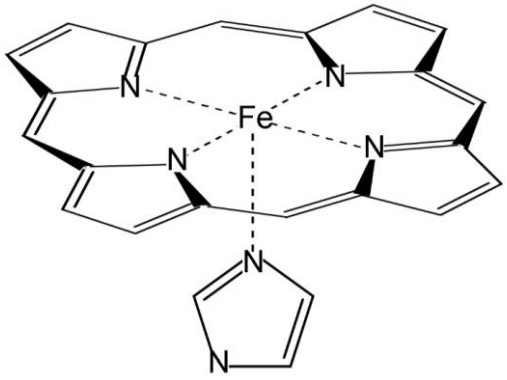

Figure 11.1. Molecular arrangement employed to model the active site of peroxidases.

It should be taken into account that this reduced model of the active site ignores the influence of the protein on heme stabilization. This effect could be separated into two different parts. On one hand, the protein directly interacts with the heme substituents by establishing covalent bonds. Posttranslationally modified heme is found in the peroxidase-cyclooxygenase superfamily,[3] with representatives showing one, two, or three covalent bonds. Additionally, non-covalent interactions including hydrogen bonding or long-distance interactions caused by charge distribution and dielectric properties of the protein have an impact on the chemical properties of both prosthetic group and the proximal ligand. In this regard, many studies explicitly compute the contribution of the protein, usually applying less resource-demanding methods, such as QM/MM, Car Parrinello, or Monte Carlo,[26, 32-34] to account for the electronic and steric effects of the protein. Other works apply solvation models to reproduce the bulk protein and solvent effect on the active site.[35] This approach seems the most adequate to combine with the simple molecular model employed in this study, and also yields more general results as desired.

11.2.2 Methods

Density functional theory (DFT) methods provide excellent geometries of porphyrins,[36-39] although typically just give

semiquantitative results for energies calculation.[40] Among these, the B3LYP functional reveals quite satisfactory due to its superior performance for calculating accurate relative energies and frequencies for small molecules and biochemical metal complexes at a reasonable computational cost.[41-43] However, the B3LYP method yields spin states very close in energy, even exchanging ground state assignments.[29]

The suitability of different DFT functionals for correct calculation of a Fe-centred porphyrin ring coordinated to an imidazole group, *i.e.*, the same model used in this work, has been studied by comparison of these methods with the results obtained with high-level CCSD(T) calculations with large basis sets for several model iron compounds.[44] All studied functionals showed a good performance in geometry optimization with respect to crystal structures. Also, hybrid DFT functionals yielded reasonably accurate relative energies of the different spin states at a lower computational cost. Additionally, some results obtained for bond dissociation energies of iron ligands suggest that B3LYP describes bonding to oxygen-containing ligands more accurately than other functionals.[44] Electron and spin densities for iron porphyrins were also calculated with both DFT and coupled cluster methods.[36, 45, 46] The good agreement between obtained results corroborates the validity of the DFT computations for the comparison of relative energies and evaluation of the stability of the different states of the considered systems.

Thus, DFT-based calculations were done using the unrestricted Becke's three-parameter hybrid method[47] with the correlation functional of Lee, Yang and Parr, which includes both local and non-local terms[48, 49] (UB3LYP). The double-ζ 6-31G and lower basis sets failed to yield appropriate geometries, namely the lack of planarity of the porphyrin group, more than the expected domed structure caused by axial ligands and/or iron out-of-plane position. Inclusion of a polarization function (6-31G*) led to a remarkable improvement. Higher basis sets were also examined and did not show any significant improvement, while the required computational resources increased notably.

Regardless of problems related to assignation of electronic ground states, geometry optimization revealed essential to adequately reproduce the structures and, as a result, their thermodynamics. Therefore, geometry optimizations were carried out with Gaussian 03[50] at UB3LYP/6-31G* computational method with the quadratically convergent SCF algorithm,[51] which showed enhanced convergence and, consequently, better performance for the minima optimization. Harmonic frequencies were calculated to obtain zero point energies and thermal corrections to enthalpies and Gibbs free energies at 298.15 K.

Furthermore, full geometry optimization was carried out within a broad range of spin multiplicities ($0 \leq S \leq 4$) to observe any possible unexpected anomaly, even though only values determined at stable low and high spin are explicitly considered for Fe(III)-PO, PO-I, and PO-II. The d^6 Fe(II) atom can exhibit three spin states: $S = 0$ (low spin), $S = 1$ (intermediate spin), and $S = 2$ (high spin). Therefore, in the case of ferrous species data from these states are collected in this work. Exceptional multiplicities ($S \geq 3$) were computed to rule out the possibility of stable species with very high number of unpaired electrons. These high spin species always revealed thermodynamically unfavourable. In the reminder of the chapter total spin will be referred to either as S (Σs) or as spin multiplicity.

Single point calculations, using the polarized continuum model (PCM),[52] were performed over the UB3LYP/6-31G* optimized structures in order to estimate the Gibbs free energy of interaction with water molecules contained in the distal heme pocket. Water has a more important effect on the four species studied than bulk protein, as the solvent interacts more closely with iron atom and oxo-ferryl group, and these interactions must differ between redox intermediates. The effect of the protein, although more remarkable on heme edges, may partially cancel out when comparing different species. Thus, the continuum has been selected with parameters corresponding to aqueous solvation. Besides, some calculations have been performed employing a dielectric constant typical for proteins ($\varepsilon = 4$) for comparison. The cavity used for PCM calculations was built employing atomic radii of the United Atom Topological Model (UA0). Additional spheres were included on H atoms in a very few cases, resulting in two disjoint cavities. Gaussian default values were selected for solvent water and for all other parameters of spheres definition.

All computational values involving solvation were corrected as for the standard state in aqueous solution. Water

concentration is usually taken as 55.5 M, but this is not the case within the distal cavity of peroxidases, where only some discrete molecules have been detected. Therefore, also 1 M concentration has been considered for this species. Published thermodynamic parameters were employed for proton in the gas phase[53] and aqueous solution[54, 55], and also for the electron in the gas phase[56].

Excitation energies were calculated with the time-dependent DFT (TD-DFT) approach considering the lowest 50 singlet excited states, both with and without solvation. UV-Vis convoluted spectra were extracted from Gaussian output files using the SWizard program[57] by using Gaussian distributions with a peak half-width of 2500 cm^{-1}. This combination was successfully applied to obtain UV-Vis spectra for similar chemical systems,[35] and yields adequate maximum heights of the Soret band for comparison with experimental values.

Position of the iron atom with respect to heme plane was worked out as depicted in Figure 11.2. Best-fitting plane was obtained from the four pyrrole nitrogen atoms (pyrrole plane), and distance to Fe (Fe–pp) was calculated. Relevant bond orders in all considered species were calculated using the natural bond orbital (NBO) analysis of Weinhold *et al*.[58-60]

The dissociation equilibrium of water complexes, the thermodynamics of protonation processes reported as pK_as, and reduction potentials were calculated as shown below. Reduction potentials are usually reported as relative to the standard hydrogen electrode (SHE) with an absolute reduction potential $E°$ = 4.44 V at 298.15 K,[61] although a small deviation is obtained if other values proposed for the absolute potential of SHE are employed.[62]

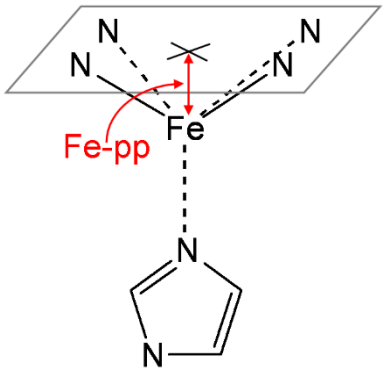

Figure 11.2. Iron out-of-plane distance (Fe–pp), described as the distance between iron atom and the plane defined by the four pyrrole nitrogen atoms.

11.2.3 Calculation of some thermodynamic parameters

The dissociation equilibrium of water complexes *in vacuo* is expressed by the following equation:

$$A\text{-}H_2O \xrightleftharpoons{\Delta G_{H2O}} A + H_2O$$

whereas the thermodynamic cycle shown in Scheme 11.2 was used for the aquo complexes equilibrium in solution, where $\Delta G°_{H2O}$(aq) is the standard-state Gibbs free energy of dissociation in aqueous solution, and ΔG_i(solv) is the solvation free energy of "i".

Thermodynamics of protonation processes are generally reported by the corresponding pK_a value. Its computational estimation requires the calculation of the optimized geometry and corresponding Gibbs free energy of the protonated and unprotonated forms of the ionizable groups under study, according to the following acid-base equilibrium:

$$AH \xrightleftharpoons{\Delta G°_{AH}} A^- + H^+$$

The protonated form, denoted AH, has a net positive charge one unit higher than the unprotonated form, A^-. The expression utilized for the absolute pK_a calculation is given by:

$$pK_a = \Delta G^\circ_{AH} / 2.303RT$$

This equation can be used in the gas phase, which is less relevant and cannot be compared to empirical results, or in solution by using a thermodynamic cycle equivalent to that shown in Scheme 11.2. Again, solvation values must be corrected to take into account the transformation of concentration units in the aqueous phase (atm to M).

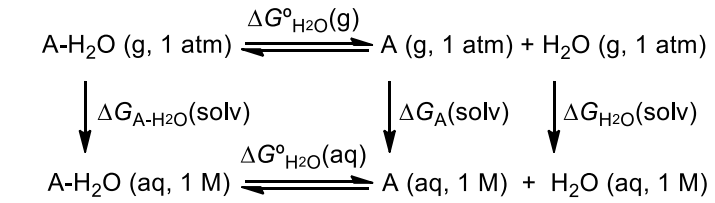

$$\Delta G^\circ_{H_2O}(aq) = \Delta G^\circ_{H_2O}(g) + \Delta G_A(solv) + \Delta G_{H_2O}(solv) - \Delta G_{A\text{-}H_2O}(solv)$$

Scheme 11.2. Thermodynamic cycle used to calculate the Gibbs free energy for the dissociation of the aquo complexes involving solvation. pK_a calculation implies the replacement of the water molecule by a proton.

One-electron reduction potential of any species A can be calculated through the thermodynamic cycle shown in Scheme 11.3. Note that the standard state for e^- is the gas phase.

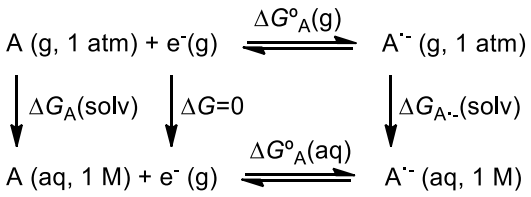

$$\Delta G^\circ_A(aq) = \Delta G^\circ_A(g) + \Delta G_{A^{\bullet-}}(solv) - \Delta G_A(solv)$$

Scheme 11.3. Thermodynamic cycle used to calculate absolute reduction potentials.

The absolute reduction potential is calculated as:

$$E^\circ = -\frac{\Delta G^\circ_A(aq)}{nF}$$

where n is the number of electrons generated in the half-reaction and *F* is the Faraday constant.

11.3 Results

11.3.1 Geometry and charges

All structures, fully optimized at the most stable spin state (see thermodynamic section for details), are shown in Figure 11.3. Ferric native enzyme (Fe(III)-PO) and ferrous species (Fe(II)-PO), as well as aquo complex of the latter are depicted at

high-spin state. The protonated ferrous state, Fe(II)-PO-H, shows an intermediate-spin state. All other species correspond to low-spin. Relevant geometrical parameters are collected in Table S11.1. Representative corresponding geometrical data empirically measured for HRP,[63, 64] CCP,[13, 18, 23] APX,[13, 24, 65] LPO (lactoperoxidase),[66] and MPO[67] are also gathered in Table S11.2, and are employed as experimental reference values along the manuscript for comparison. It is not our aim to show an exhaustive collection of data that would be difficult to analyze, as some geometries found in the literature differ greatly from most of the other structures. In this model, imidazole is not linked to the protein and, therefore, exhibits free rotation around its axial position, while this movement would be more constrained if the proximal His and whole peptide chain were considered. Furthermore, according to previous computational studies this rotation only accounts for a few kJ·mol^{-1}.[68] Thus, calculated orientation of this imidazole is disregarded in the discussion. Significant net Mulliken charges[69] calculated at the UB3LYP/6-31G* level with and without PCM aqueous solvation are shown in Table S11.3.

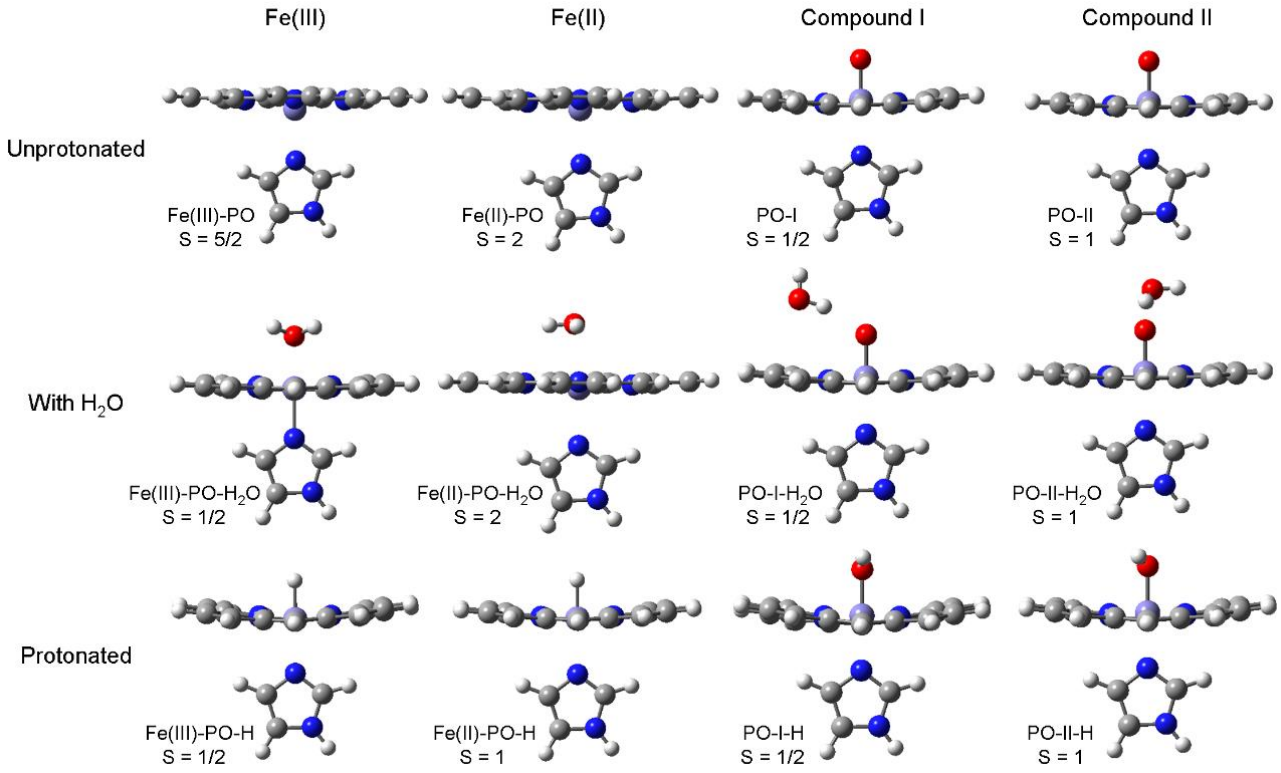

Figure 11.3. Structures optimized *in vacuo* at the UB3LYP/6-31G* computational level and at the most stable feasible spin state (according to their Gibbs free energy) for Fe(III) native peroxidase, ferrous species, compound I, and compound II, either unprotonated or with a bonded H_2O discrete molecule or protonated at a distal axial position.

Bare Fe(III)-PO and Fe(II)-PO share similar geometry, even closer when considering equivalent spin states. Slightly out-of-plane Fe atom in the proximal direction is observed, more evident in the case of ferric species, while heme planarity remains despite shift of the metal. Metal bonding to imidazole is clearly tighter for low-spin species, as indicated by both Fe–N_i (imidazole N) distances and bond orders. Distances between the heme iron and pyrrole nitrogens, Fe–N_p (pyrrole N), are nearly equal for Fe(III)-PO and Fe(II)-PO, with variations of only *ca.* 0.02 Å. Computed values for both high spin species adequately fit in the empirical ranges observed, but the outer position of Fe with respect to heme plane is more pronounced in the calculations, probably due to the lack of distal interactions in the model. Higher positive charge (approx. 0.2 a.u.) is observed on Fe(III) atom with respect to Fe(II). Additionally, *ca.* 0.7 a.u. more negative values were obtained for the

porphine ring in the case of Fe(II)-PO, accounting for the one-electron reduction process in going from ferric to ferrous species, and the fact that formation of this species should involve the gain of a proton at the heme moiety. Mulliken net charges calculated with the PCM solvation model are slightly higher than *in vacuo*. The polarized continuum stabilizes atomic charges (typical of polar solvents like water) and charge polarization increases.

Addition of one water molecule causes minor molecular reorganization, primarily a displacement of Fe atom into porphyrin plane, more evident in the case of the ferric species, which results in some lengthening of the Fe–N_i bond. Again heme planarity is retained. Obtained geometry of these two compounds is, therefore, more similar than observed with bare species. A very weak bond is formed between the metal and water oxygen (O_W). Associated Wiberg bond indices[70] are characteristic of hydrogen bonding. Fe–O_W distance calculated for the ferric species is shorter than for most of the reference peroxidases, although APX shows a water molecule even closer to the metal. On the other hand, calculations on the aquo-ferrous complex yield the water molecule situated at a further distance compared with experimental data. These complexes were produced by photoreduction of a ferryl species (compound I), and in this process ferryl oxygen converts into water. Thus, structures obtained by direct reduction of ferric native enzymes could be different, at least with regard to the location of this water molecule. The water molecule is axially placed, as revealed by a ~180° angle with respect to N_i, as observed in crystallographic structures as well, and shows a net positive charge, indicating that charge transfer takes place from the porphine ring to the water molecule. A stronger Fe–O_W bond is formed for low spin species and more charge is transferred in this case.

Despite the addition of net positive charge, protonation does not produce any significant effect on heme structure either. A shift is observed in Fe position, the metal atom becoming closer to heme pyrrole plane except in a few particular cases (with non-feasible spins), where the contrary effect was obtained. These anomalous structures correspond to some species where the proton could not be optimized in the close proximity of Fe. In general, the bond to imidazole nitrogen weakens although not always accompanied by a longer Fe–N_i distance. The proton effectively binds to iron (apart from the exceptions above mentioned) losing most of its proton character, as revealed by its low residual positive charge with the lost charge being gained by the porphine ring. Proton addition to ferrous and ferric species produces some distortion on heme planarity. The shorter the Fe–H bond, the more evident the effect, causing a saddle-shape conformation of heme (displacement of two opposite pyrrole units towards distal side while the other two move in the proximal direction) that is not observed experimentally in any case, and is coupled with asymmetric Fe–N_p linkages.

Compounds I and II exhibit almost the same geometry. The iron atom is hexacoordinate, forming a strong bond with ferryl oxygen (O_{Fe}), characterized by a short distance (< 1.62 Å) and bond orders ~1.5 (unless $S \geq 3$). This results in a somewhat longer Fe–N_i bond with respect to Fe(III)-PO and Fe(II)-PO. Similar Fe–O_{Fe} distances have been measured for CCP compound I both by X-ray and neutron diffraction crystallography, whereas other peroxidases show a slightly longer bond. This bond distribution involves an out-of-plane metal centre displaced towards the distal direction, which is closely related to the Fe–O_{Fe} bond strength. In all cases O_{Fe} exhibits a charge around –0.45 a.u. (–0.55 a.u. with solvation) mostly counterweighed by less negative charge in the porphine ring and slightly higher positive charge on Fe. Compound I in most heme peroxidases contains a porphyrin π-cation radical, therefore, lower negative charge on this ring is obtained in the case of PO-I with respect to other unprotonated species. This charge must be more positive considering the effect of heme side chains and interactions with adjacent protein. Upon addition of ferryl oxygen to the model, heme planarity is mostly conserved, although minor saddle-type conformation is observed.

Contrary to previous heme-aquo complexes, addition of H-bonded water to PO-I and PO-II causes only a minor polarization on both the water molecule and the heme moiety, almost no charge transfer takes place in this step. This discrete water molecule does not lie at the distal axis. Connecting H forms a ~120° angle with respect to Fe, typical of an sp^2 hybridized orbital, which corresponds to the electronic configuration of a double bonded oxygen atom (Fe=O).[71] Wiberg bond analysis yields a very low O_{Fe}–H value, which indicates a weak H-bond, accompanied by a slight change in the length and strength of the Fe–O_{Fe} ferryl bond and, in some cases, an opposite effect on the Fe–N_i bond. Still, calculated forces seem

stronger than in peroxidase crystals, where the angles are also different, as water molecules in the distal cavity generally lie at a further distance from O_{Fe} and are stabilized by other surrounding interactions.

Of great significance is the evident lengthening coupled with bond order decrease observed for Fe–O_{Fe} in the case of protonation of PO-I and PO-II. The distance calculated for PO-I-H with S = 1/2 is pretty similar to APX compound I, whereas Fe–O_{Fe} bond obtained for PO-II-H with $S \geq 2$ is in good agreement with all four compound II structures used as reference. Lower spin states yield too short distances. A concerted strengthening of the Fe–N_i interaction both in terms of distance and bond order is produced as the metal approaches to the heme pyrrole plane (PO-II-H at spin S = 2 reveals anomalous). This effect is not clearly observed in the experimental data. Besides, heme planarity becomes distorted, attaining saddle-like conformation, more apparent at the two lowest spin states. The proton effectively binds to O_{Fe} and transfers some charge to the heme but, in this case, keeping its proton character, *i.e.,* computations yield a remaining positive charge between 0.4 and 0.5 a.u. on this atom. Further polarization is also observed upon protonation. Thus, O_{Fe} increases its negative charge (0.2 - 0.3 a.u.) while the positive charge mostly accumulates on the porphine ring. The weakening of the Fe–O_{Fe} bond results in a different hybridization of O_{Fe} atom, approaching to sp^3, revealed by the lower value calculated for the Fe–O_{Fe}–H angle. However, the opposite behaviour is observed for protonated APX compound II (142°), perhaps related to other distal interactions, although this proton does not form a linear H-bond to any other neighboured atom but the proximity of a water molecule could be responsible for some steric distortion. Changes in structure and charge distribution are rather similar for the protonation of these two species, and also equivalent to the effect observed upon water addition, although to a much higher extent.

11.3.2 Thermodynamic parameters

Relative free energy values are collected in Table 11.1. The parent unprotonated species with the experimental most stable spin was used as reference. Absolute and relative free energy, enthalpy, and entropy values, as well as data for other spin states are compiled in Tables S11.4 and S11.5.

In vacuo UB3LYP/6-31G* computations yield a high spin Fe(III)-PO 32 kJ·mol^{-1} more stable than the doublet. A greater difference (~50 kJ·mol^{-1}) was obtained between high and low species in the case of Fe(II)-PO, while the triplet is around 60 kJ·mol^{-1} above the resting state. The presence of water at the sixth coordination site stabilizes preferentially low and intermediate spin species, which possess more adequate electron configuration for a hexacoordinate iron, and also present higher Fe–O_W bond order, but still insufficient to modify heme ground state. Thus, all four species exhibit a more favourable high spin state, as expected from the pentacoordinate iron centre. Conversely, protonated Fe(III)-PO-H presents a more stable low spin, which develops from the hexacoordinate Fe(III) atom, while S = 1 species is more favoured for Fe(II)-PO-H. Furthermore, addition of water to Fe(III)-PO is slightly favourable, which is not the case of the aquo-Fe(II) complex. On the other hand, gas phase protonation involves an important stabilization effect on the ferrous species, whereas protonated Fe(III)-PO-H develops stable but not that much.

Gas phase calculations yielded an appreciably more stable low spin in the case of hexacoordinate-Fe compounds PO-I and PO-II. This spin preference remains in the aquo and protonated forms. However, according to the calculated Gibbs free energy, addition of the water molecule is unfavourable while protonation *in vacuo* is spontaneous. Stabilization of PO-I upon protonation amounts to 704 kJ·mol^{-1}, and even more significant (1036 kJ·mol^{-1}) for PO-II.

Free energy results obtained at other spin states are collected as supplementary material (Tables S11.4 & S11.5). All ferric species appear more stable at intermediate spin (S = 3/2). This spin state is the most thermodynamically favoured in the case of compound I variants as well (PO-I-H only in gas phase), although spins 1/2 and 3/2 are almost degenerate. To confirm whether computations at higher multiplicities could yield even lower free energies, calculations were performed at spin states up to S = 7/2 (or 4) for species with an odd (or even) number of electrons. Most $\Delta G°$ values obtained at these spin states are higher than all the others by far.

Data contained in Table S11.4 show that the thermodynamic effect of protonation *in vacuo* is mostly enthalpic, since the entropic contribution is almost negligible. On the other hand, the Gibbs free energy of the gas-phase water addition

processes arises from a combined effect of the enthalpic and entropic contributions. Another noticeable outcome is that the higher the spin multiplicity, the less negative is the obtained $T\Delta S°$ value. Electronic contribution to $T\Delta S°$ accounts only 3.4 kJ·mol^{-1} when going from S = 1/2 to 7/2, or 5.4 kJ·mol^{-1} for the S = 0 to 4 spin shift, while the remaining $T\Delta S°$ variation must be attributed to vibrational contributions, which are associated to a significant change on low-frequency intramolecular vibrations upon spin conversion.[72, 73]

Table 11.1. Gibbs free energy for all compounds under study at low and high spin (and intermediate spin for ferrous species), obtained with UB3LYP/6-31G* (T = 298.15 K). Values of $\Delta G°$ obtained with PCM continuum model in italics. Most stable species of each unprotonated compound (with regard to Gibbs free energy, only for feasible spins) was taken as reference. Relative data of protonated and aquo complexes were worked out with respect to separate parent unprotonated species plus H^+ or H_2O as appropriate.

Species	Spin	$\Delta G°$ / kJ·mol^{-1}	
Fe(III)-PO	1/2	31.60	*13.99*
	5/2	0.00	*0.00*
Fe(III)-PO-H_2O	1/2	1.04	*–4.48*
	5/2	–4.76	*4.44*
Fe(III)-PO-H	1/2	–469.50	*248.39*
	5/2	–433.66	*290.47*
Fe(II)-PO	0	49.46	*37.20*
	1	60.37	*58.98*
	2	0.00	*0.00*
Fe(II)-PO-H_2O	0	31.76	*36.41*
	1	16.30	*35.05*
	2	12.55	*32.38*
Fe(II)-PO-H	0	–847.19	*136.13*
	1	–884.49	*98.21*
	2	–557.24	*435.45*
PO-I	1/2	0.00	*0.00*
	5/2	168.69	*169.94*
PO-I-H_2O	1/2	6.69	*24.52*
	5/2	43.82	*65.79*
PO-I-H	1/2	–703.74	*1.60*
	5/2	–637.73	*86.52*
PO-II	1	0.00	*0.00*
	2	153.12	*155.12*
PO-II-H_2O	1	3.65	*21.77*
	2	47.88	*72.57*
PO-II-H	1	–1035.88	*–47.57*
	2	–1029.07	*–30.01*

11.3.3 Spectral properties

Despite the particular structure of the different proteins, the position and intensity of the Soret band for the different redox intermediates are pretty conserved for the whole peroxidase family. Differences arise from the specific protein environment surrounding heme moiety and, in particular, from the covalent linkages between heme and protein. Soret band of ferric peroxidases is located around 405 nm with a molar absorption coefficient *ca.* 100000 cm^{-1}·M^{-1}. In the case of compound I the intensity is reduced to approximately 50% at the same wavelength. On the contrary, compound II exhibits a band of similar intensity to that of ferric species (~90000 cm^{-1}·M^{-1}) but shifted to the 420 nm region. Ferrous species presents a more red-shifted Soret band (440 nm) with ε = 85000 cm^{-1}·M^{-1}. All these data are average values of experimental results found in the literature for several peroxidases after excluding outliers, namely MPO, which holds three covalent bonds to the protein via two ester bonds and one sulfonium linkage, and nonplanar porphyrin group. As a consequence

MPO exhibits a particularly red shifted band scheme.[35, 74]

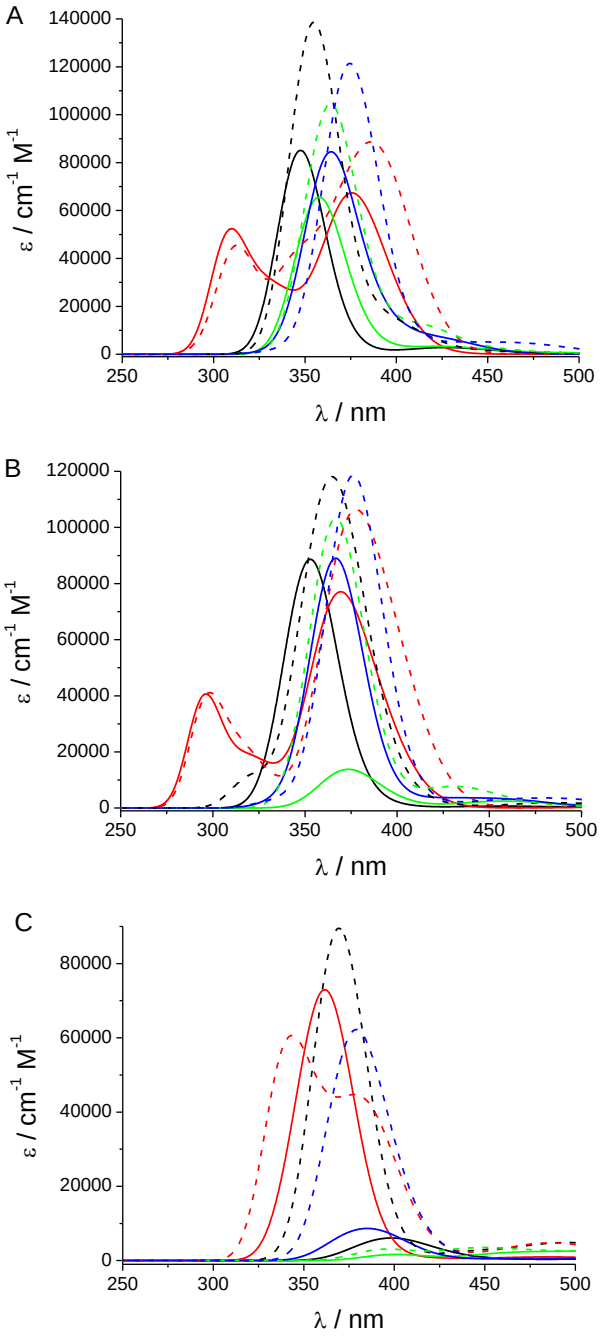

Figure 11.4. UV-Vis spectra (Soret region) obtained by TD-DFT calculations at the UB3LYP/6-31G* computational level *in vacuo* (solid line) and with PCM solvation (dashed line), and at the most stable spin multiplicity for (A) unprotonated Fe(III)-PO (—), Fe(II)-PO (—), PO-I (—), and PO-II (—); (B) corresponding aquo complexes; and (C) protonated species.

Convoluted calculated spectra at the UV region, showing the Soret band area, of the four here studied unprotonated species *in vacuo* at the most stable spin state are collected in Figure 11.4A (more spectral data are presented as supplementary material, Table S11.6). Absorption maxima exhibit a net blue shift of 50 - 65 nm relative to the experimental data, along with an adequate intensity profile, although predicted relative wavelength and extinction coefficient of PO-I are too high

and Fe(II)-PO presents a second relevant band (> 50000 $cm^{-1}·M^{-1}$) at 310 nm. This blue shift has been previously reported and is due to the known low performance of the employed TD-DFT functional in the description of excitation energies,[75, 76] as well as the absence of the porphyrin side chains in the molecular model.[35] As the origin of this deviation is the same, the absolute error obtained in the calculations can be expected to be similar for all considered species. Thus, relative wavelengths would reproduce experimental spectral shifts more accurately.

Different effects on the computed Soret spectrum were obtained when a water molecule is considered, depending on the particular species (Figure 11.4B). Thus, the spectral change upon water addition is not significant in the case of Fe(III)-PO and PO-II. A 5 nm red shift is observed in the former, and a 3 nm red shift in the latter, while a 7 nm blue shift accompanied by an increase of 15% in intensity is obtained for Fe(II)-PO-H_2O. The spectrum of the aquo complex of compound I, PO-I-H_2O, is different with a particularly low Soret band showing a maximum at λ = 374 nm and ε = 13791 $cm^{-1}·M^{-1}$.

Computed protonated enzymatic complexes yield UV-Vis absorption profiles at the Soret band region that are much distorted with respect to both unprotonated species and experimental spectral properties (Figure 11.4C). Full depletion of the band is observed, only Fe(II)-PO-H shows a significant peak (72960 $cm^{-1}·M^{-1}$ at 362 nm), and the secondary band disappears.

UV-Vis spectra obtained with PCM solvation model are also displayed in Figure 11.4. Band intensity increases around 50%, this rise being much higher for some of the species showing very low peaks *in vacuo* (Fe(III)-PO-H, PO-I-H_2O, and PO-II-H). Furthermore, minor differences are found in the position of the bands, usually a ~10 nm red shift, so that the blue shift with respect to empirical values decreases to 40 - 55 nm.

UV-Vis spectra both *in vacuo* and in aqueous solution are strongly spin-dependent. It should be noted, that all Fe(III) species with the non-feasible spin 3/2, which yield the most stable free energies, exhibit low intensity peaks in the Soret region. Thus, despite the well documented shortcoming of DFT calculations for the thermodynamical assignment of correct spin in heme systems, this method seems to produce better spectral properties for the adequate spin multiplicity.

11.4 Discussion

The obtained results present a reasonably good agreement with experimental data. However, some values need further analysis and discussion as they do not fit previous empirical studies and, besides, other conclusions can be obtained. First, it should be noted that most of the calculated bond distances adequately reproduce the experimental values, and the differences could be mostly attributed to interactions within the distal cavity. As expected, calculated geometrical parameters are quite similar for each of the couples studied (Fe(III)-PO/Fe(II)-PO and PO-I/PO-II, either unprotonated, protonated, or aquo complexes), with structures not particularly affected by spin states and, furthermore, only some distances change significantly upon addition of water or H^+. However, the distance determined for the oxo-ferryl Fe–O_{Fe} couple is very similar for both compounds I and II, contrary to what has been experimentally observed.[13, 19, 64] This issue is extensively analyzed below. Conversely, spin multiplicity as well as water addition and protonation show a much more relevant effect on charge distribution, thermodynamics, and spectral properties.

Most stable spin obtained for each parent species agrees with the well-established experimental spin values (Table 11.1). Both pentacoordinate Fe(III)-PO and Fe(II)-PO present more stable high spin states (*S* = 5/2 and 2, respectively), whereas low spin state is preferred for hexacoordinate PO-I (*S* = 1/2) and PO-II (*S* = 1). Known erroneous assignment of spin states with DFT methods is not observed at this particular UB3LYP/6-31G* computational level, at least when only considering the feasible spin multiplicities for each species. This Gibbs free energy preference is also maintained when solvation is taken into account. Relative spectral data (*i.e.*, subtracting the ~60 nm blue shift) calculated with the UB3LYP/6-31G* computational method for these unprotonated species mirror adequately the empirical values, although a ~10 nm red shift was obtained for PO-I.

When solvation (PCM) is considered some atomic charges are stabilized, mostly on the most exposed atoms, while

decreasing the net charge on the porphyrin ring. Thus, charge distribution is slightly affected, leading to Gibbs free energy stabilization, which does not alter the preferred spin state in any case. The effect of the environment on heme stabilization must be quite different from just simulating water as a polarizable continuum model. However, although the interaction exerted from the protein on the heme edges and imidazole is neglected, it should be similar among different systems (bare, protonated, or aqueous complex) within the same enzymatic species (Fe(III)-PO, Fe(II)-PO, PO-I, or PO-II). According to literature, peroxidase crystals contain some water molecules in their cavity, representing the closest moieties to central iron atom and the oxo-ferryl group. It is reasonable to assume that the number in solution is higher. In this study protonation and water addition are located around the distal heme axis, in the close vicinity of the Fe atom and the ferryl group, where the effect of water is higher than that of the protein. Despite the deficient description of the interaction with the edges of the system, this approach seems to be the most adequate to obtain proper energy stabilization of the close surroundings of the metal centre, and the obtained errors can be disregarded since we use relative energies for comparing different systems, where protein effects should partially cancel out. PCM was also tested with a dielectric continuum corresponding to a protein environment showing somewhat poorer results (see section 11.4.5).

Calculated Soret bands (Figure 11.4A) show an evident increase in intensity upon PCM addition, while the wavelength is not affected to such a large extent (a red shift about 10 nm in average is obtained with respect to spectral data *in vacuo*). Nevertheless, relative values obtained for the four species are consistent with empirical results except for the again observed deviation of PO-I band.

11.4.1 Aquo complexes

Addition of a water molecule in distal axial position reveals that this molecule exerts a different effect depending on the enzymatic species considered. In the case of Fe(III)-PO-H_2O, low spin species is more stabilized, arising from the effective hexacoordination of the metal atom (Fe–O_W bond order = 0.32, almost twice the high spin value), due to the more adequate electronic occupancy of iron *d*-orbitals for distal binding. The species with $S = 5/2$ is still preferred *in vacuo*, but the ordering is inverted when solvation is considered. The water molecule linked to Fe(II)-PO-H_2O presents an interaction with Fe that becomes stronger for decreasing spin values. It modifies consequently the relative stability of spin states but the Gibbs free energy preference is not altered. Water addition also causes a charge polarization for these two species, the positive charge on Fe increases and some positive charge is transferred to H_2O, mostly balanced by a more negative charge on the porphyrin ring; this effect is more evident for the ferric complex, where obtained Fe–O_W bond orders are higher (Tables S11.1 & S11.3).

The most evident effect of the water molecule on PO-I-H_2O and PO-II-H_2O is a slight elongation of the Fe–O distance accompanied by a weakening of the ferryl bond, and charge polarization between metalloporphyrin and the ferryl oxygen. The negative charge increase on the latter atom *in vacuo* is similar to that obtained with PCM solvation of bare PO-I and PO-II. Net charge transfer from water is not observed, but this molecule undergoes certain charge polarization as well. Thermodynamic values are consequently affected but the $\Delta G°$ stability order is not modified.

Addition of PCM causes a destabilization of all aquo complexes. About 15 kJ·mol^{-1} can be just attributed to the solvation free energy value obtained for free H_2O. In the particular case of Fe(III)-PO-H_2O, aqueous solvation promotes a spin change, as the $S = 1/2$ species is more stable than the corresponding high spin, indicating the hexacoordination of Fe atom following bonding of the water molecule. Spectral properties at the Soret region obtained with PCM model are not particularly modified upon water addition.

Obtained $\Delta G°_{H2O}$(aq) values at preferred spin states are collected in Table 11.2. Since any weak H-bond or Coulomb forces between water molecule and heme moiety *in vacuo*, *i.e.*, in the absence of any other interactions, lowers the energy of the aquo-complex with respect to independent species, all calculations in the gas phase ($\Delta G°_{H2O}$(g)) yield more positive values. PCM data are, therefore, more relevant to extrapolate to empirical results, where other interactions are also present. In the case of Fe(III)-PO-H_2O the stabilization caused by Fe–O interaction is weak and fully compensated by aqueous solvation. Besides, hydrogen bonding of the water molecule to either other water molecules or available adequate residues in the distal cavity (typically 5 to 30 kJ·mol^{-1} per H-bond) rules out the possibility of formation of thermodynamically favourable

aquo-complexes. This result is consistent with empirical data showing that ferric iron of native peroxidases is pentacoordinated while a water molecule is situated at a distal position but at a long non-bonding distance.

Other aquo complexes (Fe(II)-PO-H_2O, PO-I-H_2O, and PO-II-H_2O) are more unfavourable. Bonding to ferrous centre and mainly to ferryl oxygen is weak, yielding bond orders ~0.04 for the latter and $\Delta G°_{H2O}$(aq) values ranging from –22 to –32 kJ·mol^{-1}. The effect on oxygen charge, and length and strength of the Fe–O_{Fe} double bond is quite similar for both ferryl species. The calculated Fe–O_{Fe} distance is adequate in the case of PO-I-H_2O, while the short elongation observed for this bond does not seem enough to reproduce the longer Fe–O_{Fe} distance determined by crystallography for compound II. The interaction is weak and the dissociation process is favourable, more evident if considering solvation and other hydrogen bonding possibilities of the water molecule. However, the position of the water molecule in this case (distance from metal to water oxygen > 3.8 Å) could allow a less stressed cooperative interaction of H_2O with both the ferryl group and other suitable residues placed above heme in the distal cavity, taking advantage of the stabilization by extensive H-bonding. Therefore, water molecules, present in the distal cavity, may easily interact with compounds I and II while they keep away from the metal centre of ferric and ferrous species, as this sole interaction reveals thermodynamically unfavourable. To study this effect in more detail, in addition to computations with one discrete water molecule, these compounds were also computed with one and two extra H_2O molecules. Obtained results do not particularly differ from the data above. Thus, hydrogen bonding cannot solely explain the differences observed between compounds I and II (see section 11.4.4).

Table 11.2. Gibbs free energy values in kJ·mol^{-1} for the dissociation equilibrium of the different considered aquo complexes ($\Delta G°_{H2O}$(aq)), and pK_a values for corresponding protonation processes. Data calculated by PCM//UB3LYP/6-31G* (T = 298.15 K). The most favourable spin multiplicities were used; first value under spin columns refers to unprotonated species, second number to the aquo complex or protonated compound.

Species	Spin	$\Delta G°_{H2O}$(aq)	Spin	pK_a
Fe(III)-PO	5/2 – 1/2	4.48	5/2 – 1/2	–43.5
Fe(II)-PO	2 – 2	–32.38	2 – 1	–17.2
PO-I	1/2 – 1/2	–24.52	1/2 – 1/2	–0.3
PO-II	1 – 1	–21.77	1 – 1	8.3

11.4.2 Protonated species

The effect of protonation on geometry, charge, and spectral properties is more relevant than in the previous results obtained with water complexes. Positive charge (a total of 1 a.u.) is added to the model and part of it transferred from H^+ to heme moiety, while H_2O only caused certain bond polarization and the net charge transferred from the water molecule is almost negligible. This leads to some structural modification and a noticeable change in the Soret spectrum.

Formation of a bond between H^+ and the iron atom of the ferric and ferrous species (Fe(III)-PO-H and Fe(II)-PO-H) seems a very unfavourable process in the gas phase, as it involves a cation with no electron density available for donation acting as sixth ligand of Fe^{3+} / Fe^{2+}. However, when linked to the metal centre, the hydrogen atom loses its proton character; the calculated charge on this atom approaches to zero for any spin state, while effective Fe–H bonding is observed (bond orders around 0.75). In the case of Fe(III)-PO-H with S = 7/2 and Fe(II)-PO-H with S = 3 (and to a lower extent S = 4), geometry was only optimized with proton at a distant position. At those spin states no stable minimum could be achieved with hydrogen atom linked to Fe and, thus, the corresponding bond orders are close to 0. Since charged H^+ is quite unstable in gas phase, an unpaired electron is transferred from heme and resulting neutral atom accounts for 1/2 to the total spin. Spin preference is altered for these protonated species, exhibiting more stable low (ferric) and intermediate (ferrous) spins. The positive charge on proton is fully transferred to the porphine ring. No relevant geometrical changes are observed for the two species upon protonation, but a remarkable decrease in the Soret band intensity is obtained.

The effect of PCM solvation is striking in the thermodynamic values obtained, and it mostly arises from the fact that proton is extremely unstable in gas phase. However, the expected charge stabilization is not observed. Atomic charges do not practically vary with respect to *in vacuo* results. The Soret region is deeply affected as well, the intensity of the band increases with respect to *in vacuo*, and a dramatic rise is observed for some spin states.

Protonation of PO-I and PO-II takes place on the distal oxygen. Hydrogen keeps its proton character but some electronic density is transferred to this atom, mostly from the porphine (more than 0.5 a.u. in all cases). Furthermore, it causes certain polarization of the oxo-ferryl bond with an increase of the negative charge associated to O_{Fe}, coupled with weakening and lengthening of this bond. This effect is much more important than in the case of the aquo complexes. Still, no change in the relative stability of the different spin states is observed in this case, and low spin species are again preferred. O_{Fe}–H bonding yields a bond order ~0.75, compensating the decrease of the Fe–O_{Fe} bond order. The metal binds pyrrol and imidazole N atoms more tightly and undergoes a slight in-plane shift. This effective O_{Fe}–H linkage must be the responsible of the more favourable free energy values obtained for these protonated species in the gas phase. It must be noted that the stabilization upon protonation is always higher for PO-II-H, and this process remains favourable also with PCM solvation for compound II. Following protonation the Soret band fully disappears in gas phase, but it is partially recovered by including solvation in the case of PO-II-H.

Although current molecular model and computational level are not expected to yield very accurate pK_a values, which would require more complete molecular models and computationally demanding methods, our pK_a values obtained with PCM solvation allow a qualitative discussion at least. Both Fe(III)-PO and Fe(II)-PO present very negative pK_a values (Table 11.2). This arises from the noticeable destabilization observed when the metal centre was protonated (see Table 11.1). This can be explained by the high positive charge on the iron atom plus the partial desolvation of H^+ in the distal cavity. These two species do not accept a proton coordinated to iron even at high acidic aqueous conditions. Besides, extreme acid media lead to inactivation and denaturalization of the enzymes, which would occur ahead of any iron protonation. Thus, protonation does not occur on these centres in any case. The protonation processes observed for ferric and ferrous species must be assigned to other ionizable groups in the heme or its close vicinity.

Formation of ferrous species involves the gain of a proton, and current data suggest that protonation does not take place on the metal. Chiavarino *et al.* studied computationally the relative energies of ferrous heme protonated at different sites.[33] A much more favourable protonated species (61.9 $kJ \cdot mol^{-1}$) was obtained at the β carbon atom of a vinyl group, and this position was assigned to the gained proton. Anyway, the observed stabilization relative to protonated iron would only lead to an increase of ~10 pK_a units, still insufficient to account for the proton addition upon Fe(II)-PO formation. The correct allocation of this proton may be required to calculate the Soret spectrum with a single band and at the corresponding wavelength.

The pK_a obtained for compound I is close to zero, which means that this species is neither protonated at the normal enzyme function. Still, PO-I-H is much more stable than the species protonated at the metal centre. The protonated form of compound II presents a geometry very similar to PO-I-H but with lower Gibbs free energy with respect to the unprotonated species, resulting in a more positive pK_a value (8.3). This number fits in the pK_a range found in the literature for compound II of HRP A (6.9),[14, 77] other HRP isozymes (8.5),[14] or other peroxidases (~9).[78, 79] As commented above, protonation on ferryl oxygen of compound II is still controversial. Often, this process has been ascribed to the distal histidine, despite the pK_a corresponding to the deprotonation of free histidine imidazole is only 6.0, much lower than the value observed in peroxidases. Besides, the neutral form of imidazole should be favoured in the interior of a protein. It does not seem reasonable that the effect of a ferryl O situated at 3.6 - 3.8 Å from imidazole N atom[13, 64] could cause such an increase (2.5 to 3 pK_a units). However, the presence of this neighbouring distal imidazole and some water molecules could lead to a more moderate variation of the ferryl oxygen pK_a (*ca.* ± 1 unit). Thus, even considering that this effect is neglected in the molecular model used and the error of the computational method, we could assume that the pK_a value around 8.5 - 9.0 measured for compound II actually corresponds to the ionization of protonated ferryl group. Recently another study

obtained pK_a values for a basic compound II ferryl oxygen of porphyrins[80] similar to the model used in this paper but lacking the proximal imidazole. The effect of this coordination bond is quite relevant as other hemoproteins with different proximal ligands show pretty dissimilar activities and, presumably, the acidity of this proton also diverges.

According to X-ray diffraction crystallographic structures, the oxo-ferryl group presents dissimilar Fe–O_{Fe} distances for compounds I and II. Upon one-electron oxidation of the former, the bond weakens and there is an increment in the Fe–O_{Fe} distance. Typical bond lengths shift from 1.65 to 1.75 - 1.80 Å. Some papers already explained this elongation by protonation on ferryl O,[81] which has also been observed in the current study. On the other hand, EXAFS experiments yield Fe–O_{Fe} distances pretty similar for both ferryl species and, therefore, reject any protonation on this atom.[17] Finally, the publication of the neutron diffraction structure of APX compound II protonated at the ferryl oxygen[24] sheds light on the debate, with its sound support for the protonated state. However, the noticeable decrease obtained for the Soret band of PO-II-H (not experimentally observed) seems to rule out this possibility and needs further analysis.

Protonated species were calculated with one and two water molecules as well (see below). These discrete waters display some effect on the oxo-ferryl group charges and geometry, and also on the Soret band, although not as important as PCM solvation. No definite, new conclusions can be obtained from those results.

Considering that compound I exhibits a negative pK_a value and that the pK_a obtained for compound II seems to be equivalent to the experimentally measured value around 8.5 - 9.0, the ferryl oxygen of these species must be unprotonated and protonated, respectively, as observed with neutron diffraction crystallography.[23, 24] On the other hand, the presence of adequate interactions with surrounding groups seems essential to achieve a satisfactory Soret band intensity for PO-II-H. However, according to our results, similar interactions on unprotonated PO-I causes a red shift of the Soret band. Thus, the inconsistent displacement of this peak with respect to the other species is aggravated.

The nature of ferryl group interactions within distal cavity should be different for PO-I and PO-II-H. We could suggest a different protonation state of distal His as the interaction with unprotonated or protonated ferryl group must also have a different effect on this imidazole, but this does not conform to neutron diffraction results, as this group appears protonated in both CCP compound I and APX compound II.

Resonance Raman experiments yield alike oxo-ferryl stretching frequencies for compounds I and II of peroxidases, and a shift of only 11 cm^{-1} was observed for HRP compound II connected to the pK_a around 8.5 - 9.0.[14, 15] Fe–O_{Fe} stretching vibration has been determined computationally for all considered ferryl complexes, relevant values are shown in Table 11.3.

Table 11.3. Fe–O_{Fe} stretching frequencies calculated for relevant ferryl species at the most favourable spin multiplicities employing the UB3LYP/6-31G* computational level (T = 298.15 K).

Species	Spin	ν / cm^{-1}
PO-I	1/2	937
PO-I-H_2O	1/2	934
PO-I-H	1/2	710
PO-II	1	945
PO-II-H_2O	1	941
PO-II-H	1	702

Results obtained for PO-I and PO-II are rather similar, and the addition of water causes a slight shift (3 - 4 cm^{-1}) in both cases. The interaction of O_{Fe} with a water molecule can be correlated with the effect of a neighbouring protonated group H-bonded to the ferryl moiety. On the other hand, protonation of the ferryl oxygen leads to a noticeable shift in the stretching frequency (*ca.* 200 cm^{-1}) that, although can be modulated to some extent via hydrogen bonding (Table S11.8), is quite different from the unprotonated species in all cases and does not support the protonated form, as considered in most

of the recent studies.[82]

11.4.3 Redox properties

Peroxidases participate in one- and two-electron oxidation processes. The native ferric state is oxidized to compound I, which is either directly reduced by two-electron donors (*e.g.* halides) to the ferric state or by one-electron donors to compound II and subsequently to the resting state (Scheme 11.1). Both redox intermediates exhibit a higher oxidation capacity compared to the ferric and ferrous species. Redox properties of all these intermediates have been measured for different peroxidases. The standard reduction potential of the redox couple Fe(III)/Fe(II) typically ranges between –120 and –310 mV.[83] Human myeloperoxidase is unique in having a globin-like reduction potential at +5 mV[84] due to an electron withdrawing covalent sulfonium ion bond between the prosthetic group and a methionine.

The redox intermediate with the highest oxidation capacity is compound I. In heme *b* peroxidases the reduction potential *E*°' of the couple compound I/ferric state and compound I/compound II were reported to be in the range 750 - 950 mV and 900 - 1150 mV, respectively.[83] By contrast, in representatives of the peroxidase cyclooxygenase superfamily, which typically have posttranslationally modified and covalently linked heme, the *E*°' values of the redox couples compound I/compound II and compound I/ferric state are more positive, namely 1000 - 1150 mV and 1150 - 1350 nm, respectively.[85, 86] Reduction potentials for the redox couple compound II/ferric state were reported to be in the range of 750 - 950 mV for heme *b* peroxidases and 950 - 1050 mV for members of the peroxidase-cyclooxygenase superfamily.[3] All individual redox processes involved in the peroxidase cycle were studied, including oxidation of native peroxidase to yield compound I, reduction of compound I to compound II and, finally, reduction of compound II to the ferric state:

$$\text{Fe(III)-PO} + \text{H}_2\text{O} \rightarrow \text{PO-I} + 2\text{H}^+ + 2\text{e}^-$$

$$\text{PO-I} + \text{H}^+ + \text{e}^- \rightarrow \text{PO-II-H}$$

$$\text{PO-II-H} + \text{H}^+ + \text{e}^- \rightarrow \text{Fe(III)-PO} + \text{H}_2\text{O}$$

The respective standard reduction potentials relative to SHE, *E*°, for all these individual redox steps have been calculated (Table 11.4). Additionally, the standard reduction potential of the couple Fe(III)/Fe(II) was obtained. Half reactions were modified to account for different feasible species as previously described, *i.e.*, considering other protonation possibilities as well as complexes involving water molecules (see below, section 11.4.4). Oxidation of Fe(III)-PO to PO-I yields an *E*° value of –963 mV, which is within the experimental peroxidase range. The reduction potential of the couple compound I/compound II was calculated to be 503 mV, while *E*° = 996 mV was obtained for protonated compound II, which better mirrors the experimental values. Similarly, *E*° of the redox couple compound II/ferric state was calculated to be 1422 mV for the unprotonated compound II and 929 mV for the protonated intermediate, respectively, again suggesting the presence of protonated compound II.

The reduction potential of the couple Fe(III)/Fe(II) was calculated to be –465 mV, significantly more negative compared to the experimental values. Assuming that the protonated ferrous species, Fe(II)-PO-H* complex (protonated on a position other than ferrous centre), is more stable than unprotonated Fe(II)-PO, more positive reduction potential is obtained, which is closer to experimental values.

These data indicate that the origin of the redox properties of the different peroxidase intermediates mostly lies on the metalloporphyrin ring together with proximal imidazole, which is not the case for other enzymes. The H-bonding interaction of the proximal imidazole strongly influences its imidazolate character and thus the electron density shifted from the ligand to the heme iron (see section 11.4.5). Additionally, interactions of the heme substituents with the protein and the presence of residues in the distal cavity modulate the reduction potentials. In any case, protonation of the ferryl oxygen in compound II is necessary to obtain adequate *E*° values for the redox couples compound I/ferric state and compound I/compound II.

Table 11.4. Standard reduction potential ($E°$) values relative to SHE calculated by PCM//UB3LYP/6-31G* (T = 298.15 K) at preferred spins.

Half-reaction	$E°$ (mV)
Compound I (S = 1/2) → Ferric (S = 5/2)	
$PO\text{-}I + 2H^+ + 2e^- \rightarrow Fe(III)\text{-}PO + H_2O$	963
Compound I (S = 1/2) → Compound II (S = 1)	
$PO\text{-}I + e^- \rightarrow PO\text{-}II$	503
$PO\text{-}I + H^+ + e^- \rightarrow PO\text{-}II\text{-}H$	996
Compound II (S = 1) → Ferric (S = 5/2)	
$PO\text{-}II + 2H^+ + e^- \rightarrow Fe(III)\text{-}PO + H_2O$	1422
$PO\text{-}II\text{-}H + H^+ + e^- \rightarrow Fe(III)\text{-}PO + H_2O$	929
Ferric (S = 5/2) → Ferrous (S = 2)	
$Fe(III)\text{-}PO + e^- \rightarrow Fe(II)\text{-}PO$	–465

11.4.4 Expansion of compounds I and II with water molecules

The geometries of compounds I and II were also optimized with more water molecules. Relevant parameters obtained for PO-I-$(H_2O)_n$ and PO-II-$(H_2O)_n$ (n = 0 to 3) are collected in Table S11.7. Addition of two discrete water molecules produces a polarization of the ferryl group, coupled with lengthening and weakening of this bond, more pronounced than with a single water molecule. However, the species computed with three water molecules do not show such further increase of the effect on oxygen charge and length of the oxo-ferryl bond. First water molecule causes a slight elongation of ferryl bond, less than 0.010 Å, and the effect of the second molecule is similar. However, no relevant effect is observed upon addition of a third water molecule.

The total effect of water molecules is similar for compounds I and II and only accounts for around 0.010 - 0.015 Å. The observed tendency indicates that further addition of water molecules must not be significant. This reveals that the longer $Fe–O_{Fe}$ bond observed for compound II cannot be achieved just by hydrogen bonding. Therefore, interactions with protonated distal histidine or other residues situated at a distance beyond 3 Å are not responsible for this weaker $Fe–O_{Fe}$ bond. Furthermore, it should be noted that the effect of discrete water molecules on the Soret band of compound II (or both ferryl species if PCM solvation is considered) is minor. The negative charge on the porphyrin ring calculated for PO-I-$(H_2O)_n$ slightly lowers upon addition of an increasing number of water molecules, but this cannot solely account for the empirically observed radical cation. Consideration of side chains must be necessary to obtain an adequate charge distribution, although all species would be similarly affected by the substituents. In any case, it should be noted that the charge on the porphyrin ring is always less negative for compound I.

Protonated compounds I and II were also optimized with one and two water molecules. These aquo complexes can be an adequate model for the interaction of these species with the water molecules present in the distal cavity, but also for feasible hydrogen bonding with surrounding residues. First water molecule may interact either with ferryl O (denoted PO-I-H···H_2O and PO-II-H···H_2O) or with linked H (PO-I-H···OH_2 and PO-II-H···OH_2). Both possibilities are reported for PO-II-H, whereas optimization of a minimum of PO-I-H with H_2O H-bonded to ferryl O was not possible except for S = 7/2 (the water molecule always moved to PO-I-H···OH_2 complex during geometry optimization at other spin states, as this position must be much more stable). Two water molecules were successfully optimized situated on both positions, one molecule H-bonded to O_{Fe} and the other one acting as H-acceptor (PO-I-H-$(H_2O)_2$ and PO-II-H-$(H_2O)_2$). Results obtained for relevant parameters are also collected in Table S11.7. Again, these water molecules have some effect on oxygen charge and $Fe–O_{Fe}$ bond. In the case of PO-II-H···H_2O, H-donor water causes the elongation and weakening of $Fe–O_{Fe}$ bond, coupled with a more negatively charged O_{Fe}. On the other hand, the H-acceptor water molecule (H-bonded to PO-I-H or PO-II-H) partially counterbalances the effect of protonation on ferryl bond, *i.e.*, a stronger $Fe–O_{Fe}$ bond is obtained, mostly at low spin, while

the oxygen negative charge is slightly increased *in vacuo* but not if solvation is considered. The addition of the combined two discrete water molecules yields a spin-dependent effect on ferryl group while negative charge on O_{Fe} increases both *in vacuo* and with PCM in this case. Again, obtained Fe–O_{Fe} distances reproduce X-ray diffraction geometry in the case of compound II, but are too long for compound I.

Spectral properties are also affected by these H-bonds. The intensity of the Soret band increases in the case of some aqueous complexes of PO-II-H. Thus, the strong effect on this band observed upon protonation is partially compensated by other interactions with surrounding adequate groups. Either water molecules or peptide residues in the distal cavity, all of them modelled here as discrete water molecules, or bulk solvent simulated with PCM. This is not the case of PO-I-H, since its Soret band suffers some increment but it is still very low with respect to other species and unprotonated PO-I, also suggesting the inadequacy of this species. Furthermore, water molecules added on PO-II-H modify the oxo-ferryl stretching frequency to some extent, but still insufficient to reach the much higher values calculated for unprotonated PO-I and PO-II (Table S11.8).

Calculated spectra of PO-II-H complexes indicate that other interactions, with water or other feasible moieties at the distal cavity, are needed to obtain adequate Soret intensities. Therefore, complexes with H-bonded water molecules are also considered for the calculation of redox potentials (Table S11.9). Presumably, interactions of PO-II-H with other surrounding groups are different than for PO-I, since the former may form hydrogen bonds with H-donor (to ferryl oxygen) and H-acceptor (from ferryl hydrogen) moieties. Thus, several combinations were taken into account. The addition of a H-acceptor water molecule to compound II (PO-II-H$\cdots OH_2$) causes an increase in the reduction potential of the compound II/ferric state couple and, as a result, it does not fit so adequately the experimental values, at least for heme *b* enzymes. Considering this water complex in the reduction process of compound I to compound II, yields a slightly lower value when PO-I without any other interaction is considered. In fact, such a H-acceptor group (apart from water molecules with free rotation) would not interact with unprotonated PO-I. A somewhat higher value is obtained if PO-I-H_2O is used. The H-donor water molecule complex (PO-II-H$\cdots H_2O$) produces less adequate potential values for its reduction to Fe(III)-PO or the reduction of bare PO-I. Once more, better computational data are obtained when the same interaction is applied in both compounds (reduction of PO-I-H$\cdots H_2O$ to PO-II-H$\cdots H_2O$). The species with both discrete water molecules (PO-II-H-$(H_2O)_2$) shows even worse reduction potentials for the couples compound II/ferric state (too high) or compound I/compound II (too low). The latter value is again counterbalanced if other interactions are also considered for PO-I.

11.4.5 Adequacy of the computational molecular model and method

It was our clear aim to select a molecular model comprised of ferriporphine and a proximal imidazole, the only fully common part for three out of four heme peroxidase superfamilies. Distal catalytic residues were not incorporated in the model as their chemistry and distance from the metal centre significantly varies in peroxidases from the four superfamilies. Also heme side chains are modified in members of the peroxidase-cyclooxygenase superfamily, and the position and environment of proximal histidine greatly differs among peroxidases. In this regard, the protonation state of the proximal imidazole of myeloperoxidase has been examined in a joint experimental-computational study.[87] It has been suggested that in MPO, and probably other mammalian peroxidases, the proximal ligand has a strongly pronounced imidazolate character in view of the steric clash observed in crystal structures between either His336 and Asn421, or Asn421 and Arg333, when His336 is protonated. This could be supported by molecular dynamics simulations. The protonation state of this imidazolate was already revealed in the presented crystallographic structure represented by a Fe–N_i coordination bond of only 1.87 - 1.88 Å, which is clearly shorter than in other myeloperoxidase structures displaying a less pronounced imidazolate character (2.17 to 2.24 Å, data collected in Table 11.5).[67, 87, 88] This movement can be adequately predicted with our model. The Fe–N_i distance changes from 2.087 Å in high spin Fe(III)-PO to 1.955 Å upon proximal imidazole deprotonation (from 1.930 Å to 1.846 Å with low spin), although the observed experimental shift is even higher.

The reduced molecular model employed in the study also corresponds to the active site of other heme enzymes as globins. However, it should be taken into account that some significant differences in their active sites are not considered in the

model. The position of distal His with respect to heme is different in both families, the most significant change is a shorter distance from Fe in the case of globins.[89] This fact results in a preferential stabilization of Fe-bound O_2 via hydrogen bonding for these enzymes, while a further position of distal His in peroxidases seems to be more suitable for interacting with H_2O_2 and participating in the oxidation step leading to compound I. Thus, these processes and the transient intermediates involved have not been studied employing this model, since it would not be so adequate. Only stable intermediates were examined, where interaction with distal His is not essential, as confirmed with obtained results showing suitable values. Furthermore, ferric/ferrous reduction potential in globins is different than in peroxidases, although similar to the outlier MPO. This difference must arise from some interactions between heme and protein (covalent bonding in the case of MPO), which are not considered here either. Therefore, obtained results indicate that, while this model is appropriate to study some general features of peroxidases, it should be enlarged to obtain information on globins, as their behaviour must be strongly affected by some interactions that are out of scope of this research.

Table 11.5. Distance (Å) between iron and imidazole nitrogen atom (Fe–N_i), measured from some crystallographic structures of ferric MPO. The two different values correspond to the distances observed for hemes A and B.

Species	PDB entry	Fe–Ni	
Native	3F9P[a]	1.868	1.876
Native	1CXP[b]	2.187	2.189
Bromide complex	1D2V[b]	2.168	2.197
Cyanide complex	1D5L[c]	2.196	2.197
Thiocyanate complex	1DNU[c]	2.183	2.182
Cyanide-bromide complex	1D7W[c]	2.177	2.239
Cyanide-thiocyanate complex	1DNW[c]	2.228	2.230

[a] Ref. 87. [b] Ref. 67. [c] Ref. 88.

The employed basis set has been selected after some systematic trial. As stated above, double-ζ 6-31G and lower basis sets failed to yield appropriate geometries, while basis sets higher than 6-31G* did not show relevant improvements in the depiction of the studied system. A comparison of low and high spin Fe(III)-PO and Fe(III)-PO-H_2O, and low spin PO-I, PO-I-H, PO-II, and PO-II-H has been performed among 6-31G*, 6-31G**, 6-31++G**, 6-311G**, and 6-311++G** basis sets. The use of diffuse functions is usually recommended for anionic molecules, which is not the case under study, but they still have an effect on a number of computed parameters,[90] and they have also been tested. Benefits and limitations of additional polarization functions and the use of triple-ζ basis sets were also analyzed. In order to avoid any unintended manipulation of the results, Gaussian 03 default values were used when possible. Thus, double-ζ basis sets use Cartesian d functions (6D), triple-ζ basis sets use spherical d basis functions, and spherical f functions (7F) are used in all cases. Besides, calculations were performed with the default integration pruned grid (75 radial shells and 302 angular points per shell). Large integration grids have been sometimes recommended for DFT methods when employed together with big basis sets.[91] However, the use of the Grid=UltraFine option in Gaussian 03 (a pruned grid defined as 99 radial shells and 590 angular points) did not show any relevant improvement.

Changes in optimized geometries were negligible for the purpose of this study and, more important, the maximum difference obtained in Gibbs free energies was as low as 2 $kJ \cdot mol^{-1}$, which does not affect the conclusions of this work. Furthermore, it should be noted that any modification in the definition of the cavities used in the continuum model could have an important effect on the solvation energies. Thus, to prevent any unconscious influence on the results, default cavity parameters were used. Obtained results validate the approach employed.

Very slight geometrical changes have been obtained (Table S11.10). The most important difference occurs when adding diffuse functions, as bond distances and bond orders increase with respect to parent basis sets. On the other hand, while

6-31G* and 6-31G** yield almost identical Mulliken charges (Table S11.11), and some irrelevant differences are calculated with 6-311G**, results obtained with 6-31++G** and 6-311++G** are bizarre, even values of opposite sign were obtained. Mulliken charges calculation often fails for non-minimal basis sets, but the examination of natural bond orbitals population analysis (not shown) also indicates that the two basis sets with added diffusion functions lead to wrong charge distribution, although not as strange as Mulliken.

Thermodynamic results obtained with 6-31G*, 6-31G**, and 6-311G** basis sets (Table S11.12) are again consistent. Almost equivalent energies are obtained for ferric species, high spin pentacoordinate Fe(III)-PO and low spin hexacoordinate Fe(III)-PO-H_2O are preferred, and very similar $\Delta G°_{H2O}$(aq) values were also achieved. Besides, pK_a values determined for compounds I and II are pretty similar, although 6-31G** results are higher (*ca*. 2 units) than the others. Adequate reduction potentials are calculated on condition that compound II is protonated, but increasing numbers are obtained with higher basis sets, so that 6-31G** and 6-311G** values are overestimated with respect to empirical data. Conversely, thermodynamic results calculated with 6-31++G** and 6-311++G** basis sets seem defective, and some values obtained are not only quite different from the other methods, but they are also different between them.

An analysis of the excitation energies (Table S11.13) shows again a similar performance for 6-31G*, 6-31G**, and 6-311G** basis sets. A small shift in Soret wavelength is observed for the latter. Addition of diffuse functions seems more relevant in this case as higher extinction coefficients are obtained for PO-II-H, and the partial depletion of the Soret band is not so pronounced.

Table 11.6. Comparison of the performance of PCM with different dielectric constants (ε). Values of $\Delta G°$(aq) in kJ·mol^{-1}, absolute values obtained for Fe(III)-PO with S = 5/2 were taken as reference. Relative data of aquo complexes were worked out with respect to separate parent unprotonated species plus H_2O. $\Delta G°_{H2O}$(aq) stands for Gibbs free energy for the dissociation equilibrium of the aquo complexes, pK_a values for protonation processes, and reduction potential values in mV relative to SHE.

	Spin	**$\Delta G°$(aq)**	**Spin**	**$\Delta G°$(aq)**		
	Fe(III)-PO		Fe(III)-PO-H_2O			
ε (water)	1/2	13.99	1/2	–4.48		
ε = 4	1/2	15.83	1/2	1.42		
ε (water)	5/2	0.00	5/2	4.44		
ε = 4	5/2	0.00	5/2	7.84		
	Spin	**$\Delta G°_{H2O}$(aq)**	**Spin**	**pK_a**	**Spin**	**pK_a**
	Ferric		Compound I		Compound II	
ε (water)	5/2 – 1/2	4.48	1/2	–0.3	1	8.3
ε = 4	5/2 – 1/2	–1.42	1/2	–16.7	1	4.8

Reduction potential	PO-I / Fe(III)-PO	PO-I / PO-II	PO-I / PO-II-H	PO-II / Fe(III)-PO	PO-II-H / Fe(III)-PO
ε (water)	963	503	996	1422	929
ε = 4	1001	730	1017	1271	984

A comparison of the continuum model employing PCM with two dielectric constants (ε) has been also performed and most relevant results are collected in Table 11.6. Water solvation corresponds to ε = 78.39, while another dielectric continuum with ε = 4 and all other parameters set as default, *i.e.*, corresponding to water, has been also employed. This value is in the range predicted for inner protein medium of cytochrome c,[92] and it has been previously used to study computationally the active site of myeloperoxidase.[35] High spin pentacoordinate Fe(III)-PO and low spin hexacoordinate Fe(III)-PO-H_2O are preferred in both models. Very low pK_a values were computed for compound I, and notably higher for compound II, although pK_a determined with ε = 4 does not support the protonation of this species at neutral pH. However, protonated

compound II is again necessary to obtain an adequate profile of reduction potentials, so that the pK_a of compound II must be higher to account for the observed potentials. Therefore, values computed with a dielectric continuum that represents the protein surrounding the active site are slightly worse. This supports that the water molecules present in the distal cavity exert a more variable effect that sharply depends on the particular intermediate under study, than the effect of surrounding bulk protein. Thus, the latter can be neglected when employing relative energies as it cancels out. In any case, same general conclusions can be drawn with both dielectric contants.

To summarize, the reduced molecular model employed is adequate to study peroxidases, same outcomes are reached from both 6-31G* and 6-311G** basis sets, but the former yields redox data more similar to experimental values and has a much lower computational cost, an important aspect if the molecular model is enlarged. Addition of diffusion functions may lead to inappropriate results, although their use should be considered when dealing with excitation energies. The use of PCM continuum with water parameters seems also more adequate as it yields better values than with a dielectric constant corresponding to the protein environment.

We do not claim that this reduced model of the active site of peroxidases could reproduce the detailed behaviour of a particular enzyme as it does not include the effect of heme side chains, heme-protein linkages, and full protein environment. However, it does include the most important common structural features of their active site, and reproduces the general behaviour and common characteristics. Despite their different protein structure, peroxidases share a variety of physicochemical properties (pretty similar spectroscopic and redox characteristics, reactivity, active site geometry, etc), and the specific features of any particular peroxidase must be attributed to slight variations of external influences on the core of the active site. Therefore, this simple molecular arrangement coupled with PCM solvation at the UB3LYP/6-31G* computational level revealed quite adequate for a general elucidation of several common properties of peroxidases, which tells about the capability of the employed methodology.

11.5 Conclusions

Electronic structure calculations have been carried out to examine the effect of protonation and hydrogen-bonded water molecules on peroxidase species at a distal axial position. This is the first comprehensive computational study on ferric and ferrous states, as well as compounds I and II of peroxidases, by using a minimal molecular model common to all these enzymes and at different spin multiplicities. The use of this simple molecular arrangement together with UB3LYP/6-31G* full geometry optimization and frequency calculations, with unspecific surrounding interactions simulated by means of PCM water solvation, allowed a quite reasonable description of the relative energy profiles as well as UV-Vis spectra at the Soret region, $\Delta G°_{H2O}$(aq) and pK_a values, and reduction potentials ($E°$). Besides, electronic ground states were correctly predicted (if only considering feasible spin values for each species).

Obtained geometries show a good correlation with experimental structures. Also, computed UV-Vis spectra essentially depict the experimental profiles at the Soret region measured with most peroxidases (with an absolute ~60 nm blue shift), but the peaks corresponding to compound I and protonated compound II are not so well reproduced. Specific interactions of ferryl oxygen with other groups within the distal cavity must account for the different wavelength and intensity.

Gibbs free energy data revealed that distal bonding of a water molecule at the sixth position of ferric peroxidases is thermodynamically unstable, thus supporting five-coordinate metal atom of these enzymes with a water molecule axially situated but at non-bonding distance from the Fe(III) centre. Furthermore, unfavourable interaction with discrete water molecules was also obtained for other studied species since aquo complexes are less stable than separate solvated corresponding heme model and H_2O ($\Delta G°_{H2O}$(aq) < 0). Similarly, axial proton addition at the distal side does not occur under physiological conditions, as revealed by the calculated negative pK_a values, except for a more favourable ferryl oxygen protonation in the case of compound II. This proton is responsible for the longer Fe–O_{Fe} distance observed with X-ray

diffraction experiments, not often corroborated by EXAFS studies; whereas the comparison of calculated stretching frequencies with Resonance Raman measurements points towards the unprotonated species. It must be considered that the use of ionizing radiation (X-rays) or a powerful laser beam (RR) arises as a potential shortcoming of these experimental techniques when studying easily reducing metals as in ferryl species, leading to some ambiguity in the measurements. However, neutron diffraction experiments unequivocally point to protonated APX compound II. Another approach has been here employed: protonated ferryl oxygen of compound II was found necessary to justify the redox potential measured for processes involving this species, which is also a reliable measurement. Current computational results indicate that this feature must be common to all peroxidases, not only APX, and the pK_a has been estimated (pK_a = 8.5 - 9.0), the first time a value has been proposed.

In summary, although specific characteristics of particular enzymes arise from the environment and heme-peptide linkages, and the absolute effect of the protein must be quite different from the approach here used with a continuum simulating water, obtained results tell about the adequacy of both the employed methodology and the molecular model for characterization of most common peroxidase features. Observed agreement between computation and experiment suggests that the origin of the general oxidative profile of peroxidase species, as well as of their reactivity towards water and protons, and of Soret spectral properties, mostly resides on just the iron porphyrin and the proximal histidine moiety.

11.6 References

1. J. Everse, K. E. Everse, and M. B. Grisham, *Peroxidases in chemistry and biology*. 1991, Boca Raton, FL: CRC Press.
2. P. R. Ortiz de Montellano, *Cytochrome P-450: structure, mechanism, and biochemistry*. 1986, New York: Plenum Press.
3. M. Zámocký, S. Hofbauer, I. Schaffner, B. Gasselhuber, A. Nicolussi, M. Soudi, K. F. Pirker, P. G. Furtmüller, and C. Obinger, *Independent evolution of four heme peroxidase superfamilies.* Arch. Biochem. Biophys., 2015 **574** 108-119.
4. D. R. Ramos, M. V. García, M. Canle L., J. A. Santaballa, P. G. Furtmüller, and C. Obinger, *Myeloperoxidase-catalyzed taurine chlorination: initial versus equilibrium rate.* Arch. Biochem. Biophys., 2007 **466** (2) 221-233.
5. T. L. Poulos and J. Kraut, *The stereochemistry of peroxidase catalysis.* J. Biol. Chem., 1980 **255** (17) 8199-8205.
6. G. Barea, F. Maseras, and A. Lledós, *Theoretical assessment on the viability of possible intermediates in the reaction mechanism of catalase and peroxidase models.* J. Mol. Struct.-Theochem, 2003 **632** (1-3) 323-333.
7. D. L. Harris and G. H. Loew, *Identification of putative peroxide intermediates of peroxidases by electronic structure and spectra calculations.* J. Am. Chem. Soc., 1996 **118** (43) 10588-10594.
8. G. Loew and M. Dupuis, *Structure of a model transient peroxide intermediate of peroxidases by ab initio methods.* J. Am. Chem. Soc., 1996 **118** (43) 10584-10587.
9. H. B. Dunford, *Heme peroxidases*. 1999, New York: John Wiley & Sons, Inc.
10. H. Spalteholtz, O. M. Panasenko, and J. Arnhold, *Formation of reactive halide species by myeloperoxidase and eosinophil peroxidase.* Arch. Biochem. Biophys., 2006 **445** (2) 225-234.
11. I. I. Vlasova, J. Arnhold, A. N. Osipov, and O. M. Panasenko, *pH-dependent regulation of myeloperoxidase activity.* Biochem., Moscow, 2006 **71** (6) 667-677.
12. D. R. Ramos, M. V. García, M. Canle L., J. A. Santaballa, P. G. Furtmüller, and C. Obinger, *Myeloperoxidase-catalyzed chlorination: The quest for the active species.* J. Inorg. Biochem., 2008 **102** (5-6) 1300-1311.
13. A. Gumiero, C. L. Metcalfe, A. R. Pearson, E. L. Raven, and P. C. E. Moody, *Nature of the ferryl heme in compounds I and II.* J. Biol. Chem., 2011 **286** (2) 1260-1268.
14. A. J. Sitter, C. M. Reczek, and J. Terner, *Heme-linked ionization of horseradish peroxidase compound II monitored*

by the resonance Raman Fe(IV)=O stretching vibration. J. Biol. Chem., 1985 **260** (12) 7515-7522.

15. J. R. Kincaid, Y. Zheng, J. Al-Mustafa, and K. Czarnecki, *Resonance Raman spectra of native and mesoheme-reconstituted horseradish peroxidase and their catalytic intermediates.* J. Biol. Chem., 1996 **271** (46) 28805-28811.
16. M. T. Green, *Application of Badger's rule to heme and non-heme iron-oxygen bonds: An examination of ferryl protonation states.* J. Am. Chem. Soc., 2006 **128** (6) 1902-1906.
17. J. E. Penner-Hahn, K. S. Eble, T. J. McMurry, M. Renner, A. L. Balch, J. T. Groves, J. H. Dawson, and K. O. Hodgson, *Structural characterization of horseradish peroxidase using EXAFS spectroscopy. Evidence for Fe = O ligation in compounds I and II.* J. Am. Chem. Soc., 1986 **108** (24) 7819-7825.
18. C. A. Bonagura, B. Bhaskar, H. Shimizu, H. Li, M. Sundaramoorthy, D. E. McRee, D. B. Goodin, and T. L. Poulos, *High-resolution crystal structures and spectroscopy of native and compound I cytochrome c peroxidase.* Biochemistry, 2003 **42** (19) 5600-5608.
19. B. Chance, L. Powers, Y. Ching, T. Poulos, G. R. Schonbaum, I. Yamazaki, and K. G. Paul, *X-ray absorption studies of intermediates in peroxidase activity.* Arch. Biochem. Biophys., 1984 **235** (2) 596-611.
20. K. L. Stone, R. K. Behan, and M. T. Green, *Resonance Raman spectroscopy of chloroperoxidase compound II provides direct evidence for the existence of an iron(IV)–hydroxide.* Proc. Natl. Acad. Sci. U.S.A., 2006 **103** (33) 12307-12310.
21. M. T. Green, J. H. Dawson, and H. B. Gray, *Oxoiron(IV) in chloroperoxidase compound II is basic: Implications for P450 chemistry.* Science, 2004 **304** (5677) 1653-1656.
22. T. H. Yosca, R. K. Behan, C. M. Krest, E. L. Onderko, M. C. Langston, and M. T. Green, *Setting an upper limit on the myoglobin iron(IV)hydroxide pK_a: Insight into axial ligand tuning in heme protein catalysis.* J. Am. Chem. Soc., 2014 **136** (25) 9124-9131.
23. C. M. Casadei, A. Gumiero, C. L. Metcalfe, E. J. Murphy, J. Basran, M. G. Concilio, S. C. M. Teixeira, T. E. Schrader, A. J. Fielding, A. Ostermann, M. P. Blakeley, E. L. Raven, and P. C. E. Moody, *Neutron cryo-crystallography captures the protonation state of ferryl heme in a peroxidase.* Science, 2014 **345** (6193) 193-197.
24. H. Kwon, J. Basran, C. M. Casadei, A. J. Fielding, T. E. Schrader, A. Ostermann, J. M. Devos, P. Aller, M. P. Blakeley, P. C. E. Moody, and E. L. Raven, *Direct visualization of a Fe(IV)–OH intermediate in a heme enzyme.* Nat. Commun., 2016 **7** (13445).
25. H. Maskill, *The investigation of organic reactions and their mechanisms*. 2006, Oxford: Blackwell publishing.
26. M. J. Ramos and P. A. Fernandes, *Computational enzymatic catalysis.* Acc. Chem. Res., 2008 **41** (6) 689-698.
27. Y. Zhang, J. Mao, N. Godbout, and E. Oldfield, *Mössbauer quadrupole splittings and electronic structure in heme proteins and model systems: A density functional theory investigation.* J. Am. Chem. Soc., 2002 **124** (46) 13921-13930.
28. L. Banci, I. Bertini, H. B. Gray, C. Luchinat, T. Reddig, A. Rosato, and P. Turano, *Solution structure of oxidized horse heart cytochrome c.* Biochemistry, 1997 **36** (32) 9867-9877.
29. C. Rovira, K. Kunc, J. Hutter, P. Ballone, and M. Parrinello, *Equilibrium geometries and electronic structure of iron-porphyrin complexes: A density functional study.* J. Phys. Chem. A, 1997 **101** (47) 8914-8925.
30. C. Rovira and M. Parrinello, *Factors influencing ligand binding properties of heme models: a first principles study of picket-fence and protoheme complexes.* Chem. Eur. J., 1999 **5** (1) 250-262.
31. C. Rovira and M. Parrinello, *Harmonic and anharmonic dynamics of Fe-CO and Fe-O_2 in heme models.* Biophys. J., 2000 **78** (1) 93-100.
32. F. Maseras, *Binding of dioxygen in a picket-fence porphyrin complex of iron. A theoretical QM/MM study.* New. J. Chem., 1998 **22** (4) 327-332.

33. B. Chiavarino, M. E. Crestoni, S. Fornarini, and C. Rovira, *Protonated heme.* Chem. Eur. J., 2007 **13** (3) 776-785.

34. K. Kühnel, E. Derat, J. Terner, S. Shaik, and I. Schlichting, *Structure and quantum chemical characterization of chloroperoxidase compound 0, a common reaction intermediate of diverse heme enzymes.* Proc. Natl. Acad. Sci. U.S.A., 2007 **104** (1) 99-104.

35. A. Devarajan, A. V. Gaenko, and U. Ryde, *Effect of covalent links on the structure, spectra, and redox properties of myeloperoxidase - A density functional study.* J. Inorg. Biochem., 2008 **102** (8) 1549-1557.

36. M. P. Johansson, D. Sundholm, G. Gerfen, and M. Wikström, *The spin distribution in low-spin iron porphyrins.* J. Am. Chem. Soc., 2002 **124** (39) 11771-11780.

37. A. Ghosh, *First-principles quantum chemical studies of porphyrins.* Acc. Chem. Res., 1998 **31** (4) 189-198.

38. K. P. Jensen and U. Ryde, *Comparison of the chemical properties of iron and cobalt porphyrins and corrins.* ChemBioChem, 2003 **4** (5) 413-424.

39. K. M. Vogel, P. M. Kozlowski, M. Z. Zgierski, and T. G. Spiro, *Determinants of the FeXO [X=C,N,O] vibrational frequencies in heme proteins and models from experiment and density functional theory.* J. Am. Chem. Soc., 1999 **121** (43) 9915-9921.

40. K. Morokuma, D. G. Musaev, T. Vreven, H. Basch, M. Torrent, and D. V. Khoroshun, *Model studies of the structures, reactivities, and reaction mechanisms of metalloenzymes.* IBM J. Res. & Dev., 2001 **45** (3-4) 367.

41. C. W. Bauschlicher Jr., *A comparison of the accuracy of different functionals.* Chem. Phys. Lett., 1995 **246** (1-2) 40-44.

42. F. Neese, *A critical evaluation of DFT, including time-dependent DFT, applied to bioinorganic chemistry.* J. Biol. Inorg. Chem., 2006 **11** (6) 702-711.

43. P. E. M. Siegbahn, *The performance of hybrid DFT for mechanisms involving transition metal complexes in enzymes.* J. Biol. Inorg. Chem., 2006 **11** (6) 695-701.

44. N. Strickland and J. N. Harvey, *Spin-forbidden ligand binding to the ferrous-heme group: Ab initio and DFT Studies.* J. Phys. Chem. B, 2007 **111** (4) 841-852.

45. M. P. Johansson, M. R. A. Blomberg, D. Sundholm, and M. Wikström, *Change in electron and spin density upon electron tranfer to haem.* Biochim. Biophys. Acta, 2002 **1553** (3) 183-187.

46. M. P. Johansson and D. Sundholm, *Spin and charge distribution in iron porphyrin models: a coupled cluster and density-functional study.* J. Chem. Phys., 2004 **120** (7) 3229-3236.

47. A. D. Becke, *Density-functional thermochemistry. III. The role of exact exchange.* J. Chem. Phys., 1993 **98** (7) 5648-5652.

48. C. Lee, W. Yang, and R. G. Parr, *Development of the Colle-Salvetti correlation-energy formula into a functional of the electron density.* Phys. Rev. B, 1988 **37** (2) 785-789.

49. B. Miehlich, A. Savin, H. Stoll, and H. Preuss, *Results obtained with the correlation energy density functionals of Becke and Lee, Yang and Parr.* Chem. Phys. Lett., 1989 **157** (3) 200-206.

50. M. J. Frisch, G. W. Trucks, H. B. Schlegel, G. E. Scuseria, M. A. Robb, J. R. Cheeseman, J. A. Montgomery Jr., T. Vreven, K. N. Kudin, J. C. Burant, J. M. Millam, S. S. Iyengar, J. Tomasi, V. Barone, B. Mennucci, M. Cossi, G. Scalmani, N. Rega, G. A. Petersson, H. Nakatsuji, M. Hada, M. Ehara, K. Toyota, R. Fukuda, J. Hasegawa, M. Ishida, T. Nakajima, Y. Honda, O. Kitao, H. Nakai, M. Klene, X. Li, J. E. Knox, H. P. Hratchian, J. B. Cross, C. Adamo, J. Jaramillo, R. Gomperts, R. E. Stratmann, O. Yazyev, A. J. Austin, R. Cammi, C. Pomelli, J. W. Ochterski, P. Y. Ayala, K. Morokuma, G. A. Voth, P. Salvador, J. J. Dannenberg, V. G. Zakrzewski, S. Dapprich, A. D. Daniels, M. C. Strain, O. Farkas, D. K. Malick, A. D. Rabuck, K. Raghavachari, J. B. Foresman, J. V. Ortiz, Q. Cui, A. G. Baboul, S. Clifford, J. Cioslowski, B. B. Stefanov, G. Liu, A. Liashenko, P. Piskorz, I. Komaromi, R. L. Martin, D. J. Fox, T. Keith, M. A. Al-Laham, C. Y. Peng,

A. Nanayakkara, M. Challacombe, P. M. W. Gill, B. Johnson, W. Chen, M. W. Wong, C. Gonzalez, and J. A. Pople, *Gaussian 03*. 2004, Gaussian, Inc.: Wallingford CT.

51. G. B. Bacskay, *A quadratically convergent Hartree-Fock (QC-SCF) method. Application to closed shell systems* Chem. Phys., 1981 **61** (3) 385-404.
52. J. Tomasi and M. Persico, *Thermodynamics of the electron and the proton.* Chem. Rev., 1994 **94** (7) 2027-2094.
53. J. E. Bartmess, *Thermodynamics of the electron and the proton.* J. Phys. Chem., 1994 **98** (25) 6420-6424.
54. M. D. Tissandier, K. A. Cowen, W. Y. Feng, E. Gundlach, M. H. Cohen, A. D. Earhart, J. V. Coe, and T. R. Tuttle Jr., *The proton's absolute aqueous enthalpy and Gibbs free energy of solvation from cluster-ion solvation data.* J. Phys. Chem. A, 1998 **102** (40) 7787-7794.
55. I. A. Topol, G. J. Tawa, S. K. Burt, and A. A. Rashin, *On the structure and thermodynamics of solvated monoatomic ions using a hybrid solvation model.* J. Chem. Phys., 1999 **111** (24) 10998-11014.
56. J. Ho, M. L. Coote, C. J. Cramer, and D. G. Truhlar, *Organic electrochemistry*, in *Theoretical calculation of reduction potentials*, O. Hammerich and B. Speiser, Editors. 2015, CRC Press: Boca Raton. 229-259.
57. S. I. Gorelsky, *SWizard program, revision 4.5*.
58. J. E. Carpenter and F. Weinhold, *Analysis of the geometry of the hydroxymethyl radical by the "different hybrids for different spins" natural bond orbital procedure.* J. Mol Struct.-Theochem, 1988 **169** 41-62.
59. E. D. Glendening, A. E. Reed, J. E. Carpenter, and F. Weinhold, *NBO Version 3.1*.
60. A. E. Reed, L. A. Curtiss, and F. Weinhold, *Intermolecular interactions from a natural bond orbital, donor-acceptor viewpoint.* Chem. Rev., 1988 **88** (6) 899-926.
61. IUPAC, *Compendium of chemical terminology (the "Gold Book")*. 2nd ed. ed. 1997, Oxford: Blackwell Scientific Publications.
62. A. A. Isse and A. Gennaro, *Absolute potential of the standard hydrogen electrode and the problem of interconversion of potentials in different solvents.* J. Phys. Chem. B, 2010 **114** (23) 7894-7899.
63. G. H. Carlsson, P. Nicholls, D. Svistunenko, G. I. Berglund, and J. Hajdu, *Complexes of horseradish peroxidase with formate, acetate, and carbon monoxide.* Biochemistry, 2005 **44** (2) 635-642.
64. G. I. Berglund, G. H. Carlsson, A. T. Smith, H. Szöke, A. Henriksen, and J. Hajdu, *The catalytic pathway of horseradish peroxidase at high resolution.* Nature, 2002 **417** (6887) 463-468.
65. K. H. Sharp, M. Mewies, P. C. E. Moody, and E. L. Raven, *Crystal structure of the ascorbate peroxidase-ascorbate complex.* Nat. Struct. Mol. Biol., 2003 **10** (4) 303-307.
66. A. K. Singh, N. Singh, S. Sharma, S. B. Singh, P. Kaur, A. Bhushan, A. Srinivasan, and T. P. Singh, *Crystal structure of lactoperoxidase at 2.4 Å resolution.* J. Mol. Biol., 2008 **376** (4) 1060-1075.
67. T. J. Fiedler, C. A. Davey, and R. E. Fenna, *X-ray crystal structure and characterization of halide-binding sites of human myeloperoxidase at 1.8 Å resolution.* J. Biol. Chem., 2000 **275** (16) 11964-11971.
68. A. S. Galstyan, S. D. Zarić, and E. W. Knapp, *Computational studies on imidazole heme conformations.* J. Biol. Inorg. Chem., 2005 **10** (4) 343-354.
69. R. S. Mulliken, *Electronic population analysis on LCAO–MO molecular wave functions. I.* J. Chem. Phys., 1955 **23** (10) 1833-1840.
70. K. B. Wiberg, *Application of the pople-santry-segal CNDO method to the cyclopropylcarbinyl and cyclobutyl cation and to bicyclobutane.* Tetrahedron, 1968 **24** (3) 1083-1096.
71. P. Murray-Rust and J. P. Glusker, *Directional hydrogen bonding to sp2- and sp3-hybridized oxygen atoms and its relevance to ligand-macromolecule interactions.* J. Am. Chem. Soc., 1984 **106** (4) 1018-1025.

72. A. Bousseksou, J. J. McGarvey, F. Varret, J. A. Real, J. P. Tuchagues, A. C. Dennis, and M. L. Boillot, *Raman spectroscopy of the high- and low-spin states of the spin crossover complex $Fe(phen)_2(NCS)_2$: an initial approach to estimation of vibrational contributions to the associated entropy change.* Chem. Phys. Lett., 2000 **318** (4-5) 409-416.

73. M. Sorai and S. Seki, *Phonon coupled cooperative low-spin 1A1 high-spin 5T2 transition in $[Fe(phen)_2(NCS)_2]$ and $[Fe(phen)_2(NCSe)_2]$ crystals.* J. Phys. Chem. Solids, 1974 **35** (4) 555-570.

74. R. E. Fenna, *Myeloperoxidase*, in *Handbook of metalloproteins*, A. Messerschmidt, et al., Editors. 2001, John Wiley & Sons: Chichester. 211-221.

75. M. Parac and S. Grimme, *A TDDFT study of the lowest excitation energies of polycyclic aromatic hydrocarbons.* Chem. Phys., 2003 **292** (1) 11-21.

76. D. Jacquemin, E. A. Perpète, G. E. Scuseria, I. Ciofini, and C. Adamo, *TD-DFT performance for the visible absorption spectra of organic dyes: conventional versus long-range hybrids.* J. Chem. Theory Comput., 2008 **4** (1) 123-135.

77. S. Hashimoto, R. Nakajima, I. Yamazaki, Y. Tatsuno, and T. Kitagawa, *Oxygen exchange between the Fe(IV)=O heme and bulk water for the A2 isozyme of horseradish peroxidase.* FEBS Lett., 1986 **208** (2) 305-307.

78. W. A. Oertling, H. Hoogland, G. T. Babcock, and R. Wever, *Identification and properties of an oxoferryl structure in myeloperoxidase compound II.* Biochemistry, 1988 **27** (15) 5395-5400.

79. H. Zhang and H. B. Dunford, *Hammett ρσ correlation for reactions of lactoperoxidase compound II with phenols.* Can. J. Chem., 1993 **71** (12) 1990-1994.

80. N. C. Boaz, S. R. Bell, and J. T. Groves, *Ferryl protonation in oxoiron(IV) porphyrins and its role in oxygen transfer.* J. Am. Chem. Soc., 2015 **137** (8) 2875-2885.

81. R. K. Behan and M. T. Green, *On the status of ferryl protonation.* J. Inorg. Biochem., 2006 **100** (4) 448-459.

82. G. Chreifi, E. L. Baxter, T. Doukov, A. E. Cohen, S. E. McPhillips, J. Song, Y. T. Meharenna, S. M. Soltis, and T. L. Poulos, *Crystal structure of the pristine peroxidase ferryl center and its relevance to proton-coupled electron transfer.* Proc. Natl. Acad. Sci. U.S.A., 2016 **113** (5) 1226-1231.

83. G. Battistuzzi, M. Bellei, C. A. Bortolotti, and M. Sola, *Redox properties of heme peroxidases.* Arch. Biochem. Biophys., 2010 **500** (1) 21-36.

84. G. Battistuzzi, M. Bellei, M. Zederbauer, P. G. Furtmüller, M. Sola, and C. Obinger, *Redox thermodynamics of the Fe(III)/Fe(II) couple of human myeloperoxidase in its high-spin and low-spin forms.* Biochemistry, 2006 **45** (42) 12750-12755.

85. P. G. Furtmüller, J. Arnhold, W. Jantschko, H. Pichler, and C. Obinger, *Redox properties of the couples compound I/compound II and compound II/native enzyme of human myeloperoxidase.* Biochem. Biophys. Res. Commun., 2003 **301** (2) 551-557.

86. P. G. Furtmüller, J. Arnhold, W. Jantschko, M. Zederbauer, C. Jakopitsch, and C. Obinger, *Standard reduction potentials of all couples of the peroxidase cycle of lactoperoxidase.* J. Inorg. Biochem., 2005 **99** (5) 1220-1229.

87. X. Carpena, P. Vidossich, K. Schroettner, B. M. Calisto, S. Banerjee, J. Stampler, M. Soudi, P. G. Furtmüller, C. Rovira, I. Fita, and C. Obinger, *Essential role of proximal histidine-asparagine interaction in mammalian peroxidases.* J. Biol. Chem., 2009 **284** (38) 25929-25937.

88. M. Blair-Johnson, T. Fiedler, and R. Fenna, *Human myeloperoxidase: Structure of a cyanide complex and its interaction with bromide and thiocyanate substrates at 1.9 Å resolution.* Biochemistry, 2001 **40** (46) 13990-13997.

89. T. Matsui, S. Ozaki, E. Liong, G. N. Phillips Jr., and Y. Watanabe, *Effects of the location of distal histidine in the reaction of myoglobin with hydrogen peroxide.* J. Biol. Chem., 1999 **274** (5) 2838-2844.

90. E. Papajak, J. Zheng, X. Xu, H. R. Leverentz, and D. G. Truhlar, *Perspectives on basis sets beautiful: Seasonal plantings of diffuse basis functions.* J. Chem. Theory Comput., 2011 **7** (10) 3027-3034.

91. J. M. L. Martin, C. W. Bauschlicher Jr., and A. Ricca, *On the integration accuracy in molecular density functional theory calculations using Gaussian basis sets.* Comput. Phys. Commun., 2001 **133** (2-3) 189-201.

92. T. Simonson and D. Perahia, *Internal and interfacial dielectric properties of cytochrome c from molecular dynamics in aqueous solution.* Proc. Natl. Acad. Sci. U.S.A., 1995 **92** (4) 1082-1086.

CHAPTER 12

Protonation site of ferrous peroxidases

Human beings, who are almost unique in having the ability to learn from the experience of others, are also remarkable for their apparent disinclination to do so.

Douglas Adams,
in Last Chance to See

12.1 Introduction

The prosthetic group of heme peroxidases is constituted by protoporphyrin IX and a central iron atom coordinated to the imidazole of a proximal histidine. Formation of the ferrous species via a one-electron reduction of the ferric native enzyme involves the gain of a proton. This ferrous intermediate does not participate in the reactions catalyzed by peroxidases nor play a role in their biological activity. However, for a detailed analysis of the reactivity, reaction mechanisms, and other features of peroxidases, the study of the protonation site of this oxidation intermediate is also necessary to obtain a comprehensive knowledge on the subject.

Recently Chiavarino *et al.* published a joint empirical and computational study to determine the protonated site of ferrous heme, employing the Fe(II)-protoporphyrin IX complex (see Figure 12.1).[1] Gas-phase experimental measurements were performed by FTICR mass spectrometry on protonated ferrous ions obtained by electrospray ionization. The calculations were carried out by using an analogous molecular model together with the Car-Parrinello method, based on the combination of density functional theory (DFT) with molecular dynamics.[2]

The most favourable protonated species was obtained at the β-carbon atom of a vinyl group (61.9 $kJ \cdot mol^{-1}$ lower than the second preferred isomer), so this position was assigned to the extra proton. However, this result may not be valid for peroxidases, not only due to the use of gas phase in the measurements and calculations, but also because the employed model included all porphine substituents whereas it did not take into account the important axial interaction at the proximal side.

The molecular model of the active site of peroxidases already employed for the calculations incorporates an imidazole axially coordinated to iron, simulating the proximal histidine (Chapter 11). This link between Fe and a nitrogen atom of the imidazole leads to a charge distribution between both moieties and, therefore, it may present an important influence on the protonation properties of ferrous heme. In fact, some research has already revealed that axial coordination ligands show a relevant role in the reactivity of heme proteins,[3, 4] whereas substituents on the porphyrin ring have not such a significant effect.[5]

The aim of this study is to establish the site of protonation at the ferrous intermediate of peroxidases, necessary to determine other features correctly, like redox potentials or ligand binding properties; and, besides, test the validity of the computational method for peroxidases (a minimal molecular model plus a DFT computational level) already employed in the previous chapter.

12.2 Computational procedure

Atom numbering used for the description of iron protoporphyrin IX (or heme *b*) is depicted in Figure 12.1, numbers were assigned according to IUPAC recommendations and letters A to D indicate the location of each pyrrole ring.[6]

Two molecular models were considered. Model I is the same model already employed in the previous chapter, composed of porphine, central iron, and an imidazole ring axially coordinated to iron. Besides, an extended model was also used, with the addition of a vinyl group in position 3 (model II), as represented in Figure 12.2.

Different protonation possibilities were tested by optimizing the ferrous species (Fe(II)-PO) upon addition of an extra proton on the iron atom (Fe(II)-PO-H_{Fe}), a pyrrole nitrogen (Fe(II)-PO-H_{N21}), pyrrole α-carbon (Fe(II)-PO-H_{C1}), pyrrole β-carbon (Fe(II)-PO-H_{C2}), and meso carbon atom of a methine bridge (Fe(II)-PO-H_{C5}) with molecular model I. Moreover, model II was used to analyze the protonation on a vinyl β-carbon (Fe(II)-PO-$H_{C3\beta}$) and on N_{21} for comparison. Besides, other peroxidase intermediates (ferric species and compounds I and II) were calculated with this model.

Proton affinity (PA) is a frequently used measure of the gas-phase basicity. Thus, for a deprotonation reaction:

$$AH \rightleftharpoons A^- + H^+$$

It has been defined as:

$$\mathrm{PA} = \Delta H°$$

Results in aqueous solution are reported as pK_a values. They were obtained applying the following expression:

$$\mathrm{p}K_\mathrm{a} = \Delta G°_{(\mathrm{aq})}/2.303\mathrm{RT}$$

Values of $\Delta H°_f$ (H^+) = 6.20 kJ·mol^{-1} [7] and $\Delta G°_f$ (H^+)$_{(aq)}$ = –1138.71 kJ·mol^{-1} [7-9] were employed. Absolute reduction potentials were calculated according to:

$$E° = -\frac{\Delta G°_{(\mathrm{aq})}}{\mathrm{n}F}$$

where n is the number of electrons generated in the half-reaction and *F* is the Faraday constant. All reduction potentials are reported relative to the standard hydrogen electrode (SHE) with an absolute reduction potential $E°$ = 4.44 V. Standard free energy values in solution were corrected for 1.0 M as already explained. All calculations were performed with Gaussian 03 package[10] at the unrestricted DFT UB3LYP/6-31G* computational level, and PCM solvation model was used to estimate solvation free energies in water.

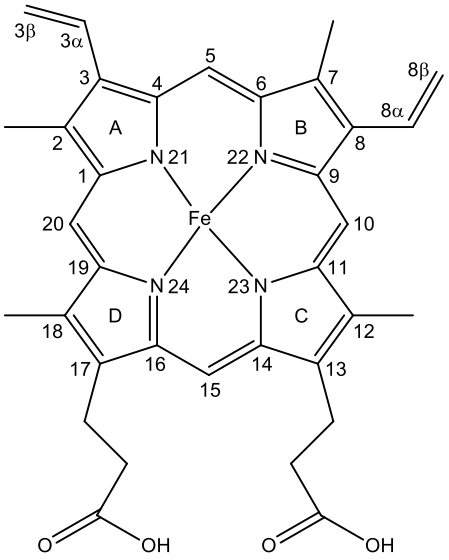

Figure 12.1. Heme numbering convention for iron protoporphyrin IX.

UV-Vis spectra were obtained from the lowest 50 singlet excited states calculated with time-dependent DFT (TD-DFT) considering PCM solvation. Convoluted spectra were extracted with the SWizard program[11] applying Gaussian distributions with a peak half-width of 2500 cm^{-1}.

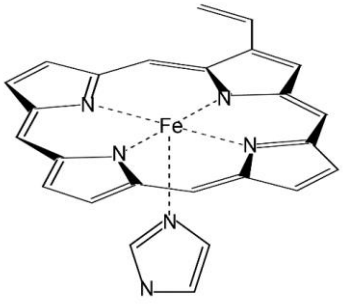

Figure 12.2. Model II. A vinyl substituent in position 3 is incorporated in the molecular model.

12.3 Results and discussion

The optimized structures obtained for unprotonated ferrous species, and this intermediate protonated at the metal centre (Fe), pyrrole nitrogen (N_{21}), pyrrole α- and β-carbons (C_1 and C_2, respectively), and meso carbon (C_5) with model I are collected in Figure 12.3. Some relevant thermodynamic parameters and atomic charges from all these compounds are collected in Table 12.1.

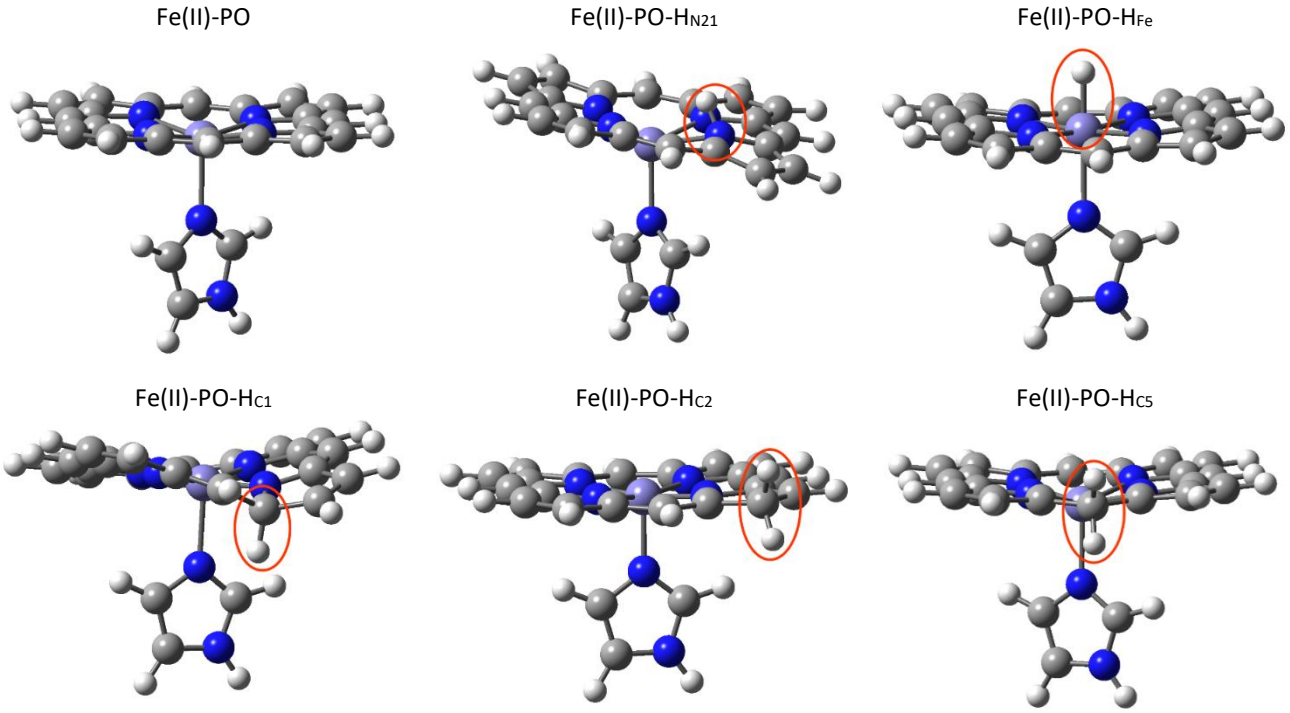

Figure 12.3. Most stable optimized structures for the unprotonated ferrous intermediate of peroxidases and its protonated isomers calculated with model I and at the UB3LYP/6-31G* computational level.

The planarity observed at the unprotonated intermediate is conserved at the isomers with protonated Fe, C_2, or C_5 atoms. In Fe(II)-PO-H$_{Fe}$ the additional proton is axially bonded on the vacant coordination position. Protonation onto C_2 and C_5 is accompanied by a hybridization switch of these atoms, from the trigonal planar sp^2 to tetrahedral sp^3, resulting in a high displacement of the already attached proton while the carbon atoms keep in plane. The associated ideal angle transition from 120° to 109° is not possible as the angles in the porphyrin structure (C_1–C_2–C_3 and C_4–C_5–C_6) are quite restricted, then a decrease of only about 5° is observed upon protonation. Besides, a shift of the central iron into the heme plane is observed for Fe(II)-PO-H$_{Fe}$ and Fe(II)-PO-H$_{C2}$ structures.

On the other hand, protonation on N_{21} and C_1 causes more important geometry changes as these atoms have not bonded hydrogens. The addition of the proton at Fe(II)-PO-H$_{N21}$ shows an important steric hindrance with the bulky Fe atom, thus the orthogonal position of the imidazole with respect to heme is lost and some distortion of porphine is produced. The proton added on N_{21} is rather more stable at the distal side, avoiding being even more hindered by neighbouring Fe as it lies slightly out-of-plane but displaced towards proximal side. The change from planar to tetrahedral bonding in C_1 leads to a higher effect on the overall porphine structure. Therefore, heme distortion is much more evident in Fe(II)-PO-H$_{C1}$ than in other isomers. In this case, proximal protonation is thermodynamically preferred.

Protonation on the metal centre has been already analyzed in Chapter 11. Relevant obtained data are again collected for

the comparative study. The charge on Fe upon protonation reflects that the hydrogen atom has not a proton character but acts as hydride anion. This process is the least favourable and consequently protonation does not take place on the metal in any case.

Table 12.1. Relative free energies and proton affinities in kJ·mol^{-1}, pK_a values, and Mulliken atomic charges in atomic units for the optimized structures of protonated ferrous isomers under study obtained with model I and calculated with UB3LYP/6-31G* at the most stable spin. Values of ΔG° obtained with PCM continuum model in italics. Charges in solution at the different protonation sites are shown for the protonated and unprotonated species, values with attached hydrogens summed into heavy atoms in parentheses. Other thermodynamic parameters are collected in Table S12.1.

Protonation site	Spin	ΔG°		PA	pK_a	Charge			
						Unprotonated		Protonated	
N_{21}	2	0.00	*0.00*	1012.12	0.1	–0.78	(–0.78)	–0.84	(–0.39)
Fe	1	98.66	*106.57*	920.76	–18.5	1.27	(1.27)	1.15	(1.08)
C_1	1	69.52	*72.74*	951.36	–12.6	0.35	(0.35)	–0.04	(0.21)
C_2	0	73.39	*70.12*	955.80	–12.2	–0.22	(–0.05)	–0.41	(0.06)
C_5	2	0.72	*14.45*	1008.52	–2.4	–0.32	(–0.15)	–0.47	(–0.01)

Despite some distorted geometry, Fe(II)-PO-H_{N21} is relatively stable and yields higher PA and pK_a values than the other protonated isomers. The couple N_{21}+H shows a charge 0.40 a.u. more positive than unprotonated N_{21}, indicating that proton charge is only partially delocalized, while isomers in C_1, C_2, or C_5 are much more effective in charge delocalization. However, nitrogen is a better base than carbon atoms; therefore, this protonation is preferred.

Atom C_5 corresponds to the meso carbon atom of a methine bridge, protonation at this position is slightly more energetic than the observed with Fe(II)-PO-H_{N21} but it is also quite stable compared to the other sites. Current data evidence that compounds protonated on pyrrole carbons, Fe(II)-PO-H_{C1} and Fe(II)-PO-H_{C2}, are energetically similar, although the former is more stable in gas phase and the latter with solvation, but far more unstable than N_{21} and C_5 isomers.

According to this model, computed proton affinities range from 920 (protonation at Fe) to 1012 (N_{21}) kJ·mol^{-1}. Microscopic pK_a values may be better related to the macroscopically observed events and the effect of pH on the reactivity. However, pK_a values calculated for these five protonated compounds are very low. Protonation is more stable in N_{21} both in gas phase and *in vacuo*, but its pK_a is close to 0, still too low to explain the observed protonation state. C_5 is the second choice, and the other studied positions (C_1, C_2, and Fe) are much more acid and present pK_a values lower than –10. A comparison with previously published results[1] shows quite different trends, since the preferred order of protonation differs in both studies.

The negative charge of porphine is focused on the four pyrrolic nitrogens (N_{21} to N_{24}, or N_P), and the high electronic density of these atoms explains their strong coordination with the metal centre. The addition of an axial ligand in the fifth coordination position of iron, as the considered imidazole ring mimicking the proximal histidine common to all peroxidases, leads to a slight out-of-plane shift of the iron, accompanied by lengthening and weakening of Fe–N_P bonds. This displacement facilitates the attachment of a proton on a N_P from the distal side, and this protonation reveals more stable than on any other atom at the porphyrin ring. However, axial coordination positions remained vacant in the molecular model used by Chiavarino *et al*. Therefore, their results could not profit from this effect, disfavouring protonation on N_{21}. Furthermore, protonation on the central iron is quite unstable with the imidazole-coordinated model, but this was not the case with a heme without any axial ligand. The differences observed at other positions cannot be so easily explained in terms of the fifth coordination, nor can be with reference to porphine substituents.

The reduction potential obtained for the formation of the protonated ferrous species from the native ferric intermediate ranges from –1589 mV with Fe(II)-PO-H_{Fe} to –485 mV obtained for Fe(II)-PO-H_{N21}. The second potential is better and closer to experimental values measured for peroxidases, although it is very similar to the reduction potential calculated for

unprotonated Fe(II)-PO in the previous chapter (–465 mV).

Model I does not allow the possibility of a protonation site at any of the porphyrin substituents. However, the previously mentioned study on protonation of ferrous heme also considered both carbons of vinyl groups and a carboxyl oxygen as protonation alternatives.[1] Oxygen atoms at heme propanoate substituents present pK_a values around 4 - 5 and, although slight variations from this value can be specifically produced by the particular environment, these carboxylic acids should keep unprotonated under neutral pH. Furthermore, the oxidation state of the distant metal centre does not exert a very relevant influence on the acidity of these carboxylic acids.[12] Therefore, it can be presumed that the protonation state of these carboxyl groups is the same for all redox intermediates, *i.e.*, protonated propanoic acid substituents could not be exclusive to ferrous species, and this option is ruled out. Besides, protonation on the α-carbon of a vinyl substituent would lead to a rare and unstable carbocation at β-position, so this site is rejected as well:

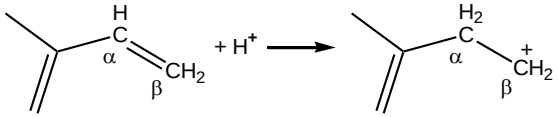

On the other hand, protonation on β-carbon is consistent with the Markownikoff Rule:[13] considering the protonation process as the first step of the usual Brønsted acid addition to an alkene, the proton binds the least substituted carbon atom (β-carbon here) to yield a more stable carbocation. Besides, the addition of H^+ on β-carbon in this case permits the delocalization of the extra positive charge to the porphyrin moiety, with a very important stabilization effect. This process must be much more influenced by the oxidation state of the Fe atom:

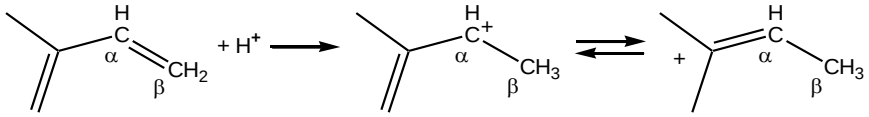

Furthermore, the computational study of Chiavarino *et al*. estimates a higher proton affinity of this β-carbon than both α-carbon and carboxyl oxygen, as expected. Thus, only this protonation site has been here analyzed, and corresponding calculations were performed by using a different molecular model incorporating a vinyl group on C_3, model II (Figure 12.2). The structures for Fe(II)-PO, Fe(II)-PO-H_{N21}, and Fe(II)-PO-$H_{C3\beta}$ were optimized with this model (Figure 12.4). Some relevant thermodynamic and geometric parameters, and atomic charges are collected in Table 12.2.

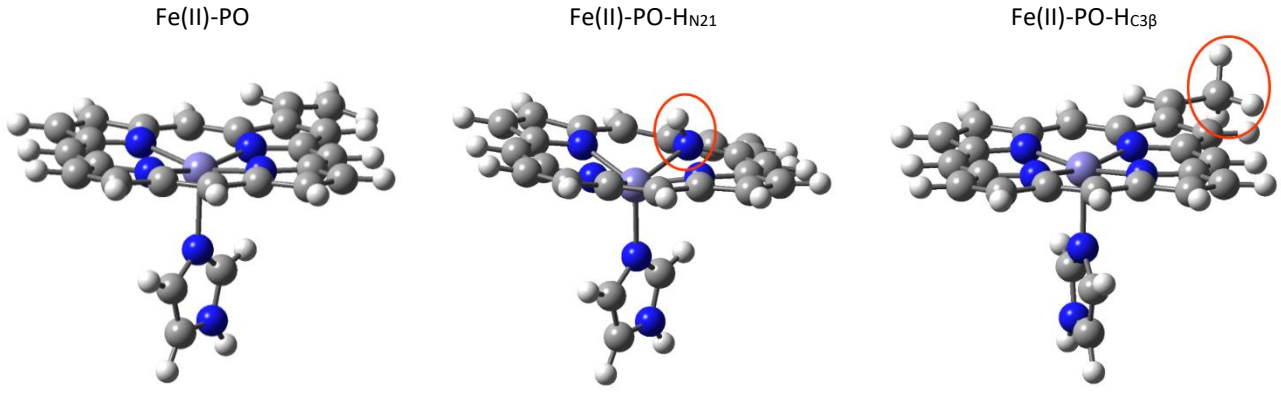

Figure 12.4. Most stable optimized structures for the unprotonated ferrous intermediate of peroxidases and its protonated isomers calculated with model II and at the UB3LYP/6-31G* computational level.

The presence of a vinyl substituent does not affect the geometry of the structures of ferrous species either unprotonated or protonated on N_{21}. A slight difference in pK_a of Fe(II)-PO-H_{N21} (0.4 units) is found between both models, and the vinyl

substituent has no significant effect on the atomic charge on N_{21}.

The isomer protonated at the β-carbon (Fe(II)-PO-$H_{C3\beta}$) is thermodynamically more favourable, yielding a higher proton affinity, 1048 kJ·mol^{-1}, closer to the value obtained at this position with Car-Parrinello calculations on a full heme model (1220 kJ·mol^{-1}).[1] This protonation yields a pK_a higher than all the other values, although still too low, which can be attributed to a defective combination of computational level and molecular model.

The addition of a proton on $C_{3\beta}$ has no effect on the planarity of the porphyrin ring, however it modifies the C–C distances of the vinyl group. These parameters as well as corresponding bond orders and charges on these atoms are collected in Table 12.2. The values obtained for Fe(II)-PO and Fe(II)-PO-H_{N21} are very similar: $C_{3\alpha}$–$C_{3\beta}$ shows a short distance with a bond order close to 2, in agreement with the vinyl double bond, and C_3–$C_{3\alpha}$ distance and bond order are typical of a C–C single bond. The double bond is broken upon protonation at $C_{3\beta}$, leading to a single $C_{3\alpha}$–$C_{3\beta}$ bond and to an intermediate situation between a single and a double bond for C_3–$C_{3\alpha}$, as an equilibrium for charge delocalization is achieved (see above). In fact, the positive charge on the vinyl substituent observed for Fe(II)-PO-$H_{C3\beta}$ hardly increases with respect to the unprotonated species, and it is just the same amount calculated with PCM for Fe(II)-PO-H_{N21}. This indicates that the charge is completely transferred to porphine, despite the geometry does not correspond to a full double C_3=$C_{3\alpha}$ bond. The chemical-bond arrangement at the vinyl substituents of heme cannot be confirmed with crystallographic structures of ferrous peroxidases and other redox intermediates, since the electronic density maps, even at the highest available resolution, do not yield unequivocal distances for these vinyl groups.

Table 12.2. Relative free energies and proton affinities in kJ·mol^{-1}, pK_a values, and Mulliken atomic charges in atomic units for the optimized structures of protonated ferrous isomers under study obtained with model II and calculated with UB3LYP/6-31G* at high spin. Values of Δ*G*° obtained with PCM continuum model in italics. Charges in solution at three different positions are shown for the protonated and unprotonated species, values with attached hydrogens summed into heavy atoms in parentheses; also distances and bond orders (in parentheses) determined for the C–C bonds at the vinyl substituent. Other thermodynamic parameters are collected in Table S12.2.

		Δ*G*°	**PA**	**pK_a**
Protonation site	**$C_{3\beta}$**	0.00 *0.00*	1047.91	3.8
	N_{21}	30.12 *23.43*	1015.52	–0.3
		Fe(II)-PO	**Fe(II)-PO-$H_{C3\beta}$**	**Fe(II)-PO-H_{N21}**
Charge	**$C_{3\alpha}$**	–0.14 (0.02)	–0.19 (0.00)	–0.14 (0.04)
	$C_{3\beta}$	–0.37 (–0.06)	–0.51 (0.03)	–0.36 (–0.01)
	N_{21}	–0.79 (–0.79)	–0.81 (–0.81)	–0.86 (–0.41)
Distance and bond order	**C_3–$C_{3\alpha}$**	1.458 (1.10)	1.387 (1.42)	1.458 (1.10)
	$C_{3\alpha}$–$C_{3\beta}$	1.342 (1.88)	1.492 (1.07)	1.341 (1.88)

The reduction potential calculated for the formation of the ferrous intermediate protonated at N_{21} is –517 mV, similar as with model I, and –274 mV is obtained for Fe(II)-PO-$H_{C3\beta}$. This value is in the experimental range measured for peroxidases and very close to the potential determined for horseradish peroxidase (–270 mV).[14]

Due to the very efficient charge delocalization to the porphyrin ring, the proton affinity and pK_a of the species protonated at the vinyl β-carbon must be strongly influenced by the charged central metal atom. In order to confirm that this protonation only takes place at the ferrous species, other redox intermediates have been also computed with model II. Thus, it can be observed the important effect of the iron oxidation state on the acidity at this position. Ferric peroxidase produces pK_a = –10.4, while ferryl compounds I and II yield –13.0 and –9.2, respectively (compound II already protonated on ferryl oxygen). The possibility of a protonated vinyl substituent at these species is then discarded. It should be noted

that compound II, as the ferrous intermediate, contains an extra proton. The alternative protonation on $C_{3\beta}$ rather than on ferryl oxygen has been also analyzed, but the pK_a values obtained with model II (6.8 for O and –3.4 for $C_{3\beta}$) ruled out this possibility.

The general molecular model of the active site employed to study peroxidases (here model I) cannot simulate accurately the geometry and thermodynamics of the ferrous state, because of the wrong allocation of the additional proton. Therefore, the correct heme protonation site at a vinyl substituent must be incorporated (model II) for the proper calculation of any properties of this intermediate.

12.4 Conclusions

The ferrous intermediate of peroxidases features a protonated heme, the protonation site has been studied computationally employing two different simple molecular models with a DFT method. Both structures contain a coordinated axial imidazole to simulate the distal histidine, which plays a role in biological activity, but only one model incorporates a vinyl substituent.

The most basic position at porphine is a pyrrolic nitrogen atom. It presents a very low pK_a (~0 with both models) but higher than any other atom of the porphyrin ring or the ferrous centre. However, protonation at the β-carbon of a vinyl group is more favoured (pK_a = 3.8), as previously referred by Chiavarino *et al*. for a ferrous heme lacking axial ligands.[1] Conjugated π bonds are decisive for the stabilization of the carbocation formed at the α-position as the charge is effectively delocalized throughout porphine.

The employed methodology allowed the confirmation of the protonation site but it failed in the estimation of an accurate associated pK_a value, too low to explain empirical observations. Nevertheless, the ferrous species protonated at the vinyl substituent yielded a very adequate potential for the reduction of the native ferric state of peroxidases.

The molecular model comprising only Fe-centred porphine plus axial imidazole is valid for a correct description of peroxidase properties and processes not involving ferrous species, but a protonated vinyl substituent must be incorporated when this intermediate is considered.

12.5 References

1. B. Chiavarino, M. E. Crestoni, S. Fornarini, and C. Rovira, *Protonated heme.* Chem. Eur. J., 2007 **13** (3) 776-785.
2. R. Car and M. Parrinello, *Unified approach for molecular dynamics and density-functional theory.* Phys. Rev. Lett., 1985 **55** (22) 2471-2474.
3. A. R. Groenhof, M. Swart, A. W. Ehlers, and K. Lammertsma, *Electronic ground states of iron porphyrin and of the first species in the catalytic reaction cycle of cytochrome P450s.* J. Phys. Chem. A, 2005 **109** (15) 3411-3417.
4. D. M. A. Smith, M. Dupuis, E. R. Vorpagel, and T. P. Straatsma, *Characterization of electronic structure and properties of a bis(histidine) heme model complex.* J. Am. Chem. Soc., 2003 **125** (9) 2711-2717.
5. C. Rovira and M. Parrinello, *Factors influencing ligand binding properties of heme models: a first principles study of picket-fence and protoheme complexes.* Chem. Eur. J., 1999 **5** (1) 250-262.
6. J. E. Merritt and K. L. Loening, *Nomenclature of tetrapyrroles.* Pure Appl. Chem., 1979 **51** (11) 2251-2304.
7. J. E. Bartmess, *Thermodynamics of the electron and the proton.* J. Phys. Chem., 1994 **98** (25) 6420-6424.
8. M. D. Tissandier, K. A. Cowen, W. Y. Feng, E. Gundlach, M. H. Cohen, A. D. Earhart, J. V. Coe, and T. R. Tuttle Jr., *The proton's absolute aqueous enthalpy and Gibbs free energy of solvation from cluster-ion solvation data.* J. Phys. Chem. A, 1998 **102** (40) 7787-7794.
9. I. A. Topol, G. J. Tawa, S. K. Burt, and A. A. Rashin, *On the structure and thermodynamics of solvated monoatomic*

ions using a hybrid solvation model. J. Chem. Phys., 1999 **111** (24) 10998-11014.

10. M. J. Frisch, G. W. Trucks, H. B. Schlegel, G. E. Scuseria, M. A. Robb, J. R. Cheeseman, J. A. Montgomery Jr., T. Vreven, K. N. Kudin, J. C. Burant, J. M. Millam, S. S. Iyengar, J. Tomasi, V. Barone, B. Mennucci, M. Cossi, G. Scalmani, N. Rega, G. A. Petersson, H. Nakatsuji, M. Hada, M. Ehara, K. Toyota, R. Fukuda, J. Hasegawa, M. Ishida, T. Nakajima, Y. Honda, O. Kitao, H. Nakai, M. Klene, X. Li, J. E. Knox, H. P. Hratchian, J. B. Cross, C. Adamo, J. Jaramillo, R. Gomperts, R. E. Stratmann, O. Yazyev, A. J. Austin, R. Cammi, C. Pomelli, J. W. Ochterski, P. Y. Ayala, K. Morokuma, G. A. Voth, P. Salvador, J. J. Dannenberg, V. G. Zakrzewski, S. Dapprich, A. D. Daniels, M. C. Strain, O. Farkas, D. K. Malick, A. D. Rabuck, K. Raghavachari, J. B. Foresman, J. V. Ortiz, Q. Cui, A. G. Baboul, S. Clifford, J. Cioslowski, B. B. Stefanov, G. Liu, A. Liashenko, P. Piskorz, I. Komaromi, R. L. Martin, D. J. Fox, T. Keith, M. A. Al-Laham, C. Y. Peng, A. Nanayakkara, M. Challacombe, P. M. W. Gill, B. Johnson, W. Chen, M. W. Wong, C. Gonzalez, and J. A. Pople, *Gaussian 03*. 2004, Gaussian, Inc.: Wallingford CT.

11. S. I. Gorelsky, *SWizard program, revision 4.5*.

12. D. K. Das and O. K. Medhi, *The role of heme propionate in controlling the redox potential of heme: square wave voltammetry of protoporphyrinato IX iron (III) in aqueous surfactant micelles.* J. Inorg. Biochem., 1998 **70** (2) 83-90.

13. W. Markownikoff, *I. Ueber die Abhängigkeit der verschiedenen Vertretbarkeit des Radicalwasserstoffs in den isomeren Buttersäuren.* Justus Liebigs Ann. Chem., 1870 **153** (2) 228-259.

14. H. A. Harbury, *Oxidation-reduction potentials of horseradish peroxidase.* J. Biol. Chem., 1957 **225** (2) 1009-1024.

CHAPTER 13

Modulation of the redox potential of peroxidases by simple geometrical manipulation

If at first you don't succeed, try, try again.
Then give up, there's no use being a damn fool about it.

W. C. Fields

13.1 Introduction

Heme is an important metal-organic group, ubiquitous in multiple biological compounds. Its importance lies in its particular structure, a flat porphine constituted by four pirrole rings covalently bonded to a central metal ion. This aromatic geometry permits that ferriprotoporphyrin IX presents a very notable resonance among all porphine atoms, and also two conjugated vinyl substituents, which results in a π electronic cloud with as many as 26 π electrons. This special configuration together with the metal centre are determinant for the significant biological activity of this group. It must be noted that planarity of heme is essential for keeping the aromaticity, making the compound exceptionally stable. Heme is the prosthetic group at the active site of peroxidases and the distinctive specificities of different peroxidases may be mostly ascribed to structural changes within the heme or in its close vicinity.

According to their phylogenetic affiliation, heme peroxidases can be classified into two superfamilies,[1] peroxidase-cyclooxygenase (previously animal peroxidases) and peroxidase-catalase (previously bacterial, fungal, and plant peroxidases), and three families. More recently, classification into four different superfamilies has been proposed.[2] The peroxidase-cyclooxygenase superfamily includes several subfamilies,[3] with mammalian peroxidases playing a significant biological role.

The oxidation intermediates of peroxidases present particular redox profiles that reveal essential for their enzymatic function. Besides, the differences in these oxidation potentials fully determine the observed disparity in their reactivity. In particular, the reduction potentials of compound I/ferric and compound I/compound II couples in mammalian peroxidases are higher with respect to most peroxidases, allowing them to catalyze the typical two-electron oxidation of halides, including bromide and chloride, that seems to be the main physiological enzymatic activity of these proteins.[2] These differences must arise from some changes in the structure and geometry of the enzymes, most probably, in the proximity of the active site.

Peroxidases belonging to peroxidase-cyclooxygenase superfamily display hemes covalently bonded to protein: the prosthetic group is linked via two ester bonds with conserved Asp and Glu residues.[4] As a result, heme becomes distorted and these enzymes present some different biophysical and chemical properties. Additionally, myeloperoxidase (MPO), which has a third bond (a sulfonium ion linkage with Met243),[5] is an enzyme that shows some unique features: the heme groups are particularly bent, a red-shifted Soret band with respect to other peroxidases (MPO is green in contrast to other red or brown peroxidases), and it presents a redox profile that explains its ability to oxidize chloride producing the bactericidal agent hypochlorous acid (HClO). As a result, this enzyme of the innate immune system is a key agent in host defense against infection.[6, 7]

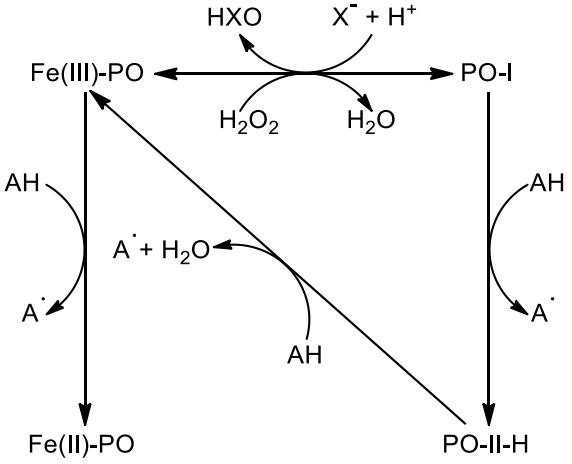

Scheme 13.1. Peroxidase cycle showing both peroxidation and halogenation reactions, as well as formation of ferrous intermediate. X^- stands for halides (I^-, Br^-, Cl^-) or thiocyanate (SCN^-).

Peroxidases participate in oxidation processes, namely peroxidation and halogenation, according to the reactions collected in Scheme 13.1. The native ferric state (Fe(III)-PO) is oxidized to compound I (PO-I), which is two oxidizing equivalents above resting state and is active for both reactions. PO-I can be one-electron reduced to compound II (PO-II-H), only active for peroxidation, and subsequent one-electron reduction leads back to native enzyme. Further reduction of this species yields inactive ferrous state (Fe(II)-PO). Compound I shows higher reduction potentials and also participate in two-electron oxidation of halides, while the other species reveal not so oxidizing.

As already described in Chapter 11, both superfamilies exhibit different redox profiles. Some data are collected in Table 13.1. It must be noted that MPO lies at the edge of some ranges. Furthermore, it is an outlier in the case of the ferric/ferrous couple, displaying a positive value (5 to 24 mV) more typical of globins. These values account for iodide oxidation from compound I of plant peroxidases, while animal peroxidases are also able to oxidize bromide, or even chloride (primarily MPO). The origin of the PO-I/Fe(III)-PO reduction potential resides in the structural differences within and/or in the environs of the prosthetic group.

Table 13.1. General reduction potential ranges obtained for peroxidases. All values in mV.

Reduction process	Superfamily	
	Peroxidase-catalase	**Peroxidase-cyclooxygenase**
PO-I/Fe(III)-PO	750 - 950	1000 - 1150
PO-I/PO-II-H	900 - 1150	1150 - 1350
PO-II-H/Fe(III)-PO	750 - 950	950 - 1050
Fe(III)-PO/Fe(II)-PO	–180 - –280	–180 - –280

Covalent bonding between protein and heme exerts an electronic effect on the latter, but it may be also the source of its curvature. The lack of planarity of the prosthetic group could affect its aromaticity and, therefore, modify the stability of these distorted porphyrins as well as influence their spectroscopic properties. Besides, some research proposes that proximal histidine of MPO (and, by extension, enzymes belonging to peroxidase-cyclooxygenase superfamily) is unprotonated at N_π. Thus, the strong interaction between proximal imidazole and a conserved asparagine (Asn421 in MPO) leads to a proton transfer between these two residues, which also has an impact on the Fe-ligand bond.[8] Furthermore, we have observed that the position of the proximal histidine is not the same for all peroxidases and it could even be a distinctive feature of both superfamilies. This is mostly evident in the rotation angle of the imidazole with respect to an axis perpendicular to porphyrin plane. This angle depends on the position of the peptide bonds of histidine and other interactions with surrounding groups, as with the mentioned asparagine.

We discuss whether covalent bonding, heme curvature, and angle and protonation state of the proximal imidazole are responsible for the particular spectral and redox properties of peroxidases.

13.2 Computational methods

The active site of peroxidases has been simulated with the simple model that has performed quite adequately in previous studies, *i.e.*, Fe-centred porphine and an imidazole ring coordinated to the metal in an axial position. Ferric (S = 5/2) and ferrous (S = 2) species, and compounds I (S = 1/2) and II (S = 1) have been considered with either imidazole or imidazolate, compound II has always been considered protonated on the ferryl oxygen and, since a vinyl substituent is not included in the model, protonation of ferrous intermediate was applied on N_{21} (or N_A, nitrogen atom of pyrrole A).

Heme numbering is used as in Chapter 12 (see Figure 12.1). Imidazole atoms are numbered according to the IUPAC recommendations: this group is linked to the histidine via C_4, adjacent to this atom are N_π and C_5, and the other two atoms are N_τ and C_2. Here, carbons also include Im indicating imidazole (C_{4Im}, and so on) to avoid confusion with heme carbon

atoms.

Calculations were performed with either free rotation angle of imidazole or the rotation of this group around distal axis fixed at –72° and 45° angles, as depicted in Figure 13.1, to simulate the position in peroxidase-catalases and peroxidase-cyclooxygenases, respectively.

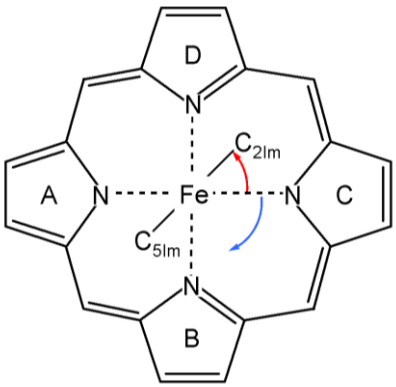

Figure 13.1. Axial rotation angle of proximal imidazole with respect to heme, view from distal side. The angle is defined with respect to position of N_C (nitrogen atom of pyrrole C). Thus, for angle = 45° (as imidazole shown in the figure, red arrow) the dihedral angle N_C–Fe–N_τ–C_{2Im} was fixed at 45° and the dihedral angle N_C–Fe–N_τ–C_{5Im} at 225°; and for angle –72° (blue arrow) these parameters were fixed at –72° and 108°, respectively.

Furthermore, we have analyzed the effect of heme doming according to the following description. Heme of MPO is linked to the protein at the distal side through three covalent bonds. Besides, iron is linked to the imidazole of a proximal histidine through a coordination bond. These linkages exert a strain on the structure and, as a result, the porphyrin ring becomes slightly curved. On the assumption that a plane can be defined passing through the three affected carbon atoms of the porphine (C_2, C_3, and C_{12}, see Figure 12.1), the variation of the distance from the carbon atom of the imidazole where this group is bound to remainder of the histidine (C_{4Im}) may produce different degrees of curvature. Thus, employing Cartesian coordinates the three porphyrin carbons were kept at the plane y = 0, while y_{C4Im} was situated at different values (Figure 13.2).

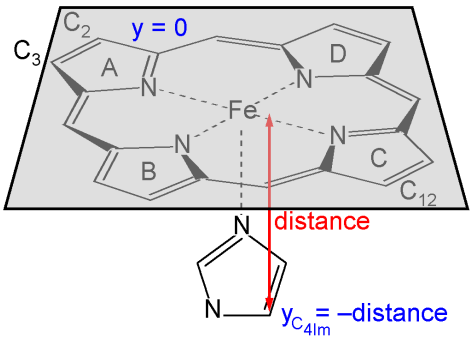

Figure 13.2. Plane y = 0 passing through atoms C_2, C_3, and C_{12}, the distance from imidazole carbon atom C_{4Im} to this plane corresponds to its Cartesian coordinate y value (y_{C4Im}).

DFT-based calculations were carried out with Gaussian 03.[9] Geometry optimizations were performed and a polarized continuum (with solvent water parameters) was used to simulate the environment. Thus, PCM//UB3LYP/6-31G* computational level was always employed. Besides, Gaussian default parameters were considered in all cases, and all solvated free-energy values were corrected as for standard state in aqueous solution.

pK_a values were worked out from the Gibbs free energy of the protonated and unprotonated forms according to the acid-base equilibrium:

$$AH \xrightleftharpoons{\Delta G^{o}_{AH}} A^- + H^+$$

and applying the following expression:

$$pK_a = \Delta G^{o}_{AH} / 2.303RT$$

Absolute reduction potentials were calculated as:

$$E^{o} = -\frac{\Delta G^{o}_{A}(aq)}{nF}$$

where n is the number of electrons generated in the half-reaction and F the Faraday constant. All reduction potentials are reported relative to the standard hydrogen electrode (SHE) with an absolute reduction potential $E°$ = 4.44 V.

UV-Vis spectra were calculated with time-dependent DFT (TD-DFT) considering the lowest 50 singlet excited states and then extracted with the SWizard program[10] by using Gaussian distributions with a peak half-width of 2500 cm^{-1}.

13.3 Results and discussion

The electronic effect of covalent bonding has already been studied computationally and the obtained results published in a paper entitled *Effect of covalent links on the structure, spectra, and redox properties of myeloperoxidase - A density functional study*.[11] Those authors use the same molecular model as in this work (Fe-porphine plus imidazole) to simulate horseradish peroxidase (HRP), while the two ester bonds were modelled with two $–CH_2–O–CO–CH_3$ groups (as for lactoperoxidase, LPO), and myeloperoxidase also incorporates a $–CH_2–CH_2–S(CH_3)^+–CH_2–CH_3$ group to simulate the sulfonium ion link, and some other variations of these structures.

The environment around the active site was modelled with COSMO dielectric continuum model,[12] employing a dielectric constant ε = 4 (typical of proteins) or 80 (water). With these premises the four intermediates, ferric, ferrous, and compounds I and II, were computed and thermodynamics and spectral properties were determined.

Geometries were fully optimized, and the obtained structures hardly show any heme distortion. This indicates that this curvature does not originate merely from covalent bonding, but the whole structure may be strained and the protein pulls the heme through the linkages. Furthermore, rotation of imidazole was not restricted and it could turn around distal axis freely, so optimized structures show this group at different positions. Thus, both the strain exerted on the porphyrin and the specific position of imidazole were not taken into account

With these calculations some experimental shifts observed for the Soret band could be fairly explained, as the difference in Fe(III)-PO between HRP and LPO, while the typical large red-shift of MPO was clearly underestimated. Also, redox potentials were calculated for Fe(III)-PO/Fe(II)-PO and PO-I/PO-II-H couples. Acceptable values were obtained for these processes, which account for the difference between HRP and MPO.

However, adequate results are only obtained when using ε = 80 in the first case and ε = 4 in the second. Furthermore, MPO at ferric and ferrous states was modelled with three covalent bonds, whereas in compounds I and II just the sulfonium bond was considered. Besides, reduction potentials for the PO-I/Fe(III)-PO and PO-II-H/Fe(III)-PO processes are not presented, and no satisfactory explanation is given for the use of different procedures to obtain the results. Therefore, some important information is provided, but the origin of the spectral and redox properties of MPO is not certainly elucidated.

Contrary to the research discussed above, in our study the electronic effects of covalent bonding between protein and prosthetic group are not considered, but the model incorporates the coordination bond from the proximal histidine. An important advantage of the use of a reduced molecular model, just comprising part of the active site, is that it permits a better observation of the effect of any changes inferred in this structure, without any interference from or interaction with surrounding peptide that could modulate the monitored physicochemical properties. The changes observed can be only ascribed to the modifications performed on the structure.

Using the same methodology described in Figure 13.2, *i.e.*, measuring the distance from the atom C_{4Im} to the plane formed by the three atoms C_2, C_3, and C_{12}, heme curvature was obtained for some peroxidases at different oxidation states (Table 13.2). Only ferric structures are available for LPO and MPO, so the curvatures of other intermediates have been extrapolated from HRP differences.

Table 13.2. Relevant structural parameters of selected peroxidases. Heme curvature, measured as $-y_{C4Im}$, and distances in Å, and angles in degrees. Data were obtained from RCSB Protein Data Bank (PDB) files as stated, but the values marked with *, which were worked out from extrapolation. 1W4W,[13] 1H58,[14] 1HCH,[14] 1H55,[14] 2GJ1,[15] 1D2V,[5] 1ZBY,[16] 2XJ8,[17] 1ZBZ,[16] 2XIL,[17] 2XJ5,[17] 3F9P,[8] and 1CXP.[5]

Curvature ($-y_{C4Im}$)	**Fe(III)-PO**	**Fe(II)-PO**	**PO-I**	**PO-II-H**
HRP	4.551 (1W4W)	4.731 (1H58)	4.440 (1HCH)	4.462 (1H55)
LPO	4.663 (2GJ1)	4.843*	4.552*	4.574*
MPO	4.884 (1D2V)	5.064*	4.773*	4.795*
Imidazole angle	**Fe(III)-PO**	**Fe(II)-PO**	**PO-I**	**PO-II-H**
HRP	–71 (1W4W)	–72 (1H58)	–73 (1HCH)	–71 (1H55)
CCP	–71 (1ZBY)	–72 (2XJ8)	–70 (1ZBZ)	–72 (2XJ5)
			–72 (2XIL)	
LPO	45 (2GJ1)			
MPO	46 & 47 (1D2V)			
	48 & 44 (3F9P)			
Fe-N_τ distance	**Fe(III)-PO**	**Fe(II)-PO**	**PO-I**	**PO-II-H**
HRP	2.093 (1W4W)	2.133 (1H58)	2.141 (1HCH)	2.140 (1H55)
CCP	2.107 (1ZBY)	2.062 (2XJ8)	2.102 (1ZBZ)	2.121 (2XJ5)
			2.099 (2XIL)	
LPO	2.145 (2GJ1)			
MPO	2.168 & 2.197 (1D2V)			
	2.187 & 2.189 (1CXP)			
	1.868 & 1.876 (3F9P)			

The geometrical optimization of our model simulating the four intermediates at different heme curvatures and with unrestricted rotation of imidazole led to free energy values that show a strong dependence on the y_{C4Im} parameter, while rotation angle of the imidazole varies in order to adjust to the lowest energy position. Highly divergent behaviours can be observed for ferric species and compound II (Table 13.3). Data obtained for Fe(II)-PO and PO-I are also collected as supplementary information (Table S13.1). Thus, in the case of Fe(III)-PO, structures obtained with imidazole situated at ~90° (except one outlier) yielded free energy values that present a parabola-like distribution. However, most geometries optimized with other angles produced more unstable energies (Figure 13.3A). On the other hand, the optimization of PO-II-H at increasing curvatures yielded Gibbs energies that are reasonably arranged in a parabolic shape despite structures with distinct imidazole angles were obtained (Figure 13.3B). Parabolic plots display a particular heme curvature (or $-y_{C4Im}$ value) that corresponds to the thermodynamic minimum, *i.e.*, the equilibrium position, where the energy increases when moving away from this value to more unstable configurations. In any case, it can be inferred that the turning of imidazole

around the proximal axis has a significant effect on heme thermodynamics.

Table 13.3. Relative Gibbs free energy in kJ·mol^{-1} obtained for Fe(III)-PO and PO-II-H at different $-y_{C4Im}$ values in Å. Imidazole rotation is unrestricted, approximate angle (°) resulted upon geometry optimization is also displayed. Species with shortest y_{C4Im} distance were taken as reference.

Fe(III)-PO			PO-II-H		
$-y_{C4Im}$	$\Delta G°$	Angle	$-y_{C4Im}$	$\Delta G°$	Angle
4.75	0.00	95	4.15	0.00	45
4.80	146.60	96	4.20	–0.01	45
4.85	0.97	90	4.25	–0.30	45
4.90	65.04	75	4.30	–6.68	40
4.95	65.88	75	4.35	–3.65	40
5.00	4.87	90	4.40	2.42	40
5.00	66.21	75	4.45	–1.73	30
5.05	67.86	75	4.50	4.80	30
5.10	158.41	95	4.55	2.24	30
5.15	208.23	90	4.60	6.53	25
5.20	11.46	90	4.65	6.29	30
5.25	164.88	95	4.70	9.03	–45
5.30	15.02	90	4.75	9.54	–45
5.35	16.97	90	4.80	12.50	–45
5.45	21.87	90	4.85	14.61	–45
5.50	24.02	90	4.90	16.62	–45
5.55	26.11	90	4.95	19.13	–45
5.60	29.22	90	5.00	21.11	–45
5.65	32.23	90	5.05	23.18	–50
5.75	37.57	90	5.10	27.31	–50
			5.15	29.78	–50
			5.20	33.59	–50
			5.30	35.72	–50

Free rotation of imidazole is hindered in peroxidases as it belongs to a proximal histidine linked to protein via two peptide bonds. Besides, some forces established with surrounding residues, as the strong interaction between imidazole and a conserved asparagine observed in peroxidase-cyclooxygenase enzymes,[8] may also help align this group in a particular orientation.

The position of this group has been examined in available crystal structures and some relevant data are collected in Table 13.2. The angle in HRP and CCP keeps reasonably constant for both enzymes and at the four oxidation states, with a value close to –72°. However, native LPO and MPO show the imidazole situated at ~45°, and it can be assumed that this particular orientation does not depend on the oxidation state either. Thus, rotation of this group must be quite restricted since a specific angle is common to all members of each superfamily (–72° for peroxidase-catalases and 45° for peroxidase-cyclooxygenases) and it is highly conserved upon redox transformations. Hence, this parameter is taken into account and these two fixed angles are employed in all the calculations coming after.

Based on a crystal structure of MPO that shows an important steric clash in the close proximity of the active site, the protonation state of proximal imidazole has been discussed and the migration of the proton on N_π atom to a neighbouring Asn residue has been proposed for enzymes belonging to the peroxidase-cyclooxygenase superfamily. Thus, we have also computed all molecular structures considering that this proton is either present or absent.

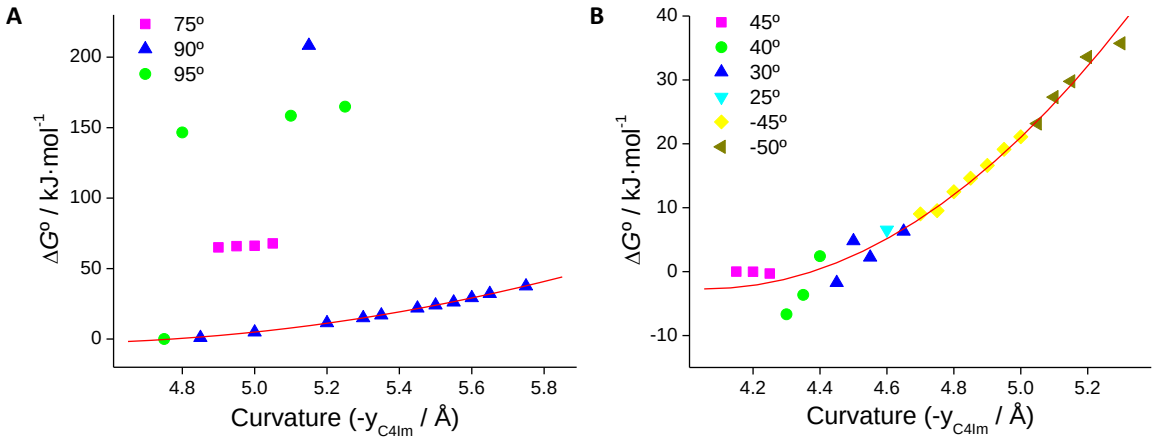

Figure 13.3. Relative Gibbs free energy in kJ·mol^{-1} *vs*. heme curvature, measured as $-y_{C4Im}$ parameter in Å, for geometries optimized with unrestricted rotation angle of imidazole, data symbols indicate the angle obtained. Values calculated for (A) Fe(III)-PO and (B) PO-II-H.

Systematic modification of these variables (heme curvature and imidazole rotation and protonation), followed by geometry optimization, allows the calculation of thermodynamics and spectral information for every combination. Geometries achieved for two enzymatic intermediates with rather different values employed for these parameters are displayed in Figure 13.4. Free energy and Fe–N_τ distance values obtained for Fe(III)-PO are collected in Table 13.4, corresponding data for other species are compiled in Table S13.2.

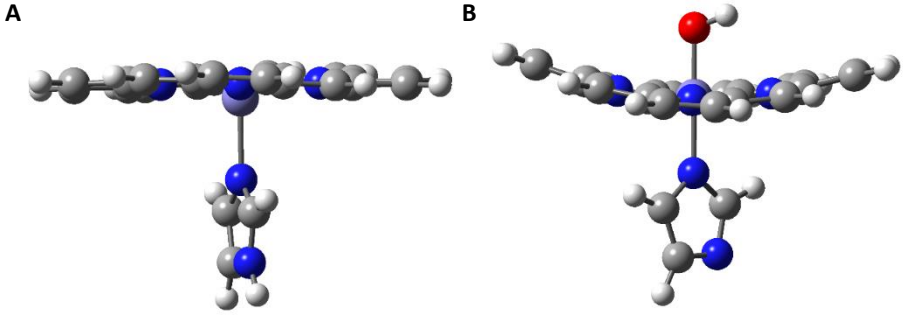

Figure 13.4. Optimized structures of (A) Fe(III)-PO with $-y_{C4Im}$ = 4.4 Å and imidazole angle = –72°, and (B) PO-II-H with $-y_{C4Im}$ = 4.85 Å and imidazolate angle = 45°.

Fe–N_τ distance is strongly dependent on the redox intermediate and it is deeply influenced by ligands on the distal side. This is observed in both the experimental studies (Table 13.2) and this computational work (Tables 13.4 and S13.2). However, heme curvature has not a great impact on this distance: despite the exerted force affects this bond directly, this important strain is not translated into a relevant lengthening. Some effect is also observed from imidazole rotation angle. The dependence of Fe–N_τ distance on heme curvature for ferric species is displayed in Figure 13.5 (see Figure S13.1 for other species).

Fe–N_τ distance increases with heme curvature, but the maximum elongation upon a 1.0 Å increase of $-y_{C4Im}$ is lower than 0.1 Å for Fe(III)-PO, Fe(II)-PO, and PO-II-H. This is a strong coordination bond not easily stretched, hence any increment in $-y_{C4Im}$ is mostly converted into additional curvature of the porphyrin ring and some out-of-plane displacement of the metal

centre towards proximal side. Higher variations were only obtained for compound I. The interaction between Fe and imidazole N_τ atom is weaker for this species (due to the strong Fe=O bond formed at distal side), resulting in a longer Fe–N_τ distance that is also more readily modified when stressed. An important tension was applied on the model structures corresponding to the four oxidation intermediates, causing their distortion, but in no case the imidazole group was pulled apart. Experimental geometries (Table 13.2) show an increase in the Fe–N_τ distance when going from the flat heme of ferric HRP (2.093 Å) to the bent structure of MPO (2.168 to 2.197 Å) similar to the change predicted by our calculations.

Table 13.4. Relative Gibbs free energy in kJ·mol^{-1} and Fe–N_τ distance in Å obtained for Fe(III)-PO at different $-y_{C4Im}$ values in Å. Data calculated with either protonated or unprotonated proximal imidazole, situated at –72° or 45° orientation. Species with shortest $-y_{C4Im}$ distance and 45° were taken as reference. Corresponding data for other species are available in Table S13.2.

$-y_{C4Im}$	Protonated				Unprotonated			
	–72°		45°		–72°		45°	
	Δ*G*°	Fe–N_τ	Δ*G*°	Fe–N_τ	Δ*G*°	Fe–N_τ	Δ*G*°	Fe–N_τ
4.20	5.81	2.075	0.00	2.068	4.22	1.947	0.00	1.941
4.25	5.21	2.076	–0.15	2.069	3.77	1.947	–1.15	1.942
4.30	4.61	2.076	–0.88	2.070	2.85	1.947	–2.24	1.943
4.35	4.04	2.077	–1.40	2.071	3.23	1.948	–3.51	1.944
4.40	3.82	2.077	–1.84	2.073	2.50	1.948	–4.58	1.946
4.45	3.67	2.078	–2.76	2.075	1.73	1.949	–5.55	1.947
4.50	2.59	2.080	–3.67	2.077	0.96	1.950	–6.44	1.948
4.55	2.60	2.081	–1.18	2.079	1.24	1.951	–7.18	1.949
4.60	3.32	2.082	–4.33	2.081	1.16	1.952	–7.25	1.951
4.65	3.34	2.084	–5.77	2.083	1.50	1.952	–5.58	1.952
4.70	3.74	2.086	1.92	2.085	1.58	1.954	–5.20	1.953
4.75	4.10	2.087	2.61	2.088	2.04	1.955	–4.53	1.955
4.80	4.91	2.089	3.11	2.090	2.46	1.956	–3.58	1.956
4.85	5.74	2.091	–3.53	2.093	2.95	1.958	–2.57	1.958
4.90	6.93	2.094	–1.32	2.096	4.22	1.959	–1.39	1.960
4.95	7.93	2.096	–0.71	2.099	5.48	1.961	–1.52	1.961
5.00	7.56	2.099	1.31	2.102	–4.25	1.962	–0.70	1.963
5.05	–2.74	2.102	2.71	2.106	–2.04	1.964	0.59	1.965
5.10	1.91	2.105	3.94	2.109	–0.47	1.966	1.77	1.967
5.15	4.37	2.108	5.73	2.113	1.34	1.967	3.10	1.969
5.20	7.13	2.111	7.65	2.117	3.21	1.969	4.75	1.971

When heme is flat (low $-y_{C4Im}$ values) higher values of Fe–N_τ bond length were obtained at –72°. The reverse situation, or at least similar values with both orientations, is found for bent structures. Thus, the coordination bond between the metal centre and the proximal ligand at flat heme configuration is stronger when imidazole is situated at 45°, while the other orientation yields longer distances and, therefore, weaker interactions, indicating that this group may feel constrained at this position. This rotation angle (–72°) implies that the protons on C_{2Im} and C_{5Im} are located close to pyrroles B and D, in particular close to atoms N_B and N_D, respectively. On the other hand, 45° orientation is associated with these two protons pointing to the empty area between pyrroles. This result is more pronounced at lower $-y_{C4Im}$ values, where the steric effect is more relevant. However, in some cases the position at –72° presents shorter Fe–N_τ lengths but at remarkably distorted porphines, where heme-imidazole hindrance must not be so important.

Following deprotonation of imidazole the interaction between Fe and N_τ becomes much stronger and Fe–N_τ distance shortens at least 0.1 Å, except for PO-I. Negatively charged imidazolate interacts more powerfully with the metal centre and the two involved atoms approach, this is coupled with an out-of-plane displacement of Fe so further heme bending is not developed. Fe is already strongly bonded to ferryl oxygen in the case of compound I, avoiding the intimate interaction

with a proximal ligand. This short Fe–N_τ bond length was already obtained in the X-ray structure of a mixture of glycoforms of human MPO (PDB ID: 3F9P).[8] This crystal structure displays an unusual value for Fe–N_τ, which corresponds to an unprotonated imidazole. In fact, that study first introduces the idea of an imidazolate as proximal ligand of peroxidase-cyclooxygenase enzymes, but the short distance obtained for this coordination bond is not mentioned, despite it is the main evidence of this exceptional protonation state. However, although this file represents a MPO structure that corresponds to imidazolate ligands, all other peroxidase PDB files show Fe–N_τ distances that are in agreement with a protonated proximal imidazole (Table 13.2).

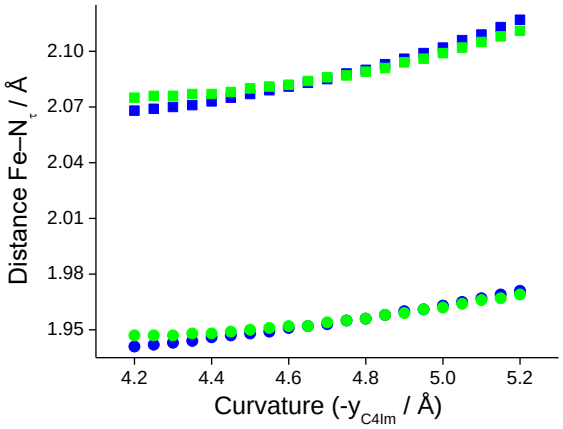

Figure 13.5. Fe–N_τ distance *vs*. heme curvature measured as $-y_{C4Im}$ parameter, both in Å, calculated for Fe(III)-PO with either protonated (■) or unprotonated (●) imidazole. Values calculated with rotation angle –72° displayed in green, and with 45° in blue.

Geometry optimization with several frozen variables was required for the calculation of these model structures with particular heme curvatures and imidazole rotation angles. Obtaining correct structures, corresponding to the absolute free energy minimum (considering these constraints), became more difficult as the number of constants increased. Thus, geometry optimization often failed, yielding structures that may correspond to local minima, and search for the global energy minimum was arduous and probably not always achieved. In any case, the geometries with the lowest free energy available were always selected. Therefore, calculated free energy values show an important fluctuation and consequently the data cannot be easily fitted to a unique parabolic curve. This can be better observed in a plot of Gibbs free energy values *versus* curvature. The data obtained for Fe(III)-PO are displayed in Figure 13.6, similar graphs for the other three species are collected in Figure S13.2.

This figure shows that the data obtained with imidazole situated at –72° are distributed in two different curves: for high values of curvature, the thermodynamics are similar for structures computed with both angles, but when heme is not so bent (these are the values more relevant for catalases-peroxidases as they present flat heme and imidazole at –72°) the curved traced by –72° points indicates that this orientation is unstable with respect to 45° angle. The jump observed around $-y_{C4Im}$ = 5 Å is not associated with any geometrical change, there are no particular differences between the structures before and after the transition. However, it must be related to the variables kept frozen at the optimization process, as the structures with $-y_{C4Im}$ < 5 Å yield one imaginary vibrational frequency, which corresponds to a vibration of imidazole rotating around the proximal axis, whereas data corresponding to the other curve ($-y_{C4Im}$ > 5 Å) present only positive frequencies. This also happens with the three anomalous data points at 45° and $-y_{C4Im}$ = 4.70 to 4.80 Å in Figure 13.6A. Similar behaviours can be also observed in Figures S13.2A, S13.2E, and S13.2F. Besides, all the data with angle = –72° plotted in Figures S13.2B, S13.2C, and S13.2D correspond to geometries with one negative vibrational frequency. These negative frequencies may arise from the steric hindrance between imidazole and porphyrin ring, more pronounced at –72° orientation as already

commented. Furthermore, we have obtained other incorrect values that do not lie on the curve, despite those structures do not present imaginary frequencies. We have always tried to acquire better values, repeatedly computing these structures in different ways, and the best results achieved are displayed, even if they seem to be outliers. These deviant data have not been used when calculating other results as reduction potentials, to avoid inferring mistaken conclusions. For this reason, some thermodynamic results obtained in this study should be taken with caution.

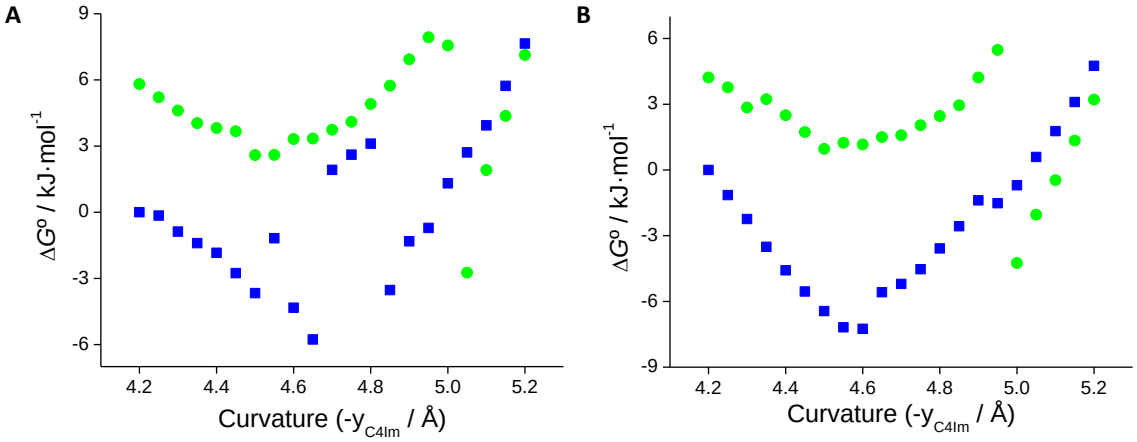

Figure 13.6. Relative Gibbs free energy in kJ·mol^{-1} *vs*. heme curvature, measured as $-y_{C4Im}$ parameter in Å, for geometries optimized with restricted rotation angle of imidazole (● for –72° and ■ for 45°). Values calculated for Fe(III)-PO with (A) protonated and (B) unprotonated imidazole.

According to these parabolic curves, the lowest point indicates the $-y_{C4Im}$ distance of the most stable geometry for each species. It can be observed (Tables 13.2, 13.4 & S13.2) that they do not match experimental values for peroxidases-catalases, although their prosthetic group should adopt the most favourable conformation as it is not covalently linked to the protein. Despite there are not covalent bonds between heme and peptide, the coordinated proximal histidine is part of the protein and other interactions with heme are present, so the displacement of these moieties must also be somehow restricted. Furthermore, the computational model neglects the possible effect of the lateral substituents at the porphyrin ring.

Enzymes belonging to the peroxidase-catalase superfamily exhibit rather flat hemes, whereas the porphyrins of peroxidase-cyclooxygenase members are more distorted. They present barrel-vaulted shapes, particularly in MPO, which also has exceptional oxidative and spectroscopic properties. Therefore, for the following discussion, the structures of HRP, as representative of one superfamily, and of MPO, as extreme example of the other group, are employed to describe flat and curved hemes, respectively (Table 13.2). Thus, $-y_{C4Im}$ values of 4.40 Å (Fe(III)-PO), 4.70 Å (Fe(II)-PO), and 4.40 Å (PO-I and PO-II-H) stand for flat hemes, while 4.90, 5.10, and 4.80 Å are employed for the corresponding curved hemes. These values are similar to the distances observed for these enzymes, while avoiding the use of outliers (Figures 13.6 & S13.2). However, some of them show one imaginary frequency. It has been verified that the use of other close values has not any important effect regarding the final outcomes derived from them.

We have obtained reduction potentials for the four studied processes that are in the typical range of peroxidases (Table 13.5). All values determined with 45° (except one) were calculated from structures without imaginary frequencies, so these data may be correct. Most potentials with –72° were obtained from two geometries with one negative frequency each. It seems that the possible effect of these imaginary vibrations is counterbalanced, as the results are very similar to the data with 45° angle. Other values were worked out from only one structure that presents one imaginary frequency; some of these results are quite different from 45° values. They could still be correct or, on the contrary, the difference could arise

just from such negative frequency. Therefore, these data are not considered.

The couples PO-I/Fe(III)-PO and PO-II-H/Fe(III)-PO yielded redox potentials that are in general higher than the values computed for PO-I/PO-II-H reduction, whereas the opposite trend is usually found in peroxidases. These results may be modulated by the interactions of the ferryl-oxo moiety (PO-I and PO-II-H) with appropriate groups within the distal cavity (see Chapter 11).

Table 13.5. Reduction potential values relative to SHE in mV calculated for the four processes displayed in Scheme 13.1. Data calculated with heme curvatures ($-y_{C4Im}$ values) at the limits of the ranges defined by HRP-MPO: Fe(III)-PO, 4.40-4.90 Å; Fe(II)-PO, 4.70-5.10 Å; and PO-I and PO-II-H, 4.40-4.80 Å, stand for flat and curved hemes, respectively. Values obtained with imidazolate in italics.

	Flat		**Curved**	
	–72°	**45°**	**–72°**	**45°**
PO-I/Fe(III)-PO	956**	962	992**	1018
	*1038***	*1048*	*1063***	*1072*
PO-I/PO-II-H	885**	896	957*	884
	*978***	*974*	*981**	*880*
PO-II-H/Fe(III)-PO	1027**	1028	1028*	1152
	*1098***	*1121*	*1146**	*1263*
Fe(III)-PO/Fe(II)-PO	–520*	–561*	–494*	–486
	*–703***	*–717*	*–689***	*–690*

* One structure has one imaginary frequency

** Both structures have one imaginary frequency each

The difference between 45° and –72° potentials is low (≤ 26 mV), but the values are usually higher (more positive, or more negative) with 45° angle, which corresponds to the peroxidases that show higher redox potential, the enzymes belonging to the peroxidase-cyclooxygenase superfamily. This small difference is not enough to establish a clear dependence of the redox potentials on imidazole orientation. However, this does not refuse the existence of such influence as imidazole rotation has an effect on the thermodynamics of the calculated structures.

Heme curvature affects noticeably the thermodynamics of the structures as shown in Figures 13.6 and S13.2. Besides, the free energy change observed with respect to $-y_{C4Im}$ parameter is different for each species. Therefore, a progressive change in the reduction potentials would be expected, but we have only considered two extreme situations, referred as flat and curved. They correspond to the $-y_{C4Im}$ values that represent the whole change in heme bending observed when going from HRP to MPO.

The two-electron oxidation of native peroxidase to compound I shows a higher potential when the heme is curved, as experimentally observed, but not to such an extent. Contrarily, the formation of compound II from compound I has a lower potential with higher $-y_{C4Im}$ distances (although not very significant with protonated imidazole), in contrast to empirical measurements. Subsequent one-electron reduction of PO-II-H presents reduction potentials that are evidently greater for bent hemes, in agreement with the behaviour observed for these enzymes. The negative potential obtained for the formation of ferrous intermediate seems to slightly decrease its absolute value for curved hemes. In any case, indistinct numbers are determined experimentally for both superfamilies, as in this work, and the particular positive potential measured for MPO has not been obtained here. The effect of heme curvature on the reduction potential seems moderately adequate for three of four studied processes, although it does not explain the observed variations in full.

The absolute values of the reduction potentials always increase when imidazolate is considered, apart from the result calculated for reduction of PO-I to PO-II-H at 45° with curved heme. Besides, this increment is significant, around 100 mV

in most cases. Therefore, the possibility of members of the peroxidase-cyclooxygenase superfamily containing an unprotonated imidazole ligand is consistent with the higher reduction potentials obtained for the three processes involved in peroxidation. However, experimental values of the reduction of Fe(III)-PO to Fe(II)-PO do not show such variation, and the behaviour is quite the opposite in the case of MPO. Furthermore, since all PDB files (but one MPO structure, with ID: 3F9P) correspond to peroxidases with a protonated proximal imidazole according to observed Fe–N_τ distances, this possibility should be ruled out.

These computational results indicate that some effect on the redox properties is obtained from imidazole rotation. The effect is more important from heme curvature, and the deprotonation of the imidazole affects greatly the potentials of the considered processes. Thus, all these factors must be taken into account for an accurate description of the origin of the observed differences in redox profiles of peroxidases as they modulate the values.

UV-Vis spectra of peroxidases display a characteristic very high Soret band. Native ferric state of peroxidase-catalases presents a peak around 400 nm with an extinction coefficient *ca*. 100 $cm^{-1}{\cdot}mM^{-1}$, whereas the absorption in compound I occurs at the same wavelength but is half intense. Ferrous species and compound II show red-shifted Soret bands (~40 and ~15 nm, respectively) with a height similar to the ferric peak. Enzymes belonging to the peroxidase-cyclooxygenase superfamily display analogous absorption spectra, the main difference is that all bands increase 10 to 15 nm in wavelength. MPO again presents particular values, more red-shifted than the other enzymes, *ca*. 30 nm.

The spectral data calculated with the TD-DFT functional are collected in Table 13.6. As already noticed (Chapter 11) the absorption maxima exhibit a net blue shift of *ca*. 50 nm relative to the experimental data, along with an adequate intensity profile. The spectrum of Fe(II)-PO with flat heme and protonated imidazole situated at –72° orientation could not been obtained, even using structures with diverse $-y_{C4Im}$ values around 4.70 Å. Besides, the other three spectra of this species display a second relevant band at ~330 nm (> 60 $cm^{-1}{\cdot}mM^{-1}$, not collected in the table), whereas only one peak is observed for the structures with imidazolate.

Table 13.6. Wavelength (λ) in nm and extinction coefficient (ε) in $cm^{-1}{\cdot}mM^{-1}$ of the Soret band obtained for the four considered species calculated with flat and curved hemes, and two orientations of the proximal imidazole. Values obtained with imidazolate in italics.

	Flat				**Curved**			
	–72°		**45°**		**–72°**		**45°**	
	λ	**ε**	**λ**	**ε**	**λ**	**ε**	**λ**	**ε**
Fe(III)-PO	354	130	354	127	355	141	356	141
	378	*82*	*379*	*81*	*378*	*81*	*379*	*79*
Fe(II)-PO	–	–	392	81	390	89	390	84
	359	*108*	*362*	*115*	*359*	*105*	*361*	*107*
PO-I	366	69	364	106	364	101	364	105
	372	*126*	*373*	*126*	*373*	*125*	*373*	*125*
PO-II-H	379	56	367	99	375	59	367	99
	401	*12*	*402*	*13*	*399*	*14*	*402*	*11*

Neither imidazole orientation nor heme curvature modifies significantly the wavelength and absorption of the Soret band, only some shift is observed between –72° and 45° results of compound II with protonated imidazole, and also some differences in peak height are found both in the mentioned data and in one value of compound I. On the other hand, the maximum absorption is quite affected, both in wavelength and intensity, upon deprotonation of N_π in the proximal imidazole. Computed structures with imidazolate show red-shifted (6 to 35 nm) bands for Fe(III)-PO, PO-I, and PO-II-H, and the wavelength of Fe(II)-PO peaks decreases ~30 nm. Higher extinction coefficients were obtained for Fe(II)-PO and PO-I,

whereas lower peaks are obtained for the other two species; in the particular case of PO-II-H the absorption reduces dramatically.

These results do not follow the trends experimentally measured, only the charge on coordinated imidazole seems to regulate the spectral properties of peroxidases. This is consistent with spectral changes that mostly depend on the covalent bonding between prosthetic group and protein, as stated in the already published computational study.[11] The migration of the proton on N_π to neighbouring Asn421 was proposed to explain a strong steric clash observed in the electron density maps of peroxidase-cyclooxygenases.[8] However, Fe–N_τ distances measured in most PDB files reject this hypothesis. Thus, we have also estimated the pK_a value at this position in order to throw some light on N_π protonation state.

Calculated pK_a values are collected in Table S13.3, they are much affected by the variability obtained in thermodynamic data. Thus, better than discussing tabulated numbers, the tendencies observed in the plot of pK_a values *versus* heme curvature are much more descriptive (Figure 13.7).

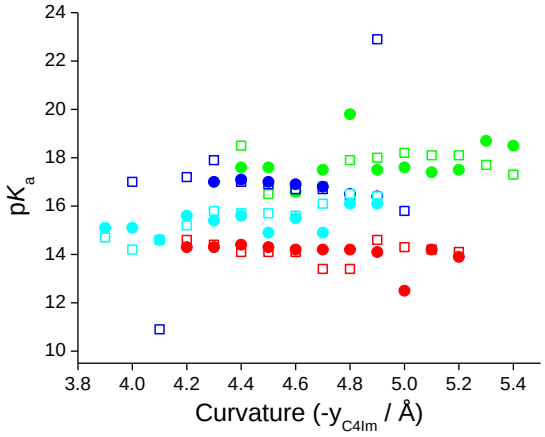

Figure 13.7. pK_a of N_π proton *vs*. heme curvature, measured as $-y_{C4Im}$ parameter in Å, calculated for Fe(III)-PO (●□), Fe(II)-PO (●□), PO-I (●□), and PO-II-H (●□) with imidazole at rotation angle –72° (●) or 45° (□).

The rotational position of the imidazole does not play any relevant role in the acidity of the proton on N_π, while the strain caused by increasing the curvature does not affect the pK_a of Fe(III)-PO and Fe(II)-PO intermediates, but it shows some effect on compound I (pK_a slightly decreases with increasing curvature) and compound II (the opposite behaviour). Much more important is the effect of the oxidation state of the heme species: ferric native state presents the most acidic proton, followed by PO-II-H, PO-I, and finally Fe(II)-PO. These differences can be related to the charge on Fe (Table S13.2, solvated Mulliken charge is 1.53, 1.39, 1.38, and 1.27 a.u., respectively), the more positive this atom the greater electronic charge withdrawn from N_τ and, consequently, from the imidazole moiety, facilitating the proton release at N_π. Thus, the possibility of the presence of an imidazolate only in some intermediates is considered below.

Reduction potentials have been calculated with either only Fe(III)-PO or both Fe(III)-PO and PO-II-H (the two species with lower pK_a values) incorporating an unprotonated proximal ligand, and the cycle is protonated in the other species. Since thermodynamic data obtained with –72° are perhaps not very reliable, and taking into account that pK_a results were hardly affected by imidazole rotation, only reduction potentials calculated with 45° angle are displayed in Table 13.7. Besides, the strong interaction of proximal imidazole with a nearby Asn residue has only been observed in enzymes belonging to peroxidase-cyclooxygenase superfamily, which show imidazoles situated at this orientation.

The ferric state containing a proximal imidazolate leads to a dramatic decrease in the reduction potentials of PO-I/Fe(III)-PO and PO-II-H/Fe(III)-PO. This result is contrary to experimental observations. Besides, reduction of unprotonated Fe(III)-PO to Fe(II)-PO produces positive potentials, as in MPO, but too high. The reduction process of compound I to compound II

with the latter having an imidazolate yields slightly negative values, inconsistent with empirical results. Therefore, the selective deprotonation of the proximal imidazole in only some intermediates cannot account for the diverse redox profiles of peroxidases.

Table 13.7. Reduction potential values relative to SHE in mV calculated for the four processes displayed in Scheme 13.1. Data calculated with heme curvatures ($-\gamma_{C4Im}$ values) as in Table 13.5, and proximal ligand oriented at 45°. Species incorporating an imidazolate have been employed as stated in the table, and the other intermediates contain protonated imidazole.

	Imidazolate			
	Fe(III)-PO		**Fe(III)-PO & PO-II-H**	
	Flat	**Curved**	**Flat**	**Curved**
PO-I/Fe(III)-PO	544	586	544	586
PO-I/PO-II-H	896	884	–33	–91
PO-II-H/Fe(III)-PO	192	288	1121	1263
Fe(III)-PO/Fe(II)-PO	275*	378	275*	378

* One structure has one imaginary frequency

As already stated, the observed Fe–N_τ distance excludes the presence of a fully unprotonated imidazolate coordinated to heme iron, but the imidazole and neighbouring asparagine, both protonated, cannot coexist either. Thus, this amino acid must be unprotonated and the proton on N_π interacts with the negatively charged atom. Some electronic charge may be transferred to imidazole, or even a partial proton transference, with the two groups sharing this proton. In any case, the ligand would have some imidazolate character. This charge distribution may still affect the reduction potentials, although not as much as in the tabulated data, which correspond to fully unprotonated imidazoles.

13.4 Conclusions

Computational studies have been conducted to determine the origin of the different oxidative behaviours and spectral properties observed in peroxidases. Thus, the effect of covalent bonding between prosthetic group and protein, heme bending, and orientation and protonation state of proximal imidazole are discussed, but their particular influence could not be unequivocally assessed.

The linkages between heme and the peptide can explain some differences in the UV-Vis spectra and they also affect redox attributes of peroxidases to some extent.[11] Likewise, heme curvature and the position and protonation state of the proximal ligand must also play a role in the properties of these enzymes.

Contrary to the imidazolate proposed as proximal ligand in members of the peroxidase-cyclooxygenase superfamily, presented results reveal that this group must be protonated, although it may accept some negative charge from a neighbouring unprotonated asparagine residue.

It can be highlighted that this study opens the door to further research on this topic, taking into account that not only the electronic effect of covalent bonding but also these other structural features may provide an explanation for the different enzymatic activities and properties of peroxidases.

13.5 References

1. C. Obinger, *Heme peroxidase biochemistry: Facts and perspectives.* Arch. Biochem. Biophys., 2010 **500** (1) 1-2.
2. M. Zámocký, S. Hofbauer, I. Schaffner, B. Gasselhuber, A. Nicolussi, M. Soudi, K. F. Pirker, P. G. Furtmüller, and C. Obinger, *Independent evolution of four heme peroxidase superfamilies.* Arch. Biochem. Biophys., 2015 **574** 108-

119.

3. M. Zamocky, C. Jakopitsch, P. G. Furtmüller, C. Dunand, and C. Obinger, *The peroxidase-cyclooxygenase superfamily: Reconstructed evolution of critical enzymes of the innate immune system.* Proteins, 2008 **72** (2) 589-605.
4. M. Zederbauer, P. G. Furtmüller, S. Brogioni, C. Jakopitsch, G. Smulevich, and C. Obinger, *Heme to protein linkages in mammalian peroxidases: impact on spectroscopic, redox and catalytic properties.* Nat. Prod. Rep., 2007 **24** (3) 571-584.
5. T. J. Fiedler, C. A. Davey, and R. E. Fenna, *X-ray crystal structure and characterization of halide-binding sites of human myeloperoxidase at 1.8 Å resolution.* J. Biol. Chem., 2000 **275** (16) 11964-11971.
6. S. J. Klebanoff, *Myeloperoxidase-halide-hydrogen peroxide antibacterial system.* J. Bacteriol., 1968 **95** (6) 2131-2138.
7. C. C. Winterbourn, M. C. M. Vissers, and A. J. Kettle, *Myeloperoxidase.* Curr. Opin. Hematol., 2000 **7** (1) 53-58.
8. X. Carpena, P. Vidossich, K. Schroettner, B. M. Calisto, S. Banerjee, J. Stampler, M. Soudi, P. G. Furtmüller, C. Rovira, I. Fita, and C. Obinger, *Essential role of proximal histidine-asparagine interaction in mammalian peroxidases.* J. Biol. Chem., 2009 **284** (38) 25929-25937.
9. M. J. Frisch, G. W. Trucks, H. B. Schlegel, G. E. Scuseria, M. A. Robb, J. R. Cheeseman, J. A. Montgomery Jr., T. Vreven, K. N. Kudin, J. C. Burant, J. M. Millam, S. S. Iyengar, J. Tomasi, V. Barone, B. Mennucci, M. Cossi, G. Scalmani, N. Rega, G. A. Petersson, H. Nakatsuji, M. Hada, M. Ehara, K. Toyota, R. Fukuda, J. Hasegawa, M. Ishida, T. Nakajima, Y. Honda, O. Kitao, H. Nakai, M. Klene, X. Li, J. E. Knox, H. P. Hratchian, J. B. Cross, C. Adamo, J. Jaramillo, R. Gomperts, R. E. Stratmann, O. Yazyev, A. J. Austin, R. Cammi, C. Pomelli, J. W. Ochterski, P. Y. Ayala, K. Morokuma, G. A. Voth, P. Salvador, J. J. Dannenberg, V. G. Zakrzewski, S. Dapprich, A. D. Daniels, M. C. Strain, O. Farkas, D. K. Malick, A. D. Rabuck, K. Raghavachari, J. B. Foresman, J. V. Ortiz, Q. Cui, A. G. Baboul, S. Clifford, J. Cioslowski, B. B. Stefanov, G. Liu, A. Liashenko, P. Piskorz, I. Komaromi, R. L. Martin, D. J. Fox, T. Keith, M. A. Al-Laham, C. Y. Peng, A. Nanayakkara, M. Challacombe, P. M. W. Gill, B. Johnson, W. Chen, M. W. Wong, C. Gonzalez, and J. A. Pople, *Gaussian 03*. 2004, Gaussian, Inc.: Wallingford CT.
10. S. I. Gorelsky, *SWizard program, revision 4.5*.
11. A. Devarajan, A. V. Gaenko, and U. Ryde, *Effect of covalent links on the structure, spectra, and redox properties of myeloperoxidase - A density functional study.* J. Inorg. Biochem., 2008 **102** (8) 1549-1557.
12. A. Klamt and G. Schüürmann, *COSMO: a new approach to dielectric screening in solvents with explicit expressions for the screening energy and its gradient.* J. Chem. Soc., Perkin Trans. 2, 1993 (5) 799-805.
13. G. H. Carlsson, P. Nicholls, D. Svistunenko, G. I. Berglund, and J. Hajdu, *Complexes of horseradish peroxidase with formate, acetate, and carbon monoxide.* Biochemistry, 2005 **44** (2) 635-642.
14. G. I. Berglund, G. H. Carlsson, A. T. Smith, H. Szöke, A. Henriksen, and J. Hajdu, *The catalytic pathway of horseradish peroxidase at high resolution.* Nature, 2002 **417** (6887) 463-468.
15. A. K. Singh, N. Singh, S. Sharma, S. B. Singh, P. Kaur, A. Bhushan, A. Srinivasan, and T. P. Singh, *Crystal structure of lactoperoxidase at 2.4 Å resolution.* J. Mol. Biol., 2008 **376** (4) 1060-1075.
16. C. A. Bonagura, B. Bhaskar, H. Shimizu, H. Li, M. Sundaramoorthy, D. E. McRee, D. B. Goodin, and T. L. Poulos, *High-resolution crystal structures and spectroscopy of native and compound I cytochrome c peroxidase.* Biochemistry, 2003 **42** (19) 5600-5608.
17. A. Gumiero, C. L. Metcalfe, A. R. Pearson, E. L. Raven, and P. C. E. Moody, *Nature of the ferryl heme in compounds I and II.* J. Biol. Chem., 2011 **286** (2) 1260-1268.

CHAPTER 14

Chloride ion in the myeloperoxidase-mediated chlorination reaction: substrate and inhibitor

No human investigation can be called real science
if it cannot be demonstrated mathematically.

Leonardo da Vinci,
in Pensieri (*ca*. 1492)

14.1 Introduction

Peroxidases can oxidize halides and pseudohalides to the corresponding hypohalous acids according to their redox potential. The oxidation readiness of (pseudo)halide ions commonly oxidized by these enzymes is $SCN^- > I^- > Br^- > Cl^-$.[1, 2] Thus, all peroxidases can oxidize iodide and thiocyanate, and some do bromide. However, at neutral pH, only myeloperoxidase (MPO) oxidizes chloride at a high rate. Different anions compete as substrates for several redox intermediates of MPO, and although chloride oxidation is slower than other processes, this halide is the major physiological substrate due to its high extracellular concentration.

The peroxidase cycle applied to MPO, also showing the formation of ferrous species and the chlorination steps, is depicted in Scheme 14.1. Besides, chloride binding equilibria are represented for the four enzymatic intermediates: ferric (Fe(III)-MPO) and ferrous (Fe(II)-MPO-H) MPO, and compounds I (MPO-I) and II (MPO-II-H).

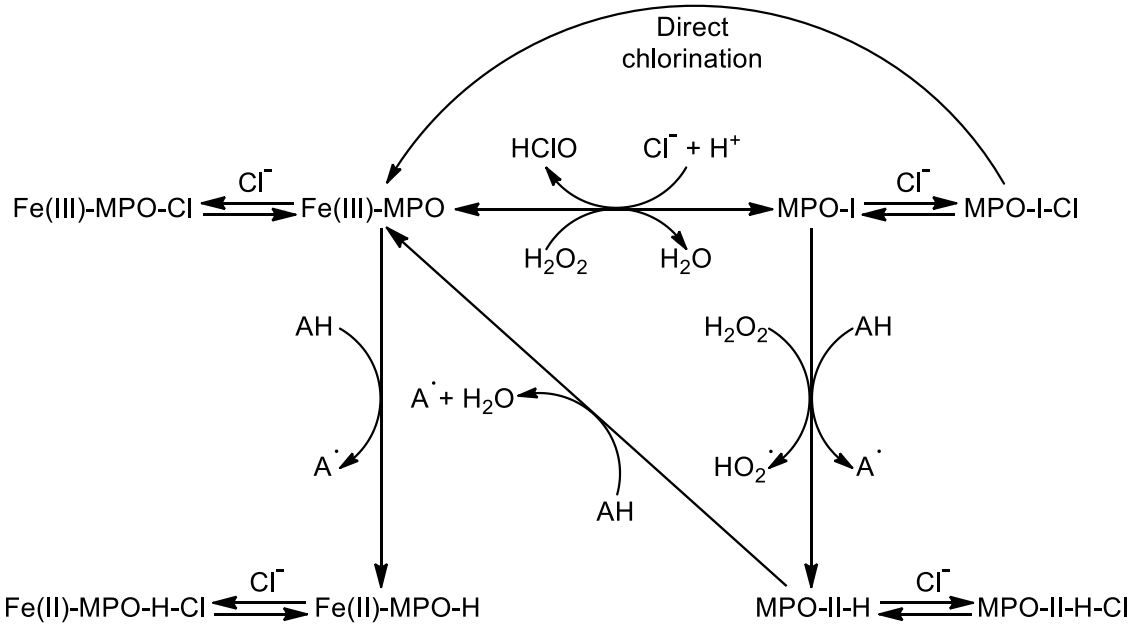

Scheme 14.1. Normal peroxidase cycle of MPO showing both peroxidation and chlorination reactions, as well as formation of ferrous intermediate. Chloride binding with the four redox species is also depicted.

The crystallographic structure of native ferric MPO shows five water molecules in the distal cavity, designated W_1–W_5 (Figure 14.1).[3] W_1 is axially situated between N_τ of the imidazole of the distal histidine (His95) and heme iron (distances N_τ–O_{W1} and Fe–O_{W1} = 2.9 Å). Therefore, it is interacting, but not coordinated, with Fe(III) and hydrogen-bonded to the former, and also to W_2 and W_3. W_2 is approximately situated above δ-methine bridge carbon between pyrroles A and D, interacting with this meso carbon (C_{20}, see Figure 12.1) at a distance C_{20}–O_{W2} = 3.9 Å, and hydrogen-bonded to the amide nitrogen of Gln91, W_1, and W_5.

Halides bind ferric native MPO at the distal cavity. Chloride binding site at the sixth coordination position of ferric iron, displacing W_1, has been considered on several evidences: changes in the resonance Raman spectrum[4] and EPR signal[5, 6] upon chloride binding, the dependence on His95 protonation,[7] or the inhibition of the reaction of ferric MPO with H_2O_2,[8] HClO,[9] and other substrates.[10] Furthermore, the pseudohalide cyanide binds directly to heme iron, as confirmed by X-ray crystallography,[11] yielding a low-spin species that has been analyzed by magnetic circular dichroism, circular dichroism, and EPR and RR spectroscopies,[12, 13] supporting a tight Fe-CN interaction. C_{CN} is coordinated to iron (Fe–C_{CN} = 2.1 Å) while N_{CN} forms three hydrogen bonds with His95, W_2, and W_3. This complex shows a bent Fe-C_{CN}-N_{CN} angle

of approximately 157 degrees.[11] Formation of the MPO-cyanide adduct also presents a strong dependence on His95 protonation.[7, 8]

However, a different binding site has been later proposed based on the crystallographic structure of the MPO-bromide complex.[3] This halide anion replaces W_2, above the meso carbon between pyrrole rings A and D. Although located at a further distance (Br–C_{20} = 3.8 Å, Br–Fe = 5.0 Å, and Br– N_τ = 3.6 Å), this binding site is assumed to interact sufficiently with the heme to explain the spectroscopic differences, and with the imidazole of His95 to inhibit compound I formation and induce the observed pH dependence. Besides, adducts of ferric MPO with halides, including MPO-chloride, are high spin species, supporting a binding position other than as metal ligands at the sixth coordination site, although this structure has not been observed for chloride.

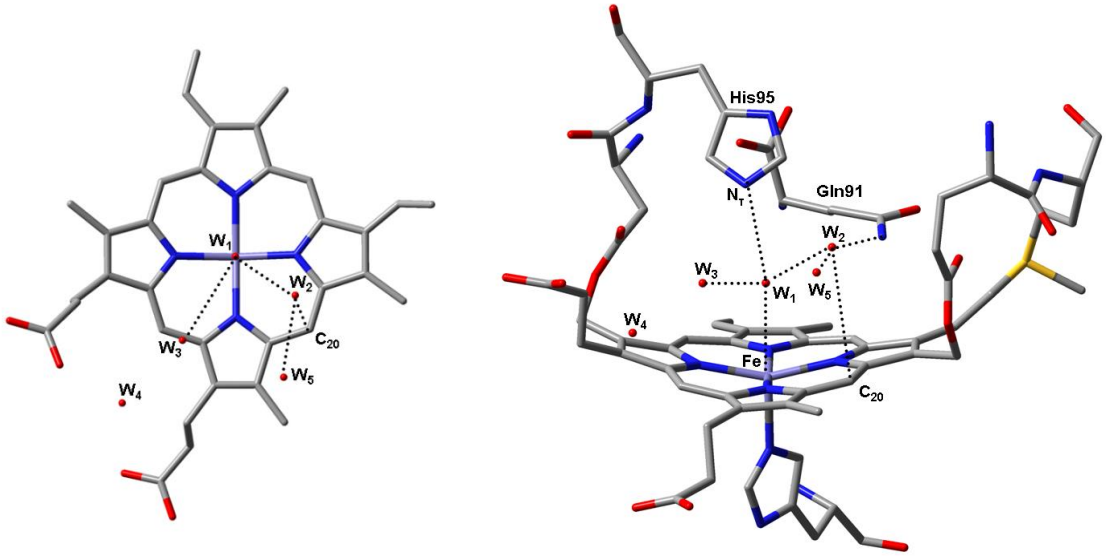

Figure 14.1. Position of the five water molecules in the distal heme cavity of MPO and relevant interactions with W_1 and W_2. Geometries were obtained from the RCSB Protein Data Bank 1CXP file.[3]

There are also some evidences supporting the possibility of two different distal binding sites for halides, such as kinetic measurements[14] or crystallographic results like the structure of the MPO-cyanide-bromide complex, where cyanide binds iron and bromide binds in place of W_5.[11] Therefore, the position of chloride binding for the inhibition of reactions with ferric native state has not been undoubtedly established.

The possible role of ferrous species of peroxidases is unknown, and it is only formed via strong reduction of the native ferric species, although the reduction potential for the Fe(III)/Fe(II) couple is not so unfavourable in the case of MPO, in fact it is similar to globins. Binding of or reaction with halides has not been observed, but a ferrous heme adduct with the pseudohalide cyanide.[11, 15] This chemical is unique (as well as nitric oxide) in binding to both the ferric and ferrous forms of these enzymes.[16] EPR measurements show that, again, cyanide anion binds the metal at the distal axial position.[17]

Compound I is the most oxidizing intermediate of the peroxidase cycle. This species is responsible for the two-electron oxidation of (pseudo)halides to corresponding hypohalous acids, or the formation of a proposed halogenating enzyme complex.[18, 19] MPO compound I efficiently oxidizes chloride[2] and it has been established that binding of this anion occurs near a protonated site in the close vicinity of the oxoferryl group (Fe(IV)=O) as the EPR spectrum at acidic pH is halide-dependent.[20]. Furthermore, ferryl oxygen departs in the HClO released as chlorinating agent, and the high oxidizing power of compound I (and compound II as well) most probably resides in this group. These facts also support a halide binding site very close to Fe(IV)=O moiety. Despite bromide was situated at a substantial distance from both the

porphyrin ring and the axial oxoferryl group for the oxidation process to occur, the positions at the distal cavity above a heme meso carbon (W_2)[3] or in the proximity of the pyrrole ring D methyl carbon (W_5)[21] have been considered viable chloride binding sites for compound I.

Compound II is not as oxidizing as compound I. Thus, the one-electron oxidation of iodide can be carried out by compound II of peroxidases,[22, 23] whereas the oxidation of other halides is not possible as the potential for the compound II/ferric couple reveals insufficient. Additionally, the one-electron oxidation of the pseudohalides cyanide and thiocyanate has also been observed.[24, 25] Although feasible, these reactions are usually irrelevant for the enzymes belonging to the peroxidase-cyclooxygenase superfamily, with a compound I already capable of oxidizing these anions to the corresponding hypohalite anions, which are the major stable oxidation products. Still, a detailed analysis of the interaction of (pseudo)halides with MPO compound II is also required.

Hardly any information on the reactivity and interaction of halides with other oxidation intermediates of peroxidases is available in related literature and, therefore, these possibilities are not considered in this study either. Here, the interaction of chloride anion (and also bromide and cyanide anions for comparison) within MPO heme pocket is analyzed at a distal axial position, exploring the possibility of a direct binding of halides onto Fe for ferric and ferrous species, and ferryl O for compounds I and II; or interacting with the δ-methine bridge carbon between pyrroles A and D for all four species. Structure and thermodynamics of these computed halocomplexes are discussed and the results are also analysed with respect to experimental values of MPO and other peroxidases.

14.2 Computational procedure

As previously stated, ferriprotoporphyrin IX with all methyl, vinyl and propionate side chains substituted by hydrogen atoms, and with the imidazole group of His336 coordinated to iron at the proximal side, has been used as model of MPO (at ferric state and compounds I and II). Ferrous species also includes a protonated vinyl substituent in position 3. Atom numbering used for the description of heme *b* has been depicted in Figure 12.1, numbers were assigned according to IUPAC recommendations and letters A to D indicate the location of each pyrrole ring.[26]

Calculations have been performed with Gaussian03[27] using an unrestricted DFT method for the optimization of the structures (UB3LYP/6-31G*), and coupled with a polarized continuum model to obtain water solvation free-energy values (PCM//UB3LYP/6-31G*). Solvated values were corrected for standard state in aqueous solution as already explained in previous chapters.

Binding of chloride, bromide, and cyanide anions at the sixth coordination position of ferrous and ferric species, as well as interacting with ferryl oxygen of compounds I and II, the latter with ferryl oxygen both protonated and unprotonated, has been analyzed by optimization of all corresponding halide-bound intermediates. Furthermore, halide adducts were computed with Cl^-, Br^-, and CN^- directly bound to the meso bridge carbon between pyrrole rings A and D, C_{20}. All calculations have been performed at feasible spin states, *i.e.*, low and high spin for all species plus intermediate spin for ferrous compounds. Besides, main results obtained with chloride were also calculated with increased basis sets (6-311G** and 6-311++G**) for comparison purposes.

14.3 Results

Upon optimization of the corresponding structures, thermodynamic information has been obtained for the formation of the halide-enzyme adducts of Cl^-, Br^-, and CN^- (X^- denotes any (pseudo)halide anion) with four oxidation intermediates of MPO: ferric (Fe(III)-MPO) and ferrous (Fe(II)-MPO-H) species, and compounds I (MPO-I) and II (MPO-II and MPO-II-H). It must be taken into account that this model of the active site of MPO is common to other peroxidases and, thus, it does not consider the particular redox properties of this enzyme. Optimized structures with halides axially bound to iron (complex-X_{Fe}) or ferryl oxygen (complex-X_O) are shown in Figure 14.2, while adducts with halides bound to the meso carbon between

pyrroles A and D (compound-X_{C20}) are represented in Figure 14.3. Relevant results obtained with other basis sets are collected as Supplementary Information. These data are not explicitly mentioned in the text, but they support the same conclusions.

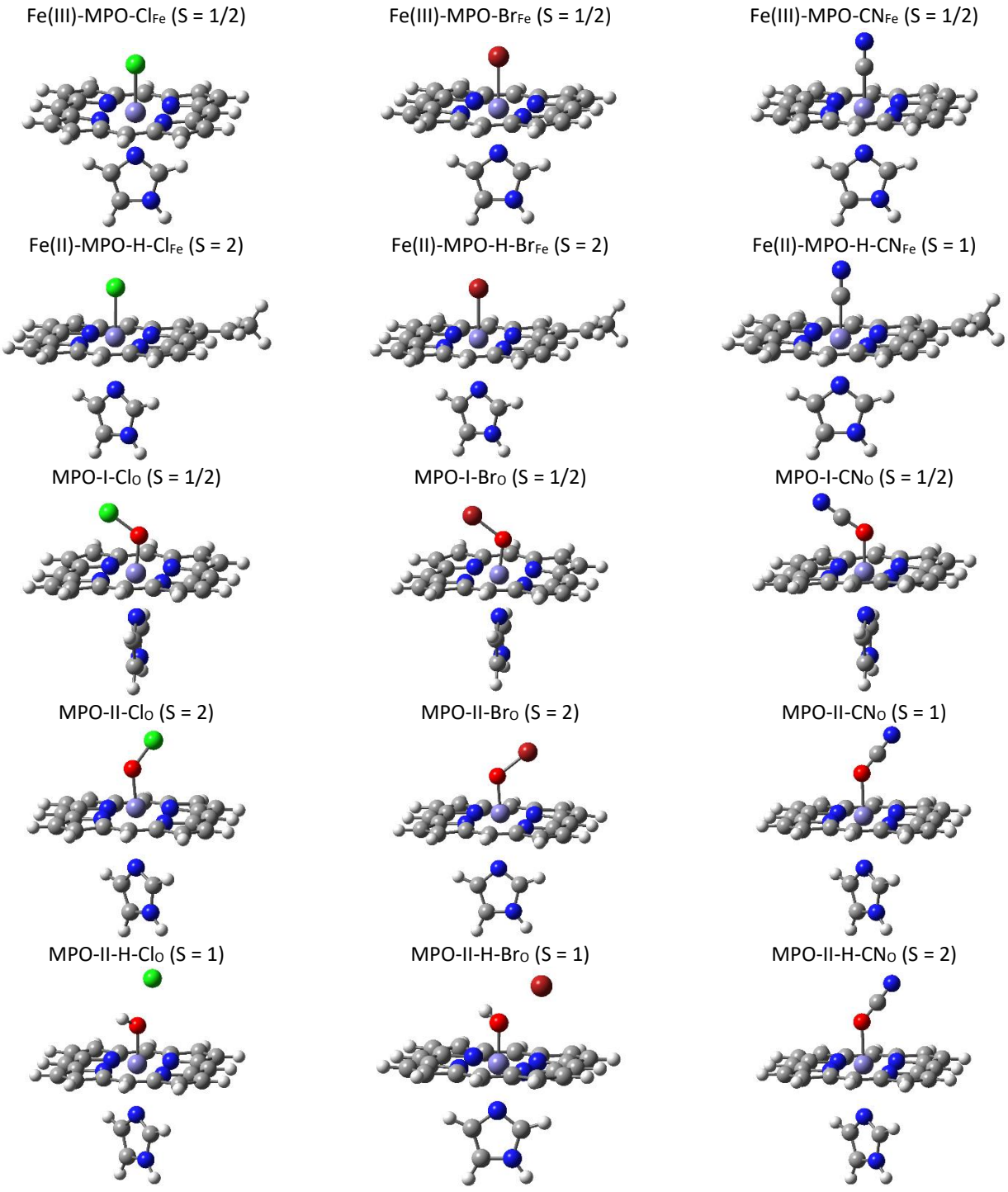

Figure 14.2. Structures optimized *in vacuo* at the UB3LYP/6-31G* computational level and at the most stable spin state, according to Gibbs free energy, for halocomplexes of ferric native myeloperoxidase, ferrous species, compound I, and compound II (either unprotonated or protonated), with Cl^-, Br^-, or CN^- anions at the distal axial binding position.

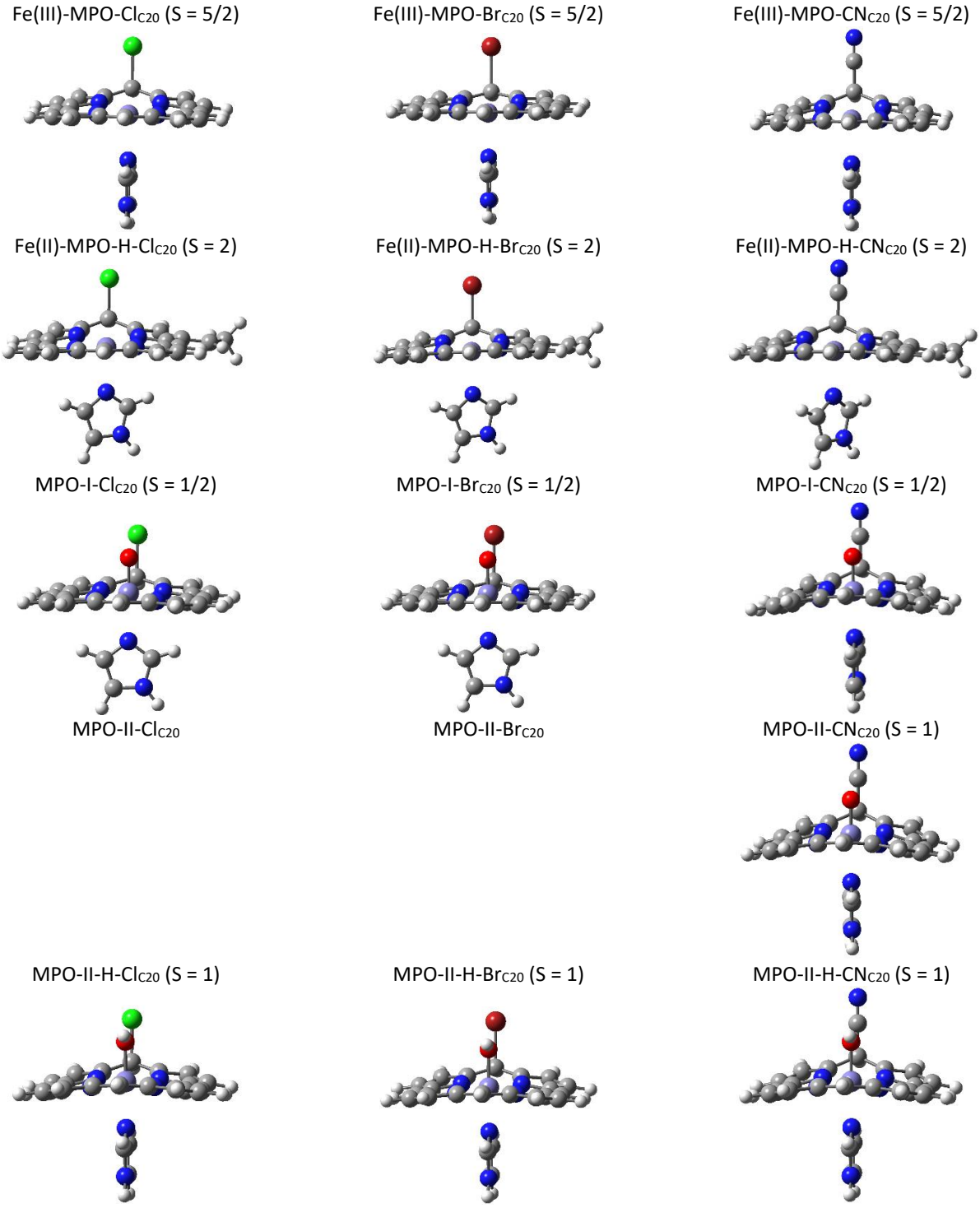

Figure 14.3. Structures optimized *in vacuo* at the UB3LYP/6-31G* computational level and at the most stable spin state, according to Gibbs free energy, for halocomplexes of ferric native myeloperoxidase, ferrous species, compound I, and compound II (either unprotonated or protonated), with Cl^-, Br^-, or CN^- anions bound to the δ-meso bridge carbon, C_{20}.

Gibbs free energy values obtained for the formation of halo-complexes are collected in Table 14.1 (more thermodynamic values in Table S14.1). When substrate binding is not accompanied by further relevant chemical reorganization of the

substrate or enzyme, the values calculated *in vacuo* mainly correspond to the Gibbs free energy of interaction and this mostly represents the forces between both parts ($\Delta H°_{(g)}$) minus the entropy loss ($T\Delta S°_{(g)}$) that is a much smaller term. This is the case of the halo-complexes of ferric and ferrous species calculated with the axial binding position, where the general structure results barely affected upon X^- binding. Some differences arise for halo-complexes of compounds I and II, where relevant changes in the electronic configuration are observed, as commented below. On the other hand, binding of X^- onto C_{20} always disrupts the planarity and aromaticity of heme to a greater or lesser extent, and the analysis is not so simple. Besides, the structures calculated at this binding site differ from natural MPO, where other interactions with the protein and water molecules can stabilize an unbound halide in the distal cavity. Thus, the lack of this particular environment could be considered as a shortcoming of the employed molecular model. However, it still permits interesting comparative analyses. Furthermore, the effect of surrounding interactions has been roughly estimated in the results calculated with PCM. Halide ions in aqueous solution are strongly stabilized by the interaction with water molecules. Thus, their desolvation upon heme binding accounts for the high difference observed between both data sets.

Chloride binding to ferric iron (Fe(III)-MPO-Cl_{Fe}) shows a strong interaction ($\Delta G°_{(g)}$) that is fully counterbalanced by desolvation of independent reactants, so that a positive value is obtained for $\Delta G°_{(aq)}$ (Table 14.1). Fe–Br interaction is greater, and Fe–C_{CN} even stronger, but again both solvated complexes are not so stable although $\Delta G°_{(aq)}$ is still negative in these cases.

Table 14.1. Gibbs free energies in kJ·mol^{-1} obtained for the formation of MPO-halide complexes calculated with UB3LYP/6-31G*, relative values with respect to independent enzyme and anion. Subscripts indicate X^- binding position: Fe, O, and C_{20} stand for ferric/ferrous iron, ferryl oxygen, and meso carbon C_{20}, respectively. Values of $\Delta G°_{(aq)}$ obtained with PCM continuum model in italics. Other thermodynamic values are collected as Supplementary Information.

Species	Spin	X					
		Cl		Br		CN	
Fe(III)-MPO-X_{Fe}	1/2	–366.77	*30.67*	–417.06	*–26.65*	–465.71	*–91.70*
	5/2	–384.73	*36.35*	–430.25	*–20.59*	–426.67	*–38.06*
Fe(III)-MPO-X_{C20}	1/2	–222.87	*193.02*	–246.34	*150.98*	–367.25	*27.09*
	5/2	–265.10	*147.57*	–278.32	*121.34*	–409.96	*–14.86*
Fe(II)-MPO-H-X_{Fe}	0	–280.69	*88.84*	–334.50	*27.59*	–388.82	*–40.67*
	1	–343.24	*53.03*	–397.16	*–9.93*	–442.66	*–70.20*
	2	–360.32	*41.59*	–407.82	*–14.35*	–384.68	*–4.89*
Fe(II)-MPO-H-X_{C20}	0	–220.93	*189.82*	–240.46	*157.43*	–367.92	*20.61*
	1	–278.13	*141.65*	–301.63	*107.15*	–428.74	*–28.41*
	2	–280.40	*135.19*	–300.00	*102.38*	–432.23	*–37.17*
MPO-I-X_O	1/2	–369.92	*65.22*	–424.29	*–4.84*	–699.26	*–310.82*
	5/2	–361.86	*86.92*	–414.79	*17.50*	–702.29	*–300.51*
MPO-I-X_{C20}	1/2	–291.16	*126.28*	–351.26	*46.47*	–445.56	*–55.23*
	5/2	–293.52	*130.49*	–314.49	*91.65*	–309.78	*84.43*
MPO-II-X_O	1	112.30	*273.64*	60.43	*205.74*	–273.34	*–155.39*
	2	83.75	*252.15*	35.58	*184.53*	-	-
MPO-II-X_{C20}	1	-	-	-	-	28.41	*151.79*
	2	-	-	-	-	28.43	*157.84*
MPO-II-H-X_O	1	–314.72	*89.20*	–351.31	*48.64*	-	-
	2	–314.01	*110.29*	–337.44	*69.41*	–315.02	*72.67*
MPO-II-H-X_{C20}	1	–321.08	*96.65*	–341.88	*58.95*	–472.00	*–78.03*
	2	–308.81	*125.23*	–333.36	*80.98*	–454.73	*–44.70*

An interesting result arises: Fe(III)-MPO-Cl_{Fe} and Fe(III)-MPO-Br_{Fe} are slightly more stable at high spin *in vacuo* and at low spin with solvation, while S = 1/2 is always preferred for Fe(III)-MPO-CN_{Fe}. High-spin Fe(III)-MPO-X_{Fe} molecules (X^- = Cl^- or

Br^-) present a longer and weaker Fe–X bond with respect to complexes at S = 1/2 (Table 14.2). This result is accompanied by some distal out-of-plane shift of the metal centre and an important elongation of Fe–N_i distance, *i.e.*, the imidazole separates from the ferric iron, presenting a very low bond order of only 0.15. This effect is not relevant in the case of the cyano-complex. Formation of Fe(III)-MPO-X_{Fe} complexes leads to an important charge transference and bound halides present only half of their initial negative charge (Table 14.3).

Table 14.2. Relevant distances in Å obtained for MPO-halide complexes calculated with UB3LYP/6-31G*. Corresponding bond orders are shown in parentheses. Subscripts indicate X^- binding position: Fe, O, and C_{20} stand for ferric/ferrous iron, ferryl oxygen, and meso carbon C_{20}, respectively.

X	Spin	Species	Fe–X	Fe–N_i	Species	C_{20}–X
Cl	1/2	Fe(III)-MPO-X_{Fe}	2.253 (0.83)	2.038 (0.37)	Fe(III)-MPO-X_{C20}	1.973 (0.78)
	5/2		2.277 (0.66)	2.515 (0.15)		1.987 (0.77)
Br	1/2		2.369 (0.93)	2.062 (0.35)		2.236 (0.65)
	5/2		2.400 (0.73)	2.475 (0.15)		2.227 (0.65)
CN	1/2		1.910 (0.85)	2.086 (0.34)		1.485 (1.00)
	5/2		2.070 (0.58)	2.480 (0.16)		1.485 (1.00)
Cl	0	Fe(II)-MPO-H-X_{Fe}	2.338 (0.78)	2.029 (0.37)	Fe(II)-MPO-H-X_{C20}	1.951 (0.81)
	1		2.252 (0.83)	2.036 (0.37)		1.942 (0.82)
	2		2.341 (0.58)	2.490 (0.15)		1.935 (0.83)
Br	0		2.435 (0.88)	2.037 (0.36)		2.156 (0.74)
	1		2.370 (0.92)	2.045 (0.35)		2.135 (0.75)
	2		2.458 (0.67)	2.484 (0.15)		2.133 (0.78)
CN	0		1.908 (0.86)	2.102 (0.33)		1.486 (1.00)
	1		1.909 (0.85)	2.086 (0.34)		1.484 (1.00)
	2		1.925 (0.83)	2.110 (0.34)		1.484 (1.00)

X	Spin	Species	O_{Fe}–X	Fe–O_{Fe}	Fe–N_i	Species	C_{20}–X
Cl	1/2	MPO-I-X_O	1.736 (0.94)	1.794 (0.78)	2.074 (0.33)	MPO-I-X_{C20}	1.945 (0.81)
	5/2		1.703 (0.97)	1.886 (0.48)	2.464 (0.15)		1.939 (0.83)
Br	1/2		1.867 (0.92)	1.783 (0.79)	2.076 (0.33)		2.183 (0.70)
	5/2		1.835 (0.94)	1.872 (0.49)	2.483 (0.14)		2.162 (0.71)
CN	1/2		1.268 (1.24)	1.880 (0.53)	2.033 (0.38)		1.484 (1.00)
	5/2		1.263 (1.25)	1.945 (0.35)	2.365 (0.18)		1.484 (0.99)
Cl	1	MPO-II-X_O	1.751 (0.96)	1.943 (0.65)	2.664 (0.14)	MPO-II-X_{C20}	-
	2		1.768 (0.91)	1.905 (0.57)	2.847 (0.09)		-
Br	1		1.875 (0.95)	1.926 (0.67)	2.653 (0.14)		-
	2		1.891 (0.91)	1.893 (0.46)	2.739 (0.09)		-
CN	1		1.253 (1.34)	2.100 (0.26)	2.535 (0.13)		1.486 (1.00)
	2		-	-	-		1.489 (1.00)
Cl	1	MPO-II-H-X_O	2.362 (0.24)	1.891 (0.52)	2.465 (0.15)	MPO-II-H-X_{C20}	1.924 (0.84)
	2		2.346 (0.18)	1.872 (0.43)	2.443 (0.15)		1.963 (0.79)
Br	1		2.449 (0.20)	1.824 (0.66)	2.057 (0.34)		2.139 (0.75)
	2		2.503 (0.21)	1.977 (0.37)	2.494 (0.14)		2.218 (0.66)
CN	1		-	-	-		1.484 (1.00)
	2		2.043 (0.28)	2.020 (0.33)	2.449 (0.15)		1.484 (1.00)

Ferric adducts of Cl^- and Br^- computed with C_{20} binding site revealed much less stable both *in vacuo* and with PCM solvation. Fe(III)-MPO-CN_{C20} yields also less favourable $\Delta G°$ values but more similar to axial complex. An important difference is that high spin is more favourable for the three (pseudo) halides, as the metal centre is always pentacoordinated. The bonds formed between halides and the carbon atom are strong, yielding bond orders not far from the unity (about 0.78, 0.65, and 1.00 for Cl^-, Br^-, and CN^-, respectively). This leads to a C_{20} shift towards distal side and some heme bending. The effect of C_{20}–X bond on the porphyrin structure is more remarkable in the case of CN^- complexes, where C_{20}–C_{CN} bond is stronger

and heme adopts a non-planar saddle-like conformation (Figure 14.3). More electronic density is transferred from the halides upon binding to C_{20}, in particular for Fe(III)-MPO-CN_{C20}, where the anion only retains –0.15 a.u.

Table 14.3. Mulliken atomic charges in a.u. on (pseudo)halogens bound to different MPO species obtained in solution at the PCM//UB3LYP/6-31G* computational level. Corresponding hypohalous acids are also shown for comparison. Values calculated on other relevant atoms are collected in Table S14.3.

Species	Spin	X		
		Cl	Br	CN
Fe(III)-MPO-X_{Fe}	1/2	–0.52	–0.45	–0.49
	5/2	–0.55	–0.48	–0.58
Fe(III)-MPO-X_{C20}	1/2	–0.26	–0.37	–0.15
	5/2	–0.30	–0.36	–0.15
Fe(II)-MPO-H-X_{Fe}	0	–0.66	–0.58	–0.59
	1	–0.52	–0.45	–0.50
	2	–0.62	–0.54	–0.49
Fe(II)-MPO-H-X_{C20}	0	–0.24	–0.31	–0.14
	1	–0.24	–0.29	–0.14
	2	–0.22	–0.29	–0.14
MPO-I-X_O	1/2	0.04	0.05	–0.07
	5/2	0.10	0.12	–0.08
MPO-I-X_{C20}	1/2	–0.21	–0.30	–0.12
	5/2	–0.20	–0.28	–0.13
MPO-II-X_O	1	–0.10	–0.10	–0.22
	2	–0.11	–0.12	-
MPO-II-X_{C20}	1	-	-	–0.16
	2	-	-	–0.15
MPO-II-H-X_O	1	–0.59	–0.42	-
	2	–0.47	–0.41	–0.45
MPO-II-H-X_{C20}	1	–0.20	–0.28	–0.13
	2	–0.22	–0.32	–0.13
HXO	0	0.13	0.13	0.03

Halide binding to ferrous intermediate yielded structures very similar to ferric complexes (Figures 14.2 & 14.3). The most noticeable difference is a little longer Fe–X bond and a little shorter C_{20}–X distance with respect to equivalent ferric compounds for $X^- = Cl^-$ or Br^-, coupled with lower and higher bond order values, respectively. Furthermore, somewhat less negative charge is transferred from the anion to heme moiety in axial ferrous complexes, whereas halide charge is slightly more delocalized in C_{20} adducts than in ferric corresponding species.

As observed for ferric species, Fe(II)-MPO-H-CN is more favourable than Fe(II)-MPO-H-Br, and this one also more stable than Fe(II)-MPO-H-Cl, for both binding sites. Chloro and bromo Fe(II)-MPO-H-X_{Fe} adducts are more unstable than corresponding ferric compounds, both *in vacuo* and with PCM solvation, and high spin is preferred. On the other hand, Fe(II)-MPO-H-CN_{Fe} is a few kJ·mol^{-1} more favourable than its ferric counterpart, and S = 1 is preferred in this case. Fe(II)-MPO-H-X_{C20} complexes are again less stable than the axial ligands, not so remarkable in the case of CN^-, and all present a more favourable high spin, *i.e.*, no spin change is observed upon halogen binding. Still, the addition of (pseudo)halides on C_{20} seems more thermodynamically convenient than in the ferric species.

The metal centre is hexacoordinated in compound I, and thus axial addition of halides takes place on ferryl oxygen (O_{Fe}). A strong O_{Fe}–X bond develops upon MPO-I-X_O formation (bond orders around 1.0), in particular with CN^- (1.25), while the oxoferryl bond weakens accordingly. Furthermore, it results in a strengthening of the interaction between Fe and N_i, both in terms of distance and bond order, in low spin species, whereas high spin MPO-I-XO compounds show a very weak Fe–N_i

bond. The C_{20}–X covalent bond is similar to those in Fe(III)-MPO-X_{C20} and Fe(II)-MPO-X_{C20} adducts. The stability of compound I-halide complexes again follows the order MPO-I-CN > MPO-I-Br > MPO-I-Cl, and spin S = 1/2 is always preferred but MPO-I-CN_O *in vacuo*. It is noteworthy that the differences of the calculated $\Delta G°$ values between MPO-I-X_O complexes of different anions are much higher than for other enzymatic oxidation intermediates. Thus, while the chloro adduct is more stable on C_{20} than on O_{Fe}, the reverse is obtained for MPO-I-CN. The negative charge of the (pseudo)halide ions is fully transferred to the heme moiety in MPO-I-X_O, so that Mulliken atomic charges on Cl, Br, and CN are close to 0, and the polarization of the oxoferryl bond increases (Table S14.3). On the other hand, halogen charges in MPO-I-X_{C20} are much the same as in the ferrous species.

Compound II-(pseudo)halide adducts have been tested for both the unprotonated species and the complex protonated on ferryl oxygen, as this proton could be lost upon halide binding. MPO-II-X_O geometries are similar to MPO-I-X_O, apart from ferryl axial bonds (Fe–O_{Fe} and Fe–N_i) that are in general longer and weaker. In the case of MPO-II-H-X_O the bond with the incoming halide is very weak, bond order < 0.3, and it barely shows any effect on the structure, so that ferryl axial bonds resemble those of MPO-II-H. Geometries of high spin MPO-II-CN_O and low spin MPO-II-H-CN_O could not be optimized. Every attempt of calculation of the former led to rupture of the Fe–N_i bond, and of the latter led to independent HNCO and heme via Fe–O_{Fe} breakage. The Mulliken negative charge on the halogen in MPO-II-H-X_O is comparable to the values obtained for ferric and ferrous complexes, and it is closer to 0 in MPO-II-X_O, but still lower than in the case of MPO-I-X_O.

Effective binding of X^- on C_{20} has been obtained for only MPO-II-CN_{C20} and all protonated compound II complexes; MPO-II-Cl_{C20} and MPO-II-Br_{C20} could not be optimized. Heme structure and charge distribution are distorted in a similar way to previous C_{20} adducts.

Again, cyano compounds are the most stable while chloro adducts show higher energies than the others, except in the case of MPO-II-H-X_O, which do not present important differences among the three (pseudo)halides. Much higher values have been obtained for the solvation Gibbs free energy in all unprotonated MPO-II-X species with respect to any other halocompounds. This led to more similar thermodynamics observed in this case for *in vacuo* and PCM solvated data.

14.4 Discussion

The use of the current model for the calculation of complexes with axial halides excludes the interactions with His95 and water molecules in the distal cavity (W_2 and W_3.) but, apart from that, the same structure obtained experimentally is essentially studied, following the cyanide-native MPO complex.[11] On the other hand, the binding site observed for the MPO-bromide adduct[3] is rather different than in the complexes here calculated. The anion is situated above the meso carbon between pyrroles A and D (C_{20}), but at a long non-bonding distance (Br–C_{20} = 3.8 Å). The anion is stabilized at this position by hydrogen bonding to neighbouring Gln91 and water molecules W_1 and W_5, which are not present in the molecular model employed. Thus, adducts at this binding site were calculated without these surrounding interactions, which results in the halides binding tightly the porphyrin atom C_{20}. Biologically produced organohalides are very rare, and their formation involves more steps than the simple addition of a halide anion.

The interactions of halides with the protein at a particular binding site, either axial or above C_{20}, are reasonably common for all MPO redox species, apart from some protonation differences, and also different halides may present similar forces. Therefore, computed results excluding this environment still allow an adequate comparison. Furthermore, the most important interactions of halides are established with the porphine ring or the metal centre / ferryl oxygen, which are here explicitly considered, and other interactions within the distal cavity have been roughly simulated by the employed PCM solvation model.

Our results indicate that the Gibbs free energy of formation of halocomplexes is always lower for cyanide, then bromide, and chloride presents the least favourable interaction. This occurs either at axial position, binding to Fe or O_{Fe}, or on C_{20}, and for the four enzymatic intermediates analyzed, both in gas phase and with PCM solvation, but for MPO-II-H-X_O, where the Br-adduct is the most favourable species.

Binding of (pseudo)halides is reasonably strong for all obtained complexes with reference to $\Delta G°_{(g)}$, except MPO-II-Cl_O, MPO-II-Br_O, and MPO-II-CN_{C20}, and also in terms of the order of the bond formed with incoming X^-, but MPO-II-H-X_O. However, Gibbs free energy is not so favourable when solvation is considered. Halide anions are strongly solvated in aqueous solution and, therefore, $\Delta G°_{(aq)}$ values are much higher, around 400 kJ·mol^{-1} for most compounds. This is mostly due to the important contribution of X^- desolvation (313, 296, and 290 kJ·mol^{-1} for Cl^-, Br^-, and CN^-, respectively). However, full desolvation (or at least partial, but almost complete) must already occur when the halide crosses the funnel-shaped substrate channel, with a narrow entry to the distal heme pocket,[19] and then the bare anion occupies the most stable position, if any, which must correspond to the distal binding site.

14.4.1 Ferric

According to obtained results, axial Fe(III)−X interaction is more favourable than binding at C_{20} for all Fe(III)-MPO-X species. This suggests that halides bind iron, as experimentally observed for the cyano adduct, but in contradiction with the crystallographic structure obtained for the complex with Br^-.

It has been observed that a distal cavity group (presumably His95) of the ferric native enzyme must be protonated prior to Cl^- binding. Its N_τ is situated axially to heme at 5.6 Å from ferric iron, at a suitable position when protonated for the formation of a H-bond with a halide displacing W_1 (Figure 14.4A). However, the interaction with a halide at W_2 position would be much weaker. This water molecule is not only situated further from the imidazole (N_τ−O_{W2} = 3.5 Å, and N_τ−Br = 3.6 Å) than W_1 (N_τ−O_{W1} = 2.9 Å), but also the orientation of His95 is not so adequate for a H-bond. According to X-ray crystal geometries, distal imidazole does not turn to the halide in the MPO-bromide complex (Figure 14.4B). N_τ-H-Br angle is clearly not linear (~115°), hampering the formation of a strong H-bond linking these two groups, as hydrogen bonds are directional.[28] However, the protonated imidazole can still act as a stronger hydrogen donor to W_1 (N_τ-H-O_{W1} angle ~142°), so that this water molecule becomes more polarized and then forms a stronger H-bond with Br^-. Still, the pH influence is better explained with Cl^- directly attached to Fe and displacing W_1.

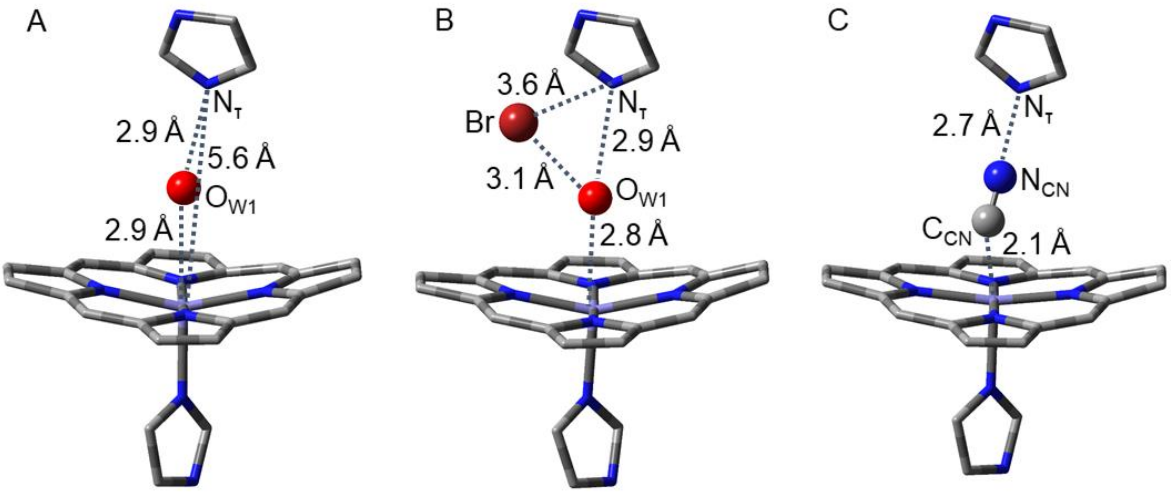

Figure 14.4. Relevant distances at the active site of MPO measured for (A) native ferric state (PDB: 1CXP[3]), (B) bromide complex (PDB: 1D2V[3]), and (C) cyanide complex (PDB: 1D5L[11]).

The two different binding positions observed for Br^- and CN^- can be explained in terms of steric effects. Bromide is a bulky anion (ionic radius 1.82 Å), bigger than chloride (1.67 Å). This is also reflected in the distance calculated for Fe−Br (2.369 Å), longer than for Cl^- (2.277 Å) and CN^- (1.902 Å). Therefore, Fe-coordinated Br^- could lie too close to N_τ for the formation of a H-bond with a proton attached to this atom. In the case of cyanide, despite it forms a strong, stable, and shorter Fe−C_{CN}

bond with Fe via the carbon atom, this anion is longer and the minimum energy structure was calculated for a Fe-C_{CN}-N_{CN} linear arrangement. This ~180° Fe-C_{CN}-N_{CN} angle typical of nitriles and cyano-metal complexes arises from the *sp* hybridization of the C_{CN} atom, triply bonded to N_{CN}, and it would lead again to some steric impediment. However, the crystallographic structure (Figure 14.4C) shows that this problem is overridden as cyanide binds to Fe(III) with a bent Fe-C_{CN}-N_{CN} angle of approximately 157°,[11] more characteristic of cyano-bridged complexes, then minimizing the hindrance with the imidazole moiety. This bending may be also responsible for some weakening of the Fe−C_{CN} bond, as the distance experimentally observed (2.1 Å) is considerably longer than the computed value (1.902 Å). In this case, orientation of His95 imidazole is quite adequate for the formation of a H-bond with N_{CN}.

Hexacoordinate Fe(III) complexes are usually low spin species. However, calculated structure of MPO-Fe(III)-Cl_{Fe} is more stable *in vacuo* at S = 5/2. Fe−Cl distance obtained at high spin is slightly longer than for low spin, and the bond order between both atoms is notably lower. Besides, this interaction is accompanied by a distal out-of-plane shift of iron and an important elongation of Fe−N_i distance, *i.e.*, the metal centre separates from the imidazole, presenting a very low bond order of only 0.15. Therefore, although iron is apparently hexacoordinated in this complex, Fe−N_i bond is mostly exchanged for Fe−Cl, and the proximal imidazole is hardly coordinated to Fe(III), so this could account for the stable high spin experimentally observed. On the other hand, halogenation on C_{20} has no effect on the spin preference: obtained spin multiplicities are the same as for the enzymatic intermediates without halides, since iron coordination is not particularly affected by the anions binding at the porphine edge.

Reported K_d values for chloride and bromide binding to ferric MPO at pH 5.5 are on the order of 5 mM and 20 mM, respectively,[29] indicating a more favourable formation of the chloride complex. According to calculated thermodynamics, binding of bromide is obviously preferred in both positions, contrary to experimental observations. The most likely explanation is that these two halides bind ferric MPO at different sites. Thus, as chloride anion is smaller than bromide, it seems feasible that it could fit in the restricted gap between Fe(III) and protonated distal imidazole, then binding iron directly. This possibility explains the higher affinity measured for this halide.

Nevertheless, it is important to keep in mind that positive $\Delta G°_{(aq)}$ values were calculated for MPO-Fe(III)-Cl_{Fe} and MPO-Fe(III)-Br_{C20}. An analogy can be drawn between this situation and the results obtained for Fe(III)-MPO + H_2O at experimentally observed high spin (see Chapter 11), where the slightly unfavourable $\Delta G°_{(aq)}$ value must be compensated with other interactions within the distal cavity, namely His95, W_2, and W_3, which are not considered in the molecular model. The interaction of a water molecule with Fe(III) is very weak ($\Delta G°_{(g)}$ = −4.76 kJ·mol^{-1}) and, thus, it is stabilized in an axial position over iron atom but at a non-bonding distance. However, the interaction of Cl^- with Fe(III) is stronger, explaining that this halide is able to replace the water molecule situated over Fe (W_1) at a concentration much lower than that of water (5 mM *vs*. 55.5 M) provided that His95 is protonated.

On the other hand, the interaction of CN^- with ferric atom is stronger and formation equilibrium is favourable even considering solvation. The high stability of this cyanocomplex, MPO-Fe(III)-CN_{Fe}, explains the observed inactivation of peroxidases by CN^-.[25] However, MPO is still able to oxidize this anion as long as it is present at low, non-inhibitory concentrations.[30]

According to our data it seems reasonable to propose that chloride anion binds ferric native MPO in an axial position, interacting with Fe as occurs with CN^-. Experimental data support that Br^- binds replacing W_2, and the reason for these two different binding sites is the steric hindrance between protonated imidazole of distal His95 and bulky bromide anion.

14.4.2 Ferrous

The main differences between MPO ferrous heme and that of ferric species are the oxidation state of the central iron atom, and consequently its lower positive charge, and the presence of a protonated vinyl substituent on a pyrrol ring, which also affects the charge distribution of the whole system. The atomic charge on Fe calculated for Fe(III)-MPO (1.53 a.u.) decreases slightly to 1.43 a.u. upon reduction to Fe(II)-MPO-H. Thus, coordination of Cl^- or Br^- with the ferrous centre shows a little longer distance, accompanied by a lower bond order; this effect is negligible in the case of Fe(II)-MPO-H-CN_{Fe}. Furthermore,

the interaction seems to be less favourable with the halides (Cl^- and Br^-), both *in vacuo* (22 to 24 kJ·mol^{-1}) and PCM solvated (6 to 12 kJ·mol^{-1}), whereas the ferrous cyanocomplex is more stable than its ferric counterpart (6 to 10 kJ·mol^{-1}). Halide anions do not act as substrates for reduced peroxidases, therefore $\Delta G°$ values higher than for ferric complexes are consistent with experimental results, and also with the lower oxidation state (and thus, atomic charge) of Fe. However, the relative stability of Fe(II)-MPO-H-CN_{Fe} was an unexpected outcome. For comparison, it has been experimentally determined that the Fe(III)-CN bond of cytochrome *c* is 48 kJ·mol^{-1} more favourable than binding to the ferrous state,[31] whereas our data predict a more stable Fe(II)-CN bond. This difference may arise from the H-bond formed with protonated distal His in the ferric species.

According to our previous calculations and considering the reduced model employed, ferrous heme is protonated on the β-carbon of a vinyl substituent. This protonation associated with a subsequent attachment of a chloride to the adjacent carbon atom can be assimilated to the well-known addition of hydrochloric acid to a C=C double bond. In the particular case of the heme group, the vinyl is conjugated with the aromatic porphyrin ring, so that the extra positive charge upon protonation can be transferred to many other positions where chloride addition is then promoted, as with a conjugated diene:

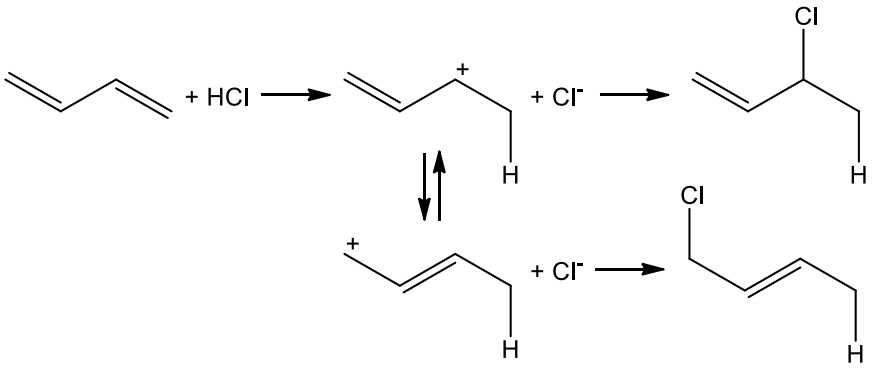

However, the proton added on the vinyl substituent only donates ~80 % of its positive charge to heme, which means less charge than that transferred from Fe(III) atom with respect to Fe(II), ~0.9 a.u. (according to the calculations in Chapters 11 and 12, data not presented). Besides, this charge can be delocalized quite effectively through the heme network of conjugated π bonds, so that individual porphyrin atoms barely modify their charge. Thus, charge on C_{20} only increases 0.03 a.u. upon vinyl protonation, and this position shows the same negative charge (−0.29 a.u.) at both Fe(II)-MPO-H and Fe(III)-MPO. Carbon atoms adjacent to C_{20} are more positively charged (~0.37 a.u.), and they can also interact with halide anions at W_2 position.

Again, the efficiency of the interaction in Fe(II)-MPO-H-X_{C20} follows $CN^- > Br^- > Cl^-$. These complexes are less favourable than the metal-coordinated compounds but more stable (12 to 23 kJ·mol^{-1}) than corresponding ferric adducts. Therefore, considering that the ferric-bromide complex at C_{20} position has been observed, the ferrous bromo complex should be also viable, however it has not been experimentally determined. The geometry obtained by crystallographic studies indicates that Br^- does not lie directly linked to C_{20} but further, at a non-bonding distance, and the anion is stabilized at this position via interaction with W_1, W_5, and Gln91 (and perhaps His95). The forces with W_5 and Gln91 may be very similar in ferric and ferrous species, whereas W_1 in Fe(III)-MPO is more polarized due to its interaction with Fe(III) atom and His95 protonated imidazole. Thus, formation of a stronger H-bond with W_1 is a possible explanation for the specific binding of Br^- to the ferric enzyme but not to the reduced form of MPO.

14.4.3 Compound I

The great difference obtained in the Gibbs free energy of MPO-I-X_O adducts could be ascribed to the fact that, in this case, the formation of the complex does not only represent the building up of some interaction or coordination between heme or iron and (pseudo)halide, but a more important electronic rearrangement, as the anions are oxidized upon binding. The

calculated charge on X atoms in MPO-I-X_O is close to 0 in all cases, slightly positive for Cl^- and Br^- complexes, and the cyano moiety keeps a small amount of its initial negative charge. These values are only ~0.10 a.u. lower than the charges observed in the corresponding hypohalous acids. This indicates that the halides are effectively oxidized upon binding. On the other hand, the charge on X in Fe(III)-MPO-X_{Fe} and Fe(II)-MPO-H-X_{Fe} adducts is always about −0.50 a.u., so the binding of halides to iron does not cause any change in their oxidation state.

Reduction potentials of hypohalites according to the reaction:

$$XO^- + H_2O + 2e^- \rightarrow X^- + 2HO^-$$

are 0.89, 0.76, and −0.97 V for Cl^-, Br^-, and CN^-, respectively. Thus, applying the following equation, where n is the number of electrons generated in the half-reaction and *F* is the Faraday constant:

$$E° = -\frac{\Delta G°_{(aq)}}{nF}$$

Gibbs free energies can be obtained for this process. It results in a Br^- value 334 kJ·mol^{-1} higher than for CN^-, and 359 kJ·mol^{-1} higher in the case of Cl^-. Similarly, MPO-I-X_O with respect to MPO-I + X^- presents a value for Br^- 306 kJ·mol^{-1} higher than for CN^-, and 376 kJ·mol^{-1} for the Cl^- value. These amounts also suggest that the halides are two e^- oxidized upon binding to the oxoferryl group of MPO-I. Thus, only peroxidases with a highly oxidizing compound I may bind some halides and catalyze the corresponding oxidation reaction. Therefore, a heme model lacking MPO particularities (covalent bonds between heme and protein, heme bending, etc) does not yield a compound I able to oxidize Cl^-. This explains that Gibbs free energy obtained here for the formation of MPO-I-Cl_O is positive.

MPO-I-Cl_O may also represent an intermediate for the hypochlorous acid formation (breakage of the oxo-ferryl bond would produce ClO^- and Fe(III)-MPO), and the reverse reaction (chloride departure leading to MPO-I) is the oxidation of ferric MPO by hypochlorous acid to yield compound I. Besides, since the axial O-X moiety in MPO-I-X_O clearly resembles corresponding hypohalous acids, we propose that these complexes act the enzymatic halogenating intermediates, which were already suggested to take part in MPO-mediated chlorination. Furthermore, our MPO-I-Cl_O may correspond to the MPO-Fe(III)-OCl complex proposed for the first step of the reaction between ferric MPO and HClO, in the HClO-mediated MPO heme destruction.[32]

Formation of Fe(III)-MPO-X_{Fe} with bulky halides is prevented by steric hindrance with His95 protonated imidazole. However, halides bind oxoferryl group forming a ~120° Fe-O-X angle, and imidazole protonation seems unnecessary for this process. Thus, all (pseudo)halides may bind ferryl oxygen of compound I provided that it is oxidizing enough. Besides, MPO-I-X_O complexes are more stable than MPO-I-X_{C20}, so the last position is not an option.

It could be expected a stronger bond in C_{20} position than in other peroxidase redox intermediates, as compound I presents a porphyrin π-cation radical and, therefore, more positive charge is presumed on this atom. However, the value calculated for this species (–0.26 a.u.) and the charge on C_{20} observed with other intermediates (–0.25 to –0.29, Chapters 11 & 12, data not presented) are alike. Still, Gibbs free energy in solution for MPO-I-X_{C20} is lower than for ferric and ferrous adducts, but similar to compound II.

14.4.4 Compound II

Interaction between MPO compound II and halides has not been observed experimentally. Still, we have examined the feasibility of a MPO-II-(H)-X complex, where Cl^-, Br^-, or CN^- binds either ferryl oxygen or the meso carbon between pyrroles A and D (C_{20}).

Halides bind O_{Fe} in MPO-II-X_O tightly, with a bond order close to 1 (or higher in the case of CN^-). However, this new bond is compensated by a similar Fe-O_{Fe} weakening in terms of bond order. Thus, *in vacuo* Gibbs free energy is positive for Cl^- and Br^-, and is a low negative value for CN^-, indicating that this interaction is less favourable than in previous intermediates. The only halocompound in C_{20} position, MPO-II-CN_{C20}, is far more unstable than corresponding oxoferryl adduct, which would be much preferred. Halide anions are strongly solvated in aqueous solution and, therefore, $\Delta G°_{(aq)}$ values are

considerably higher than $\Delta G°_{(g)}$, around 400 kJ·mol^{-1} for most compounds. However, solvation energy reveals also high in MPO-II-X adducts and consequently the difference is smaller, *ca*. 150 kJ·mol^{-1}. Thus, MPO-II-Cl_O, MPO-II-Br_O, and MPO-II-CN_{C20} are very unfavourable both *in vacuo* and with PCM solvation, while MPO-II-CN_O shows a stable $\Delta G°_{(aq)}$ value, not as much as MPO-I-CN_O but more than ferric and ferrous species. It must be taken into account that MPO-II-H is preferred under physiological conditions, and that the less stable unprotonated intermediate has been used as reference for MPO-II-X compounds.

The particular charge observed on the halides in MPO-II-X_O (values close to −0.1 for Cl and Br, and −0.22 for CN) is closer to 0 than when bound to iron, but different than in MPO-I-X_O, where they are two-electron oxidized. These values may indicate that here the (pseudo)halide anions are one-electron oxidized (according to the reaction: $X^- \rightarrow X^{\cdot} + e^-$). It is also consistent with the high $\Delta G°$ difference between Cl^-, Br^-, and CN^-, as in compound I. Therefore, if any peroxidase has a compound II with enough potential to oxidize the anion, the corresponding radical plus ferric species could be formed through this intermediate. Thus, despite cyanide is used as an inhibitor of peroxidases, its oxidation to cyanyl radical has been observed with several of these enzymes.[24] Besides, the one-electron oxidation of iodide can be also achieved by compound II of peroxidases.[22, 23]

All MPO-II-H-X compounds present more favourable thermodynamics, both *in vacuo* and with PCM solvation, than corresponding unprotonated species, but MPO-II-H-CN_O. Furthermore, starting MPO-II-H is also more stable than unprotonated compound II. Therefore, these halocompounds seem to be preferred to MPO-II-X (but MPO-II-CN_O).

Halogens interact with ferryl oxygen at long distances, more than 2 Å in all cases, which correspond to very low bond orders. Besides, while Fe-O_{Fe}-H presents a ~116° angle adequate for two atoms bound to oxygen, halides are situated forming Fe-O_{Fe}-X angles around 150°. Furthermore, CN^- does not form the O_{Fe}-C-N linear arrangement consistent with a bond linking both moieties. Thus, halides interact with the oxoferryl group of MPO-II-H but no real bonds are formed. Therefore, these atoms maintain an important part of their initial negative charge, and keep their anionic character.

In compound II the porphyrin ring is not a cation, but the charge on C_{20} is −0.25, both in MPO-II and MPO-II-H, very similar to compound I and the other intermediates. Interaction with a halide over this position should then be similar to other MPO redox species, and also between unprotonated and protonated compound II. However, binding of (pseudo)halides to δ-meso carbon is much more stable for the protonated species; in fact in MPO-II-Cl_{C20} and MPO-II-Br_{C20} the halides could not be optimized at this position, as they always escaped. Besides, MPO-II-H-X_{C20} adducts are more stable than other halocompounds with this binding position for ferric and ferrous intermediates, and also with respect to compound I in the case of MPO-II-H-CN_{C20}. Still, adducts at O_{Fe} position are always preferred: protonated compounds for Cl^- and Br^-, and unprotonated MPO-II-CN_O for CN^-, as explained below.

Oxoferryl group in compound II is protonated, but the presence of halides in the distal cavity must have an effect on its acidity, as they bind strongly unprotonated O_{Fe} stabilizing this form. Therefore, we can calculate pK_a of compound II with a (pseudo)halide present, considering that X^- binds O_{Fe} upon deprotonation according to this substitution reaction (X^- is not linked to O_{Fe} in the protonated complex):

$$\text{MPO-II-H-}X_O \rightarrow \text{MPO-II-}X_O + H^+$$

where published thermodynamic parameters were employed for proton in the gas phase[33] and aqueous solution.[34, 35] pK_a values determined with most stables spins are 37, 32, and −32 for Cl^-, Br^-, and CN^-, respectively. In the case of CN^-, the adduct MPO-II-H-CN_{C20} presents lower Gibbs free energy than in the other binding position. Using this species for the calculation pK_a = −5, although covalently bound halides are considered in the study and the unbound compounds at this binding site must not be so stable. Therefore, this substitution is not possible with Cl^- and Br^- anions, apart from any peroxidase that could be able to stabilize MPO-II-Cl_O and MPO-II-Br_O adducts extremely. Displacement of H^+ by CN^- is much favoured, though. However, structures of both MPO-II-CN_O with S = 2 and MPO-II-H-CN_O with S = 1 could not be optimized, since some bond breaking processes occurred. Regarding MPO-II-H-CN_O, HNCO was always released, which can be involved in reactions like:

$$\text{Ferrous species} + HXO \leftrightarrows \text{Compound II} + X^-$$

Formation of free HNCO could indicate a 2-electron oxidation of CN^- by compound II, yielding isocyanic acid and the ferrous enzymatic intermediate. The oxidation of ferrous peroxidases with H_2O_2 to yield compound II is known for many years.[36] The reaction has been also observed for MPO,[37] and it takes place with peroxynitrite as well.[38] Thus, in a similar way as HClO can replace H_2O_2 in the 2-electron oxidation of ferric MPO to compound I,[39] it may also mediate the oxidation of ferrous MPO to compound II. This process will be feasible if the oxidation potential of the substrate is enough. In that case, it may take place through the chloro intermediates here exposed. On the other hand, as HNCO is much less oxidant, studied cyanocompounds could play the intermediate role in the reverse reaction, or even a transition structure. This could explain that the optimization led to a real energy minimum that corresponds to separate Fe(II)-MPO + HNCO, and even more stable if protonated on a vinyl substituent.

14.5 Conclusions

Computational methodologies allow a better insight in reaction mechanisms. However, theoretical results should always be considered carefully and contrasted with empirical data when possible. Here, the use of a reduced model of the protein revealed quite adequate to estimate some features of peroxidases, but it ignores the effect of and interactions with other functional groups within distal cavity. Despite the results can also be applied to other members of this family, this study is mainly focused on MPO. Thus, computational general outcomes were contrasted and complemented with more specific empirical data obtained with MPO, or other enzymes if necessary.

According to this approach, Cl^- binds ferric iron as observed for CN^-, whereas Br^- is situated at W_2 position. This distribution can be explained in terms of steric hindrance. Halocomplexes with ferrous intermediate are less stable than with ferric enzyme, but in the case of CN^-, and again metal-coordinated complexes are more favourable. This is consistent with the observation of the ferro cyano compound as the only feasible ferrous complex with halides.

This analysis indicates that halides oxidized by compounds I and II interact directly with ferryl oxygen for the electronic transference to proceed. This interaction is possible as the non-linear Fe-O_{Fe}-X position allows binding of bulky substrates at this site without any hampering by His95 imidazole. The adduct formed by compound I and Cl^- must be the enzymatic chlorinating species, as well as an intermediate for $HClO/ClO^-$ formation. A similar cyano adduct with unprotonated compound II, upon substitution of H^+ by CN^-, could lead the one-electron oxidation reaction of the substrate, while the interaction of halides with protonated compound II may represent a transition structure for the conversion between ferrous species and compound II: direct or reverse reaction would occur depending on the oxidation potential of HXO and the particular peroxidase.

Therefore, chloride anion may play substrate and inhibitor roles in the MPO-mediated chlorination reaction. These conclusions can also be adapted and applied to other peroxidases and halides.

14.6 References

1. C. J. van Dalen, M. W. Whitehouse, C. C. Winterbourn, and A. J. Kettle, *Thiocyanate and chloride as competing substrates for myeloperoxidase.* Biochem. J., 1997 **327** (Pt. 2) 487-492.
2. P. G. Furtmüller, U. Burner, and C. Obinger, *Reaction of myeloperoxidase compound I with chloride, bromide, iodide, and thiocyanate.* Biochemistry, 1998 **37** (51) 17923-17930.
3. T. J. Fiedler, C. A. Davey, and R. E. Fenna, *X-ray crystal structure and characterization of halide-binding sites of human myeloperoxidase at 1.8 Å resolution.* J. Biol. Chem., 2000 **275** (16) 11964-11971.
4. M. Ikeda-Saito, P. V. Argade, and D. L. Rousseau, *Resonance Raman evidence of chloride binding to the heme iron in myeloperoxidase.* FEBS Lett., 1985 **184** (1) 52-55.

5. R. Wever and A. R. J. Bakkenist, *The interaction of myeloperoxidase with ligands as studied by EPR.* Biochim. Biophys. Acta, 1980 **612** (1) 178-184.

6. M. Ikeda-Saito and R. C. Prince, *The effect of chloride on the redox and EPR properties of myeloperoxidase.* J. Biol. Chem., 1985 **260** (14) 8301-8305.

7. M. Ikeda-Saito, *A study of ligand binding to spleen myeloperoxidase.* Biochemistry, 1987 **26** (14) 4344-4349.

8. B. G. J. M. Bolscher and R. Wever, *A kinetic study of the reaction between myeloperoxidase, hydroperoxides and cyanide. Inhibition by chloride and thiocyanate.* Biochim. Biophys. Acta, 1984 **788** (1) 1-10.

9. R. Floris and R. Wever, *Reaction of myeloperoxidase with its product HOCl.* Eur. J. Biochem., 1992 **207** (2) 697-702.

10. R. Floris, S. R. Piersma, G. Yang, P. Jones, and R. Wever, *Interaction of myeloperoxidase with peroxynitrite. A comparison with lactoperoxidase, horseradish peroxidase and catalase.* Eur. J. Biochem., 1993 **215** (3) 767-775.

11. M. Blair-Johnson, T. Fiedler, and R. Fenna, *Human myeloperoxidase: structure of a cyanide complex and its interaction with bromide and thiocyanate substrates at 1.9 Å resolution.* Biochemistry, 2001 **40** (46) 13990-13997.

12. D. G. Eglinton, D. Barber, A. J. Thomson, C. Greenwood, and A. W. Segal, *Studies of cyanide binding to myeloperoxidase by electron paramagnetic resonance and magnetic circular dichroism spectroscopies.* Biochim. Biophys. Acta, 1982 **703** (2) 187-195.

13. J. J. Lopez-Garriga, W. A. Oertling, R. T. Kean, H. Hoogland, R. Wever, and G. T. Babcock, *Metal-ligand vibrations of cyanoferric myeloperoxidase and cyanoferric horseradish peroxidase: evidence for a constrained heme pocket in myeloperoxidase.* Biochemistry, 1990 **29** (40) 9387-9395.

14. G. Proteasa, Y. R. Tahboub, S. Galijasevic, F. M. Raushel, and H. M. Abu-Soud, *Kinetic evidence supports the existence of two halide binding sites that have a distinct impact on the heme iron microenvironment in myeloperoxidase.* Biochemistry, 2007 **46** (2) 398-405.

15. C. Phelps, E. Antonini, and M. Brunori, *The binding of cyanide to ferroperoxidase.* Biochem. J., 1971 **122** (1) 79-87.

16. J. B. Wittenberg, R. W. Noble, B. A. Wittenberg, E. Antonini, M. Brunori, and J. Wyman, *Studies on the equilibria and kinetics of the reactions of peroxidase with ligands. II. The Reaction of Ferroperoxidase with Oxygen.* J. Biol. Chem., 1967 **242** (4) 626-634.

17. W. E. Blumberg, J. Peisach, B. A. Wittenberg, and J. B. Wittenberg, *The electronic structure of protoheme proteins I. An electron paramagnetic resonance and optical study of horseradish peroxidase and its derivatives.* J. Biol. Chem., 1968 **243** (8) 1854-1862.

18. L. A. Marquez and H. B. Dunford, *Chlorination of taurine by myeloperoxidase. Kinetic evidence for an enzyme-bound intermediate.* J. Biol. Chem., 1994 **269** (11) 7950-7956.

19. D. R. Ramos, M. V. García, M. Canle L., J. A. Santaballa, P. G. Furtmüller, and C. Obinger, *Myeloperoxidase-catalyzed chlorination: The quest for the active species.* J. Inorg. Biochem., 2008 **102** (5-6) 1300-1311.

20. H. C. Lee, K. S. Booth, W. S. Caughey, and M. Ikeda-Saito, *Interaction of halides with the cyanide complex of myeloperoxidase: a model for substrate binding to compound I.* Biochim. Biophys. Acta, 1991 **1076** (2) 317-320.

21. P. G. Furtmüller, M. Zederbauer, W. Jantschko, J. Helm, M. Bogner, C. Jakopitsch, and C. Obinger, *Active site structure and catalytic mechanisms of human peroxidases.* Arch. Biochem. Biophys., 2006 **445** (2) 199-213.

22. R. Roman, H. B. Dunford, and M. Evett, *Studies on horseradish peroxidase VII. A kinetic study of the oxidation of iodide by horseradish peroxidase compound II.* Can. J. Chem., 1971 **49** (18) 3059-3063.

23. J. E. Critchlow and H. B. Dunford, *Studies on horseradish peroxidase X. The mechanism of the oxidation of p-cresol, ferrocyanide, and iodide by compound II.* J. Biol. Chem., 1972 **247** (12) 3714-3725.

24. S. N. J. Moreno, K. Stolze, E. G. Janzen, and R. P. Mason, *Oxidation of cyanide to the cyanyl radical by*

peroxidase/H_2O_2 systems as determined by spin trapping. Arch. Biochem. Biophys., 1988 **265** (2) 267-271.

25. S. Adak, A. Mazumdar, and R. K. Banerjee, *Low catalytic turnover of horseradish peroxidase in thiocyanate oxidation. Evidence for concurrent inactivation by cyanide generated through one-electron oxidation of thiocyanate.* J. Biol. Chem., 1997 **272** (17) 11049-11056.
26. J. E. Merritt and K. L. Loening, *Nomenclature of tetrapyrroles.* Pure Appl. Chem., 1979 **51** (11) 2251-2304.
27. M. J. Frisch, G. W. Trucks, H. B. Schlegel, G. E. Scuseria, M. A. Robb, J. R. Cheeseman, J. J. A. Montgomery, T. Vreven, K. N. Kudin, J. C. Burant, J. M. Millam, S. S. Iyengar, J. Tomasi, V. Barone, B. Mennucci, M. Cossi, G. Scalmani, N. Rega, G. A. Petersson, H. Nakatsuji, M. Hada, M. Ehara, K. Toyota, R. Fukuda, J. Hasegawa, M. Ishida, T. Nakajima, Y. Honda, O. Kitao, H. Nakai, M. Klene, X. Li, J. E. Knox, H. P. Hratchian, J. B. Cross, V. Bakken, C. Adamo, J. Jaramillo, R. Gomperts, R. E. Stratmann, O. Yazyev, A. J. Austin, R. Cammi, C. Pomelli, J. W. Ochterski, P. Y. Ayala, K. Morokuma, G. A. Voth, P. Salvador, J. J. Dannenberg, V. G. Zakrzewski, S. Dapprich, A. D. Daniels, M. C. Strain, O. Farkas, D. K. Malick, A. D. Rabuck, K. Raghavachari, J. B. Foresman, J. V. Ortiz, Q. Cui, A. G. Baboul, S. Clifford, J. Cioslowski, B. B. Stefanov, G. Liu, A. Liashenko, P. Piskorz, I. Komaromi, R. L. Martin, D. J. Fox, T. Keith, M. A. Al-Laham, C. Y. Peng, A. Nanayakkara, M. Challacombe, P. M. W. Gill, B. Johnson, W. Chen, M. W. Wong, C. Gonzalez, and J. A. Pople, *Gaussian03*. 2004, Gaussian, Inc.: Wallingford CT.
28. A. Shahi and E. Arunan, *Why are hydrogen bonds directional?* J. Chem. Sci., 2016 **128** (10) 1571-1577.
29. A. R. J. Bakkenist, J. E. G. D. Boer, H. Plat, and R. Wever, *The halide complexes of myeloperoxidase and the mechanism of the halogenation reactions.* Biochim. Biophys. Acta, 1980 **613** (2) 337-348.
30. C. Delporte, K. Z. Boudjeltia, P. G. Furtmüller, R. A. Maki, M. Dieu, C. Noyon, M. Soudi, D. Dufour, C. Coremans, V. Nuyens, F. Reye, A. Rousseau, M. Raes, N. Moguilevsky, M. Vanhaeverbeek, J. Ducobu, J. Nève, B. Robaye, L. Vanhamme, W. F. Reynolds, C. Obinger, and P. Van Antwerpen, *Myeloperoxidase-catalyzed oxidation of cyanide to cyanate: A potential carbamylation route involved in the formation of atherosclerotic plaques?* J. Biol. Chem., 2018 **293** (17) 6374-6386.
31. A. Schejter, M. D. Ryan, E. R. Blizzard, C. Zhang, E. Margoliash, and B. A. Feinberg, *The redox couple of the cytochrome c cyanide complex: the contribution of heme iron ligation to the structural stability, chemical reactivity, and physiological behavior of horse cytochrome c.* Protein Sci., 2006 **15** (2) 234-241.
32. D. Maitra, F. Shaeib, I. Abdulhamid, R. M. Abdulridha, G. M. Saed, M. P. Diamond, S. Pennathur, and H. M. Abu-Soud, *Myeloperoxidase acts as a source of free iron during steady-state catalysis by a feedback inhibitory pathway.* Free Radic. Biol. Med., 2013 **63** 90-98.
33. J. E. Bartmess, *Thermodynamics of the electron and the proton.* J. Phys. Chem., 1994 **98** (25) 6420-6424.
34. M. D. Tissandier, K. A. Cowen, W. Y. Feng, E. Gundlach, M. H. Cohen, A. D. Earhart, J. V. Coe, and T. R. Tuttle Jr., *The proton's absolute aqueous enthalpy and Gibbs free energy of solvation from cluster-ion solvation data.* J. Phys. Chem. A, 1998 **102** (40) 7787-7794.
35. I. A. Topol, G. J. Tawa, S. K. Burt, and A. A. Rashin, *On the structure and thermodynamics of solvated monoatomic ions using a hybrid solvation model.* J. Chem. Phys., 1999 **111** (24) 10998-11014.
36. R. W. Noble and Q. H. Gibson, *The reaction of ferrous horseradish peroxidase with hydrogen peroxide.* J. Biol. Chem., 1970 **245** (9) 2409-2413.
37. W. Jantschko, P. G. Furtmüller, M. Zederbauer, M. Lanz, C. Jakopitsch, and C. Obinger, *Direct conversion of ferrous myeloperoxidase to compound II by hydrogen peroxide: an anaerobic stopped-flow study.* Biochem. Biophys. Res. Commun., 2003 **312** (2) 292-298.
38. P. G. Furtmüller, W. Jantschko, M. Zederbauer, M. Schwanninger, C. Jakopitsch, S. Herold, W. H. Koppenol, and C. Obinger, *Peroxynitrite efficiently mediates the interconversion of redox intermediates of myeloperoxidase.*

Biochem. Biophys. Res. Commun., 2005 **337** (3) 944-954.

39. P. G. Furtmüller, U. Burner, W. Jantschko, G. Regelsberger, and C. Obinger, *The reactivity of myeloperoxidase compound I formed with hypochlorous acid.* Redox Rep., 2000 **5** (4) 173-178.

ADDENDUM

In the race for quality, there is no finish line.

David T. Kearns

Scientific research is quite often an endless task or, at least, its conclusion is a rather fluid concept since the knowledge in the subject under study can always be improved or extended. This dissertation shows a more or less complete study, in the sense that it fulfils some objectives and it is able to reach some conclusions. However, to keep the dissertation at a reasonable length and to avoid further delay of its completion, it has been abridged and an important part of the produced data were not shown in the previous chapters. Then, other results already obtained are summarized in this final chapter, as well as the ongoing research in the topic.

15.1 Computational studies

The research was initially intended with experimental techniques, but the complexity of the reaction mechanisms under study made the use of other tools desirable. Electronic structure calculations are the perfect tool to support traditional experimental studies, determining structures, stabilities, or activation barriers for a better interpretation of empirical data. Then, different methods of computational chemistry have been employed in the three parts of the dissertation to obtain additional information not accessible by empirical means, or to gain further insight in the detailed reactivity.

The dramatic increase in computational power and speed is associated to a continuous improvement in the available methodology to obtain more and more accurate thermochemical properties for a wide range of systems. Thus, the capabilities of computational chemistry have developed notably during the years spent performing this long research. However, in order to obtain easily comparable results and to keep some consistency along each study, the computational methods employed were not updated and so more uniform data are displayed.

In the present study, structure and thermodynamics of myeloperoxidase have been analyzed employing a small molecular model and the lowest computational level that was found to yield adequate results. The use of this reduced model of the active site of myeloperoxidase (and peroxidases in general) was fully deliberate, to find out what properties of these enzymes arise from this minor but common part of their structures. Employed DFT method (PCM//UB3LYP/6-31G*) yielded good results, with an excellent agreement with experimental observations. We estimate that this concurrence was mostly due to the use of relative energies, where protein environment effects, solvation deficiencies, exchange-correlation functional shortcomings, and others, cancel out. However, it can be argued that this good correlation is in fact an artifact caused by accidental but favourable error cancellation of a too simple computational model.[1] Therefore, calculations with higher level methods are being performed to obtain more accurate values and to confirm the adequacy of previous outcomes and conclusions.

The four possible degradation pathways of secondary *N*-halo ethanolamines were computed with either B3LYP/6-31++G** or MP2=full/6-31++G**. Aqueous solvation was simulated by using discrete and hybrid discrete-polarized continuum models. Results obtained with these computational methods were already published in scientific journals.[2-4] Subsequent reactions, *i.e.*, hydrolysis of imines, and intramolecular fragmentation and hydrolysis of ethanolimines, where also calculated at the B3LYP/6-31++G** computational level, while the effect of water was described incorporating PCM (polarized continuum model) solvation over microsolvated optimized structures. This method was chosen for a better comparison among results acquired for all related processes. Therefore, corresponding values were collected in previous chapters. However, additional computational work has been performed with more powerful methods, employing current optimized geometries as starting point, to obtain more adequate data for publication. So far, same conclusions can be inferred from those results, which also support quite similar reaction mechanisms.

A particular hybrid continuum-microsolvated method, where the effect of an increasing number of discrete water molecules was analyzed, is described in Chapter 7. This work on cysteine pK_a values has been already published,[5] but it does not provide any conclusive order of $-NH_3^+$ and –SH acidities. More calculations have been executed to determine correct pK_a assignments of cysteine, but this compound is particularly challenging, as it needs the calculation of adequate thermodynamics in aqueous solution of two anions, one of them a dianion, and two zwitterions, one of them incorporating three different charged groups.[6]

A comparative examination of the acid dissociation thermodynamics of thiols and amines was also prepared. Several compounds with known pK_a values were calculated at different computational levels and with various solvent models. Experimental and computational data were compared in order to find out any reliable method for obtaining adequate pK_a values of both thiols and amines, and then apply it to Cys. This study has not reached any definite outcome until now.

15.2 Amines

The first part of this dissertation focused on the base-assisted decomposition of secondary *N*-halo ethanolamines, and on the reactions undergone by *N*-Cl,*N*-methylethanolamine in particular. Other secondary ethanolamines were studied by both empirical and computational means: *N*-ethylethanolamine, *N*-isopropylethanolamine, and *N*-benzylethanolamine. Results obtained with these compounds, both experimental and computational, were briefly described in Chapter 6, and are fully compatible with the behaviour observed with *N*-methylethanolamine.

Table 15.1. Second-order kinetic constants measured at T =298 K for the HO^--mediated decomposition of the *N*-Cl alcoholamines under study and corresponding parent *N*-Cl amines, and ratio between them. Values obtained for *N*-Cl,*N*-methylethylamine and *N*-Cl,*N*-methylethanolamine are collected for comparison purposes.

Amine	k_{HO^-} ($M^{-1}\cdot s^{-1}$)	Alcoholamine	k_{HO^-} ($M^{-1}\cdot s^{-1}$)	Ratio
N-methylethylamine	1.9×10^{-4}	*N*-methylethanolamine	6.8×10^{-2}	362
N,*N*-dimethylethylamine	2.5×10^{-4}	*N*,*N*-dimethylethanolamine	7.0×10^{-2}	279
2-ethylpiperidine	7.1×10^{-4}	2-ethanolpiperidine	1.2×10^{-3}	1.7

Besides, decomposition of the halo derivatives of other alcoholamines has been also studied, showing a different reactivity than previous compounds. *N*,*N*-dimethylethanolamine and parent *N*,*N*-dimethylethylamine were taken as an example of tertiary ethanolamines, while 2-ethanolpiperidine and 2-ethylpiperidine were model compounds for the study of secondary propanolamines. Kinetic constants obtained for the reaction between these chloramines and HO^- show that degradation rate of *N*-Cl,*N*,*N*-dimethylethanolamine is very similar to that of *N*-Cl,*N*-methylethanolamine, and also the increase with respect to parent *N*-Cl amines (Table 15.1). However, decomposition of *N*-Cl,2-ethanolpiperidine is slower, and less than a twofold rise with respect to *N*-Cl,2-ethylpiperidine was observed.

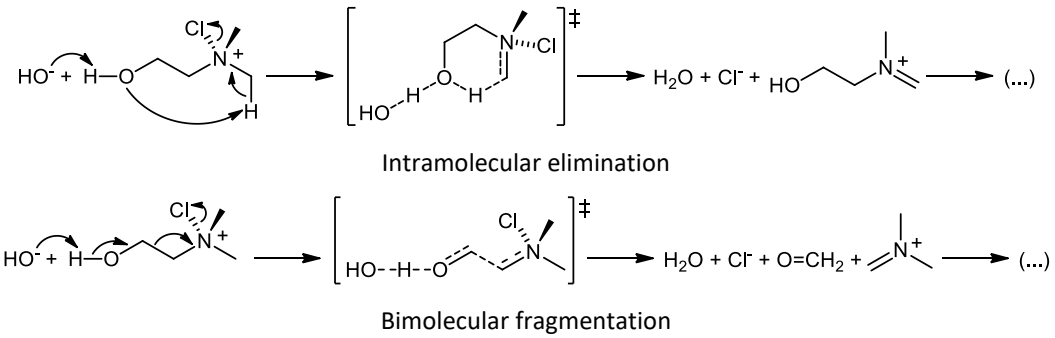

Scheme 15.1. Reaction mechanism proposed for the HO^--promoted decomposition of *N*-Cl,*N*,*N*-dimethylethanolamine. Intermolecular elimination pathways are omitted.

Reaction of HClO with tertiary amines leads to chlorinated quaternary ammonium species.[7] This type of compounds

actively participate in several oxidation processes during chlorination.[8, 9] They present a positively charged N atom, which, however, seems not to exert any relevant effect on their degradation rate. As with secondary ethanolamines, the increase with respect to the same reaction of the parent *N*-Cl ethylamine is due to the participation of two proposed additional pathways, intramolecular elimination and bimolecular fragmentation (Scheme 15.1). The participation ratio of these two processes has not been determined, neither by computational means nor by product analysis. Besides, this could yield misleading results since, again, the iminium cations produced in these reactions may undergo hydrolysis[10] or other unknown processes.

The situation is quite different when dealing with propanolamines. The bimolecular fragmentation is not possible, but intramolecular eliminations can take place in two positions, as in the case of intermolecular eliminations. Intramolecular elimination at the Hofmann position proceeds via a cyclic 7-membered transition structure, whereas the process at the Zaitsev position occurs via a cyclic 5-membered activated complex (Scheme 15.2). Both of them are much less stable than 6-atom rings, as the transition structures in the case of ethanolamines, and therefore, these processes must be not so favourable. Furthermore, as the N atom already belongs to a piperidine ring, transition structures are bicyclic, which means that they must have an important structural strain, especially at the C atom(s) in α position to N.

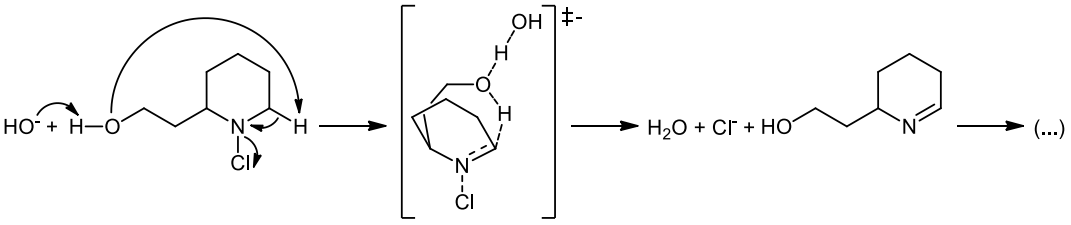

Intramolecular Hofmann elimination

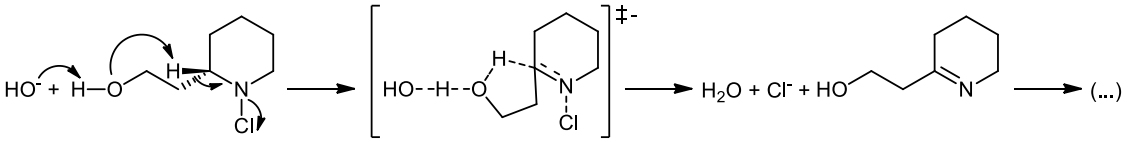

Intramolecular Zaitsev elimination

Scheme 15.2 Reaction mechanism proposed for the HO^--promoted decomposition of *N*-Cl,2-ethanolpiperidine. Intermolecular elimination pathways are omitted.

Decomposition rate only increased 70 % upon addition of the hydroxyl group. This difference may arise from very ineffective intramolecular competitive processes, as expected from those unfavourable strained cyclic transition states, or just from some electronic effect of this functional group on the intermolecular elimination reaction with no participation of additional pathways.

15.3 Thiols

15.3.1 Cysteine

Some computational work on the microscopic pK_a equilibria of the α-amino acid cysteine (Cys) has already been included in Chapter 7, and other computational studies performed afterwards have been briefly explained above in this chapter. Besides, experimental procedures for the determination of pK_a values of Cys were also evaluated. These studies did not yield any useful result. Thus, further experimental work in this matter would be necessary to obtain correctly assigned pK_a values.

Furthermore, a different approach to the problem was used, by comparison of experimental pK_a values of Cys with other amines and thiols through quantitative structure-activity relationships (QSAR). Hammett σ inductive (σ_i) was selected as the most consistent parameter for these processes.[11] Total inductive effects on the C_α were considered for amine acidities, while cumulative σ_i values on the C_β were used for thiol pK_a values; this has been proven necessary to derive $\Sigma\sigma_i$ for Cys. Then, amines and thiols employed in the study were methodically chosen as follows: from all amine-thiol couples with both acidities in water published in the reference books *Critical Stability Constants*[12] and *The Proton: Applications to Organic Chemistry*[13], only the compounds with substituents that permit the evaluation of their $\Sigma\sigma_i$ value were selected. Thus, plots of pK_a values for amines and thiols, including Cys, *vs*. inductive effect are depicted in Figure 15.1.

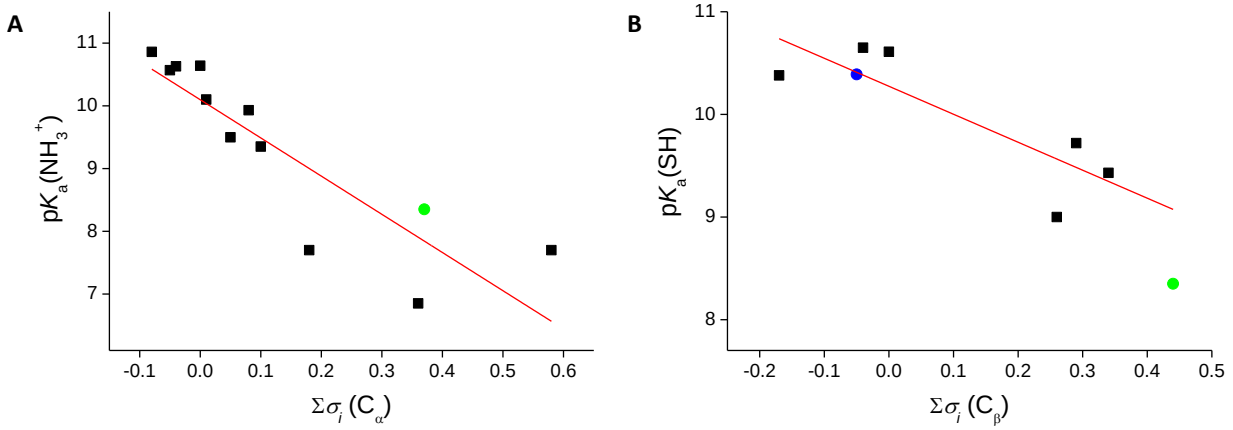

Figure 15.1. Scatter plots of experimental pK_a values of amines (A) and thiols (B) *vs*. $\Sigma\sigma_i$ calculated on C_α and C_β, respectively. Hypothetical experimental data points for $^-O_2CCH(NH_3^+)CH_2SH$ (●) and $^-O_2CCH(NH_2)CH_2SH$ (●) are shown. Total inductive effect of the substituents on C_α to N in $^-O_2CCH(NH_3^+)CH_2S^-$ cannot be estimated, and this point is not represented.

According to these linear fits, predicted pK_a values of the second ionization of Cys, that is, ionization of $^-O_2CCH(NH_3^+)CH_2SH$, are 7.84 for the amine and 9.07 for the thiol. Therefore, amine is more acidic and the prediction is even lower (0.51 units) than the experimental macroscopic value (8.35), whereas thiol predicted pK_a is 1.23 units higher. On the other hand, the third Cys pK_a value, estimated for the thiol of $^-O_2CCH(NH_2)CH_2SH$ according to its substituents, is 10.41, extremely close to the empirical macroscopic pK_a (10.39).

Computational studies did not allow a conclusive discrimination of the correct deprotonation sequence. However, from the QSAR approach, it follows that $–NH_3^+$ must be more acidic than –SH in Cys and, therefore, the pK_a value about 8 should be assigned to the amino end. This outcome opposes most assignations of acid dissociations of Cys found in scientific literature.

15.3.2 Glutathione

Reduced glutathione (GSH) is the major non-protein thiol present in most animal cells and intracellular fluids.[14] It is an important antioxidant that is easily oxidized by halogenating agents, like those produced by activated neutrophils through the enzymatic system myeloperoxidase / H_2O_2 / Cl^-. Upon reaction with HClO or *N*-Cl taurine, glutathione is oxidized to sulfenyl chloride, GSCl. An *in vitro* kinetic study of the chlorination of GSH by HClO and subsequent reactions has been performed. The influence of the acidity of the medium has been also analyzed around myeloperoxidase/H_2O_2/Cl^- optimal pH working range.

Results showed that formation of GSCl is very fast; a typical kinetic trace is displayed in Figure 15.2A. Chlorination in other position than the thiol group has not been observed in any case. The pH influence on the observed kinetic constant shows a bell-shaped fit, which corresponds to a reaction comprising two fast protonation equilibria (for HClO and GSH) and a rate-limiting chlorination step (Figure 15.2B). The rate constant value obtained for the latter is 1.6×10^{10} $M^{-1}{\cdot}s^{-1}$, close to the

diffusion control limit. When using a less powerful oxidizing agent like *N*-Cl taurine, observed kinetic constants are four orders of magnitude lower for the same chlorination reaction.[15]

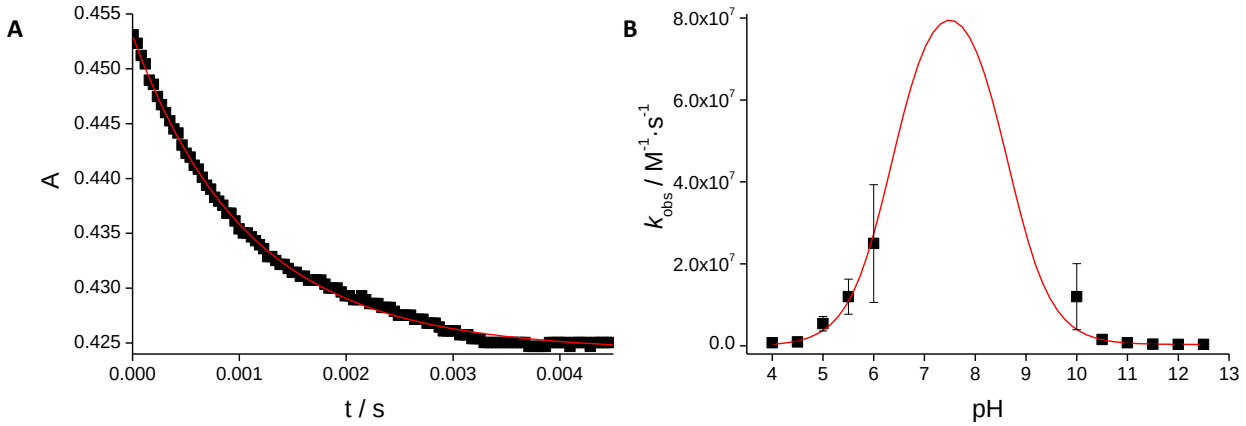

Figure 15.2. Typical kinetic trace measured for GSH chlorination (A) and pH influence on the chlorination kinetic constant (B). Data obtained by M. Isabel Fernández.

Chlorination of reduced glutathione is immediately followed by two other slower consecutive decomposition steps. The three processes occur within different time scales and present rates in decreasing order. Thus, they can be measured and fitted independently. Exponential fitting of the kinetic traces of both subsequent processes indicate that they correspond to two competitive reactions each (Figure 15.3).

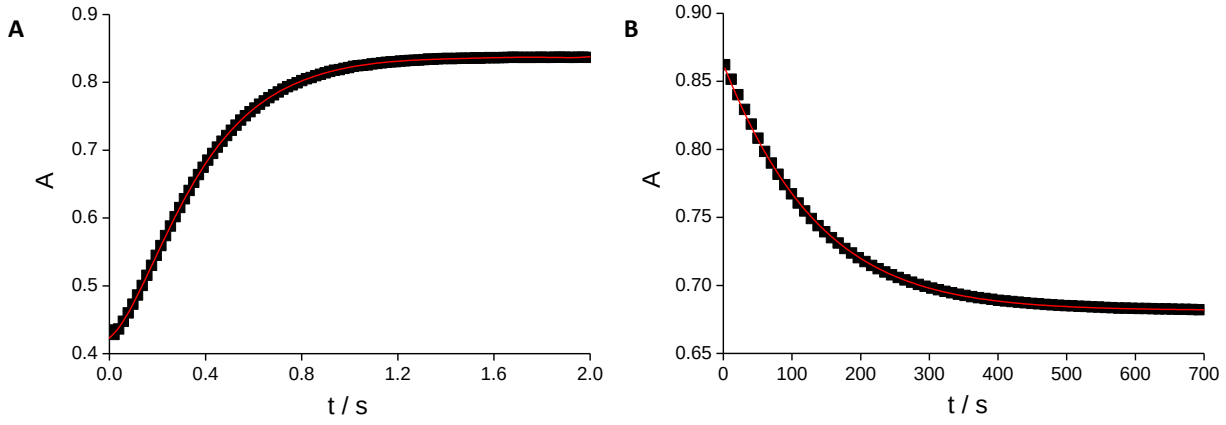

Figure 15.3. Typical kinetic traces measured for the first decomposition step of GSCl (A) and subsequent process (B).

GSCl decomposes via a complex mechanism including several concurrent and consecutive processes. Taking into account these data and some previous research,[16] a possible mechanism has been proposed (Scheme 15.3). Reaction of the chlorinated species with unreacted GSH may lead to the oxidation form of glutathione, GSSG. The rate constant observed for this process decreases exponentially with increasing pH (Figure 15.4A). On the other hand, further HClO-oxidation of GSCl yields the sulfonyl chloride derivative (GSO_2Cl). This reaction seems to be controlled by acid ionization of both reactants and, therefore, the rate constant shows a maximum value about pH = 4.0 - 4.5 (Figure 15.4B).

GSSG is a stable compound that can be reduced back to GSH by the enzyme glutathione reductase. The equilibrium between

reduced and oxidized species of glutathione is essential for maintaining reducing conditions in the cell, playing an important antioxidant role by scavenging different reactive oxygen species.[17] Therefore, subsequent processes correspond to the other product.

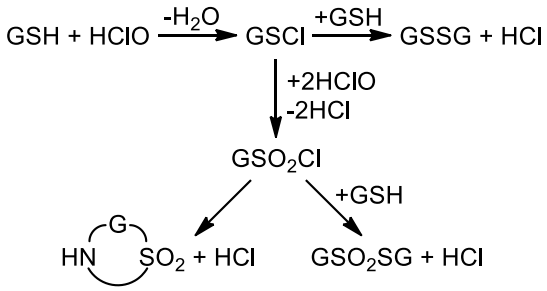

Scheme 15.3. Proposed mechanism for the reaction between GSH and HClO.

Decomposition of GSO_2Cl takes place via two competitive mechanisms. The reaction with unreacted GSH yields glutathione thiosulfonate (GSO_2SG) and the rate constant decreases dramatically with increasing pH (Figure 15.4C). On the other hand, GSO_2Cl may undergo an intramolecular cyclization, leading to the formation of a cyclic sulfonamide (see Scheme 15.3). This process presents a similar influence of pH, but here the observed kinetic constant reaches a minimum value about pH = 5 (Figure 15.4D).

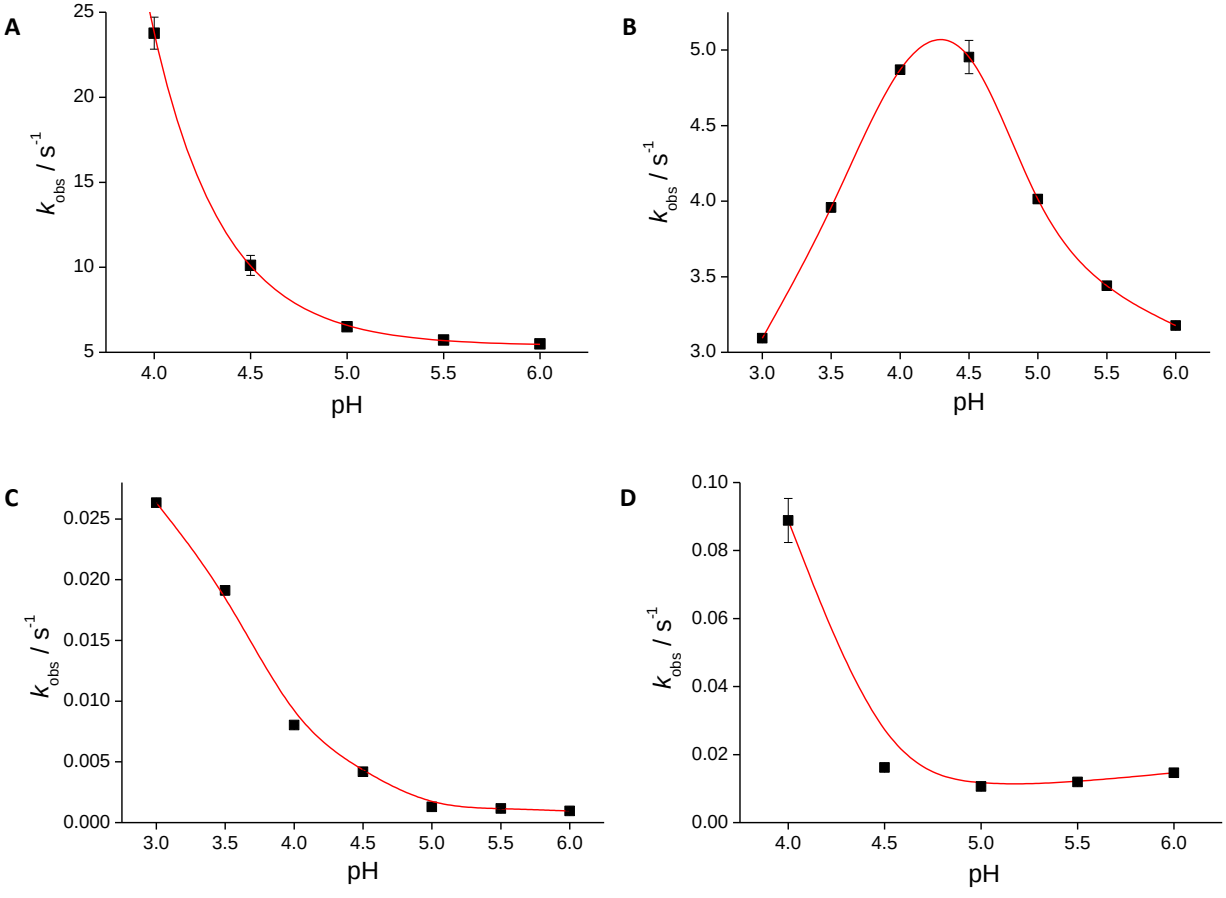

Figure 15.4. pH influence on the observed kinetic constants for the decomposition processes of GSCl. The plots correspond to formation of GSSG (A), GSO_2Cl (B), GSO_2SG (C), and cyclic glutathione sulfonamide (D).

The spectrophotometric kinetic study here presented must be finished and experiments with other techniques should be used to confirm the proposed reaction mechanism. A complete product analysis would be very useful. Still, these are the first kinetic values obtained for the chlorination of GSH with HClO and subsequent decomposition reactions.

The study of the generation of highly oxidized products, more than GSSG, by HClO is relevant to understand the antioxidant role of glutathione against activated neutrophils. These products, contrary to GSSG, cannot be recycled by glutathione reductase and their oxidation could be irreversible. In this case, GSH should be replaced by new synthesis.

15.4 Myeloperoxidase

Chapters 8 to 14 collect most of the experimental and computational research about myeloperoxidase (MPO), but more studies have been performed, which are summarized below.

15.4.1 Taurine and Pro-Gly-Gly chlorination

The experimental study on MPO-mediated taurine (Tau) chlorination, including the influence of pH and [H_2O_2], has already been published,[18] as well as another similar study performed with the tripeptide Pro-Gly-Gly.[19] However, more experimental results have been obtained, like the effects of temperature and concentrations of substrate and chloride.

According to the rate equations proposed for this process (Chapter 8), the rate is controlled by the formation of chlorinating agents: ClO^- and/or MPO-I-Cl. This step is previous to chlorination and, therefore, initial and equilibrium equation rates are independent of substrate concentration:

$$v_0 = \frac{k_2 \cdot K_1 \cdot [\mathrm{MPO_0}] \cdot [\mathrm{H_2O_2}] \cdot [\mathrm{Cl^-}]}{1 + K_4 \cdot [\mathrm{H^+}] \cdot (1 + K_6 \cdot [\mathrm{Cl^-}])}$$

$$v_{eq} = \frac{k_2 \cdot [\mathrm{MPO_0}] \cdot [\mathrm{Cl^-}]}{\frac{1 + K_4 \cdot [\mathrm{H^+}] \cdot (1 + K_6 \cdot [\mathrm{Cl^-}])}{K_1 \cdot [\mathrm{H_2O_2}]} + 1 + K_5 \cdot [\mathrm{H^+}] + \frac{K_7' \cdot [\mathrm{H_2O_2}]}{[\mathrm{H^+}]}}$$

Thus, kinetic studies performed with different amounts of the chlorination target showed that the rate is not affected by substrate concentration (Figure 15.5). Despite kinetic constants look slightly different (Figure 15.5A), initial rates are statistically equivalent (Figure 15.5B).

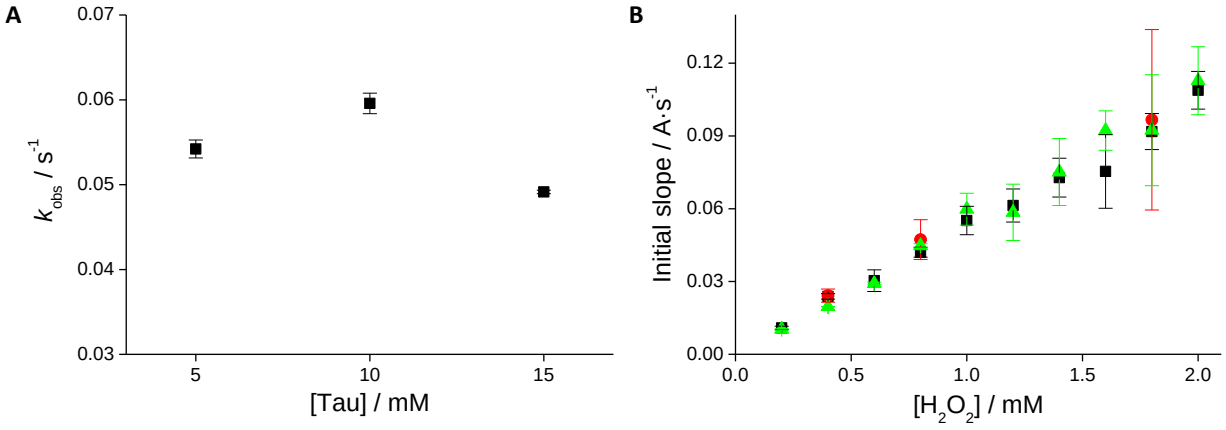

Figure 15.5. (A) Observed kinetic constant (k_{obs}) at T = 298 K for the MPO-mediated chlorination of Tau *vs*. Tau concentration. (B) Initial rate of chlorination of Tau *vs*. [H_2O_2]. [Tau] = 5 (■), 10 (●), and 15 (▲) mM.

Chloride may act as substrate or inhibitor of MPO, as reported in Chapter 14. Therefore, this anion participates in several reactions (Scheme 14.1), although only the processes involving ferric species and compound I are relevant.

The influence of [Cl⁻] on the chlorination rate is more complex than that of [substrate]. According to the initial rate equation, the effect on the observed kinetic constant is:

$$k_{obs} = \frac{v_0}{[H_2O_2]} = \frac{a \cdot [Cl^-]}{1 + b \cdot [Cl^-]}$$

However, results obtained for the MPO-catalyzed chlorination of Pro-Gly-Gly using different concentrations of this substrate (Figure 15.6) show a different trend.

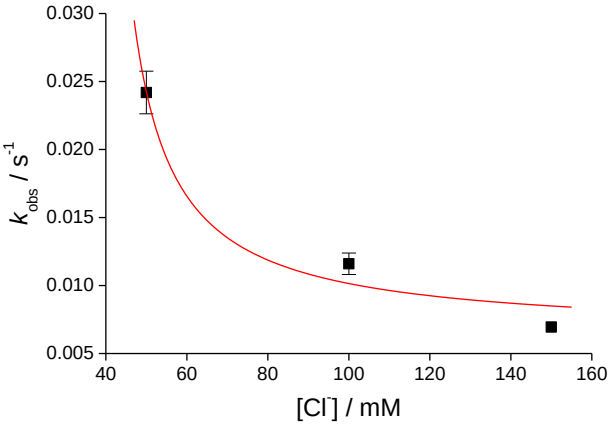

Figure 15.6. Observed kinetic constant (k_{obs}) at T = 298 K for the MPO-mediated chlorination of Pro-Gly-Gly *vs*. chloride concentration. Data fit: $a = -1.74 \times 10^{-4}$, $b = -2.72 \times 10^{-2}$.

Data cannot be adequately fitted with this equation, and the best fit corresponds to negative values for *a* and *b* parameters, which have not any chemical meaning. Besides, the function depicting the effect of [Cl⁻] at equilibrium state is more difficult. Therefore, this aspect needs further analysis to understand the results. Finally, measurements performed at different temperatures have not been yet analyzed.

15.4.2 Redox properties

The source of the particularly high oxidation potential of compound I of MPO, and also the differences in the redox profiles among peroxidases, is still unknown. According to our computational research (Chapter 13), heme curvature and proximal imidazole rotation angle show some effect on redox properties, but they cannot solely explain the differences found in enzymes belonging to peroxidase-cyclooxygenase superfamily with respect to other peroxidases, and in particular the distinct behaviour observed for MPO. The protonation state of this imidazole seems not to be responsible of these oxidative properties either. Besides, the presence of an imidazolate has been discarded on a geometry basis. The electronic effect of covalent linkages between heme and peptide in MPO has been previously analyzed in a computational study.[20] However, it has not been proved that this bonding scheme induces the oxidation properties of the enzyme. In order to shed light on this issue, further computational research is being performed.

Calculations to determine the influence of the position of vinyl and propionate substituents of heme on its thermodynamics are in progress. Propionates are usually situated normal to heme, so they can be located at either distal or proximal side. Some studies have already reported on the effect of this position in heme proteins by examining their structural role, interactions, etc.,[21] but not their impact on energetics. Besides, we have determined that rotation of vinyl groups may notably alter the relative free energy between different oxidation intermediates (Figure 15.7). However, this result should be considered with much caution, as it may be algorithm-dependant: it has only been observed with some Gaussian versions so far.

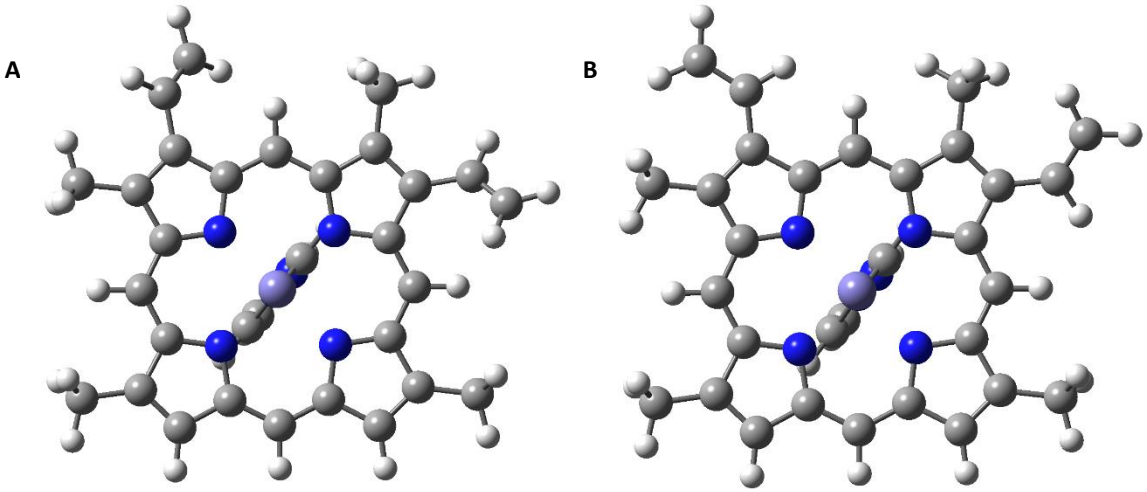

Figure 15.7. Optimized heme at ferric state showing two different rotation angles for vinyl substituents.

The relevance of covalent bonding between prosthetic group and protein is assessed by further calculations including those bonds explicitly in the model. The effect of these links on the structure, charge distribution, and thermodynamics of the intermediates are then evaluated. Several molecular models are being tested, gradually incorporating more protein residues to the full prosthetic group. The model comprising heme and entire residues covalently bonded to heme or coordinated to central iron is represented in Figure 15.8. The structures of protonated compound ll optimized for lactoperoxidase (A) and myeloperoxidase (B) with this model are depicted. It is expected that a comprehensive analysis of covalent bonding together with the other considered structural features may provide an explanation for the different enzymatic activities of peroxidases.

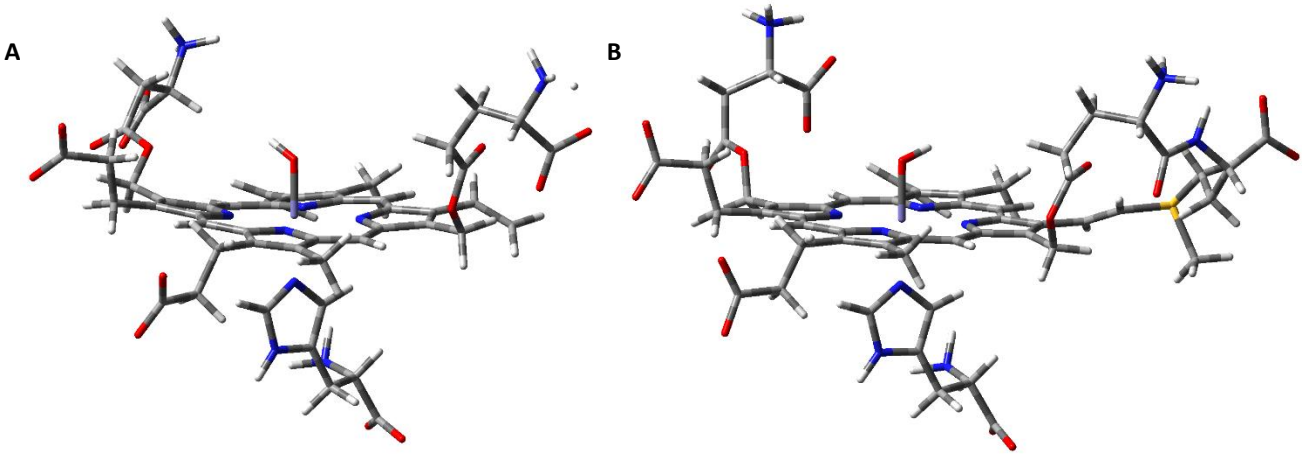

Figure 15.8. Protonated compound II of lactoperoxidase (A) and myeloperoxidase (B) computed with molecular models including all residues directly bound to heme.

15.4.3 Compound III and compound II-hydroperoxyl complex

Structure and properties of MPO intermediates participating in the peroxidase cycle (ferric species, Fe(III)-MPO, and compounds I and II, MPO-I and MPO-II, respectively) have been calculated, as explained in previous chapters. Furthermore, the inactive ferrous species, Fe(II)-MPO, has been also considered, and attention was paid on all halogenated complexes as well. Compound III (MPO-III) is another intermediate of MPO inactive for its chlorination and peroxidation activities.

Besides, it has been also proposed (Chapter 8) that hydroperoxyl radical ($HO_2^{\cdot}$) is not released upon reduction of compound I to compound II by H_2O_2, at least under acidic conditions, and that a compound II-hydroperoxyl complex (MPO-II-HO_2) accumulates. This species does not participate in reactions catalyzed by MPO either. Processes involving those intermediates are depicted in Scheme 15.4.

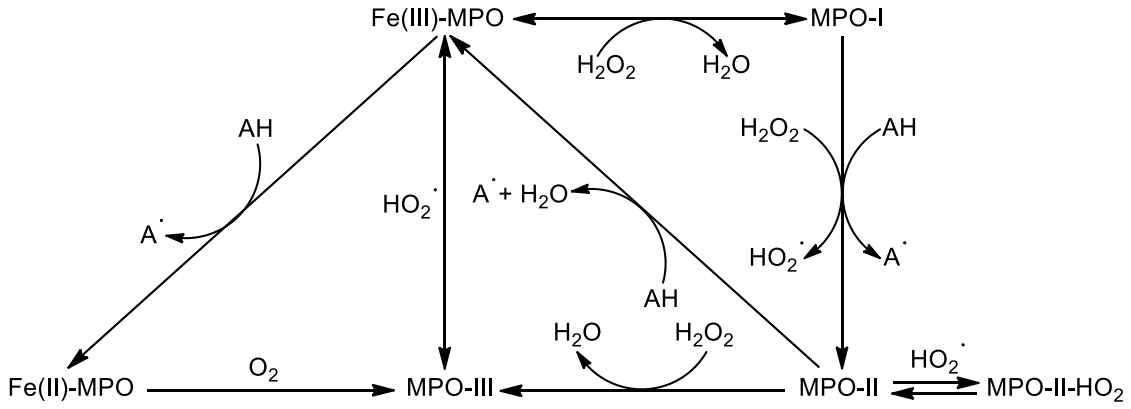

Scheme 15.4. Peroxidase cycle of MPO showing also the reactions leading to compound III and compound II-hydroperoxyl complex.

Contrary to the oxo-ferryl compounds I and II, compound III contains dioxygen linked to a ferrous or ferric centre. It is rapidly produced by reaction of superoxide anion ($O_2^{\cdot-}$) with native Fe(III)-MPO and an extra proton (or $HO_2^{\cdot}$, although its pK_a is 4.8),[22] but it can also be formed by reaction of a large excess of hydrogen peroxide (H_2O_2) with MPO-II,[23] or by addition of molecular oxygen (O_2) to ferrous species.[24] As in the case of ferrous enzyme and compound II, MPO-III also contains an additional proton in the active site compared to native ferric state and compound I, but its precise location is unknown. This hexacoordinate species is a stable complex that decays slowly to ferric enzyme,[25] although it is accelerated at basic media.[24] Central iron in MPO-III has been described as ferric or ferrous, and according to some authors an equilibrium is stablished between both species, although the ferric form is dominant.[26]

In the MPO-mediated chlorination reaction, in order to explain the dramatic deceleration at equilibrium phase, the feasibility of a stable complex between compound II and $HO_2^{\cdot}$ has been considered. Formation of MPO-II-HO_2 is pH sensitive, the process revealed relevant at pH > 5 and it increases to at least pH 6. According to the few kinetic evidences available about this species, its accumulation decreases the rate of chlorination. Thus, it is inactive at least for the halogenation reaction. This inactivation seems reversible, as the chlorination rate increases again when H_2O_2 concentration decreases upon consumption, but no other information is available on this complex. The reaction between H_2O_2 and MPO-I in the distal cavity to yield MPO-II and $HO_2^{\cdot}$, or MPO-II-HO_2, most probably takes place in an axial position. Therefore, the possibility of a MPO-II-HO_2 complex, with either superoxide anion or hydroperoxyl radical bound to the protonated or unprotonated ferryl oxygen of MPO-II, has been analyzed.

Apart from some transient intermediates (as postulated for the mechanism of the reaction of ferric MPO with H_2O_2 to yield compound I), these are the only MPO complexes with more than one oxygen atom bound to the heme metal centre. A complete knowledge on the inactive MPO complexes, *i.e.*, ferrous species (already analyzed in Chapter 12), compound III, and compound II-$HO_2^{\cdot}$ complex, is also quite relevant since they act as efficient MPO inhibitors with the advantage of being fully reversible.

All structural possibilities of these two compounds have been computed, in order to provide an overall view of the systems under study. Unprotonated compound III can be depicted with a dioxygen moiety linked to iron by one oxygen atom and

also with both oxygen atoms interacting with the metal; the protonated form incorporates an extra proton on the terminal or on the central oxygen. These alternatives are represented in Scheme 15.5. Besides, since iron may be present in the ferrous state, protonation on a vinyl substituent was also considered, and all species have been computed at a full range of spin multiplicities (S = 0 to 3).

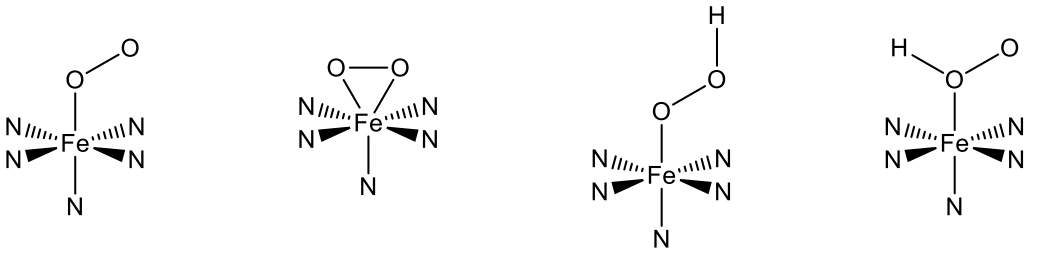

Scheme 15.5. Schematic geometries of the four structures of compound III under study.

Both analyzed complexes of unprotonated compound III, MPO-III$_{(Fe\text{-}O\text{-}O)}$ and MPO-III$_{(Fe<O2)}$, could be correctly optimized, but the former is much more stable. This complex presents a strong Fe–O interaction (bond order = 1.0) at low spin. However, the interaction is weaker (bond order = 0.6) at the much more stable species with intermediate spin (Figure 15.9A). Heme and $O_2^{\bullet -}$ are independent at high spin, which has a Gibbs free energy slightly higher than the intermediate form. Minimized geometries of protonated complexes showed that a proton is preferred on the terminal oxygen (MPO-III-H$_{(Fe\text{-}O\text{-}OH)}$). Again, a bond order = 1.0 is obtained at low spin but the species with intermediate spin is more stable and presents a weaker Fe–O interaction (bond order = 0.8, Figure 15.9B). However, in this case the unconnected high spin structure is slightly preferred.

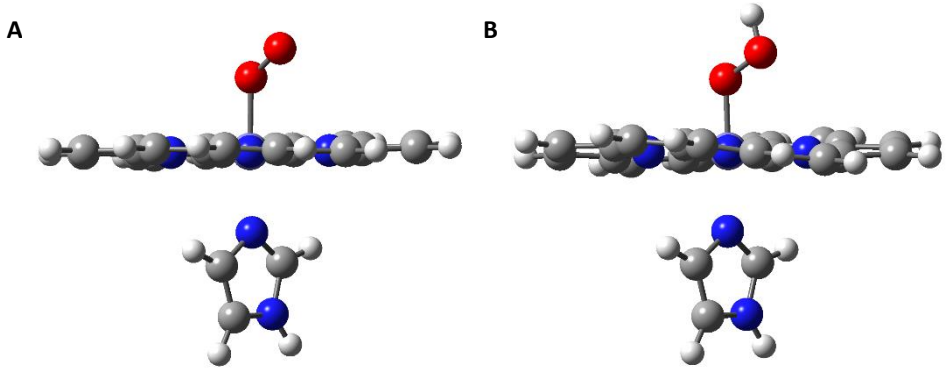

Figure 15.9. Optimized geometries obtained for the most stable compound III species. (A) MPO-III$_{(Fe\text{-}O\text{-}O)}$ with S = 1 and (B) MPO-III-H$_{(Fe\text{-}O\text{-}OH}$ with S = 1.

Incorporation of a vinyl substituent in the molecular model has an important effect on spin multiplicity of compound III. Thus, in all cases intermediate spin is preferred, and the proton reveals more stable on the terminal oxygen than on the vinyl group, which points to a more ferric character of the iron atom.

Potential structures of MPO-II-HO$_2$ have been calculated as adducts of compound II with superoxide anion or hydroperoxyl radical bound to ferryl oxygen. All possibilities of interaction between protonated and unprotonated forms of both the radical and the enzymatic species have been studied in a similar way as with compound III, even if they do not make much sense from a chemical point of view (Scheme 15.6).

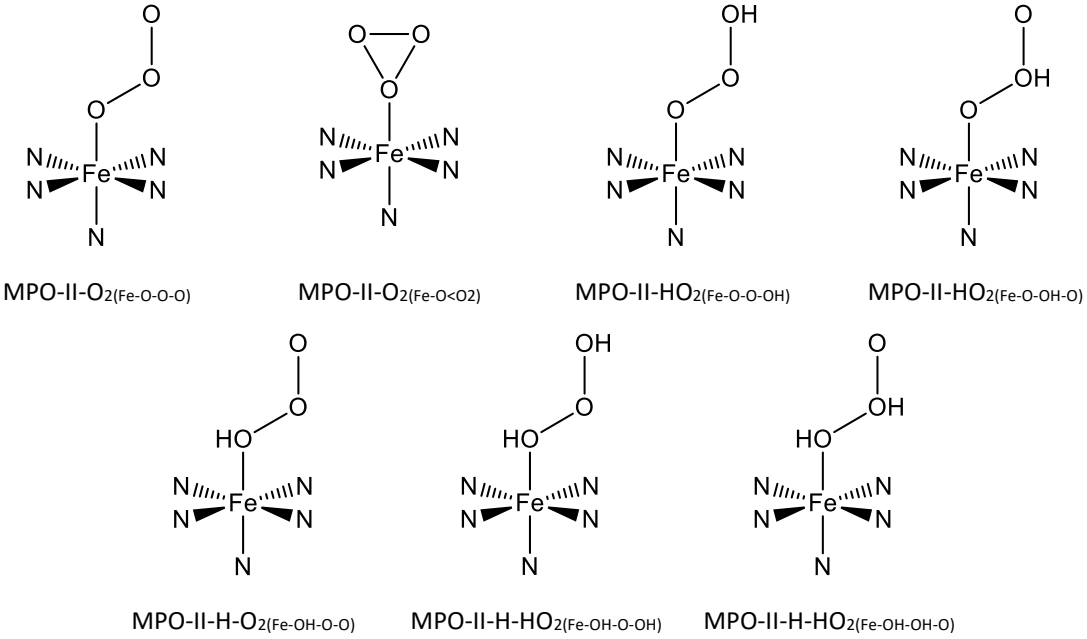

Scheme 15.6. Schematic geometries of the seven structures of compound II-$HO_2^{\bullet}$ complex under study.

The unprotonated form of the compound II-$HO_2^{\bullet}$ complex has been only optimized as MPO-II-$O_{2(Fe\text{-}O\text{-}O\text{-}O)}$, whereas the other structure could not be geometry-minimized. Still, this complex is unstable as it presents a much higher Gibbs free energy than separate unprotonated MPO-II and $O_2^{\bullet -}$. A favourable species with $HO_2^{\bullet}$ could be obtained provided that it is protonated on the terminal oxygen, while MPO-II-$HO_{2(Fe\text{-}O\text{-}O\text{-}OH)}$ is not feasible. Geometry optimization of MPO-II-H-$O_{2(Fe\text{-}OH\text{-}O\text{-}O)}$ did not yield any viable structure. Finally, a stable diprotonated complex has been only obtained with protons on ferryl and terminal oxygen atoms. The most relevant calculated structures are shown in Figure 15.10.

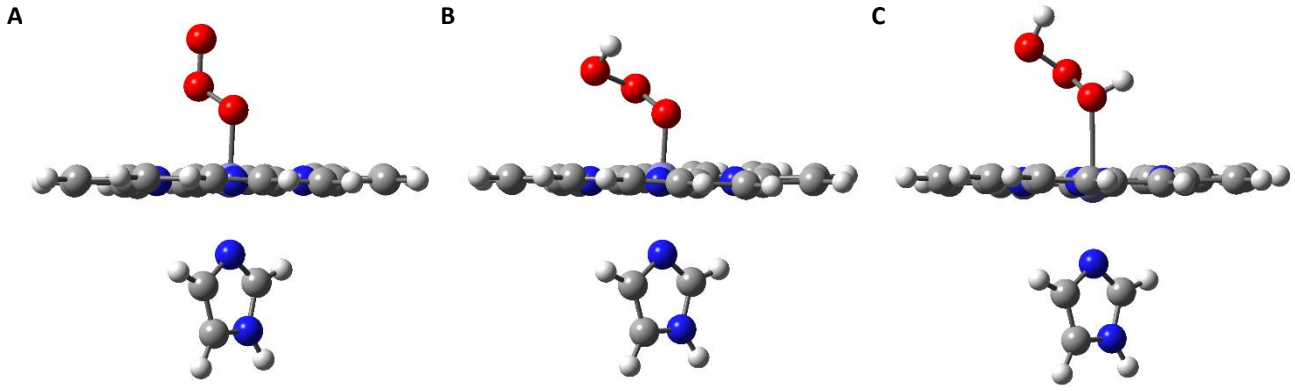

Figure 15.10. Optimized geometries obtained for the most stable compound II-$HO_2^{\bullet}$ complexes. (A) MPO-II-$O_{2(Fe\text{-}O\text{-}O\text{-}O)}$ with S = 1/2, (B) MPO-II-$HO_{2(Fe\text{-}O\text{-}O\text{-}OH)}$ with S = 1/2, and (C) MPO-II-H-$HO_{2(Fe\text{-}OH\text{-}O\text{-}OH)}$ with S = 3/2.

According to these results, compound III is feasible with or without a proton on dioxygen. However, it is well known that this species has an extra proton compared to ferric native enzyme, so this proton could be either on the terminal oxygen or at one of the vinyl substituents. The fact that this compound decays faster to ferric species at basic media suggests that it fragments preferentially when unprotonated, with $O_2^{\bullet -}$ departing from the active site.

On the other hand, compound II-$HO_2^{\cdot}$ complex only presents stable structures when the terminal oxygen is protonated. When this proton is lost, the species with MPO-II-H could not be optimized, and the geometry obtained for unprotonated MPO-II is thermodynamically unfavourable. This means that, again, the complex fragments upon deprotonation of the terminal O atom, releasing $O_2^{\cdot -}$ to the outer medium. Therefore, the reduction of compound I to produce compound II could be better depicted as:

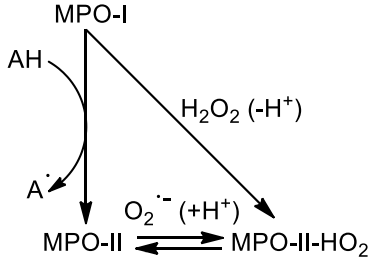

Scheme 15.7. Proposed pathways for the reduction reaction of compound I to compound II of MPO.

Therefore, the reaction with H_2O_2 takes place via formation of MPO-II-HO_2, which inactivates the enzyme at acid pH, but decomposes rapidly to MPO-II, yielding superoxide, at more alkaline conditions. This process does not occur when MPO-I oxidizes other substrates rather than H_2O_2. This complex explains that MPO-mediated chlorination rate is maximum at pH about 5,[18] while it catalyzes peroxidation preferentially around neutral pH.[27, 28]

15.4.4 Myeloperoxidase protection against oxidative damage

MPO catalyzes the production of strong oxidizing agents. It primarily catalyzes the oxidation of chloride anion to the oxidizing and chlorinating agent hypochlorous acid, but it also produces other reactive oxygen species.[29] This feature makes it especially vulnerable to self-damage through out-of-control oxidative processes. Nevertheless, the enzyme still exerts its catalytic function under aggressive chemical conditions with no apparent inactivation. Therefore, there must be a protection system that prevents active-site damage via regulation of enzyme turnover and product release.

The active site of MPO is hidden deep inside the protein, connected to the outer medium through a narrow substrate channel (Figure 15.11). This architecture contributes to selectivity and it seems to permit easy access (and exit) only to anions and neutral molecules of limited size, probably due to negative charge stabilization from the protein environment. The only cation full involved in MPO reactivity is the proton, which could enter via either a Grotthuss mechanism through the hydrogen bond network of water molecules placed in the substrate channel and distal cavity, or a proton relay mechanism through protein ionizable groups.

These distribution and negative charge stabilization may also have a protective purpose. Some implications consistent with this view are described below.

MPO was reacted with solvated electrons, the strongest reducing agent in water, with a reduction potential of –2.9 V, and extremely reactive. This was studied by pulse radiolysis: water was irradiated to form hydroxyl radical and electrons, radicals are removed with a scavenger, and solvated electrons react with MPO.

One-electron reduction of MPO intermediates was not observed in any case. Electrons rather react with several different functional groups, according to relaxation kinetics constants and absorption spectra measured after irradiation. Thus, the damage caused to MPO structure and activity was monitored following the decrease in the chlorination rate of the amino acid glycine (Gly).

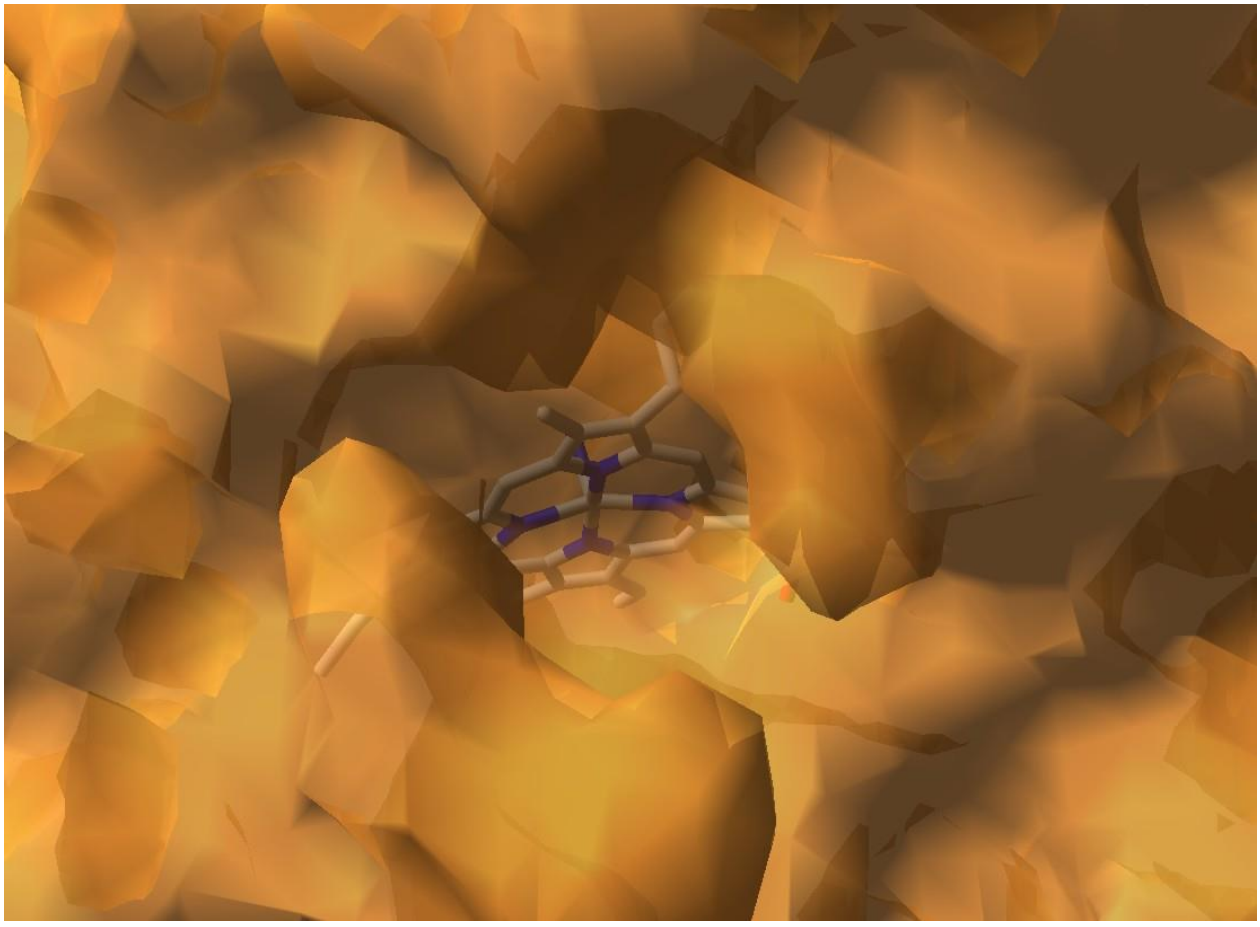

Figure 15.11. View through the substrate channel of the active centre of MPO deeply buried inside the protein.

The activity of MPO decreases upon irradiation (Figure 15.12). However, the enzyme is still able to chlorinate after a very high dose. These results indicate that electrons do not enter the enzyme but react on the surface, with the protein playing the role of a scavenger. Although this experiment is performed under reducing conditions, it still suggests that the peptide surrounding the active site may have a protective function against oxidative damage.

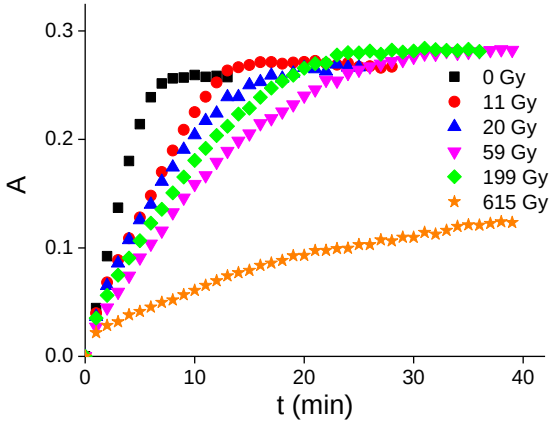

Figure 15.12. Kinetic traces obtained for the MPO-mediated chlorination of Gly after an increasing irradiation dose.

A reaction mechanism derived from experimental studies on the MPO-catalyzed chlorination of Tau and Pro-Gly-Gly has been proposed. According to the observed pH influence, protons are not involved in the step leading to formation of the chlorinating agent, so it is initially produced unprotonated:

$$\text{MPO-I} + \text{Cl}^- \xrightarrow{k_2} \text{MPO} + \text{ClO}^- \quad \text{or} \quad \text{MPO-I} + \text{Cl}^- \xrightarrow{k_{2b}} \text{MPO-I-Cl}$$

It has been proposed that both an enzymatic complex (MPO-I-Cl) or a free chlorinating agent (ClO^-) can be formed. HClO pK_a is 7.54, so this form is predominant at the acidic medium where chlorination occurs. On the hypothesis that the inner part of MPO stabilizes negative charges, it would be expected that hypochlorite anion would not be protonated before reaching the medium out of the protein.

This fact is quite important since this species presents quite different reduction potentials depending on its protonation state:

$E°$ (HClO, Cl^-) = 1.495 V

$E°$ (ClO^-, Cl^-) = 0.885 V

In consequence, HClO is a stronger oxidant than ClO^- and, in addition, it reacts faster with amino acids. These compounds can be chlorinated on N or S atoms, preferentially with the protonated agent and faster on the latter position (Table 15.2).

Table 15.2. Second-order rate constants at T = 298 K for the chlorination of S-containing amino acids by HClO and ClO^-. Values taken from [30].

k ($M^{-1}·s^{-1}$)	Cys	Met
HClO	1.2×10^9	8.7×10^8
ClO^-	1.9×10^5	0

Therefore, the presence of HClO inside the enzyme means a potential danger, while ClO^- is much safer for its integrity. This outcome is consistent with the peptide acting as a protective shield against oxidative damage at the active site.

A similar case is observed for the hydroperoxyl radical / superoxide anion pair. $HO_2^·$ presents a pK_a = 4.8 and, therefore, the presence of the protonated radical is negligible at the typical peroxidation neutral pH. However, at chlorination optimal conditions both hydroperoxyl radical and superoxide anion are relevant. Again they have very different oxidation properties:

$E°$ ($HO_2^·$, H^+/H_2O_2) = 1.46 V

$E°$ ($O_2^{·-}$, $2H^+/H_2O_2$) = 0.91 V

This results in much higher oxidation rates for the protonated species and, once more, kinetics of their reactions with S-compounds are more favourable than with amines. Therefore, Cys and Met residues represent the natural oxidation targets inside the protein (Table 15.3).

Table 15.3. Second-order rate constants at T = 298 K for the oxidation of S-containing amino acids by $HO_2^·$ and $O_2^{·-}$. Values taken from [31].

k ($M^{-1}·s^{-1}$)	Cys	Met
$HO_2^·$	< 600	< 49
$O_2^{·-}$	< 15	< 0.33

Superoxide anion must be released from the decomposition of MPO-II-HO_2 and MPO-III to yield MPO-II and Fe(III)-MPO,

respectively, and it must be present exclusively in the anionic form to avoid inactivation of the enzyme due to oxidative damage. Thus, surrounding protein must stabilize superoxide preferentially in the distal cavity and the substrate channel with respect to the conjugated acid. Moreover, it seems that MPO-II-HO_2 complex is stable under chlorination conditions, and the radical is only delivered upon deprotonation above pH = 6.

Furthermore, superoxide anion can react with different MPO intermediates (Fe(III)-MPO, MPO-I, MPO-II, and MPO-III) to yield enzymatic complexes at different oxidation states (MPO-III, MPO-II, Fe(III)-MPO, and MPO-I, respectively).[32] In several of these processes the radical is oxidized, which is easier in the unprotonated form. Besides, the reaction of superoxide anion with iron (either ferric or ferrous) is faster than that of hydroperoxyl radical,[33] so these processes would occur more readily with $O_2^{\bullet-}$.

In conclusion, a pulse radiolysis study indicated that the active site of MPO is effectively protected by surrounding protein moiety with only a narrow channel allowing access to heme. Experimental analysis of the MPO-catalyzed chlorination reaction showed that it takes place via formation of unprotonated hypochlorite anion, and both experimental and computational studies supported the possibility of a complex between protonated hydroperoxyl radical and compound II, which only releases superoxide anion upon deprotonation. Inner stabilization of negative charges rules out the presence in the heme pocket and substrate channel of the protonated counterparts, which are only formed outside the enzyme. Thus, MPO inactivation is prevented, since HClO and $HO_2^{\bullet}$ are much more reactive with the protein. Therefore, the structure of the substrate channel and of the protein around the active centre constitutes a very effective protective shield against oxidative damage from both external potential harmful species and oxidizing agents produced by the enzyme.

15.4.5 Myeloperoxidase inhibitors

MPO is a cornerstone of human innate immune system. This heme enzyme is the most abundant protein in neutrophils and is released during the oxidative burst. It primarily catalyzes the oxidation of chloride anion to the oxidizing and chlorinating agent hypochlorous acid, but also produces other reactive oxidative species. Furthermore, it participates in several types of cancer, neurodegenerative diseases, arthritis, and, in general, all disorders involving inflammation.[34] Therefore, it is important to discover new therapeutic strategies to prevent oxidative damage produced by MPO-derived ROS.[35, 36] A detailed knowledge on reaction mechanism, structure of redox intermediates, and thermodynamics is essential to understand the enzymatic activity and to develop more efficient inhibitors.

There are numerous studies on possible inhibitors of MPO, which have been found through trial and error. The use of rational drug design could lead to faster development of improved inhibitors that permit a better modulation of MPO catalytic activity. In this sense, understanding the way these already identified compounds inhibit the enzymatic function is of critical relevance. It seems that the most usual mode of action consists in establishing in the heme pocket, where the inhibitor can interact with iron, porphyrin ring, and other distal residues, sterically hindering the access for other substrates. A more detailed inhibition mechanism was first proposed in a study of 2-thioxanthines, where the inhibitor reacts with compound I and the so-formed radical binds covalently a methyl substituent of heme.[37] However, inhibition of these compounds is irreversible and not very effective.

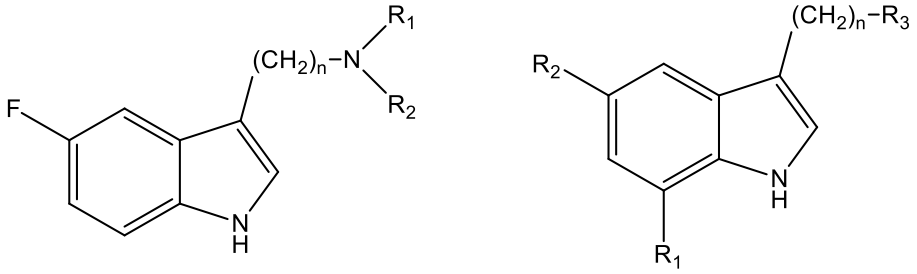

1 **2**

Scheme 15.8. General structure of (**1**) 3-aminoalkyl,5-fluoroindole and (**2**) 3-alkylindole derivatives.

The earliest systematic research into this field is the study of the 3-aminoalkyl,5-fluoroindole series (Scheme 15.8).[38] These compounds present reversible inhibition with IC_{50} (the concentration of inhibitor required to inhibit a catalyzed reaction by 50 %) values as low as 0.005 µM for low-density lipoproteins (LDL) oxidation. The inhibition process has been investigated by molecular docking, supporting interactions between fluorine and iron atoms, and between indole and pyrrole rings. However, obtained binding energies were not consistent with corresponding IC_{50} values.

A later study on the inhibitory effect of other very efficient similar compounds, the derivatives of 3-alkylindole (Scheme 15.8), could determine some relationship between this efficiency and their substituents.[39] But, again, IC_{50} values cannot be directly related to free energies of binding.

A qualitative, or even quantitative, relationship between structure and inhibitory effect is necessary to predict the ability of other compounds to inhibit MPO and to guide the development of new inhibitors. This has been computationally done by characterizing the structure and properties of the compounds shown above, and evaluating their interaction with the active site of MPO. Only some of the inhibitors from these references have been studied so far.

Thus, structures of several inhibitors have been energy minimized and different properties were tested, searching a pattern that could explain their efficiency. Some dependence between Mulliken charge on F atom and IC_{50} has been found. IC_{50} parameter is related to enzyme-inhibitor interaction through Cheng-Prusoff equation:[40]

$$K_{\mathrm{i}} = \frac{\mathrm{IC}_{50}}{1 + \frac{[\mathrm{S}]}{K_{\mathrm{m}}}}$$

where [S] is the substrate concentration used in the assay, K_m is Michaelis constant, and K_i is the dissociation constant of the enzyme-inhibitor complex. The latter is connected to Gibbs free energy of formation of this complex:

$$\Delta G = \mathrm{RT} \ln K_i$$

Thus, assuming that the charge on F is proportional to the interaction between inhibitor and MPO, an exponential relationship between Mulliken charge on this atom and IC_{50} would be expected (Figure 15.13).

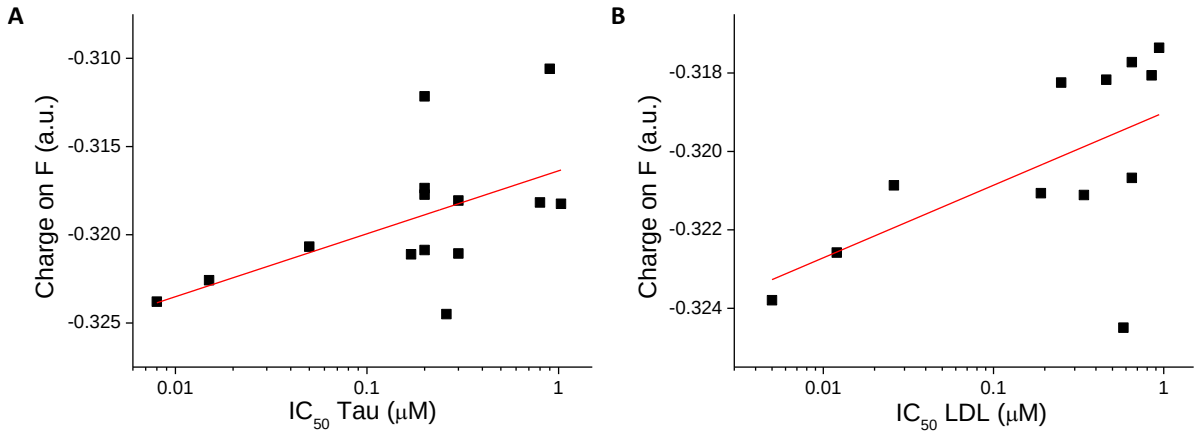

Figure 15.13. Scatter plots of calculated Mulliken charge on fluorine atom *vs*. experimental IC_{50} values obtained for Tau chlorination (A) and LDL oxidation (B) with some 3-aminoalkyl,5-fluoroindole derivatives.

It seems evident from these correlations that charge on F atom exerts a relevant influence on the inhibitory effect, but other parameters may also be important as well. Therefore, not only interaction forces but other structural features should be considered. Thus, for instance, it has been observed that the position of fluorine shows a remarkable effect (Figure 15.14).

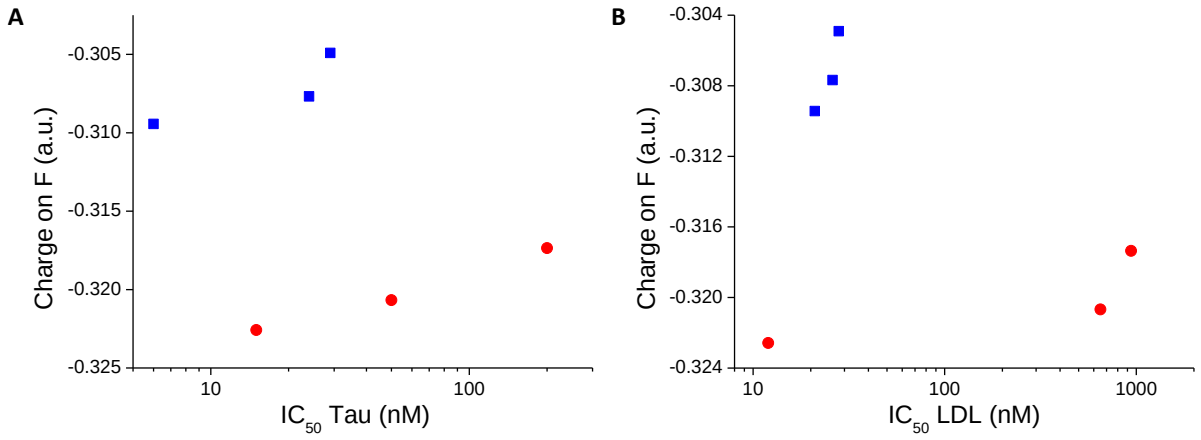

Figure 15.14. Scatter plots of calculated Mulliken charge on fluorine atom *vs*. experimental IC_{50} values obtained for (A) Tau chlorination and (B) LDL oxidation with two series of inhibitors only differing in fluorine position, either (●) 5-fluoroindoles or (■) 7-fluoroindoles.

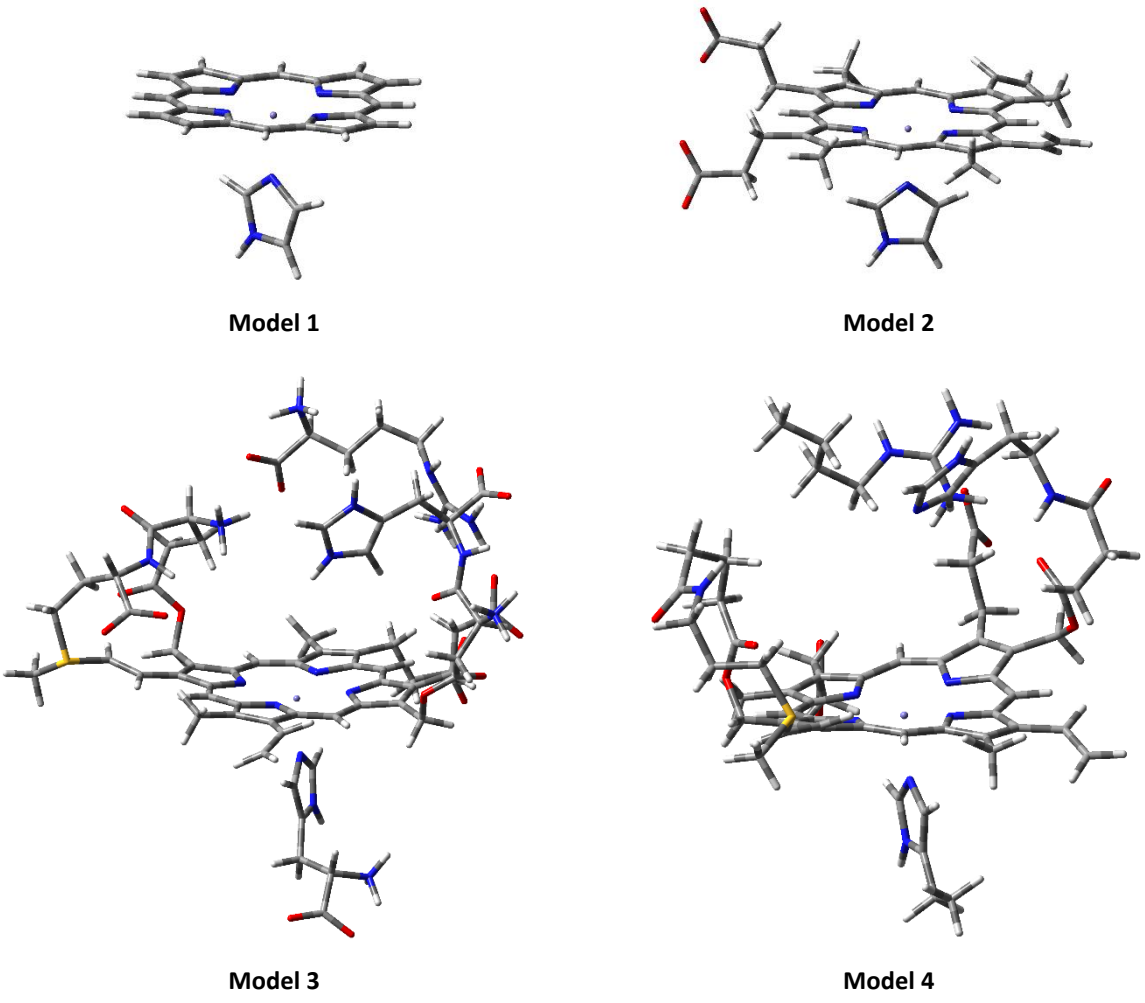

Figure 15.15. Ferric native state optimized with the four molecular models employed to simulate the active site of MPO.

With the aim of acquiring a full understanding of inhibition mechanisms, the calculation of independent inhibitors must be completed with a computational study of the corresponding enzyme-inhibitor complexes. This has been performed employing several molecular models of the active site of MPO (Figure 15.15). Model 1 has been extensively employed in this thesis, whereas model 2 incorporates all heme substituents. These two models may be adequate for an initial approach, analyzing the interaction with the prosthetic group, but they are insufficient for the determination of the interaction between inhibitor and protein. Thus, model 3 simulates full active centre including complete proximal histidine (His336), the residues covalently bound to heme (Asp94, Glu242, and Met243), distal histidine (His95), and the arginine that delimits the entrance to heme pocket from the substrate channel (Arg239). Finally, terminal protonated amines and carboxylates are exchanged for hydrogens in model 4 to avoid additional charges in the system.

Optimization of the enzyme-inhibitor complex with models 1 and 2 yields structures with the inhibitor placed either normal to heme or more parallel to the porphyrin ring but at a too long distance (Figure 15.16). These arrangements are not possible inside MPO due to steric hindrance within the distal cavity, so both models revealed deficient in this respect. On the contrary, residues incorporated in models 3 and 4 restrict the movement of the inhibitors. However, calculations with these models yielded unexpected preliminary results, as the compounds were always optimized too far from iron for interacting with either metal or porphine.

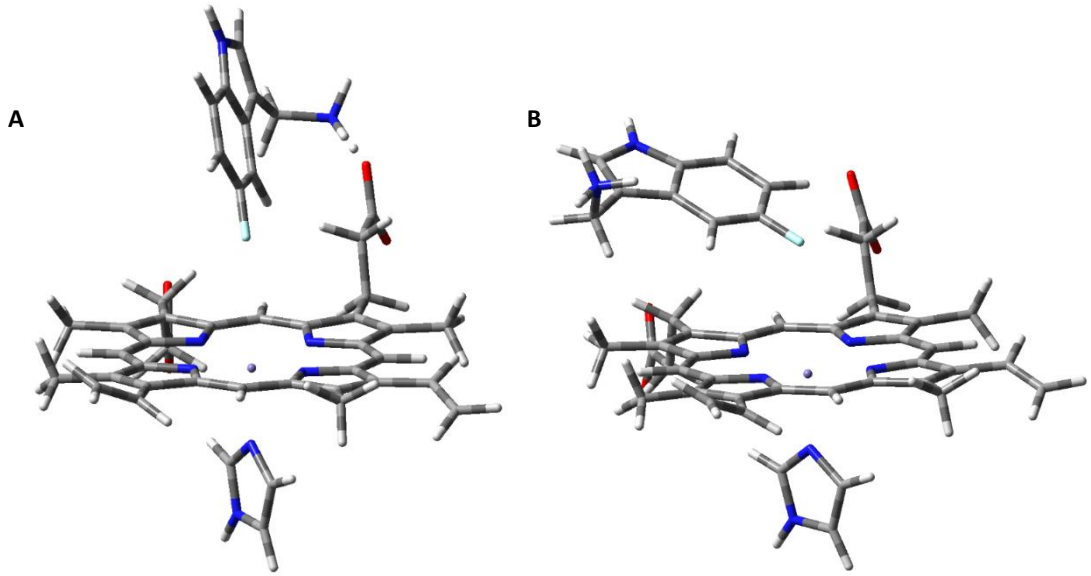

Figure 15.16. Enzyme-inhibitor complex calculated with model 2 for the interaction of 3-aminomethyl,5-fluoroindole with MPO. Geometries of minimum potential energy optimized for the inhibitor (A) perpendicular and (B) parallel to heme, which correspond to global and local minima, respectively.

Further studies are still necessary for a complete understanding of the inhibition mechanism of these compounds and, as a result, for being able to design, just computationally, new substances with enhanced inhibitory activity.

15.5 References

1. E. Cancès and G. Dusson, *Discretization error cancellation in electronic structure calculation: toward a quantitative study.* ESAIM-Math. Model Num., 2017 **51** (5) 1617-1636.

2. J. Andrés, X. L. Armesto, M. Canle L., M. V. García, D. R. Ramos, and J. A. Santaballa, *Understanding the mechanism of base-assisted decomposition of (N-halo),N-alkylalcoholamines.* Org. Biomol. Chem., 2003 **1** (23) 4323-4328.

3. D. R. Ramos, R. Castillo, M. Canle L., M. V. García, J. Andrés, and J. A. Santaballa, *Density functional study of the Hoffmann elimination of (N-Cl),N-methylethanolamine in gas phase and in aqueous solution.* Chem. Phys. Lett., 2006 **429** (4-6) 425-429.
4. D. R. Ramos, R. Castillo, M. Canle L., M. V. García, J. Andrés, and J. A. Santaballa, *A theoretical study on the mechanism of the base-promoted decomposition of N-chloro,N-methylethanolamine.* Org. Biomol. Chem., 2009 **7** (9) 1807-1814.
5. M. Canle L., D. R. Ramos, and J. A. Santaballa, *DFT study on the microscopic ionization of cysteine in water.* Chem. Phys. Lett., 2006 **417** (1-3) 28-33.
6. D. M. Chipman, *Computation of pK_a from dielectric continuum theory.* J. Phys. Chem. A, 2002 **106** (32) 7413-7422.
7. A. J. Ellis and F. G. Soper, *Studies of N-halogeno-compounds. Part VI. The kinetics of chlorination of tertiary amines.* J. Chem. Soc., 1954 (0) 1750-1755.
8. W. A. Prütz, *Reactions of hypochlorous acid with biological substrates are activated catalytically by tertiary amines.* Arch. Biochem. Biophys., 1998 **357** (2) 265-273.
9. K. Huang and A. D. Shah, *Role of tertiary amines in enhancing trihalomethane and haloacetic acid formation during chlorination of aromatic compounds and a natural organic matter extract.* Environ. Sci.: Water Res. Technol., 2018 **4** (5) 663-679.
10. G. A. Reynolds and J. A. VanAllan, *Pyranylidene iminium salts. I. Iminium salts derived from alkyl-substituted pyrylium salts and their hydrolysis products.* J. Org. Chem., 1969 **34** (9) 2736-2741.
11. C. Hansch and A. Leo, *Substituent constants for correlation analysis in chemistry and biology*. 1979, New York: John Wiley & Sons, Inc.
12. A. E. Martell and R. M. Smith, *Critical stability constants. Second supplement*. Critical stability constants. 1989, New York: Springer.
13. R. Stewart, *The proton: Applications to organic chemistry*. 1985, Orlando: Academic Press, Inc.
14. D. A. Dickinson and H. J. Forman, *Cellular glutathione and thiols metabolism.* Biochem. Pharmacol., 2002 **64** (5-6) 1019-1026.
15. M. I. Fernández, M. V. García, X. L. Armesto, M. Canle L., and J. A. Santaballa, *Unravelling the mechanism of intracellular oxidation of thiols by (N-Cl)-Taurine.* J. Phys. Org. Chem., 2013 **26** (12) 1098-1104.
16. C. C. Winterbourn and S. O. Brennan, *Characterization of the oxidation products of the reaction between reduced glutathione and hypochlorous acid.* Biochem. J., 1997 **326** (1) 87-92.
17. K. Das and A. Roychoudhury *Reactive oxygen species (ROS) and response of antioxidants as ROS-scavengers during environmental stress in plants*. Front. Environ. Sci., 2014 **2**.
18. D. R. Ramos, M. V. García, M. Canle L., J. A. Santaballa, P. G. Furtmüller, and C. Obinger, *Myeloperoxidase-catalyzed taurine chlorination: Initial versus equilibrium rate.* Arch. Biochem. Biophys., 2007 **466** (2) 221-233.
19. D. R. Ramos, M. V. García, M. Canle L., J. A. Santaballa, P. G. Furtmüller, and C. Obinger, *Myeloperoxidase-catalyzed chlorination: The quest for the active species.* J. Inorg. Biochem., 2008 **102** (5-6) 1300-1311.
20. A. Devarajan, A. V. Gaenko, and U. Ryde, *Effect of covalent links on the structure, spectra, and redox properties of myeloperoxidase - A density functional study.* J. Inorg. Biochem., 2008 **102** (8) 1549-1557.
21. T. Hayashi, T. Matsuo, Y. Hitomi, K. Okawa, A. Suzuki, Y. Shiro, T. Iizuka, Y. Hisaeda, and H. Ogoshi, *Contribution of heme-propionate side chains to structure and function of myoglobin: chemical approach by artificially created prosthetic groups.* J. Inorg. Biochem., 2002 **91** (1) 94-100.
22. R. A. Cuperus, A. O. Muijsers, and R. Wever, *The superoxide dismutase activity of myeloperoxidase; formation of*

Compound III. Biochim. Biophys. Acta, 1986 **871** (1) 78-84.

23. E. Lee, Y. Miki, H. Katsura, and K. Kariya, *Mechanism of inactivation of myeloperoxidase by propylthiouracil.* Biochem. Pharmacol., 1990 **39** (9) 1467-1471.

24. H. M. Abu-Soud, F. M. Raushel, and S. L. Hazen, *A novel multistep mechanism for oxygen binding to ferrous hemoproteins: Rapid kinetic analysis of ferrous-dioxy myeloperoxidase (compound III) formation.* Biochemistry, 2004 **43** (36) 11589-11595.

25. L. A. Marquez and H. B. Dunford, *Reaction of compound III of myeloperoxidase with ascorbic acid.* J. Biol. Chem., 1990 **265** (11) 6074-6078.

26. H. B. Dunford, *Heme peroxidases*. 1999, New York: John Wiley & Sons, Inc.

27. I. I. Vlasova, J. Arnhold, A. N. Osipov, and O. M. Panasenko, *pH-dependent regulation of myeloperoxidase activity.* Biochemistry-Moscow, 2006 **71** (6) 667-677.

28. H. Spalteholtz, O. M. Panasenko, and J. Arnhold, *Formation of reactive halide species by myeloperoxidase and eosinophil peroxidase.* Arch. Biochem. Biophys., 2006 **445** (2) 225-234.

29. S. J. Klebanoff, *Myeloperoxidase: friend and foe.* J. Leukoc. Biol., 2005 **77** (5) 598-625.

30. X. L. Armesto, M. Canle L., M. I. Fernández, M. V. García, and J. A. Santaballa, *First steps in the oxidation of sulfur-containing amino acids by hypohalogenation: Very fast generation of intermediate sulfenyl halides and halosulfonium cations.* Tetrahedron, 2000 **56** (8) 1103-1109.

31. B. H. J. Bielski, D. E. Cabelli, R. L. Arudi, and A. B. Ross, *Reactivity of HO_2/O_2^- radicals in aqueous solution.* J. Phys. Chem. Ref. Data, 1985 **14** (4) 1041-1100.

32. C. C. Winterbourn and A. J. Kettle, *Reactions of superoxide with myeloperoxidase and its products.* Jpn. J. Infect. Dis., 2004 **57** (5) S31-S33.

33. J. D. Rush and B. H. J. Bielski, *Pulse radiolytic studies of the reactions of HO_2/O_2^- with Fe(II)/Fe(III) ions. The reactivity of HO_2/O_2^- with ferric ions and its implication on the occurrence of the Haber-Weiss reaction.* J. Phys. Chem., 1985 **89** (23) 5062-5066.

34. A. Hoy, B. Leininger-Muller, D. Kutter, G. Siest, and S. Visvikis, *Growing significance of myeloperoxidase in non-infectious diseases.* Clin. Chem. Lab. Med., 2002 **40** (1) 2-8.

35. E. Malle, P. G. Furtmüller, W. Sattler, and C. Obinger, *Myeloperoxidase: a target for new drug development?* Br. J. Pharmacol., 2007 **152** (6) 838-854.

36. M. J. Davies, C. L. Hawkins, D. I. Pattison, and M. D. Rees, *Mammalian heme peroxidases: from molecular mechanisms to health implications.* Antioxid. Redox. Signal., 2008 **10** (7) 1199-1234.

37. A. K. Tidén, T. Sjögren, M. Svensson, A. Bernlind, R. Senthilmohan, F. Auchère, H. Norman, P. O. Markgren, S. Gustavsson, S. Schmidt, S. Lundquist, L. V. Forbes, N. J. Magon, L. N. Paton, G. N. Jameson, H. Eriksson, and A. J. Kettle, *2-Thioxanthines are mechanism-based inactivators of myeloperoxidase that block oxidative stress during inflammation.* J. Biol. Chem., 2011 **286** (43) 37578-37589.

38. J. Soubhye, M. Prévost, P. Van Antwerpen, K. Z. Boudjeltia, A. Rousseau, P. G. Furtmüller, C. Obinger, M. Vanhaeverbeek, J. Ducobu, J. Néve, M. Gelbcke, and F. O. Dufrasne, *Structure-based design, synthesis, and pharmacological evaluation of 3-(aminoalkyl)-5-fluoroindoles as myeloperoxidase inhibitors.* J. Med. Chem., 2010 **53** (24) 8747-8759.

39. J. Soubhye, I. Aldib, B. Elfving, M. Gelbcke, P. G. Furtmüller, M. Podrecca, R. Conotte, J. M. Colet, A. Rousseau, F. Reye, A. Sarakbi, M. Vanhaeverbeek, J. M. Kauffmann, C. Obinger, J. Nève, M. Prévost, K. Z. Boudjeltia, F. Dufrasne, and P. Van Antwerpen, *Design, synthesis, and structure-activity relationship studies of novel 3-alkylindole derivatives as selective and highly potent myeloperoxidase inhibitors.* J. Med. Chem., 2013 **56** (10) 3943-3958.

40. Y. C. Cheng and W. H. Prusoff, *Relationship between the inhibition constant (K_I) and the concentration of inhibitor which causes 50 per cent inhibition (I_{50}) of an enzymatic reaction.* Biochem. Pharmacol., 1973 **22** (23) 3099-3108.

CONCLUSIONS

Were I to await perfection,

my book would never be finished.

Tai T'ung,
in History of Chinese Writing (13th century)

Conclusions of every chapter were presented in the corresponding sections. Nevertheless, main general outcomes obtained in this dissertation are summarized below:

- The presence of the alcohol group in secondary *N*-halo ethanolamines increases the rate of base-assisted decomposition relative to corresponding parent *N*-halo ethylamines. This enhancement is due to the involvement of two extra pathways, apart from the usual intermolecular eliminations, Hofmann or Zaitsev: intramolecular elimination and bimolecular fragmentation. All initial elementary steps are rate limiting and take place through asynchronous concerted processes, where proton transfer to the base is ahead of the rest of the molecular events. Chloride anion is always released as leaving group, losing any chlorination activity.

- Calculations on imines hydrolysis reveal that the reaction proceeds via a stepwise mechanism, as experimentally observed. The attack of a water molecule (asynchronous concerted addition of H^+ and HO^-) on the N=C double bond takes place in the first step, which is rate limiting. Subsequently, the so-formed hemiaminal collapses, leading to the parent amine (or ammonia) and carbonyl compound. In both steps proton-transfer to the nitrogen atom is well ahead of the rest of bond forming/breaking processes.

- According to the computational study, decomposition of *N*-(2-hydroxyethyl) imines, or ethanolimines, takes places via two concurrent pathways: hydrolysis and intramolecular fragmentation reactions. Hydrolysis is equivalent to the process without the alcohol group, while intramolecular fragmentation may also proceed in the absence of water via a stable six-membered cyclic transition structure. This rearrangement leads to formaldehyde and another imine, which then hydrolyses.

- The most favourable decomposition pathway in the reaction between HO^- and *N*-Cl,*N*-methylethanolamine is a base-assisted intramolecular elimination, which takes place via an unstrained six-membered cyclic transition structure. Generated *N*-ethanolmethanimine undergoes two concurrent reactions, hydrolysis (33 %) and intramolecular fragmentation (67 %); and the imine produced in the latter also suffers hydrolysis, yielding the same products expected from the bimolecular fragmentation pathway. This result is common in base-mediated decomposition of secondary *N*-halo ethanolamines, but with different ratios of the competitive processes, which also explain the observed discrepancies between empirical and computational studies.

- The computational study on the acidities of cysteine in aqueous solution deals with the pK_a calculation of two anions, one of them a dianion, and two zwitterions, one of them incorporating three different charged groups; therefore, this is a quite challenging system to obtain adequate thermodynamics. Thus, computational results do not allow discriminating conclusively the correct deprotonation sequence. However, quantitative structure-activity relationships employing experimental pK_a values point to a more acidic amino group.

- The role of solvent water in all these processes was analysed by using discrete and hybrid discrete-polarized continuum models to describe both the solute-solvent interaction in the first solvation shell and the effect of bulk water. The aqueous solvent plays a fundamental role in several reactions, such as eliminations, hydrolysis, and acid ionizations. In hydrolysis reactions, a water molecule must act as reactant, but results indicate that much more favourable formation of transition structures is obtained when two water molecules participate in a cooperative process. In this six-membered cyclic arrangement, bonds are formed and broken among all species, mimicking the possibility of HO^- and H^+ ions from different water molecules. On the other hand, in elimination reactions aqueous solvent is not involved in proton relay mechanisms, but water causes a polarization effect enhancing the charge redistribution at the transition structure. Thus, this reaction can be viewed as a prototype for water-assisted elimination rearrangement. Finally, a novel approach was applied to acid dissociation of cysteine. Solvation was simulated by an increasing number of water molecules and obtained results were then extrapolated to infinity. All these examples indicate how this research contributes to a qualitative understanding of solvent effects on chemical reactivity.

- Decomposition of *S*-Cl glutathione is a fast chemical transformation that comprises several pathways. Kinetic results indicate that two initial competitive processes are followed by other two concurrent reactions. According to these data, a feasible reaction mechanism has been proposed, but additional results, namely product analysis, are still necessary for its validation.
- It has been demonstrated that kinetic studies on complex enzymatic mechanisms can be performed at different stages of the process to obtain different information. In the case of human myeloperoxidase, the rate dependence on pH and [H_2O_2] (at [Cl^-] = 100 mM, [Tau] = 10 mM, and [MPO] = 100 nM) shows a different behaviour for initial rates and for rates at equilibrium regime. The slow taurine chlorination rate under equilibrium conditions can be quantitatively ascribed to the chemical equilibrium between compounds I and II, and supporting the existence of a stable enzymatic complex between compound II and hydroperoxyl radical (MPO-II-HO_2). Thus, the maximum steady chlorination rate is obtained approximately at [H_2O_2] = 0.4 mM and pH = 5. This result is in agreement with the fact that the chlorination activity of myeloperoxidase is optimal at acidic pH values, while its peroxidative effect takes place around neutral pH.
- The comparative analysis of the chlorination of taurine and the tripeptide Pro-Gly-Gly showed that Pro-Gly-Gly reacts with HClO faster than taurine, while the MPO-mediated chlorination of the latter occurs more readily. This observation supports the participation of a chlorinating enzymatic complex (MPO-I-Cl), available for small compounds that can access the active site through the narrow substrate channel. On the other hand, bulky substrates are chlorinated only (or mostly) outside the heme pocket by HClO or other free chlorinating agents like *N*-Cl taurine.
- The reaction mechanism of the MPO-mediated chlorination of substrates has been obtained and is depicted below. Derived rate equations fit kinetic data adequately, provided that the chlorinating agent (either HClO or a complex between compound I and chloride) is formed unprotonated. In the case of chlorination by free HClO outside the heme cavity, ClO^- must be released from the active center, diffuse away the heme cavity, and undergo protonation to HClO.

$$\mathrm{MPO} + \mathrm{H_2O_2} \overset{K_1}{\rightleftarrows} \mathrm{MPO\text{-}I} + \mathrm{H_2O}$$

$$\mathrm{MPO\text{-}I} + \mathrm{Cl^-} \underset{k_{-2a}}{\overset{k_{2a}}{\rightleftarrows}} \mathrm{MPO} + \mathrm{ClO^-} \;/\; \mathrm{MPO\text{-}I} + \mathrm{Cl^-} \underset{k_{-2b}}{\overset{k_{2b}}{\rightleftarrows}} \mathrm{MPO\text{-}I\text{-}Cl}$$

$$\mathrm{ClO^-} + \mathrm{Tau} + \mathrm{H^+} \overset{k_3}{\rightarrow} \mathit{N}\text{-}\mathrm{Cl\ Tau} + \mathrm{H_2O} \;/\; \mathrm{MPO\text{-}I\text{-}Cl} + \mathrm{Tau} + \mathrm{H^+} \overset{k_{3b}}{\rightarrow} \mathit{N}\text{-}\mathrm{Cl\ Tau} + \mathrm{MPO} + \mathrm{H_2O}$$

$$\mathrm{MPO} + \mathrm{H^+} \overset{K_4}{\rightleftarrows} \mathrm{MPO\text{-}H}$$

$$\mathrm{MPO\text{-}I} + \mathrm{H^+} \overset{K_5}{\rightleftarrows} \mathrm{MPO\text{-}I\text{-}H}$$

$$\mathrm{MPO\text{-}H} + \mathrm{Cl^-} \overset{K_6}{\rightleftarrows} \mathrm{MPO\text{-}H\text{-}Cl}$$

$$\mathrm{MPO\text{-}I} + \mathrm{H_2O_2} \overset{K_7}{\rightleftarrows} \mathrm{MPO\text{-}II\text{-}HO_2} + \mathrm{H^+}$$

$$\mathrm{MPO\text{-}II\text{-}HO_2} + \mathrm{H^+} \overset{k_8}{\rightarrow} \mathrm{MPO} + \mathrm{H_2O} + \mathrm{O_2}$$

- Pulse radiolysis experiments were performed to study the reaction of solvated electrons, the strongest reducing agent in water, with myeloperoxidase. One-electron reduction of different oxidation intermediates could not be observed, indicating that the reaction does not take place at the intensely chromophoric heme group, which is hindered in the

core of myeloperoxidase superstructure, but on other parts of the molecule. Wavelength-dependent relaxation kinetics indicates that excitation occurs at different functional groups placed at the more accessible surface of the enzyme. Furthermore, the enzyme was still able to chlorinate after receiving a very high irradiation dose, revealing that the active site, hindered at the end of the substrate channel, has not been damaged.

- Computational studies showed that distal bonding of a water molecule at the sixth position of ferric peroxidases is thermodynamically unstable, supporting five-coordinate metal atom of these enzymes with a water molecule axially situated but at non-bonding distance from the Fe(III) center. Besides, protonated ferryl oxygen of compound II was found necessary to justify the redox potential measured for processes involving this species. This protonation has been recently observed for ascorbate peroxidase by neutron diffraction experiments. Current computational results indicate that this feature must be common to all peroxidases, and the pK_a has been estimated (pK_a = 8.5 – 9.0), the first time a value has been proposed.

- A reduced model of the active site of myeloperoxidase, where only the common part of all peroxidases -at least for three superfamilies- has been employed, yielded very adequate computational results. It consists of the Fe-centered porphine ring coordinated to the proximal histidine imidazole. This outcome suggests that the prevalent behaviour of these enzymes just arises from a rather small part of their active site, while the specific performance of every particular peroxidase develops from the other part of the active site and its environment.

- This molecular model revealed suitable for most computational studies on native ferric species, compounds I and II, and other enzymatic complexes of peroxidases, but it needs to incorporate a vinyl substituent when ferrous state is also considered. This species is protonated and the most basic position is at the β-carbon of a vinyl group. Therefore, this protonated ferrous intermediate yields a much better potential for the reduction of the native ferric state of peroxidases. This arrangement also corresponds to the active site of other heme proteins as globins, but some significant differences are not considered, in particular the position of distal His with respect to heme. Thus, the model should be enlarged to obtain adequate information on these other proteins.

- Computational studies have been conducted to determine the origin of the different oxidative profiles observed in peroxidases. The effect of heme bending and orientation and protonation state of proximal imidazole were analysed, but their influence on the potentials could not be assessed unequivocally. However, it can be clearly stated that, contrary to the imidazolate proposed as proximal ligand in members of the peroxidase-cyclooxygenase superfamily, this group must be always protonated. This outcome has been drawn from geometry parameters rather than from the effect on redox potential. Further calculations are being executed in order to examine other relevant factors, as rotation of heme vinyls or covalent bonding between prosthetic group and protein, which could shed some light on this issue.

- The binding site of halides in the active site of myeloperoxidase at different oxidation states has been determined by a computational-experimental approach. Thus, computational general outcomes were contrasted and balanced with more specific empirical data obtained with myeloperoxidase, or with other enzymes if necessary. Chloride binds ferric iron as observed for cyanide (a pseudohalide), whereas bromide is situated above the meso carbon between heme pyrroles A and D. This distribution is explained in terms of steric hindrance with distal histidine (His95). Ferrous halocomplexes are less stable than the ferric ones, but in the case of cyanide, and again metal-coordinated complexes are more favoured. This result is consistent with the observation of the ferro-cyano compound as the only feasible ferrous complex with halides. On the other hand, all halides oxidized by compounds I and II may interact directly with ferryl oxygen for the electronic transference to proceed. This interaction is possible as the non-linear Fe-O_{Fe}-X arrangement allows binding of bulky substrates at this site without any hampering by His95 imidazole. The adduct formed by compound I and chloride must be the enzymatic chlorinating species, as well as an intermediate for ClO^-/HClO formation.

- The active site of myeloperoxidase is situated in the heme cavity, hindered at the end of the substrate channel. Surrounding protein is necessary to locate adequately some proximal and distal residues essential for enzyme reactivity, and for the formation of three covalent bonds between the prosthetic group and the peptide. We have observed that the protein also plays a relevant protective role**.** Pulse radiolysis experiments showed that the reaction of myeloperoxidase with solvated electrons takes place in the surface of the enzyme, as they could not access the heme cavity. Besides, chlorination activity is not lost after very high irradiation doses, indicating that the protein provides an effective barrier for protection of the active site. Furthermore, this environment must stabilize negative charges, favouring the presence of anionic species inside the enzyme. Thus, both hypochlorous acid and hydroperoxyl radical are produced and released unprotonated from the heme cavity, and they only undergo protonation outside the enzyme. Hypochlorite and superoxide anions are also strong oxidants, but milder than protonated counterparts. Therefore, this quality of the protein helps to prevent oxidative damage on the active site and along the access channel.

- All reactions occurring among all the redox intermediates of myeloperoxidase studied in this work, and adjusted to include the major outcomes obtained on this topic, are depicted in the following scheme:

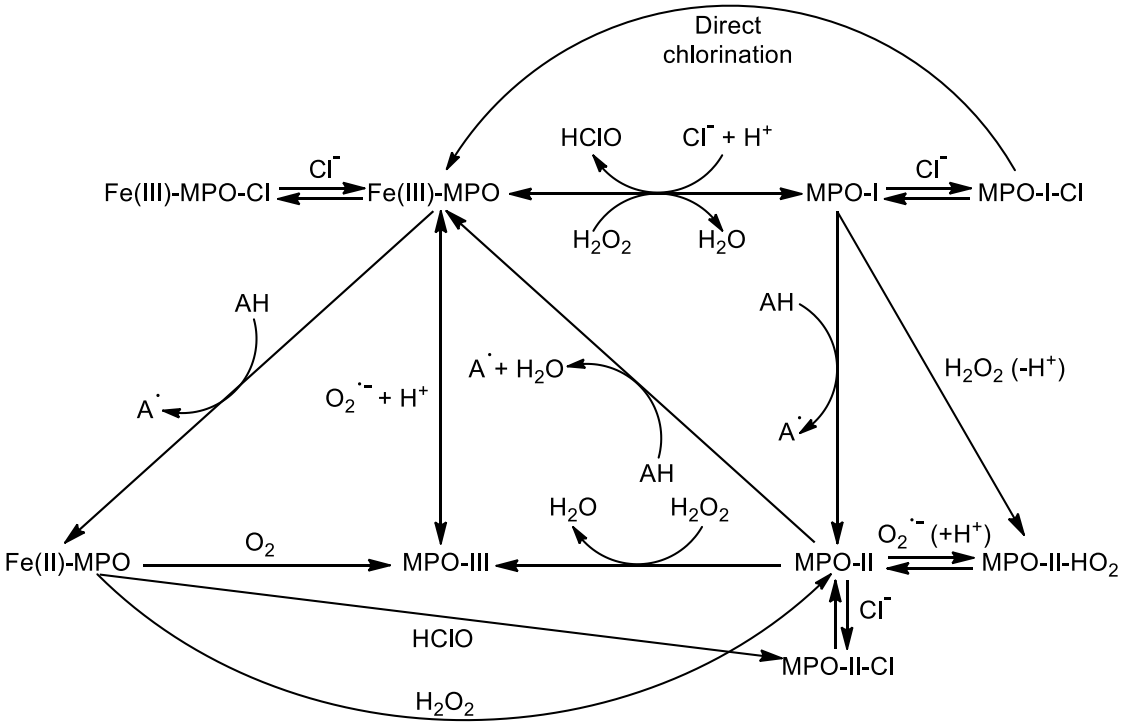

RESUMEN

We learn wisdom from failure much more than from success.
We often discover what will do, by finding what will not do;
and probably he who never made a mistake
never made a discovery.

Samuel Smiles,
in The Lives of George and Robert Stephenson

Mecanismo de cloración enzimática de compuestos nitrogenados catalizada por el sistema mieloperoxidasa-peróxido de hidrógeno-anión cloruro. Aproximación cinética y computacional.

La halogenación es un proceso fundamental en la reactividad química y biológica. El halógeno más abundante es el cloro, presente en el agua de mar en elevada concentración, así como en algunos minerales y numerosos compuestos orgánicos. Además, en el cuerpo humano el ion cloruro es el anión mayoritario en el fluido extracelular y el plasma sanguíneo, por ello resulta esencial para diversas funciones biológicas. Los procesos de cloración desempeñan un papel crucial en el sistema inmunitario innato, participando en la función antimicrobiana de los leucocitos y también presentan un rol activo en las enfermedades de tipo inflamatorio.

Las peroxidasas constituyen una familia enzimática cuya acción catalítica consiste principalmente en la oxidación de un sustrato mediante la reducción de peróxido de hidrógeno (H_2O_2). La mieloperoxidasa (MPO) es la proteína más abundante de los neutrófilos y su actividad resulta decisiva en el sistema inmunitario de los mamíferos. Este enzima es responsable de la formación de numerosas especies reactivas de oxígeno y es el productor primordial de ácido hipocloroso (HClO), un agente oxidante y clorante con gran acción antimicrobiana.

La taurina es un aminoácido sulfónico presente en diversos tejidos del cuerpo humano que se encuentra en los leucocitos en muy elevada concentración, hasta 50 mM. La taurina es frecuentemente considerada el objetivo principal del HClO producido por el sistema MPO/H_2O_2/Cl^-, formándose así otro compuesto oxidante más estable y menos tóxico, la monoclorotaurina (*N*-Cl Tau). Esta cloramina mantiene la capacidad de clorar otras moléculas e igualmente posee una importante actividad antibacteriana, participando en enfermedades inflamatorias asociadas con el estrés oxidativo.

Se realizaron estudios cinéticos de la cloración de taurina por el sistema enzimático MPO/H_2O_2/Cl^- con el fin de establecer el mecanismo de reacción que tiene lugar. La reacción de cloración no sigue un comportamiento típico de Michaelis-Menten, ya que las medidas no han mostrado saturación del centro activo. Sin embargo se observa un importante descenso de velocidad respecto al estado inicial al alcanzar el régimen de equilibrio, que se ha podido asignar a un equilibrio químico establecido entre los intermedios enzimáticos compuesto I y compuesto II, que no participa en el proceso de cloración. De este modo se ha podido determinar que, en las condiciones de estudio, el máximo de velocidad se obtiene aproximadamente con [H_2O_2] = 0,4 mM y a pH = 5. Este resultado se corresponde con la observación previa de que este enzima en medios ácidos cataliza principalmente procesos de cloración, mientras que la peroxidación sucede en ambiente neutro. Se ha logrado establecer un mecanismo de reacción que ajusta correctamente los resultados cinéticos en estado inicial y de equilibrio, y la influencia del pH en la reacción. Este mecanismo se muestra a continuación:

$$\mathrm{MPO} + \mathrm{H_2O_2} \overset{K_1}{\rightleftarrows} \mathrm{MPO\text{-}I} + \mathrm{H_2O}$$

$$\mathrm{MPO\text{-}I} + \mathrm{Cl^-} \underset{k_{-2a}}{\overset{k_{2a}}{\rightleftarrows}} \mathrm{MPO} + \mathrm{ClO^-} \;/\; \mathrm{MPO\text{-}I} + \mathrm{Cl^-} \underset{k_{-2b}}{\overset{k_{2b}}{\rightleftarrows}} \mathrm{MPO\text{-}I\text{-}Cl}$$

$$\mathrm{ClO^-} + \mathrm{Tau} + \mathrm{H^+} \overset{k_3}{\rightarrow} \textit{N}\text{-Cl Tau} + \mathrm{H_2O} \;/\; \mathrm{MPO\text{-}I\text{-}Cl} + \mathrm{Tau} + \mathrm{H^+} \overset{k_{3b}}{\rightarrow} \textit{N}\text{-Cl Tau} + \mathrm{MPO} + \mathrm{H_2O}$$

$$\mathrm{MPO} + \mathrm{H^+} \overset{K_4}{\rightleftarrows} \mathrm{MPO\text{-}H}$$

$$\mathrm{MPO\text{-}I} + \mathrm{H^+} \overset{K_5}{\rightleftarrows} \mathrm{MPO\text{-}I\text{-}H}$$

$$\text{MPO-H} + \text{Cl}^- \overset{K_6}{\rightleftarrows} \text{MPO-H-Cl}$$

$$\text{MPO-I} + \text{H}_2\text{O}_2 \overset{K_7}{\rightleftarrows} \text{MPO-II-HO}_2 + \text{H}^+$$

$$\text{MPO-II-HO}_2 + \text{H}^+ \overset{k_8}{\rightarrow} \text{MPO} + \text{H}_2\text{O} + \text{O}_2$$

Este resultado sugiere la formación de un complejo estable entre Compuesto II y el radical hidroperoxilo (MPO-II-HO_2), pero no hace distinción entre la formación de HClO libre o la existencia de un complejo enzimático entre Compuesto I y cloruro (MPO-I-Cl) con capacidad halogenante. Los datos cinéticos descartan en ambos casos la participación de un protón en la formación del agente clorante, por lo que se propone la formación del ion ClO^- en el centro activo, situado en el interior de la proteína, que inmediatamente se difunde al exterior donde se protonará rápidamente a HClO.

El centro activo de MPO se encuentra situado en una cavidad en el interior del enzima, conectado con el exterior a través de un estrecho canal de acceso para los sustratos. Si bien se ha observado la presencia de compuestos relativamente voluminosos en la cavidad distal al grupo hemo, resulta evidente que su acceso será más lento y complejo que el de las pequeñas moléculas capaces de atravesar el canal de sustratos. Esta característica se ha aprovechado para el diseño de otro experimento de cloración enzimática. El tripéptido Pro-Gly-Gly reacciona con HClO mucho más rápido que la taurina, es más voluminoso que ésta y el derivado clorado resulta estable. Por todo ello es el sustrato de elección ideal para un estudio comparativo de la cloración de ambos compuestos por el sistema MPO/H_2O_2/Cl^-.

Este tripéptido muestra un comportamiento que se corresponde totalmente con el observado con taurina. Los resultados cinéticos se ajustan correctamente a las mismas ecuaciones de velocidad tanto en estado inicial como en régimen de equilibrio. Sin embargo, se ha observado que la reacción es más lenta para este compuesto. Esta diferencia no resulta compatible con un proceso de cloración equivalente con ambos sustratos, como el que tiene lugar en el exterior del enzima por reacción con un agente oxidante libre como el HClO. Este resultado indica la existencia de una vía alternativa de cloración que favorece la oxidación de taurina. Así se confirma que la cloración de sustratos catalizada por el enzima mieloperoxidasa transcurre a través de dos mecanismos diferentes, uno en el exterior de la proteína por reacción con HClO adecuado para compuestos más voluminosos, y otro en la cavidad distal del hemo válido para especies de menor tamaño que reaccionan directamente con un complejo enzimático con capacidad clorante (MPO-I-Cl).

Se han realizado otras medidas experimentales con este enzima. Además de un análisis del efecto de diversos parámetros (temperatura, [Cl^-], etc), se ha estudiado la reacción de la mieloperoxidasa, capaz de producir especies altamente oxidantes, con electrones solvatados, que suponen el agente más reductor en disolución acuosa. No se ha logrado observar reducción del átomo de hierro del grupo hemo, ya que los electrones parecen reaccionar con diferentes grupos funcionales situados en la superficie del enzima. De este modo se evita el deterioro del centro activo, de modo que el enzima es capaz de mantener una importante actividad catalítica tras recibir dosis electrónicas muy elevadas.

La investigación experimental se ha complementado con diversos estudios computacionales, con el fin de obtener información que se encuentra fuera del alcance de los métodos exclusivamente empíricos. Esto sucede habitualmente cuando el estudio se realiza sobre reacciones con elevada complejidad, como es el caso de la actividad enzimática de la mieloperoxidasa, y también cuando se pretende alcanzar un nivel de detalle difícilmente accesible para las técnicas experimentales. Los cálculos de estructura electrónica constituyen un potente instrumento para la elucidación de estructuras y mecanismos de reacción y han sido ampliamente utilizados en el desarrollo de esta investigación.

En el estudio computacional se ha empleado un modelo molecular reducido del centro activo de la mieloperoxidasa que sólo incluye la estructura común a todas las peroxidasas, es decir, el anillo de porfina con el átomo de hierro central coordinado al imidazol de la histidina proximal. Con este modelo se ha podido describir adecuadamente el comportamiento observado para los miembros de esta familia enzimática, lo que indica que la reactividad general de las peroxidasas reside

precisamente en esta pequeña parte del centro activo, mientras que la acción más específica de cada enzima será debida al resto del centro activo, así como su entorno más cercano y la interacción entre ambos.

Este modelo se ha empleado para optimizar geometrías y calcular valores termodinámicos de las tres especies integrantes del ciclo peroxidativo de la mieloperoxidasa, enzima férrico nativo y compuestos I y II, permitiendo confirmar que la especie férrica presenta un átomo de hierro pentacoordinado, con una molécula de agua situada en posición distal, interaccionando con el metal pero a una distancia no enlazante. Asimismo, se ha logrado determinar el estado de protonación del grupo oxoferrilo en el compuesto II, un aspecto que ha estado en discusión durante décadas. Sólo un compuesto II protonado sobre el átomo de oxígeno unido al hierro permite calcular adecuadamente el potencial de los procesos redox en los que este intermedio participa. Este protón se ha observado por primera vez en un reciente estudio por cristalografía de difracción de neutrones de la estructura del compuesto II del enzima ascorbato peroxidasa, pero los datos aquí obtenidos permiten extrapolar ese resultado al resto de peroxidasas. Además se ha podido estimar que el pK_a de este grupo protonado corresponde al proceso observado en torno a pH = 8,5 - 9,0 para diversos enzimas de esta familia.

El intermedio ferroso de las peroxidasas, al contrario que en otras familias enzimáticas, no interviene en su actividad catalítica, ya que no participa en el ciclo de peroxidación ni en el de halogenación. Las peroxidasas actúan en medios oxidantes, por lo que la presencia de este estado reducido del grupo hemo es residual. Sin embargo, el potencial de reducción férrico/ferroso de la mieloperoxidasa difiere del resto de miembros de la familia y presenta valores similares a las globinas, en donde este intermedio sí es activo y muy relevante para su función de transporte o almacenamiento de gases. Por ello, su estudio computacional, similar al de los otros intermedios que participan en el ciclo peroxidativo, resulta relevante.

El estado ferroso de las peroxidasas presenta el hemo protonado, y se ha determinado la posición más favorable para ese protón. Todas las posiciones posibles en la ferroporfina resultan demasiado ácidas; la modificación del modelo molecular para incluir un sustituyente vinilo ha permitido determinar que el C_β de este grupo es el átomo más favorable para dicha protonación. De este modo se obtiene un potencial de reducción adecuado para la reducción del estado férrico nativo en la mayoría de las peroxidasas, aunque no para la mieloperoxidasa, que presenta un valor excepcional.

La mieloperoxidasa tiene un perfil redox particular dentro de la familia de las peroxidasas. No sólo el proceso de reducción férrico/ferroso, sino que también presenta un compuesto I más oxidante, lo que explica su capacidad de catalizar la oxidación bielectrónica de ion cloruro a hipoclorito. Se supone que el origen de estas diferencias se encuentra íntimamente relacionado con los tres enlaces covalentes existentes entre la proteína y el grupo prostético, aunque no ha podido ser demostrado. Un estudio computacional previo ha intentado establecer esta conexión, pero los resultados obtenidos no resultaban concluyentes en absoluto. Por lo tanto, en esta tesis se ha realizado una investigación computacional con el fin de determinar si otras variables estructurales podrían contribuir al especial comportamiento redox de la mieloperoxidasa.

Se ha estudiado el efecto de los siguientes factores sobre el potencial redox de los intermedios férrico, ferroso, y compuestos I y II: curvatura del anillo porfirínico, ángulo de giro del imidazol proximal respecto al eje transversal al grupo hemo y estado de protonación del mismo. La presencia de un imidazolato proximal supone cierta diferencia en los potenciales de reducción en estudio. Sin embargo, esta carga negativa produce una disminución relevante de la distancia existente entre el átomo de hierro central y el N_τ del imidazol, que no corresponde a la geometría obtenida experimentalmente para las peroxidasas. Por lo tanto, aunque la existencia de este imidazolato ha sido propuesta en una publicación previa, los datos obtenidos desmienten esta posibilidad.

Las estructuras cristalográficas de diversos enzimas de esta familia indican que la rotación axial de este grupo presenta distintos ángulos de giro y el anillo porfirínico no siempre se mantiene totalmente plano. Las peroxidasas pertenecientes a la superfamilia peroxidasa-ciclooxigenasa, que presentan mayor poder oxidante y un hemo curvado, particularmente en el caso de la mieloperoxidasa, poseen un imidazol situado de modo que se minimiza el efecto estérico entre dos hidrógenos de este anillo y los pirroles porfirínicos. Sin embargo, el grupo hemo de las peroxidasas de otras superfamilias es más plano y el imidazol proximal muestra un giro que implica un mayor impedimento con los nitrógenos pirrólicos.

El estudio computacional orientado a evaluar el efecto de estos parámetros geométricos en el potencial redox de las peroxidasas ha mostrado que todos ellos poseen cierta influencia en su capacidad oxidante. Sin embargo, por sí mismos no logran justificar las importantes diferencias observadas entre distintas superfamilias. De ello se deduce que junto a estas variables es necesario considerar los enlaces covalentes entre grupo prostético y péptido con el fin de obtener una imagen válida y global del potencial redox de los enzimas del grupo peroxidasa-ciclooxigenasa.

El ion cloruro participa como cosustrato en la reacción de cloración catalizada por la mieloperoxidasa. Es oxidado por el compuesto I para formar HClO, que se libera en su forma aniónica (ClO^-) al exterior, o un complejo enzimático con capacidad de cloració, (MPO-I-Cl). Este anión haluro también puede interaccionar con otros intermedios enzimáticos actuando como inhibidor. Se ha estudiado la estabilidad de los complejos enzimáticos tipo MPO-X (X = Cl, Br, y CN) para cada uno de los intermedios redox (especies férrica y ferrosa y compuestos I y II), en dos posibles sitios de unión: en posición axial, interaccionando con el átomo de hierro central o con el oxígeno del grupo oxoferrilo, o sobre el átomo de carbono en posición meso entre los pirroles A y D del anillo porfirínico.

El análisis computacional indica que todos estos complejos presentan mayor estabilidad con el grupo ciano, mientras que los compuestos con cloro son los menos estables. La comparación de estos resultados con otros datos experimentales ha permitido establecer que el ion cloruro se sitúa sobre el átomo metálico en el intermedio férrico, al igual que se ha observado por medidas cristalográficas para el cianuro. Sin embargo, el ion bromuro se une al centro activo de la mieloperoxidasa en estado nativo en diferente posición debido a su mayor volumen: el imidazol protonado de la histidina distal produce un impedimento estérico en posición axial. Por el contrario, se ha determinado que los tres aniones pueden enlazarse al átomo de oxígeno del compuesto I, siempre que éste sea suficientemente oxidante, ya que la formación de dicho enlace supone la oxidación bielectrónica de los (pseudo)haluros. Por ello se puede postular que el complejo de cloro resultante es el intermedio enzimático con capacidad clorante previamente determinado por métodos experimentales (MPO-I-Cl). Los (pseudo)haluros también pueden unirse al oxígeno del grupo oxoferril del compuesto II, de nuevo condicionado al potencial de reducción del intermedio enzimático, aunque en este caso posiblemente tenga lugar una oxidación monoelectrónica.

El compuesto III y el novedoso complejo propuesto entre el compuesto II y el radical hidroperoxilo son los únicos intermedios estables que poseen más de un átomo de oxígeno sobre el hierro del grupo hemo (dos y tres oxígenos, respectivamente). En ambos casos se ha observado que su estabilidad depende considerablemente de su estado de protonación. Los dos compuestos se disocian con facilidad al desprotonarse, liberando aniones superóxido ($O_2^{\bullet -}$) que precisan estabilizar su carga negativa en el interior del enzima por interacción con el entorno proteínico hasta su salida al medio exterior. Este resultado es muy relevante, puesto que tanto este ion como el anión hipoclorito (ClO^-) son mucho menos reactivos que las correspondientes especies protonadas, radical hidroperoxilo ($HO_2^{\bullet}$) y ácido hipocloroso (HClO). La formación de compuestos menos agresivos en el interior del enzima, así como la capacidad de la proteína de restringir el acceso de los electrones hidratados observada en el estudio correspondiente, demuestran que la mieloperoxidasa posee un mecanismo de defensa contra el daño oxidativo, con la proteína actuando de escudo frente a las agresiones externas y estabilizando en su interior, donde se encuentra protegido el centro activo, las especies aniónicas menos dañinas.

El conocimiento detallado del mecanismo de reacción de este enzima fundamental en la actividad antimicrobiana del sistema inmune, e implicado en numerosas enfermedades inflamatorias, resulta imprescindible para entender la acción de los fármacos empleados en su control y los mecanismos de inhibición que tienen lugar. En este sentido se han estudiado computacionalmente dos series de inhibidores derivados del 3-alquilindol, pudiéndose observar una relación cuantitativa entre la distribución de cargas en la molécula y su IC_{50} (concentración necesaria para inhibir la actividad catalítica en un 50 %). Es un resultado prometedor que indica el camino a seguir para avanzar en el diseño racional de fármacos inhibidores de la mieloperoxidasa.

Las reacciones e intermedios de la mieloperoxidasa estudiados en esta tesis, incluyendo los principales resultados obtenidos acerca de este sistema enzimático se encuentran representados en el siguiente esquema:

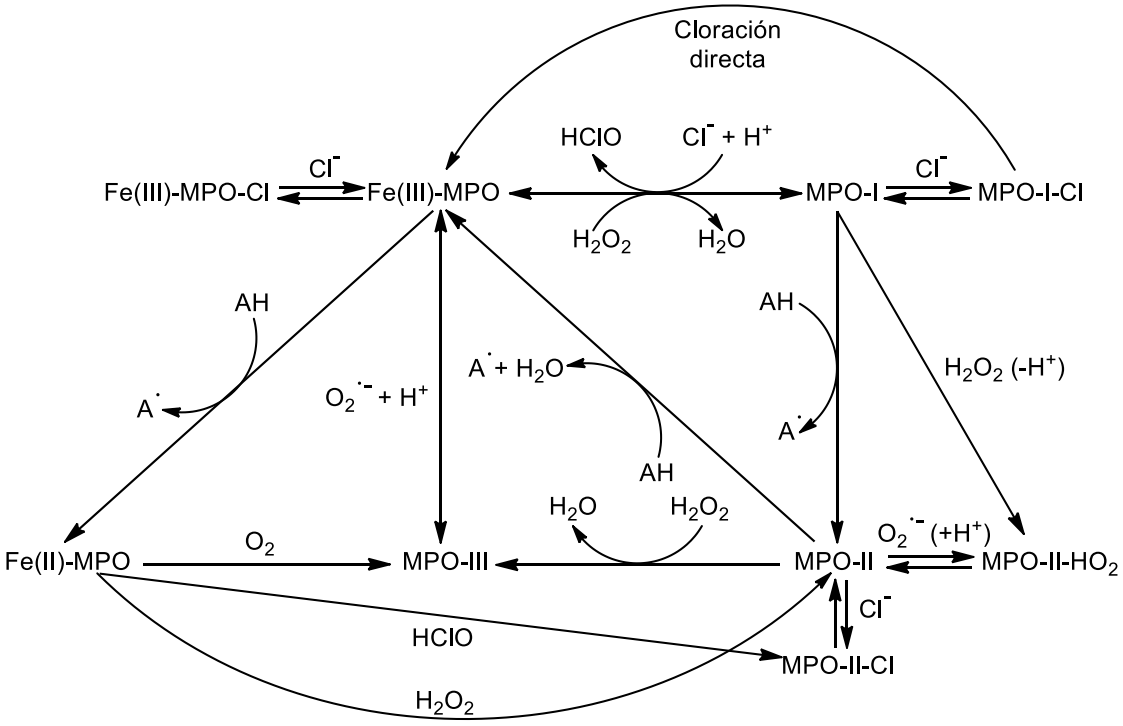

Donde Fe(III)-MPO, Fe(II)-MPO, MPO-I, MPO-II y MPO-III son las especies férrica y ferrosa de la mieloperoxidasa, así como los compuestos I, II y III, respectivamente; Fe(III)-MPO-Cl, MPO-I-Cl y MPO-II-Cl son los compuestos clorados de los correspondientes intermedios; y MPO-II-HO_2 es el complejo formado por el compuesto I y el radical hidroperoxilo.

Aunque la taurina posee un rol central, existen muchos otros compuestos diana para los procesos de cloración catalizados por la mieloperoxidasa, principalmente aminas y tioles. Las cloraminas son más estables que el HClO pero presentan la particularidad de mantener la capacidad clorante, de modo que pueden propagar el daño oxidativo desde el punto inicial donde se produce la generación de HClO hasta zonas más alejadas. Los tioles, por su parte, se oxidan con mucha facilidad y con velocidades de reacción muy elevadas, por lo que resultan objetivos no sólo del HClO sino también de las cloraminas. Por este motivo, los aminoácidos azufrados (cisteína y metionina) son los puntos débiles de las proteínas frente al ataque de estos oxidantes. Además, el glutatión, un tripéptido con un grupo tiol, es un antioxidante esencial para el mantenimiento del equilibrio redox celular.

Algunas cloraminas son inestables y se descomponen con facilidad liberando el cloro en forma de anión cloruro, perdiendo su potencial clorante y actuando *de facto* como antioxidantes. En esta tesis se ha estudiado la rápida descomposición de las *N*-halo etanolaminas secundarias en medio básico, por medio de técnicas experimentales y computacionales, así como los procesos que experimentan posteriormente los productos de decomposición.

La presencia de la función alcohol acelera extraordinariamente la reacción de descomposición de las *N*-Cl etanolaminas respecto a las correspondientes *N*-Cl etilaminas. Este incremento no se debe a un efecto electrónico del grupo hidroxilo sobre las típicas eliminaciones intermoleculares de cloraminas en posición Hofmann o Zaitsev, sino a la participación de dos reacciones competitivas adicionales: una fragmentación bimolecular y una eliminación intramolecular. Todos estos procesos presentan una etapa inicial bimolecular de tipo concertado asincrónico, en la que la transferencia protónica se encuentra adelantada al resto de eventos moleculares. Este primer paso representa la etapa limitante de velocidad en todos los casos. Las cuatro vías de descomposición de *N*-Cl, *N*-metiletanolamina se describen a continuación:

Eliminación en posición Hofmann

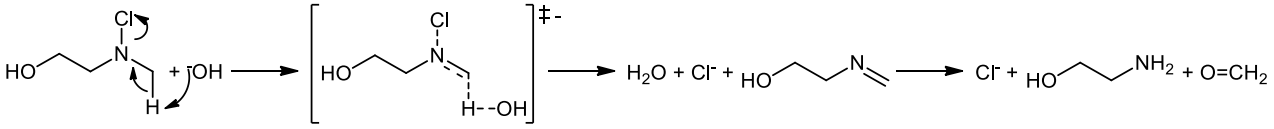

Eliminación en posición Zaitsev

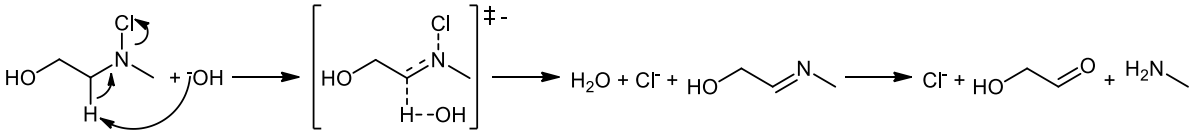

Eliminación intramolecular

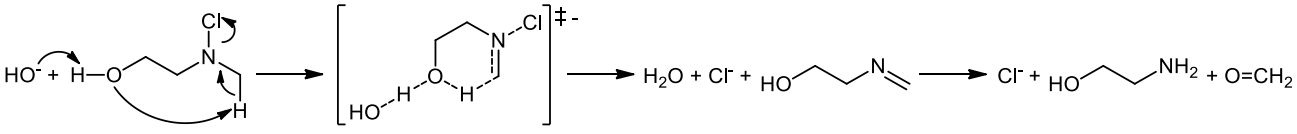

Fragmentación bimolecular

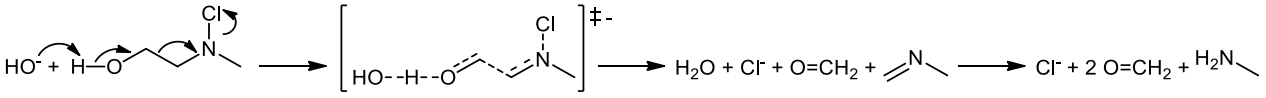

El estudio computacional de estos procesos ha permitido confirmar la mayoría de las conclusiones obtenidas a partir de los resultados experimentales. El estudio cinético de la reacción no permite la obtención de datos en las etapas posteriores a la inicial, aunque la participación de los distintos procesos se ha realizado mediante el análisis de productos de reacción. Sin embargo, las energías de activación obtenidas computacionalmente difieren en el peso de cada vía de reacción en el proceso global. Los productos de reacción sugieren que la fragmentación bimolecular es el proceso mayoritario, mientras que el estudio de estructura electrónica indica un predominio evidente de la eliminación intramolecular.

En este primer paso se forman iminas y etanoliminas, inestables en disolución acuosa. La investigación cinética no permite obtener datos sobre los procesos que suceden a continuación de la etapa limitante, por ello se ha procedido a estudiar computacionalmente la descomposición de esos compuestos. La hidrólisis de iminas sucede en dos pasos, se inicia con el ataque de una molécula de agua al doble enlace N=C para formar un hemiaminal, que colapsa en la segunda etapa dando lugar a una amina y un compuesto carbonílico, con la intervención de al menos dos moléculas de agua, según se indica en el siguiente esquema. En ambas reacciones elementales las transferencias protónicas al átomo de nitrógeno suceden adelantadas respecto al resto de procesos moleculares. Los resultados obtenidos concuerdan con los datos experimentales publicados.

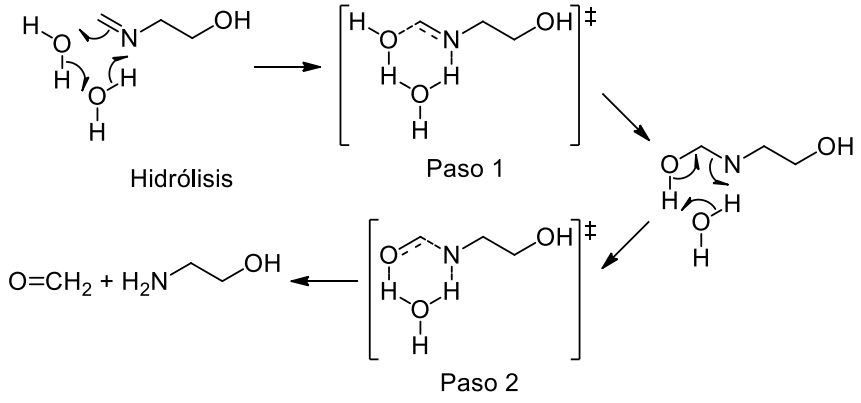

La descomposición de etanoliminas tiene lugar a través de dos procesos competitivos. La primera vía es una reacción de hidrólisis similar a la de iminas, ya que apenas se ve alterada por la presencia del grupo alcohol. También se descompone a través de una fragmentación intramolecular, produciendo una nueva imina que sufre hidrólisis a continuación. Éste es el primer estudio sobre la descomposición de etanoliminas, de las que no existe apenas información, puesto que son compuestos inestables incluso en ausencia de agua, que se ha revelado no necesaria para el proceso de fragmentación. El mecanismo de descomposición de la *N*-etanolmetanimina se detalla a continuación:

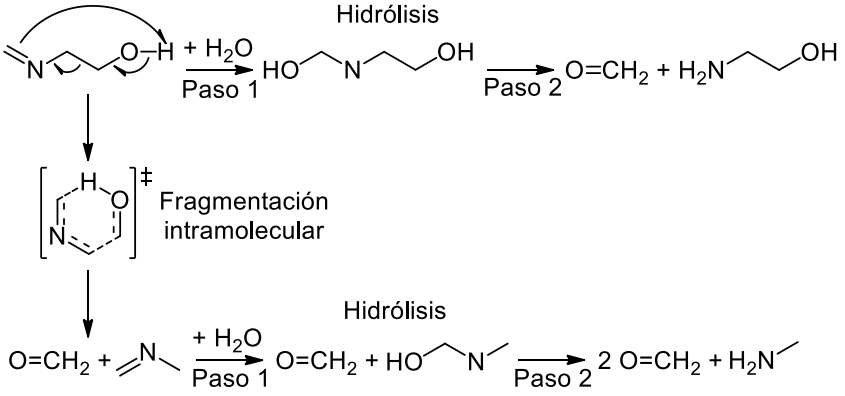

El estudio combinado de técnicas experimentales y computacionales ha permitido establecer que la descomposición de *N*-Cl etanolaminas en medio básico tiene lugar muy mayoritariamente a través de la eliminación intramolecular. La distribución de los productos finales de reacción determina la cuota de participación de la fragmentación intramolecular y la hidrólisis en la descomposición de la etanolimina obtenida del primer proceso.

La cisteína es un aminoácido proteico que posee un sustituyente con un grupo tiol susceptible de una muy rápida oxidación por parte del ácido hipocloroso producido por el sistema MPO/H_2O_2/Cl^-. Esta cloración se encuentra regulada por los equilibrios de ionización de los grupos amino y tiol de la cisteína, con valores de pK_a asignados aplicando diversas teorías de acidez, ya que no se han podido medir independientemente de manera adecuada. El cálculo de estos equilibrios microscópicos se ha realizado de diversos modos, incluyendo un método de solvatación inédito, en el que el medio acuoso se ha representado con un número creciente de moléculas discretas de agua, posteriormente extrapolado a infinito. Sin embargo, los estudios computacionales no han permitido la asignación irrefutable de los valores macroscópicos de pK_a obtenidos experimentalmente. Por otro lado, sí se ha podido establecer una relación cuantitativa estructura-actividad entre distintas aminas y tioles que apuntan a una mayor acidez del grupo amino, al contrario de lo considerado habitualmente.

En todos estos procesos (descomposición de cloraminas y etanoliminas, hidrólisis de iminas y disociación ácida de cisteína) se ha analizado en profundidad el papel que desempeña el agua como disolvente empleando modelos discretos e híbridos de tipo discreto-continuo polarizado, incluyendo una novedosa extrapolación a infinito de un número creciente de moléculas explícitas de agua. Algunas moléculas de agua muestran un efecto catalítico reduciendo la energía de activación, bien por estabilización de cargas o participando activamente en las estructuras de transición. Mientras que las moléculas discretas de agua describen la interacción soluto-disolvente en la capa de hidratación, los modelos continuos han permitido estudiar el efecto conjunto de la masa de agua a mayor distancia.

El glutatión es un importante antioxidante que, al igual que la cisteína, reacciona con mucha facilidad con el ácido hipocloroso. Si bien los productos de oxidación de este tripéptido son conocidos, no existía más información de la reacción que tiene lugar. En esta tesis se presenta un estudio cinético en el que se analizan velocidad de reacción y la influencia del pH del medio en los distintos procesos que experimenta el derivado clorado tras su formación. Algunos de los productos

de esta reacción no son reversibles e implican la generación de más glutatión para el mantenimiento del potencial reductor de la célula.

Según se ha expuesto de manera muy resumida en esta última sección, en esta tesis doctoral se han cumplido ampliamente los objetivos propuestos inicialmente, proporcionando una nueva visión amplia y detallada sobre el mecanismo enzimático de cloración catalizado por el sistema MPO/H_2O_2/Cl^-. Asimismo, se han estudiado y descrito los procesos que tienen lugar tras la cloración de diversos compuestos de importancia biológica.

APPENDIX

Research is what I am doing
when I don't know what I am doing.

Wernher von Braun

Supplementary information 3

A theoretical study on the mechanism of the base-promoted decomposition of *N*-Cl,*N*-methylethanolamine

Table S3.1. Percentage of negative charge transferred from the HO^-, and degree of evolution for selected bonds at RICs and TSs, using the microsolvated model. Atom labels are the same as in Figure 3.2. Bonds being formed and broken are labelled f and b, respectively.

	Hofmann elim.		**Zaitsev elim.**		**Bimol. fragm.**		**Intram. elim.**	
	RIC	**TS**	**RIC**	**TS**	**RIC**	**TS**	**RIC**	**TS**
% $q_{transferred}$	21.2	44.1	62.4	70.9	15.1	62.4	18.1	64.3
				% Evolution				
O_{OH}–H_T (f)	3.1	34.8	1.4	58.5	-	-	-	-
O_{OH}–H_O (f)	-	-	-	-	19.8	74.3	23.3	75.0
O–H_O (b)	-	-	-	-	27.6	82.8	30.8	83.3
O–C_3 (f)	-	-	-	-	4.0	29.5	-	-
C_3–C_2 (b)	-	-	-	-	2.3	33.5	-	-
O–H_T (f)	-	-	-	-	-	-	1.4	28.2
C_1–H_T (b)	7.4	42.4	-	-	-	-	4.1	38.5
C_2–H_T (b)	-	-	4.5	66.7	-	-	-	-
C_1–N (f)	–1.7	8.8	-	-	-	-	–0.8	17.0
C_2–N (f)	-	-	–2.2	0.8	–2.2	23.2	-	-
N–Cl (b)	0.7	15.9	0.1	7.1	0.4	37.5	0.7	29.4
S_y		0.68		0.43		0.74		0.68

Table S3.2. Mulliken atomic charges and dipole moments (in debye) obtained by using MP2=full/6-31++G(d,p) level. Atom labels are the same as in Figure 3.2.

	C_1	N	Cl	C_2	C_3	O	H_T	H_O	O_{OH}	H_{OH}	O_{WO}	H_{WO}	O_{WN}	H_{WN}	μ
Hofmann elimination															
R	–0.15	–0.31	–0.11	–0.09	0.02	–0.59	0.14	0.39	–1.21	0.21	–0.72	0.36	–0.72	0.36	-
RIC	–0.20	–0.43	–0.14	0.04	–0.09	–0.64	0.21	0.41	–1.17	0.31	–0.93	0.55	–0.84	0.52	10.60
TS	–0.42	–0.33	–0.31	–0.02	–0.05	–0.64	0.41	0.43	–1.03	0.31	–0.86	0.52	–0.88	0.54	6.16
PIC	–0.07	–0.36	–0.80	–0.04	–0.08	–0.64	0.36	0.43	–0.78	0.40	–0.78	0.36	–0.86	0.51	8.37
P	–0.04	–0.27	–1.00	–0.19	0.07	–0.58	0.36	0.38	–0.72	0.36	–0.72	0.36	–0.72	0.36	-
Zaitsev elimination															
R	–0.15	–0.31	–0.11	–0.09	0.02	–0.59	0.13	0.39	–1.21	0.21	–0.72	0.36	–0.72	0.36	-
RIC	–0.25	–0.42	–0.10	0.07	–0.08	–0.64	0.10	0.40	–1.18	0.31	–0.91	0.55	–0.82	0.52	10.43
TS	–0.21	–0.32	–0.23	–0.55	–0.03	–0.65	0.50	0.40	–0.86	0.32	–0.80	0.48	–0.83	0.52	9.80
PIC	–0.21	–0.43	–0.82	0.00	–0.04	–0.65	0.36	0.47	–0.80	0.38	–0.83	0.42	–0.79	0.46	11.64
P	–0.24	–0.26	–1.00	–0.07	0.01	–0.57	0.36	0.36	–0.72	0.36	–0.72	0.36	–0.72	0.36	-
Bimolecular fragmentation															
R	–0.15	–0.31	–0.11	–0.09	0.02	–0.59	-	0.39	–1.21	0.21	–0.72	0.36	–0.72	0.36	-
RIC	–0.21	–0.38	–0.13	–0.15	0.15	–0.73	-	0.55	–1.21	0.31	–0.89	0.54	–0.79	0.49	15.73
TS	–0.19	–0.21	–0.48	–0.20	0.18	–0.80	-	0.53	–0.95	0.35	–0.80	0.48	–0.79	0.48	15.41
PIC	–0.23	–0.36	–0.82	–0.03	0.34	–0.52	-	0.44	–0.90	0.47	–0.80	0.47	–0.75	0.36	9.50
P	–0.25	–0.24	–1.00	–0.04	0.27	–0.44	-	0.36	–0.72	0.36	–0.72	0.36	–0.72	0.36	-
Intramolecular elimination															
R	–0.15	–0.31	–0.11	–0.09	0.02	–0.59	0.14	0.39	–1.21	0.21	–0.72	0.36	–0.72	0.36	-
RIC	–0.21	–0.39	–0.14	0.08	–0.13	–0.72	0.16	0.57	–1.21	0.33	–0.84	0.52	–0.79	0.51	11.78
TS	–0.34	–0.18	–0.44	–0.08	0.04	–0.83	0.30	0.56	–0.93	0.35	–0.79	0.47	–0.80	0.49	7.54
PIC	0.00	–0.33	–0.85	–0.22	0.07	–0.68	0.41	0.51	–0.87	0.36	–0.79	0.45	–0.77	0.34	12.34
P	–0.04	–0.27	–1.00	–0.19	0.07	–0.58	0.38	0.36	–0.72	0.36	–0.72	0.36	–0.72	0.36	-

Table S3.3. Relevant geometrical parameters of the stationary points (distances in Å and angles in degrees) for the HO^--promoted decomposition of *N*-Cl,*N*-methylethanolamine. Atom labels are the same as in Figure 3.2. Superscripts to values refer to the respective parameters, as indicated in left column.

	Hofmann elim.	Zaitsev elim.	Bimol. fragm.	Intram. elim.
		R		
H_T–C_1[c]/C_2[d]/O[e]	1.095[c]	1.097[d]	-	1.095[c]/4.783[e]
C_1–N		1.465		
N–Cl		1.761		
N–C_2		1.469		
C_2–C_3		1.516		
C_3–O		1.423		
O–H_O		0.970		
		RIC		
O_{OH}–H_T[a]/H_O[b]	1.978[a]	2.302[a]	1.511[b]	1.465[b]
H_T–C_1[c]/C_2[d]/O[e]	1.095[c]	1.092[d]	-	1.087[c]/2.218[e]
C_1–N	1.473	1.478	1.476	1.472
N–Cl	1.778	1.773	1.778	1.782
N–C_2	1.486	1.482	1.480	1.480
C_2–C_3	1.520	1.517	1.530	1.530
C_3–O	1.437	1.437	1.408	1.404
O–H_O	0.970	0.970	1.036	1.051
H_{WO}–O_{OH}	1.452	1.063	1.518	1.599
H_{WN}–N	1.772	1.770	1.864	1.877
H_O–O_{WN}	2.058	2.122	-	-
O_{OH}–H_T[a]/H_O[b]–C_1[c]/C_2[d]/O[e]	152.31[ac]	166.07[ad]	168.51[be]	169.62[be]
		TS		
O_{OH}–H_T[a]/H_O[b]	1.316[a]	1.108[a]	1.019[b]	1.021[b]
H_T–C_1[c]/C_2[d]/O[e]	1.296[c]	1.569[d]	-	1.264[c]/1.377[e]
C_1–N	1.415	1.470	1.455	1.390
N–Cl	1.967	1.866	2.126	2.048
N–C_2	1.477	1.455	1.362	1.441
C_2–C_3	1.525	1.492	1.804	1.561
C_3–O	1.427	1.470	1.302	1.390
O–H_O	0.976	0.971	1.560	1.549
H_{WO}–O_{OH}	1.625	1.754	1.804	1.816
H_{WN}–N	1.680	1.736	1.877	1.890
H_O–O_{WN}	1.928	2.255	-	-
O_{OH}–H_T[a]/H_O[b]–C_1[c]/C_2[d]/O[e]	170.29[ac]	174.15[ad]	175.92[be]	176.91[be]
		PIC		
O_{OH}–H_T[a]/H_O[b]	0.974[a]	0.967[a]	0.972[b]	0.985[b]
H_T–C_1[c]/C_2[d]/O[e]	3.303[c]	2.511[d]	-	3.328[c]/0.974[e]
C_1–N	1.285	1.466	1.464	1.285
N–Cl	4.256	3.965	4.169	4.193
N–C_2	1.466	1.287	1.285	1.468
C_2–C_3	1.519	1.507	3.650	1.516
C_3–O	1.427	1.420	1.232	1.449
O–H_O	0.974	0.981	1.995	1.736
H_{WO}–O_{OH}	2.850	2.319	1.827	1.882
H_{WN}–N	1.757	1.963	5.137	3.716
H_O–O_{WN}	1.969	6.012	-	-
O_{OH}–H_T[a]/H_O[b]–C_1[c]/C_2[d]/O[e]	88.37[ac]	144.49[ad]	168.69[be]	174.59[be]

Table S3.3. Cont.

	Hofmann elim.	Zaitsev elim.	Bimol. fragm.	Intram. elim.
		P		
O_{OH}–H_T[a]/H_O[b]	0.963[a]	0.963[a]	0.963[b]	0.963[b]
H_T–C_1[c]/C_2[d]/O[e]	-	-	-	3.570[c]/0.969[e]
C_1–N	1.280	1.462	1.456	1.280
N–C_2	1.458	1.283	1.279	1.458
C_2–C_3	1.519	1.513	-	1.519
C_3–O	1.422	1.425	1.223	1.422
O–H_O	0.969	0.965	-	-

Supplementary information 4

Neutral hydrolysis of aliphatic imines: A quantum chemical study

Table S4.1. Relevant distances in Å at the different stationary points obtained for the hydrolysis of the imines with R_1, R_2, and R_3 = H or CH_3, with models I to IV at the B3LYP/6-31++G** computational level.

R_1	R_2	R_3	Model	Stationary Point	N–C_I	N–H_1	N–H_2	C_I–O_C	O_C–H_1	O_C–H_2	O_C–H_O	N–H_N	O_2–H_1	O_2–H_2
H	H	H		R	1.272	-	-	-	0.965	0.965	-	-	0.965	-
				I	1.428	1.016	3.198	1.444	2.610	0.968	-	-	-	-
				P	-	1.016	1.016	1.209	-	-	-	-	-	-
			I	RIC_1	1.273	1.944	3.393	3.573	0.979	0.964	-	-	-	-
				TS_1	1.307	1.069	3.285	2.274	1.656	0.969	-	-	-	-
				PIC_1	1.428	1.016	3.198	1.444	2.610	0.968	-	-	-	-
				RIC_2	1.452	1.016	2.405	1.417	2.746	0.969	-	-	-	-
				TS_2	1.585	1.021	1.186	1.346	2.897	1.420	-	-	-	-
				PIC_2	2.850	1.017	1.017	1.213	4.099	3.151	-	-	-	-
			II	RIC_1	1.270	1.896	3.368	4.012	0.985	0.964	1.871	-	-	-
				TS_1	1.290	1.038	3.379	2.449	1.893	0.967	1.621	-	-	-
				PIC_1	1.418	1.015	3.210	1.467	2.653	0.968	1.894	-	-	-
				RIC_2	1.444	1.017	2.405	1.434	2.736	0.970	1.919	-	-	-
				TS_2	1.538	1.022	1.212	1.376	2.688	1.392	1.791	-	-	-
				PIC_2	2.666	1.022	1.017	1.220	3.053	3.570	1.909	-	-	-
			III	RIC_1	1.276	3.308	4.484	3.293	0.982	0.964	-	1.845	-	-
				TS_1	1.366	1.370	2.942	1.771	1.209	0.974	-	1.881	-	-
				PIC_1	1.440	1.018	3.193	1.435	2.572	0.967	-	1.942	-	-
			IV	RIC_1	1.276	1.845	3.308	3.293	-	0.982	-	-	0.989	1.827
				TS_1	1.309	1.142	2.462	2.083	-	1.140	-	-	1.413	1.307
				PIC_1	1.418	1.017	2.838	1.467	-	1.894	-	-	2.400	0.977
				RIC_2	1.476	1.018	1.918	1.403	-	2.673	-	-	3.408	0.986
				TS_2	1.598	1.020	1.119	1.333	-	2.364	-	-	3.052	1.471
				PIC_2	2.666	1.017	1.022	1.220	-	3.053	-	-	3.607	2.139
H	H	CH_3		R	1.275	-	-	-	0.965	0.965	-	-	0.965	-
				I	1.435	1.018	3.190	1.449	2.589	0.968	-	-	-	-
				P	-	1.016	1.016	1.214	-	-	-	-	-	-
			I	RIC_1	1.277	1.926	3.404	3.592	0.981	0.964	-	-	-	-
				TS_1	1.317	1.082	3.270	2.285	1.613	0.969	-	-	-	-
				PIC_1	1.435	1.018	3.190	1.449	2.589	0.968	-	-	-	-
				RIC_2	1.458	1.018	2.354	1.423	2.712	0.968	-	-	-	-
				TS_2	1.599	1.021	1.185	1.350	2.909	1.410	-	-	-	-
				PIC_2	3.164	1.017	1.017	1.216	4.085	2.696	-	-	-	-
			II	RIC_1	-	-	-	-	-	-	-	-	-	-
				TS_1	-	-	-	-	-	-	-	-	-	-
				PIC_1	-	-	-	-	-	-	-	-	-	-
				RIC_2	1.453	1.019	2.371	1.439	2.687	0.969	1.921	-	-	-
				TS_2	1.558	1.021	1.206	1.378	2.723	1.384	1.790	-	-	-
				PIC_2	3.925	1.022	1.017	1.222	3.630	4.540	1.886	-	-	-
			III	RIC_1	1.279	4.892	3.485	3.947	0.964	0.980	-	1.839	-	-
				TS_1	1.366	1.310	3.011	1.864	1.247	0.972	-	1.902	-	-
				PIC_1	1.449	1.019	3.183	1.442	2.563	0.967	-	1.926	-	-
			IV	RIC_1	1.279	1.839	3.479	3.931	-	0.980	-	-	0.990	1.851
				TS_1	1.313	1.109	2.459	2.150	-	1.149	-	-	1.496	1.297
				PIC_1	1.427	1.019	2.849	1.473	-		-	-	2.456	0.977
				RIC_2	1.482	1.020	1.902	1.409	-	2.666	-	-	3.378	0.987
				TS_2	1.607	1.021	1.116	1.337	-	2.354	-	-	3.061	1.475
				PIC_2	3.108	1.017	1.022	1.222	-	3.233	-	-	3.627	2.133

Table S4.1. (Cont.)

R_1	R_2	R_3	Model	Stationary Point	$N–C_I$	$N–H_1$	$N–H_2$	$C_I–O_C$	$O_C–H_1$	$O_C–H_2$	$O_C–H_O$	$N–H_N$	$O_2–H_1$	$O_2–H_2$
H	CH_3	CH_3		R	1.279	-	-	-	0.965	0.965	-	-	0.965	-
				I	1.443	1.017	3.186	1.457	2.545	0.968	-	-	-	-
				P	-	1.016	1.016	1.219	-	-	-	-	-	-
			I	RIC_1	1.281	1.905	3.366	3.627	0.983	0.964	-	-	-	-
				TS_1	1.322	1.066	3.300	2.325	1.678	0.968	-	-	-	-
				PIC_1	1.443	1.017	3.186	1.457	2.545	0.968	-	-	-	-
				RIC_2	1.466	1.018	2.344	1.431	2.642	0.969	-	-	-	-
				TS_2	1.621	1.020	1.183	1.355	2.901	1.401	-	-	-	-
				PIC_2	3.787	1.016	1.020	1.223	3.744	2.211	-	-	-	-
			II	RIC_1	-	-	-	-	-	-	-	-	-	-
				TS_1	-	-	-	-	-	-	-	-	-	-
				PIC_1	-	-	-	-	-	-	-	-	-	-
				RIC_2	1.461	1.019	2.371	1.447	2.617	0.970	1.914	-	-	-
				TS_2	1.570	1.021	1.204	1.386	2.703	1.380	1.774	-	-	-
				PIC_2	3.996	1.022	1.017	1.228	3.616	4.532	1.850	-	-	-
			III	RIC_1	1.283	4.926	3.648	4.386	0.964	0.982	-	1.813	-	-
				TS_1	1.356	1.195	3.137	2.064	1.358	0.970	-	1.957	-	-
				PIC_1	1.457	1.019	3.177	1.449	2.508	0.968	-	1.919	-	-
			IV	RIC_1	1.283	1.816	3.455	3.916	-	0.981	-	-	0.993	1.841
				TS_1	1.315	1.083	2.473	2.226	-	1.184	-	-	1.570	1.252
				PIC_1	1.434	1.018	2.838	1.482	-	1.878	-	-	2.436	0.978
				RIC_2	1.489	1.019	1.899	1.418	-	2.677	-	-	3.332	0.987
				TS_2	1.627	1.020	1.110	1.343	-	2.349	-	-	3.060	1.490
				PIC_2	3.997	1.017	1.022	1.228	-	3.618	-	-	3.625	2.102
CH_3	H	H		R	1.268	-	-	-	0.965	0.965	-	-	0.965	-
				I	1.424	1.016	3.198	1.447	2.636	0.967	-	-	-	-
				P	-	1.016	1.016	1.209	-	-	-	-	-	-
			I	RIC_1	1.269	1.937	3.362	3.629	0.980	0.964	-	-	-	-
				TS_1	1.300	1.048	3.334	2.302	1.794	0.968	-	-	-	-
				PIC_1	1.424	1.016	3.198	1.447	2.636	0.967	-	-	-	-
				RIC_2	1.452	1.017	2.429	1.414	2.613	0.969	-	-	-	-
				TS_2	1.569	1.021	1.197	1.352	2.820	1.403	-	-	-	-
				PIC_2	2.781	1.017	1.017	1.214	3.278	3.278	-	-	-	-
			II	RIC_1	1.269	1.839	3.318	3.731	0.990	0.965	1.842	-	-	-
				TS_1	1.292	1.026	3.477	2.378	2.129	0.967	1.585	-	-	-
				PIC_1	1.414	1.017	3.210	1.472	2.654	0.968	1.887	-	-	-
				RIC_2	1.444	1.019	2.420	1.430	2.626	0.970	1.915	-	-	-
				TS_2	1.532	1.023	1.230	1.380	2.647	1.370	1.780	-	-	-
				PIC_2	2.552	1.021	1.017	1.223	2.973	3.443	1.887	-	-	-
			III	RIC_1	1.273	3.348	4.527	3.327	0.981	0.964	-	1.838	-	-
				TS_1	1.353	1.320	2.992	1.845	1.247	0.973	-	1.907	-	-
				PIC_1	1.438	1.018	3.194	1.438	2.585	0.967	-	1.921	-	-
			IV	RIC_1	1.273	1.838	3.348	3.326	-	0.981	-	-	0.992	1.829
				TS_1	1.299	1.098	2.489	2.163	-	1.156	-	-	1.522	1.288
				PIC_1	1.414	1.017	2.844	1.472	-	1.887	-	-	2.428	0.977
				RIC_2	1.473	1.019	1.892	1.403	-	2.657	-	-	3.325	0.989
				TS_2	1.582	1.021	1.105	1.338	-	2.354	-	-	3.040	1.505
				PIC_2	2.552	1.017	1.021	1.223	-	2.972	-	-	3.609	2.136

Table S4.1. (Cont.)

R_1	R_2	R_3	Model	Stationary Point	N–C_I	N–H_1	N–H_2	C_I–O_C	O_C–H_1	O_C–H_2	O_C–H_O	N–H_N	O_2–H_1	O_2–H_2
CH_3	H	CH_3		R	1.271	-	-	-	0.965	0.965	-	-	0.965	-
				I	1.431	1.017	3.190	1.452	2.605	0.967	-	-	-	-
				P	-	1.016	1.016	1.214	-	-	-	-	-	-
			I	RIC_1	1.273	1.919	3.377	3.597	0.983	0.964	-	-	-	-
				TS_1	1.304	1.048	3.318	2.374	1.810	0.968	-	-	-	-
				PIC_1	1.431	1.017	3.190	1.452	2.605	0.967	-	-	-	-
				RIC_2	1.458	1.018	2.357	1.422	2.637	0.969	-	-	-	-
				TS_2	1.583	1.021	1.196	1.356	2.820	1.395	-	-	-	-
				PIC_2	3.136	1.017	1.017	1.216	4.128	2.710	-	-	-	-
			II	RIC_1	1.272	1.820	3.293	3.726	0.993	0.965	1.841	-	-	-
				TS_1	1.292	1.020	3.461	2.506	2.311	0.966	1.529	-	-	-
				PIC_1	1.422	1.018	3.203	1.478	2.626	0.967	1.884	-	-	-
				RIC_2	1.453	1.019	2.370	1.438	2.617	0.970	1.923	-	-	-
				TS_2	1.547	1.023	1.225	1.383	2.644	1.364	1.786	-	-	-
				PIC_2	3.956	1.021	1.017	1.222	3.632	4.535	1.885	-	-	-
			III	RIC_1	1.275	1.828	3.247	3.706	0.993	0.965	-	3.699	-	-
				TS_1	1.319	1.080	3.278	2.293	1.623	0.968	-	2.135	-	-
				PIC_1	1.446	1.019	3.186	1.444	2.568	0.967	-	1.908	-	-
			IV	RIC_1	1.275	1.829	3.699	4.372	-	0.981	-	-	0.993	1.813
				TS_1	1.304	1.075	2.481	2.227	-	1.175	-	-	1.612	1.266
				PIC_1	1.422	1.018	2.849	1.478	-	1.884	-	-	2.472	0.977
				RIC_2	1.481	1.020	1.876	1.410	-	2.623	-	-	3.337	0.990
				TS_2	1.599	1.022	1.103	1.341	-	2.323	-	-	3.065	1.504
				PIC_2	3.099	1.017	1.021	1.222	-	3.204	-	-	3.625	2.145
CH_3	CH_3	CH_3		R	1.279	-	-	-	0.965	0.965	-	-	0.965	-
				I	1.445	1.016	3.190	1.459	2.573	0.967	-	-	-	-
				P	-	1.016	1.016	1.219	-	-	-	-	-	-
			I	RIC_1	1.281	1.886	3.314	3.653	0.985	0.964	-	-	-	-
				TS_1	1.315	1.047	3.330	2.383	1.795	0.968	-	-	-	-
				PIC_1	1.445	1.016	3.190	1.459	2.573	0.967	-	-	-	-
				RIC_2	1.467	1.015	2.377	1.433	3.210	0.969	-	-	-	-
				TS_2	1.620	1.021	1.196	1.360	2.791	1.380	-	-	-	-
				PIC_2	3.811	1.016	1.019	1.223	3.738	2.230	-	-	-	-
			II	RIC_1	1.283	1.789	3.708	3.700	0.997	0.965	1.809	-	-	-
				TS_1	1.304	1.018	3.520	2.527	2.337	0.966	1.450	-	-	-
				PIC_1	1.435	1.015	3.201	1.481	2.578	0.968	1.878	-	-	-
				RIC_2	1.465	1.019	2.356	1.448	2.501	0.970	1.909	-	-	-
				TS_2	1.569	1.023	1.224	1.391	2.569	1.358	1.769	-	-	-
				PIC_2	4.045	1.021	1.017	1.228	3.639	4.576	1.851	-	-	-
			III	RIC_1	1.280	1.786	3.236	3.732	0.997	0.965	-	4.629	-	-
				TS_1	1.331	1.073	3.295	2.316	1.638	0.968	-	2.122	-	-
				PIC_1	1.461	1.018	3.184	1.451	2.529	0.967	-	1.897	-	-
			IV	RIC_1	1.283	1.796	3.499	4.089	-	0.980	-	-	0.996	1.845
				TS_1	1.311	1.062	2.500	2.303	-	1.225	-	-	1.659	1.211
				PIC_1	1.435	1.017	2.848	1.485	-	1.873	-	-	2.480	0.978
				RIC_2	1.493	1.019	1.875	1.421	-	2.643	-	-	3.251	0.991
				TS_2	1.621	1.021	1.099	1.350	-	2.318	-	-	3.016	1.522
				PIC_2	4.035	1.017	1.021	1.228	-	3.621	-	-	3.640	2.110

Table S4.2. Mulliken charges on relevant atoms at the different stationary points obtained for the hydrolysis of the imines with R_1, R_2, and R_3 = H or CH_3, with models I to IV at the B3LYP/6-31++G** computational level.

R_1	R_2	R_3	Model	Stationary Point	N	C_I	O_C	H_1	H_2	H_N	H_O
H	H	H		R	–0.32	–0.20	–0.69	0.34	0.34	0.34	0.34
				I	–0.58	–0.15	–0.50	0.30	0.33	0.34	0.34
				P	–0.85	0.11	–0.32	0.28	0.28	0.34	0.34
			I	RIC_1	–0.43	–0.14	–0.75	0.42	0.33	-	-
				TS_1	–0.36	–0.09	–0.95	0.38	0.34	-	-
				PIC_1	–0.58	–0.15	–0.50	0.30	0.33	-	-
				RIC_2	–0.57	–0.17	–0.48	0.30	0.35	-	-
				TS_2	–0.60	0.00	–0.65	0.32	0.39	-	-
				PIC_2	–0.91	0.17	–0.35	0.29	0.32	-	-
			II	RIC_1	–0.41	–0.17	–0.77	0.42	0.36	-	0.41
				TS_1	–0.35	–0.08	–1.07	0.39	0.37	-	0.44
				PIC_1	–0.57	–0.16	–0.57	0.30	0.35	-	0.42
				RIC_2	–0.56	–0.19	–0.54	0.33	0.37	-	0.41
				TS_2	–0.62	–0.04	–0.67	0.37	0.38	-	0.40
				PIC_2	–0.96	0.18	–0.38	0.37	0.30	-	0.40
			III	RIC_1	–0.47	–0.14	–0.78	0.42	0.35	0.45	-
				TS_1	–0.78	–0.10	–0.57	0.40	0.36	0.46	-
				PIC_1	–0.75	–0.12	–0.47	0.33	0.36	0.43	-
			IV	RIC_1	–0.47	–0.14	–0.78	0.45	0.42	-	-
				TS_1	–0.41	–0.16	–0.77	0.44	0.51	-	-
				PIC_1	–0.57	–0.16	–0.57	0.33	0.42	-	-
				RIC_2	–0.70	–0.13	–0.49	0.31	0.44	-	-
				TS_2	–0.66	–0.07	–0.58	0.35	0.47	-	-
				PIC_2	–0.96	0.18	–0.38	0.30	0.37	-	-
H	H	CH_3		R	–0.35	–0.02	–0.69	0.34	0.34	0.34	0.34
				I	–0.52	–0.03	–0.47	0.29	0.34	0.34	0.34
				P	–0.85	0.23	–0.37	0.28	0.28	0.34	0.34
			I	RIC_1	–0.46	0.04	–0.76	0.43	0.33	-	-
				TS_1	–0.37	0.05	–0.90	0.37	0.34	-	-
				PIC_1	–0.52	–0.03	–0.47	0.29	0.34	-	-
				RIC_2	–0.53	–0.13	–0.47	0.29	0.37	-	-
				TS_2	–0.57	–0.09	–0.62	0.31	0.41	-	-
				PIC_2	–0.90	0.28	–0.39	0.29	0.31	-	-
			II	RIC_1	-	-	-	-	-	-	-
				TS_1	-	-	-	-	-	-	-
				PIC_1	-	-	-	-	-	-	-
				RIC_2	–0.44	–0.37	–0.49	0.31	0.40	-	0.42
				TS_2	–0.54	–0.13	–0.62	0.35	0.40	-	0.41
				PIC_2	–0.95	0.23	–0.41	0.37	0.28	-	0.41
			III	RIC_1	–0.46	0.03	–0.77	0.34	0.42	0.45	-
				TS_1	–0.67	–0.12	–0.58	0.42	0.34	0.46	-
				PIC_1	–0.72	0.06	–0.45	0.32	0.36	0.44	-
			IV	RIC_1	–0.46	0.03	–0.77	0.45	0.42	-	-
				TS_1	–0.36	–0.01	–0.77	0.42	0.51	-	-
				PIC_1	–0.47	–0.22	–0.50	0.32	0.43	-	-
				RIC_2	–0.67	–0.05	–0.49	0.31	0.44	-	-
				TS_2	–0.66	–0.01	–0.57	0.35	0.47	-	-
				PIC_2	–0.96	0.40	–0.41	0.28	0.36	-	-

Table S4.2. (Cont.)

R_1	R_2	R_3	Model	Stationary Point	N	C_I	O_C	H_1	H_2	H_N	H_O
H	CH_3	CH_3		R	–0.35	0.14	–0.69	0.34	0.34	0.34	0.34
				I	–0.46	–0.08	–0.43	0.30	0.34	0.34	0.34
				P	–0.85	0.41	–0.42	0.28	0.28	0.34	0.34
			I	RIC_1	–0.48	0.31	–0.75	0.43	0.33	-	-
				TS_1	–0.31	0.23	–0.93	0.38	0.34	-	-
				PIC_1	–0.46	–0.08	–0.43	0.30	0.34	-	-
				RIC_2	–0.48	–0.15	–0.43	0.30	0.38	-	-
				TS_2	–0.54	–0.01	–0.59	0.31	0.42	-	-
				PIC_2	–0.91	0.47	–0.44	0.28	0.34	-	-
			II	RIC_1	-	-	-	-	-	-	-
				TS_1	-	-	-	-	-	-	-
				PIC_1	-	-	-	-	-	-	-
				RIC_2	–0.43	–0.29	–0.47	0.33	0.39	-	0.42
				TS_2	–0.51	–0.04	–0.60	0.36	0.41	-	0.42
				PIC_2	–0.96	0.51	–0.45	0.37	0.28	-	0.42
			III	RIC_1	–0.50	0.37	–0.77	0.34	0.43	0.46	-
				TS_1	–0.52	0.02	–0.71	0.44	0.33	0.43	-
				PIC_1	–0.64	0.00	–0.43	0.32	0.36	0.44	-
			IV	RIC_1	–0.46	0.30	–0.77	0.46	0.43	-	-
				TS_1	–0.28	0.04	–0.78	0.42	0.52	-	-
				PIC_1	–0.40	–0.24	–0.48	0.34	0.44	-	-
				RIC_2	–0.62	–0.23	–0.42	0.31	0.46	-	-
				TS_2	–0.66	–0.13	–0.51	0.35	0.48	-	-
				PIC_2	–0.96	0.51	–0.45	0.28	0.37	-	-
CH_3	H	H		R	–0.11	–0.17	–0.69	0.34	0.34	0.34	0.34
				I	–0.37	–0.12	–0.50	0.30	0.34	0.34	0.34
				P	–0.57	0.11	–0.32	0.28	0.28	0.34	0.34
			I	RIC_1	–0.20	–0.12	–0.74	0.40	0.33	-	-
				TS_1	–0.14	–0.07	–1.00	0.37	0.36	-	-
				PIC_1	–0.37	–0.12	–0.50	0.30	0.34	-	-
				RIC_2	–0.37	–0.12	–0.46	0.30	0.35	-	-
				TS_2	–0.47	0.05	–0.64	0.33	0.39	-	-
				PIC_2	–0.63	0.14	–0.34	0.32	0.32	-	-
			II	RIC_1	–0.21	–0.14	–0.80	0.44	0.36	-	0.42
				TS_1	–0.16	–0.06	–1.07	0.38	0.37	-	0.45
				PIC_1	–0.35	–0.11	–0.57	0.34	0.36	-	0.41
				RIC_2	–0.35	–0.15	–0.53	0.34	0.37	-	0.41
				TS_2	–0.49	0.02	–0.66	0.38	0.40	-	0.40
				PIC_2	–0.69	0.15	–0.39	0.39	0.31	-	0.41
			III	RIC_1	–0.23	–0.12	–0.78	0.42	0.35	0.44	-
				TS_1	–0.51	–0.09	–0.61	0.40	0.36	0.44	-
				PIC_1	–0.59	–0.06	–0.48	0.33	0.36	0.43	-
			IV	RIC_1	–0.23	–0.12	–0.78	0.44	0.42	-	-
				TS_1	–0.15	–0.12	–0.82	0.44	0.51	-	-
				PIC_1	–0.35	–0.11	–0.57	0.34	0.41	-	-
				RIC_2	–0.52	–0.08	–0.48	0.33	0.43	-	-
				TS_2	–0.52	–0.03	–0.58	0.36	0.48	-	-
				PIC_2	–0.69	0.15	–0.39	0.31	0.39	-	-

Table S4.2. (Cont.)

R_1	R_2	R_3	Model	Stationary Point	N	C_I	O_C	H_1	H_2	H_N	H_O
CH_3	H	CH_3		R	–0.13	0.09	–0.69	0.34	0.34	0.34	0.34
				I	–0.30	–0.09	–0.47	0.30	0.35	0.34	0.34
				P	–0.57	0.23	–0.37	0.28	0.28	0.34	0.34
			I	RIC_1	–0.21	0.12	–0.74	0.40	0.33	-	-
				TS_1	–0.12	0.09	–1.00	0.36	0.36	-	-
				PIC_1	–0.30	–0.09	–0.47	0.30	0.35	-	-
				RIC_2	–0.35	–0.01	–0.46	0.30	0.36	-	-
				TS_2	–0.44	0.10	–0.63	0.33	0.41	-	-
				PIC_2	–0.61	0.28	–0.38	0.30	0.31	-	-
			II	RIC_1	–0.23	0.12	–0.80	0.43	0.36	-	0.42
				TS_1	–0.08	0.06	–1.06	0.38	0.36	-	0.45
				PIC_1	–0.23	–0.31	–0.49	0.34	0.36	-	0.42
				RIC_2	–0.26	–0.23	–0.48	0.33	0.39	-	0.41
				TS_2	–0.41	0.04	–0.62	0.37	0.42	-	0.40
				PIC_2	–0.67	0.23	–0.41	0.38	0.29	-	0.41
			III	RIC_1	–0.23	0.17	–0.81	0.43	0.36	0.45	-
				TS_1	–0.29	0.07	–0.92	0.39	0.37	0.38	-
				PIC_1	–0.55	0.04	–0.47	0.33	0.36	0.44	-
			IV	RIC_1	–0.23	0.17	–0.77	0.45	0.43	-	-
				TS_1	–0.12	0.09	–0.83	0.41	0.50	-	-
				PIC_1	–0.23	–0.31	–0.49	0.34	0.42	-	-
				RIC_2	–0.53	0.06	–0.48	0.33	0.44	-	-
				TS_2	–0.53	0.07	–0.57	0.36	0.49	-	-
				PIC_2	–0.68	0.39	–0.40	0.29	0.37	-	-
CH_3	CH_3	CH_3		R	–0.15	0.30	–0.69	0.34	0.34	0.34	0.34
				I	–0.25	–0.18	–0.42	0.31	0.35	0.34	0.34
				P	–0.57	0.41	–0.42	0.28	0.28	0.34	0.34
			I	RIC_1	–0.30	0.47	–0.73	0.40	0.33	-	-
				TS_1	–0.12	0.40	–0.99	0.37	0.36	-	-
				PIC_1	–0.25	–0.18	–0.42	0.31	0.35	-	-
				RIC_2	–0.26	–0.23	–0.43	0.29	0.37	-	-
				TS_2	–0.41	–0.02	–0.59	0.32	0.43	-	-
				PIC_2	–0.63	0.49	–0.43	0.28	0.36	-	-
			II	RIC_1	–0.32	0.49	–0.81	0.45	0.36	-	0.43
				TS_1	–0.08	0.32	–1.04	0.39	0.35	-	0.47
				PIC_1	–0.21	–0.24	–0.48	0.30	0.37	-	0.40
				RIC_2	–0.23	–0.27	–0.47	0.34	0.40	-	0.42
				TS_2	–0.36	–0.04	–0.59	0.37	0.43	-	0.41
				PIC_2	–0.67	0.55	–0.45	0.38	0.29	-	0.42
			III	RIC_1	–0.31	0.49	–0.80	0.43	0.36	0.34	-
				TS_1	–0.25	0.31	–0.93	0.40	0.36	0.39	-
				PIC_1	–0.47	–0.08	–0.43	0.33	0.37	0.44	-
			IV	RIC_1	–0.28	0.47	–0.77	0.45	0.42	-	-
				TS_1	–0.09	0.22	–0.84	0.42	0.52	-	-
				PIC_1	–0.15	–0.36	–0.47	0.36	0.43	-	-
				RIC_2	–0.45	–0.21	–0.42	0.33	0.46	-	-
				TS_2	–0.48	–0.20	–0.51	0.36	0.50	-	-
				PIC_2	–0.66	0.55	–0.45	0.29	0.38	-	-

Table S4.3. Thermodynamic parameters, Δ*H°*, *T*Δ*S°*, and Δ*G°*, for the hydrolysis of imines with R_1, R_2, and R_3 = H or CH_3, obtained with models I to IV and B3LYP/6-31++G** computational level. Reactants (R) were taken as reference. All values in kJ·mol^{-1}, data obtained with PCM continuum model in italics.

Compound			Stationary point	Model I			Model II			Model III			Model IV		
R_1	R_2	R_3		Δ*H°*	*T*Δ*S°*	Δ*G°*	Δ*H°*	*T*Δ*S°*	Δ*G°*	Δ*H°*	*T*Δ*S°*	Δ*G°*	Δ*H°*	*T*Δ*S°*	Δ*G°*
H	H	H	RIC_1	-21.38	-31.02	9.63	-53.81	-74.15	20.34	-56.09	-75.83	19.74	-56.09	-75.83	19.74
				6.29		*34.09*			*46.03*			*34.09*			*34.09*
			TS_1	160.42	-45.23	205.64	98.76	-85.52	184.28	139.01	-79.64	218.64	41.25	-92.96	134.21
				181.75		*123.50*			*181.14*			*216.84*			*123.50*
			PIC_1	-49.81	-45.96	-3.86	-72.51	-82.53	10.02	-71.61	-76.57	4.96	-72.48	-82.59	10.11
				-15.99		*13.49*			*13.12*			*-2.07*			*13.49*
			I	-49.81	-45.96	-3.86	-49.81	-45.96	-3.86	-49.81	-45.96	-3.86	-49.81	-45.96	-3.86
				-15.99		*-15.99*			*-15.99*			*-15.99*			*-15.99*
			RIC_2	-47.73	-46.44	-1.29	-70.34	-82.66	12.32	-	-	-	-79.46	-87.78	8.33
				-10.37		*19.25*			*18.89*						*19.25*
			TS_2	108.55	-47.69	156.24	67.01	-87.45	154.46	-	-	-	-1.04	-95.67	94.62
				112.90		*62.95*			*145.76*						*62.95*
			PIC_2	-17.61	-24.26	6.65	-44.89	-72.98	28.10	-	-	-	-44.88	-72.98	28.09
				17.32		*57.26*			*57.30*						*57.26*
			P	-10.41	1.32	-11.73	-10.41	1.32	-11.73	-10.41	1.32	-11.73	-10.41	1.32	-11.73
				5.04		*5.04*			*5.04*			*5.04*			*5.04*
H	H	CH_3	RIC_1	-24.41	-33.95	9.54	-	-	-	-51.83	-71.17	19.35	-51.82	-71.01	19.20
				7.87		*30.24*						*30.48*			*30.24*
			TS_1	165.42	-46.63	212.04	-	-	-	141.70	-82.19	223.88	48.17	-94.95	143.12
				193.63		*138.10*						*224.01*			*138.10*
			PIC_1	-36.48	-48.32	11.84	-	-	-	-60.05	-82.02	21.98	-58.87	-85.14	26.27
				4.14		*33.89*						*20.64*			*33.89*
			I	-36.48	-48.32	11.84	-36.48	-48.32	11.84	-36.48	-48.32	11.84	-36.48	-48.32	11.84
				4.14		*4.14*			*4.14*			*4.14*			*4.14*
			RIC_2	-35.99	-48.73	12.75	-55.90	-82.74	26.84	-	-	-	-68.52	-90.09	21.57
				8.06		*36.92*			*35.20*						*36.92*
			TS_2	115.49	-49.50	164.99	78.74	-87.51	166.25	-	-	-	5.90	-97.64	103.54
				128.97		*78.23*			*158.26*						*78.23*
			PIC_2	-26.26	-22.85	-3.41	-55.45	-70.62	15.17	-	-	-	-55.45	-68.28	12.84
				12.45		*47.40*			*47.97*						*47.40*
			P	-21.17	2.21	-23.38	-21.17	2.21	-23.38	-21.17	2.21	-23.38	-21.17	2.21	-23.38
				-9.90		*-9.90*			*-9.90*			*-9.90*			*-9.90*
H	CH_3	CH_3	RIC_1	-26.43	-33.90	7.46	-	-	-	-57.88	-73.81	15.92	-55.19	-74.54	19.34
				6.63		*32.90*						*28.02*			*32.90*
			TS_1	156.43	-46.51	202.94	-	-	-	136.86	-78.91	215.76	42.86	-95.24	138.11
				183.40		*132.50*						*218.53*			*132.50*
			PIC_1	-28.63	-51.36	22.72	-	-	-	-53.57	-86.39	32.82	-51.61	-88.66	37.05
				15.40		*45.00*						*32.57*			*45.00*
			I	-28.63	-51.36	22.72	-28.63	-51.36	22.72	-28.63	-51.36	22.72	-28.63	-51.36	22.72
				15.40		*15.40*			*15.40*			*15.40*			*15.40*
			RIC_2	-28.43	-51.53	23.09	-48.88	-86.68	37.80	-	-	-	-60.59	-93.57	32.99
				18.07		*47.38*			*46.88*						*47.38*
			TS_2	120.10	-51.93	172.03	82.36	-90.42	172.77	-	-	-	13.13	-100.52	113.65
				139.31		*90.51*			*167.21*						*90.51*
			PIC_2	-39.60	-28.32	-11.28	-68.42	-70.74	2.32	-	-	-	-68.46	-70.62	2.17
				6.34		*34.84*			*35.00*						*34.84*
			P	-30.69	7.54	-38.22	-30.69	7.54	-38.22	-30.69	7.54	-38.22	-30.69	7.54	-38.22
				-26.13		*-26.13*			*-26.13*			*-26.13*			*-26.13*

Table S4.3. (Cont.)

Compound			Stationary point	Model I			Model II			Model III			Model IV		
R_1	R_2	R_3		*ΔH°*	*TΔS°*	*ΔG°*	*ΔH°*	*TΔS°*	*ΔG°*	*ΔH°*	*TΔS°*	*ΔG°*	*ΔH°*	*TΔS°*	*ΔG°*
CH_3	H	H	RIC_1	-21.42	-30.66	9.24	-51.90	-74.14	22.25	*35.09*	-54.75	-75.33	20.58	*36.02*	-54.71	-75.50	20.79	*36.27*
			TS_1	165.81	-44.26	210.08	*178.78*	101.45	-84.13	185.57	*165.28*	159.74	-77.06	236.80	*236.80*	49.32	-91.03	140.35	*130.69*
			PIC_1	-28.34	-45.99	17.65	*-0.51*	-51.39	-82.54	31.15	*30.07*	-50.37	-79.20	28.83	*16.07*	-51.39	-82.54	31.15	*30.06*
			I	-28.34	-45.99	17.65	*-0.51*	-28.34	-45.99	17.65	*-0.51*	-28.34	-45.99	17.65	*-0.51*	-28.34	-45.99	17.65	*-0.51*
			RIC_2	-27.40	-46.84	19.44	*3.63*	-49.66	-83.06	33.40	*36.83*	-	-	-	-	-60.56	-88.51	27.95	*33.48*
			TS_2	119.03	-48.34	167.37	*121.81*	76.45	-87.34	163.79	*157.68*	-	-	-	-	9.21	-95.67	104.87	*75.42*
			PIC_2	12.74	-27.80	40.54	*41.50*	-15.24	-72.26	57.02	*76.06*	-	-	-	-	-15.24	-72.27	57.03	*76.07*
			P	19.87	2.97	16.91	*22.55*	19.87	2.97	16.91	*22.55*	19.87	2.97	16.91	*22.55*	19.87	2.97	16.91	*22.55*
CH_3	H	CH_3	RIC_1	-23.71	-34.22	10.51	*10.14*	-52.78	-74.02	21.25	*33.80*	-53.87	-73.93	20.06	*31.48*	-53.80	-73.97	20.17	*31.59*
			TS_1	170.64	-46.03	216.67	*187.25*	105.51	-84.34	189.86	*167.39*	162.64	-74.42	237.06	*226.86*	53.24	-92.57	145.81	*137.27*
			PIC_1	-17.57	-48.31	30.74	*16.01*	-40.40	-85.18	44.78	*46.66*	-41.06	-83.28	42.22	*33.72*	-40.41	-85.18	44.77	*46.66*
			I	-17.57	-48.31	30.74	*16.01*	-17.57	-48.31	30.74	*16.01*	-17.57	-48.31	30.74	*16.01*	-17.57	-48.31	30.74	*16.01*
			RIC_2	-17.17	-49.11	31.94	*18.67*	-37.37	-83.72	46.36	*50.21*	-	-	-	-	-49.13	-90.68	41.55	*48.33*
			TS_2	124.13	-49.73	173.86	*135.58*	85.52	-88.44	173.95	*168.26*	-	-	-	-	16.06	-97.24	113.29	*88.15*
			PIC_2	1.77	-23.70	25.47	*31.12*	-26.97	-68.46	41.49	*63.92*	-	-	-	-	-26.86	-66.04	39.19	*65.67*
			P	6.05	4.08	1.97	*2.51*	6.05	4.08	1.97	*2.51*	6.05	4.08	1.97	*2.51*	6.05	4.08	1.97	*2.51*
CH_3	CH_3	CH_3	RIC_1	-26.35	-35.09	8.74	*8.44*	-56.86	-75.45	18.60	*30.40*	-56.47	-73.55	17.07	*29.75*	-53.82	-69.88	16.06	*28.99*
			TS_1	151.89	-49.84	201.73	*176.66*	73.96	-94.96	168.91	*146.40*	141.30	-80.09	221.40	*214.79*	37.68	-95.87	133.54	*127.39*
			PIC_1	-18.54	-53.78	35.24	*25.07*	-36.31	-86.00	49.69	*47.02*	-43.84	-89.60	45.76	*42.20*	-42.02	-90.17	48.15	*53.38*
			I	-18.54	-53.78	35.24	*25.07*	-18.54	-53.78	35.24	*25.07*	-18.54	-53.78	35.24	*25.07*	-18.54	-53.78	35.24	*25.07*
			RIC_2	-20.46	-54.69	34.23	*26.03*	-40.13	-90.39	50.26	*58.29*	-	-	-	-	-51.08	-96.72	45.64	*55.73*
			TS_2	118.49	-53.72	172.20	*139.78*	78.99	-94.28	173.27	*173.94*	-	-	-	-	12.70	-103.68	116.39	*96.47*
			PIC_2	-27.58	-28.19	0.61	*14.75*	-56.18	-71.28	15.11	*43.39*	-	-	-	-	-56.27	-70.34	14.06	*42.47*
			P	-19.70	7.27	-26.97	*-21.78*	-19.70	7.27	-26.97	*-21.78*	-19.70	7.27	-26.97	*-21.78*	-19.70	7.27	-26.97	*-21.78*

Table S4.4. Absolute thermodynamic values, Δ*H*° (Hartree), Δ*S*° (cal/K·mol), and Δ*G*° (Hartree), for the imines with R_1, R_2, and R_3 = H, CH_3, or CH_2CH_3, and water, obtained with B3LYP/6-31++G** computational level. Free energy of solvation, ΔG_{solv} (kcal/mol), obtained with PCM continuum model.

Imine			Absolute thermodynamic values			
R_1	**R_2**	**R_3**	**Δ*H*°**	**Δ*S*°**	**Δ*G*°**	**ΔG_{solv}**
H	H	H	–94.597006	54.266	–94.622789	–2.10
H	H	CH_3	–133.896800	62.741	–133.926611	–1.15
H	H	CH_2CH_3	–173.182590	70.691	–173.216177	–0.9
H	CH_3	CH_3	–173.192869	71.091	–173.226647	1.39
H	CH_3	CH_2CH_3	–212.479879	78.088	–212.516981	2.84
H	CH_2CH_3	CH_2CH_3	–251.765475	85.29	–251.805999	3.67
CH_3	H	H	–133.883210	62.218	–133.912772	2.87
CH_3	H	CH_3	–173.181838	70.508	–173.215339	4.25
CH_3	H	CH_2CH_3	–212.462304	81.511	–212.501032	3.78
CH_3	CH_3	CH_3	–212.471725	80.578	–212.510010	5.35
CH_3	CH_3	CH_2CH_3	–251.757873	87.996	–251.799683	5.89
CH_3	CH_2CH_3	CH_2CH_3	–291.043229	93.771	–291.087783	7.45
CH_2CH_3	H	H	–173.173713	69.829	–173.206891	3.51
CH_2CH_3	H	CH_3	–212.472311	78.148	–212.509442	4.99
CH_2CH_3	H	CH_2CH_3	–251.753286	89.108	–251.795624	4.38
CH_2CH_3	CH_3	CH_3	–251.762641	87.283	–251.804112	6.45
CH_2CH_3	CH_3	CH_2CH_3	–291.048818	94.527	–291.093731	7.03
CH_2CH_3	CH_2CH_3	CH_2CH_3	–330.333343	101.928	–330.381772	8.66
	H_2O		–76.409077	46.48	–76.431161	–6.68

Table S4.5. Relevant distances in Å at the different stationary points obtained for the hydrolysis of the imines with R_1, R_2 and R_3, = H, CH_3, or CH_2CH_3, with model IV at the B3LYP/6-31++G** computational level. Data already collected in Table S4.1 are not reported.

R_1	R_2	R_3	Stationary Point	N–C_I	N–H_1	N–H_2	C_I–O_C	O_C–H_2	O_2–H_1	O_2–H_2
H	H	CH_2CH_3	R	1.275	-	-	-	0.965	0.965	-
			RIC_1	1.279	1.816	3.306	3.345	0.982	0.993	1.819
			TS_1	1.309	1.106	2.471	2.184	1.173	1.488	1.263
			PIC_1	1.426	1.018	2.817	1.472	1.883	2.387	0.977
			I	1.458	1.018	-	1.423	-	-	0.965
			RIC_2	1.481	1.020	1.901	1.409	2.661	3.382	0.987
			TS_2	1.602	1.021	1.116	1.338	2.350	3.062	1.473
			PIC_2	3.140	1.017	1.022	1.222	3.244	3.636	2.133
			P	-	1.016	1.016	1.214	-	-	-
H	CH_3	CH_2CH_3	R	1.278	-	-	-	0.965	0.965	-
			RIC_1	1.282	1.811	3.472	3.960	0.981	0.994	1.836
			TS_1	1.313	1.077	2.479	2.259	1.202	1.593	1.233
			PIC_1	1.434	1.018	2.831	1.483	1.876	2.450	0.978
			I	1.443	1.017	-	1.458	-	-	0.965
			RIC_2	1.488	1.019	1.897	1.419	2.681	3.312	0.988
			TS_2	1.623	1.020	1.108	1.345	2.347	3.058	1.496
			PIC_2	4.209	1.017	1.022	1.228	3.604	3.611	2.108
			P	-	1.016	1.016	1.220	-	-	-
H	CH_2CH_3	CH_2CH_3	R	1.279	-	-	-	0.965	0.965	-
			RIC_1	1.282	1.809	3.691	4.445	0.982	0.994	1.810
			TS_1	1.314	1.077	2.481	2.257	1.199	1.595	1.236
			PIC_1	1.433	1.018	2.824	1.484	1.874	2.424	0.978
			I	1.465	1.018	-	1.433	-	-	0.965
			RIC_2	1.488	1.019	1.900	1.420	2.675	3.325	0.987
			TS_2	1.625	1.020	1.109	1.346	2.339	3.066	1.491
			PIC_2	4.011	1.017	1.022	1.230	3.621	3.626	2.110
			P	-	1.016	1.016	1.219	-	-	-
CH_3	H	CH_2CH_3	R	1.274	-	-	-	0.965	0.965	-
			RIC_1	1.279	1.797	3.361	3.413	0.982	0.996	1.819
			TS_1	1.304	1.078	2.505	2.258	1.207	1.578	1.228
			PIC_1	1.428	1.017	2.826	1.477	1.875	2.420	0.978
			I	1.458	1.018	-	1.423	-	-	0.965
			RIC_2	1.481	1.020	1.873	1.411	2.613	3.349	0.990
			TS_2	1.597	1.022	1.104	1.342	2.318	3.071	1.501
			PIC_2	3.140	1.017	1.021	1.223	3.227	3.642	2.142
			P	-	1.016	1.016	1.214	-	-	-
CH_3	CH_3	CH_2CH_3	R	1.279	-	-	-	0.965	0.965	-
			RIC_1	1.281	1.787	3.427	5.194	0.982	0.997	1.824
			TS_1	1.311	1.061	2.502	2.306	1.230	1.663	1.206
			PIC_1	1.435	1.017	2.840	1.486	1.871	2.458	0.978
			I	1.444	1.017	-	1.460	-	-	0.965
			RIC_2	1.494	1.019	1.868	1.421	2.633	3.261	0.991
			TS_2	1.620	1.021	1.099	1.351	2.316	3.017	1.521
			PIC_2	3.397	1.017	1.021	1.228	3.219	3.642	2.168
			P	-	1.016	1.016	1.220	-	-	-
CH_3	CH_2CH_3	CH_2CH_3	R	1.279	-	-	-	0.965	0.965	-
			RIC_1	1.283	1.799	3.789	4.582	0.981	0.997	1.817
			TS_1	1.312	1.059	2.503	2.322	1.234	1.671	1.203
			PIC_1	1.437	1.017	2.829	1.485	1.870	2.469	0.978
			I	1.472	1.018	-	1.432	-	-	0.965
			RIC_2	1.493	1.020	1.905	1.422	2.654	3.152	0.989
			TS_2	1.619	1.021	1.108	1.353	2.317	2.953	1.495
			PIC_2	3.923	1.017	1.021	1.229	3.570	3.648	2.129
			P	-	1.016	1.016	1.219	-	-	-

Table S4.5. (Cont.)

R_1	R_2	R_3	Stationary Point	N–C_I	N–H_1	N–H_2	C_I–O_C	O_C–H_2	O_2–H_1	O_2–H_2
CH_2CH_3	H	H	R	1.269	-	-	-	0.965	0.965	-
			RIC_1	1.273	1.838	3.351	3.331	0.981	0.992	1.830
			TS_1	1.299	1.096	2.491	2.169	1.156	1.529	1.288
			PIC_1	1.414	1.018	2.842	1.472	1.884	2.435	0.977
			I	1.424	1.017	-	1.448	-	-	0.965
			RIC_2	1.474	1.020	1.891	1.403	2.654	3.327	0.989
			TS_2	1.581	1.022	1.102	1.339	2.353	3.054	1.516
			PIC_2	2.566	1.018	1.022	1.223	2.978	3.635	2.147
			P	-	1.017	1.017	1.209	-	-	-
CH_2CH_3	H	CH_3	R	1.271	-	-	-	0.965	0.965	-
			RIC_1	1.275	1.825	3.695	4.374	0.981	0.994	1.815
			TS_1	1.304	1.073	2.484	2.232	1.174	1.621	1.266
			PIC_1	1.422	1.019	2.848	1.478	1.882	2.477	0.978
			I	1.431	1.018	-	1.453	-	-	0.965
			RIC_2	1.481	1.021	1.879	1.411	2.619	3.341	0.990
			TS_2	1.598	1.022	1.100	1.342	2.321	3.082	1.515
			PIC_2	3.109	1.018	1.022	1.222	3.212	3.655	2.156
			P	-	1.017	1.017	1.214	-	-	-
CH_2CH_3	H	CH_2CH_3	R	1.274	-	-	-	0.965	0.965	-
			RIC_1	1.280	1.810	3.371	3.405	0.982	0.995	1.818
			TS_1	1.304	1.075	2.514	2.266	1.204	1.592	1.230
			PIC_1	1.428	1.018	2.830	1.477	1.872	2.439	0.978
			I	1.457	1.019	-	1.424	-	-	0.965
			RIC_2	1.480	1.021	1.876	1.411	2.608	3.353	0.990
			TS_2	1.595	1.022	1.101	1.344	2.315	3.089	1.511
			PIC_2	3.148	1.018	1.022	1.222	3.233	3.680	2.153
			P	-	1.017	1.017	1.214	-	-	-
CH_2CH_3	CH_3	CH_3	R	1.278	-	-	-	0.965	0.965	-
			RIC_1	1.282	1.806	3.633	5.277	0.981	0.996	1.829
			TS_1	1.310	1.060	2.510	2.310	1.221	1.678	1.214
			PIC_1	1.435	1.018	2.852	1.486	1.870	2.497	0.978
			I	1.445	1.018	-	1.459	-	-	0.965
			RIC_2	1.493	1.021	1.876	1.421	2.639	3.255	0.991
			TS_2	1.619	1.022	1.096	1.351	2.317	3.029	1.532
			PIC_2	4.058	1.018	1.022	1.228	3.639	3.680	2.121
			P	-	1.017	1.017	1.219	-	-	-
CH_2CH_3	CH_3	CH_2CH_3	R	1.279	-	-	-	0.965	0.965	-
			RIC_1	1.284	1.823	3.824	4.576	0.981	0.995	1.818
			TS_1	1.311	1.060	2.512	2.312	1.223	1.681	1.212
			PIC_1	1.435	1.019	2.847	1.487	1.866	2.484	0.978
			I	1.444	1.018	-	1.460	-	-	0.965
			RIC_2	1.492	1.019	1.865	1.425	2.591	3.310	0.991
			TS_2	1.633	1.022	1.100	1.351	2.273	3.073	1.514
			PIC_2	3.464	1.018	1.021	1.228	3.237	3.630	2.169
			P	-	1.017	1.017	1.220	-	-	-
CH_2CH_3	CH_2CH_3	CH_2CH_3	R	1.278	-	-	-	0.965	0.965	-
			RIC_1	1.283	1.816	3.841	4.634	0.981	0.996	1.820
			TS_1	1.312	1.057	2.514	2.330	1.228	1.692	1.208
			PIC_1	1.437	1.018	2.841	1.485	1.867	2.502	0.978
			I	1.446	1.018	-	1.459	-	-	0.965
			RIC_2	1.493	1.018	1.863	1.425	2.604	3.262	0.992
			TS_2	1.632	1.021	1.099	1.353	2.275	3.052	1.516
			PIC_2	3.410	1.018	1.021	1.228	3.210	3.644	2.171
			P	-	1.017	1.017	1.219	-	-	-

Table S4.6. Mulliken charges on relevant atoms at the different stationary points obtained for the hydrolysis of the imines with R_1, R_2, and R_3 = H, CH_3, or CH_2CH_3, with model IV at the B3LYP/6-31++G** computational level. Data collected in Table S4.2 are not reported.

R_1	R_2	R_3	Stationary Point	N	C_I	H_1	O_C	H_2
H	H	CH_2CH_3	R	–0.33	–0.08	0.34	–0.69	0.34
			RIC_1	–0.49	0.14	0.46	–0.78	0.43
			TS_1	–0.30	–0.29	0.45	–0.81	0.53
			PIC_1	–0.46	–0.24	0.34	–0.54	0.42
			I	–0.47	–0.30	0.30	–0.49	0.34
			RIC_2	–0.63	–0.24	0.32	–0.50	0.45
			TS_2	–0.63	–0.16	0.36	–0.58	0.47
			PIC_2	–0.97	0.28	0.28	–0.40	0.36
			P	–0.85	0.15	0.28	–0.37	0.28
H	CH_3	CH_2CH_3	R	–0.37	0.09	0.34	–0.69	0.34
			RIC_1	–0.48	0.27	0.45	–0.78	0.43
			TS_1	–0.29	–0.05	0.42	–0.81	0.53
			PIC_1	–0.38	–0.47	0.34	–0.48	0.44
			I	–0.47	–0.26	0.30	–0.42	0.34
			RIC_2	–0.63	–0.39	0.32	–0.41	0.46
			TS_2	–0.65	–0.38	0.35	–0.49	0.48
			PIC_2	–0.94	0.41	0.28	–0.44	0.36
			P	–0.85	0.35	0.28	–0.42	0.28
H	CH_2CH_3	CH_2CH_3	R	–0.34	–0.05	0.34	–0.69	0.34
			RIC_1	–0.49	0.16	0.45	–0.78	0.43
			TS_1	–0.25	–0.41	0.42	–0.79	0.54
			PIC_1	–0.36	–0.71	0.34	–0.46	0.45
			I	–0.46	–0.36	0.30	–0.44	0.34
			RIC_2	–0.57	–0.65	0.32	–0.44	0.47
			TS_2	–0.65	–0.53	0.35	–0.53	0.48
			PIC_2	–0.95	0.29	0.28	–0.43	0.37
			P	–0.85	0.11	0.28	–0.40	0.28
CH_3	H	CH_2CH_3	R	–0.10	–0.26	0.34	–0.69	0.34
			RIC_1	–0.24	–0.09	0.45	–0.77	0.43
			TS_1	–0.09	–0.33	0.45	–0.85	0.51
			PIC_1	–0.25	–0.27	0.35	–0.52	0.41
			I	–0.32	–0.17	0.32	–0.47	0.34
			RIC_2	–0.52	–0.10	0.34	–0.49	0.44
			TS_2	–0.51	–0.06	0.37	–0.58	0.49
			PIC_2	–0.68	0.26	0.29	–0.39	0.37
			P	–0.57	0.15	0.28	–0.37	0.28
CH_3	CH_3	CH_2CH_3	R	–0.13	0.12	0.34	–0.69	0.34
			RIC_1	–0.28	0.27	0.43	–0.77	0.42
			TS_1	–0.04	–0.11	0.42	–0.83	0.52
			PIC_1	–0.08	–0.68	0.36	–0.45	0.45
			I	–0.18	–0.37	0.31	–0.42	0.34
			RIC_2	–0.43	–0.41	0.34	–0.43	0.46
			TS_2	–0.46	–0.35	0.37	–0.52	0.50
			PIC_2	–0.67	0.53	0.29	–0.44	0.36
			P	–0.57	0.35	0.28	–0.42	0.28
CH_3	CH_2CH_3	CH_2CH_3	R	–0.09	–0.06	0.34	–0.69	0.34
			RIC_1	–0.29	0.13	0.43	–0.78	0.42
			TS_1	–0.02	–0.36	0.41	–0.82	0.53
			PIC_1	–0.05	–0.91	0.37	–0.45	0.44
			I	–0.26	–0.60	0.33	–0.43	0.34
			RIC_2	–0.43	–0.83	0.35	–0.41	0.45
			TS_2	–0.49	–0.72	0.37	–0.52	0.50
			PIC_2	–0.65	0.21	0.29	–0.42	0.37
			P	–0.57	0.11	0.28	–0.40	0.28

Table S4.6. (Cont.)

R_1	R_2	R_3	Stationary Point	N	C_I	H_1	O_C	H_2
CH_2CH_3	H	H	R	–0.06	–0.14	0.34	–0.69	0.34
			RIC_1	–0.18	–0.11	0.44	–0.78	0.42
			TS_1	–0.11	–0.09	0.43	–0.83	0.51
			PIC_1	–0.30	–0.05	0.32	–0.57	0.41
			I	–0.32	–0.08	0.29	–0.50	0.34
			RIC_2	–0.51	–0.05	0.32	–0.48	0.43
			TS_2	–0.52	–0.01	0.36	–0.59	0.47
			PIC_2	–0.68	0.15	0.30	–0.39	0.37
			P	–0.53	0.11	0.28	–0.32	0.28
CH_2CH_3	H	CH_3	R	–0.09	0.10	0.34	–0.69	0.34
			RIC_1	–0.19	0.16	0.45	–0.77	0.43
			TS_1	–0.08	0.09	0.40	–0.83	0.51
			PIC_1	–0.21	–0.23	0.32	–0.48	0.42
			I	–0.27	–0.03	0.29	–0.47	0.34
			RIC_2	–0.53	0.12	0.32	–0.48	0.43
			TS_2	–0.54	0.11	0.35	–0.58	0.48
			PIC_2	–0.66	0.38	0.28	–0.40	0.36
			P	–0.53	0.23	0.28	–0.37	0.28
CH_2CH_3	H	CH_2CH_3	R	–0.12	–0.18	0.34	–0.69	0.34
			RIC_1	–0.29	0.01	0.44	–0.77	0.43
			TS_1	–0.08	–0.32	0.45	–0.85	0.51
			PIC_1	–0.24	–0.26	0.35	–0.51	0.41
			I	–0.33	–0.06	0.31	–0.46	0.34
			RIC_2	–0.53	–0.03	0.33	–0.48	0.43
			TS_2	–0.53	–0.02	0.37	–0.58	0.48
			PIC_2	–0.66	0.24	0.28	–0.39	0.36
			P	–0.53	0.15	0.28	–0.37	0.28
CH_2CH_3	CH_3	CH_3	R	–0.13	0.32	0.34	–0.69	0.34
			RIC_1	–0.30	0.53	0.39	–0.77	0.43
			TS_1	–0.07	0.19	0.41	–0.83	0.52
			PIC_1	–0.13	–0.42	0.35	–0.45	0.44
			I	–0.22	–0.25	0.29	–0.40	0.34
			RIC_2	–0.44	–0.19	0.32	–0.41	0.46
			TS_2	–0.48	–0.21	0.35	–0.51	0.51
			PIC_2	–0.65	0.54	0.28	–0.44	0.37
			P	–0.53	0.41	0.28	–0.42	0.28
CH_2CH_3	CH_3	CH_2CH_3	R	–0.12	0.11	0.34	–0.69	0.34
			RIC_1	–0.29	0.19	0.42	–0.78	0.42
			TS_1	–0.03	–0.18	0.41	–0.82	0.53
			PIC_1	–0.06	–0.76	0.36	–0.44	0.45
			I	–0.16	–0.45	0.30	–0.40	0.34
			RIC_2	–0.45	–0.40	0.33	–0.42	0.47
			TS_2	–0.44	–0.33	0.35	–0.53	0.51
			PIC_2	–0.62	0.47	0.27	–0.43	0.38
			P	–0.53	0.35	0.28	–0.42	0.28
CH_2CH_3	CH_2CH_3	CH_2CH_3	R	–0.05	–0.07	0.34	–0.69	0.34
			RIC_1	–0.25	0.00	0.42	–0.78	0.42
			TS_1	0.00	–0.45	0.42	–0.81	0.52
			PIC_1	–0.02	–1.05	0.37	–0.43	0.44
			I	–0.12	–0.79	0.31	–0.38	0.34
			RIC_2	–0.45	–0.89	0.33	–0.43	0.47
			TS_2	–0.46	–0.79	0.34	–0.53	0.52
			PIC_2	–0.63	0.50	0.27	–0.41	0.38
			P	–0.53	0.11	0.28	–0.40	0.28

Table S4.7. Thermodynamic parameters, Δ*H°*, *TΔS°*, and Δ*G°*, for the hydrolysis of imines with R_1, R_2, and R_3 = H, CH_3, or CH_2CH_3, obtained with model IV and B3LYP/6-31++G** computational level. Reactants (R) were taken as reference. All values in kJ·mol^{-1}, data obtained with PCM continuum model in italics.

R_1	R_2	R_3	Stationary Point	Δ*H°*	*TΔS°*	Δ*G°*	
H	H	CH_2CH_3	RIC_1	–59.43	–75.57	16.14	*36.39*
			TS_1	37.99	–93.03	131.02	*121.73*
			PIC_1	–62.53	–86.02	23.50	*38.27*
			I	–40.24	–49.42	9.18	*7.46*
			RIC_2	–72.98	–90.88	17.90	*36.31*
			TS_2	0.87	–98.35	99.22	*77.01*
			PIC_2	–57.95	–67.83	9.88	*46.99*
			P	–23.73	2.37	–26.10	*–11.84*
H	CH_3	CH_2CH_3	RIC_1	–55.88	–74.32	18.43	*32.62*
			TS_1	40.69	–94.78	135.47	*132.12*
			PIC_1	–48.28	–88.83	40.55	*47.62*
			I	–25.32	–51.43	26.10	*17.94*
			RIC_2	–55.62	–93.42	37.80	*51.36*
			TS_2	17.85	–100.29	118.14	*98.69*
			PIC_2	–62.17	–68.51	6.34	*36.76*
			P	–26.58	3.42	–30.00	*–22.80*
H	CH_2CH_3	CH_2CH_3	RIC_1	–58.21	–73.73	15.52	*31.29*
			TS_1	39.56	–94.27	133.83	*131.70*
			PIC_1	–48.33	–88.29	39.96	*48.87*
			I	–26.43	–52.20	25.77	*17.94*
			RIC_2	–57.60	–94.55	36.95	*49.08*
			TS_2	15.19	–100.71	115.89	*91.00*
			PIC_2	–62.62	–71.37	8.75	*40.38*
			P	–38.38	4.78	–43.17	*–34.17*
CH_3	H	CH_2CH_3	RIC_1	–58.29	–73.33	15.04	*36.00*
			TS_1	33.28	–94.76	128.04	*121.09*
			PIC_1	–50.34	–88.82	38.47	*49.44*
			I	–34.78	–53.36	18.58	*12.27*
			RIC_2	–66.70	–95.08	28.37	*42.14*
			TS_2	–2.42	–101.74	99.31	*81.49*
			PIC_2	–43.28	–68.90	25.61	*58.08*
			P	–10.49	0.44	–10.93	*–6.58*
CH_3	CH_3	CH_2CH_3	RIC_1	–56.37	–75.12	18.75	*32.94*
			TS_1	37.06	–95.85	132.91	*128.48*
			PIC_1	–41.42	–90.63	49.21	*56.66*
			I	–17.86	–54.25	36.39	*27.48*
			RIC_2	–49.58	–97.04	47.46	*58.96*
			TS_2	12.71	–104.04	116.75	*99.72*
			PIC_2	–51.11	–68.54	17.43	*46.64*
			P	–17.86	2.62	–20.48	*–16.38*
CH_3	CH_2CH_3	CH_2CH_3	RIC_1	–56.19	–70.37	14.18	*27.86*
			TS_1	37.10	–96.46	133.56	*126.19*
			PIC_1	–39.61	–90.60	50.99	*60.78*
			I	–17.35	–53.67	36.32	*29.83*
			RIC_2	–43.74	–96.95	53.21	*60.57*
			TS_2	17.70	–103.63	121.33	*102.97*
			PIC_2	–57.92	–69.12	11.20	*39.44*
			P	–30.29	5.76	–36.05	*–33.21*

Table S4.7. (Cont.)

R_1	R_2	R_3	Stationary Point	$\Delta H°$	$T\Delta S°$	$\Delta G°$	
CH_2CH_3	H	H	RIC_1	–54.59	–75.65	21.06	*37.17*
			TS_1	48.70	–91.03	139.73	*130.49*
			PIC_1	–51.87	–82.46	30.59	*31.43*
			I	–28.78	–46.16	17.38	*–0.44*
			RIC_2	–60.35	–88.48	28.13	*34.82*
			TS_2	8.73	–95.52	104.26	*75.18*
			PIC_2	–16.39	–72.44	56.06	*76.06*
			P	18.01	2.83	15.19	*19.58*
CH_2CH_3	H	CH_3	RIC_1	–53.85	–74.52	20.67	*32.80*
			TS_1	52.69	–92.89	145.58	*136.92*
			PIC_1	–40.82	–85.24	44.42	*48.02*
			I	–17.83	–48.57	30.74	*16.27*
			RIC_2	–48.83	–90.65	41.82	*49.94*
			TS_2	15.66	–97.18	112.83	*88.57*
			PIC_2	–28.37	–66.35	37.98	*64.80*
			P	4.11	3.90	0.21	*–0.92*
CH_2CH_3	H	CH_2CH_3	RIC_1	–57.75	–76.16	18.41	*39.24*
			TS_1	35.13	–95.12	130.24	*125.05*
			PIC_1	–48.62	–88.91	40.29	*54.35*
			I	–33.62	–53.40	19.78	*14.50*
			RIC_2	–65.11	–94.87	29.76	*45.11*
			TS_2	–1.55	–101.72	100.16	*83.59*
			PIC_2	–43.51	–68.58	25.07	*58.25*
			P	–11.08	0.32	–11.40	*–8.14*
CH_2CH_3	CH_3	CH_3	RIC_1	–53.58	–74.73	21.15	*31.61*
			TS_1	39.65	–94.73	134.37	*128.30*
			PIC_1	–40.32	–89.08	48.76	*55.58*
			I	–17.08	–52.68	35.59	*25.68*
			RIC_2	–49.40	–95.65	46.24	*57.25*
			TS_2	13.54	–102.75	116.29	*96.70*
			PIC_2	–56.57	–69.15	12.58	*40.20*
			P	–20.47	8.26	–28.73	*–26.72*
CH_2CH_3	CH_3	CH_2CH_3	RIC_1	–54.42	–74.18	19.76	*33.45*
			TS_1	39.11	–94.56	133.67	*129.49*
			PIC_1	–39.58	–89.14	49.56	*59.52*
			I	–16.18	–53.25	37.08	*29.13*
			RIC_2	–36.36	–97.19	60.83	*68.91*
			TS_2	22.92	–103.04	125.96	*106.88*
			PIC_2	–50.91	–67.99	17.08	*47.20*
			P	–18.55	3.83	–22.38	*–21.62*
CH_2CH_3	CH_2CH_3	CH_2CH_3	RIC_1	–54.85	–73.30	18.45	*31.51*
			TS_1	37.12	–97.22	134.34	*126.60*
			PIC_1	–40.15	–89.91	49.76	*60.85*
			I	–16.77	–54.49	37.71	*30.89*
			RIC_2	–37.14	–98.17	61.03	*72.32*
			TS_2	20.05	–103.29	123.34	*108.65*
			PIC_2	–60.10	–68.04	7.93	*40.52*
			P	–33.17	4.94	–38.11	*–38.90*

Table S4.8. Intrinsic activation barriers ($\Delta G^\circ_{int} = \Delta G^\circ_{TS} - \Delta G^\circ_{RIC}$) in kJ·mol^{-1} for both steps of the reverse reaction (imine formation from carbonyl compound and amine) with R_1, R_2, and R_3 = H, CH_3, or CH_2CH_3, obtained with model IV at the B3LYP/6-31++G** computational level. Values obtained with PCM continuum model in italics. Data already collected in Table 4.4 are not reported.

Imine			ΔG°_{int}	
R_1	**R_2**	**R_3**	**Step 1**	**Step 2**
H	H	CH_2CH_3	89.34	107.52
			30.01	*83.47*
H	CH_3	CH_2CH_3	111.80	94.91
			61.93	*84.49*
H	CH_2CH_3	CH_2CH_3	107.14	93.87
			50.62	*82.83*
CH_3	H	CH_2CH_3	73.70	89.56
			23.41	*71.66*
CH_3	CH_3	CH_2CH_3	99.31	83.70
			53.08	*71.82*
CH_3	CH_2CH_3	CH_2CH_3	110.14	82.57
			63.53	*65.41*
CH_2CH_3	H	H	48.20	109.14
			–0.88	*99.06*
CH_2CH_3	H	CH_3	74.85	101.16
			23.77	*88.90*
CH_2CH_3	H	CH_2CH_3	75.09	89.95
			25.34	*70.71*
CH_2CH_3	CH_3	CH_3	103.70	85.61
			56.51	*72.72*
CH_2CH_3	CH_3	CH_2CH_3	108.88	84.11
			59.68	*69.96*
CH_2CH_3	CH_2CH_3	CH_2CH_3	115.40	84.58
			68.12	*65.75*

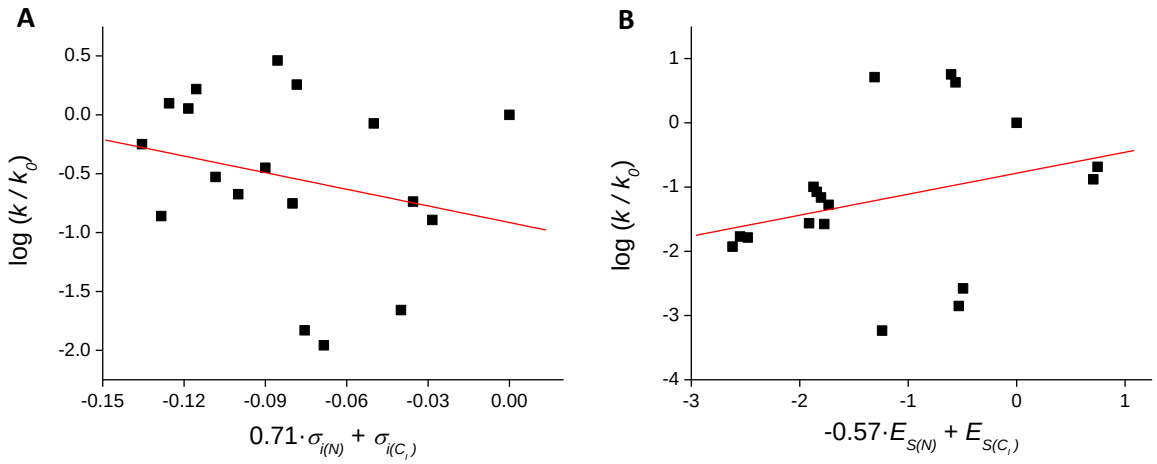

Figure S4.1. Best Hammett plots for the first step of the hydrolysis reaction calculated *in vacuo* (A) and with PCM solvation (B) employing inductive σ_i and E_S scales, respectively, at the B3LYP/6-31++G** computational level with model IV.

Supplementary information 5

Density functional study of the decomposition of ethanolimines: Hydrolysis and fragmentation reactions

Table S5.1. Thermodynamic parameters, Δ*H*°, *T*Δ*S*°, and Δ*G*°, for the hydrolysis and fragmentation processes of the simplest ethanolimine (CH_2=NCH_2CH_2OH), obtained with models I to V at the B3LYP/6-31++G** computational level. Results obtained for the hydrolysis of the parent imine (CH_2=NCH_2CH_3) with model IV are also collected. Reactants (R) were taken as reference. All values in kJ·mol^{-1}, data obtained with PCM continuum model in italics.

Hydrolysis					Fragmentation					Hydrolysis of CH_2=NCH_2CH_3				
	Δ*H*°	*T*Δ*S*°	Δ*G*°			Δ*H*°	*T*Δ*S*°	Δ*G*°			Δ*H*°	*T*Δ*S*°	Δ*G*°	
Model I														
RIC_1	–29.58	–41.98	12.39	*22.19*	RIC_{Frag}	0.08	–0.18	0.27	*0.22*					
TS_1	168.69	–44.57	213.26	*181.63*	TS_{Frag}	171.51	–5.79	177.31	*185.80*					
PIC_1	–32.76	–47.65	14.89	*–0.59*	PIC_{Frag}	49.94	18.39	31.56	*57.83*					
I	–32.76	–47.65	14.89	*–0.59*	P	55.38	49.90	5.48	*34.68*					
RIC_2	–17.02	–45.75	28.73	*9.40*										
TS_2	131.79	–49.10	180.89	*131.10*										
PIC_2	10.45	–24.64	35.09	*44.84*										
P	24.35	3.46	20.90	*16.92*										
Model II														
RIC_1	–49.96	–73.74	23.78	*38.63*	RIC_{Frag}	–20.79	–34.99	14.20	*27.17*					
TS_1	107.24	–83.38	190.63	*167.41*	TS_{Frag}	157.76	–36.40	194.17	*211.03*					
PIC_1	–56.13	–84.27	28.14	*32.41*	PIC_{Frag}	28.94	–21.48	50.42	*88.96*					
I	–32.76	–47.65	14.89	*–0.59*	P	55.38	49.90	5.48	*34.68*					
RIC_2	–41.57	–81.58	40.01	*41.56*										
TS_2	87.06	–88.02	175.08	*166.21*										
PIC_2	–14.99	–65.98	50.99	*82.62*										
P	24.35	3.46	20.90	*16.92*										
Model III														
RIC_1	–70.18	–81.11	10.92	*33.69*	RIC_{Frag}	–29.55	–41.94	12.39	*32.14*					
TS_1	148.32	–88.24	236.56	*245.09*	TS_{Frag}	150.69	–39.30	189.99	*212.29*					
PIC_1	–54.00	–86.31	32.32	*30.10*	PIC_{Frag}	20.96	–17.99	38.96	*83.47*					
I	–32.76	–47.65	14.89	*–0.59*	P	55.38	49.90	5.48	*34.68*					
RIC_2	-	-	-	-										
TS_2	-	-	-	-										
PIC_2	-	-	-	-										
P	24.35	3.46	20.90	*16.92*										
Model IV														
RIC_1	–70.16	–80.83	10.68	*33.52*	RIC_{Frag}	–71.36	–82.04	10.68	*44.77*	RIC_1	–54.59	–75.65	21.06	*37.17*
TS_1	15.54	–96.73	112.27	*111.86*	TS_{Frag}	127.59	–84.25	211.85	*248.58*	TS_1	48.70	–91.03	139.73	*130.49*
PIC_1	–58.86	–86.11	27.25	*34.57*	PIC_{Frag}	–8.19	–48.97	40.78	*104.50*	PIC_1	–51.87	–82.46	30.59	*31.43*
I	–32.76	–47.65	14.89	*–0.59*	P	55.38	49.90	5.48	*34.68*	I	–28.78	–46.16	17.38	*–0.44*
RIC_2	–57.52	–88.84	31.32	*33.79*						RIC_2	–60.35	–88.48	28.13	*34.82*
TS_2	11.84	–96.12	107.96	*75.28*						TS_2	8.73	–95.52	104.26	*75.18*
PIC_2	–13.43	–71.76	58.33	*73.94*						PIC_2	–16.39	–72.44	56.06	*76.06*
P	24.35	3.46	20.90	*16.92*						P	18.01	2.83	15.19	*19.58*
Model V														
RIC_1	–56.32	–79.98	23.66	*50.44*	RIC_{Frag}	–29.60	–41.95	12.35	*32.10*					
TS_1	146.03	–83.44	229.47	*211.35*	TS_{Frag}	205.76	–47.98	253.74	*262.15*					
PIC_1	–55.02	–81.04	26.02	*24.84*	PIC_{Frag}	28.91	–21.54	50.45	*89.03*					
I	–32.76	–47.65	14.89	*–0.59*	P	55.38	49.90	5.48	*34.68*					
RIC_2	–34.12	–77.36	43.25	*30.86*										
TS_2	116.20	–80.34	196.54	*153.86*										
PIC_2	–16.22	–59.27	43.05	*71.17*										
P	24.35	3.46	20.90	*16.92*										

Table S5.2. Absolute thermodynamic values, Δ*H*° (Hartree), Δ*S*° (cal·K^{-1}·mol^{-1}), and Δ*G*° (Hartree), for the reactants taken as reference in Table S5.1, obtained with B3LYP/6-31++G** computational level. Free energy of solvation, ΔG_{solv} (kcal·mol^{-1}), obtained with PCM continuum model.

	Absolute thermodynamic values			
	Δ*H*°	Δ*S*°	Δ*G*°	ΔG_{solv}
CH_2=NCH_2CH_2OH	–248.385443	75.843	–248.421479	–2.33
CH_2=NCH_2CH_3	–173.173713	69.829	–173.206891	3.51
H_2O	–76.409077	46.48	–76.431161	–6.68

Supplementary information 11

Understanding the origin of the shared reactivity and properties of peroxidases: a DFT study

Table S11.1. Relevant geometrical parameters for all studied species fully optimized at the UB3LYP/6-31G* computational level for all considered spin states. Distance (Å) between iron and imidazole nitrogen atom (Fe–N_i), the metal centre and either ferryl or water oxygen (Fe–O) or proton (Fe–H), and between ferryl oxygen and proton or hydrogen atom from the water molecule (O–H); mean distance (Å) between iron and the four pyrrole nitrogen atoms (Fe–N_p); and distance (Å) from Fe atom to heme pyrrole plane (Fe–pp). Positive values of the latter indicate displacement towards distal side, while negative figures stand for out-of-plane Fe placed at the opposite side. Bond orders are shown in parentheses, values under Fe–N_p account for total iron-pyrrole nitrogen bond order, *i.e.*, the overall order of those four covalent bonds. N_i–Fe–O, N_i–Fe–H, and Fe–O–H stand for the angles (°) among these atoms. Results of experimentally feasible spin multiplicities in bold.

Species	Spin	Fe–N_i	Fe–N_p	Fe–pp	Fe–O/H	O–H	N_i–Fe–O/H	Fe–O–H
Fe(III)-PO	**1/2**	**1.930 (0.48)**	**1.988 (2.06)**	**–0.213**				
	3/2	2.133 (0.27)	1.994 (1.89)	–0.215				
	5/2	**2.087 (0.27)**	**2.061 (1.79)**	**–0.383**				
	7/2	2.083 (0.28)	2.065 (1.33)	–0.338				
Fe(III)-PO-H_2O	**1/2**	**1.948 (0.50)**	**2.003 (1.96)**	**–0.068**	**2.028 (0.32)**		**179.48**	
	3/2	2.196 (0.24)	2.000 (1.82)	–0.082	2.333 (0.16)		179.23	
	5/2	**2.140 (0.26)**	**2.057 (1.27)**	**–0.149**	**2.292 (0.17)**		**179.50**	
	7/2	2.145 (0.44)	2.067 (2.00)	–0.116	2.248 (0.26)		179.15	
Fe(III)-PO-H	**1/2**	**2.106 (0.35)**	**1.983 (1.90)**	**–0.129**	**1.498 (0.81)**		**179.38**	
	3/2	2.113 (0.34)	1.981 (2.11)	–0.131	1.500 (0.78)		179.48	
	5/2	**2.080 (0.35)**	**2.061 (1.99)**	**–0.296**	**1.546 (0.72)**		**179.46**	
	7/2	2.064 (0.30)	2.064 (1.31)	–0.432	3.773 (0.03)		179.46	
Fe(II)-PO	**0**	**1.924 (0.48)**	**2.001 (1.79)**	**–0.154**				
	1	**2.249 (0.35)**	**2.001 (2.01)**	**–0.108**				
	2	**2.164 (0.25)**	**2.085 (1.78)**	**–0.311**				
	3	2.110 (0.27)	2.061 (1.41)	–0.335				
	4	2.106 (0.26)	2.068 (1.38)	–0.270				
Fe(II)-PO-H_2O	**0**	**1.972 (0.43)**	**2.011 (1.75)**	**–0.069**	**2.088 (0.26)**		**178.16**	
	1	**2.305 (0.35)**	**2.010 (1.91)**	**–0.084**	**2.656 (0.17)**		**169.67**	
	2	**2.222 (0.20)**	**2.082 (1.06)**	**–0.175**	**2.490 (0.12)**		**172.90**	
	3	2.155 (0.24)	2.064 (1.29)	–0.142	2.308 (0.16)		171.22	
	4	2.161 (0.24)	2.074 (1.27)	–0.113	2.271 (0.17)		173.04	
Fe(II)-PO-H	**0**	**2.080 (0.38)**	**2.002 (2.14)**	**–0.078**	**1.520 (0.77)**		**179.62**	
	1	**2.165 (0.31)**	**1.983 (1.96)**	**–0.085**	**1.495 (0.81)**		**179.46**	
	2	**2.127 (0.30)**	**1.977 (1.60)**	**–0.102**	**1.496 (0.72)**		**179.76**	
	3	2.089 (0.23)	2.060 (1.06)	–0.376	3.360 (0.04)		171.25	
	4	2.289 (0.27)	2.074 (2.08)	–0.010	1.767 (0.61)		179.35	
PO-I	**1/2**	**2.154 (0.28)**	**2.016 (1.77)**	**0.088**	**1.620 (1.46)**		**179.87**	
	3/2	2.152 (0.28)	2.017 (1.77)	0.090	1.620 (1.46)		179.84	
	5/2	**2.156 (0.28)**	**2.018 (1.76)**	**0.096**	**1.619 (1.46)**		**179.80**	
	7/2	2.322 (0.28)	2.081 (1.87)	0.071	1.895 (1.03)		179.83	
PO-I-H_2O	**1/2**	**2.146 (0.29)**	**2.015 (1.79)**	**0.095**	**1.625 (1.41)**	**1.920 (0.04)**	**179.83**	**123.54**
	3/2	2.146 (0.29)	2.014 (1.79)	0.097	1.625 (1.41)	1.921 (0.04)	179.93	123.32
	5/2	**2.156 (0.28)**	**2.080 (1.20)**	**0.143**	**1.619 (1.40)**	**1.956 (0.03)**	**179.98**	**122.11**
	7/2	2.305 (0.20)	2.078 (1.09)	0.058	1.913 (0.54)	1.866 (0.06)	178.68	116.34
PO-I-H	**1/2**	**2.040 (0.42)**	**1.994 (2.05)**	**0.047**	**1.744 (0.92)**	**0.976 (0.72)**	**179.57**	**115.18**
	3/2	2.044 (0.41)	1.992 (2.06)	0.048	1.745 (0.92)	0.976 (0.72)	179.40	114.92
	5/2	**2.125 (0.31)**	**2.060 (1.32)**	**0.058**	**1.787 (0.78)**	**0.972 (0.74)**	**177.52**	**117.80**
	7/2	2.379 (0.19)	2.088 (1.03)	0.230	1.803 (0.63)	0.968 (0.72)	179.39	141.82

Table S11.1. Cont.

Species	Spin	Fe–N_i	Fe–N_p	Fe–pp	Fe–O/H	O–H	N_i–Fe–O/H	Fe–O–H
PO-II	0	2.181 (0.26)	2.018 (1.84)	0.119	1.623 (1.92)		179.98	
	1	**2.196 (0.25)**	**2.018 (1.80)**	**0.119**	**1.618 (1.47)**		**179.92**	
	2	**2.179 (0.25)**	**2.029 (1.76)**	**0.119**	**1.618 (1.47)**		**179.71**	
	3	2.488 (0.16)	2.078 (1.16)	0.189	1.895 (1.05)		179.63	
	4	2.386 (0.18)	2.090 (1.16)	0.168	1.888 (1.07)		179.63	
PO-II-H_2O	0	2.179 (0.26)	2.016 (1.86)	0.123	1.625 (1.85)	1.895 (0.04)	179.75	124.80
	1	**2.184 (0.25)**	**2.016 (1.82)**	**0.122**	**1.624 (1.42)**	**1.892 (0.04)**	**179.70**	**124.65**
	2	**2.206 (0.24)**	**2.079 (1.24)**	**0.188**	**1.620 (1.40)**	**1.927 (0.04)**	**179.83**	**124.72**
	3	2.441 (0.21)	2.074 (1.79)	0.159	1.912 (0.90)	1.859 (0.05)	179.22	120.57
	4	2.355 (0.17)	2.086 (1.11)	0.141	1.905 (0.54)	1.857 (0.06)	177.70	119.59
PO-II-H	0	2.010 (0.44)	2.006 (2.17)	0.044	1.750 (1.03)	0.976 (0.74)	164.35	111.30
	1	**2.062 (0.38)**	**1.995 (2.08)**	**0.065**	**1.748 (0.92)**	**0.975 (0.73)**	**179.49**	**111.34**
	2	**2.493 (0.17)**	**2.088 (1.69)**	**0.271**	**1.817 (0.65)**	**0.969 (0.73)**	**179.56**	**124.89**
	3	2.420 (0.17)	2.092 (1.05)	0.250	1.823 (0.60)	0.968 (0.74)	179.39	128.39
	4	2.427 (0.16)	2.093 (1.05)	0.261	1.824 (0.61)	0.968 (0.74)	179.04	127.84

Table S11.2. Relevant geometrical parameters obtained experimentally for selected peroxidases: horseradish peroxidase (HRP), cytochrome c peroxidase (CCP), ascorbate peroxidase (APX), lactoperoxidase (LPO), and myeloperoxidase (MPO). Distance (Å) between iron and imidazole nitrogen atom (Fe–N_i), the metal centre and either ferryl or water oxygen (Fe–O), and between ferryl oxygen and its proton (O–H); mean distance (Å) between iron and the four pyrrole nitrogen atoms (Fe–N_p); and distance (Å) from Fe atom to heme pyrrole plane (Fe–pp). Positive values of the latter indicate displacement towards distal side, while negative figures stand for out-of-plane Fe placed at the opposite side. N_i–Fe–O and Fe–O–H stand for the angles (°) among these atoms.

Species	Peroxidase	PDB	Fe–N_i	Fe–N_p	Fe–pp	Fe–O	O–H	N_i–Fe–O	Fe–O–H
Ferric	HRP	1W4W[a]	2.093	2.021	–0.140	-		-	
	CCP	1ZBY[b]	2.107	2.039	–0.274	2.330		176.15	
	CCP*	4CVI[c]	2.024	2.055	–0.181	2.651		169.64	
	APX	1OAG[d]	2.018	2.038	–0.199	1.944		176.90	
	LPO	2GJ1[e]	2.145	2.051	–0.203	-		-	
	MPO	1CXP[f]	2.187	1.989	–0.321	2.899		178.06	
			2.189	1.986	–0.342	3.000		172.99	
Ferrous	HRP	1H58[g]	2.133	2.028	–0.245	-		-	
	CCP	2XJ8[h]	2.062	2.117	–0.253	2.017		175.54	
	APX	2XJ6[h]	2.013	2.104	–0.220	2.306		177.77	
Compound I	HRP	1HCH[g]	2.141	2.009	0.028	1.705		177.05	
	CCP	2XIL[h]	2.099	2.050	0.077	1.635		178.92	
	CCP*	4CVJ[c]	2.124	2.039	0.098	1.645		169.51	
	APX	2XI6[h]	2.033	2.092	–0.087	1.743		176.11	
Compound II	HRP	1H55[g]	2.140	2.007	0.003	1.839		176.41	
	CCP	2XJ5[h]	2.121	2.070	–0.061	1.834		178.65	
	APX	2XIF[h]	1.994	2.027	–0.134	1.830		178.12	
	APX*	5JPR[i]	1.970	2.006	–0.081	1.879	0.986	178.76	142.28

* Structures obtained by neutron diffraction. [a] Ref. 63. [b] Ref. 18. [c] Ref. 23. [d] Ref. 65. [e] Ref. 66. [f] Ref. 67. [g] Ref. 64. [h] Ref. 13. [i] Ref. 24.

Table S11.3. Mulliken atomic charges (a.u.) on relevant atoms obtained at UB3LYP/6-31G* computational level. N_i, N_p, O_{Fe}, and Por refer to imidazole nitrogen, total charge on the four pyrrole nitrogens, ferryl oxygen, and porphine, respectively. Values obtained including solvation (PCM) are shown in parentheses. Results of experimentally feasible spin multiplicities in bold.

Species	Spin	Fe	N_i	N_p	O_{Fe}	H	Por	H_2O
Fe(III)-PO	**1/2**	**1.34 (1.39)**	**–0.53 (–0.54)**	**–3.11 (–3.10)**			**–0.61 (–0.69)**	
	3/2	1.40 (1.44)	–0.56 (–0.56)	–3.18 (–3.18)			–0.58 (–0.63)	
	5/2	**1.51 (1.53)**	**–0.59 (–0.60)**	**–3.30 (–3.29)**			**–0.72 (–0.77)**	
	7/2	1.53 (1.57)	–0.59 (–0.60)	–3.30 (–3.27)			–0.74 (–0.81)	
Fe(III)-PO-H_2O	**1/2**	**1.44 (1.42)**	**–0.54 (–0.54)**	**–3.13 (–3.08)**			**–0.86 (–0.90)**	**0.18 (0.21)**
	3/2	1.45 (1.44)	–0.54 (–0.54)	–3.17 (–3.14)			–0.74 (–0.74)	0.13 (0.15)
	5/2	**1.60 (1.58)**	**–0.58 (–0.58)**	**–3.32 (–3.28)**			**–0.92 (–0.94)**	**0.14 (0.16)**
	7/2	1.60 (1.59)	–0.57 (–0.58)	–3.26 (–3.22)			–0.92 (–0.95)	0.14 (0.17)
Fe(III)-PO-H	**1/2**	**1.28 (1.27)**	**–0.58 (–0.59)**	**–3.01 (–2.99)**		**0.07 (0.07)**	**0.43 (0.42)**	
	3/2	1.28 (1.27)	–0.58 (–0.59)	–3.01 (–2.99)		0.07 (0.07)	0.43 (0.42)	
	5/2	**1.39 (1.38)**	**–0.62 (–0.62)**	**–3.15 (–3.13)**		**0.11 (0.12)**	**0.26 (0.24)**	
	7/2	1.50 (1.50)	–0.62 (–0.62)	–3.28 (–3.27)		0.03 (0.03)	0.20 (0.19)	
Fe(II)-PO	**0**	**1.20 (1.21)**	**–0.49 (–0.49)**	**–3.02 (–3.00)**			**–1.31 (–1.35)**	
	1	**1.21 (1.20)**	**–0.48 (–0.49)**	**–3.07 (–3.06)**			**–1.27 (–1.29)**	
	2	**1.28 (1.27)**	**–0.54 (–0.55)**	**–3.15 (–3.14)**			**–1.38 (–1.40)**	
	3	1.47 (1.48)	–0.57 (–0.58)	–3.33 (–3.33)			–1.64 (–1.69)	
	4	1.50 (1.53)	–0.57 (–0.58)	–3.32 (–3.30)			–1.67 (–1.74)	
Fe(II)-PO-H_2O	**0**	**1.27 (1.24)**	**–0.50 (–0.51)**	**–3.01 (–2.97)**			**–1.48 (–1.50)**	**0.14 (0.16)**
	1	**1.18 (1.15)**	**–0.48 (–0.49)**	**–3.06 (–3.05)**			**–1.35 (–1.34)**	**0.08 (0.09)**
	2	**1.30 (1.28)**	**–0.52 (–0.53)**	**–3.16 (–3.14)**			**–1.49 (–1.49)**	**0.09 (0.10)**
	3	1.55 (1.52)	–0.55 (–0.56)	–3.39 (–3.35)			–1.82 (–1.84)	0.13 (0.14)
	4	1.54 (1.52)	–0.55 (–0.56)	–3.32 (–3.28)			–1.83 (–1.86)	0.14 (0.16)
Fe(II)-PO-H	**0**	**1.14 (1.15)**	**–0.54 (–0.55)**	**–2.85 (–2.88)**		**–0.05 (–0.07)**	**–0.24 (–0.27)**	
	1	**1.26 (1.15)**	**–0.55 (–0.54)**	**–3.09 (–2.91)**		**0.05 (–0.08)**	**–0.48 (–0.25)**	
	2	**1.26 (1.25)**	**–0.56 (–0.56)**	**–3.01 (–3.00)**		**0.05 (0.04)**	**–0.49 (–0.50)**	
	3	1.47 (1.45)	–0.59 (–0.60)	–3.29 (–3.27)		0.03 (0.03)	–0.71 (–0.72)	
	4	1.28 (1.27)	–0.54 (–0.55)	–3.07 (–3.07)		–0.15 (–0.25)	–0.27 (–0.19)	

Table S11.3. Cont.

Species	Spin	Fe	N_i	N_p	O_{Fe}	H	Por	H_2O
PO-I	**1/2**	**1.40 (1.38)**	**–0.52 (–0.53)**	**–2.88 (–2.87)**	**–0.43 (–0.53)**		**–0.13 (–0.05)**	
	3/2	1.40 (1.38)	–0.72 (–0.53)	–2.87 (–2.86)	–0.43 (–0.53)		–0.13 (–0.05)	
	5/2	**1.40 (1.38)**	**–0.52 (–0.53)**	**–2.89 (–2.89)**	**–0.43 (–0.53)**		**–0.12 (–0.04)**	
	7/2	1.54 (1.53)	–0.55 (–0.54)	–3.06 (–3.07)	–0.42 (–0.51)		–0.26 (–0.18)	
PO-I-H_2O	**1/2**	**1.42 (1.40)**	**–0.52 (–0.53)**	**–2.89 (–2.87)**	**–0.49 (–0.54)**		**–0.10 (–0.05)**	**0.01 (0.00)**
	3/2	1.42 (1.40)	–0.52 (–0.53)	–2.88 (–2.87)	–0.49 (–0.55)		–0.10 (–0.05)	0.01 (–0.00)
	5/2	**1.51 (1.50)**	**–0.53 (–0.54)**	**–2.97 (–2.96)**	**–0.48 (–0.54)**		**–0.21 (–0.17)**	**0.01 (0.00)**
	7/2	1.56 (1.55)	–0.53 (–0.54)	–3.09 (–3.09)	–0.47 (–0.52)		–0.23 (–0.18)	0.00 (–0.02)
PO-I-H	**1/2**	**1.54 (1.38)**	**–0.55 (–0.55)**	**–3.02 (–2.85)**	**–0.64 (–0.77)**	**0.46 (0.45)**	**0.35 (0.72)**	
	3/2	1.53 (1.52)	–0.55 (–0.56)	–3.03 (–3.00)	–0.65 (–0.70)	0.46 (0.51)	0.36 (0.35)	
	5/2	**1.44 (1.43)**	**–0.56 (–0.56)**	**–2.88 (–2.88)**	**–0.74 (–0.80)**	**0.43 (0.47)**	**0.66 (0.68)**	
	7/2	1.55 (1.53)	–0.52 (–0.52)	–2.99 (–2.99)	–0.79 (–0.83)	0.44 (0.47)	0.64 (0.66)	
PO-II	0	1.36 (1.32)	–0.50 (–0.51)	–2.95 (–2.93)	–0.45 (–0.55)		–1.02 (–0.93)	
	1	**1.38 (1.35)**	**–0.49 (–0.51)**	**–2.96 (–2.94)**	**–0.45 (–0.56)**		**–1.03 (–0.93)**	
	2	**1.38 (1.35)**	**–0.50 (–0.52)**	**–2.90 (–2.89)**	**–0.45 (–0.56)**		**–1.05 (–0.95)**	
	3	1.50 (1.47)	–0.47 (–0.48)	–3.17 (–3.17)	–0.44 (–0.53)		–1.15 (–1.05)	
	4	1.51 (1.48)	–0.49 (–0.50)	–3.09 (–3.08)	–0.45 (–0.54)		–1.16 (–1.06)	
PO-II-H_2O	0	1.38 (1.36)	–0.49 (–0.51)	–2.96 (–2.94)	–0.50 (–0.57)		–0.99 (–0.92)	–0.01 (–0.02)
	1	**1.39 (1.36)**	**–0.49 (–0.51)**	**–2.97 (–2.94)**	**–0.51 (–0.59)**		**–0.99 (–0.92)**	**–0.01 (–0.02)**
	2	**1.48 (1.46)**	**–0.50 (–0.51)**	**–3.07 (–3.05)**	**–0.51 (–0.58)**		**–1.10 (–1.03)**	**0.00 (–0.01)**
	3	1.52 (1.50)	–0.48 (–0.49)	–3.19 (–3.18)	–0.48 (–0.54)		–1.12 (–1.05)	–0.02 (–0.03)
	4	1.53 (1.50)	–0.49 (–0.51)	–3.11 (–3.10)	–0.49 (–0.55)		–1.13 (–1.06)	–0.02 (–0.03)
PO-II-H	0	1.40 (1.37)	–0.52 (–0.53)	–2.95 (–2.93)	–0.63 (–0.68)	0.44 (0.48)	–0.44 (–0.43)	
	1	**1.52 (1.39)**	**–0.53 (–0.53)**	**–3.09 (–2.92)**	**–0.65 (–0.76)**	**0.45 (0.46)**	**–0.55 (–0.29)**	
	2	**1.52 (1.34)**	**–0.49 (–0.48)**	**–3.03 (–2.89)**	**–0.78 (–0.86)**	**0.43 (0.45)**	**–0.28 (–0.06)**	
	3	1.52 (1.50)	–0.50 (–0.50)	–3.02 (–3.01)	–0.79 (–0.85)	0.42 (0.46)	–0.28 (–0.25)	
	4	1.52 (1.49)	–0.49 (–0.50)	–3.05 (–3.04)	–0.79 (–0.85)	0.42 (0.46)	–0.27 (–0.24)	

Table S11.4. Thermodynamic parameters Δ*H*°, *T*Δ*S*°, and Δ*G*°, in kJ·mol^{-1} for all compounds under study obtained at UB3LYP/6-31G* computational level (*T* = 298.15 K). Values of Δ*G*° obtained with PCM continuum model in italics. Most stable species of each unprotonated compound (with regard to Gibbs free energy, only for feasible spins) was taken as reference. Relative data of protonated and aquo complexes were worked out with respect to separate parent unprotonated species plus H^+ or H_2O as appropriate. Absolute thermodynamic values used as reference are collected in Table S11.5. Results of experimentally feasible spin multiplicities in bold.

Species	Spin	Δ*H*°	*T*Δ*S*°	Δ*G*°	
Fe(III)-PO	**1/2**	**23.02**	**–8.59**	**31.60**	***13.99***
	3/2	–22.48	–2.46	–20.02	*–24.46*
	5/2	**0.00**	**0.00**	**0.00**	***0.00***
	7/2	168.94	4.31	164.63	*159.44*
Fe(III)-PO-H_2O	**1/2**	**–57.14**	**–58.18**	**1.04**	***–4.48***
	3/2	–69.36	–41.97	–27.39	*–17.85*
	5/2	**–44.83**	**–40.07**	**–4.76**	***4.44***
	7/2	108.60	–37.09	145.69	*151.51*
Fe(III)-PO-H	**1/2**	**–505.20**	**–35.70**	**–469.50**	***248.39***
	3/2	–507.16	–34.79	–472.38	*246.27*
	5/2	**–461.84**	**–28.19**	**–433.66**	***290.47***
	7/2	–398.75	–13.36	–385.39	*360.58* [a,b]
Fe(II)-PO	**0**	**34.24**	**–15.22**	**49.46**	***37.20***
	1	**58.05**	**–2.32**	**60.37**	***58.98***
	2	**0.00**	**0.00**	**0.00**	***0.00***
	3	107.38	1.01	106.37	*92.19*
	4	271.15	2.93	268.22	*248.98*
Fe(II)-PO-H_2O	**0**	**–30.12**	**–61.88**	**31.76**	***36.41***
	1	**–22.53**	**–38.84**	**16.30**	***35.05***
	2	**–27.10**	**–39.65**	**12.55**	***32.38***
	3	70.11	–42.28	112.38	*119.66*
	4	218.23	–39.79	258.02	*262.58*
Fe(II)-PO-H	**0**	**–889.33**	**–42.14**	**–847.19**	***136.13***
	1	**–920.76**	**–36.27**	**–884.49**	***98.21***
	2	**–590.00**	**–32.76**	**–557.24**	***435.45***
	3	–804.58	–17.37	–787.21	*217.58* [a,b]
	4	–625.85	–24.83	–601.02	*376.03* [a]

[a] An additional sphere is included on H^+. [b] PCM calculation is performed with two disjoint cavities.

Table S11.4. Cont.

Species	Spin	Δ*H*°	*T*Δ*S*°	Δ*G*°	
PO-I	**1/2**	**0.00**	**0.00**	**0.00**	***0.00***
	3/2	–1.77	1.87	–3.65	*–3.73*
	5/2	**174.79**	**6.10**	**168.69**	***169.94***
	7/2	127.33	16.41	110.92	*120.00*
PO-I-H_2O	**1/2**	**–28.78**	**–35.47**	**6.69**	***24.52***
	3/2	–29.87	–33.98	4.11	*21.18*
	5/2	**15.99**	**–27.83**	**43.82**	***65.79***
	7/2	94.12	–22.65	116.77	*143.30*
PO-I-H	**1/2**	**–734.24**	**–30.50**	**–703.74**	***1.60***
	3/2	–734.62	–28.92	–705.71	*3.11*
	5/2	**–658.56**	**–20.83**	**–637.73**	***86.52***
	7/2	–680.40	–14.68	–665.73	*59.65*
PO-II	0	127.44	–0.88	128.32	*127.94*
	1	**0.00**	**0.00**	**0.00**	***0.00***
	2	**157.58**	**4.46**	**153.12**	***155.12***
	3	129.37	14.58	114.79	*129.36*
	4	273.14	16.22	256.92	*267.96*
PO-II-H_2O	0	8.71	–36.41	45.12	*64.07*
	1	**–30.06**	**–33.72**	**3.65**	***21.77***
	2	**20.35**	**–27.53**	**47.88**	***72.57***
	3	97.48	–19.82	117.31	*149.69*
	4	239.83	–19.63	259.46	*288.37*
PO-II-H	0	–992.09	–36.23	–955.86	*37.76*
	1	**–1067.21**	**–31.33**	**–1035.88**	***–47.57***
	2	**–1044.84**	**–15.77**	**–1029.07**	***–30.01***
	3	–1043.28	–15.85	–1027.43	*–27.75*
	4	–869.94	–14.23	–855.71	*145.65*

Table S11.5. Thermodynamic parameters Δ*H*°, *T*Δ*S*°, and Δ*G*°, in kJ·mol^{-1} for unprotonated species at ground spin state, obtained with UB3LYP method together with 6-31G* basis set (*T* = 298.15 K); and electron and proton published values employed in the study. Values of Δ*G*° obtained with PCM continuum model in italics. Absolute values used as reference for data in Tables 11.1, 11.2, 11.4, and S11.4.

Species	Spin	Δ*H*°	*T*Δ*S*°	Δ*G*°	
e^-	1/2			–3.632[a]	
H^+	-	6.20[b]	32.48[b]	–26.28[b]	*–1130.90*[c]
Fe(III)-PO	5/2	–6505301.74	203.67	–6505505.41	*–6505630.68*
Fe(II)-PO	2	–6505811.68	206.17	–6506017.85	*–6506017.80*
PO-I	1/2	–6702595.09	200.61	–6702795.69	*–6702938.12*
PO-II	1	–6703188.14	202.00	–6703390.14	*–6703418.72*
H_2O	0	–200546.20	58.03	–200604.23	*–200619.08*

[a] Ref 56. [b] Ref. 53. [c] Refs. 53-55

Table S11.6. Wavelength (nm) and molar absorption coefficient ($cm^{-1}·M^{-1}$) of the Soret band obtained for all considered species and calculated with the UB3LYP/6-31G* computational method (PCM-solvated data in parentheses). Peaks with low intensity (ε ≤ 10000) are not reported. Results of experimentally feasible spin multiplicities in bold.

Species	Spin	λ / nm		ε / $cm^{-1}·M^{-1}$		Species	Spin	λ / nm		ε / $cm^{-1}·M^{-1}$	
Fe(III)-PO	**1/2**	**346**	**(352)**	**56663**	**(96192)**	PO-I	**1/2**	**358**	**(364)**	**65564**	**(104469)**
	3/2	360	(375)	52797	(67233)		3/2	356	(363)	40772	(108372)
	5/2	**348**	**(355)**	**85095**	**(138565)**		**5/2**	**376**	**(385)**	**35997**	**(56868)**
	7/2	359	(372)	35363	(55317)		7/2	365	(377)	22320	(33847)
Fe(III)-PO-H_2O	**1/2**	**352**	**(365)**	**96356**	**(118074)**	PO-I-H_2O	**1/2**	**374**	**(367)**	**13791**	**(103158)**
	3/2	351	(359)	72030	(98507)		3/2	368	(368)	31239	(75069)
	5/2	**353**	**(364)**	**88640**	**(146992)**		**5/2**	**371**	**(375)**	**37595**	**(63995)**
	7/2	382	(378)	31122	(62822)		7/2		(394)		(18021)
Fe(III)-PO-H	**1/2**		**(369)**		**(89502)**	PO-I-H	**1/2**				
	3/2		(368)		(53735)		3/2				
	5/2		**(397)**		**(14581)**		**5/2**		**(389)**		**(33198)**
	7/2	361	(362)	20802	(61891)		7/2	369	(378)	39938	(114691)
Fe(II)-PO	**0**	**323**	**(333)**	**46691**	**(52840)**	PO-II	0	367	(376)	90787	(136175)
		360	**(369)**	**83682**	**(118108)**		**1**	**364**	**(375)**	**84524**	**(121402)**
	1	**349**	**(359)**	**107132**	**(143789)**		**2**	**363**	**(381)**	**34562**	**(48883)**
	2	**310**	**(313)**	**52409**	**(45558)**		3	351	(369)	68502	(82714)
		376	**(386)**	**67381**	**(88654)**		4	392	(368)	28015	(43054)
	3	366	(373)	52017	(83258)	PO-II-H_2O	0	369	(378)	88775	(115364)
	4	422	(335)	25005	(15881)		**1**	**367**	**(376)**	**89030**	**(118635)**
		489	(421)	18757	(30052)		**2**	**368**	**(378)**	**80462**	**(115343)**
			(482)		(32031)		3	351	(371)	59463	(88137)
Fe(II)-PO-H_2O	**0**	**338**	**(349)**	**54266**	**(64198)**		4	394	(373)	23685	(44677)
		369	**(378)**	**67643**	**(98434)**	PO-II-H	0				
	1	**367**	**(366)**	**88408**	**(132136)**		**1**		**(379)**		**(62235)**
	2	**296**	**(298)**	**40624**	**(41153)**		**2**	**374**	**(373)**	**50987**	**(46382)**
		369	**(378)**	**77086**	**(106419)**		3	358	(364)	45538	(73263)
	3	375	(385)	53711	(90068)		4	386	(400)	35050	(55181)
	4	427	(438)	25710	(35528)						
Fe(II)-PO-H	**0**		**(384)**		**(67493)**						
	1	**362**	**(343)**	**72960**	**(60618)**						
			(378)		**(44715)**						
	2	**399**	**(367)**	**25881**	**(103564)**						
	3	349	(355)	42786	(138215)						
	4	348	(358)	25122	(32542)						
		400	(394)	23424	(38408)						

Table S11.7. Ferryl bond length (Å) and bond order (in parentheses), Mulliken atomic charge on ferryl oxygen (a.u.), and wavelength (nm) and molar absorption coefficient ($cm^{-1}·M^{-1}$) of the Soret band (PCM-solvated values in parentheses in the latter three columns) obtained for all studied complexes of compounds I and II with water molecules. All values calculated with the UB3LYP/6-31G* computational method. Peaks with low intensity (ε ≤ 10000) are not reported. Results of experimentally feasible spin multiplicities in bold.

n	Spin	Fe–O	O	λ / nm	ε / $cm^{-1}·M^{-1}$	Spin	Fe–O	O	λ / nm	ε / $cm^{-1}·M^{-1}$
			PO-I-$(H_2O)_n$					PO-II-$(H_2O)_n$		
0	**1/2**	**1.620**	**–0.43**	**358**	**65564**	0	1.623	–0.45	367	90787
		(1.46)	**(–0.53)**	**(364)**	**(104469)**		(1.92)	(–0.55)	(376)	(136175)
	3/2	1.620	–0.43	356	40772	**1**	**1.618**	**–0.45**	**364**	**84524**
		(1.46)	(–0.53)	(363)	(108372)		**(1.47)**	**(–0.56)**	**(375)**	**(121402)**
	5/2	**1.619**	**–0.43**	**376**	**35997**	**2**	**1.618**	**–0.45**	**363**	**34562**
		(1.46)	**(–0.53)**	**(385)**	**(56868)**		**(1.47)**	**(–0.56)**	**(381)**	**(48883)**
	7/2	1.895	–0.42	365	22320	3	1.895	–0.44	351	68502
		(1.03)	(–0.51)	(377)	(33847)		(1.05)	(–0.53)	(369)	(82714)
						4	1.888	–0.45	392	28015
							(1.07)	(–0.54)	(368)	(43054)
1	**1/2**	**1.625**	**–0.49**	**374**	**13791**	0	1.625	–0.50	369	88775
		(1.41)	**(–0.54)**	**(367)**	**(103158)**		(1.85)	(–0.57)	(378)	(115364)
	3/2	1.625	–0.49	368	31239	**1**	**1.624**	**–0.51**	**367**	**89030**
		(1.41)	(–0.55)	(368)	(75069)		**(1.42)**	**(–0.59)**	**(376)**	**(118635)**
	5/2	**1.619**	**–0.48**	**371**	**37595**	**2**	**1.620**	**–0.51**	**368**	**80462**
		(1.40)	**(–0.54)**	**(375)**	**(63995)**		**(1.40)**	**(–0.58)**	**(378)**	**(115343)**
	7/2	1.913	–0.47			3	1.912	–0.48	351	59463
		(0.54)	(–0.52)	(394)	(18021)		(0.90)	(–0.54)	(371)	(88137)
						4	1.905	–0.49	394	23685
							(0.54)	(–0.55)	(373)	(44677)
2	**1/2**	**1.634**	**–0.54**			0	1.636	–0.54		
		(1.35)	**(–0.59)**	**(370)**	**(96945)**		(1.77)	(–0.58)	(377)	(132214)
	3/2	1.627	–0.51	367	51446	**1**	**1.628**	**–0.56**	**368**	**86120**
		(1.39)	(–0.56)	(369)	(89738)		**(1.38)**	**(–0.61)**	**(377)**	**(114154)**
	5/2	**1.627**	**–0.54**	**388**	**9304**	**2**	**1.628**	**–0.55**	**385**	**30249**
		(1.35)	**(–0.57)**	**(378)**	**(48503)**		**(1.38)**	**(–0.61)**	**(391)**	**(42197)**
	7/2	1.627	–0.54	405	26483	3	1.927	–0.52	368	44723
		(1.35)	(–0.57)	(404)	(47829)		(0.50)	(–0.56)	(370)	(99382)
						4	1.625	–0.54	462	36314
							(1.36)	(–0.59)	(383)	(63970)
3	**1/2**	**1.634**	**–0.56**			0	1.634	–0.53		
		(1.34)	**(–0.58)**	**(370)**	**(90141)**		(1.80)	(–0.58)	(377)	(130246)
	3/2	1.634	–0.56	367	56194	**1**	**1.628**	**–0.58**	**367**	**85443**
		(1.34)	(–0.60)	(371)	(74783)		**(1.38)**	**(–0.62)**	**(376)**	**(112356)**
	5/2	**1.630**	**–0.55**			**2**	**1.626**	**–0.57**	**368**	**82765**
		(1.32)	**(–0.58)**				**(1.35)**	**(–0.61)**	**(378)**	**(111645)**
	7/2	1.942	–0.52			3	1.926	–0.53	368	37919
		(0.87)	(–0.54)				(1.03)	(–0.56)	(371)	(88981)
						4	1.929	–0.53	400	22707
							(1.03)	(–0.56)	(384)	(25838)

Table S11.7. Cont.

n	Spin	Fe–O	O	λ / nm	ε / $cm^{-1}·M^{-1}$	Spin	Fe–O	O	λ / nm	ε / $cm^{-1}·M^{-1}$
			PO-I-H					PO-II-H		
0	**1/2**	**1.744**	**–0.64**			0	1.750	–0.63		
		(0.92)	**(–0.77)**				(1.03)	(–0.68)		
	3/2	1.745	–0.65			**1**	**1.748**	**–0.65**		
		(0.92)	(–0.70)				**(0.92)**	**(–0.76)**	**(379)**	**(62235)**
	5/2	**1.787**	**–0.74**			**2**	**1.817**	**–0.78**	**374**	**50987**
		(0.78)	**(–0.80)**	**(389)**	**(33198)**		**(0.65)**	**(–0.86)**	**(373)**	**(46382)**
	7/2	1.803	–0.79	369	39938	3	1.823	–0.79	358	45538
		(0.63)	(–0.83)	(378)	(114691)		(0.60)	(–0.85)	(364)	(73263)
						4	1.824	–0.79	386	35050
							(0.61)	(–0.85)	(400)	(55181)
			PO-I-H···H_2O					PO-II-H···H_2O		
1	**1/2**	**-**	**-**	**-**	**-**	0	1.774	–0.69		
							(0.91)	(–0.73)		
	3/2	-	-	-	-	**1**	**1.814**	**–0.77**		
							(0.81)	**(–0.76)**	**(364)**	**(82560)**
	5/2	**-**	**-**	**-**	**-**	**2**	**1.897**	**–0.84**		
							(0.51)	**(–0.88)**	**(397)**	**(44936)**
	7/2	1.851	–0.83	408	11973	3	1.858	–0.83	385	13408
		(0.54)	(–0.86)	(389)	(70885)		(0.53)	(–0.87)	(361)	(66286)
						4	1.861	–0.83	406	29821
							(0.52)	(–0.87)	(406)	(50416)
			PO-I-H···OH_2					PO-II-H···OH_2		
1	**1/2**	**1.716**	**–0.68**			0	1.734	–0.66		
		(0.99)	**(–0.71)**				(1.11)	(–0.70)		
	3/2	1.716	–0.68			**1**	**1.723**	**–0.69**	**370**	**38321**
		(0.99)	(–0.71)				**(0.97)**	**(–0.73)**	**(378)**	**(58976)**
	5/2	**1.782**	**–0.81**	**378**	**13861**	**2**	**1.797**	**–0.82**	**375**	**42964**
		(0.66)	**(–0.83)**	**(377)**	**(34585)**		**(0.64)**	**(–0.88)**	**(374)**	**(37008)**
	7/2	1.786	–0.82			3	1.736	–0.69	362	58073
		(0.67)	(–0.86)	(377)	(114247)		(0.63)	(–0.89)	(375)	(75739)
						4	1.805	–0.83	377	42095
							(0.67)	(–0.88)	(390)	(56644)
			PO-I-H-$(H_2O)_2$					PO-II-H-$(H_2O)_2$		
2	**1/2**	**1.733**	**–0.73**			0	1.757	–0.73		
		(0.93)	**(–0.81)**				(0.98)	(–0.75)		
	3/2	1.734	–0.73			**1**	**1.737**	**–0.75**		
		(0.93)	(–0.74)				**(0.91)**	**(–0.81)**	**(381)**	**(57016)**
	5/2	**1.817**	**–0.86**			**2**	**1.826**	**–0.87**	**405**	**33380**
		(0.59)	**(–0.89)**				**(0.56)**	**(–0.90)**	**(388)**	**(64248)**
	7/2	1.829	–0.87	405	11972	3	1.836	–0.87	367	24828
		(0.58)	(–0.88)	(389)	(76503)		(0.56)	(–0.90)	(364)	(68918)
						4	1.838	–0.87	398	36932
							(0.55)	(–0.90)	(402)	(47340)

Table S11.8. Fe–O_{Fe} stretching frequencies in cm^{-1} calculated for relevant ferryl species at the most favourable spin multiplicities employing the UB3LYP/6-31G* computational level (T = 298.15 K).

Species	Spin	ν / cm^{-1}
PO-I	1/2	937
PO-I-H_2O	1/2	934
PO-I-H	1/2	710
PO-II	1	945
PO-II-H_2O	1	941
PO-II-H	1	702
PO-II-H···OH_2	1	757
PO-II-H···H_2O	1	623
PO-II-H-$(H_2O)_2$	1	742

Table S11.9. Standard reduction potential ($E°$) values relative to SHE calculated by PCM//UB3LYP/6-31G* (T = 298.15 K) at preferred spins.

Half-reaction	$E°$ (mV)
Compound I (S = 1/2) → Ferric (S = 5/2)	
PO-I + $2H^+$ + $2e^-$ → Fe(III)-PO + H_2O	963
PO-I-H_2O + $2H^+$ + $2e^-$ → Fe(III)-PO + $2H_2O$	1090
PO-I-$(H_2O)_2$ + $2H^+$ + $2e^-$ → Fe(III)-PO + $3H_2O$	1407
Compound I (S = 1/2) → Compound II (S = 1)	
PO-I + e^- → PO-II	503
PO-I + H^+ + e^- → PO-II-H	996
PO-I + H^+ + H_2O + e^- → PO-II-H···OH_2	890
PO-I-H_2O + H^+ + e^- → PO-II-H···OH_2	1144
PO-I + H^+ + H_2O + e^- → PO-II-H···H_2O	797
PO-I-H_2O + H^+ + e^- → PO-II-H···H_2O	1051
PO-I + H^+ + $2H_2O$ + e^- → PO-II-H-$(H_2O)_2$	617
PO-I-H_2O + H_2O + H^+ + e^- → PO-II-H-$(H_2O)_2$	871
PO-I-$(H_2O)_2$ + H^+ + e^- → PO-II-H-$(H_2O)_2$	1505
Compound II (S = 1) → Ferric (S = 5/2)	
PO-II + $2H^+$ + e^- → Fe(III)-PO + H_2O	1422
PO-II-H + H^+ + e^- → Fe(III)-PO + H_2O	929
PO-II-H···OH_2 + H^+ + e^- → Fe(III)-PO + $2H_2O$	1035
PO-II-H···H_2O + H^+ + e^- → Fe(III)-PO + $2H_2O$	1128
PO-II-H-$(H_2O)_2$ + H^+ + e^- → Fe(III)-PO + $3H_2O$	1308
Ferric (S = 5/2) → Ferrous (S = 2)	
Fe(III)-PO + e^- → Fe(II)-PO	–465

Table S11.10. Comparison of the performance of different basis sets. Distance (Å) between iron and imidazole nitrogen atom (Fe–N_i), the metal centre and either ferryl or water oxygen (Fe–O), and between ferryl oxygen and proton (O–H); mean distance (Å) between iron and the four pyrrole nitrogen atoms (Fe–N_p); and distance (Å) from Fe atom to heme pyrrole plane (Fe–pp). Positive values of the latter indicate displacement towards distal side, while negative figures stand for out-of-plane Fe placed at the opposite side. Bond orders are shown in parentheses, values under Fe–N_p account for total iron-pyrrole nitrogen bond order, *i.e.*, the overall order of those four covalent bonds. N_i–Fe–O and Fe–O–H stand for the angles (°) among these atoms.

	Spin	Fe–N_i	Fe–N_p	Fe–pp	Fe–O	O–H	N_i–Fe–O	Fe–O–H
Fe(III)-PO								
6-31G*	1/2	1.930 (0.48)	1.988 (2.06)	–0.213				
6-31G**	1/2	1.929 (0.49)	1.988 (2.07)	–0.212				
6-31++G**	1/2	1.935 (0.60)	1.996 (2.50)	–0.221				
6-311G**	1/2	1.915 (0.47)	1.995 (1.61)	–0.222				
6-311++G**	1/2	1.945 (0.60)	1.996 (2.51)	–0.218				
6-31G*	5/2	2.087 (0.27)	2.061 (1.79)	–0.383				
6-31G**	5/2	2.086 (0.28)	2.061 (1.37)	–0.381				
6-31++G**	5/2	2.093 (0.41)	2.066 (1.85)	–0.386				
6-311G**	5/2	2.085 (0.18)	2.061 (1.54)	–0.361				
6-311++G**	5/2	2.103 (0.36)	2.068 (1.69)	–0.392				
Fe(III)-PO-H_2O								
6-31G*	1/2	1.948 (0.50)	2.003 (1.96)	–0.068	2.028 (0.32)		179.48	
6-31G**	1/2	1.947 (0.50)	2.003 (1.96)	–0.069	2.028 (0.32)		179.59	
6-31++G**	1/2	1.955 (0.54)	2.009 (2.11)	–0.067	2.052 (0.36)		179.69	
6-311G**	1/2	1.957 (0.43)	2.008 (1.50)	–0.067	2.037 (0.22)		179.79	
6-311++G**	1/2	1.961 (0.64)	2.009 (2.48)	–0.066	2.062 (0.40)		179.48	
6-31G*	5/2	2.140 (0.26)	2.057 (1.27)	–0.149	2.292 (0.17)		179.50	
6-31G**	5/2	2.137 (0.26)	2.057 (1.27)	–0.153	2.299 (0.17)		179.39	
6-31++G**	5/2	2.139 (0.34)	2.061 (1.59)	–0.175	2.386 (0.19)		178.67	
6-311G**	5/2	2.145 (0.16)	2.060 (0.78)	–0.146	2.285 (0.07)		179.39	
6-311++G**	5/2	2.149 (0.35)	2.061 (1.65)	–0.174	2.389 (0.18)		178.44	
PO-I								
6-31G*	1/2	2.154 (0.28)	2.016 (1.77)	0.088	1.620 (1.46)		179.87	
6-31G**	1/2	2.154 (0.28)	2.016 (1.77)	0.090	1.620 (1.46)		179.90	
6-31++G**	1/2	2.168 (0.34)	2.022 (1.92)	0.085	1.629 (1.33)		179.75	
6-311G**	1/2	2.165 (0.17)	2.020 (1.35)	0.074	1.622 (1.23)		179.91	
6-311++G**	1/2	2.180 (0.39)	2.021 (2.26)	0.085	1.629 (1.40)		179.83	
PO-I-H								
6-31G*	1/2	2.040 (0.42)	1.994 (2.05)	0.047	1.744 (0.92)	0.976 (0.72)	179.57	115.18
6-31G**	1/2	2.040 (0.42)	1.994 (2.05)	0.051	1.742 (0.93)	0.972 (0.71)	179.64	115.37
6-31++G**	1/2	2.064 (0.44)	2.018 (1.92)	0.001	1.800 (0.84)	0.969 (0.75)	176.63	114.53
6-311G**	1/2	2.048 (0.31)	1.997 (1.57)	0.042	1.743 (0.76)	0.969 (0.76)	179.68	115.73
6-311++G**	1/2	2.057 (0.54)	1.999 (2.49)	0.048	1.755 (0.97)	0.969 (0.74)	178.56	115.49
PO-II								
6-31G*	1	2.196 (0.25)	2.018 (1.80)	0.119	1.618 (1.47)		179.92	
6-31G**	1	2.195 (0.25)	2.018 (1.80)	0.121	1.618 (1.47)		179.97	
6-31++G**	1	2.207 (0.36)	2.024 (2.27)	0.115	1.627 (1.41)		179.97	
6-311G**	1	2.204 (0.15)	2.022 (1.37)	0.103	1.619 (1.24)		179.94	
6-311++G**	1	2.216 (0.36)	2.023 (2.28)	0.116	1.627 (1.41)		179.93	
PO-II-H								
6-31G*	1	2.062 (0.38)	1.995 (2.08)	0.065	1.748 (0.92)	0.975 (0.73)	179.49	111.34
6-31G**	1	2.062 (0.38)	1.995 (2.08)	0.070	1.746 (0.92)	0.971 (0.72)	179.38	111.38
6-31++G**	1	2.069 (0.43)	2.001 (2.18)	0.070	1.754 (0.88)	0.972 (0.71)	179.89	111.78
6-311G**	1	2.070 (0.27)	1.998 (1.60)	0.061	1.747 (0.76)	0.968 (0.77)	178.97	111.86
6-311++G**	1	2.084 (0.49)	2.022 (2.29)	0.021	1.807 (0.89)	0.965 (0.79)	177.17	112.22

Table S11.11. Comparison of the performance of different basis sets. Mulliken atomic charges (a.u.) obtained on relevant atoms. N_i, N_p, O_{Fe}, and Por refer to imidazole nitrogen, total charge on the four pyrrole nitrogens, ferryl oxygen, and porphine, respectively. Values obtained including solvation (PCM) are shown in parentheses.

	Spin	Fe	N_i	N_p	O_{Fe}	H	Por	H_2O
Fe(III)-PO								
6-31G*	1/2	1.34 (1.39)	–0.53 (–0.54)	–3.11 (–3.10)			–0.61 (–0.69)	
6-31G**	1/2	1.35 (1.39)	–0.55 (–0.56)	–3.12 (–3.10)			–0.61 (–0.69)	
6-31++G**	1/2	–2.21 (–2.22)	0.58 (0.61)	1.19 (1.07)			1.66 (1.57)	
6-311G**	1/2	1.44 (1.49)	–0.51 (–0.52)	–2.78 (–2.75)			–0.69 (–0.77)	
6-311++G**	1/2	–2.35 (–2.41)	0.62 (0.66)	1.35 (1.22)			2.38 (2.34)	
6-31G*	5/2	1.51 (1.53)	–0.59 (–0.60)	–3.30 (–3.29)			–0.72 (–0.77)	
6-31G**	5/2	1.51 (1.53)	–0.61 (–0.62)	–3.31 (–3.30)			–0.72 (–0.77)	
6-31++G**	5/2	–3.02 (–2.90)	0.46 (0.46)	1.21 (1.06)			2.54 (2.38)	
6-311G**	5/2	1.74 (1.78)	–0.59 (–0.61)	–3.09 (–3.06)			–0.88 (–0.94)	
6-311++G**	5/2	–2.59 (–2.49)	0.52 (0.53)	1.44 (1.28)			2.49 (2.35)	
Fe(III)-PO-H_2O								
6-31G*	1/2	1.44 (1.42)	–0.54 (–0.54)	–3.13 (–3.08)			–0.86 (–0.90)	0.18 (0.21)
6-31G**	1/2	1.46 (1.45)	–0.56 (–0.56)	–3.13 (–3.09)			–0.86 (–0.90)	0.17 (0.20)
6-31++G**	1/2	0.57 (0.66)	–0.04 (–0.05)	–0.44 (–0.49)			–0.48 (–0.61)	0.18 (0.19)
6-311G**	1/2	1.44 (1.44)	–0.48 (–0.48)	–2.68 (–2.64)			–0.85 (–0.89)	0.14 (0.17)
6-311++G**	1/2	–1.72 (–1.79)	–0.06 (–0.06)	1.39 (1.40)			2.42 (2.42)	0.36 (0.41)
6-31G*	5/2	1.60 (1.58)	–0.58 (–0.58)	–3.32 (–3.28)			–0.92 (–0.94)	0.14 (0.16)
6-31G**	5/2	1.61 (1.60)	–0.59 (–0.60)	–3.32 (–3.29)			–0.91 (–0.94)	0.12 (0.14)
6-31++G**	5/2	–1.39 (–1.29)	–0.02 (–0.05)	–0.12 (–0.18)			1.54 (1.41)	0.17 (0.18)
6-311G**	5/2	1.79 (1.79)	–0.54 (–0.55)	–3.01 (–2.97)			–1.00 (–1.03)	0.07 (0.08)
6-311++G**	5/2	–2.64 (–2.61)	–0.02 (–0.03)	1.62 (1.60)			3.22 (3.15)	0.17 (0.20)
PO-I								
6-31G*	1/2	1.40 (1.38)	–0.52 (–0.53)	–2.88 (–2.87)	–0.43 (–0.53)		–0.13 (–0.05)	
6-31G**	1/2	1.40 (1.39)	–0.54 (–0.55)	–2.88 (–2.88)	–0.43 (–0.53)		–0.13 (–0.05)	
6-31++G**	1/2	3.04 (3.23)	–0.18 (–0.19)	–0.40 (–0.47)	–0.81 (–1.03)		–1.46 (–1.47)	
6-311G**	1/2	1.35 (1.37)	–0.47 (–0.48)	–2.46 (–2.44)	–0.37 (–0.48)		–0.12 (–0.06)	
6-311++G**	1/2	–0.37 (–0.23)	–0.14 (–0.15)	1.91 (1.87)	–0.39 (–0.59)		1.84 (1.90)	
PO-I-H								
6-31G*	1/2	1.54 (1.38)	–0.55 (–0.55)	–3.02 (–2.85)	–0.64 (–0.77)	0.46 (0.45)	0.35 (0.72)	
6-31G**	1/2	1.55 (1.54)	–0.57 (–0.57)	–3.03 (–3.00)	–0.56 (–0.60)	0.36 (0.41)	0.35 (0.34)	
6-31++G**	1/2	2.08 (2.27)	–0.21 (–0.22)	–0.13 (–0.13)	–0.80 (–1.01)	0.38 (0.44)	–0.04 (–0.08)	
6-311G**	1/2	1.46 (1.46)	–0.50 (–0.51)	–2.61 (–2.58)	–0.46 (–0.51)	0.30 (0.35)	0.40 (0.38)	
6-311++G**	1/2	–1.16 (–1.19)	–0.03 (–0.03)	1.77 (1.87)	–0.32 (–0.43)	0.35 (0.42)	3.07 (3.14)	
PO-II								
6-31G*	1	1.38 (1.35)	–0.49 (–0.51)	–2.96 (–2.94)	–0.45 (–0.56)		–1.03 (–0.93)	
6-31G**	1	1.38 (1.35)	–0.51 (–0.52)	–2.96 (–2.95)	–0.45 (–0.56)		–1.03 (–0.93)	
6-31++G**	1	3.46 (3.74)	–0.23 (–0.25)	–0.69 (–0.88)	–0.86 (–1.10)		–2.69 (–2.80)	
6-311G**	1	1.37 (1.39)	–0.44 (–0.46)	–2.53 (–2.50)	–0.40 (–0.53)		–1.06 (–0.99)	
6-311++G**	1	–0.28 (–0.07)	–0.14 (–0.17)	1.83 (1.69)	–0.45 (–0.69)		1.01 (1.00)	
PO-II-H								
6-31G*	1	1.52 (1.39)	–0.53 (–0.53)	–3.09 (–2.92)	–0.65 (–0.76)	0.45 (0.46)	–0.55 (–0.29)	
6-31G**	1	1.53 (1.51)	–0.55 (–0.55)	–3.10 (–3.07)	–0.57 (–0.62)	0.35 (0.39)	–0.55 (–0.55)	
6-31++G**	1	2.10 (2.27)	–0.02 (–0.03)	–0.48 (–0.54)	–0.80 (–0.94)	0.42 (0.49)	–1.29 (–1.42)	
6-311G**	1	1.47 (1.47)	–0.48 (–0.49)	–2.67 (–2.64)	–0.47 (–0.53)	0.28 (0.33)	–0.53 (–0.54)	
6-311++G**	1	–1.04 (–0.89)	–0.14 (–0.15)	1.72 (1.66)	–0.42 (–0.63)	0.29 (0.35)	2.30 (2.29)	

Table S11.12. Comparison of the performance of different basis sets. Thermodynamic parameters Δ*H*°, *T*Δ*S*°, and Δ*G*°, in kJ·mol^{-1}. Values of Δ*G*° obtained with PCM continuum model in italics. Absolute vales obtained for Fe(III)-PO with *S* = 5/2 were taken as reference. Relative data of aquo complexes were worked out with respect to separate parent unprotonated species plus H_2O. Gibbs free energy values in kJ·mol^{-1} for the dissociation equilibrium of the aquo complexes ($\Delta G°_{H2O}$(aq)), pK_a values for protonation processes, and reduction potential values in mV relative to SHE.

	Spin	**Δ*H*°**	***T*Δ*S*°**	**Δ*G*°**	
Fe(III)-PO					
6-31G*	1/2	23.02	–8.59	23.02	*13.99*
6-31G**	1/2	22.93	–8.33	22.93	*15.15*
6-31++G**	1/2	19.57	–5.79	19.57	*6.20*
6-311G**	1/2	29.96	–2.31	29.96	*16.38*
6-311++G**	1/2	23.88	–6.46	23.88	*17.28*
Fe(III)-PO-H_2O					
6-31G*	1/2	–57.14	–58.18	1.04	*–4.48*
6-31G**	1/2	–56.60	–57.86	1.27	*–5.97*
6-31++G**	1/2	–31.93	–56.62	24.70	*20.64*
6-311G**	1/2	–56.19	–56.12	–0.07	*–4.72*
6-311++G**	1/2	–24.87	–56.04	31.17	*28.07*
6-31G*	5/2	–44.83	–40.07	–4.76	*4.44*
6-31G**	5/2	–44.58	–40.26	–4.33	*3.66*
6-31++G**	5/2	–20.51	–39.25	18.74	*31.71*
6-311G**	5/2	–44.57	–38.45	–6.12	*5.30*
6-311++G**	5/2	–19.18	–38.87	19.69	*33.91*

	Spin	**Δ*G*°$_{H2O}$(aq)**	**Spin**	**p*K*$_a$**	**Spin**	**p*K*$_a$**
	Ferric		Compound I		Compound II	
6-31G*	5/2 – 1/2	4.48	1/2	–0.3	1	8.3
6-31G**	5/2 – 1/2	5.97	1/2	1.8	1	10.2
6-31++G**	5/2 – 1/2	–20.64	1/2	–0.1	1	6.5
6-311G**	5/2 – 1/2	4.72	1/2	0.0	1	8.4
6-311++G**	5/2 – 1/2	–28.07	1/2	–1.8	1	8.4

Reduction potential	PO-I / Fe(III)-PO	PO-I / PO-II	PO-I / PO-II-H	PO-II / Fe(III)-PO	PO-II-H / Fe(III)-PO
6-31G*	963	503	996	1422	929
6-31G**	1097	503	1109	1690	1085
6-31++G**	1295	708	1094	1883	1496
6-311G**	1252	713	1208	1791	1296
6-311++G**	1413	806	1305	2020	1521

Table S11.13. Comparison of the performance of different basis sets. Wavelength (nm) and molar absorption coefficient ($cm^{-1}·M^{-1}$) of the Soret band (PCM-solvated data in parentheses).

	Spin	λ / nm		ε / $cm^{-1}·M^{-1}$			Spin	λ / nm		ε / $cm^{-1}·M^{-1}$	
Fe(III)-PO						PO-I					
6-31G*	1/2	346	(352)	56663	(96192)	6-31G*	1/2	358	(364)	65564	(104469)
6-31G**	1/2	347	(352)	57327	(96743)	6-31G**	1/2	360	(364)	39756	(104475)
6-31++G**	1/2	356	(359)	58169	(108026)	6-31++G**	1/2	362	(372)	73423	(115325)
6-311G**	1/2	353	(358)	53541	(102094)	6-311G**	1/2	360	(367)	44814	(97062)
6-311++G**	1/2	356	(359)	56258	(107800)	6-311++G**	1/2	360	(372)	73720	(94066)
Fe(III)-PO						PO-I-H					
6-31G*	5/2	348	(355)	85095	(138565)	6-31G*	1/2				
6-31G**	5/2	348	(355)	87897	(138220)	6-31G**	1/2		(379)		(20392)
6-31++G**	5/2	353	(362)	98626	(150399)	6-31++G**	1/2				
6-311G**	5/2	350	(357)	85405	(139402)	6-311G**	1/2				
6-311++G**	5/2	353	(362)	100220	(153120)	6-311++G**	1/2				
Fe(III)-PO-H_2O						PO-II					
6-31G*	1/2	352	(365)	96356	(118074)	6-31G*	1	364	(375)	84524	(121402)
6-31G**	1/2	353	(365)	100587	(117531)	6-31G**	1	365	(375)	84170	(121285)
6-31++G**	1/2	359	(372)	104503	(134575)	6-31++G**	1	373	(384)	95766	(131424)
6-311G**	1/2	355	(368)	99082	(123063)	6-311G**	1	367	(377)	87836	(126844)
6-311++G**	1/2	359	(372)	102700	(133087)	6-311++G**	1	372	(384)	95259	(130948)
Fe(III)-PO-H_2O						PO-II-H					
6-31G*	5/2	353	(364)	88640	(146992)	6-31G*	1	385	(379)	8655	(62235)
6-31G**	5/2	353	(365)	90623	(146712)	6-31G**	1	383	(380)	9859	(63739)
6-31++G**	5/2	357	(372)	102062	(153750)	6-31++G**	1	392	(386)	10033	(75422)
6-311G**	5/2	354	(367)	100136	(154825)	6-311G**	1	376	(382)	16869	(67046)
6-311++G**	5/2	356	(371)	104015	(152994)	6-311++G**	1	360	(368)	70420	(103719)

Supplementary information 12

Protonation site of ferrous peroxidases

Table S12.1. Thermodynamic parameters, Δ*H*°, TΔ*S*°, and Δ*G*°, in kJ·mol^{-1} for the optimized structures of all protonated ferrous isomers under study obtained with model I and calculated with UB3LYP/6-31G*. Values of Δ*G*° obtained with PCM continuum model in italics. Values of the most stable spin of each protonation site (with regard to Gibbs free energy) in bold, and the most stable isomer was taken as reference. Absolute thermodynamic values used as reference are collected in Table S12.3.

Protonation site	Spin 0				Spin 1				Spin 2			
	Δ*H*°	**TΔ*S*°**	**Δ*G*°**		**Δ*H*°**	**TΔ*S*°**	**Δ*G*°**		**Δ*H*°**	**TΔ*S*°**	**Δ*G*°**	
N_{21} (distal)	78.44	–15.93	94.36	*69.05*	41.83	–6.83	48.65	*45.39*	0.00	0.00	0.00	*0.00*
N_{21} (proximal)	84.50	–17.07	101.57	*86.30*	38.60	–8.48	47.08	*50.26*	21.80	–5.18	26.98	*29.24*
Fe	122.79	–13.24	136.03	*141.26*	91.36	–7.30	98.66	*106.57*	422.12	–3.95	426.06	*443.97*
C_1 (distal)	119.96	–18.74	138.69	*131.24*	69.16	–10.27	79.42	*79.59*	87.63	–8.35	95.98	*99.07*
C_1 (proximal)	111.63	–17.38	129.01	*122.44*	60.76	–8.75	69.52	*72.74*	86.02	–6.29	92.31	*95.07*
C_2	56.32	–17.07	73.39	*70.12*	78.76	–12.44	91.20	*88.07*	136.80	–2.86	139.66	*143.81*
C_5	62.69	–13.76	76.45	*70.59*	10.00	–7.88	17.87	*27.75*	3.60	2.87	0.72	*14.45*

Table S12.2. Thermodynamic parameters, Δ*H*°, TΔ*S*°, and Δ*G*°, in kJ·mol^{-1} for the optimized structures of all protonated ferrous isomers under study obtained with model II and calculated with UB3LYP/6-31G*. Values of Δ*G*° obtained with PCM continuum model in italics. Values of the most stable spin of each protonation site (with regard to Gibbs free energy) in bold, and the most stable isomer was taken as reference. Absolute thermodynamic values used as reference are collected in Table S12.3.

Protonation site	Spin 0				Spin 1				Spin 2			
	Δ*H*°	**TΔ*S*°**	**Δ*G*°**		**Δ*H*°**	**TΔ*S*°**	**Δ*G*°**		**Δ*H*°**	**TΔ*S*°**	**Δ*G*°**	
$C_{3\beta}$	46.29	–13.83	60.12	*52.76*	42.95	–6.14	49.10	*38.05*	0.00	0.00	0.00	*0.00*
N_{21}	110.09	–11.90	121.99	*90.23*	73.50	–2.18	75.68	*56.02*	32.40	2.27	30.12	*23.43*

Table S12.3. Thermodynamic parameters, Δ*H*°, TΔ*S*°, and Δ*G*°, in kJ·mol^{-1} for several species at ground spin state, obtained with models I and II and calculated with UB3LYP/6-31G*. Values of Δ*G*° obtained with PCM continuum model in italics. Absolute values used as reference for data in other tables.

Species	Model	Spin	**Δ*H*°**	**TΔ*S*°**	**Δ*G*°**	
Fe(II)-PO	I	2	–6505811.68	206.17	–6506017.85	*–6506017.76*
	II	2	–6708934.56	222.20	–6709156.75	*–6709147.84*
Fe(II)-PO-H_{N21}	I	2	–6506817.60	209.84	–6507027.44	*–6507157.18*
Fe(II)-PO-$H_{C3\beta}$	II	2	–6709976.27	222.25	–6710198.52	*–6710308.27*

Supplementary information 13

Modulation of the redox potential of peroxidases by simple geometrical manipulation

Table S13.1. Relative Gibbs free energy in kJ·mol^{-1} obtained for Fe(II)-PO and PO-I at different $-y_{C4Im}$ values in Å. Imidazole rotation is unrestricted, approximate angle (°) resulted upon geometry optimization is also displayed. Species with shortest y_{C4Im} distance were taken as reference. Absolute values for the oxidation intermediates used as reference are also collected.

Fe(II)-PO			PO-I		
$-y_{C4Im}$	$\Delta G°$	Angle	$-y_{C4Im}$	$\Delta G°$	Angle
4.90	0.00	95	4.20	0.00	45
5.00	–0.74	95	4.23	5.25	45
5.10	5.11	95	4.30	0.40	45
5.12	5.93	95	4.33	0.95	45
5.20	6.89	95	4.40	1.96	45
5.22	7.42	95	4.43	2.74	45
5.30	8.36	95	4.50	4.03	45
5.32	9.98	95	4.53	4.49	45
5.40	11.61	95	4.60	6.21	45
5.42	12.16	95	4.63	6.50	45
5.50	11.02	95	4.70	9.40	25
5.52	13.18	95	4.73	9.66	25
5.60	14.96	95	4.80	9.85	–45
5.62	15.74	95	4.83	10.76	–45
5.72	19.45	95	4.90	–23.94	–45
5.82	20.14	95	4.93	15.65	–45
5.92	24.46	170	5.00	–19.53	–45
6.02	37.83	90	5.03	19.78	–45
6.12	37.21	85	5.10	–14.50	–45
			5.13	–12.86	–45
			5.20	–9.07	–45
			5.23	–7.07	–45
			5.30	–2.62	–45
			5.40	3.95	–45

	Reference Values			
$\Delta G°$	Fe(III)-PO	Fe(II)-PO	PO-I	PO-II-H
	–6505640.94	–6507163.69	–6702908.48	–6704601.60

Table S13.2. Relative Gibbs free energy in kJ·mol^{-1} and Fe–N_τ distance in Å obtained for Fe(II)-PO, PO-I, and PO-II-H at different $-y_{C4Im}$ values in Å. Data calculated with either protonated or unprotonated proximal imidazole, situated at –72° or 45° orientation. Species with shortest $-y_{C4Im}$ distance and 45° were taken as reference. Absolute values for the oxidation intermediates used as reference are also collected.

Fe(II)-PO	**Protonated**				**Unprotonated**			
	–72°		**45°**		**–72°**		**45°**	
$-y_{C4Im}$	**ΔG°**	**Fe–N_τ**	**ΔG°**	**Fe–N_τ**	**ΔG°**	**Fe–N_τ**	**ΔG°**	**Fe–N_τ**
4.40	4.95	2.096	0.00	2.089	–0.47	1.977	0.00	1.973
4.45	4.54	2.096	–2.49	2.089	–0.82	1.977	7.61	1.973
4.50	7.44	2.096	3.61	2.090	2.51	1.977	–7.74	1.973
4.55	3.94	2.096	2.87	2.090	–2.13	1.978	–8.29	1.973
4.60	8.26	2.096	2.25	2.090	–2.57	1.978	–8.32	1.973
4.65	2.51	2.096	1.51	2.091	–3.02	1.979	–8.47	1.973
4.70	3.00	2.097	1.26	2.091	–2.92	1.979	–8.61	1.974
4.75	2.89	2.098	–5.59	2.093	–3.17	1.980	–8.81	1.975
4.80	–7.61	2.099	–5.96	2.094	–0.20	1.981	–9.27	1.976
4.85	–8.02	2.100	–6.42	2.095	–3.73	1.981	–8.79	1.977
4.90	2.03	2.102	–6.68	2.096	–3.83	1.982	–9.47	1.978
4.95	4.64	2.103	–7.92	2.097	–3.55	1.983	–9.46	1.979
5.00	2.24	2.105	–7.90	2.099	–3.00	1.984	–9.40	1.980
5.05	2.98	2.107	–6.94	2.101	–3.06	1.985	–8.18	1.982
5.10	3.53	2.109	–5.44	2.099	–2.50	1.986	–8.00	1.983
5.15	4.04	2.112	–5.83	2.101	–1.73	1.987	–7.80	1.985
5.20	5.20	2.114	–4.05	2.104	–0.73	1.988	–6.62	1.986
5.25	–2.19	2.117	–2.43	2.107	–0.31	1.990	–7.47	1.988
5.30	–0.19	2.120	–2.20	2.110	0.68	1.991	–6.65	1.989
5.35	1.31	2.124	4.09	2.113	1.66	1.992	–5.56	1.991
5.40	2.99	2.127	2.00	2.116	2.70	1.994	–4.79	1.993

	Reference Values			
ΔG°	**Fe(III)-PO**	**Fe(II)-PO**	**PO-I**	**PO-II-H**
Prot.	–6505639.27	–6507161.55	–6702908.63	–6704603.64
Unprot.	–6504417.14	–6505917.23	–6701672.73	–6703380.80

Table S13.2. Cont.

PO-I	Protonated				Unprotonated			
	–72°		45°		–72°		45°	
$-y_{C4Im}$	$\Delta G°$	$Fe–N_\tau$	$\Delta G°$	$Fe–N_\tau$	$\Delta G°$	$Fe–N_\tau$	$\Delta G°$	$Fe–N_\tau$
4.00	–30.24	2.154	0.00	2.135	8.44	2.155	0.00	2.129
4.05	–31.32	2.155	–2.29	2.134	–29.62	2.156	–36.50	2.139
4.10	–31.53	2.156	–1.34	2.137	8.70	2.152	–36.23	2.144
4.15	–32.10	2.158	–37.36	2.144	7.96	2.166	–35.03	2.150
4.20	–31.98	2.160	–37.13	2.149	7.93	2.163	–36.21	2.155
4.25	–30.65	2.163	–34.97	2.153	–30.20	2.180	–35.71	2.162
4.30	–30.38	2.167	–35.54	2.158	–30.38	2.185	–30.55	2.168
4.35	–31.22	2.171	–35.13	2.162	–30.25	2.191	–35.59	2.175
4.40	–30.59	2.175	–35.11	2.168	–29.96	2.197	–35.05	2.182
4.45	–29.76	2.180	–34.20	2.173	–29.33	2.204	–34.48	2.190
4.50	–29.02	2.185	–33.15	2.178	–28.99	2.212	–34.12	2.199
4.55	–28.04	2.190	–31.95	2.184	–28.47	2.220	–33.13	2.208
4.60	–26.94	2.196	–30.38	2.191	–27.79	2.230	–32.28	2.218
4.65	–25.77	2.201	–29.41	2.197	–26.84	2.240	–30.82	2.229
4.70	–24.35	2.207	–27.69	2.204	–25.62	2.251	–29.77	2.241
4.75	15.40	2.210	–25.49	2.212	–24.60	2.264	–28.98	2.254
4.80	–20.51	2.220	–23.79	2.219	–23.27	2.278	–27.32	2.269
4.85	–19.49	2.227	–21.50	2.228	–21.75	2.293	–25.73	2.286
4.90	–17.39	2.235	–19.57	2.237	–20.92	2.311	13.94	2.296
4.95	22.52	2.240	–17.05	2.247	19.49	2.323	–22.55	2.330
5.00	–12.99	2.252	–14.70	2.257	21.27	2.346	–21.98	2.359
PO-II-H	**Protonated**				**Unprotonated**			
	–72°		**45°**		**–72°**		**45°**	
$-y_{C4Im}$	$\Delta G°$	$Fe–N_\tau$	$\Delta G°$	$Fe–N_\tau$	$\Delta G°$	$Fe–N_\tau$	$\Delta G°$	$Fe–N_\tau$
3.90	7.70	2.059	0.00	2.050	9.57	1.927	0.00	1.919
3.95	10.86	2.061	–2.87	2.052	9.23	1.928	–1.26	1.920
4.00	5.92	2.062	0.61	2.055	8.21	1.929	–2.57	1.922
4.05	3.74	2.065	–6.62	2.065	7.41	1.931	–1.59	1.923
4.10	8.37	2.067	1.78	2.061	7.72	1.932	0.99	1.925
4.15	3.80	2.070	–2.45	2.064	7.78	1.934	2.04	1.927
4.20	3.17	2.073	–1.28	2.068	7.82	1.936	1.54	1.929
4.25	5.11	2.077	–1.31	2.072	7.63	1.938	3.70	1.931
4.30	4.69	2.080	–2.13	2.075	8.35	1.940	4.07	1.934
4.35	5.27	2.084	–0.73	2.080	8.98	1.942	4.93	1.936
4.40	5.72	2.088	0.12	2.084	10.47	1.944	5.69	1.938
4.45	6.72	2.092	0.79	2.087	11.33	1.947	5.97	1.941
4.50	11.69	2.097	2.87	2.091	12.43	1.949	8.24	1.943
4.55	9.76	2.101	4.04	2.096	13.36	1.951	9.03	1.946
4.60	11.60	2.106	6.57	2.102	16.17	1.954	11.51	1.949
4.65	15.55	2.111	7.93	2.107	17.28	1.957	14.95	1.952
4.70	8.76	2.117	9.30	2.113	9.41	1.960	17.19	1.955
4.75	11.51	2.123	10.92	2.119	13.49	1.963	19.86	1.958
4.80	8.90	2.129	12.58	2.126	16.82	1.966	22.54	1.961
4.85	10.57	2.136	15.50	2.133	18.84	1.969	24.03	1.964
4.90	13.85	2.143	17.57	2.141	21.88	1.972	26.79	1.968

Table S13.3. pK_a values obtained for deprotonation at N_π position.

	Fe(III)-PO		Fe(II)-PO		PO-I		PO-II-H	
$-\gamma_{C4Im}$	**–72°**	**45°**	**–72°**	**45°**	**–72°**	**45°**	**–72°**	**45°**
3.9							15.1	14.7
4.0						17.0	15.1	14.2
4.1						10.9	14.6	14.6
4.2	14.3	14.6				17.2	15.6	15.2
4.3	14.3	14.4			17.0	17.9	15.4	15.8
4.4	14.4	14.1	17.6	18.5	17.1	17.0	15.6	15.7
4.5	14.3	14.1	17.6	16.5	17.0	16.9	14.9	15.7
4.6	14.2	14.1	16.6	16.6	16.9	16.7	15.5	15.6
4.7	14.2	13.4	17.5	16.8	16.8	16.7	14.9	16.1
4.8	14.2	13.4	19.8	17.9	16.5	16.4	16.1	16.5
4.9	14.1	14.6	17.5	18.0	16.4	22.9	16.1	16.4
5.0	12.5	14.3	17.6	18.2		15.8		
5.1	14.2	14.2	17.4	18.1				
5.2	13.9	14.1	17.5	18.1				
5.3			18.7	17.7				
5.4			18.5	17.3				

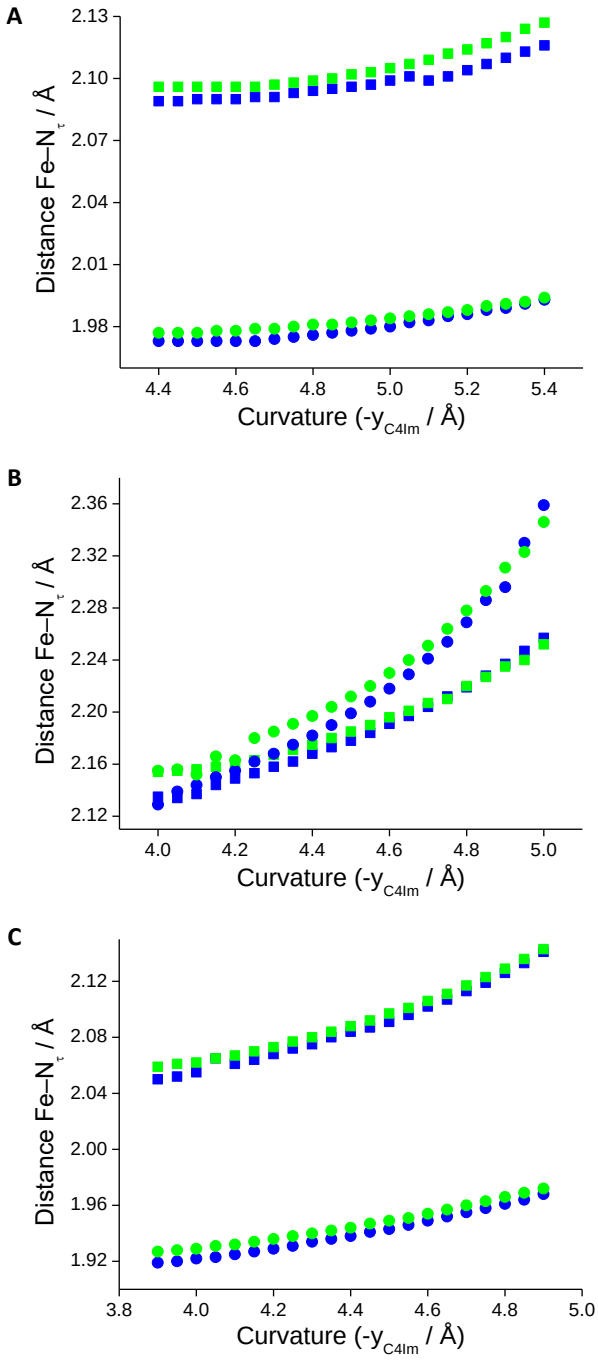

Figure S13.1. Fe–N_τ distance *vs*. heme curvature, measured as $-y_{C4Im}$ parameter, both in Å, calculated for (A) Fe(II)-PO, (B) PO-I, and (C) PO-II-H with either protonated (■) or unprotonated (●) imidazole. Values calculated at rotation angle –72° displayed in green, and with 45° in blue.

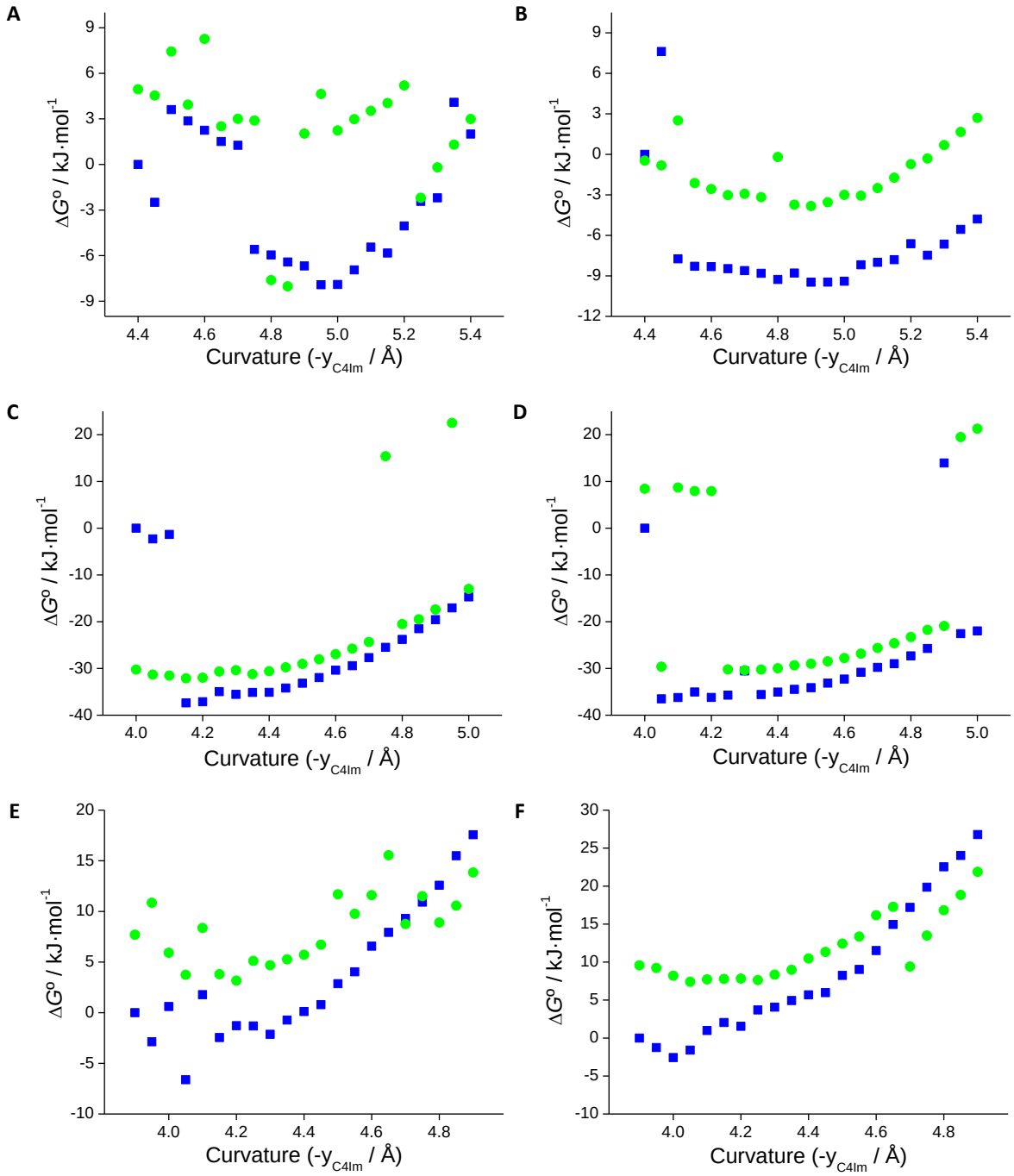

Figure S13.2. Relative Gibbs free energy *vs*. heme curvature, measured as $-y_{C4Im}$ parameter, for geometries optimized with restricted rotation angle of imidazole (● for –72° and ■ for 45°). Values calculated for Fe(II)-PO (A & B), PO-I (C & D), and PO-II-H (E & F), with protonated and unprotonated imidazole, respectively.

Supplementary information 14

Chloride ion in the myeloperoxidase-mediated chlorination reaction: substrate and inhibitor

Table S14.1. Thermodynamic parameters, $\Delta H°$, $T\Delta S°$, and $\Delta G°$, in kJ·mol^{-1} for all MPO-halide complexes under study calculated with UB3LYP/6-31G*, relative values with respect to corresponding independent peroxidase intermediate and (pseudo)halide anion. Values of $\Delta G°_{(aq)}$ obtained with PCM continuum model in italics. Absolute thermodynamic values used as reference are collected in Table S14.2.

Species	X	Spin	$\Delta H°$	$T\Delta S°$	$\Delta G°$	
Fe(III)-MPO-X_{Fe}	Cl	1/2	–414.55	–47.78	–366.77	*30.67*
		5/2	–416.30	–31.58	–384.73	*36.35*
	Br	1/2	–463.98	–46.93	–417.06	*–26.65*
		5/2	–464.00	–33.75	–430.25	*–20.59*
	CN	1/2	–521.06	–55.35	–465.71	*–91.70*
		5/2	–466.87	–40.20	–426.67	*–38.06*
Fe(III)-MPO-X_{C20}	Cl	1/2	–263.79	–40.92	–222.87	*193.02*
		5/2	–295.74	–30.64	–265.10	*147.57*
	Br	1/2	–285.13	–38.80	–246.34	*150.98*
		5/2	–304.93	–26.62	–278.32	*121.34*
	CN	1/2	–419.51	–52.26	–367.25	*27.09*
		5/2	–451.08	–41.12	–409.96	*–14.86*
Fe(II)-MPO-H-X_{Fe}	Cl	0	–328.70	–48.01	–280.69	*88.84*
		1	–387.80	–44.56	–343.24	*53.03*
		2	–389.94	–29.61	–360.32	*41.59*
	Br	0	–382.81	–48.31	–334.50	*27.59*
		1	–441.74	–44.58	–397.16	*–9.93*
		2	–438.43	–30.62	–407.82	*–14.35*
	CN	0	–445.29	–56.47	–388.82	*–40.67*
		1	–494.14	–51.48	–442.66	*–70.20*
		2	–429.22	–44.55	–384.68	*–4.89*
Fe(II)-MPO-H-X_{C20}	Cl	0	–270.32	–49.40	–220.93	*189.82*
		1	–316.96	–38.83	–278.13	*141.65*
		2	–314.39	–33.98	–280.40	*135.19*
	Br	0	–288.80	–48.34	–240.46	*157.43*
		1	–338.29	–36.67	–301.63	*107.15*
		2	–331.00	–31.01	–300.00	*102.38*
	CN	0	–427.81	–59.89	–367.92	*20.61*
		1	–476.81	–48.07	–428.74	*–28.41*
		2	–475.29	–43.07	–432.23	*–37.17*
MPO-I-X_O	Cl	1/2	–406.86	–36.94	–369.92	*65.22*
		5/2	–379.65	–17.79	–361.86	*86.92*
	Br	1/2	–461.04	–36.75	–424.29	*–4.84*
		5/2	–434.34	–19.56	–414.79	*17.50*
	CN	1/2	–746.34	–47.08	–699.26	*–310.82*
		5/2	–732.50	–30.21	–702.29	*–300.51*
MPO-I-X_{C20}	Cl	1/2	–325.20	–34.04	–291.16	*126.28*
		5/2	–322.24	–28.73	–293.52	*130.49*
	Br	1/2	–383.93	–32.67	–351.26	*46.47*
		5/2	–342.17	–27.68	–314.49	*91.65*
	CN	1/2	–491.71	–46.16	–445.56	*–55.23*
		5/2	–350.66	–40.88	–309.78	*84.43*

Table S14.1. Cont.

Species	X	Spin	Δ*H*°	*T*Δ*S*°	Δ*G*°	
MPO-II-X_O	Cl	1	95.87	–16.44	112.30	*273.64*
		2	75.91	–7.84	83.75	*252.15*
	Br	1	45.30	–15.13	60.43	*205.74*
		2	23.93	–11.65	35.58	*184.53*
	CN	1	–299.89	–26.55	–273.34	*–155.39*
		2	-	-	-	-
MPO-II-X_{C20}	Cl	1	-	-	-	-
		2	-	-	-	-
	Br	1	-	-	-	-
		2	-	-	-	-
	CN	1	–13.31	–41.72	28.41	*151.79*
		2	0.49	–27.94	28.43	*157.84*
MPO-II-H-X_O	Cl	1	–328.88	–14.16	–314.72	*89.20*
		2	–325.99	–11.98	–314.01	*110.29*
	Br	1	–381.15	–29.84	–351.31	*48.64*
		2	–355.15	–17.71	–337.44	*69.41*
	CN	1	-	-	-	-
		2	–339.48	–24.46	–315.02	*72.67*
MPO-II-H-X_{C20}	Cl	1	–352.99	–31.91	–321.08	*96.65*
		2	–328.97	–20.16	–308.81	*125.23*
	Br	1	–372.82	–30.93	–341.88	*58.95*
		2	–352.81	–19.45	–333.36	*80.98*
	CN	1	–514.30	–42.31	–472.00	*–78.03*
		2	–484.97	–30.23	–454.73	*–44.70*

Table S14.2. Thermodynamic parameters, $\Delta H°$, $T\Delta S°$, and $\Delta G°$, in kJ·mol^{-1} for starting species at ground spin state, obtained with UB3LYP/6-31G* (T = 298.15 K), and proton published values employed in the study. Values of $\Delta G°_{(aq)}$ obtained with PCM continuum model in italics. Absolute values used as reference for data in Tables 14.1, S14.1, and part of S14.6.

Species	Spin	Basis set	$\Delta H°$	$T\Delta S°$	$\Delta G°$	
H^+			6.20[a]	32.48[a]	–26.28[a]	*–1130.90*[b]
Cl^-	0	6-31G*	–1208385.93	45.64	–1208431.56	*–1208744.65*
		6-311G**	–1208513.20	45.64	–1208558.84	*–1208854.65*
		6-311++G**	–1208521.12	45.64	–1208566.76	*–1208855.88*
Br^-	0	6-31G*	–6752152.55	48.67	–6752201.21	*–6752497.40*
CN^-	0	6-31G*	–243689.31	58.70	–243748.01	*–244038.09*
Fe(III)-MPO	5/2	6-31G*	–6505301.74	203.67	–6505505.41	*–6505630.68*
		6-311G**	–6506270.77	202.32	–6506473.10	*–6506605.98*
		6-311++G**	–6506327.12	203.55	–6506530.67	*–6506662.51*
Fe(II)-MPO-H	2	6-31G*	–6709976.27	222.25	–6710198.52	*–6710308.31*
		6-311G**	–6710997.99	223.27	–6711221.25	*–6711340.87*
		6-311++G**	–6711052.67	222.13	–6711274.80	*–6711392.62*
MPO-I	1/2	6-31G*	–6702595.09	200.61	–6702795.69	*–6702938.12*
		6-311G**	–6703610.79	202.92	–6703813.71	*–6703958.18*
		6-311++G**	–6703667.36	201.96	–6703869.32	*–6704016.89*
MPO-II	1	6-31G*	–6703188.14	202.00	–6703390.14	*–6703418.72*
		6-311G**	–6704226.67	202.32	–6704428.99	*–6704458.99*
		6-311++G**	–6704292.40	202.33	–6704494.73	*–6704526.70*
MPO-II-H	1	6-31G*	–6704249.15	203.15	–6704452.30	*–6704597.19*
		6-311G**	–6705285.96	204.56	–6705490.52	*–6705637.71*
		6-311++G**	–6705347.30	205.89	–6705553.19	*–6705705.74*

[a] Ref. 32. [b] Refs. 33, 34.

Table S14.3. Mulliken atomic charges (a.u.) on relevant atoms obtained at PCM//UB3LYP/6-31G* computational level for all MPO-halide complexes under study.

Species		Spin	Fe	N_i	X
Fe(III)-MPO-X_{Fe}	Cl	1/2	1.24	–0.52	–0.52
		5/2	1.40	–0.47	–0.55
	Br	1/2	1.20	–0.51	–0.45
		5/2	1.36	–0.47	–0.48
	CN	1/2	1.21	–0.52	–0.49
		5/2	1.40	–0.47	–0.58
Fe(II)-MPO-H-X_{Fe}	Cl	0	1.17	–0.50	–0.66
		1	1.25	–0.52	–0.52
		2	1.29	–0.47	–0.62
	Br	0	1.10	–0.51	–0.58
		1	1.20	–0.52	–0.45
		2	1.24	–0.47	–0.54
	CN	0	1.09	–0.50	–0.59
		1	1.21	–0.52	–0.50
		2	1.29	–0.53	–0.49

Species		Spin	O_{Fe}	Fe	N_i	X
MPO-I-X_O	Cl	1/2	–0.62	1.42	–0.51	0.04
		5/2	–0.69	1.55	–0.48	0.10
	Br	1/2	–0.60	1.39	–0.51	0.05
		5/2	–0.67	1.53	–0.47	0.12
	CN	1/2	–0.60	1.43	–0.51	–0.07
		5/2	–0.64	1.59	–0.50	–0.08
MPO-II-X_O	Cl	1	–0.69	1.26	–0.43	–0.10
		2	–0.70	1.29	–0.41	–0.11
	Br	1	–0.67	1.24	–0.43	–0.10
		2	–0.69	1.29	–0.42	–0.12
	CN	1	–0.62	1.25	–0.44	–0.22
		2	-	-	-	-
MPO-II-H-X_O	Cl	1	–0.67	1.42	–0.48	–0.59
		2	–0.70	1.55	–0.49	–0.47
	Br	1	–0.69	1.42	–0.52	–0.42
		2	–0.71	1.39	–0.47	–0.41
	CN	1	-	-	-	-
		2	–0.68	1.37	–0.48	–0.45

Table S14.3. Cont.

Species		Spin	C_{20}	Fe	X
Fe(III)-MPO-X_{C20}	Cl	1/2	–0.40	1.22	–0.26
		5/2	–0.38	1.39	–0.30
	Br	1/2	–0.32	1.21	–0.37
		5/2	–0.32	1.23	–0.36
	CN	1/2	–0.36	1.22	–0.15
		5/2	–0.35	1.35	–0.15
Fe(II)-MPO-H-X_{C20}	Cl	0	–0.40	1.19	–0.24
		1	–0.41	1.27	–0.24
		2	–0.39	1.32	–0.22
	Br	0	–0.32	1.17	–0.31
		1	–0.33	1.24	–0.29
		2	–0.31	1.31	–0.29
	CN	0	–0.36	1.19	–0.14
		1	–0.36	1.24	–0.14
		2	–0.35	1.31	–0.14
MPO-I-X_{C20}	Cl	1/2	–0.40	1.33	–0.21
		5/2	–0.40	1.44	–0.20
	Br	1/2	–0.33	1.33	–0.30
		5/2	–0.33	1.43	–0.28
	CN	1/2	–0.36	1.35	–0.12
		5/2	–0.35	1.34	–0.13
MPO-II-X_{C20}	Cl	1	-	-	-
		2	-	-	-
	Br	1	-	-	-
		2	-	-	-
	CN	1	–0.36	1.27	–0.16
		2	–0.37	1.20	–0.15
MPO-II-H-X_{C20}	Cl	1	–0.40	1.34	–0.20
		2	–0.42	1.34	–0.22
	Br	1	–0.32	1.33	–0.28
		2	–0.34	1.33	–0.32
	CN	1	–0.35	1.34	–0.13
		2	–0.37	1.34	–0.13

Species	O	X
HClO	–0.63	0.13
HBrO	–0.62	0.13
HCNO	–0.57	0.03

Table S14.4. Comparison of the performance of different basis sets with UB3LYP. Relevant distances in Å obtained for significant MPO-chloride complexes under study. Corresponding bond orders are shown in parentheses.

	Spin	Fe–Cl	Fe–N_i	
Fe(III)-MPO-Cl_{Fe}				
6-31G*	1/2	2.253 (0.83)	2.038 (0.37)	
6-311G**		2.253 (0.58)	2.048 (0.27)	
6-311++G**		2.248 (0.93)	2.066 (0.50)	
6-31G*	5/2	2.277 (0.66)	2.515 (0.15)	
6-311G**		2.293 (0.37)	2.409 (0.07)	
6-311++G**		2.274 (0.79)	2.538 (0.21)	
Fe(II)-MPO-H-Cl_{Fe}				
6-31G*	2	2.341 (0.58)	2.490 (0.15)	
6-311G**		2.355 (0.32)	2.424 (0.07)	
6-311++G**		2.412 (0.61)	2.490 (0.22)	
	Spin	**C_{20}–Cl**		
Fe(III)-MPO-Cl_{C20}				
6-31G*	1/2	1.973 (0.78)		
6-311G**		1.985 (0.77)		
6-311++G**		1.964 (0.79)		
6-31G*	5/2	1.987 (0.77)		
6-311G**		1.990 (0.76)		
6-311++G**		1.962 (0.80)		
	Spin	**O_{Fe}–Cl**	**Fe–O_{Fe}**	**Fe–N_i**
MPO-I-Cl_O				
6-31G*	1/2	1.736 (0.94)	1.794 (0.78)	2.074 (0.33)
6-311G**		1.736 (0.95)	1.798 (0.64)	2.084 (0.24)
6-311++G**		1.725 (0.97)	1.811 (0.82)	2.090 (0.48)
MPO-II-Cl_O				
6-31G*	2	1.768 (0.91)	1.905 (0.57)	2.847 (0.09)
6-311G**		1.766 (0.93)	1.927 (0.29)	2.583 (0.04)
6-311++G**		1.751 (0.96)	1.958 (0.47)	2.825 (0.12)
MPO-II-H-Cl_O				
6-31G*	1	2.362 (0.24)	1.891 (0.52)	2.465 (0.15)
6-311G**		2.383 (0.21)	1.834 (0.53)	2.063 (0.26)
6-311++G**		2.385 (0.04)	1.845 (0.72)	2.073 (0.49)

Table S14.5. Comparison of the performance of different basis sets with PCM//UB3LYP. Mulliken atomic charges (a.u.) obtained on relevant atoms for significant MPO-chloride complexes under study

	Spin	**Fe**	**N_i**	**Cl**	
Fe(III)-MPO-Cl_{Fe}					
6-31G*	1/2	1.24	–0.52	–0.52	
6-311G**		1.37	–0.48	–0.63	
6-311++G**		4.02	–0.15	–1.50	
6-31G*	5/2	1.40	–0.47	–0.55	
6-311G**		1.69	–0.45	–0.68	
6-311++G**		3.96	–0.48	–0.86	
Fe(II)-MPO-H-Cl_{Fe}					
6-31G*	2	1.29	–0.47	–0.62	
6-311G**		1.52	–0.45	–0.75	
6-311++G**		3.53	–0.33	–1.43	
	Spin	**C_{20}**	**Fe**	**Cl**	
Fe(III)-MPO-Cl_{C20}					
6-31G*	1/2	–0.40	1.22	–0.26	
6-311G**		–0.37	1.36	–0.27	
6-311++G**		–0.32	–1.45	–0.47	
6-31G*	5/2	–0.38	1.39	–0.30	
6-311G**		–0.36	1.63	–0.29	
6-311++G**		–0.04	–1.69	–0.53	
	Spin	**O_{Fe}**	**Fe**	**N_i**	**Cl**
MPO-I-Cl_O					
6-31G*	1/2	–0.62	1.42	–0.51	0.04
6-311G**		–0.58	1.41	–0.46	0.00
6-311++G**		–0.26	–1.82	–0.05	0.00
MPO-II-Cl_O					
6-31G*	2	–0.70	1.29	–0.41	–0.11
6-311G**		–0.74	1.60	–0.39	–0.16
6-311++G**		–0.43	–0.60	–0.34	–0.23
MPO-II-H-Cl_O					
6-31G*	1	–0.67	1.42	–0.48	–0.59
6-311G**		–0.49	1.45	–0.47	–0.59
6-311++G**		–0.37	–1.48	–0.17	–0.63

Table S14.6. Comparison of the performance of different basis sets with UB3LYP. Thermodynamic parameters, Δ*H*°, *T*Δ*S*°, and Δ*G*°, in kJ·mol^{-1} for significant MPO-chloride complexes under study, relative values with respect to corresponding independent peroxidase intermediate and chloride anion. Values of Δ*G*°$_{(aq)}$ obtained with PCM continuum model in italics. Absolute thermodynamic values used as reference are collected in Table S14.2.

	Spin	**Δ*H*°**	***T*Δ*S*°**	**Δ*G*°**	
Fe(III)-MPO-Cl_{Fe}					
6-31G*	1/2	–414.55	–47.78	–366.77	*30.67*
6-311G**		–388.30	–45.90	–342.40	*39.52*
6-311++G**		–393.44	–46.87	–346.56	*33.64*
6-31G*	5/2	–416.30	–31.58	–384.73	*36.35*
6-311G**		–382.58	–33.45	–349.13	*50.99*
6-311++G**		–393.88	–32.18	–361.70	*42.89*
Fe(III)-MPO-Cl_{C20}					
6-31G*	1/2	–263.79	–40.92	–222.87	*193.02*
6-311G**		–247.59	–39.61	–207.98	*193.05*
6-311++G**		–254.46	–40.63	–213.83	*182.32*
6-31G*	5/2	–295.74	–30.64	–265.10	*147.57*
6-311G**		–274.05	–29.38	–244.68	*156.11*
6-311++G**		–281.78	–29.85	–251.93	*150.41*
Fe(II)-MPO-H-Cl_{Fe}					
6-31G*	2	–389.94	–29.61	–360.32	*41.59*
6-311G**		–356.95	–33.31	–323.64	*60.66*
6-311++G**		–303.68	–29.32	–274.36	*97.51*
MPO-I-Cl_O					
6-31G*	1/2	–406.86	–36.94	–369.92	*65.22*
6-311G**		–382.34	–38.80	–343.53	*71.27*
6-311++G**		–390.92	–36.83	–354.09	*58.08*
MPO-II-Cl_O					
6-31G*	2	75.91	–7.84	83.75	*252.15*
6-311G**		97.91	–16.69	114.60	*257.36*
6-311++G**		66.66	–10.74	77.40	*221.37*
MPO-II-H-Cl_O					
6-31G*	1	–328.88	–14.16	–314.72	*89.20*
6-311G**		–321.69	–30.27	–291.42	*92.26*
6-311++G**		–317.32	–30.89	–286.43	99.88